Elliptical Galaxies: Structure, Stellar Content, and Evolution

Thesis by

Michael Andrew Pahre

In Partial Fulfillment of the Requirements

for the Degree of

Doctor of Philosophy

California Institute of Technology

Pasadena, California

1998

(Submitted February 3, 1998)

Abstract

A near–infrared imaging survey of 341 nearby early–type galaxies, combined with optical imaging and spectroscopic data from the literature, are used to construct the global scaling relations for this population of galaxies. These data demonstrate a number of important features of the early–type galaxy sequence: (1) the slope of the Fundamental Plane (FP) correlations systematically increases with wavelength; (2) the slope of these FP correlations deviates from the virial expectation at all wavelengths, implying a breakdown of either or both of the assumptions of constant mass–to–light ratio and homology; (3) the intrinsic scatter of the FP correlations is small but resolved at all wavelengths, implying a small cosmic scatter of early–type galaxy properties at any position in the galaxy sequence and contradicting any model in which various stellar populations parameters "conspire" with each other to keep the correlations thin at optical wavelengths; (4) there is no correlation among residuals of the metallicity–independent near–infrared FP and the metallicity–sensitive Mg_2–σ_0 relation, implying that both age and metallicity variations contribute to the cosmic scatter of both correlations; and (5) the effective radii systematically decrease with increasing wavelength, fully consistent with the general presence of stellar populations gradients in early–type galaxies. A comprehensive and self–consistent model is described which simultaneously explains these and other global properties of the early–type galaxy sequence. This model demonstrates that age, metallicity, deviations from a dynamically homologous family, and populations gradients are all contributing to the form of the global scaling relations; the latter two effects are the least constrained by the observations and model, respectively.

Additional constraints on the role of age in the global scaling relations is obtained by observing early–type galaxies at higher redshifts. This has been studied using three approaches: color evolution, evolution of the slope and intercept of the K–band FP correlations, and evolution of the absorption line strengths. The galaxies in each cluster are identified in a systematic way using two color (three bandpass) imaging—sampling approximately the U, V, and I bandpasses in the rest frame—to eliminate late–type cluster member and general field interloper galaxies. This method is $> 90\%$ effective in identifying

early–type galaxies at the target cluster redshift.

Weak color evolution in rest–frame $(U-V)_0$ has been detected in 26 rich clusters of galaxies. The bluing trend in color is 0.05 ± 0.03 mag at $z = 0.2$, 0.12 ± 0.04 mag at $z = 0.4$, and $\sim 0.23 \pm 0.05$ mag at $z = 0.54$. Using stellar population synthesis models from the literature, this color evolution is fully consistent with the galaxy population as a whole having formed at $1 < z_f < 5$.

The FP correlations are studied for 128 galaxies in eight rich clusters at $0.1 < z < 0.6$ using moderate dispersion spectroscopy (110 of the measurements are new) and imaging in the near–infrared K–band. These data more than quadruple the data in the literature which can be used to study the FP at high redshift. The near–infrared FP is constructed at high redshifts for the first time. The intercept of the FP on the surface brightness axis is observed to dim with redshift, as expected for the Tolman signal in an expanding world model. A small amount of luminosity evolution $\Delta K \approx -2.5 \log(1+z)$ mag is detected on top of the Tolman signal, which is consistent with the passive evolution of a stellar population that formed at high redshift. The slope of the near–infrared FP is observed to flatten with redshift, implying that the least luminous galaxies are evolving faster than the luminous galaxies. This is strong evidence that low luminosity ellipticals have a stellar content that is up to a factor of two times younger than high luminosity ellipticals, but age spreads much larger than this appear to be excluded, and age spreads somewhat smaller than this are still allowed depending on the choice of nearby galaxy sample used in the comparison.

The absorption line strengths of the galaxies are observed to evolve slowly with redshift: the Mg_2 and $\langle \mathrm{Fe} \rangle$ indices weaken while the $\mathrm{H}\beta_G$ index strengthens. The latter effect in particular is another strong indication that the mean age of the stellar populations in early–type galaxies formed at redshifts $3 < z_f < 5$. All of these properties are moderately consistent with the models derived above based on the samples of nearby galaxies, implying that age is an important physical parameter underlying the global scaling relations for early–type galaxies.

Acknowledgments

For a thesis like this one, in which a large quantity of data is collected from many sources, it is difficult to fully acknowledge every person who has made a significant contribution along the way towards this final product. Professor George Djorgovski provided timely advice, wonderful encouragement, marvelous amounts of money for traveling to meetings and observing runs, tall back scratcher drinks on the coast of Hawaii, large quantities of powdered drugs from Colombia (the dark brown variety), observing time galore, and many a not–so–gentle shove to finish some of the many projects we started. Above all, he showed patience in allowing me to run amok designing the various surveys reported here. Many thanks also go to that special woman for her moderating influence.

I have spent many a night, cloudy and clear, shooting the breeze and sharing a mug of java with the night assistants of the Palomar and Las Campanas Observatories and the Observing Assistants of the Keck Observatories. The efficient professionalism of the staffs of these observatories has made the collection of all those ExaByte tapes proceed smoothly and resulted in beautiful data. The cooks of Palomar and Las Campanas Observatories are thanked for making even a cloudy run pleasurable. The directors of these observatories, and the Time Allocation Committees, have my highest gratitude for granting large blocks of observing time to pursue this thesis project. I pray that in the end they will find the product well worth the considerable investment.

The year spent among the Santa Barbarians of Carnegie building a near–infrared camera was memorable due to their collective enthusiasm and remarkable scientific insights. I now hold an even greater respect for the wide–ranging abilities possessed by the instrumentation teams at OCIW, and wish them great luck on their Magellanic expedition. It was a joy learning first–hand from Drs. Eric Persson, David Murphy, and Anand Sivaramakrishnan the right way to build an instrument.

Professor Jeremy Mould deserves special appreciation for getting me started in infrared observing and surface brightness fluctuations, and for his super–human patience and persistence in our continued collaborations. Many of the things I know about elliptical galaxies stem directly from the untold numbers of conversations I have had over the years with Dr.

Reinaldo de Carvalho. I have also learned a great deal through collaborations, or extensive discussions, with many other members of the Caltech astronomy community: Professors Roger Blandford, Judy Cohen, Shri Kulkarni, Keith Matthews, Mark Metzger, Gerry Neugebauer, Tom Soifer, and Chuck Steidel; post–doctoral researchers John Blakeslee, Chris Clemens, Laura Ferrarese, and Ian Smail; and graduate students Chris Fassnacht, John Gizis, David Hogg, and James Larkin. Laura Ferrarese also read an early version of several chapters of this thesis and provided insightful comments. Many office mates have shown patience with the ever–expanding masses of papers, folders, and tapes which occupy the surfaces of my desks. Martin Shepherd has proved to be a highly valuable source for all sorts of "nawk–ing." Finally, my thesis committee—George Djorgovski (chair), Roger Blandford, Andrew Lange, Eric Persson, Steve Shectman, and Chuck Steidel—have shown great encouragement and offered excellent advice, comments, and six unique perspectives on this ambitious project.

My family has shown great support and encouragement not only while I have spun deeper and faster into this black hole, but also all along my various routes which eventually led to Caltech. And Suzanne, the most complicated and fascinating person I have ever had the pleasure to know, to you I owe gratitude for your patience with my crazy work and travel habits, your unbridled enthusiasm for science and me, your excellent proofreading ability, and your constant love and affection. Ah yes, and many thanks to the support from Mieza Ekyii, Nyame Bekyereh, and Kofi Mieza.

Contents

Abstract **iii**

Acknowledgments **v**

1 Introduction **1**

1.1 The Standard Paradigm for Elliptical Galaxies 1

1.2 The Fundamental Plane Correlations 2

1.3 Outline of Thesis 4

References 5

2 Near–Infrared Photometry of Early–Type Galaxies in the Local Universe: Global Photometric Parameters **7**

2.1 Introduction 8

2.2 Description of the Near–Infrared Imaging Survey 11

2.3 Observations and Data Reduction 17

2.3.1 Palomar 60–inch Telescope Data 17

2.3.2 Las Campanas 1.0 m Swope Telescope Data 18

2.3.3 Las Campanas 2.5 m du Pont Telescope Data 19

2.3.4 Data Reduction 19

2.3.5 Photometric Calibration 20

2.4 Surface Photometry 23

2.5 Seeing Corrections 25

2.6 Measurement of Global Photometric Parameters 32

2.7 Estimation of Internal Uncertainties 34

2.7.1 Aperture Magnitudes 35

2.7.2 Surface Photometry 35

2.7.3 Global Photometric Parameters 35

2.8 Estimation of External Uncertainties 39

2.8.1 Aperture Magnitudes 40
2.8.2 Surface Photometry 42
2.9 Additional Global Properties Drawn from the Literature 48
2.9.1 Photometric Parameters 48
2.9.2 Spectroscopic Parameters 52
2.9.3 Catalogs of Global Photometric and Spectroscopic Parameters for Various Optical Bandpasses 53
2.10 Discussion 55
References 56

3 The Near–Infrared Fundamental Plane of Early–Type Galaxies 59
3.1 Introduction 60
3.2 Description of the Data 62
3.3 Analysis of the Elliptical Galaxy Correlations 64
3.3.1 The Near–Infrared Fundamental Plane 64
3.3.2 The D_K–σ_0 Relation 70
3.3.3 The FP As Seen in κ–Space 72
3.3.4 The Mg_2–σ_0 Relation 75
3.3.5 The Mg_2 Near–Infrared Fundamental Plane 75
3.3.6 The Faber–Jackson Relation 85
3.3.7 The Modified Faber–Jackson Form of the FP 85
3.3.8 The Kormendy Relation 87
3.3.9 The Radius–Luminosity Relation 89
3.4 Exploring Simple Models for the Origins of the Elliptical Galaxy Scaling Relations in the Near–Infrared 89
3.5 Discussion 93
References 95

4 The Physical Origins of the Fundamental Plane Scaling Relations for Early–Type Galaxies 99
4.1 Introduction 100
4.2 Description of the Data 102
4.3 Comparing Optical and Near–Infrared Effective Radii 102

4.4 The Difference in Slope Between the Optical and Near–Infrared FP 105
4.4.1 The Traditional Method to Measure the Change in Slope of the FP 105
4.4.2 The New, Distance–Independent Method to Measure the Change in Slope of the FP 105
4.4.3 Possible Environmental Effects on the FP 111
4.5 Comparing the Fundamental Plane Among Various Optical Bandpasses . . 113
4.6 General Constraints from the Elliptical Galaxy Scaling Relations 115
4.7 A Self–Consistent Model for the Underlying Physical Parameters Which Produce the FP Correlations 119
4.7.1 Modeling the Changes in the Slope of the FP Between Bandpasses . 120
4.7.2 Additional Equations of Constraint 121
4.7.3 Solutions to the Physical Quantities in the Model for the Scaling Relations 124
4.7.4 The Relative Roles of Various Constraints on the Model Solution . 127
4.8 Discussion 129
4.9 Summary 136
References 137

5 Color Evolution in the Early–Type Galaxy Population in 26 Rich Clusters at $0 < z < 0.6$ **141**
5.1 Introduction 142
5.2 Observations 146
5.2.1 Calibration 150
5.2.2 k–corrections 150
5.2.3 Galactic Extinction 155
5.3 Object Detection and Measurement of Colors 158
5.4 The Color–Morphology Selection Criteria to Identify Cluster Ellipticals . . 159
5.4.1 Summary of Selection Criteria Used 159
5.4.2 Abell 665 ($z = 0.182$) as a Worked Example 159
5.4.3 Comparing the Effects of Each of the Selection Criteria 161
5.4.4 The Field Galaxy Contamination as Measured from Blank Fields . 161

5.5 Comparison of Color-Morphology Selection Results with Spectroscopic Information . . . 166
5.5.1 New Spectroscopy of Galaxies from These Complete Samples 166
5.5.2 Comparison to Redshift Surveys from the Literature 172
5.5.3 The Exclusion of K+A Type Galaxies 173
5.6 Color Evolution in the Early–Type Galaxy Population in Rich Clusters of Galaxies . . . 173
5.7 Summary . . . 182
References . . . 184

6 Global Spectroscopic and Photometric Properties of Early–Type Galaxies in Eight Clusters at $0.1 < z < 0.6$ 187
6.1 Introduction . . . 187
6.2 Selection of Galaxy Sample in Each Cluster . . . 189
6.3 Spectroscopy . . . 193
6.3.1 Observations . . . 193
6.3.2 Data Reductions . . . 207
6.3.3 Stellar Template Spectra . . . 210
6.3.4 Measurement of Velocities and Velocity Dispersions . . . 217
6.3.5 Measurement of Line Indices . . . 223
6.3.6 Spectroscopic Parameters From the Literature . . . 233
6.4 Photometry . . . 235
6.4.1 K–band Imaging . . . 235
6.4.2 Measuring Global Photometric Parameters . . . 238
6.4.3 Optical Global Photometric Parameters . . . 242
6.5 Summary . . . 243
References . . . 244

7 The Evolution of the Fundamental Plane of Early–Type Galaxies for $0 < z < 0.6$ 247
7.1 Introduction . . . 248
7.2 Summary of Data . . . 250
7.3 Evolution of the Surface Brightness Intercept of the FP . . . 251

7.4 Evolution of the Slope of the FP 254
7.5 Evolution of the Line Strengths 259
7.6 Discussion 263
References 265

8 Summary: The Physical Properties Underlying the Sequence of Elliptical Galaxies 269

8.1 The Sequence of Elliptical Galaxies 269
8.2 Summary of Results in This Thesis 270
8.3 A Picture for the History of Elliptical Galaxies 273
8.3.1 Can These Results be Reconciled with the Line Index Measurements of Trager (1997)? 274
8.3.2 The Formation Epoch for Elliptical Galaxies 277
8.3.3 Hierarchical Structure Formation and Elliptical Galaxies 278
8.4 Future Work 281
References 282

A Tables of Global Photometric and Spectroscopic Parameters for Nearby Early–Type Galaxy Surveys 285

List of Figures

2.1 Distribution of K–band Survey Galaxies in Galactic Coordinates 13
2.2 Comparison of K_s and K Filters 22
2.3 Histogram of the Seeing Distribution for the Survey 25
2.4 Seeing Corrections Derived from Model Grid Galaxies 30
2.5 Comparison of Seeing Corrections with the Literature 31
2.6 The Similarity of Curves of Growth for Elliptical Galaxies 33
2.7 Internal Comparison of Surface and Aperture Photometry 36
2.8 Comparison of Global Photometric Parameters Derived from Circular Aperture Photometry 37
2.9 Comparison of Global Photometric Parameters Derived from Surface Photometry 38
2.10 Comparison of Aperture Magnitudes with the Literature 43
2.11 Comparison of Surface Photometry with Peletier (1989) 45
2.12 Comparison of Surface Photometry with Silva & Elston (1994) 46
2.13 Comparison of Surface Photometry with Ferrarese (1996) 47
2.14 Histograms of Global Colors for Early–Type Galaxies 50

3.1 The Fundamental Plane (FP) in the K–band for Each Cluster 67
3.2 The FP in the K–band in Edge–On and Face–On Perspectives 69
3.3 The D_K–σ_0 Relation 71
3.4 The K–band FP Viewed in κ–Space 73
3.5 The Mg_2–σ_0 Relation 76
3.6 The Mg_2 Form of the Near–Infrared Fundamental Plane 78
3.7 The Effects of a 10% Young, 5 Gyr Population on Top of a 90% Old Stellar Population 81
3.8 The Residuals of the Near–Infrared FP Plotted Against the Residuals of the Mg_2–σ_0 Relation 83
3.9 The Residuals from the Mg_2–σ_0 and κ_3–κ_1 Relations 84

3.10 The Faber–Jackson Relation 86
3.11 The Modified Faber–Jackson Relation Form of the FP 88
3.12 The Kormendy Relation Between Effective Radius and Mean Surface Brightness 90
3.13 The Relation Between Luminosity and Effective Radius 91

4.1 Comparison of the Effective Radii and Diameters Derived From Optical and Near–Infrared Photometry 104
4.2 Comparison of the Slope of the Optical and Near–Infrared Fundamental Plane 109
4.3 Comparison of the Slope of the Optical and Near–Infrared D_n–σ_0 Relation 110
4.4 Comparison of the D_V–σ_0 and D_K–σ_0 Relations in Different Environments and Regions 112
4.5 Comparison of the Slope of the Fundamental Plane Among Optical Bandpasses 116
4.6 Comparison of the Slope of the D_n–σ_0 Relation Among Optical Bandpasses 117
4.7 Comparison of the Slope of the FP Among Various Optical Bandpasses Using the Color Information From Prugniel & Simien (1996) 118
4.8 Comparison of M/L_V and M/L_K for Four Different Stellar Populations Models 122
4.9 Contours of χ^2/ν for the Self–Consistent Model for the FP 128
4.10 The Evolution of the FP With Redshift for the Self–Consistent Model Describing the FP 133

5.1 Comparison of k–corrections into $(U-V)_0$ Color 152
5.2 Comparison of k–corrections for Solar Metallicity Models Only 153
5.3 Comparison of Galactic Extinction Estimates 157
5.4 Identification of the Early–Type Galaxy Sequence in Abell 665 160
5.5 Selection Effects Due to the $(U-V)_0$ versus $V_{\rm tot,0}$ Color–Magnitude Relation in Abell 665 162
5.6 Selection Effects Due to the $(V-I)_0$ versus $V_{\rm tot,0}$ Color–Magnitude Relation in Abell 665 163
5.7 Selection Effects Due to the Concentration Index in Abell 665 164

5.8 Selection Effects Due to the $(U-V)_0$ versus $(V-I)_0$ in Abell 665 165
5.9 Field Galaxy Contamination Estimated from Three "Blank" Fields Observed in the $BR_{\rm C}I_{\rm C}$ Bandpasses 167
5.10 Field Galaxy Contamination in Abell 665 As Estimated from Three "Blank" Fields 168
5.11 Field Galaxy Contamination at $z = 0.12$ from Two "Blank" Fields Observed in UVI Filters 169
5.12 Field Galaxy Contamination at $z = 0.37$ from Three "Blank" Fields Observed in BRI Filters 170
5.13 Color–Magnitude Relations for Clusters Observed in $(U-V)$ at $0.062 < z < 0.125$ 175
5.14 Color–Magnitude Relations for Clusters Observed in $(U-V)$ at $0.129 < z < 0.231$ 176
5.15 Color–Magnitude Relations for Clusters Observed in $(B-R)$ at $0.171 < z < 0.231$ 177
5.16 Color–Magnitude Relations for Clusters Observed in $(B-R)$ at $0.308 < z < 0.390$ 178
5.17 Color–Magnitude Relations for Clusters Observed in $(B-R)$ at $0.402 < z < 0.460$ and in $(V-I)$ at $0.539 < z < 0.546$ 179
5.18 Color–Magnitude Relations Binned by Redshift 180
5.19 Color Evolution $(U-V)_0$ for the Individual Clusters at $0.024 < z < 0.546$. 181
5.20 Color Evolution $(U-V)_0$ for the Binned Data at $0.024 < z < 0.546$ 182

6.1 Finding Chart for Galaxies in Abell 655 194
6.2 Finding Chart for Galaxies in Abell 665 195
6.3 Finding Chart for Galaxies in Abell 2390 196
6.4 Finding Chart for Galaxies in Abell 370 197
6.5 Finding Chart for Galaxies in Abell 851 198
6.6 Finding Chart for Galaxies in MS0015.9+1609 199
6.7 Spectra of Galaxies in Abell 655 211
6.8 Spectra of Galaxies in Abell 665 212
6.9 Spectra of Galaxies in Abell 2390 213

6.10 Spectra of Galaxies in Abell 370 214
6.11 Spectra of Galaxies in Abell 851 215
6.12 Spectra of Galaxies in MS0015.9+1609 216
6.13 Fits to Several Galaxy Spectra for Abell 665 Using Stellar Template HD134190 (G7.5 III) 221
6.14 Comparison of Mg_2 and Mg_b for High Redshift Galaxies Observed 232
6.15 K–corrections for the K and K_s Filters 238
6.16 Comparison of Model Photometric Fits in K and K_s Filters for Eight Galaxies in MS0015.9+1609 242

7.1 Detection of the Tolman Surface Brightness Dimming Signal for an Expanding World Model 252
7.2 Detection of Luminosity Evolution from the Near–Infrared FP 253
7.3 Evolution of the Surface Brightness Intercept of the FP in the K–band . . . 255
7.4 The Individual Fits to the Slope of the K–band Fundamental Plane for Clusters at $0 < z < 0.6$ 257
7.5 The Evolution With Redshift of the Slope and Intercept of the K–band FP 258
7.6 The Relations Between Line Strength and Central Velocity Dispersion . . . 260
7.7 The Evolution of the Mean Line Strengths With Redshift 262

8.1 Comparison of Models From This Thesis With Ages and Metallicities from Trager (1997) 276

List of Tables

2.1 Clusters, Groups and Other Galaxies in the K–band Photometry Survey . . 14
2.2 Model Grid for Calculating Seeing Corrections 27
2.3 Internal Comparison of Global Photometric Parameters 39
2.4 Comparison of Aperture Magnitudes with the Literature 41
2.5 Literature Sources for Global Photometric Parameters 51
2.6 Literature Sources for Spectroscopic Parameters 54

3.1 Fits for Each Cluster or Group for the Near–Infrared FP 66
3.2 Variations in Magnitude and Mg_2 for an Old Population With and Without a 10% Young Population By Mass for the Worthey (1994) Models 80

4.1 Comparison of the Slope of the FP in the Optical and Near–Infrared 108
4.2 Comparison of the Slope of the FP Among Various Optical Bandpasses . . 114
4.3 Variations in Magnitude for Various Bandpasses for the Bruzual & Charlot (1996) and Vazdekis *et al.* (1996) Models 123

5.1 Summary of Observations 148
5.2 Measurements of $(U-V)_0$ by Cluster 156

6.1 Summary of All Available Data Appropriate for Studying the Evolution of the Early–Type Galaxy Scaling Relations 190
6.2 Photometric Properties for Galaxies in Abell 655 200
6.3 Photometric Properties for Galaxies in Abell 665 201
6.4 Photometric Properties for Galaxies in Abell 2390 202
6.5 Photometric Properties for Galaxies in Abell 370 203
6.6 Photometric Properties for Galaxies in Abell 851 204
6.7 Photometric Properties for Galaxies in MS0015.9+1609 205
6.8 Spectroscopic Properties for Galaxies in Abell 655 224
6.9 Spectroscopic Properties for Galaxies in Abell 665 225
6.10 Spectroscopic Properties for Galaxies in Abell 2390 225

6.11 Spectroscopic Properties for Galaxies in Abell 370 226
6.12 Spectroscopic Properties for Galaxies in Abell 851 227
6.13 Spectroscopic Properties for Galaxies in MS0015.9+1609 228
6.14 Photometric and Spectroscopic Properties for Galaxies in ZwCL0024+1652 234
6.15 Photometric and Spectroscopic Properties for Galaxies in MS2053.7-0447 . 236

7.1 Individual Fits to the K–band Fundamental Plane Slope 256
7.2 Evolution of the Line Strengths With Redshift 261

A.1 All Measurements of K–Band Global Photometric Parameters 287
A.2 Combined Catalog of Global Parameters for All Program Galaxies 296
A.3 Comparisons of K–band Quantities with B–band Quantities from Faber *et al.* (1989) 303
A.4 Comparisons of K–band Quantities with B–band Quantities from Dressler *et al.* (1991) 307
A.5 Comparisons of K–band Quantities with V–band Quantities from Lucey & Carter (1988) and Lucey *et al.* (1991a, b; 1997) 308
A.6 Comparisons of K–band Quantities with R–band Quantities from Smith *et al.* (1997) 312
A.7 Comparisons of K–band Quantities with r–band Quantities from Jørgensen *et al.* (1995a) 313
A.8 Comparisons of K–band Quantities with U–band Quantities from Jørgensen *et al.* (1996) 315
A.9 Comparisons of K–band Quantities with B–band Quantities from Jørgensen *et al.* (1996) 316
A.10 Comparisons of K–band Quantities with g–band Quantities from Jørgensen *et al.* (1996) 317
A.11 Comparisons of K–band Quantities with I–band Quantities from Scodeggio *et al.* (1997) 318
A.12 Comparisons of K–band Quantities with V–band Quantities from Bower *et al.* (1992a) 320
A.13 Comparisons of K–band Quantities with V–band Quantities from Sandage & Visvanathan (1978) and Persson *et al.* (1979) 322

A.14 Comparisons of r–band and U–band Quantities from Jørgensen *et al.* (1995a; JFK95a) 324
A.15 Comparisons of r–band and B–band Quantities from JFK95a 325
A.16 Comparisons of r–band and g–band Quantities from JFK95a 326
A.17 Comparisons of r–band Quantities from Jørgensen *et al.* (1995a) and B–band Quantities from Faber *et al.* (1989) 328
A.18 Comparisons of r–band Quantities from Jørgensen *et al.* (1995a) and V–band Quantities from Lucey & Carter (1988) and Lucey *et al.* (1991a,b; 1997) 330
A.19 Comparisons of $R_{\rm C}$–band Quantities from Smith *et al.* (1997) and V–band Quantities from Lucey & Carter (1988) and Lucey *et al.* (1991a,b; 1997) . . 332
A.20 Comparisons of $I_{\rm C}$–band Quantities from Scodeggio *et al.* (1997) and V–band Quantities from Lucey & Carter (1988) and Lucey *et al.* (1991a,b; 1997) 333
A.21 Comparisons of $I_{\rm C}$–band Quantities from Scodeggio *et al.* (1997) and r–band Quantities from Jørgensen *et al.* (1995a) 335

Chapter 1

Introduction

1.1 The Standard Paradigm for Elliptical Galaxies

The standard picture of elliptical galaxies is that they each formed early in the universe's history after a monolithic collapse and a massive burst of star formation. When the first generation of supernovae exploded, the combined output energy of their winds blew the gas out of these galaxies thus abruptly halting the formation of additional stars. The remainder of the history of these galaxies up to the present day consisted of the slow stellar evolution, as the stars began to evolve off the main sequence at progressively lower masses. In this way elliptical galaxies are said to contain "old" stellar populations, since they have not experienced star formation since early in the history of the universe. The stellar content of these galaxies is likewise referred to as "early–type," which means that the stars the galaxies contain formed at early times.[1] Elliptical galaxies take their name from their smooth, featureless, ellipsoidal morphology which stands in stark contrast to the composite of grand spiral arms, dust lanes, bars, disks, and bulges which typify the morphologies of spiral galaxies.

In this simple picture, elliptical galaxies do not contain gas (molecular or atomic, neutral or ionized) or dust that typically accompanies the formation of stars, since the interstellar medium (ISM) of these galaxies was blown out early on by the first generation of supernovae. They contain uniformly old stars that are nearly as old as the universe itself. Their shapes are perfectly smooth and regular, such that they can be viewed mathematically as a homologous family in the distribution of their light and stellar velocities. Finally, ellipti-

[1]This elementary distinction of terminology is essential to grasp from the beginning. Elliptical galaxies are also called "early–type" galaxies and contain *old* stellar populations; they are comprised of old, low mass stars which themselves are referred to as "late–type" stars. Spiral galaxies are called "late–type" galaxies and contain a number of different stellar populations; their most distinctive stellar population is "early–type," *young* stars that have been forming very recently, right up to the present day. Thus "early–type galaxies" (ellipticals) are old and contain "late–type stars," while "late–type galaxies" (spirals) also contain a younger stellar population of "early–type stars." I do not take responsibility for this confusing historical terminology.

cal galaxies are dynamically "hot," which means that they are supported by pressure (the apparently random motions of their stars) rather than by ordered rotation (as in a disk galaxy).

At first glance, the observable properties of elliptical galaxies appear to provide strong support for this picture of an extremely homogeneous population of galaxies. For example, their colors are red, their light profiles are well fit by a two parameter (de Vaucouleurs) function $I \propto I_e \exp\left[1 - (r/r_e)^{1/4}\right]$ such that they are homologous to a scaling by the half–light radius r_e, and their distribution of ellipticities appears to imply triaxiality.

Many observations made during the last decade, however, are now showing that elliptical galaxies are not so simple.[2] There appears not to be a single, unimpeachable case for triaxiality in a real elliptical galaxy. There are clear and systematic departures of the light profiles from the de Vaucouleurs shape, such that the galaxies either have $I \propto I_e \exp\left[1 - (r/r_e)^{1/n}\right]$, where n correlates with galaxy luminosity, or are a composite disk plus bulge:

$$I \propto I_b \exp\left[1 - \left(\frac{r}{r_b}\right)^{1/4}\right] + I_d \exp\left[1 - \left(\frac{r}{r_d}\right)\right]. \tag{1.1}$$

Detection of these galaxies at far infrared wavelengths by the IRAS satellite in the 1980s argues for the presence of a warm dust component to their ISM. Residuals from fits of smooth models to the two–dimensional light distributions reveal the presence of dust lanes and disks which have short dynamical times. Ionized gas is detected in the core regions of these galaxies, as are rings of neutral hydrogen gas at large radii. It is beginning to look like elliptical galaxies are not such an elegant and pure class of galaxies after all.

1.2 The Fundamental Plane Correlations

Fortunately, all of these departures of real elliptical galaxies from the ideal concept of an elliptical galaxy are small. The global properties of elliptical galaxies obey simple correlations with very small scatter. A simple (mono-variate) correlation between two variables appears not to be sufficient to fully describe the properties of elliptical galaxies; instead, the correlations with the minimal scatter require three observables. These bivariate correlations are called the Fundamental Plane correlations (FP; Dressler *et al.* 1987; Djorgovski & Davis

[2]See the proceedings volume edited by Arnaboldi, Da Costa, & Saha (1997) for discussions of many of the following points.

1987) since the properties of elliptical galaxies are found to occupy only a planar surface within the three–dimensional space of the observables. While it is truly remarkable that elliptical galaxies tightly obey the FP correlations, it is even more remarkable that they do so despite the many small variations that exist among galaxies in their profile shapes, dust and gas contents, and even galaxy environment.

The standard form of the FP is the relationship between one quantity which measures galaxy size (the half–light, or effective, radius $r_{\rm eff}$), another quantity which measures the luminosity density (mean surface brightness), and a third quantity which measures the dynamical state (the central velocity dispersion, a measure of the random motions of the stars in a galaxy). The correlation of these quantities is thus effectively a relationship between the luminosity, size, and dynamical mass of a galaxy. This thesis will use these FP correlations liberally as the optimal tool *by construction* with which to study the global properties of elliptical galaxies.

Since the FP correlations have such small scatter, they are well suited for studying in detail the way that the early–type galaxy population evolves with redshift. The global properties of ellipticals are so uniform that they probably comprise the best class of galaxy for performing some of the neoclassical cosmological tests. One such test will be addressed in this thesis: the dimming of surface brightness SB with redshift z. Tolman (1934) and Hubble & Tolman (1935) proposed that surface brightness should vary as $(1+z)^{-4}$ in an expanding universe, or as $(1+z)^{-1}$ in a non–expanding ("tired light") universe. This signal is well–detected using elliptical galaxies, as will be shown in Chapter 7; galaxy evolution is then detected as a small brightening on top of this strong SB dimming due to the expanding world model. The spectral energy distribution of the cosmic microwave background radiation (CMBR, measured recently by the COBE satellite) is by far the most significant observation that constrains the world model to be one of expansion. The complementary constraint imposed by SB dimming of the early–type galaxy population, however, requires any non–standard cosmological model to explain simultaneously both the CMBR and the SB dimming effects. Such improbable cosmologies will thus suffer from Occam's razor.

1.3 Outline of Thesis

The basic question that is addressed by this thesis is: What are the underlying physical properties that vary systematically from one elliptical galaxy to the next along the galaxy sequence? Subtle effects—such as variations in heavy element abundance, mean solar age, and so on—can be derived from the exact form of the FP correlations at various wavelengths and at different redshifts.

This thesis is neatly divided into two parts: studies of nearby early–type galaxies (Chapters 2–4) and three investigations of how this population of galaxies evolves with redshift (Chapters 5–7).

The thesis begins with a near–infrared imaging survey of 341 early–type galaxies in the $\lambda = 2.2\mu$m atmospheric window. These data comprise the first large–scale study of its kind since the single element, aperture photometry measurements of Persson, Frogel, and collaborators in the 1970s. The Fundamental Plane (FP) bivariate correlations among the properties of these galaxies will be presented in Chapter 3. The systematic variation of the slope of the FP correlations with wavelength will be described in Chapter 4 using a distance independent construction of the observables. These correlations and a number of other global properties of early–type galaxies are then drawn together in Chapter 4, and a complete and self–consistent model is developed for the first time to explain the underlying physical parameters which produce the correlations. Chapter 4 ends the first part of the thesis with predictions based on this model for how the slope of the FP correlations should evolve with redshift.

The second part of the thesis begins in Chapter 5 with the development of a method of reliably identifying this same population of early–type galaxies in distant clusters of galaxies at $0 < z < 0.6$. The method is shown to be $> 90\%$ effective in identifying galaxies that belong to this population at the target cluster redshift. The remainder of the thesis consists of using galaxy samples identified in this manner to measure the evolution of early–type galaxies.

Chapter 5 concludes with the detection of weak color evolution in rest–frame $(U - V)_0$ in the early–type galaxy population for $0 < z < 0.6$. This is followed by the description of a new study of the global properties of early–type galaxies at these redshifts in Chapter 6. The new data use moderate dispersion spectroscopy to measure central velocity dispersions

and line strengths, and near–infrared imaging to measure effective radii and mean surface brightnesses. The first near–infrared FP at high redshift is presented in Chapter 7. The galaxies are observed to evolve in three ways: the characteristic luminosity (as measured by the surface brightness intercept of the near–infrared FP) evolves slowly; the slope of the near–infrared FP relations evolves by flattening with redshift, implying a differential evolutionary rate among early–type galaxies; and the absorption line strengths in general, and Hβ in particular, evolve slowly with redshift. Models are compared with all of these evolutionary trends in Chapters 5 and 7 in order to determine if the evolution is passive.

References

Arnaboldi, M., Da Costa, G. S., & Saha, P., eds. 1997, The Nature of Elliptical Galaxies, Proceedings of the Second Stromlo Symposium, ASP Conf. Ser. Vol. 116 (San Francisco: ASP)

Djorgovski, S., & Davis, M. 1987, ApJ, 313, 59

Dressler, A., Lynden-Bell, D., Burstein, D., Davies, R. L., Faber, S. M., Terlevich, R. J., & Wegner, G. 1987, ApJ, 313, 42

Hubble, E., & Tolman, R. C. 1935, ApJ, 82, 302

Tolman, R. C. 1934, Relativity, Thermodynamics and Cosmology (Oxford: Oxford Univ. Press)

Chapter 2

Near–Infrared Photometry of Early–Type Galaxies in the Local Universe: Global Photometric Parameters

Abstract

An imaging survey of 341 nearby early–type galaxies in the the near–infrared K–band atmospheric window (2.2μm) is described. The survey galaxies were primarily drawn from 13 nearby rich clusters (85%), with additional galaxies in loose groups (12%) and the general field (3%). Surface photometry was measured for the entire sample. Detailed corrections were derived from an extensive grid of seeing–convolved $r^{1/4}$ models and then applied to the isophotal surface brightness, aperture magnitude, and ellipticity profiles. Global photometric parameters were derived from these seeing–corrected photometry. More than 25% of the sample has been observed at least twice, and these repeat measurements demonstrate the small internal uncertainties on the derived global photometric parameters. Extensive comparisons with aperture photometry from the literature demonstrate that the photometry is fully–consistent with those photometric systems to ≤ 0.01 mag and confirm the estimates of internal random uncertainties. Additional global parameters (central velocity dispersion, line indices, optical surface brightness, effective radii, D_n diameters, and aperture magnitudes) are drawn from the literature in a homogeneous manner in order to construct a large catalog of galaxy properties: 95% of the galaxies have a velocity dispersion, 69% have a Mg_2 index, 80% have an optical $r_{\rm eff}$ and $\langle\mu\rangle_{\rm eff}$, 82% have a D_n, and 81% have a derived optical–infrared color measurement. This large data set provides excellent source material for investigations of the physical origins of the global scaling relations of early–type galaxies, velocity fields in the local universe, and comparisons to higher redshift early–type galaxies.

2.1 Introduction

Early–type galaxies form a homogeneous population both in their structure (luminous and dynamical) and stellar content. The bivariate correlations called the Fundamental Plane (Dressler *et al.* 1987; Djorgovski & Davis 1987) among their global properties describes a systematic sequence of galaxy properties within this population; the small scatter of these correlations implies a similarly small scatter in early–type galaxy properties throughout that sequence. While it can be argued (Schechter 1997) that there is no such thing as a "perfect elliptical galaxy," there appears to be little influence on the global properties of early–type galaxies caused by such complicating factors as gas (ionized and neutral), dust, young stars, or the presence of an ordered disk component. Despite the high frequency of dust features (van Dokkum & Franx 1995) and ionized gas (Goudfrooij & de Jong 1995) in the core regions of a large fraction of elliptical galaxies, the small scatter of the optical FP (Jørgensen, Franx, & Kjærgaard 1996), near–infrared FP (Pahre, Djorgovski, & de Carvalho 1995), and the color–magnitude relations (Bower, Lucey, & Ellis 1992b) all imply that the global properties of these elliptical galaxies are relatively unaffected.

As a result of this uniformity of global properties for early–type galaxies, the specific form of these correlations (slope and intercept) provide insight into the underlying physical properties such as stellar content (age, metallicity, and initial mass function), mass, radius, and the distribution of stars and velocities within the galaxy. The color–magnitude relation—more luminous early–type galaxies are redder than less luminous galaxies—could be the result of systematic variations in metal abundance, or mean stellar age, or both. The key question to be addressed by any investigation into the global properties of early–type galaxies is: what underlying physical properties drive these correlations? A related question is immediately raised: what is the distribution of these underlying physical properties among the family of early–type galaxies?

The stellar content of early–type galaxies is, in general, enriched in heavy elements to near–solar abundances, so the integrated optical light in the galaxies is sensitive to the line–blanketing effects of metallicity. For this reason, optical light may not be a good tracer of the stellar mass in these galaxies. Near–infrared light at 2.2μm, however, is a good tracer of bolometric luminosity, which in turn varies only weakly with metallicity (for example, in the models of Bruzual & Charlot 1996 or Vazdekis *et al.* 1996; see the discussion in Pahre,

de Carvalho, & Djorgovski 1998b, Chapter 4 of this thesis). Since late–type giant stars dominate the near–infrared light of early–type galaxies (Frogel 1971), the composite nature of the stellar populations is simplified in this bandpass. Near–infrared light is therefore a good tracer of the stellar mass for early–type galaxies.

Large–scale surveys to study the global properties of early–type galaxies have, in general, utilized optical light for the photometric properties. A limited number studies stand out against this trend (Frogel *et al.* 1975, 1978; Persson, Frogel, & Aaronson 1979; Peletier 1989; Bower, Lucey, & Ellis 1992ab; Silva & Elston 1994; Pahre *et al.* 1995; Ferrarese 1996; Mobasher *et al.* 1997). All but the last four studies used single element aperture photometry as the source data.

The rapid technological advances of the last decade have produced a series of ever larger near–infrared imaging detectors with high quantum efficiency, small dark current, low numbers of dead pixels, and photometric stability. Compared to optical wavelengths, observing in the near–infrared has the further advantages that the seeing is better on average, corrections for Galactic extinction are smaller and hence less important, the presence of dust in the early–type galaxies themselves is virtually irrelevant, and the stellar populations effects are simpler. There is, however, a strong disadvantage to observing in the near–infrared from the ground: the sky is much brighter than in the optical. For example, while a typical sky brightness in the V–band is 21.8 mag arcsec^{-2}, the equivalent sky brightness in the K_s–band on a cold night is 13.5 mag arcsec^{-2}. Early–type galaxies typically have a color of $(V-K) \sim 3.2$ mag (Persson, Frogel, & Aaronson 1979), hence there is a loss of ~ 5 mag in the ratio of galaxy to sky surface brightness, equivalent to a loss of a factor of ten in signal–to–noise ratio. Additionally, the near–infrared imaging detectors are much smaller (256×256 pixel^2 is the current standard format) than modern, large format CCD arrays, which causes problems as many of the larger galaxies overfill the field–of–view (FOV) with the smaller detector. Nonetheless, substantial portions of the optical data in the literature (Djorgovski & Davis 1987; Franx, Illingworth, & Heckman 1989; Colless *et al.* 1993; Jørgensen, Franx, & Kjærgaard 1995) on early–type galaxies have been taken with a FOV that is similar to that of most of the near–infrared imaging data (2.6×2.6 arcmin^2 instantaneous, or 3.5×3.5 arcmin^2 after dithering) utilized for the survey described in this paper.

As a result of these technological advances, and despite the challenges posed by near–

infrared observations of nearby early–type galaxies, it became apparent that a large, new survey of early–type galaxy properties using *imaging* detectors was timely. The survey of 327 early–type galaxies described in this paper is larger by more than a factor of two in the number of galaxies studied than any previous investigation at 2.2μm. The unusually large number of repeat observations in this survey—more than 120—will establish its internal homogeneity and reliability, as well as provide reasonable estimates of the uncertainties of each measured and derived quantity. Many previous studies in the near–infrared (Frogel *et al.* 1975, 1978; Persson *et al.* 1979; Peletier *et al.* 1989; Silva & Elston 1994) used samples dominated by nearby, luminous, field elliptical galaxies, while the present survey draws the bulk of the sample from the cores of rich clusters of galaxies—the special environment occupied primarily by early–type galaxies. A small number of early–type galaxies in the field and loose groups have been included in this survey in order to sample a wide variety of density environments.

The data in this paper comprise a large and homogeneous sample of galaxy photometry suitable for a wide range of follow–up studies. The primary purpose for this study was to study the wavelength dependence of the slope of the FP correlations in order to determine the influence of stellar populations parameters in defining the early–type galaxy sequence. A related issue is the small scatter of the FP in the optical: if it is due to an age–metallicity "conspiracy," then the scatter of the near–infrared FP will be large due to the minimized metallicity effects in the near–infrared bandpass. A comparison between the global properties of field and cluster early–type galaxies can be investigated on the basis of this near–infrared photometry, and possible age variations can be constrained between those two distinct environments. An investigation of the universality of the color–magnitude relation is possible with these data, as this survey includes galaxies from 13 rich clusters—compared to only Virgo and Coma in Bower *et al.* (1992b). The key element to study the optical–infrared color–magnitude relation is to choose galaxies for which high quality optical photometry already exists in the literature; as is described in §2.2, this was a key consideration in planning this near–infrared survey. There are only a limited number of optical–infrared color gradient measurements in the literature (Peletier 1989; Silva & Elston 1994), hence this survey will be unique in its potential to derive color gradients for more than *ten* times the number of galaxies that have been studied previously. A comparison between optical–optical and optical–infrared color gradients should be capable of

distinguishing between stellar populations gradients (age and/or metallicity) and diffuse distributions of dust as the underlying physical cause. A comparison of the near–infrared and optical deviations of the fitted isophotes from perfect ellipses is a potential tool for determining if the disks in S0 galaxies could be comprised of a different stellar population from the bulges. Finally, these survey data provide a nearby galaxy "calibration" for studies of the near–infrared FP correlations at higher redshifts.

2.2 Description of the Near–Infrared Imaging Survey

The primary scientific goals to be achieved by this near–infrared imaging survey of early–type galaxies are: (1) to measure the change (if any) in the slope of the FP from the optical to the near–infrared; and (2) to construct a nearby, near–infrared "calibration" sample for future FP observations at high redshifts. To these primary goals, several secondary goals can also be introduced: (3) to measure any changes in the FP (slope and/or intercept) between cluster and field galaxies; (4) to investigate optical–infrared colors and color gradients which could indicate properties of possible stellar populations gradients and/or dust distributions; (5) to investigate deviations of the shapes of early–type galaxies from pure ellipses as indicators of the possible presence of disk structures; (6) to determine if systematic errors caused by Galactic extinction corrections are the cause of any particular cases of peculiar velocities, as the K–band is relatively unaffected by this correction; and (7) to construct models of the structural, kinematical, and stellar content properties of early–type galaxies as a family which are consistent with all relevant data.

The two primary goals of the project require that a sufficiently large sample be observed, in order that the slope of the FP can be determined to an accuracy comparable to that for the optical FP; for example, a total of 226 galaxies in 10 clusters were used by JFK96 in measuring the Gunn r–band FP. In order to reduce the effects of distance uncertainties on the FP distance–dependent parameter, rich clusters with large early–type galaxy populations are preferable; in this way, many galaxies at the same distance can be observed. In order that cluster peculiar velocity effects be minimized, it is necessary to avoid nearby clusters or at least minimize their proportion within the entire survey. The Coma cluster is an ideal target, as its redshift velocity of $\sim$ 7200 km s^{-1} places it far enough to have little or no deviation from the Hubble flow, while it is a rich cluster with 146 early–type

galaxies within the central 1 degree^2 and Gunn $r \leq 15.3$ mag (Jørgensen & Franx 1994). A number of other rich clusters—Perseus, Pisces, Abell 194, Abell 2199, Abell 2199, and Klemola 44—were chosen to add additional galaxies to the sample, and to determine if there is any variation of the FP parameters among clusters.

Two nearby clusters—Virgo and Fornax—and five loose groups (Leo, Eridanus, Pegasus, Cetus, and NGC 5846) were added to the sample, as they have many galaxies that have been well–studied at many wavelengths. Detailed comparisons of optical–optical and optical–infrared color gradients are possible for these galaxies. The challenge for interpreting the FP data derived for these galaxies, however, is that the Virgo cluster has well–known depth effects (Tonry, Ajhar, & Luppino 1990) including a background W Cloud; Fornax, Leo, and Eridanus effectively have unresolved depths (Tonry 1991) as derived by the surface brightness fluctuations method. Nearby galaxy motions are strongly affected by Virgo infall, and possibly by bulk motion in the direction of the Hydra–Centaurus Supercluster.

The investigation of possible differences in the FP between different clusters, or between clusters and the field, could be tested in the Hydra–Centaurus region. Large peculiar velocities were derived for some clusters and field galaxies in this region from the Seven Samurai survey (Lynden-Bell *et al.* 1988) which resulted in the identification of a "Great Attractor."

The galaxy lists were drawn from the literature (Lucey & Carter 1988; Faber *et al.* 1989; Lucey *et al.* 1991a; Lucey *et al.* 1991b; Jørgensen & Franx 1994; Smith *et al.* 1997), based on the requirement that there be central velocity dispersion measurements and optical global photometric parameters already measured for survey galaxies. In a significant number of cases, additional galaxies fell within the detector's field–of–view which do not have kinematical and/or optical photometry available in the literature.

Information on the clusters, groups, and other galaxies included in this survey are listed in Table 2.1. The location of the survey galaxies on the sky are plotted in Figure 2.1 in Galactic coordinates.

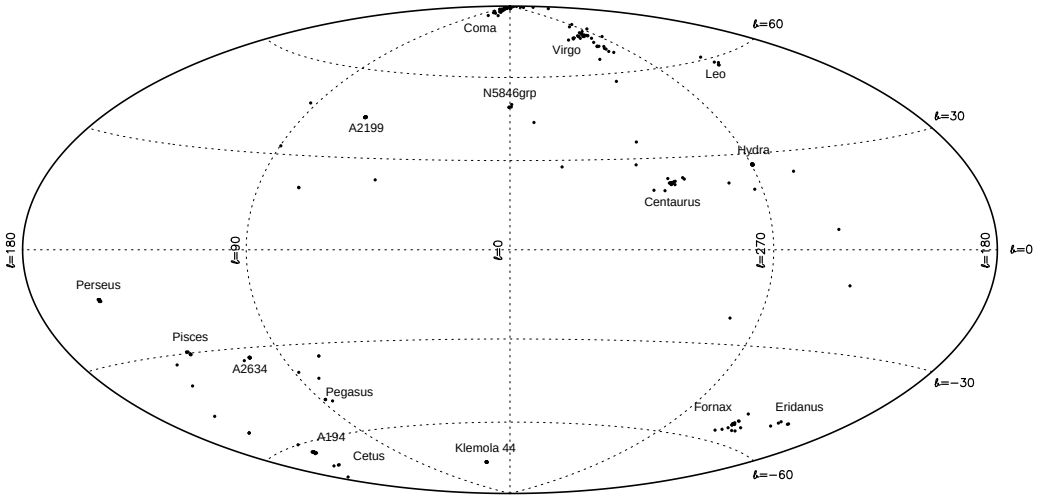

Figure 2.1: The distribution of the K–band early–type galaxy survey galaxies, plotted in Galactic coordinates using the Aitoff projection. Each point represents a separate galaxy. Rich clusters and groups with ≥ 3 galaxies in the survey are identified.

Table 2.1: Clusters, Groups and Other Galaxies in the K–band Photometry Survey

Name	α (1950)	δ (1950)	l (deg)	b (deg)	cz_{CMB} (km s^{-1})	$S_{100\mu m}$ (MJy/ster)	A_B (mag)	N_{obs}
CLUSTERS:								
Pisces	01^h00^h	$+30°02'$	126	–33	4581	2.8	0.20	11
Abell 194	01^h23^h	$-01°36'$	142	–63	5176	3.5	0.25	21
Perseus = Abell 426	03^h15^h	$+41°20'$	150	–13	5169	8.9	0.64	24
Fornax	03^h37^h	$-35°37'$	237	–54	1301	0.2	0.02	20
Hydra = Abell 1060	10^h34^h	$-27°16'$	270	26	4033	4.0	0.29	23
Virgo	12^h24^h	$+13°00'$	280	74	1493	2.4	0.17	37
Centaurus–Low (30)	12^h46^h	$-41°02'$	302	21	3332	8.9	0.63	15
Centaurus–High (45)	12^h47^h	$-41°07'$	303	21	4835	9.3	0.67	7
Coma = Abell 1656	12^h57^h	$+28°15'$	58	88	7202	0.0	0.00	70
Abell 2199	16^h27^h	$+39°40'$	63	44	8997	–0.4	0.00	28
Pegasus	23^h18^h	$+07°55'$	88	–48	3116	4.0	0.28	4
Abell 2634	23^h36^h	$+26°45'$	103	–33	9063	2.7	0.19	19
Klemola 44 = DC2345-28	23^h45^h	$-28°25'$	25	–76	8569	0.6	0.04	12
GROUPS:								
Local (M 32)	00^h40^h	$+40°36'$	121	–22	···	···	0.31	1
Cetus	01^h30^h	$-07°17'$	151	–68	1555	2.3	0.16	3
GH18	01^h46^h	$+27°24'$	138	–33	3358	3.6	0.26	1
GH20 = NGC 691 Group	01^h48^h	$+21°39'$	141	–39	2606	5.3	0.38	1
NGC 720 Group	01^h50^h	$-13°45'$	173	–70	1437	0.4	0.03	1
NGC 741 Group	01^h54^h	$+05°23'$	151	–54	4963	3.5	0.25	3
Eridanus	03^h26^h	$-20°55'$	211	–54	1444	1.3	0.09	5
HG1 = NGC 2442 Group	07^h33^h	$-69°24'$	281	–22	1454	11.6	0.83	1
IC 2311 Group	08^h17^h	$-25°13'$	245	6	2088	7.1	0.51	1
HG36 = NGC 2986 Group	09^h42^h	$-21°03'$	255	24	2520	3.0	0.21	1
Antlia	10^h28^h	$-35°35'$	273	19	3314	4.5	0.32	1
Leo I	10^h46^h	$+12°56'$	234	58	1142	3.6	0.26	5
NGC 3557 Group	11^h08^h	$-37°08'$	282	21	3337	6.1	0.44	1
NGC 4373 Group	12^h23^h	$-39°29'$	297	23	3625	6.7	0.48	2
NGC 5011 Group	13^h10^h	$-42°50'$	307	20	3525	9.1	0.65	1
HG35 = NGC 5084 Group	13^h15^h	$-26°34'$	310	36	2184	5.8	0.41	1
Centaurus A	13^h23^h	$-43°46'$	310	19	590	9.9	0.70	1
HG22 = IC 4296 Group	13^h31^h	$-33°22'$	313	28	3997	4.8	0.34	1
NGC 5846 Group	15^h03^h	$+01°53'$	0	49	1883	3.0	0.21	5
7S71 = NGC 5898 Group	15^h17^h	$-23°40'$	341	28	2517	11.8	0.84	1
GH158	15^h38^h	$+59°14'$	93	47	2832	0.2	0.01	1
7S86	22^h12^h	$+13°36'$	75	–34	7497	3.3	0.24	2
GH163 = NGC 7448 Group	22^h59^h	$+15°57'$	88	–39	1729	4.0	0.28	1

Table 2.1—*Continued*

Name	α (1950)	δ (1950)	l (deg)	b (deg)	cz_{CMB} (km s^{-1})	$S_{100\mu\mathrm{m}}$ (MJy/ster)	A_B (mag)	N_{obs}
NGC 7768 (Abell 2666)	$23^{\mathrm{h}}48^{\mathrm{h}}$	$+26°52'$	107	–34	7601	4.0	0.28	1
OTHER GALAXIES:								
NGC 821	$02^{\mathrm{h}}05^{\mathrm{h}}$	$+10°46'$	152	–48	1431	5.9	0.42	1
NGC 2325	$07^{\mathrm{h}}01^{\mathrm{h}}$	$-28°37'$	240	–10	2406	6.4	0.46	1
NGC 5812	$14^{\mathrm{h}}58^{\mathrm{h}}$	$-07°15'$	350	43	2288	6.7	0.48	1
NGC 6411	$17^{\mathrm{h}}35^{\mathrm{h}}$	$+60°51'$	90	33	3641	2.1	0.15	1
NGC 6482	$17^{\mathrm{h}}50^{\mathrm{h}}$	$+23°05'$	48	23	3950	7.8	0.56	1
NGC 6702	$18^{\mathrm{h}}46^{\mathrm{h}}$	$+45°39'$	75	20	4600	5.0	0.36	1
NGC 6703	$18^{\mathrm{h}}46^{\mathrm{h}}$	$+45°30'$	75	20	2244	4.8	0.34	1
NGC 7385	$22^{\mathrm{h}}47^{\mathrm{h}}$	$+11°21'$	82	–41	7528	3.7	0.27	1

NOTES:

(1) cz_{group} is with respect to the CMBR and is taken from Faber *et al.* (1989).

(2) $S_{100\mu\mathrm{m}}$ is measured from the IRAS 100 μm maps.

(3) A_B is converted from $S_{100\mu\mathrm{m}}$ using the relation of Laureijs *et al.* (1994): $A_B(\mathrm{mag}) = S_{100\mu\mathrm{m}}/14$.

The Galactic extinction has been calculated from the 100μm emission, under the assumption that cool dust emission is a better tracer of dust absorption than neutral hydrogen gas. The emission at 100μm has been measured for each cluster, group, or galaxy using the IRAS maps. Each measurement typically used samples in a 3×3 grid with internal spacing of $\sim$ 5 arcmin. Obvious 100μm sources were excluded visually from the measurements, as some of the nearest early–type galaxies contain a cool dust component and have been detected at this wavelength (Jura *et al.* 1987; Goudfrooij & de Jong 1995). The 100μm emission was then converted to A_B using the formula from Laureijs, Helou, & Clark (1994):

$$A_B = \frac{S_{100\mu\mathrm{m}}}{14 \pm 2 \mathrm{MJy\ ster}^{-1}}\ \mathrm{mag.} \tag{2.1}$$

These values of $S_{100\mu\mathrm{m}}$ and A_B have been entered into Tables 2.1. The extinction in the K–band are calculated by assuming the Galactic extinction curve of Cardelli, Clayton, & Mathis (1989) with $R = 3.05$, resulting in $A_K = 0.085 A_B$.

These estimates of A_B correlate well with those from other studies, although there appear to be significant departures in the Hydra–Centaurus region. In particular, the estimate of A_B is 0.12 mag larger for the Hydra cluster than in Faber *et al.* (1989), $\sim$ 0.13 mag larger for the NGC 4373 group and $\sim$ 0.18 mag larger in Centaurus than in Dressler, Faber, & Burstein (1991). Since $E(V-K) = 0.668 A_B$, the $(V-K)$ color derived in this paper for galaxies in those regions would have to be corrected by +0.1 mag to agree with the Burstein & Heiles (1982) reddening estimates, but this would create many galaxies with $(V-K)_0$ that is too red in the final catalog. It is interesting that if the *underestimate* of A_B by Faber *et al.* (1989) in the Hydra–Centaurus is corrected, the galaxies in this region then have smaller distances and larger peculiar velocities. The origin of this discrepancy in estimating A_B is uncertain, but could be a result of variations in gas–to–dust ratio or dust size distribution along this Galactic line–of–sight. Future work in this region should utilize the new IRAS/DIRBE dust extinction maps as constructed by Schlegel, Finkbeiner, & Davis (1997), which show a significant improvement over the Burstein & Heiles (1982) maps.

2.3 Observations and Data Reduction

Data for this survey were acquired during runs on the 60–inch telescope at Palomar Observatory, and the 1.0 m Swope and 2.5 m du Pont Telescopes at Las Campanas Observatory. All instruments used are based on NICMOS–3 256×256 pixel^2 HgCdTe arrays manufactured by Rockwell with 40μm pixels. A K_s ("K–short") filter was used in all cases in order to reduce the thermal background contribution.

The observing sequence was typically three exposures of 60 seconds each (or six exposures of 30 seconds each during the summer months) taken in each of five positions; those positions were offset in an "X" pattern by 15–30 arcsec in each direction. The total on–source exposure time was therefore 900 seconds. The nearest early–type galaxies (i.e., in the Leo I group and the Virgo cluster) used half the total exposure time or 450 seconds. Sets of exposures on a region of "blank" sky separated 5–15 arcmin away from the target galaxy were interleaved with the object exposures. Early in the project, the telescope guider was used during the object exposures in case there were no stacking stars available in the individual data frames. In time, it became clear that there was virtually always a sufficient number of usable stacking stars in the frame of each galaxy, so the guider was not used for the remainder of the survey, which slightly improved the observing efficiency.

Except for the 1993 March observing run at the 2.5 m du Pont Telescope, all of the observations were calibrated using observations of the new HST $K \sim 11$ mag G dwarf standard stars (Persson 1997). A typical photometric night included observations of 5–20 standard stars at up to two or three airmasses. Several observing programs were pursued concurrently with these instruments so that during non–photometric conditions a backup project was observed.

2.3.1 Palomar 60–inch Telescope Data

A total of 212 early–type galaxy fields were observed with the near–infrared camera (Murphy *et al.* 1995) on the Palomar Observatory 60–inch (P60) Telescope during 27 photometric nights between 1994 October and 1997 August. This instrument uses an all–mirror, 1:1 reimaging Offner design at the f/8.75 Cassegrain focus of the Ritchey–Chretien telescope, producing a projected pixel size of 0.6200 ± 0.0004 arcsec and an instantaneous field–of–view (FOV) of 158×158 arcsec^2. This pixel scale was measured using a large number of

stars in the field of globular cluster Messier 15 with an accurate photographic plate solution for their coordinates (this list was provided by K. Cudworth to J. Cohen) and shows very little geometric distortion over the entire FOV. The electronics have an inverse gain of 7.8 e^- DN^{-1} and a read–noise of $\sim$ 40 e^-. The instrument FOV was limited slightly (by $\sim$ 3%) during 1994 October due to vignetting caused by misalignment of a cold mask at the telescope focal plane which was subsequently fixed.

On this telescope, the seeing FWHM in the near–infrared varied between 1.0 and 2.5 arcsec during the course of the survey. In order that the survey be conducted in a way that a more similar resolution *in physical units* be obtained, it was decided to observe the higher redshift galaxies during times of optimal seeing. The result of this decision was that many of the nearest galaxies, such as in the Leo I Group or the Virgo cluster, were imaged under the worst seeing conditions. The advantage of this decision was that the seeing corrections would be manageably small in the Coma cluster—the top priority cluster for the study—as well as in the Virgo cluster.

The data acquired from this telescope form $\sim$ 50% of the entire survey data. The Virgo, Coma, Abell 194, Abell 2199, Abell 2634, Perseus, Pisces, and Pegasus clusters, the Leo I and Cetus groups, M 32, and many of the "field" galaxies were imaged with this telescope.

2.3.2 Las Campanas 1.0 m Swope Telescope Data

Observations at the Las Campanas 1.0 m Swope Telescope (C40) were made during two runs, each using a different near–infrared imaging camera.

The instrument described by Persson *et al.* (1992) was used during four photometric nights in 1995 March (the same instrument was also mounted on the Las Campanas 2.5 m telescope for the runs described in §2.3.3) to obtain 45 images of galaxies primarily in the Hydra–Centaurus Supercluster region. The instrument was mounted at the standard f/7 focus of the telescope and used in "medium resolution" mode, producing a 0.920 arcsec project pixel size and a 236 $\times$ 236 arcsec^2 instantaneous FOV. The seeing FWHM was typically significantly undersampled with the large pixel size. The electronics have an inverse gain of 4.8 e^- DN^{-1} and a read–noise of $\sim$ 40 e^-.

Observations were obtained in 1995 October–November on the same telescope using a new near–infrared camera which is nearly identical with that used on the P60 and described in §2.3.1. This instrument, however, is placed at the telescope's Cassegrain focus with the

f/13.5 secondary—which is not the standard Ritchey–Chretien f/7 secondary. The 1:1 reimaging optics produce a projected pixel size of 0.600 arcsec and an instantaneous FOV of 154×154 arcsec^2. As for the P60 instrument, the electronics have an inverse gain of 7.8 e$^-$ DN^{-1} and a read–noise of $\sim$ 40 e$^-$. A total of 32 galaxy images were obtained primarily in the Fornax cluster and the Eridanus group during three photometric nights. The seeing was typically marginally–sampled for these data at 1.0–1.3 arcsec FWHM.

2.3.3 Las Campanas 2.5 m du Pont Telescope Data

Observations were obtained during six photometric nights in 1993 March and three photometric nights in 1994 December using the near–infrared camera (Persson *et al.* 1992) on the Las Campanas 2.5 m du Pont Telescope (C100). The "medium resolution" mode was used producing a projected pixel size of 0.348 arcsec and an instantaneous FOV of 89×89 arcsec^2. The electronics for this instrument have an inverse gain of 4.8 e$^-$ DN^{-1} and a read–noise of $\sim$ 40 e$^-$. A total of 53 images of 38 different galaxies were obtained during the two observing runs.

These data were acquired for a different observing program on near–infrared surface brightness fluctuations. The 1993 March data of nine Virgo cluster elliptical galaxies are described by Pahre & Mould (1994), while in 1994 December the Fornax cluster was the primary target. The different science goal for this program resulted in much longer exposure times than the rest of the survey, typically between 1000 and 3000 seconds; when coupled with the larger telescope aperture, these images reach much fainter flux limits than the C40 or P60 data. The smaller FOV of this instrument, however, causes the sky–subtraction to be far more problematical than for the rest of the survey—since the galaxies imaged with this instrument have the largest angular sizes in the survey.

2.3.4 Data Reduction

All of the data were reduced within the IRAF environment using scripts written by the author (or E. Persson) for near–infrared data reductions with these instruments. The basic procedure consisted of: (1) correcting for non–linearity; (2) subtracting an appropriate dark frame; (3) flat–fielding, using either a dome flat, a twilight sky flat, or a dark sky flat; (4) subtraction of an appropriately normalized sky frame; (5) flagging of bad pixels; (6) image registration using bright stars in the field; (7) delta–sky subtraction using a region

common to all frames of a given galaxy; and (8) averaging of all the data frames using a sigma–rejection algorithm into a single stack.

The choice of flat–field was investigated in detail. There was no statistically–significant variation between choices of dome, twilight, or dark sky flats on the resultant photometry. In some cases, due to substantial changes in airmass during a galaxy observing sequence, a dark sky flat was the only method to produce low noise. The choice was usually made for a night based on visual inspection of the final, stacked data.

There are several important issues regarding the subtraction of a sky frame which need to be addressed. First, the sky varies sufficiently on the order of 5–25 DN pixel^{-1} (out of a typical sky value of 1–1.5$\times 10^4$ DN pixel^{-1}—even during the photometric conditions used for this survey—on times faster than the exposure time (i.e., < 30 second). It is apparent that these sky frames would not be sufficient to determine the absolute sky level on the object frames. Second, the largest galaxies (25–50% of the galaxies) have extents that overfill the detector FOV such that the absolute sky level on the object frames cannot be determined from the frames themselves. The combination of these two issues causes a fundamental problem for near–infrared imaging of extended objects: the absolute sky level will need to be estimated during the analysis in a more sophisticated manner. Subtraction of sky in a more accurate manner using the surface brightness profiles themselves will be discussed in §2.4.

2.3.5 Photometric Calibration

With the exception of the C100 run in 1993 March, the new HST standard star list of Persson (1997) was used for calibration for the entire survey. For the C100 run, the faint UKIRT standards (Casali & Hawarden 1992) were used. Between five and 20 standard stars were typically observed on a photometric night or partial night at up to two (or sometimes three) airmasses. Each standard was usually placed at five different places on the array for each measurement. The atmospheric extinction coefficient was measured for each night separately; for some runs, the coefficient and zero–points were determined to be stable for several consecutive nights, allowing for the extinction to be measured for all such nights simultaneously. More the 85% of the nights had rms ≤ 0.02 mag, while $> 40\%$ had rms ≤ 0.01 mag for the standard star measurements.

The HST standards are all $K \sim 11$ mag G dwarf stars with $(J-K) \sim 0.35$ mag, while

the galaxies observed are typically $(J-K) \sim 1.0$ mag (Persson, Frogel, & Aaronson 1979). Since a K_s filter was used throughout this survey—which is not only narrower than the standard Johnson K filter, but also has a bluer effective wavelength—there is expected to be a color term between the hotter standard stars and the cooler K giant stars which dominate the near–infrared light of early–type galaxies. This color term will be in the sense that the K_s magnitudes will be measured too faint relative to the K magnitudes. Furthermore, the near–infrared light in early–type galaxies is dominated by late–type giant stars (Frogel 1971), hence there is significant absorption at rest–frame $\lambda > 2.29\mu$m due to the onset of the CO bandhead. This absorption will affect K magnitudes more than K_s magnitudes, in the sense that the K_s magnitudes will be measured too bright relative to the K magnitudes.

No correction has been applied to the photometry of this survey to account for these color differences, but they will be applied in all comparisons with observations through standard K filters from the literature. These terms can be estimated using simple stellar populations models. Using the Worthey (1994) model for [Fe/H] = 0 dex and 11 Gyr, k–corrections have been derived for both K_s and K filters using the definition adopted by Mayall, Humason, & Sandage (1956), i.e., $m_{true}(z) = m_{obs}(z) - k(z)$. Atmospheric effects and detector sensitivity are assumed constant across the filter bandpass. These are displayed in Figure 2.2. A simple polynomial fit (rms = 0.002 mag) to the K_s–band k–correction for $z \leq 0.05$ is

$$k_{K_s}(z) = -3.83z + 21.9z^2. \tag{2.2}$$

The K–band k–correction was also calculated and is reasonably consistent with that derived by Persson, Frogel, & Aaronson (1979) for $z \leq 0.025$, i.e., $k_K(z) = -3.5z$. The combined effect of the calibration due to the use of G dwarf standard stars and the CO bandhead on the K_s to K magnitude comparisons was calculated (assuming the stars to be blackbodies radiating at 5800 K) to be $(K_s - K) = -0.029$ mag. Thus, the prediction is $(K_s - K) = -0.028$ mag at $z = 0.0045$ (Virgo cluster) and $(K_s - K) = -0.007$ mag at $z = 0.024$ (Coma cluster).

As a consistency check, the CO index can be estimated for the program galaxies relative to Vega. This calculation was performed using top–hat filters simulating the narrowband

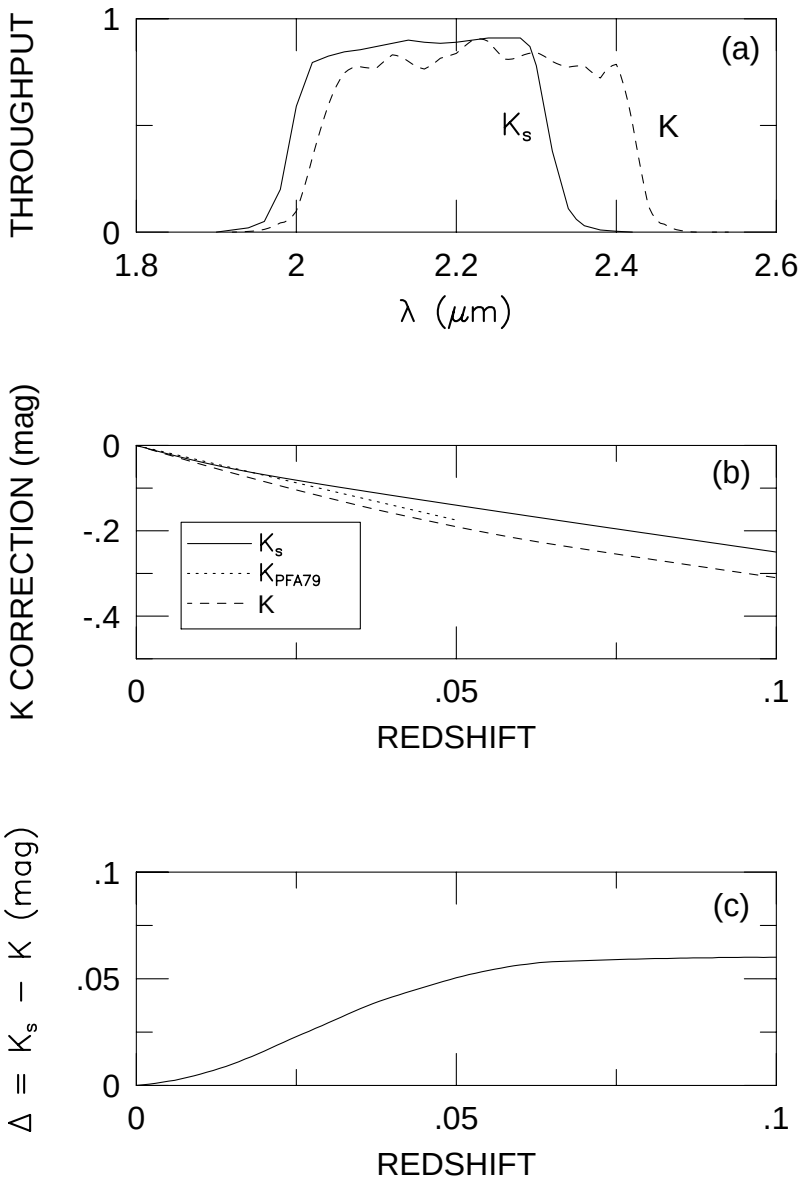

Figure 2.2: (a) Comparison of the throughput for the K_s filter (used for this survey) and the standard Johnson K filter. The K_s filter has a narrower $\Delta\lambda$ and a bluer λ_0. (b) Comparison of the k–corrections for the two filters. These have been calculated for a Worthey (1994) [Fe/H] = 0, 11 Gyr, single–burst model. (c) The difference in k–correction between the two filters as a function of redshift. The difference arises primarily due to the CO bandhead absorption at $\lambda > 2.29\mu$m which is much stronger at K than at K_s due to the filter responses. The filter differences flatten out for $z > 0.05$ after the CO bandhead has moved redwards of the K filter cutoff.

and CO filter observations of Frogel *et al.* (1988) using the same Worthey model as above, but this time calibrating with respect to a A0 star with $T = 9900$ K. (Frogel *et al.* defined Vega to have a CO index of 0 mag.) A value of 0.162 mag was calculated, which is fully consistent with the observed value of 0.16 mag for luminous galaxies as measured by Frogel *et al.*

As another consistency check, the CO absorption and G–dwarf calibration can be compared to the $(K_s - K)$ of red standard stars of Persson (1997). The CO absorption of 0.16 mag affects approximately one–fourth of the K filter bandpass, so it should produce ~ -0.04 mag absorption on the K magnitudes; the K_s filter bandpass can be assumed to be unaffected by CO absorption. The color term due to the G dwarf standard stars is estimated by comparing $(K_s - K) = +0.006 \pm 0.001$ mag (rms = 0.009 mag) for the $(J - K) \sim 0.35$ mag G dwarfs with $(K_s - K) = +0.019 \pm 0.002$ mag for the $(J - K) = 1.0 \pm 0.3$ mag (rms = 0.006 mag) standard stars (both from Persson 1997). The difference is +0.013 mag; when combined with the CO effect, this produces $(K_s - K) = -0.027$ mag, consistent with the -0.029 mag calculated above for $z = 0$.

The aperture used to measure instrumental magnitudes for the standard stars is an important effect for the detailed surface photometry that will be described in §2.4, as well as for comparisons with single element, circular aperture photometry from the literature. For this reason, the largest practical aperture size of diameter 25 arcsec was used for the standard stars. For purposes of comparisons of aperture magnitudes with the literature, it is possible that this could introduce small but systematic differences as a function of magnitude. As will be described below in §2.8.1, if such differences exist they are probably at a level significantly smaller than the random errors of the photometric comparisons.

In summary, the systematic photometric errors due to the K_s filter choice—which affect the calibration using G dwarf stars and amount of CO absorption in the bandpass—and the photometric zero–point calibration appear to be quantifiably understood to better than ± 0.01 mag.

2.4 Surface Photometry

Several different approaches have been used in the literature to model the light distributions of early–type galaxies. These range from fitting circularized models to aperture photome-

try, to using full elliptical isophotes at all radii to construct a detailed surface brightness distribution for the galaxy. A number of light distributions have been shown to represent accurate models for early–type galaxies, including the de Vaucouleurs $r^{1/4}$ form, the Sersic $r^{1/n}$ form, an exponential disk plus $r^{1/4}$ bulge, and the Hubble model. Each of these models has at least one scale–length parameter to describe its size, and at least one parameter to describe the total luminosity and/or mean surface brightness evaluated at that scale–length. When one model is chosen to describe a given galaxy, however, biases may be introduced if $r_{\rm model} \neq r_{\rm galaxy}$. Fortunately, the FP correlations typically involve the quantity $r_{\rm eff} - 0.32\langle\mu\rangle_{\rm eff}$, which is very insensitive to systematic errors in $r_{\rm eff}$ (Jørgensen, Franx, & Kjærgaard 1995, and §2.7.3 below). For this reason, the choice of model for fitting to the surface brightness distribution of an early–type galaxy should not be a significant contributor to bias in the FP correlations.

The choice was made to fit elliptical isophotes to the images, as well as to measure total magnitudes in circular apertures, in order to provide independent checks on the derivation of global photometric parameters. Isophotal surface brightness has the disadvantage of being very sensitive to seeing effects near the center of a galaxy and errors in sky subtraction at large radii; this latter effect, however, can be useful as a more accurate estimator of the true sky value. Circular aperture magnitudes, on the other hand, are very insensitive to sky subtraction errors and the effects of seeing are straightforward to model; unfortunately, they do not directly trace out the shape of the galaxy, and hence may suffer from subtle systematic biases as a function of ellipticity.

The surface photometry and aperture magnitudes were measured from the images using the STSDAS package ISOPHOTE within the IRAF environment. The ELLIPSE task was used to do the actual fitting to the images. A set of IRAF scripts was developed around this package to provide for interactive flagging of pixels (due to stars, other galaxies, or bad pixels), identification of sky regions, iterative removal of overlapping galaxies, iterative improvement of the sky estimation, calculation of derived (such as mean surface brightness) and seeing–corrected quantities, and fitting of various models to the surface brightness and aperture magnitude profiles. In fitting the global quantities, minimization of the absolute deviation orthogonally from the fitting function was performed. Error bars were used in fitting all quantities, hence there is no statistical advantage to be gained from rebinning the data at large radii.

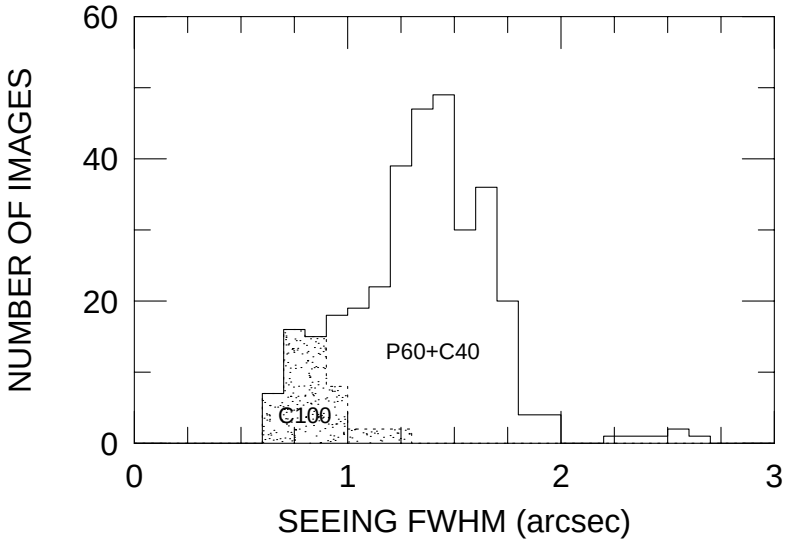

Figure 2.3: Histogram of the seeing distribution for the entire survey. The data taken with C100 have better seeing in general (shaded region) compared to the P60 and C40 data. The median seeing is 1.34 arcsec FWHM.

2.5 Seeing Corrections

The median seeing for this near–infrared survey is 1.34 arcsec FWHM, while the typical galaxy imaged has $r_{\rm eff}$ are in the range 1–100 arcsec. Hence, for the smaller galaxies in the sample, the effects of seeing on the derived surface photometry or global photometric parameters might be important. The total distribution of seeing for the survey is plotted in Figure 2.3.

The effects of seeing on the measurement of photometric parameters for early–type galaxies can be significant, particularly as the radii (or semimajor axis lengths) of individual measurements (aperture magnitudes m, isophotal SB μ, and ellipticity ϵ) approach the FWHM size of the seeing disk. In general, as the seeing effects become more important, light is scattered to larger radii from the center of a galaxy causing the effective radius $r_{\rm eff}$ to be overestimated; the galaxy shape is also circularized at small radii causing ϵ to be underestimated.[1] For well resolved galaxies (in which $r_{\rm eff} \gg {\rm PSF_{FWHM}}$), an overestimate

[1]The effects of seeing on m are straightforward to model, as flux is always scattered out of a given aperture. The seeing effects on isophotal μ are more complicated, however, since at semimajor axis lengths $a \lesssim 1.5{\rm PSF_{FWHM}}$ the measured μ is too faint, while at $a \gtrsim 1.5{\rm PSF_{FWHM}}$ the measured μ is too *bright* (e.g., Figure 4 in Franx, Illingworth, & Heckman 1989). This is further complicated for highly elliptical galaxies ($\epsilon \gtrsim 0.4$), in which the isophotal ellipses at small (or even modest) a are circularized due to seeing, thereby

of $r_{\rm eff}$ will be compensated by a fainter measurement of $\langle\mu\rangle_{\rm eff}$ (since it is measured at a larger radius), such that the quantity $r_{\rm eff} - 0.32\langle\mu\rangle_{\rm eff}$ (which enters the FP) will be nearly unaffected and seeing effects are unimportant. For marginally resolved galaxies (in which $r_{\rm eff} \sim {\rm PSF_{FWHM}}$), however, $r_{\rm eff}$ will also be overestimated but $\langle\mu\rangle_{\rm eff}$ will be highly underestimated due to the cumulative effects of both measuring $\langle\mu\rangle_{\rm eff}$ at a larger radius and the scattering of light to even larger radii due to the seeing; in this case, the quantity $r_{\rm eff} - 0.32\langle\mu\rangle_{\rm eff}$ will be systematically underestimated. The difference between the well resolved and the marginally resolved cases can produce a differential bias *along* the FP, resulting in a measurement of the slope of the FP that is too steep. It is therefore necessary to correct for the effects of seeing on the measurement of global photometric parameters to avoid biases in the slope of the FP.[2]

There are several different approaches for correcting galaxy data for the effects of seeing. One approach is to correct each measurement individually for seeing effects using simple models convolved with an appropriate PSF. This approach was used by Bower *et al.* (1992a) to correct their circular aperture magnitudes; the corrected values are then fit by $r^{1/4}$ models to measure the global photometric parameters; these corrections were also used in other papers by Lucey and collaborators (Lucey *et al.* 1991ab; Smith *et al.* 1997; but not Lucey & Carter 1988). Franx, Illingworth, & Heckman (1989) used a similar approach to correct for the individual measurements of μ and ϵ (and the position angle θ which can be caused by an elliptical PSF) based on an analytical, second order estimation of the effects of seeing. A different approach was used by Jørgensen, Franx, & Kjærgaard (1995a) and Saglia *et al.* (1993), in which the uncorrected individual measurements of aperture magnitudes are compared to seeing–convolved models. In effect, this amounts to applying a seeing correction to $r_{\rm eff}$, $\langle\mu\rangle_{\rm eff}$, and D_n when fitting the uncorrected aperture magnitudes, and Saglia *et al.* (1993) tabulated such corrections. The difficulty in applying these corrections is that the same fitting range for the profile must be used for the corrections to be valid.

Since the near–infrared photometry has much higher sky background and hence lower

causing a correlation of errors in μ with errors in ϵ.

[2]There exist a number of studies of the global photometric properties of early–type galaxies which do *not* correct for the effects of seeing. Most notably is the large 7 Samurai survey (Faber *et al.* 1989, plus a number of other papers by other authors based on these data); other studies are Djorgovski & Davis (1987), Lucey & Carter (1988), Dressler, Faber, & Burstein (1991), Saglia, Burstein, & Dressler (1993), and Jørgensen & Franx (1994), although it is important to note that seeing–corrected quantities were re–derived for these Coma galaxy observations (Jørgensen, Franx, & Kjærgaard 1995). Caution must be exercised if comparing seeing–corrected data to the data in any of these studies.

Table 2.2: Model Grid for Calculating Seeing Corrections

Quantity	Values							
$r_{\rm eff}$	$1''$	$2''$	$3''$	$5''$	$10''$	$30''$	$60''$	
$\rm PSF_{FWHM}$	$1.00''$	$1.25''$	$1.50''$	$2.00''$				
ellipticity	0.0	0.1	0.2	0.3	0.4	0.5	0.6	0.7

S/N, it was anticipated that the maximum fitting radius would be significantly smaller in the near–infrared than in the comparable optical studies. For this reason, the approach of correcting the individual measurements of m, μ, and ϵ was chosen.

A grid of model galaxies of de Vaucouleurs $r^{1/4}$ form was constructed to span a range of parameters ($r_{\rm eff}$, $\rm PSF_{FWHM}$, ϵ) that were representative of the galaxy survey, and are listed in Table 2.2. These models were constructed with the ARTDATA package in IRAF to have the typical pixel scale (0.62 arcsec), FOV (256×256 pixel^2), and dither pattern (±30 arcsec) of the P60 and C40 data which comprise the bulk of the galaxy sample. No attempt was made to span a range in signal–to-noise, include sky subtraction errors, or to add a disk component to the models. While Saglia *et al.* (1997) have demonstrated that when bulge plus exponential models are fit by $r^{1/4}$ models alone there are systematic errors in m_{tot} and $r_{\rm eff}$, their work showed that any systematic effects on the quantity $r_{\rm eff} - 0.32\langle\mu\rangle_{\rm eff}$ that enter the FP are extremely small and show no clear trend with bulge–to–disk ratio (i.e., see their Figure 4). Since the purpose of the present paper is to prepare a set of global photometric parameters for constructing the near–infrared FP, there is little to be gained from expanding the model grid to include a larger range of parameters. A Moffat PSF with $\beta = 3.0$ was used throughout to convolve the models, as this value of β is a typical representation of the PSF of ground–based images as shown by Saglia *et al.* (1993).

The model images were fit using the same programs as were used for the survey galaxies. Aperture magnitudes m_{obs}, isophotal SB μ_{obs}, and ellipticities ϵ_{obs} were measured for each semimajor axis length a or circular radius r. These were compared with the model values in order to compute the seeing corrections. A number of analytical forms were explored with the requirement that there should be no residual correlation with ϵ, $\rm PSF_{FWHM}$, or $r_{\rm eff}$. The variance was minimized for the fits (instead of the absolute deviation), as the data points with the largest deviation (i.e., the largest seeing corrections, which are at small

radii), were the most important to fit accurately. Extraneous terms which did not reduce the scatter significantly, or had high correlations as indicated by by the covariance matrix, were removed.

The following seeing corrections were derived:

$$\begin{aligned}
\mu_{\rm obs} - \mu &= (-2.14 + 6.80\epsilon)\left(\frac{\rm PSF_{FWHM}}{a\sqrt{1-\epsilon}}\right)^2\left(\frac{r_{\rm eff}}{\rm PSF_{FWHM}}\right)^{-0.5} \\
&\quad + (0.72 - 4.51\epsilon)\left(\frac{\rm PSF_{FWHM}}{a\sqrt{1-\epsilon}}\right)^3\left(\frac{r_{\rm eff}}{\rm PSF_{FWHM}}\right)^{-0.5} \\
&\quad 2{\rm PSF_{FWHM}} \le a \le 5r_{\rm eff},\ 0 \le \epsilon \le 0.7 \\
&\quad Q\sigma = 0.008 \text{ mag arcsec}^{-2} \\
\epsilon_{\rm obs} - \epsilon &= -\left(1.069\epsilon\,(1-\epsilon)\right)\left(\frac{a\sqrt{1-\epsilon}}{\rm PSF_{FWHM}}\right)^{-2} \\
&\quad {\rm PSF_{FWHM}} \le a \le 5r_{\rm eff},\ Q\sigma = 0.002 \\
&\quad {\rm PSF_{FWHM}} \le a \le 3\,{\rm PSF_{FWHM}},\ Q\sigma(\Delta\epsilon/\epsilon) = 0.13 \\
m_{\rm obs} - m &= 0.334\,(1 + 3.15\epsilon^3)\left(\frac{r}{\rm PSF_{FWHM}}\right)^{-2}\left(\frac{r_{\rm eff}}{\rm PSF_{FWHM}}\right)^{-0.063} \\
&\quad {\rm PSF_{FWHM}} \le r \le 3\,r_{\rm eff} \\
&\quad 0 \le \epsilon \le 0.7, Q\sigma = 0.014 \text{ mag} \\
&\quad 0 \le \epsilon \le 0.5, Q\sigma = 0.006 \text{ mag} \\
&\quad 0 \le \epsilon \le 0.3, Q\sigma = 0.004 \text{ mag}
\end{aligned} \tag{2.3}$$

which have been applied to each galaxy surface brightness profile.

No attempt was made to calculate seeing corrections for very small radii $r < {\rm PSF_{FWHM}}$. Seeing corrections at smaller radii can suffer from a bad match between model and galaxy (if the latter is not intrinsically of $r^{1/4}$ form, for example), pixellation effects for marginally sampled data, and errors in measuring the true $\rm PSF_{FWHM}$ for the galaxy image. Instead, all models will be fit to the corrected aperture magnitudes for radii $r \ge 3{\rm PSF_{FWHM}}$, as at these radii the seeing corrections vary little between different approaches.

These seeing corrections are plotted in Figure 2.4, and are compared to those in the literature in Figure 2.5.

The corrections to aperture magnitudes show an excellent match with both Bower *et al.* (1992a) for $r > \mathrm{PSF_{FWHM}}$ and Saglia *et al.* (1993) for $r > 2\mathrm{PSF_{FWHM}}$. More specifically, fitting a power–law to the table of seeing corrections to aperture magnitudes calculated by Bower, Lucey, & Ellis (1992a) produces a solution of the form

$$\begin{aligned} m_{obs} - m &= 0.22 \pm 0.01 \left[\frac{r}{\mathrm{PSF_{FWHM}}}\right]^{-1.69} \left[\frac{r_{\mathrm{eff}}}{\mathrm{PSF_{FWHM}}}\right]^{-0.079} \text{ mag}, \\ & Q\sigma = 0.007 \text{ mag} \\ & r \geq \mathrm{PSF_{FWHM}} \end{aligned} \tag{2.4}$$

where the weak dependence they found of Δm on r_{eff} is apparent in Equation 2.4. Using the new seeing corrections (limiting the comparison to $\epsilon = 0$ and $r_{\mathrm{eff}} = 10$, and fixing the power–law dependences for simplicity) produces:

$$\begin{aligned} m_{obs} - m &= 0.26 \pm 0.01 \left[\frac{r}{\mathrm{PSF_{FWHM}}}\right]^{-2} \left[\frac{r_{\mathrm{eff}}}{\mathrm{PSF_{FWHM}}}\right]^{-0.063} \text{ mag} \\ & Q\sigma = 0.001 \text{ mag} \\ & r \geq \mathrm{PSF_{FWHM}} \end{aligned} \tag{2.5}$$

Adding in the full–range of r_{eff} from the model grid only increases the scatter to $Q\sigma = 0.010$ mag. Comparing Equations 2.4 and 2.5 shows that the two sets of seeing corrections are nearly identical analytically.

The form of Franx *et al.* (1989) seeing corrections for isophotal surface brightness is

$$\mu - \mu_{obs} = 0.85 \left(\frac{\mathrm{PSF_{FWHM}}}{a\sqrt{1-\epsilon}}\right)^2 \tag{2.6}$$

This can be compared, for example, by fitting seeing corrections from the model grid using only the $e = 0$ simulations, producing:

$$\begin{aligned} \mu - \mu_{obs} &= 0.77 \pm 0.02 \left(\frac{\mathrm{PSF_{FWHM}}}{a\sqrt{1-\epsilon}}\right)^2 \\ & 2\mathrm{PSF_{FWHM}} \leq a \leq 5r_{\mathrm{eff}} \\ & \mathrm{rms} = 0.022 \text{ mag arcsec}^{-2} \end{aligned} \tag{2.7}$$

where the scatter is dominated by the innermost pixels. Allowing for an additional term

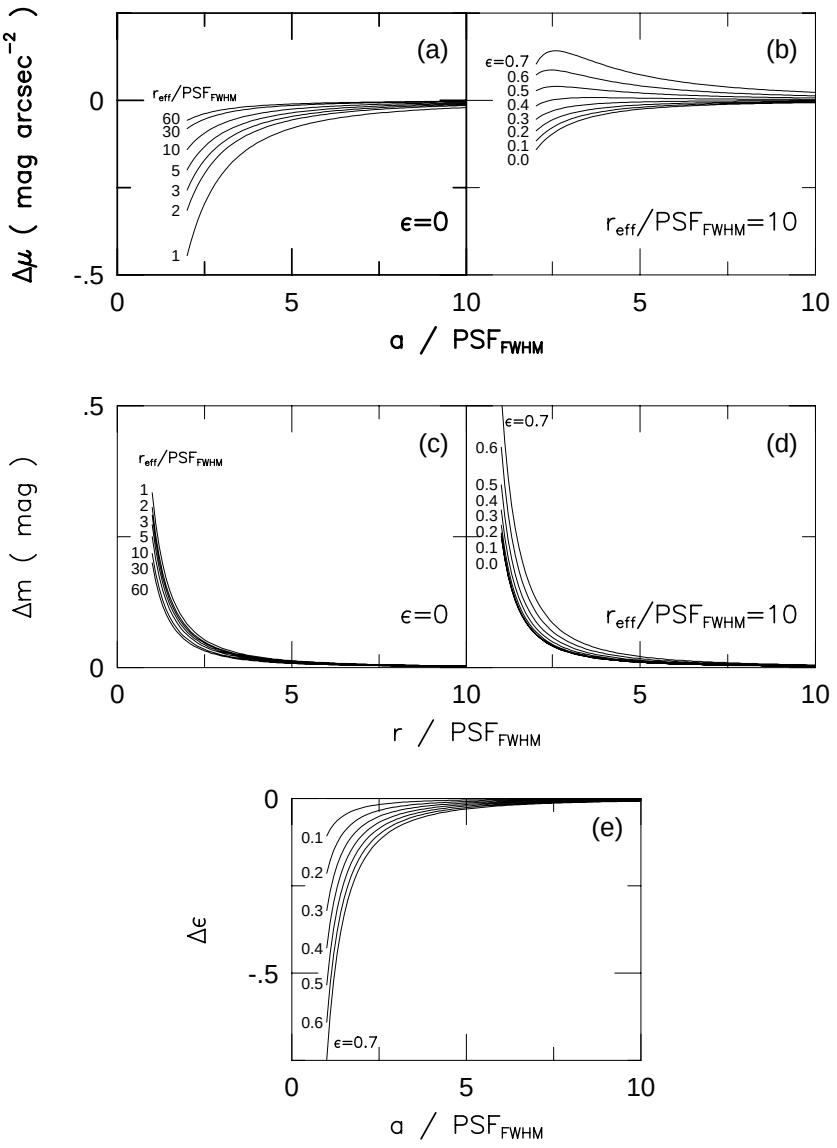

Figure 2.4: The seeing corrections for aperture magnitude m, isophotal surface brightness μ, and ellipticity ϵ, derived from the model grid in Table 2.2. Each of the plotted quantities Δm, $\Delta\mu$, and $\Delta\epsilon$ should be subtracted from observed quantities to obtain the seeing–corrected quantities. (a) Seeing corrections for isophotal surface brightness μ for fixed ellipticity $\epsilon = 0$ but variable $r_{\rm eff}/{\rm PSF}_{\rm FWHM}$. (b) Seeing corrections for isophotal surface brightness μ for fixed $r_{\rm eff}/{\rm PSF}_{\rm FWHM} = 10$ but variable ellipticity ϵ. (c) Seeing correction for circular aperture magnitudes m for fixed ellipticity $\epsilon = 0$ but variable $r_{\rm eff}/{\rm PSF}_{\rm FWHM}$. (d) Seeing corrections for circular aperture magnitudes m for fixed $r_{\rm eff}/{\rm PSF}_{\rm FWHM} = 10$ but variable ellipticity ϵ. (e) Seeing corrections for ellipticity ϵ for different ellipticities $0.1 \leq \epsilon \leq 0.7$.

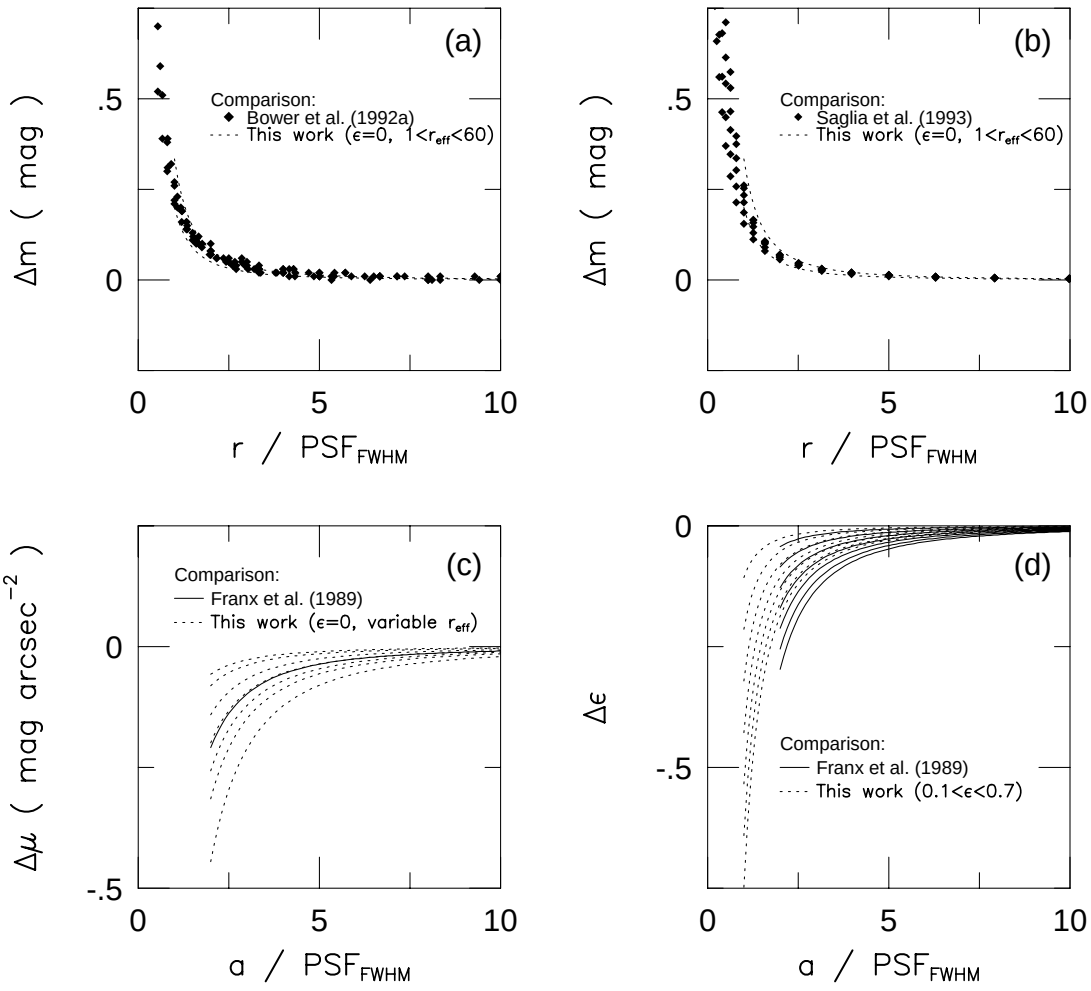

Figure 2.5: Comparison of the seeing corrections derived for this work with those in the literature.

which depends on $r_{\rm eff}$ produces

$$\begin{aligned} \mu - \mu_{obs} &= 1.64 \pm 0.02 \left(\frac{\rm PSF_{FWHM}}{a\sqrt{1-\epsilon}}\right)^2 \\ \left(\frac{r_{\rm eff}}{\rm PSF_{FWHM}}\right)^{-0.5} & \\ & {\rm rms} = 0.010 \text{ mag arcsec}^{-2} \end{aligned} \tag{2.8}$$

which shows a reduction in scatter. It is clear that the empirical method adopted here in Equation 2.8, and the analytical second–order approximations of Franx *et al.* (1989) in Equation 2.6, have a reasonable agreement. The difficulty of making the comparison for $\epsilon > 0.2$ is that there is much larger scatter, as the residuals begin to correlate more strongly with ellipticity (since the semimajor axis was fit, not $r = \sqrt{ab}$ as in the Franx *et al.* approach). Comparisons between the two forms of seeing corrections are shown in Figure 2.5.

2.6 Measurement of Global Photometric Parameters

A diameter D_K has been defined to be the circular aperture diameter at which the mean, integrated surface brightness—fully corrected for cosmological effects and Galactic extinction—drops to $\langle\mu_K\rangle = 16.6$ mag arcsec^{-2}. This quantity is similar to the D_n parameter introduced by Dressler *et al.* (1987) in the B–band, and the D_V parameter in the V–band (Lucey & Carter 1988), for a mean galaxy color of $(V-K) = 3.2$ mag. This color is typical for an elliptical galaxy (Persson, Frogel, & Aaronson 1979; Bower, Lucey, & Ellis 1992a).[3]

As noted by Dressler *et al.* (1987), the global parameters $r_{\rm eff}$, $\langle\mu\rangle_{\rm eff}$, and D_K are all closely related (and the first two are nearly equivalent to the last one) because elliptical galaxies follow very similar growth curves. A demonstration of this property is shown in Figure 2.6, where the 341 galaxies observed in the K–band show a very tight relationship between these three quantities. The majority of the galaxies obey an approximate linear relationship $\log(D_K/r_{\rm eff}) \propto -0.32\langle\mu\rangle_{\rm eff}$. This property of elliptical galaxies will be used

[3]Mobasher *et al.* have defined the same quantity D_K at 16.5 mag arcsec^{-2} implying a mean color of $(V-K) = 3.3$ mag, which is only typical for the few brightest elliptical galaxies (Persson, Frogel, & Aaronson 1979; Bower, Lucey, & Ellis 1992a). It is predicted that their definition will show a significant offset in $\log D_V - \log D_K$. The offset for the present study compared to Faber *et al.* (1989) is < 0.01 dex, demonstrating that the assumed $(V-K) = 3.2$ mag is a representative color of the elliptical galaxy population. Furthermore, the derived $(R_{\rm C}-K)$ colors using the aperture photometry of Smith *et al.* (1997) have a median value of 2.65 mag, which is only 0.02 mag different from the assumed $(R_{\rm C}-K) = 3.2-0.57 = 2.63$ mag. Converting from the Mobasher *et al.* definition to the one adopted for the present paper requires increasing their $\log D_K$ by $0.32\Delta\langle\mu_K\rangle$ or 0.032 dex.

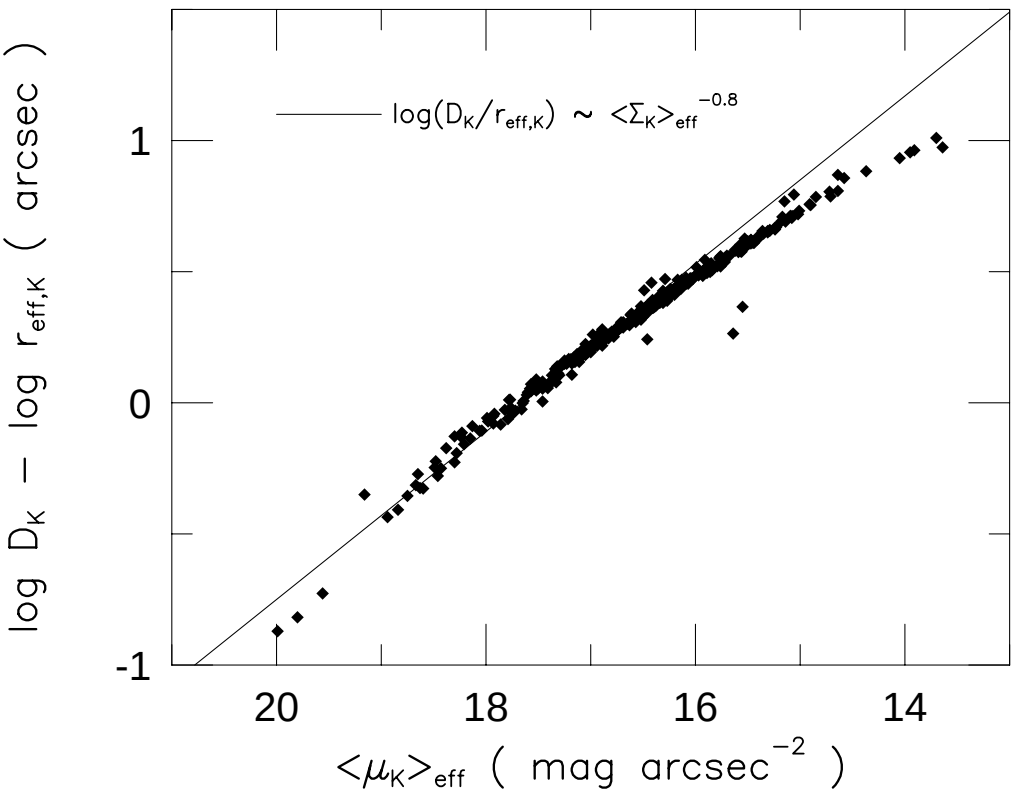

Figure 2.6: The similarity of curves of growth for ellipticals for the K–band observations of 341 galaxies. An approximate, simple scaling between $r_{\rm eff}$, $\langle\mu\rangle_{\rm eff}$, and D_K is given by $\log(D_K/r_{\rm eff}) \propto -0.32\langle\mu\rangle_{\rm eff}$. This similarity of growth curves shows why D_K can be provided as a nearly equivalent substitution for the combination $r_{\rm eff,K} - 0.32\langle\mu_K\rangle_{\rm eff}$.

below in §2.9.1 to make small corrections of optical measures of D_n to account for a different assumed extinction from that given by a particular literature source.

The half–light radius was estimated in two ways for each galaxy. The first method used fits to the isophotal surface photometry to estimate the half–light semimajor axis length $a_{\rm e}$, the ellipticity $\epsilon_{\rm e}$ at that semimajor axis length, and hence the half–light effective radius $r_{\rm e} = a_{\rm e}\sqrt{1-\epsilon_{\rm e}}$. The second method used fits to the circular aperture magnitude growth curve producing the half–light effective radius $r_{\rm eff}$. These two methods have a mean difference of 0.013 ± 0.008 dex, in the sense that the isophotal estimates are slightly larger. The scatter between these two measures is 0.14 dex, which is somewhat larger

than the quadrature sum of the internal scatter of either measure by itself of 0.11 dex (for the > 100 repeat observations described below in §2.7.3). The differences between the two methods is most likely a combination of a number of effects: seeing corrections on isophotal surface brightness are much more difficult and uncertain than for circular aperture magnitudes; systematic errors due to sky subtraction are a much larger effect on isophotal surface brightness than for circular aperture magnitudes; elliptical galaxies are not circular, so measuring their circularized structural parameters is certainly an oversimplification; and elliptical galaxies show variation in their structural light profiles, in the sense that more luminous galaxies show flatter profiles than the de Vaucouleurs $r^{1/4}$ shape. The last point should not be under-emphasized, as the reduced Chi–square χ^2/ν for fitting $r^{1/4}$ profiles (with or without an additional disk component) has a median value of 6 (Saglia *et al.* 1997) and fitting Sersic $r^{1/n}$ profiles has a median value of ~ 10 (Graham & Colless 1997). None of these models is an excellent fit to real galaxies since χ^2/ν is substantially larger than unity, so it should not be surprising that while the two different photometric measurement methods employed here have very small internal scatter, their relative scatter can be significantly larger.

The global photometric parameters derived from the aperture photometry will be adopted for two reasons. One, the vast majority of the work on the FP in the optical have used global photometric parameters derived from aperture photometry (the only significant exception being Djorgovski & Davis 1987). Since the intention was to compare optical and near–infrared measures for the same galaxies, it is essential to use similar methods to extract the global parameters. Two, it will be shown in §2.7.3 that the global photometric parameters derived from the circular aperture photometry show somewhat smaller internal uncertainties. In this way, aperture photometry is a more robust method of measuring the global parameters.

The 454 individual measurements of the global photometric parameters are tabulated in the appendix as Table A.1.

2.7 Estimation of Internal Uncertainties

One key element of any large scale photometric survey is the estimation of uncertainties. Due to the limited amount of K–band surface photometry and global photometric parameters

available in the literature, the design of this survey therefore included a large number of repeat observations both of luminous and faint galaxies in order to provide a robust internal estimation of these random uncertainties. There were 113 repeat measurements of 88 galaxies in this survey which will be discussed in this section. Some of these repeat observations were included by design, others were serendipitous in result for the more distant clusters due to the large FOV of the detector and large surface density of galaxies near the cores of the clusters.

2.7.1 Aperture Magnitudes

The seeing–corrected circular aperture magnitude profiles are compared in Figure 2.7. The uncertainty for a single measurement of an aperture magnitude is $Q\sigma = 0.038$ mag. This is somewhat larger than the scatter implied by comparisons with aperture photometry from the literature (in §2.8.1 below), but this is primarily due to the internal comparison galaxies being much fainter and the surface photometry tracing the large galaxies to much larger radii than in the external comparisons.

2.7.2 Surface Photometry

The internal comparison of the surface photometry is shown in Figure 2.7. The uncertainties for single measurements are: $\Delta\mu_K = 0.062$ mag arcsec^{-2}, $\Delta\epsilon = 0.013$, $\Delta\theta = 1.4$ degree (for measurements $\epsilon \geq 0.1$), $\Delta A_4 = 0.006$, and $\Delta B_4 = 0.006$. The $\Delta\theta$ uncertainty is somewhat large since there was no attempt made to correct for small angle changes in the camera setups from run to run. The uncertainties for μ_K are larger than for the aperture photometry due to the increased uncertainties due to seeing corrections at small radii and sky subtraction at large radii.

2.7.3 Global Photometric Parameters

A comparison of the repeat measurements of the global photometric properties derived from the circular aperture magnitudes is plotted in Figure 2.8. A comparison of the repeat measurements of the global photometric properties derived from the isophotal surface photometry is plotted in Figure 2.9. The comparisons are summarized in Table 2.3.

The measurement errors of $r_{\rm eff}$ and $\langle\mu\rangle_{\rm eff}$ for the aperture photometry, or of $a_{\rm e}$ and $\langle\mu\rangle_{\rm e}$

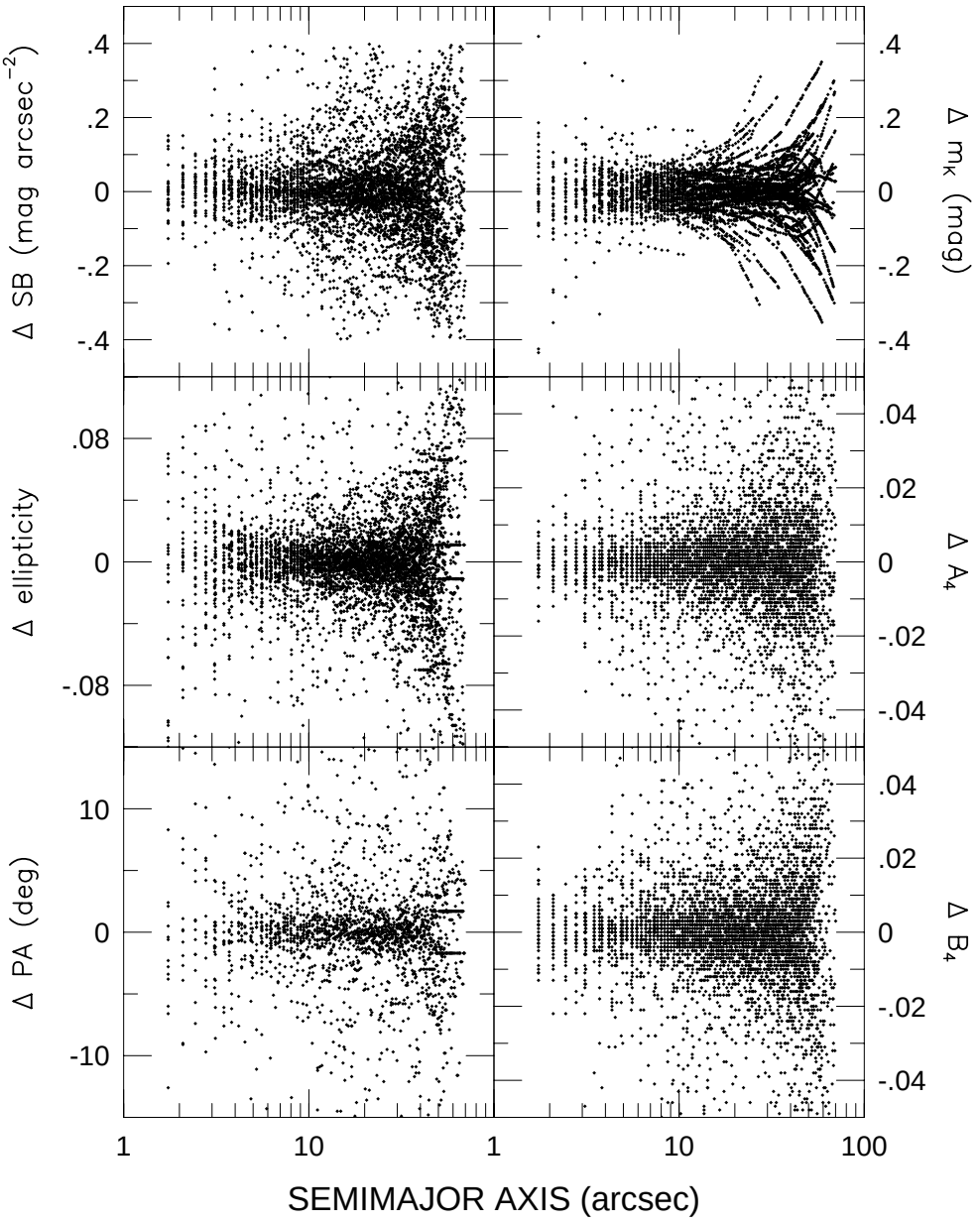

Figure 2.7: Internal comparison of surface and aperture photometry. The uncertainties for single measurements are: $\Delta m_K = 0.038$ mag, $\Delta \mu_K = 0.062$ mag arcsec^{-2}, $\Delta \epsilon = 0.013$, $\Delta \theta = 1.4$ degree (for measurements $\epsilon \geq 0.1$), $\Delta A_4 = 0.006$, and $\Delta B_4 = 0.006$.

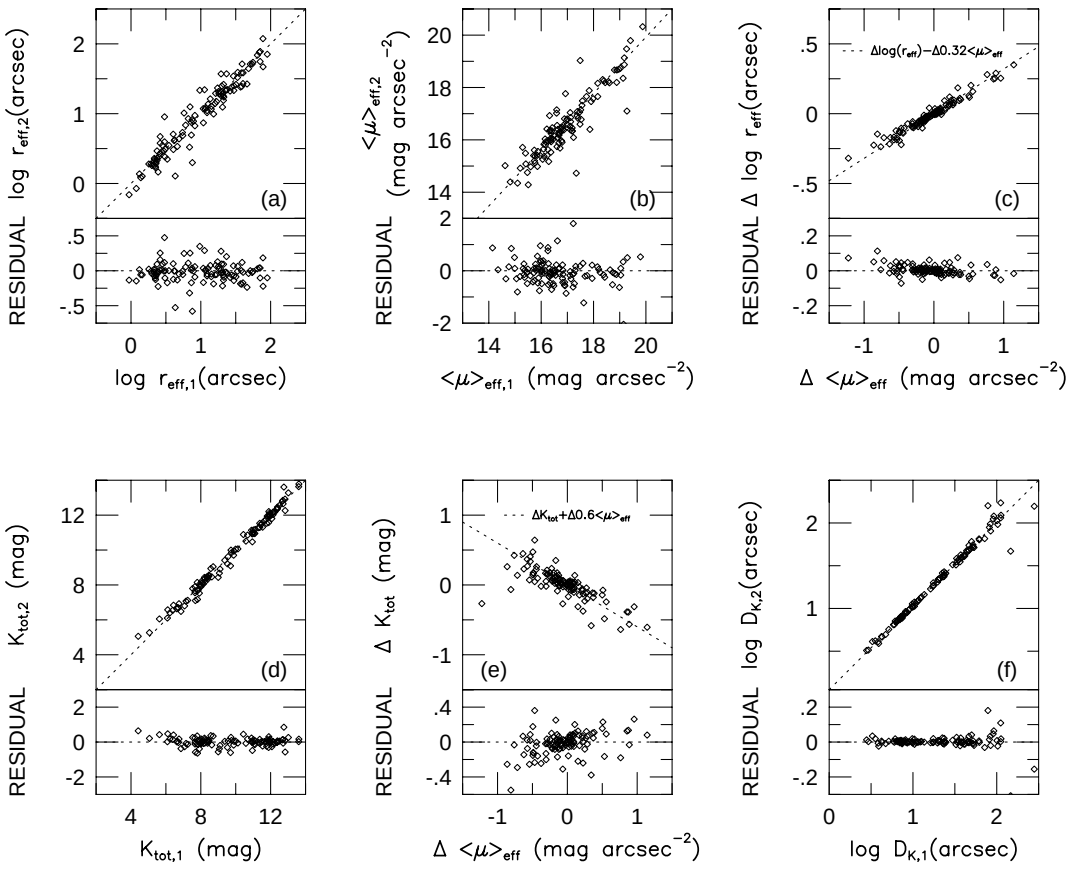

Figure 2.8: Internal comparison of global photometric parameters derived from the circular aperture photometry. (a) Comparison of repeat measurements of $\log r_{\rm eff}$. (b) Comparison of repeat measurements of $\langle\mu\rangle_{\rm eff}$. (c) Comparison of repeat measurements of $\log r_{\rm eff} - 0.32\langle\mu\rangle_{\rm eff}$, the quantity which enters the FP. Errors in the measurements of $\log r_{\rm eff}$ and $\langle\mu\rangle_{\rm eff}$ are strongly correlated, but the scatter perpendicular to this correlation is small. (d) Comparison of repeat measurements of $K_{\rm tot}$. (e) Comparison of repeat measurements of $K_{\rm tot} + 0.6\langle\mu\rangle_{\rm eff}$, the quantity which enters the luminosity version of the FP. (f) Comparison of repeat measurements of D_K, the diameter at which the mean internal surface brightness reaches 16.6 mag arcsec^{-2}.

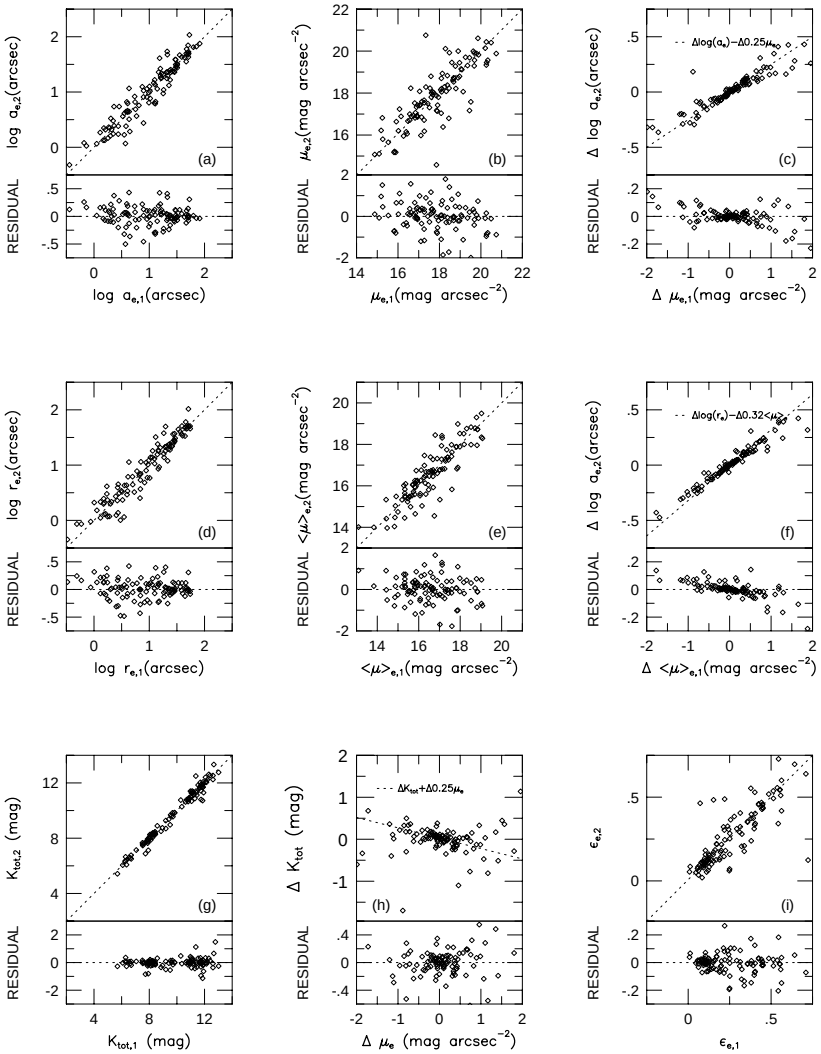

Figure 2.9: Internal comparison of global photometric parameters derived from the surface photometry. (a) Comparison of repeat measurements of the half–light semimajor length $\log a_{\rm e}$. (b) Comparison of repeat measurements of $\mu_{\rm e}$. (c) Comparison of repeat measurements of $\log a_{\rm e} - 0.25\langle\mu\rangle_{\rm e}$, the quantity which enters the FP. Errors in the measurements of $\log a_{\rm e}$ and $\mu_{\rm e}$ are strongly correlated, but the scatter perpendicular to this correlation is small. (d) Comparison of repeat measurements of the effective radius $r_{\rm e} = a_{\rm e}\sqrt{1-\epsilon}$. (e) Comparison of repeat measurements of $\langle\mu\rangle_{\rm e}$. (f) Comparison of repeat measurements of $\log r_{\rm e} - 0.32\langle\mu\rangle_{\rm e}$, the quantity which enters the FP. (g) Comparison of repeat measurements of $K_{\rm tot}$. (h) Comparison of repeat measurements of $K_{\rm tot} + 0.25\mu_{\rm e}$, the quantity which enters the luminosity version of the FP. (i) Comparison of repeat measurements of the ellipticity evaluated at the half–light semimajor axis $\epsilon_{\rm e}$.

Table 2.3: Internal Comparison of Global Photometric Parameters

Quantity	$Q\sigma$	Unit
Circular Aperture Photometry		
K_{20}	0.041	mag
$\log r_{\rm eff}$	0.060	dex
$\langle\mu\rangle_{\rm eff}$	0.209	mag
$\log r_{\rm eff} - 0.32\langle\mu\rangle_{\rm eff}$	0.015	dex
$K_{\rm tot}$	0.094	mag
$K_{\rm tot} + 0.6\langle\mu\rangle_{\rm eff}$	0.068	mag
D_K	0.010	dex
Surface Photometry		
$\log a_{\rm e}$	0.074	dex
$\epsilon_{\rm e}$	0.027	···
$\log r_{\rm e}$	0.094	dex
$\langle\mu\rangle_{\rm e}$	0.257	mag
$\log a_{\rm e} - 0.25\langle\mu\rangle_{\rm e}$	0.021	dex
$\log r_{\rm e} - 0.32\langle\mu\rangle_{\rm e}$	0.019	dex
$K_{\rm tot}$	0.098	mag
$K_{\rm tot} + 0.25\langle\mu\rangle_{\rm eff}$	0.070	mag

for the surface photometry, are strongly correlated. The uncertainty on $r_{\rm eff} - 0.32\langle\mu\rangle_{\rm eff}$, the quantity which enters the FP, is only 0.015 dex, which is substantially smaller than the uncertainties of either quantity taken separately.[4]

2.8 Estimation of External Uncertainties

At optical wavelengths there are many large–scale surveys of both surface photometry and aperture photometry to use as external comparison samples, but at near–infrared wavelengths far less data is available. Furthermore, global photometric parameters derived from K–band imaging have not been done before preventing an external comparison of those derived quantities.

[4]In early work on the FP (one example being Djorgovski & Davis 1987), the observational uncertainties due to $a_{\rm e}$ and $\langle\mu\rangle_{\rm e}$ were treated as independent variables, leading to substantial overestimates of the total observational uncertainties. This is particularly evident in their Figure 1, where the displayed "typical" error bars *exceed* the total observed scatter of the FP by more than 50%. Jørgensen *et al.* (1996) correctly showed the importance of the correlated errors on the derived intrinsic scatter of the FP.

2.8.1 Aperture Magnitudes

There are many sources of aperture photometry in the Johnson K–band dating back $\sim$ 25 years for these galaxies; the quality of these data, however, is highly irregular. For this reason, comparisons should be attempted with a subset of data that have previously been identified as externally consistent. Adding even a small number of additional observations from other sources in the literature causes the scatter to increase dramatically. As an example, comparison of a P60 observation (UT 1996 March 28) for NGC 4374 in the Virgo cluster, which has 11 observations from the PFA–79 data set, shows a mean offset of $K_s - K_{lit} = +0.013$ mag, a median offset of +0.009 mag, and a scatter of 0.042 mag; adding in four more comparisons from elsewhere in the literature increases the mean offset to +0.080 mag, the median offset to +0.050 mag, and the scatter to 0.101 mag!

The photometry of Persson and collaborators in Virgo, Fornax, Coma, and the field (Frogel *et al.* 1975; Frogel *et al.* 1978; Persson, Frogel, & Aaronson 1979), which will be referred to as PFA–79, and the photometry of Bower, Lucey, & Ellis (1992a; BLE–92a) in Coma, have been shown to be mutually consistent to high accuracy, both in zero–point and scatter (Bower, Lucey, & Ellis 1992a). As will be shown below, the K–band photometry of the present survey can be placed onto this system at a similar level of accuracy.

Aperture photometry from Recillas–Cruz *et al.* (1990, 1991) in Virgo and Coma will be compared to the present survey as an additional study. Finally, observations for Coma cluster galaxies based on near–infrared imaging data have recently appeared in the literature (Mobasher *et al.* 1997), and will be added to the comparison.

The full comparisons are plotted in Figure 2.10. For the purposes of this comparison, aperture magnitudes without k–corrections or Galactic extinction corrections are used for both the new and the literature data. In the case of the Mobasher *et al.* (1997) data, both Galactic extinction and k–corrections were removed from their published aperture magnitudes. Since the new survey used a K_s filter, while all literature observations used K filters, there is a predicted offset in the zero–point $(K_s - K)$ as described in §2.3.5 which also varies slightly with redshift.

The Coma measurements of Persson *et al.* (1979) and Bower *et al.* (1992a) show mean offsets of -0.007 ± 0.008 mag and -0.016 ± 0.008 mag, respectively, which are listed in Table 2.4. The expected offset due to the differences in the filters at $z = 0.024$ is $(K_s - K) =$

Table 2.4: Comparison of Aperture Magnitudes with the Literature

Source	r_{ap} (arcsec)	$(K_s - K)$ (mag)	$\pm$ (mag)	N	rms (mag)
Coma Cluster:					
P79	all	-0.007	0.008	26(26)	0.038
B92a	all ($r = 8.5$)	-0.016	0.008	31(31)	0.045
R90	all ($r = 7.4$)	-0.018	0.011	39(45)	0.070
M97	all ($r = 20$)	-0.005	0.010	33(41)	0.055
Predicted		-0.007			
Virgo and Fornax Clusters, and Eridanus Group:					
R91	all ($r = 7.4$)	-0.007	0.007	42(42)	0.045
F75, F78, P79	$6 < r < 9$	+0.003	0.009	19(19)	0.037
F75, F78, P79	$12 < r < 17$	-0.082	0.007	43(43)	0.045
F75, F78, P79	$23 < r < 28$	-0.044	0.006	49(51)	0.039
F75, F78, P79	$6 < r < 12$ and $r > 17$	-0.031	0.005	74(77)	0.044
Predicted		-0.028			

References: Frogel *et al.* (1975; F75), Frogel *et al.* (1978, F78), Persson *et al.* (1979, P79), Bower *et al.* (1992a, B92a), Recillas–Cruz *et al.* (1990, R90; 1991, R91), and Mobasher *et al.* (1997, M97).

-0.007 mag (see §2.3.5), suggesting that the new near–infrared data are fully consistent with both data sets.

Mobasher *et al.* (1997) removed the effect of overlapping galaxies in calculating their aperture magnitudes, hence there is expected to be significant offset for the regions around the two dominant galaxies at the core of the Coma cluster. Ignoring NGC 4872, NGC 4874, and NGC 4886 for this reason, and also galaxies NGC 4867 and D210 (which stand out from the mean relation) produces a similar mean offset of $(K_s - K) = -0.005 \pm 0.010$ mag with rms = 0.055 mag. The large scatter is no doubt due to the large, 40 arcsec diameter apertures measured by Mobasher *et al.*

The comparison between the new K_s data and Persson *et al.* (1979) for the Virgo and Fornax clusters, and the Eridanus Group, suggest that there may be a miscalibration of the aperture size for the Persson *et al.* $r \sim 15$ arcsec apertures, but not for the $r \sim 8$ or $r \sim 25$ arcsec apertures. The mean offsets between the C40+P60 and Persson *et al.* data in Virgo, Fornax, and Eridanus—where only aperture radii $6 < r < 12$ arcsec and $r > 17$ arcsec are used—is -0.031 ± 0.005 mag. The larger scatter for the smallest apertures ($r < 6$ arcsec)

is primarily an effect of seeing, and hence is not a useful comparison. The expected offset due to the differences in the filters at $z = 0.0045$ is $(K_s - K) = -0.028$ mag (see §2.3.5), demonstrating that the new near–infrared data are fully consistent with Persson *et al.* for nearby galaxies—as long as the apertures $r < 6$ arcsec (due to seeing differences) and $12 < r < 17$ arcsec (due to a possible aperture size miscalibration) are excluded.

In summary, the zero–points of the aperture magnitudes for the new near–infrared photometry survey are consistent with the studies of Persson *et al.* (1979) and Bower *et al.* (1992a) to < 0.01 mag. The scatter for each individual comparison with these studies is ~ 0.04 mag, which is fully consistent with the internal uncertainties of 0.03 mag quoted by Persson *et al.*, 0.027 mag quoted by Bower *et al.*, and 0.038 mag estimated for this new survey in §2.7.1.

2.8.2 Surface Photometry

There are three sources of comparisons for surface photometry in the 2.2μm atmospheric window: Peletier (1989), Silva & Elston (1994), and Ferrarese (1996). All three studies utilized standard K filters, and all of the galaxies in common are at group redshifted velocities less than 2000 km s^{-1}, so there should be a photometric offset of $(K_s - K) \sim -0.03$ mag (as calculated in §2.3.5).

The data of Peletier (1989) were obtained with an early version of a camera based on a 58×62 pixel^2 InSb array with very high read–noise (600 e$^-$) and dark current (100 e$^-$ pixel^{-1} second^{-1}) but modest FOV (78×83 arcsec^2). The comparisons are plotted in Figure 2.11. The zero–point for an individual comparison of surface photometry appears to have a large scatter, but the individual comparisons for each galaxy appear to have a much smaller scatter. For example, at semimajor axis lengths $a \sim 26$ arcsec, the offset among the nine galaxies is -0.03 mag and the scatter is 0.07 mag. On the other hand, for NGC 3379 alone the mean offset is K_s(P60) $- K$(P89) $= -0.062$ mag (rms = 0.024 mag) and K_s(C100) $- K$(P89) $= -0.037$ mag (rms = 0.026 mag). Hence, the major source of photometric scatter with the data of Peletier (1989) appears to be uncertainties in the zero–point for each galaxy. For semimajor axis lengths $10 < a < 50$ arcsec (with the inner cutoff due to the differences in seeing between the two studies), the mean ellipticity offset is ϵ(this study) $- \epsilon$(P89) $= +0.006$ (rms = 0.016), the mean position angle offset is θ(this study) $- \theta$(P89) $= -1.2^\circ$ (rms = 12.7°), and the mean fourth–order Fourier coeffi-

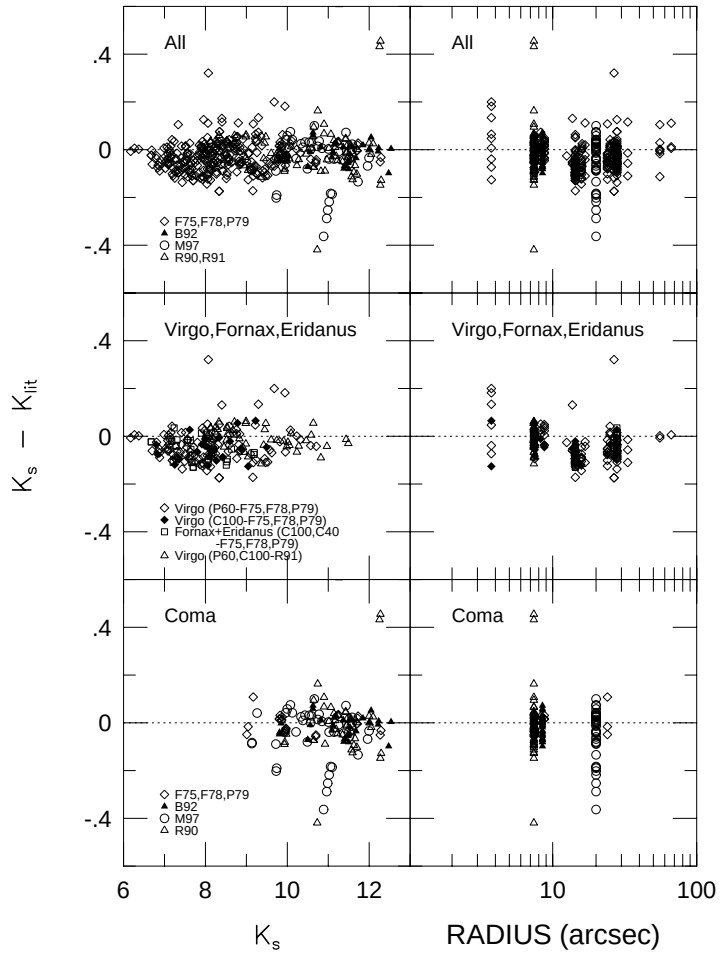

Figure 2.10: Comparison of aperture magnitudes measured from this survey with measurements from the following literature sources: Frogel *et al.* (1975, F75); Frogel *et al.* (1978, F78); Persson *et al.* (1979, P79); Bower *et al.* (1992a, B92); and Mobasher *et al.* (1997, M97). All comparisons are in the sense $K_s - K_{lit}$, where K_s is from this work. There appear to be large systematic errors as a function of K present in the Coma measurements of Mobasher *et al.* (1997). The Coma measurements of Persson *et al.* (1979), Bower *et al.* (1992a), and Recillas–Cruz *et al.* (1990) show mean offsets of $(K_s - K) = -0.007 \pm 0.008$ mag, -0.016 ± 0.008 mag, and -0.018 ± 0.011 mag, respectively. The expected offset due to the differences in the filters at $z = 0.024$ is $(K_s - K) = -0.007$ mag (see §2.3.5). The comparison between the new K_s data and F75, F78, and P79 for the Virgo and Fornax clusters, and the Eridanus Group, suggest that there may be a miscalibration of the aperture size for their $r \sim 15$ arcsec apertures. The mean offsets for the C40 and P60 data in Virgo, Fornax, and Eridanus with these authors is $(K_s - K) = -0.031 \pm 0.005$ mag ($6 < r < 12$ and $r > 17$ arcsec), while the mean offset with Recillas–Cruz *et al.* (1991) is -0.007 ± 0.007 mag. The expected offset due to the differences in the filters at $z = 0.0045$ is $(K_s - K) = -0.028$ mag (see §2.3.5). The new near–infrared data are therefore on a homogeneous photometric system with Persson *et al.*, Bower *et al.* and Recillas–Cruz *et al.* (1990, 1991) for galaxies at $z < 0.03$.

cient offset is $B_4(\text{this study}) - B_4(\text{P89}) = -0.1\%$ (rms = 0.1%, where the comparisons are affected by round–off error of $\pm 0.1\%$).

Most of the data of Silva & Elston (1994) were obtained with a low quantum efficiency PtSi 256×256 pixel^2 array with a large FOV (5.5×5.5 arcsec^2). Unfortunately, the pixel scale for this instrument is quoted to be "≈ 1.3 arcsec," suggesting that the scale may not be known to better than 5%. While the exact pixel scale was irrelevant to Silva & Elston's calculation of color gradients (as the pixel scale cancels out as long as it is constant in both bandpasses), it is clear from Figure 2.11 that there is a relative scale error between the two studies. Hence, any photometric offsets between the two data sets are not useful. There is one galaxy observed by Silva & Elston at Las Campanas Observatory with an accurate measured pixel scale: NGC 720. The offset is $K_s(\text{P60}) - K(\text{SE94}, \text{LCO}) = -0.015$ mag (rms = 0.017 mag). It is instructive to note that Silva & Elston also imaged this galaxy with the other instrument; for that comparison, the offset is $K_s(\text{P60}) - K(\text{SE94}, \text{KPNO}) = -0.102$ mag (rms = 0.054 mag).

The surface photometry of Ferrarese (1996) comprise a magnitude–limited sample of Virgo elliptical galaxies. There are 12 galaxies in common; furthermore, three of these galaxies have two measurements (i.e., P60+C100) and one has three measurements (two at P60 and one at C100), producing 17 comparisons. These comparisons are plotted in Figure 2.13. It is apparent from the SB and ellipticity offsets at small radii that the seeing for Ferrarese's observations was, on average, slightly better. The smaller FOV of Ferrarese's data (79×79 arcsec^2, with no dithering) results in a fundamental limitation: any residual sky subtraction errors cannot be modeled accurately at large radii. There do not appear to be large zero–point errors for each individual galaxy comparison (as was the case with Peletier 1989). For semimajor axis lengths $5 \leq a \leq 25$ arcsec (restricted due to the seeing and sky–subtraction effects), the offset is $K_s(\text{this study}) - K(\text{F96}) = -0.057$ mag (rms = 0.042 mag, $N = 1043$). The rms is not significantly improved by limiting the radial extent of the comparison, suggesting that the source of the scatter is not a relative scale error or sky subtraction within $5 \leq a \leq 25$ arcsec. For the same radial extent, the mean ellipticity offset is $\epsilon(\text{this study}) - \epsilon(\text{F96}) = -0.007$ (rms = 0.012), the mean position angle offset is $\theta(\text{this study}) - \theta(\text{F96}) = -2.8^\circ$ (rms = 19.6°), and the mean fourth–order Fourier coefficient offsets are $A_4(\text{this study}) - A_4(\text{F96}) = +0.18\%$ (rms = 0.10%) and $B_4(\text{this study}) - B_4(\text{F96}) = +0.14\%$ (rms = 0.06%).

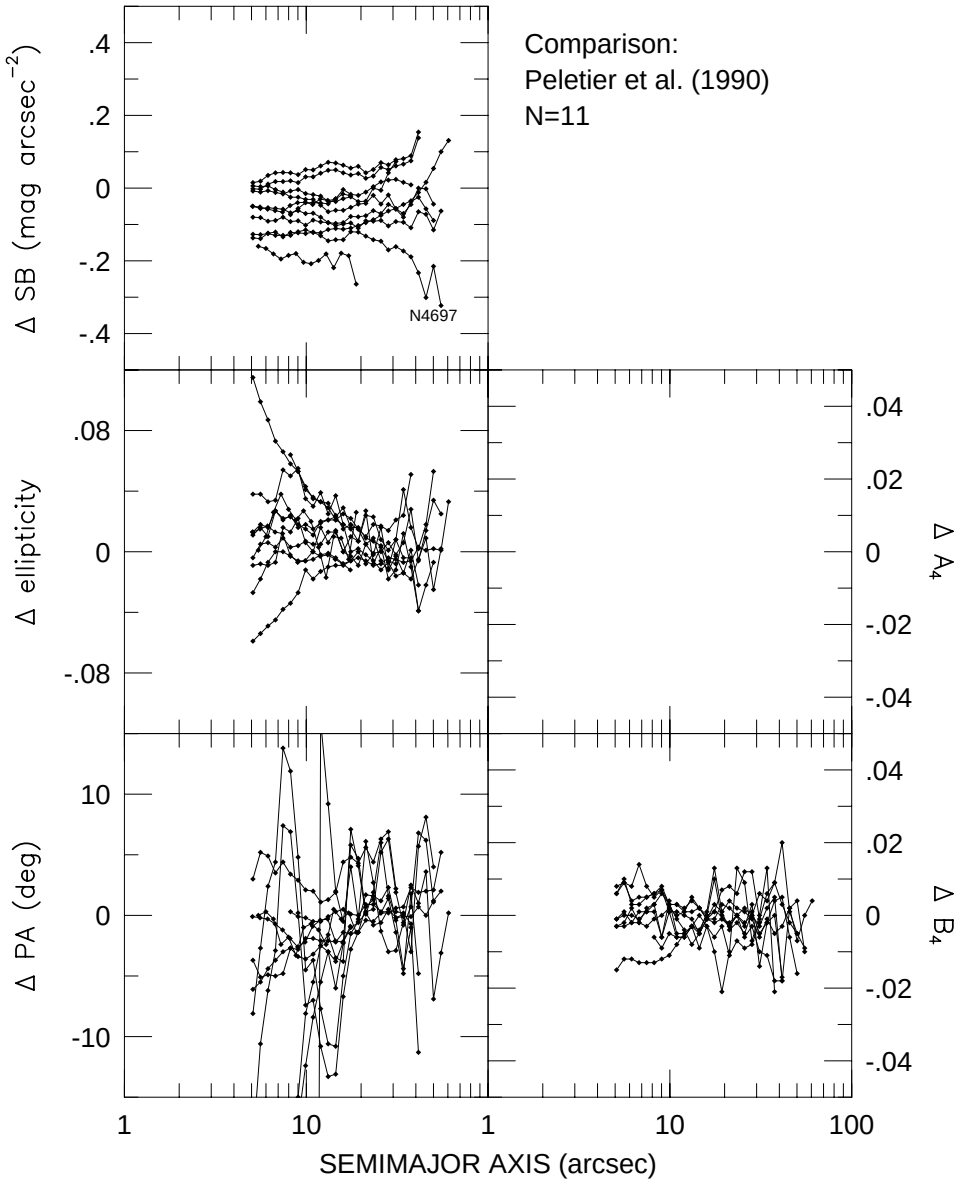

Figure 2.11: Comparison of surface photometry from this survey with Peletier (1989). All comparisons are in the sense of this work minus the literature values.

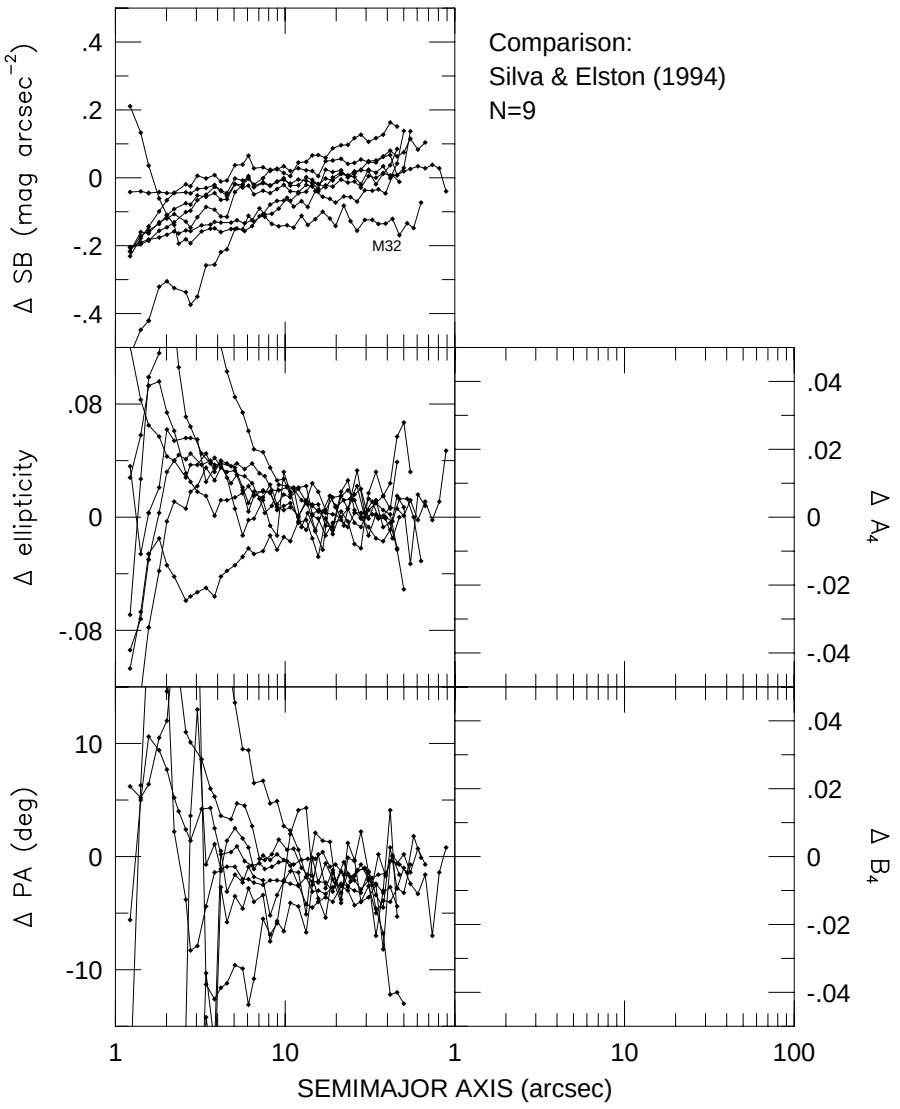

Figure 2.12: Comparison of surface photometry from this survey with Silva & Elston (1994). All comparisons are in the sense of this work minus the literature values. There appears to be a scale error in most of the Silva & Elston surface photometry.

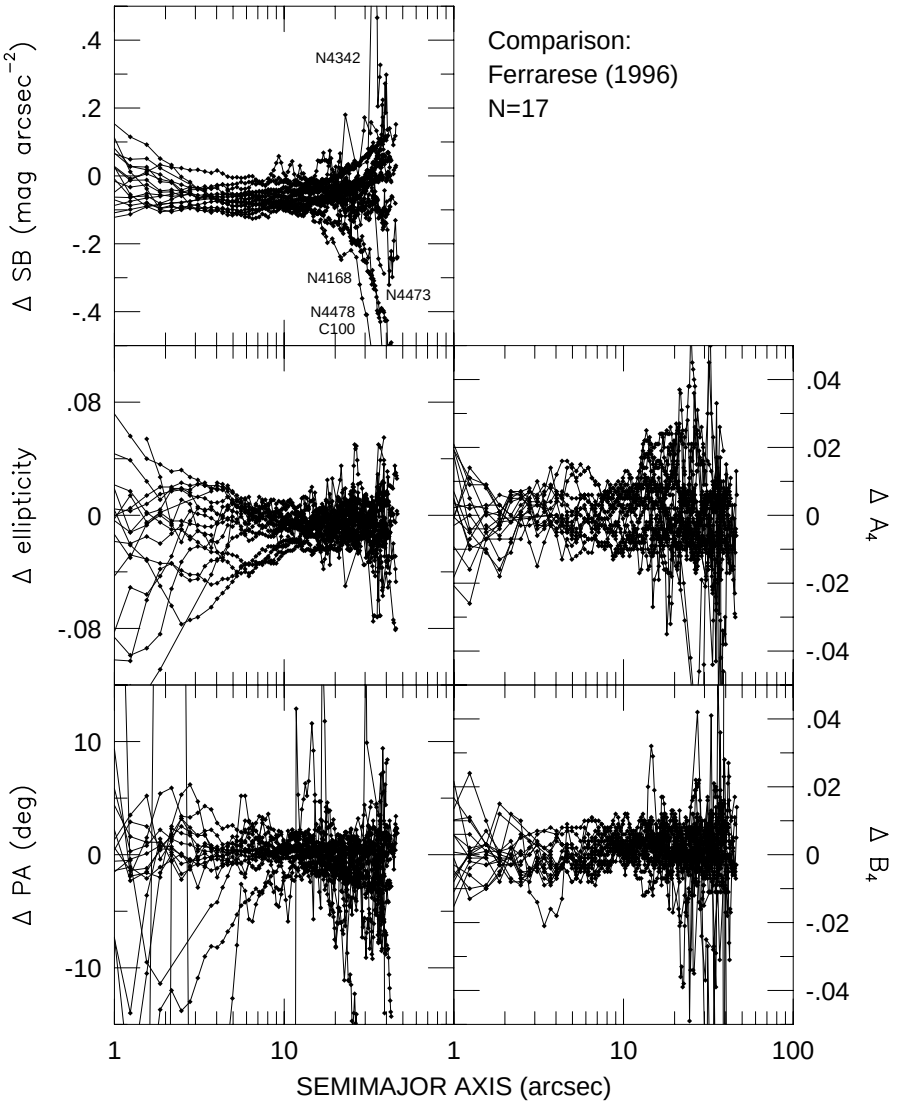

Figure 2.13: Comparison of surface photometry from this survey with Ferrarese (1996). These comparisons are all for galaxies in the Virgo cluster. All comparisons are in the sense of this work minus the literature values. The expected photometric offset is -0.029 mag (see §2.3.5), while the calculated offset is -0.057 mag.

2.9 Additional Global Properties Drawn from the Literature

The goal of this observing program was to observe early–type galaxies in the near–infrared for which optical imaging and spectroscopy data were already available. In this way, it would be possible to compare directly the near–infrared global properties to the optical global properties for the same galaxies. It is therefore necessary to construct an internally self–consistent catalog of optical photometric and spectroscopic measurements.

2.9.1 Photometric Parameters

We wish here to draw the photometric parameters of $r_{\rm eff}$, $\langle\mu\rangle_{\rm eff}$, and aperture magnitudes (to evaluate colors) from the literature. Since seeing effects can be substantial for galaxies with scale sizes comparable to the seeing, literature sources for which seeing corrections have been applied are optimal.

Colors were calculated in one of several ways. The most accurate colors were derived from matched circular apertures for the optical and near–infrared photometry. The number of galaxies for which the color could be calculated was limited to the Virgo ($r = 30$ arcsec) and Coma ($r = 10$ arcsec) clusters (V–band; Lucey *et al.* 1991b; Bower, Lucey, & Ellis 1992a), the Perseus–Pisces region ($R_{\rm C}$–band, $r = 10$ arcsec; Smith *et al.* 1997), and various galaxies in both the field and clusters from photo-electric photometry (V–band, various apertures; Sandage & Visvanathan 1978; Persson, Frogel, & Aaronson 1979). Seeing corrections, Galactic extinction corrections, and k–corrections were applied to both the optical and near–infrared data. In the case of the photo-electric photometry, no seeing corrections were applied to either the optical or near–infrared data; the three largest apertures for which both optical and near–infrared photometry were available were averaged for the color calculation. Colors derived from this method are expected to have uncertainties of order 0.06 mag based on internal comparisons. If such matched aperture magnitudes were not available, colors were calculated at the half–light radius using the curves of growth implied by the measurements of $r_{\rm eff}$ and $\langle\mu\rangle_{\rm eff}$. Since the half–light radii might be significantly different between the optical and near–infrared, the average color was calculated for those cases having the two radius estimates. In cases where only an optical total magnitude was available, the color was calculated using the difference of total magnitudes. These last two

methods are similar in their reliance on the estimate of the total magnitude. As shown in §2.7.3, total magnitudes have large uncertainties of ~ 0.09 mag which are correlated with the error in $\log r_{\rm eff}$. Colors calculated from either of these two methods are therefore identified in the catalog by a colon to designate their larger uncertainties of ~ 0.13 mag.

All color measurements used the B, V, r, $R_{\rm C}$, or $I_{\rm C}$ bandpasses; the offsets used to convert these colors into $(V-K)$ were $(B-V) = 0.95$ mag, $(V-r) = 0.25$ mag (the *observed* offset between the data of Lucey and collaborators and those of Jørgensen and collaborators, as shown by Lucey *et al.* 1997), $(V-R_{\rm C}) = 0.57$ mag (Smith *et al.* 1997), and $(V-I_{\rm C}) = 1.16$ mag (a typical color for elliptical galaxies in the survey of Tonry *et al.* 1997). In the cases of the surveys compiled by Faber *et al.* (1989) and Prugniel & Simien (1996), the observed value for each galaxy of $(B-V)_0$ was used instead of the mean value. The color–magnitude relation in either $(B-V)$ or $(V-R_{\rm C})$ has a slope of ~ -0.01 to -0.03 (Sandage & Visvanathan 1978), while that in $(V-K)$ has slope ~ -0.08, suggesting that the systematic effects on the $(V-K)$ color due to using a mean optical–optical color is small.

The photometric quantities ($\langle\mu\rangle_{\rm eff}$, $m_{\rm tot}$) were brought to a common assumption of Galactic extinction by removing the assumed A_B from each literature source, and applying the values from Table 2.1 instead. The literature measurements of $r_{\rm eff}$ are unaffected Galactic extinction, but the measurements of D_n are. By assuming that elliptical galaxies follow similar curves of growth (see Figure 4 of Dressler *et al.* 1987 and Figure 2.6), the resulting correction is $\Delta D_n = -0.32\Delta\langle\mu\rangle_{\rm eff}$ at constant $r_{\rm eff}$.

The measurements of D_n, $r_{\rm eff}$, and $\langle\mu\rangle_{\rm eff}$ of Faber *et al.* (1989) have been corrected for seeing effects according to the prescription of Saglia *et al.* (1993), using programs provided by R. Saglia and assuming an average seeing of 2 arcsec. These corrections are irrelevant for the nearby galaxies, but can be significant for Coma, Abell 2199, Abell 2634, and other distant clusters.

The literature sources used for constructing this self–consistent catalog of global, optical photometric properties are listed in Table 2.5. They are listed in order of increasing priority, such that the derived value from only the highest priority source was used for each photometric quantity. Since the random uncertainty entering the FP due to the photometric quantities is < 0.02 dex, there is no need to average multiple measurements of each quantity. There are optical $r_{\rm eff}$ and $\langle\mu\rangle_{\rm eff}$ measurements for 80% of the galaxies, D (in any bandpass)

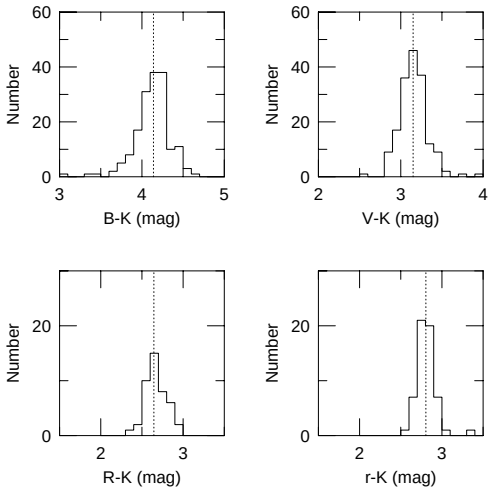

Figure 2.14: Histograms of the global colors for the early–type galaxies in the survey. The median colors are $(B-K) = 4.14$ mag, $(V-K) = 3.15$ mag, $(R_{\rm C}-K) = 2.65$ mag, and $(r-K) = 2.81$ mag. These median colors are shown by a vertical line in each panel.

measurements for 82%, an optical–infrared color for 81%, and an accurate optical–infrared color for 47%.

Histograms of the optical–infrared colors for these galaxies are shown in Figure 2.14. The median colors are $(B-K) = 4.14$ mag, $(V-K) = 3.15$ mag, $(R_{\rm C}-K) = 2.65$ mag, and $(r-K) = 2.81$ mag. These colors may differ slightly from other estimates of the mean colors for early–type galaxies, as the studies in the various optical and infrared bandpasses sample somewhat different portions of the galaxy luminosity function; since there exists a color–magnitude relation, this will contribute to small shifts in the mean color of each subsample for an optical–infrared color.

The diameters $\log D_V$ and $\log D_K$ agree very well with a median offset of 0.007 ± 0.004 dex (rms = 0.048 dex, $N = 281$). This is a strong indication that the mean galaxy color of $(V-K) = 3.2$ mag assumed in defining the D_K parameter is similar to the true mean galaxy colors. There is an expected correlation between the residuals $\log D_V - \log D_K$ and σ

Table 2.5: Literature Sources for Global Photometric Parameters

Source	Filter	Offset	Clusters	Parameters Drawn from Source
Lucey *et al.* (1991a)	V	$\cdots$	A194, A2199, A2634	$r_{\rm eff}$, $\langle\mu\rangle_{\rm eff}$, D_V
Faber *et al.* (1989)	B,V	tabulated $(B-V)_0$	All Sky	$r_{\rm eff}$, $\langle\mu\rangle_{\rm eff}$, D_B, $(B-V)_0$
Lucey & Carter (1988)	V	$\cdots$	A194, Hydra, Centaurus, Klemola 44	D_V, Type
Scodeggio *et al.* (1997)	$I_{\rm C}$	$(V-I_{\rm C})=1.16$	A2634, Coma	$r_{\rm eff}$, $\langle\mu\rangle_{\rm eff}$, Type
Jørgensen *et al.* (1995a)	r	$(V-r)=0.25$	A194, Klemola 44, Hydra, Coma	$r_{\rm eff}$, $\langle\mu\rangle_{\rm eff}$, $D_r=2r_n$
Jørgensen & Franx (1994)	r	$(V-r)=0.25$	Coma	Type
Smith *et al.* (1997)	$R_{\rm C}$	$(V-R_{\rm C})=0.57$	Pisces, Perseus, Coma, A2199	$r_{\rm eff}$, $\langle\mu\rangle_{\rm eff}$, D_R, R_{20}, Type
Lucey *et al.* (1997)	V	$\cdots$	A2199, A2634, Coma	$r_{\rm eff}$, $\langle\mu\rangle_{\rm eff}$, D_V, Type
Lucey *et al.* (1991b)	V	$\cdots$	Coma	$r_{\rm eff}$, $\langle\mu\rangle_{\rm eff}$, D_V, V_{20}
Dressler *et al.* (1991)	B	$(B-V)=0.95$	Hydra–Centaurus Region	D_B
McElroy (1995)		$\cdots$	All Sky	Type
Sandage & Visvanathan(1978)	V	$\cdots$	All Sky	various V aperture magnitudes
Persson *et al.* (1979)	V	$\cdots$	All Sky	various V aperture magnitudes
Bower *et al.* (1992a)	V	$\cdots$	Virgo	$r_{\rm eff}$, $\langle\mu\rangle_{\rm eff}$, D_V, V_{60}
Bower *et al.* (1992a)	V	$\cdots$	Coma	$r_{\rm eff}$, $\langle\mu\rangle_{\rm eff}$, D_V, V_{20}

due to the change in the slope of the FP relations between the optical and near–infrared (see, for example, Guzmán 1995). There is also a clear systematic difference between $\log r_{\rm eff,K}$ and $\log r_{\rm eff,opt}$, in the sense that the infrared effective radii are smaller than the optical ones. Both of these effects will be discussed in future papers (Pahre, Djorgovski, & de Carvalho 1998a, Chapter 3 of this thesis; Pahre, de Carvalho, & Djorgovski 1998b, Chapter 4 of this thesis).

2.9.2 Spectroscopic Parameters

Catalogs of spectroscopic quantities (redshift velocity cz, velocity dispersion σ, and Magnesium line index Mg_2) for elliptical galaxies have attempted to bring heterogeneous compilations of measurements onto a common scale by deriving a scaling number for each individual data set based on measurements in common between several different data sets (Davies *et al.* 1987; McElroy 1995; Prugniel & Simien 1996). The problem with these derivations is that they only deal with the variations in aperture size used to measure the quantity in an indirect way through that scaling constant.

Empirical aperture effects were explored by Jørgensen *et al.* (1995b) using literature data on velocity dispersion and surface brightness profiles. This study found that the velocity dispersion scales with the aperture radius r as $\log\left[\sigma(r)/\sigma(r_0)\right] = \alpha \log(r/r_0)$, where r_0 is a fiducial physical radial size (say, in kpc) and $\alpha = -0.04$ on average. There is some variation of α from galaxy to galaxy which is systematic, not random, in the sense that galaxies with larger σ have steeper profiles with $\alpha = -0.06$, while those with small σ have shallower profiles with α as low as -0.02. This effect would be expected of small, systematic variations of the velocity distributions within those galaxies from a homologous family. Instead of attempting to correct for this variation, we will adopt the null hypothesis that there is no such systematic bias of α with σ, meaning that the velocity distributions of ellipticals comprise a homologous family, and therefore scale all galaxy spectroscopic measurements using $\alpha = -0.04$.

Jørgensen *et al.* (1995b) and Smith *et al.* (1997) have both utilized this mean α to correct σ and Mg_2 for aperture effects, and then attempt to bring a large body of spectroscopic data onto a common system. The offsets for various systems are tabulated by Smith *et al.* (their Tables 6 and 7) and have been used in calculating mean σ and Mg_2 for the galaxies observed at K in the present survey. Their approach of correcting all data onto an aperture

of diameter $1.53h_{75}^{-1}$ kpc, corresponding to a 3.4 arcsec diameter circular aperture at the distance of the Coma cluster, is adopted here. Two small modifications were made. One, the three high–resolution LCO observing runs in Davies *et al.* (1987) were not subdivided, as their offsets relative to one another are small and possibly statistically insignificant; instead, an offset of $\Delta\sigma = +0.0046$ dex and $\Delta \mathrm{Mg}_2 = -0.0131$ dex, the weighted mean of the three subdivided data sets, was adopted. Two, the Dressler (1984) measurements in Virgo using a 16×16 arcsec^2 effective aperture, and similar Fornax measurements in Dressler *et al.* (1987), were incorporated into this system by assuming the "LCOHM" offset from the 1983 March run. Several additional data sets were also used and are listed in Table 2.6. Note that the FLEX measurements for Abell 2634 (Lucey *et al.* 1991a) were not used as they appear to suffer from charge transfer problems (see the discussion in Lucey *et al.* 1997), but those for Abell 2199 and Abell 194 were used.

The typical random error for a single measurement of σ is ~ 0.04 dex (Smith *et al.* 1997), so the random error for the mean value of σ is > 0.01 dex for even the best studied galaxies. Smith *et al.* note that the residual systematic errors from this data set matching method are still ~ 0.01 dex. The random uncertainty entering the near–infrared FP due to the velocity dispersion is therefore at least 0.015 dex per well–studied galaxy (due to the slope of ~ 1.5 between $\log r_{\mathrm{eff}}$ and $\log \sigma$; Pahre, Djorgovski, & de Carvalho 1995), and significantly more at $\sim 0.04 - 0.06$ dex for galaxies with only one measurement. For Mg_2 the random uncertainty of each individual measurement is typically ~ 0.013 dex. Of the 341 galaxies, only 5% have no σ available from the literature. Most of these were not targeted galaxies, but rather ones that happened to land within the FOV during observations of another galaxy. There are Mg_2 measurements for 69% of the galaxies.

2.9.3 Catalogs of Global Photometric and Spectroscopic Parameters for Various Optical Bandpasses

Catalogs comparing the global photometric parameters between various optical bandpasses have been constructed in the same manner as the optical–infrared catalog described above in §2.9.2 and §2.9.1. These catalogs use the sources of optical photometry given in Tables 2.5 and 2.6. These catalogs are provided in tabular form in Appendix A.

Table 2.6: Literature Sources for Spectroscopic Parameters

Source	Aperture (arcsec^2)	$\Delta \log \sigma$ (km s^{-1})	ΔMg$_2$ (mag)	Clusters	Parameters Drawn from Source
Lucey *et al.* (1991a)	2.55	−0.0127	···	A194, A2199, A2634	σ
Lucey *et al.* (1991b)	2.0×5.8	−0.0177	···	Coma	σ
Lucey *et al.* (1997)	3.0×3.3	+0.0080	0.0168	A2199, A2634	σ, Mg$_2$
Davies *et al.* (1987)				All sky	σ, Mg$_2$
LICK	1.5×4.0	$\equiv 0$	$\equiv 0$		
KPNO	2.3×4.2	+0.0142	−0.0034		
PAL	2.0×4.0	−0.0241	−0.0143		
LCOLO	2.0×4.0	+0.0115	−0.0032		
LCOHI	4.0×4.0	+0.0046	−0.0131		
A1	2.0×7.0	−0.0057	+0.0074		
A2	2.0×7.0	+0.0176	−0.0132		
Dressler (1984)	16×16	+0.0176	−0.0132	Virgo	σ, Mg$_2$
Dressler *et al.* (1987)	16×16	+0.0176	−0.0132	Fornax	σ, Mg$_2$
Dressler *et al.* (1991)	2.0×4.0	−0.0038	−0.0035	Hydra–Centaurus	σ, Mg$_2$
Lucey & Carter (1988)	5.73	−0.0127	···	A194, Hydra, Centaurus, Klemola 44	σ
Scodeggio *et al.* (1997)	2.0×6.0	0	···	Coma, A2634	σ
Jørgensen *et al.* (1995b)					
New measurements	2.5×8.2, 2.5×6.8, 5.31	+0.0011	−0.0017	A194, Hydra, Klemola 44, Other	σ, Mg$_2$
Literature Compilation	···	+0.0011	−0.0017	A194, Klemola 44, Coma	σ, Mg$_2$
Smith *et al.* (1997)				Perseus, Pisces, A2199, A2634, Coma, Other	σ, Mg$_2$
EEV93	3.0×3.3	−0.0014	+0.0172		
EEV94	3.0×3.3	−0.0115	···		
TEK94	3.0×3.5	−0.0063	+0.0071		
McElroy (1995)	···	0	···	All Sky	σ
Prugniel & Simien (1996)	···	0	···	All Sky	σ

2.10 Discussion

This paper presents a homogeneous body of near–infrared photometry of early–type galaxies. The quality of the photometry has been shown to be comparable to, or better than, the best such near–infrared studies in the past 20 years. The size of the galaxy sample studied is comparable to the sum of all these previous studies. This study provides the first set of global, near–infrared photometric parameters in the literature for nearby early–type galaxies.

It is hoped that these data will provide a unique perspective on early–type galaxies by studying them at a wavelength that is nearly independent of metallicity effects and dominated by the emission of the stars on the giant branch.

There are many possible uses for a data set of this size and homogeneity. Studies of the elliptical galaxy correlations at a variety of wavelengths could provide a breaking of the age–metallicity degeneracy (Worthey 1994) which has hampered investigations into the physical origins of these correlations. Other studies of the evolution of elliptical galaxies with redshift require a detailed understanding of the properties of these old stellar populations at low redshifts. The wide variety of local environments spanned by this sample will provide information suitable for comparison to both cluster and the general field at higher redshifts.

Acknowledgments

Julia Kennefick, Chris Fassnacht, and Reinaldo de Carvalho are thanked for observing several nights at the P60. Jeremy Mould kindly allowed the C100 data to be used as an external check on the C40 and P60 photometry. David Silva and Laura Ferrarese generously provided their K–band surface photometry, Roberto Saglia provided his seeing corrections, and Rafael Guzmán and Mike Hudson provided tables in electronic form. Many helpful discussions were provided by George Djorgovski, Rafael Guzmán, Mike Hudson, John Lucey, Keith Matthews, and Eric Persson. Reinaldo de Carvalho is thanked for stimulating conversations and sage advice on elliptical galaxies. This research has made use of the NASA/IPAC Extragalactic Database (NED) which is operated by the Jet Propulsion Laboratory, California Institute of Technology, under contract with the National Aeronautics and Space Administration. During the course of this project, M. A. P. received financial support from Jesse Greenstein and Kingsley Fellowships, the Bressler Foundation, and NSF

grants AST–9123646 and AST–9157412 to S. G. Djorgovski. The P60 near–infrared camera could not have been constructed without the tireless efforts of David Murphy, Eric Persson, and Anand Sivaramakrishnan at OCIW, nor without financial support from the Perkin Fund, the Jeanne Rich Foundation, and Rockwell International Corporation. The staffs at Palomar and Las Campanas Observatories are thanked for their patience, professionalism, and efficiency.

References

Bower, R. G., Lucey, J. R., & Ellis, R. S. 1992a, MNRAS, 254, 589

Bower, R. B., Lucey, J. R., & Ellis, R. S. 1992b, MNRAS, 254, 601

Burstein, D., & Heiles, C. 1982, AJ, 87, 1165

Cardelli, J. A., Clayton, G. C., & Mathis, J. S. 1989, ApJ, 345, 245

Casali, M. M., & Hawarden, T. G. 1992, JCMT-UKIRT Newsletter, 3, 33

Colless, M., Burstein, D., Wegner, G., Saglia, R. P., McMahan, R., Davies, R. L., Bertschinger, E., & Baggley, G. 1993, MNRAS, 262, 475

Davies, R. L., Burstein, D., Dressler, A., Faber, S. M., Lynden–Bell, D., Terlevich, R. J., & Wegner, G. 1987, ApJS, 64, 581

Djorgovski, S., & Davis, M. 1987, ApJ, 313, 59

van Dokkum, P. G., & Franx, M. 1995, AJ, 110, 2027

Dressler, A., Faber, S. M., & Burstein, D. 1991, ApJ, 368, 54

Dressler, A., Lynden-Bell, D., Burstein, D., Davies, R. L., Faber, S. M., Terlevich, R. J., & Wegner, G. 1987, ApJ, 313, 42

Faber, S. M., Wegner, G., Burstein, D., Davies, R. L., Dressler, A., Lynden-Bell, D., & Terlevich, R. J. 1989, ApJS, 69, 763

Ferrarese, L. 1996, Ph.D. Thesis, The Johns Hopkins University

Franx, M., Illingworth, G., & Heckman, T. 1989, AJ, 98, 538

Frogel, J. A. 1971, Ph.D. Thesis, California Institute of Technology

Frogel, J. A., Persson, S. E., Aaronson, M., Becklin, E. E., Matthews, K., & Neugebauer, G. 1978, ApJ, 220, 75

Frogel, J. A., Persson, S. E., Aaronson, M., & Matthews, K. 1978, ApJ, 220, 75

Goudfrooij, P., & de Jong, T. 1995, A&A, 298, 784

Graham, A., & Colless, M. 1997, MNRAS, 287, 221

Guzmán, R. 1995, in proceedings of the Heron Island Workshop on Peculiar Velocities in the Universe, `http://qso.lanl.gov/~heron/`

Jørgensen, I., & Franx, M. 1994, ApJ, 433, 553

Jørgensen, I., Franx, M., & Kjærgaard, P. 1992, A&A, 95, 489

Jørgensen, I., Franx, M., & Kjærgaard, P. 1993, ApJ, 411, 34

Jørgensen, I., Franx, M., & Kjærgaard, P. 1995a, MNRAS, 273, 1097

Jørgensen, I., Franx, M., & Kjærgaard, P. 1995b, MNRAS, 276, 1341

Jørgensen, I., Franx, M., & Kjærgaard, P. 1996, MNRAS, 280, 167

Jura, M., Kim, D.–W., Knapp, G. R., Guhathakurta, P. 1987, ApJ, 312, L11

Laureijs, R. J., Helou, G., & Clark, F. O. 1994, in Proceedings of The First Symposium on the Infrared Cirrus and Diffuse Interstellar Clouds, ASP Conf. Ser. Vol. 58, eds. R. M. Cutri & W. B. Latter (San Francisco, ASP), 133

Lucey, J. R., Bower, R. B., & Ellis, R. S. 1991, MNRAS, 249, 755

Lucey, J. R., & Carter, D. 1988, MNRAS, 235, 1177

Lucey, J. R., Gray, P. M., Carter, D., & Terlevich, R. J. 1991a, MNRAS, 248, 804

Lucey, J. R., Guzmán, R., Carter, D., & Terlevich, R. J. 1991b, MNRAS, 253, 584

Lucey, J. R., Guzmán, R., Steel, J., & Carter, D. 1997, MNRAS, 287, 899

Lynden–Bell, D., Faber, S. M., Burstein, D., Davies, R. L., Dressler, A., Terlevich, R. J., & Wegner, G. 1988, ApJ, 326, 19

McElroy, D. B. 1995, ApJS, 100, 105

Mobasher, B., Guzmán, R., Aragón-Salamanca, & Zepf, S. 1997, MNRAS, submitted

Murphy, D., Persson, S. E., Pahre, M. A., Sivaramakrishnan, A., & Djorgovski, S. G. 1995, PASP, 107, 1234

Pahre, M. A., & Mould, J. R. 1994, ApJ, 433, 567

Pahre, M. A., Djorgovski, S. G., & de Carvalho, R. R. 1995, ApJ, 453, L17

Pahre, M. A., Djorgovski, S. G., & de Carvalho, R. R. 1998a, in preparation [Chapter 3 of this thesis]

Pahre, M. A., de Carvalho, R. R., & Djorgovski, S. G. 1998b, in preparation [Chapter 4 of this thesis]

Peletier, R. F. 1989, Ph.D. Thesis, Rijksuniversiteit Groningen

Peletier, R. F., Davies, R. L., Illingworth, G. D., Davis, L. E., & Cawson, M. 1990, AJ, 100,

1091

Persson, S. E., Frogel, J. A., & Aaronson, M. 1979, ApJS, 39, 61

Persson, S. E., West, S. C., Carr, D. M., Sivaramakrishnan, A., & Murphy, D. C. 1992, PASP, 104, 204

Persson, S. E. 1997, private communication

Prugniel, P., & Simien, F. 1996, A&A, 309, 749

Recillas-Cruz, E., Carrasco, L., Serrano, P. G., & Cruz-González, I. 1990, A&A, 229, 64

Recillas-Cruz, E., Carrasco, L., Serrano, P. G., & Cruz-González, I. 1991, A&A, 249, 312

Saglia, R. P., Bertschinger, E., Baggley, G., Burstein, D., Colless, M., Davies, R. L., McMahan, R. K., Jr., & Wegner, G. 1997, ApJS, 109, 79

Sandage, A., & Visvanathan, N. 1978, ApJ, 223, 707

Schechter, P. L. 1997, in The Nature of Elliptical Galaxies, Proceedings of the Second Stromlo Symposium, eds. M. Arnaboldi, G. S. Da Costa, & P. Saha, ASP Conf. Ser. Vol. 116, (San Francisco: ASP), 563

Schlegel, D. J., Finkbeiner, D. P., & Davis, M. 1997, ApJ, submitted

Scodeggio, M., Giovanelli, R., & Haynes, M. P. 1997, AJ, 113, 101

Silva, D. R., & Elston, R. 1994, ApJ, 428, 511

Smith, R. J., Lucey, J. R., Hudson, M. J., & Steel, J. 1997, MNRAS, in press

Sparks, W. B., & Jørgensen, I. 1993, AJ, 105, 1753

Tonry, J. L., Ajhar, E. A., & Luppino, G. A. 1990, AJ, 100, 1416

Tonry, J. L. 1991, ApJ, 373, L1

Tonry, J. L., Blakeslee, J. P., Ajhar, E. A., & Dressler, A. 1997, ApJ, 475, 399

Worthey, G. 1994, ApJS, 95, 107

Chapter 3

The Near–Infrared Fundamental Plane of Early–Type Galaxies

Abstract

Near–infrared imaging data on 251 early–type galaxies in clusters and groups are used to construct the near–infrared Fundamental Plane (FP)

$$r_{\rm eff} \propto \sigma_0^{1.53\pm0.08} \langle \Sigma_K \rangle_{\rm eff}^{-0.79\pm0.03}.$$

The slope of the FP departs from the virial expectation of $r_{\rm eff} \propto \sigma_0^2 \langle \Sigma \rangle_{\rm eff}^{-1}$ at all wavelengths, which could be a result of the variation of M/L along the elliptical galaxy sequence, or a systematic breakdown of homology among the family of elliptical galaxies. The slope of the near–infrared FP alone excludes metallicity variations as the sole cause of the slope of the FP. Age effects, dynamical deviations from a homology, or any combination of these (with or without metallicity), however, are not excluded. The scatter of both the near–infrared and optical FP are nearly identical and substantially larger than the observational uncertainties, demonstrating small but significant intrinsic cosmological scatter for the FP at all wavelengths. The lack of a correlation of the residuals of the near–infrared FP and the residuals from the $\rm Mg_2$–σ_0 relation indicates that the thickness of these relations cannot be ascribed only to age or only to metallicity effects. Due to this metallicity independence, the small scatter of the near–infrared FP excludes a model in which age and metallicity effects "conspire" to keep the optical FP thin. The diagnostic relationship between $\log D_K/D_V$ and $\log \sigma_0$ shows no significant dependence on environment within the uncertainties of the Galactic extinction corrections, demonstrating the universality of the global scaling relations. All of these results suggest that the possible physical origins of the FP relations are complicated due to combined effects of variations of stellar populations and structural parameters among elliptical galaxies.

3.1 Introduction

Correlations among the properties of elliptical galaxies have been used both as measures of their homogeneity as a population and as indicators of the distances of individual galaxies. The discovery of a color–magnitude effect (Baum 1959) was followed by the measurement of relative distances of galaxies and clusters using the color–magnitude relation (Sandage 1972; Visvanathan & Sandage 1977; Sandage & Visvanathan 1978a,b). The relation's small scatter was used as a constraint on elliptical galaxy formation time-scales (Bower, Lucey, & Ellis 1992b). The correlation between luminosity and velocity dispersion (Faber & Jackson 1976) was likewise used as a distance indicator (Tonry & Davis 1981; Dressler 1984), but there Terlevich *et al.* (1981) discovered a weak correlation between the residuals of the relation and Mg_2, suggesting that there might be a second parameter which contributes to the intrinsic scatter of the Faber–Jackson relation.[1] Subsequent studies (Dressler *et al.* 1987; Djorgovski & Davis 1987) that included large samples of elliptical galaxies found that surface brightness was a second parameter which caused a large portion of the scatter in the Faber–Jackson relation. In this perspective, the intrinsic properties of elliptical galaxies are only found to lie on a plane within the three–dimensional parameter space of the observables. This Fundamental Plane (FP) is thus a set of bivariate correlations between the observed properties of elliptical galaxies; the color–magnitude and Faber–Jackson relations are projections of that plane onto two of the three axes.

The importance of the exact form of the slope of the FP was immediately identified (Dressler *et al.* 1987; Djorgovski & Davis 1987) as possibly providing a strong constraint on the mass–to–light ratios (M/L) of elliptical galaxies. In particular, the virial theorem produces a prediction that $r_{\rm eff} \propto \sigma_0^2 \langle\Sigma\rangle_{\rm eff}^{-1}$ if two assumptions are made: (1) that M/L is the same for all elliptical galaxies, and (2) that elliptical galaxies form a homologous family for their scaling properties. The latter assumption was generally taken to be true, hence virtually all researchers in the last decade have proceeded to explore the effects of the variations of M/L implied by the FP correlations. For example, the slope of $D_n \propto \sigma_0^{1.2}$ from Lynden–Bell *et al.* (1988) in the B–band implies that M/L varies systematically with

[1] Dressler *et al.* (1987) describe how this evidence for the bivariate nature of elliptical galaxies found by Terlevich *et al.* (1981) might actually have been driven more by distance errors in the Terlevich *et al.* sample, which was drawn primarily from the field, and from a surface brightness correlation which was later found to be the second parameter. After correcting for surface brightness effects, Dressler *et al.* found little or no correlation among the residuals of the Faber–Jackson relation and Mg_2.

the galaxy's luminosity as $M/L_B \propto L_B^{0.32}$.

More recently, there have been a variety of theoretical (Capelato, de Carvalho, & Carlberg 1995, 1997; Ciotti, Lanzoni, & Renzini 1996) and observational (Graham & Colless 1997; Busarello *et al.* 1997) investigations into the question of whether or not elliptical galaxies form a homologous scaling family. The results of these studies are not yet clear, but they seem to imply that structural deviations of the light profiles of ellipticals from a homologous family cannot effect the FP appreciably (Graham & Colless 1997), while dynamical deviations from a homologous family can (Capelato, de Carvalho, & Carlberg 1995; Busarello *et al.* 1997; cf. Graham & Colless 1997). Underlying all of these studies is an important point: if there are significant and systematic deviations from a homology, then these deviations should be strictly independent of wavelength observed in constructing the global photometric parameters which enter the FP.

In a broad sense, some of these possible implications of the FP make specific predictions which can be tested by obtaining additional data. For example, if the form of the FP is a direct result of a dependence of M/L on L due to variations in the stellar populations parameters of age and/or metallicity, then observations in the near–infrared should show a significantly different form for the FP correlations as the 2.2μm light is far less sensitive than optical light both to line–blanketing and somewhat less sensitive to age effects. Alternatively, if the origin of the FP is due to a systematic deviation of elliptical galaxies from a homologous family, then the exact form of the FP should be independent of wavelength. It is also possible that some combination of these effects could be required by a simultaneous analysis of the FP at optical and near–infrared wavelengths.

The present paper is an attempt to address these possible origins for the FP correlations by exploring their form using near–infrared imaging data. Early work on the FP in the K–band was done by Recillas–Cruz *et al.* (1990, 1991), who obtained aperture photometry for galaxies in Virgo and Coma, and Djorgovski & Santiago (1993), who used aperture photometry from Persson, Frogel, & Aaronson (1979). Both studies relied on optical estimates of $r_{\rm eff}$. It follows directly from the existence of color gradients that $r_{\rm eff}$ should be smaller for longer wavelengths and this point will be shown explicitly in a future paper (Pahre, de Carvalho, & Djorgovski 1998b, Chapter 4 of this thesis) for these optical and near–infrared data. The present paper is more than just a revisiting of the K–band FP—it is an attempt to study the global properties of elliptical galaxies using near–infrared photometry that is

fully independent of the optical photometry, while at the same time using a methodology for deriving global photometric parameters that is identical to method at optical wavelengths.

An imaging survey of this kind and scale has only recently become possible with the introduction of large format IR detectors (256×256 pixel^2). This project was initiated during the commissioning phase of a wide–field, near–infrared imaging camera (Murphy *et al.* 1995) for the Palomar 60–inch Telescope. In the first paper of this series, early results from this survey on the K–band FP (Pahre, Djorgovski, & de Carvalho 1995) indicated that there is a modest change in slope from the optical to the near–infrared, but not nearly as much variation as would be expected if stellar–populations alone were the cause of the slope of the FP (Pahre & Djorgovski 1997; Pahre, Djorgovski, & de Carvalho 1997). The full K–band survey and the complete catalogs of global properties are described in the second paper of this series (Pahre 1998a, Chapter 2 of this thesis) and are summarized in §3.2. All of the data contained in the previous contributions (Pahre, Djorgovski, & de Carvalho 1995, 1997; Pahre & Djorgovski 1997) were re–calibrated, some were re–reduced, and the global photometric parameters re–derived in a consistent manner as described in Pahre (1998, Chapter 2 of this thesis). The FP correlations and their many projections are derived in §3.3 as a way of exploring various aspects of these near–infrared data. The Mg_2–σ_0 relation is constructed from these data in §3.3.4. Simple models will be compared to these results in §3.4, but it will be shown that such naive models can neither explain the many observed properties of ellipticals nor are they unique.

3.2 Description of the Data

The data used for this paper derive from Pahre (1998, Chapter 2 of this thesis). That paper presented near–infrared K–band imaging of 341 early–type galaxies, and used these data to measure the global photometric parameters of half–light effective radius $r_{\rm eff}$, mean surface brightness $\langle\mu\rangle_{\rm eff}$ enclosed by that radius, total magnitude $K_{\rm tot}$, and the diameter D_K at which the mean surface brightness, fully corrected for cosmological effects and extinction, drops to 16.6 mag arcsec^{-2}. The latter parameter is an analog of the B–band D_n parameter defined by Dressler *et al.* (1987). The near–infrared data were corrected for the effects of seeing. As shown in that paper, the random uncertainties of the measured quantities are: 0.06 dex on $r_{\rm eff}$; 0.21 mag on $\langle\mu\rangle_{\rm eff}$; 0.09 mag on $K_{\rm tot}$; 0.010 dex on D_K; and 0.015 dex on

$r_{\rm eff} - 0.32\langle\mu\rangle_{\rm eff}$, the quantity which will enter the FP.

The galaxies in that sample are primarily drawn from nearby rich clusters of galaxies, although additional galaxies were added from groups and the general field. The galaxies were not selected according to any explicitly criteria of completeness (such as a magnitude–limited sample would be), but by the availability of companion optical imaging and spectroscopic data. The primary goal of this effort was to provide a large sample of galaxies for which the variations of the FP correlations between the optical and near–infrared wavelengths could be explored. The data probe the full range of properties ($r_{\rm eff}$, $K_{\rm tot}$, σ_0) displayed by the family of giant elliptical galaxies, and a significant portion of the sample is comprised of S0 galaxies.

The optical global photometric parameters ($r_{\rm eff}$, $\langle\mu\rangle_{\rm eff}$, and D_n) and spectroscopic parameters (central velocity dispersion σ_0 and Magnesium line index $\rm Mg_2$) were compiled from the literature by Pahre (1998, Chapter 2 of this thesis). All of the photometry were drawn from the B, V, $R_{\rm C}$ (or r) bandpasses and converted to V magnitudes for a general catalog. Furthermore, separate catalogs were constructed for individual comparisons to preserve the wavelength information between these four optical bandpasses. The spectroscopic parameters were corrected for observed aperture size effects to a common physical scale of $1.53h_{75}^{-1}$ kpc; small offsets between data sets have been applied according to prescriptions developed by other authors in the literature. The values were then averaged to reduce the random uncertainties and minimize systematic errors due to some data sets. Of the 341 galaxies imaged in the K–band, 95% have velocity dispersions, 69% have $\rm Mg_2$ indices, and 91% have optical photometric parameters (either $r_{\rm eff}$ or D_n). The typical uncertainties for individual measurements of σ_0 and $\rm Mg_2$ are 0.04 dex and 0.013 mag (Smith *et al.* 1997). A substantial fraction of the entire sample has more than one measurement of these parameters which were then averaged, so these two uncertainty estimates can be taken as a universal upper limit to the measurement uncertainties.

Many, if not most, of the literature sources suggest that their velocity dispersions are less reliable below 100 km $\rm s^{-1}$, but a bias in the slope of the FP can be introduced by imposing a cut on σ_0. It will be important to investigate what effect changing the lower cutoff for σ_0 has on the slope and scatter of the FP. Small measures of the effective radius, such as $r_{\rm eff} \leq 1$ arcsec (the median seeing was 1.34 arcsec FWHM), have large random uncertainties and probably substantial systematic errors, and should probably also be discarded. In the

sample, 4% of the galaxies have morphological type SB0 or later, and another 4% have S0/a type; caution should be exercised when studying the global properties of these galaxies. One galaxy (D45 in cluster Abell 194) appears to be a misidentification either in the optical or near–infrared as evidenced by its color $(V-K) = 1.28$ mag, which appears to be much too blue compared to the mean $(V-K) = 3.15$ mag for the entire sample. Five galaxies in the Virgo cluster were removed from the sample, as their accurate distances as derived by the surface brightness fluctuations method (provided by J. Blakeslee and J. Tonry; see Tonry *et al.* 1997) show that they are either in the background W Cloud (NGC 4168, NGC 4261, and NGC 4365) or the foreground (NGC 4660 and NGC 4697).

3.3 Analysis of the Elliptical Galaxy Correlations

3.3.1 The Near–Infrared Fundamental Plane

Galaxies were drawn from the sample described in §3.2. Only those galaxies residing in a cluster or group with four or more observed galaxies were included in the FP fits, resulting in 16 clusters/groups and 249 galaxies with $\sigma_0 > 1.8$. Two of the five Leo I Group galaxies were excluded as a result of these selection criteria, although the remaining three galaxies were retained in the sample for completeness.

The "standard" FP equation is usually written as

$$\log r_{\rm eff}({\rm arcsec}) = a \log \sigma_0({\rm km\ s^{-1}}) + b\langle\mu\rangle_{\rm eff}({\rm mag\ arcsec^{-2}}) + c_i \qquad (3.1)$$

where a is usually identified as the "slope" of the FP and c_i are the "intercepts." The intercept of the relation will vary with distance. The galaxies in each of the 16 groups and clusters are assumed to lie at the same distance, hence there are $i = 16$ different intercepts c_i.

The Equation 3.1 was fit by minimizing the sum of the absolute deviations of the points orthogonally from the relation. During the first iteration, two points which are outliers (D9 in Cen30 and S201 in Hydra) were identified and excluded from the analysis. The resulting

FP in the near–infrared K–band is

$$\begin{aligned} \log r_{\rm eff}({\rm arcsec}) &= 1.53\log\sigma_0 + \quad 0.314\langle\mu_K\rangle_{\rm eff} + c_i \quad N = 251 \quad {\rm rms} = 0.096 \text{ dex} \\ &\quad\ \pm 0.08 \qquad\quad \pm 0.011 \end{aligned} \tag{3.2}$$

The uncertainties in the coefficients were determined by 100 iterations of bootstrap resampling of the data-points. The individual intercepts c_i for the fit, and the rms about the fit for each cluster or group, are listed in Table 3.1. Since the rms is quoted in units of $\log r_{\rm eff}$, the uncertainty on each intercept is therefore ${\rm rms}/\sqrt{N-1}$. The relation in Equation 3.2 is equivalent to the scaling relation $r_{\rm eff} \propto \sigma_0^{1.53\pm0.08}\langle\Sigma_K\rangle_{\rm eff}^{-0.79\pm0.03}$.

Changing the lower cutoff for σ_0 from 1.8 dex to 2.0 dex changes the value of a by $\leq$ 0.01 dex, changes b by $\leq$ 0.001 dex, reduces the scatter by 10% to 0.089 dex, and excludes 23 galaxies (9% of the total). Hence, the solution to the FP is robust to the lower σ_0 cutoff, although the galaxies with the lowest σ_0 appear to contribute the largest to the observed scatter. Minimizing the orthogonal variance (instead of the absolute value of the deviation) from the FP relation results in a small change in the slope of the FP to:

$$\begin{aligned} \log r_{\rm eff}({\rm arcsec}) &= 1.63\log\sigma_0 + \quad 0.320\langle\mu_K\rangle_{\rm eff} + c_i \quad N = 251 \quad {\rm rms} = 0.099 \text{ dex} \\ &\quad\ \pm 0.06 \qquad\quad \pm 0.008 \end{aligned} \tag{3.3}$$

Since the coefficients in Equations 3.2 and 3.3 are equivalent within the uncertainties, the fit to the FP is insensitive to the exact fitting method. The method of minimizing the absolute value of the orthogonal deviation from the fit is to be preferred, however, as it is less sensitive to outliers.

The simultaneous fit to all clusters is displayed in Figure 3.1 with the data subdivided into the 16 individual clusters or groups. It is clear from this figure that the simultaneous fit is a representative description of the properties of the early–type galaxies in all of the clusters. There is no clear deviation from this mean relation.

The 11 clusters with more than ten galaxies were fit individually to Equation 3.1 as a test of the universality of the FP relation. The difficulty with these fits, however, is that the number of galaxies in each cluster is small enough that the slope of the relation is not accurately determined. Once again, the uncertainties on the fitted coefficients a and b have

Table 3.1: Fits for Each Cluster or Group for the Near–Infrared FP

Cluster or	Simultaneous Fit			Individual Fits					Constrained $b = 0.314$ Fits		
Group	c_i	N	rms (dex)	a	Δa	b	Δb	rms (dex)	a	Δa	rms (dex)
(1)	(2)	(3)	(4)	(5)	(6)	(7)	(8)	(9)	(10)	(11)	(12)
Coma	-7.950	60	0.086	1.33	0.19	0.302	0.03	0.082	1.57	0.15	0.088
A194	-7.734	16	0.107	1.57	0.21	0.254	0.05	0.106	1.60	0.16	0.110
A2199	-8.128	23	0.093	1.53	0.22	0.342	0.03	0.088	1.40	0.16	0.086
A2634	-8.028	15	0.076	1.19	0.74	0.292	0.06	0.061	1.24	0.30	0.063
Cen45	-7.543	6	0.071	...	...	...	...	...	...	...	...
Cen30	-7.526	14	0.124	1.72	0.41	0.299	0.08	0.123	2.05	0.39	0.139
Fornax	-7.274	15	0.137	2.56	0.65	0.339	0.06	0.156	2.11	0.30	0.128
Hydra	-7.669	17	0.086	1.76	0.34	0.344	0.03	0.080	1.77	0.15	0.086
Klemola 44	-8.041	11	0.067	1.50	0.58	0.309	0.05	0.068	1.74	0.28	0.069
Pegasus	-7.580	4	0.048	...	...	...	...	...	...	...	...
Perseus	-7.802	19	0.100	1.98	0.59	0.310	0.05	0.125	1.66	0.33	0.104
Pisces	-7.723	11	0.087	1.04	0.27	0.350	0.05	0.055	1.17	0.19	0.055
Virgo	-7.175	27	0.115	1.77	0.25	0.374	0.03	0.120	1.62	0.12	0.118
Eridanus	-7.312	5	0.061	...	...	...	...	...	...	...	...
Leo	-6.932	3	0.253	...	...	...	...	...	...	...	...
N5846grp	-7.436	5	0.101	...	...	...	...	...	...	...	...

Notes: (1) The FP fits in this table are to the form of Equation 3.1. (2) The simultaneous fit for columns 2–4 corresponds to the solution in Equation 3.2, allowing only the intercepts c_i to vary between clusters. (3) The individual cluster FP fits in columns 5–9 are for only those 11 clusters with numbers of galaxies $N \geq 10$. (4) The constrained, individual cluster fits of columns 10–12 were obtained by fixing $b = 0.314$. (5) The rms in all cases is evaluated along the $\log r_{\rm eff}$ axis.

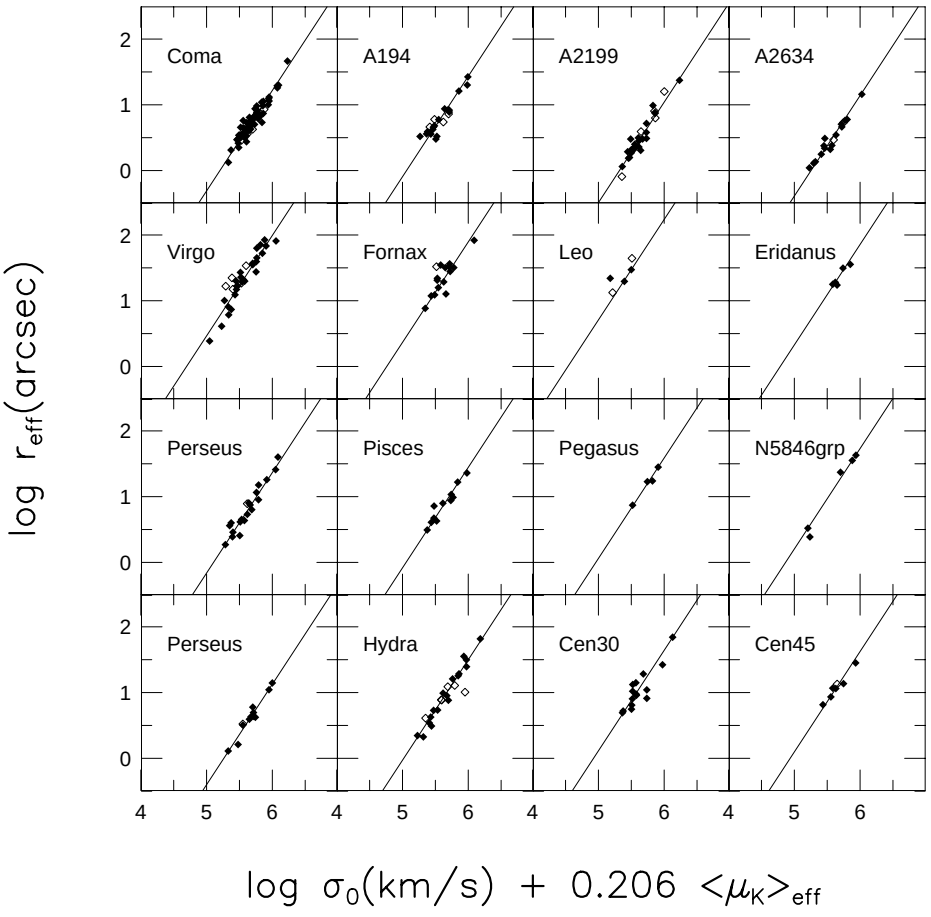

Figure 3.1: The Fundamental Plane in the near–infrared for the 16 clusters and groups in the simultaneous fit represented by the solution of Equation 3.2 and the intercepts in column 2 of Table 3.1. The FP is described by the scaling relation $r_{\rm eff} \propto \sigma_0^{1.53} \langle \Sigma_K \rangle_{\rm eff}^{-0.79}$ with a scatter of 0.096 dex in $\log r_{\rm eff}$; the scatter is reduced by 10% of the galaxies with $\sigma_0 < 100$ km s^{-1} are excluded. The fitted galaxies are plotted as solid symbols, while those excluded from the fit ($\log \sigma_0 < 1.8$, late–type morphology, $r_{\rm eff} < 1$ arcsec, or background/foreground in the Virgo cluster) are plotted as open symbols. The FP fit is plotted in each panel as a solid line.

been determined using the bootstrap procedure. In eight of the 11 cases, the fits have a within one standard deviation of the value $a = 1.53$ from the simultaneous fit, suggesting both that the uncertainties are reasonably estimated and that better fits are limited by the number of galaxies per cluster. These individual fits are listed in Table 3.1.

The same 11 clusters were also fit individually by constraining $b = 0.314$ from the previous simultaneous fit. This is possible because virtually every study of the FP (optical and near–infrared) obtains a similar value for this parameter, hence it should be possible to constrain its value *a priori*. These fits show significantly smaller uncertainty in their determination of a than the unconstrained fits, and are listed in Table 3.1. In this case, seven of the 11 clusters have a slope a within one standard deviation of the value from the simultaneous fit.

The adopted form of the FP in Equation 3.2 is plotted for all 301 galaxies in these 16 clusters and groups in Figure 3.2, both in face–on and edge–on perspectives. While the edge–on view with $\log R_{\rm eff}$ as the ordinate[2] is the most common method of displaying the FP, the edge–on view with $\log R_{\rm eff} - 0.314\langle\mu\rangle_{\rm eff}$ as the ordinate is easier to interpret. Virtually every study of the FP (optical and near–infrared) obtains the same relationship between $R_{\rm eff}$ and $\langle\mu\rangle_{\rm eff}$, but there may be significant variation in the relationship between $\log R_{\rm eff} - 0.314\langle\mu\rangle_{\rm eff}$ and $\log\sigma_0$, depending on wavelength. Furthermore, this edge–on perspective of the FP, seen from its short side, separates the correlated measurement errors in $r_{\rm eff}$ and $\langle\mu\rangle_{\rm eff}$ from the independent measurement errors in σ_0. The FP in physical units as plotted in Figure 3.2 is $\log R_{\rm eff}(h_{75}^{-1}\ {\rm kpc}) = 1.528\log\sigma_0 + 0.314\langle\mu\rangle_{\rm eff} - 8.298$.

In the face–on view of the FP in Figure 3.2(c), it is seen that galaxies do not uniformly populate this planar surface. While the K–band data in this paper are not drawn from a strictly magnitude–limited sample, they do behave as though a $K_{\rm tot} \lesssim 13$ mag limit were imposed. Most of the galaxies are found to have $15 < \langle\mu_K\rangle_{\rm eff} < 18$ mag arcsec^{-2} (long–dashed lines), although there are no clear selection effects causing this distribution of galaxy properties. Furthermore, there are no galaxies with properties in the upper–right portion of the figure, which could be caused by the lack of galaxies with central velocity dispersions $\sigma_0 > 400$ km s^{-1}, although there is no selection limit imposed on this portion of the FP.

[2]In this paper, a distinction will be made between the angular effective radius $r_{\rm eff}$, measured in arcsec, and the effective radius $R_{\rm eff}$ in physical scale, measured in kpc.

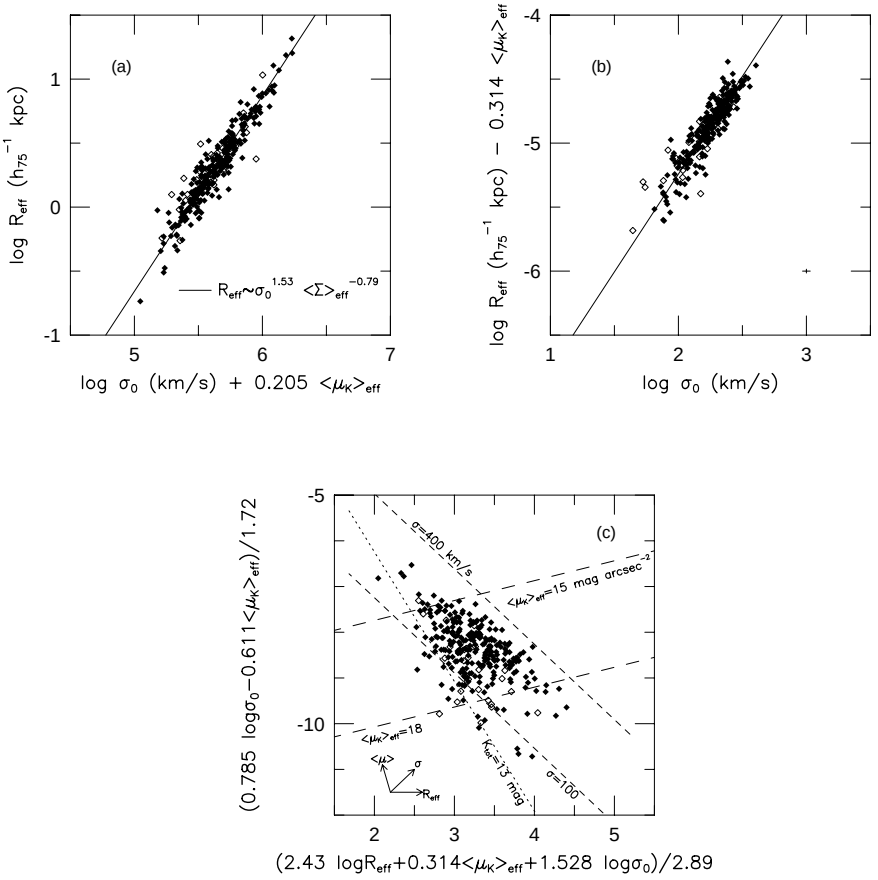

Figure 3.2: (a) The Fundamental Plane in the K–band for the combined 16 cluster and group sample, seen edge–on along its long side. The symbols are as in Figure 3.1. The ordinate is in units of kpc assuming $H_0 = 75$ km s Mpc^{-1}. (b) The FP in the K–band for the combined 16 cluster and group sample, seen edge–on along its short side. In this view of the FP, the observationally–correlated measurement errors in $R_{\rm eff}$ and $\langle\mu_K\rangle_{\rm eff}$ (ordinate) are separated from the independent measurement uncertainties in σ_0 (abscissa); the typical measurement uncertainties (0.015 dex in $\log R_{\rm eff} - 0.314\langle\mu_K\rangle_{\rm eff}$, $\sim$ 0.03 dex in σ_0) are shown in the lower right–hand corner of the panel. (c) The FP seen face–on. Galaxies do not uniformly populate this planar surface. While the K–band data in this paper are not drawn from a strictly magnitude–limited sample, they do behave as though a $K_{\rm tot} \lesssim 13$ mag limit (dotted line) were imposed. Most of the galaxies are found to have $15 < \langle\mu_K\rangle_{\rm eff} < 18$ mag arcsec^{-2} (long–dashed lines), although there are no clear selection effects causing this distribution of galaxy properties. Furthermore, there are no galaxies with properties in the upper–right portion of the figure, which could be caused by the lack of galaxies with velocity dispersions $\sigma_0 > 400$ km s^{-1} (short–dashed line). The vectors drawn in the lower left–hand corner show the direction in which each of the observed quantities varies along the plane.

3.3.2 The D_K–σ_0 Relation

Dressler *et al.* (1987) introduced a parameter D_n which was defined as the diameter at which the circular mean surface brightness (fully corrected for cosmological effects and Galactic extinction) dropped to a fiducial value. This parameter was chosen, in effect, to be a combination of the $r_{\rm eff}$ and $\langle\mu\rangle_{\rm eff}$ terms in the FP correlations, thereby simplifying the FP to a D_n–σ_0 relation. They defined this fiducial surface brightness to be 20.75 mag arcsec^{-2} in the B–band: the surface brightness was faint enough that D_B was typically much larger than the seeing disk, while bright enough that interpolation (rather than extrapolation) was used to evaluate D_B from their aperture magnitude data.[3]

Lucey & Carter (1988) defined an equivalent D_V parameter in the V–band to be the diameter at which the mean surface brightness drops to 19.8 mag arcsec^{-2} (this assumes a mean galaxy color of $(B-V)_0 = 0.95$ mag), Smith *et al.* (1997) defined D_R for the $R_{\rm C}$–band to be at $\langle\mu\rangle_{\rm eff} = 19.23$ mag arcsec^{-2} (assuming $(V-R_{\rm C}) = 0.57$ mag), Jørgensen *et al.* (1995a) defined the Gunn r–band $D_r = 2r_n$ to be at $\langle\mu\rangle_{\rm eff} = 19.6$ mag arcsec^{-2} (assuming $(V-r) = 0.2$ mag), and Pahre (1998, Chapter 2 of this thesis) defined the K–band D_K to be at $\langle\mu\rangle_{\rm eff} = 16.6$ mag arcsec^{-2} (assuming $(V-K) = 3.2$ mag). By using typical colors for early–type galaxies in constructing these definitions, the average value of D measured for a sample of galaxies should be approximately independent of bandpass. The slope of the D_n–σ_0 relation may vary between bandpasses, however, causing there to be a systematic variation of the D parameter *as a function of* σ in different bandpasses (while keeping the mean D similar). For example, if $D_V \propto \sigma^{a_V}$ and $D_K \propto \sigma^{a_K}$, then $\log D_V - \log D_K = (a_V - a_K)\log\sigma +$ constant.

The D_K–σ_0 relation was fit for the galaxies in the same 16 clusters and groups as in §3.3.1, excluding galaxies using similar criteria ($D_K < 2$ arcsec, $\log\sigma_0 < 1.8$, late types), and using the bootstrap method to estimate uncertainties in the fitted coefficients. The best fitting relation is

$$\begin{aligned} \log D_K(h_{75}^{-1}\ \mathrm{kpc}) &= 1.62\log\sigma_0 - 2.984 \quad N = 252 \quad \mathrm{rms} = 0.112\ \mathrm{dex} \\ &\quad \pm 0.07 \end{aligned} \tag{3.4}$$

[3]The notation of D_B will be adopted for the rest of the paper to distinguish the D_n parameter as defined in the B–band from the equivalent diameter as defined in another bandpass. The name "D–σ_0 relation" will refer to the correlation in all bandpasses.

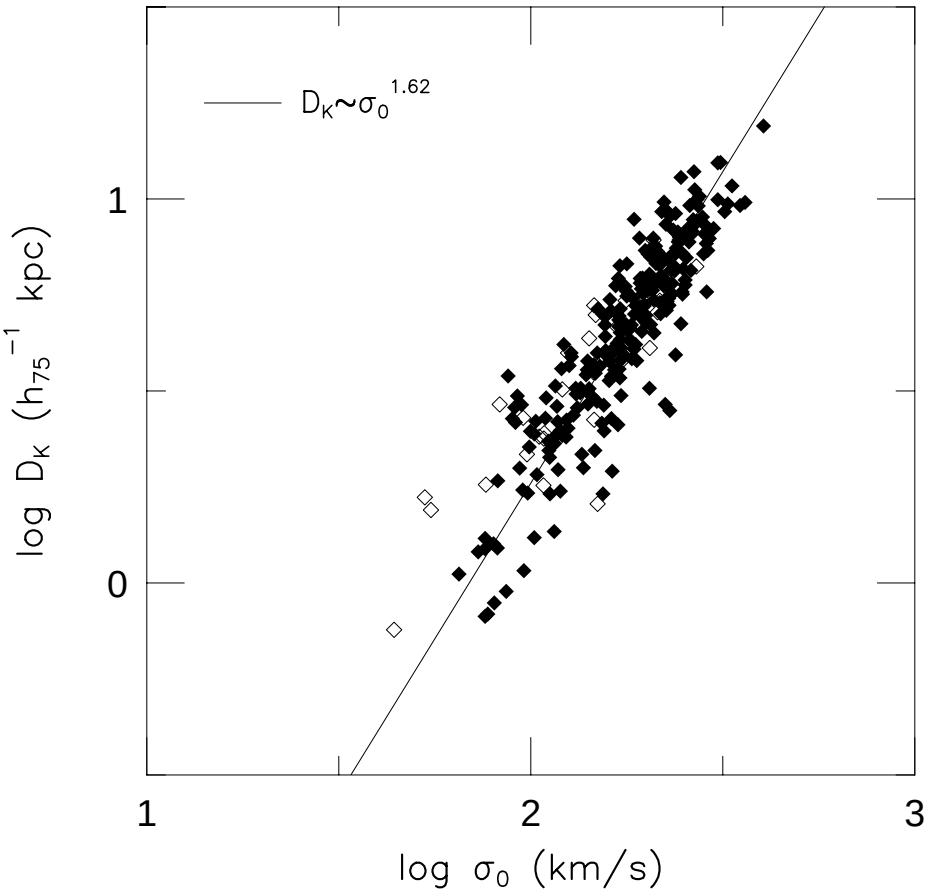

Figure 3.3: The D_K–σ_0 relation for the galaxies in the 16 clusters and groups of the survey, plotted in physical units. The scatter for this relation is 0.112 dex in $\log D_K$, which is slightly higher than the FP itself, since the D_K–σ_0 is not quite an edge–on view of the FP.

and is displayed in Figure 3.3. The slope of this relation is consistent, given the estimated uncertainties, with the full FP relation in Equations 3.2 and 3.3. The scatter of the D_K–σ_0 relation, however, is 15% higher than the K–band FP, despite the fact that the measurement uncertainty of D_K is actually smaller than that for $r_{\rm eff} - 0.32\langle\mu\rangle_{\rm eff}$ (Pahre 1998a, Chapter 2 of this thesis). This is most likely due to the fact that the D_K–$\sigma_0$relation is nearly, but not quite, viewing the FP edge–on.

3.3.3 The FP As Seen in κ–Space

Since elliptical galaxies only populate a plane in the three–dimensional space of the observables $(R_{\rm eff}, \langle\mu\rangle_{\rm eff}, \sigma_0)$, it is straightforward to construct an orthogonal transformation from this observed coordinate system to another one $(\kappa_1, \kappa_2, \kappa_3)$ which might provide a more physical interpretation. Bender, Burstein, & Faber (1992) proposed to use the transformation

$$\begin{aligned} \kappa_1 &\equiv (2\log\sigma_0 + \log R_{\rm eff})/\sqrt{2} \\ \kappa_2 &\equiv (2\log\sigma_0 + 0.8\langle\mu\rangle_{\rm eff} - \log R_{\rm eff})/\sqrt{6} \\ \kappa_3 &\equiv (2\log\sigma_0 + 0.4\langle\mu\rangle_{\rm eff} - \log R_{\rm eff})/\sqrt{3} \end{aligned} \tag{3.5}$$

where the quantities κ_i were constructed such that κ_1 is proportional to mass, κ_3 is proportional to mass–to–light ratio, and κ_2 (which is required to be orthogonal to κ_1 and κ_3) is proportional to the product of mass–to–light ratio and the third power of mean surface brightness. This "κ–space" is displayed in Figure 3.4 for the K–band survey. Given the above interpretation of κ_1 and κ_3, the fitted line between these two variables

$$\begin{array}{rcccc} \kappa_3 & = & 0.147\kappa_1 & + & 5.721\langle\mu_K\rangle_{\rm eff} \quad N = 251 \quad {\rm rms} = 0.068 \text{ dex} \\ & & \pm 0.011 & & \pm 0.038 \end{array} \tag{3.6}$$

then implies that the "observed mass–to–light ratio"[4] in the K–band varies as $(M/L_K) \propto M^{0.147\pm0.011} \propto L_K^{0.172\pm0.013}$. This conclusion is dependent on elliptical galaxies forming a dynamically homologous family in which the central velocity dispersion scales to the effective radius velocity dispersion (the radius at which surface brightness is evaluated) independently of the mass or luminosity of the galaxy. The uncertainties in Equation 3.6 were derived using bootstrap resampling of the data points. The cumulative observational uncertainties in this equation are 0.033 dex in κ_3, which is substantially smaller than the rms of the fit, implying a substantial intrinsic scatter of the "observed mass–to–light ratio" for any given "mass."

While it is desirable to choose an orthogonal coordinate system which might directly relate the observables to underlying physical properties of elliptical galaxies, this conceptu-

[4]For the reasons discussed later in this section, we prefer to distinguish between this observed relationship and the *intrinsic* M and (M/L), which may or may not be fully described by the axes κ_1 and κ_3, respectively.

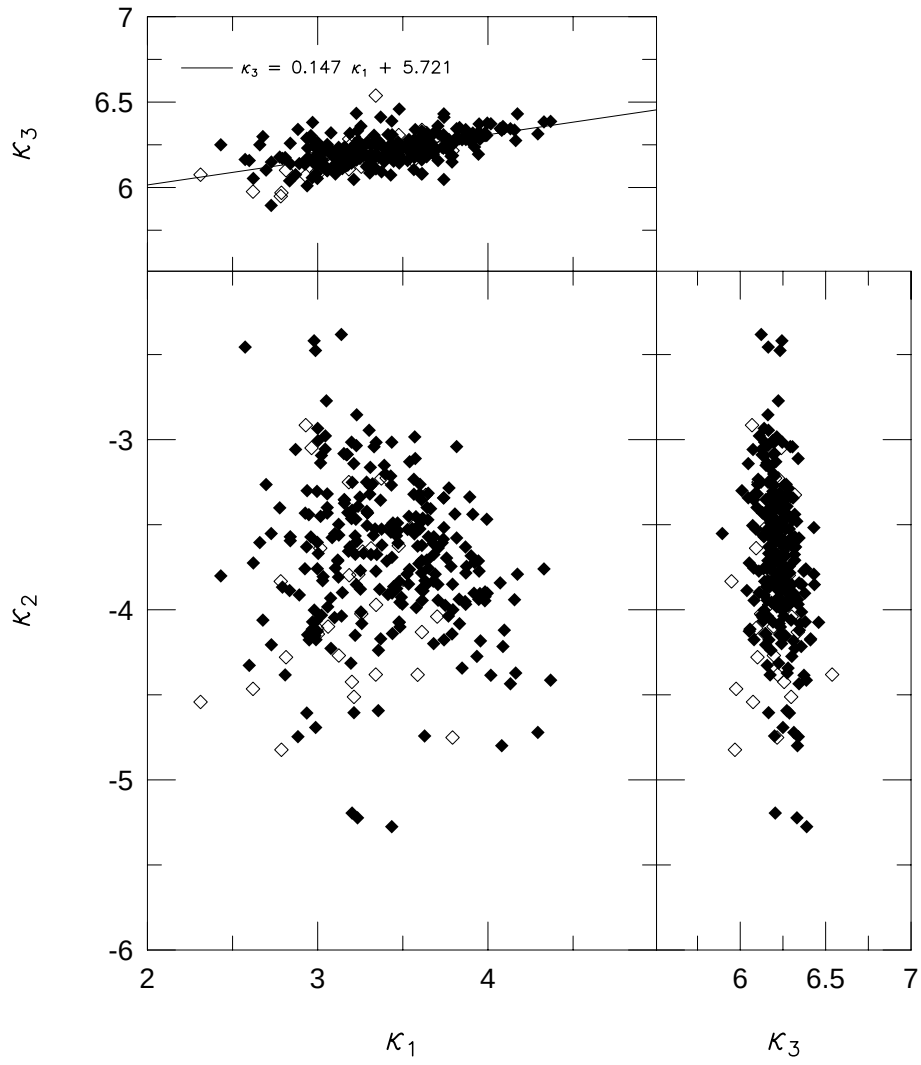

Figure 3.4: The K–band FP viewed in the κ–space perspective. This coordinate system (defined by Bender, Burstein, & Faber 1992) is given in Equation 3.5, and was designed such that κ_1 is roughly proportional to the logarithm of mass and κ_3 is roughly proportional to the logarithm of mass–to–light ratio. The fit in the top panel corresponds to the "observed" scaling relations $(M/L_K) \propto M^{0.15\pm0.01}$ or $(M/L_K) \propto L_K^{0.17\pm0.01}$, under the assumptions that there are no color gradients in elliptical galaxies and dynamical homology is preserved within the family of elliptical galaxies.

alization of the FP has a number of problems. First, the quantity $R_{\rm eff}$ is not equivalent to R_g, the half–mass radius, but instead varies with the observed wavelength. This generally follows from the presence of color gradients in elliptical galaxies (e.g., Franx, Illingworth, & Heckman 1989; Peletier *et al.* 1990a,b), but will be shown explicitly for the case of comparing V–band and K–band effective radii in the next paper in this series (Pahre, de Carvalho, & Djorgovski 1998b, Chapter 4 of this thesis). It follows that the value of κ_1, which was intended to create a quantity which is proportional to mass, *systematically varies* as a function of wavelength while mass, of course, does not. Furthermore, while the evidence is not yet strong, the lowest luminosity ellipticals show no detectable color gradients (Peletier *et al.* 1990a), suggesting that there could be a dependence of the size of the color gradient on luminosity (and hence mass). The mappings from κ_1 to mass and κ_3 to mass–to–light ratio are therefore a function of both wavelength and size of the color gradient (which is, in turn, a function of mass).

Second, the use of the central velocity dispersion σ_0 in deriving mass at the effective radius assumes dynamical homology among elliptical galaxies in mapping σ_0 (the central velocity dispersion) to $\sigma_{\rm eff}$ (the velocity dispersion within the effective radius). Whether or not the internal stellar velocity distributions of elliptical galaxies form a homologous family is a point of considerable debate. Empirical data (Jørgensen, Franx, & Kjærgaard 1995, Busarello *et al.* 1997) and numerical simulations of dissipationless merging (Capelato, de Carvalho, & Carlberg 1995) seem to suggest that the way σ_0 scales to $\sigma_{\rm eff}$ is a function of galaxy mass or luminosity. The mapping from κ_1 to mass and κ_3 to mass–to–light ratio are therefore a function of mass or luminosity, and possibly a function of other physical processes which are currently poorly understood.

In summary, because the mapping from the observables to κ–space is a *function* of wavelength, luminosity, and deviations from dynamical homology, and furthermore because the mapping from κ–space to mass and mass–to–light ratio is also a *function* of wavelength, luminosity, and deviations from dynamical homology, we eschew the use of κ–space since it is an obfuscation, rather than an illumination, of the fundamental physical quantities of elliptical galaxies which we wish to understand. At its best, the κ–space formalism is merely an intermediate orthogonal transformation between the observables $[R_{\rm eff}, \langle\mu\rangle_{\rm eff}, \sigma_0]$ and the desired physical properties $[M, L, M/L\,(\lambda)]$.

3.3.4 The Mg_2–σ_0 Relation

The Mg_2–σ_0 relation is a correlation between two distance independent quantities and hence useful both as a diagnostic and as a constraint on formation processes for elliptical galaxies as a family. Guzmán (1995), for example, found that the residuals of the Mg_2–σ_0 relation and the D_n–σ_0 relation showed systematic differences between the Hydra–Centaurus region and the Coma cluster, thereby suggesting that there are differences between the global properties of galaxies in those two environments.

Only a fraction of galaxies for which σ_0 is available also have Mg_2 values available. Of the entire sample of 301 early–type galaxies in these 16 clusters and groups, only 188 galaxies (62%) fit the criteria of $\log\sigma_0 \geq 1.8$ and have Mg_2 measurements. There are six galaxies at low σ_0 that show anomalously low Mg_2 and are therefore excluded: M32, NGC 3489 in the Leo Group, and NGC 4239, NGC 4468, NGC 4476, and NGC 4733 in the Virgo cluster (NGC 4489 was previously excluded for $\log\sigma_0 < 1.8$). Many of these are dwarf galaxies which are known to follow different FP correlations. The criterion used for this exclusion was that all galaxies satisfy $Mg_2 < \frac{5}{7}(2.2 - \log\sigma_0)$. The best fitting Mg_2–σ_0 relation is

$$\begin{array}{rcccccc} Mg_2(\text{ mag}) & = & 0.173\log\sigma_0 & -0.106 & N = 182 & \text{rms} = 0.019\text{ mag} \\ & & \pm 0.010 & \pm 0.024 & & \end{array} \tag{3.7}$$

This relation is plotted in Figure 3.5. The slope of this relation is slightly shallower than the value of 0.196 ± 0.009 found by Jørgensen (1997), and the scatter is slightly smaller than the 0.025 mag of Jørgensen. Inclusion of the six galaxies anomalously low in Mg_2 and the one galaxy with $\log\sigma < 1.8$ produces a Mg_2–σ_0 relation $Mg_2 = 0.188 \pm 0.012\log\sigma_0 - 0.140 \pm 0.026$ with a scatter of 0.021 mag; this is closer to, and statistically indistinguishable from, Jørgensen's results. The form in Equation 3.7 will be used, however, as it best represents the properties of the normal elliptical galaxies.

3.3.5 The Mg_2 Near–Infrared Fundamental Plane

An alternative form of the FP was proposed by de Carvalho & Djorgovski (1989): substitute a stellar populations indicator, such as the Mg_2 index, for the dynamical or mass indicator σ_0 in the FP relation. The motivation for this is that since Mg_2 and σ_0 are strongly correlated with each other (as shown above in §3.3.4) then metallicity could actually be

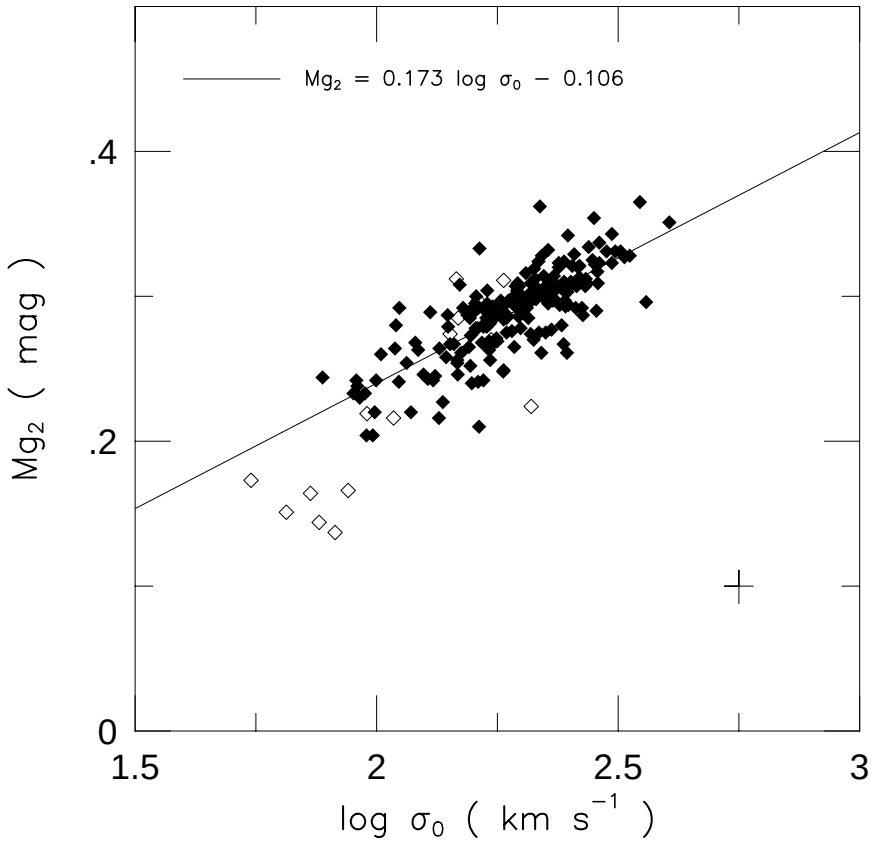

Figure 3.5: The Mg_2–σ_0 relation for the 182 galaxies with Mg_2 measurements. The scatter about this relation is 0.019 mag in Mg_2, which is significantly larger than the typical measurement uncertainties of 0.013 mag (shown in lower right–hand corner of figure).

the fundamental physical property that causes the slope of the FP to deviate from the virial expectation. de Carvalho & Djorgovski also showed that a metallicity sensitive color could be substituted for σ_0, although that approach will not be pursued here due to the heterogeneity of the derived optical–infrared colors in Paper II (see Pahre 1998a, Chapter 2 of this thesis).[5] The resulting FP in the near–infrared K–band using the Mg_2 index in place of $\log \sigma_0$ is

$$\begin{array}{rcccc} \log r_{\rm eff}({\rm arcsec}) & = & 8.3\ {\rm Mg_2} + & 0.324\langle\mu_K\rangle_{\rm eff} + c_i & N = 181 \quad {\rm rms} = 0.172\ {\rm dex} \\ & & \pm 0.9 & \pm 0.015 & \end{array} \tag{3.8}$$

The slope of this relation is 8.3 ± 0.9, as predicted by the slope of the Mg_2–σ_0 relation combined with the standard form of the near–infrared FP, i.e., $(1.53 \pm 0.08)/(0.173 \pm 0.010) = 8.8 \pm 0.7$. The observational uncertainties increase when Mg_2 is used instead of $\log \sigma_0$ since the latter quantity has ~ 3 times greater uncertainty, while the slope has changed by more than a factor of five from Equation 3.2 to Equation 3.8. The scatter in the near–infrared Mg_2 FP, however, has increased by much more than this difference, suggesting that Mg_2 is not nearly as good an indicator as the velocity dispersion in describing the fundamental and regular physical properties in elliptical galaxies that give rise to the FP. The Mg_2 index could be identifying real differences in the stellar populations among galaxies and hence shows larger scatter when it is substituted into the FP.

If part of the scatter in the $r_{\rm eff}$–$\langle\mu_K\rangle_{\rm eff}$–$\sigma_0$ FP can be attributed to differences in stellar populations among elliptical galaxies, then the introduction of a stellar populations "correction" factor based on the Mg_2 index should be able to reduce the scatter of the FP even though a small amount of additional observational uncertainty is added in the process. The idea for this comes from the attempt by Guzmán & Lucey (1993) to construct an "age–independent" distance indicator. Here the method will be applied to the near–infrared data.

[5]Basically, the fundamental requirement for such an investigation of the "color FP" is to understand the difference between an "aperture" color–magnitude relation, the standard form which relies on a color measured in a fixed physical aperture size for all galaxies, and a "global" color–magnitude relation, which is evaluated at some fiducial scaling radius. Part of the slope of the "aperture" color–magnitude relation is certainly due to the presence of color gradients which act in the sense that ellipticals are redder in their centers: the smallest galaxies have their colors evaluated at large $r/r_{\rm eff}$ where their color is bluer, while the largest galaxies have their colors evaluated at small $r/r_{\rm eff}$ where their color is redder. Future work should explicitly distinguish between the two effects of color gradients and global color differences in order to place a constraint on the global properties of ellipticals.

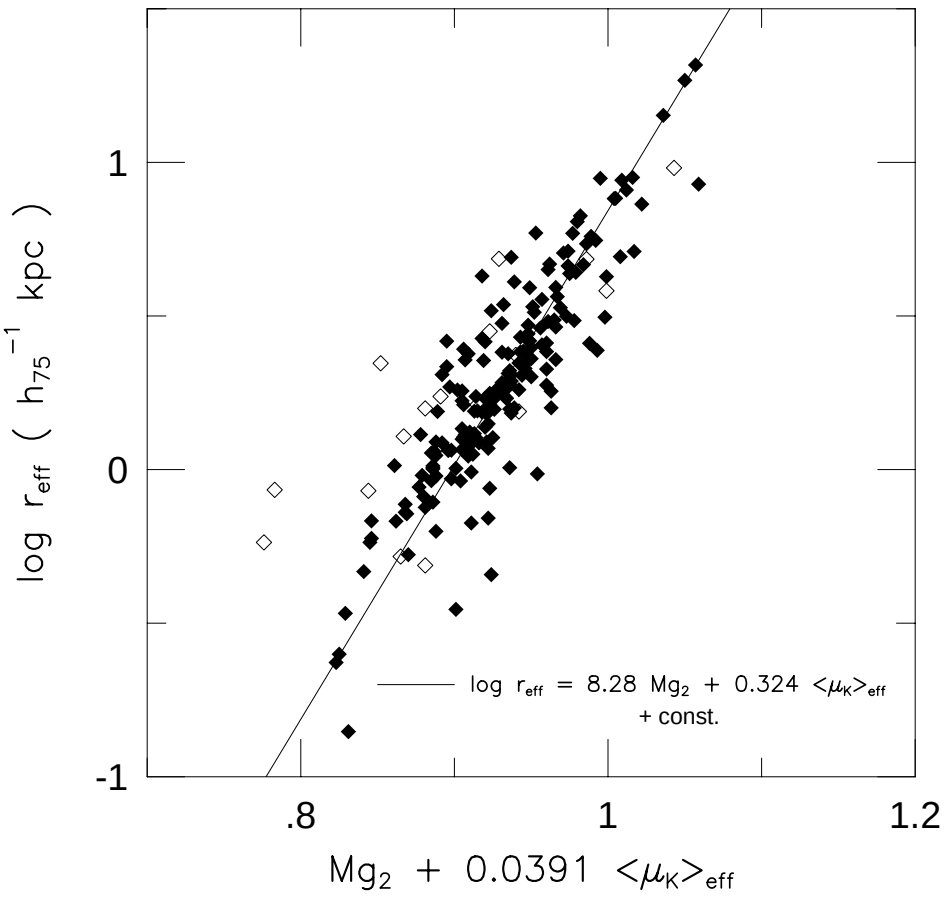

Figure 3.6: The near–infrared FP with the Mg_2 index substituted for the velocity dispersion. This figure is plotted to the same scale as Figure 3.2(a), hence a direct comparison of these two figures demonstrates how the scatter of the FP relation has increased by a factor of two by the substitution of Mg_2 for σ_0. Only a small part of this increase in scatter can be attributed to the larger measurement uncertainties of Mg_2 compared to σ_0, hence the correlation plotted in this figure cannot be an edge–on view of the FP.

Using Bruzual (1983) evolutionary spectral synthesis models, Guzmán & Lucey showed that the effects of a burst of star formation involving 10% of a galaxy's mass would appear as a change of $\Delta m/\Delta$ Mg$_2$ roughly constant for times $\gtrsim 1$ Gyr or so after the burst. Hence, an offset in magnitude Δm could be applied to each galaxy independently based on its departure Δ Mg$_2$ from the Mg$_2$–σ_0 relation. Guzmán & Lucey also showed that while the effect in the optical V–band was $\Delta m_V/\Delta \mathrm{Mg}_2 \sim 10$, the effect in the near–infrared was much smaller at

$$\frac{\Delta m_K}{\Delta\ \mathrm{Mg}_2} \sim 2. \tag{3.9}$$

This effect can basically be understood as a filling–in of the Mg$_2$ feature by the addition of a continuum flux from hot, young stars. The changes in the Mg$_2$ index are expected to be small, as Mg$_2$ is far more sensitive to metallicity than it is to age or IMF (Mould 1978).

The Guzmán & Lucey procedure is repeated here for the Worthey (1994) stellar populations models in order to determine if the size of the predicted age effects are similar despite significant differences between the Bruzual (1983) and Worthey (1994) models. The model adopted is similar to Guzmán & Lucey in that it involves 10^6 M$_\odot$ total mass, 90% of which is 15 Gyr old in the present day, 10% of which is 5 Gyr old, and all of which has solar metallicity. A similar model is investigated that involves 90% of the galaxy being which is 11 Gyr old in the present day and 10% of which is 5 Gyr old. The results from the Worthey models are listed in Table 3.2 and plotted in Figure 3.7 for the $UBVRIK$ bandpasses.

As can be seen in Table 3.2, the Worthey models show modest agreement with the Guzmán & Lucey calculations based on Bruzual (1983) models for the optical bandpasses, although the value of Δmag/Δ Mg$_2$ is systematically 30–50% higher. In the K–band, however, Worthey's models are 3–4 times higher in this quantity. The most likely explanation for this is the difficulty that many models have in producing enough Mg relative to Fe for very metal–rich populations (see Worthey, González, & Faber 1992, for example), although more fundamental problems in the treatment of cool stellar atmospheres in the infrared for the Worthey models (see Charlot, Worthey, & Bressan 1996) could also be relevant. As a result of this discrepancy, the effects of a late burst of star formation involving a small fraction of the galaxy mass on the FP cannot be assumed *a priori*.

A better approach is to measure directly the possible contribution of younger stellar

Table 3.2: Variations in Magnitude and Mg_2 for an Old Population With and Without a 10% Young Population By Mass for the Worthey (1994) Models

Age (Gyr)	U	B	V	R_C	I_C	K	Mg_2(old) (mag)	Mg_2(old+young) (mag)	Δ Mg_2 (mag)
(1)	(2)	(3)	(4)	(5)	(6)	(7)	(8)	(9)	(10)
15 Gyr old population (90%), 5 Gyr young population (10%)									
10.0	0	0	0	0	0	0	0.248	···	0
11.0	15.06	11.62	8.17	6.72	5.26	2.36	0.253	0.197	-0.055
11.5	17.70	13.57	10.62	9.44	7.67	4.42	0.255	0.221	-0.034
12.0	20.43	15.65	13.04	12.17	10.87	6.52	0.258	0.235	-0.023
12.5	21.39	17.11	14.44	13.37	11.76	8.02	0.259	0.240	-0.019
13.0	23.81	19.05	16.33	15.65	14.29	9.52	0.261	0.246	-0.015
13.5	22.46	17.39	15.22	13.77	12.32	8.70	0.262	0.248	-0.014
14.0	20.77	16.15	13.85	13.08	11.54	7.69	0.264	0.251	-0.013
14.5	20.49	15.57	13.93	12.30	10.66	6.56	0.266	0.253	-0.012
15.0	20.18	14.91	13.16	12.28	10.53	6.14	0.267	0.256	-0.011
11 Gyr old population (90%), 5 Gyr young population (10%)									
6.0	0	0	0	0	0	0	0.223	···	0
7.0	15.60	12.26	8.36	6.96	5.29	2.79	0.231	0.195	-0.036
7.5	18.54	14.63	11.71	10.24	8.78	4.88	0.235	0.214	-0.020
8.0	22.90	17.56	15.27	13.74	12.21	9.16	0.239	0.226	-0.013
8.5	23.53	19.61	16.67	15.69	14.71	9.80	0.241	0.231	-0.010
9.0	27.63	22.37	21.05	18.42	18.42	13.16	0.243	0.236	-0.008
9.5	24.32	20.27	18.92	17.57	14.86	10.81	0.245	0.238	-0.007
10.0	24.29	18.57	15.71	14.29	14.29	8.57	0.248	0.241	-0.007
10.5	20.90	17.91	14.93	14.93	11.94	8.96	0.250	0.243	-0.007
11.0	21.54	16.92	13.85	13.85	10.77	6.15	0.253	0.246	-0.007

Notes: Tabulated in columns (2) to (7) are the changes in Δ mag/Δ Mg_2 for the filter at the head of the column.

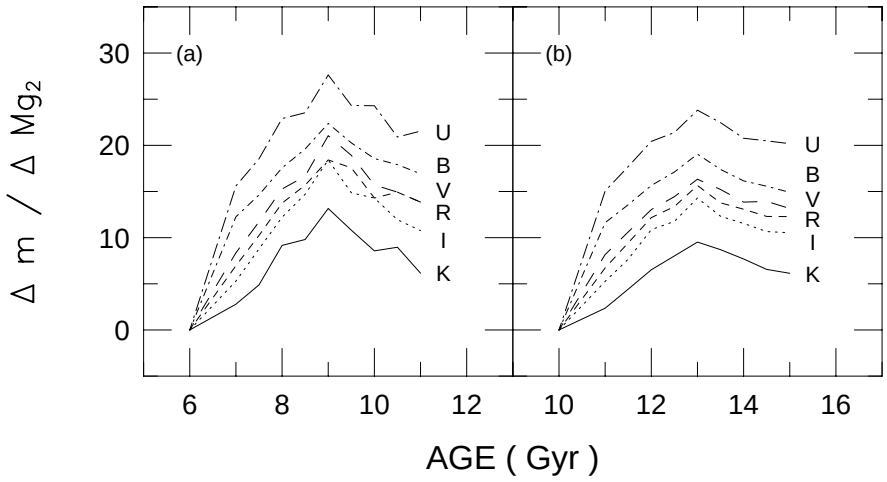

Figure 3.7: The ratio of the change in magnitude Δm to the change in the Mg_2 index for the $UBVRIK$ bandpasses using the models of Worthey (1994). The two cases considered both have a 90% (by mass) old stellar population component of 11 Gyr (a) and 15 Gyr (b) and [Fe/H]= 0 in addition to a 10% young stellar population that is 5 Gyr old at the present day.

populations using the FP itself, and then use that as an observational constraint for constraining the models. Combining Equations 3.1 and 3.7, defining $r_K = \frac{\Delta m_K}{\Delta\ \mathrm{Mg_2}}$, and assuming that the mean surface brightness term in the FP is the only one affected by r_K yields:

$$\log r_{\rm eff}(\mathrm{arcsec}) \quad = \quad a' \log \sigma_0 + b' \left(\langle \mu_K \rangle_{\rm eff} - r_K \left[\mathrm{Mg_2} - 0.173 \log \sigma_0 + 0.106 \right] \right) + c_i \tag{3.10}$$

where the primed coefficients are the "age–independent" form of the FP. The Guzmán & Lucey analysis predicts $r_K \sim 2$, while the Worthey models predict $r_K \sim 7$.

A minimization of Equation 3.10 does not reveal to optimal value of r_K since values of $|r_K| > 0$ increase the scatter of the equation due to the added measurement uncertainties. Put another way, there was no significant improvement in the scatter (by $> 2\%$) of the FP for any r_K in the range $-10 < r_K < +10$. Since the intrinsic thickness of the near–infrared FP is clearly resolved without including a Mg_2 term (i.e., Equation 3.2 and Figure 3.2), then some of that thickness could be due to variations in age among the stellar populations of elliptical galaxies. This effect can be viewed from a similar perspective by attempting to

correlate the residuals of the near–infrared FP with the residuals of the Mg_2–σ_0 relation. This Δ–Δ diagram is shown in Figure 3.8. This figure shows no correlation among the residuals in the direction of the age vectors, implying that the resolved intrinsic scatter of both the near–infrared FP and the Mg_2–σ_0 relations cannot be caused by age effects alone.

Instead, insight can be gained by looking for changes in the relative distance modulus between a given cluster and the Coma cluster. When $r_K = 2$, all 16 clusters and groups show changes in their distance moduli relative to Coma of ≤ 0.05 mag, which is smaller than the typical uncertainty of 0.1 mag in the distance to a cluster of $N = 20$ galaxies for a scatter of $\log r_{\rm eff} = 0.085$ dex. The difference in relative distance modulus between the $r_K = 0$ and $r_K = 7$ cases, however, reach as high as 0.12–0.18 mag in the case of several clusters (Virgo, Cen30, and Pegasus), which is marginally significant. Since the Worthey (1994) models probably overestimate r_K due to their difficulty in producing Mg for metal–rich populations, the conclusion is that 0.18 mag is a firm upper limit to the effects of age differences on the distance moduli derived using the near–infrared FP. This result for the K–band is similar to that found in the r–band by Jørgensen *et al.* (1996), who found a minimally–significant contribution of $r_r = 1.3 \pm 0.8$. They probably found no good correlation for the reason given above—that the increase of measurement uncertainties as r increases prevents effective minimization during the fitting—hence this may not be a significant constraint on a superimposed intermediate age contribution. Repeating the analysis using $r_V = 10$ for the Abell 2199 and Abell 2634 clusters for the galaxies in the V and K matched catalog (Table A.5) produces a similarly small change in their distance moduli relative to Coma. In summary, there is little evidence that adding a Mg_2 term (based on the Mg_2–σ_0 relation) to the near–infrared FP to account for age differences in the ellipticals in different clusters causes a significant improvement over the zero–point for the relation and hence distances derived from it.

A similar approach could be pursued by looking at the correlation between the residuals of the Mg_2–σ_0 relation and the residuals of the κ_3–κ_1 relation. If differences of Mg_2 at a fixed σ_0 indicate differences of stellar populations, and if differences of κ_3 at a fixed κ_1 indicate differences in (M/L) due to stellar populations effects, then the residuals of these two relations (Equations 3.10 and 3.6) should correlate in a manner that is consistent with stellar populations effects. These residuals are plotted against each other in Figure 3.9.

This figure is an excellent diagnostic for distinguishing between age and metallicity

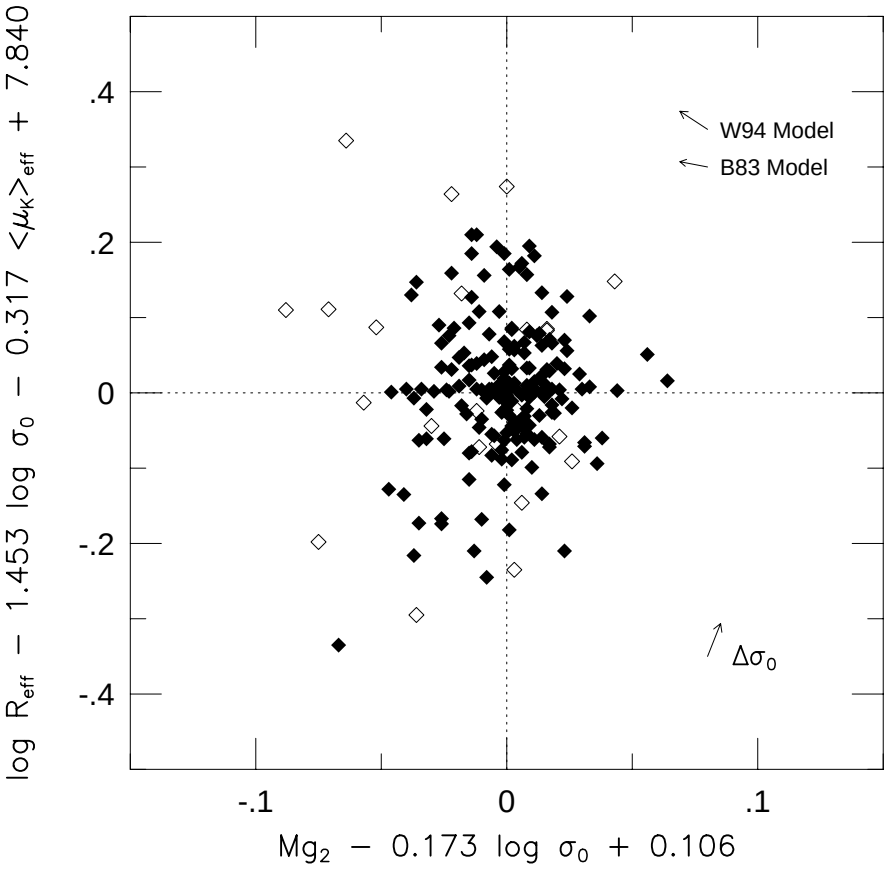

Figure 3.8: The residuals of the near–infrared FP plotted against the residuals of the Mg_2–σ_0 relation. For the purpose of this comparison, only those galaxies with good Mg_2 measurements (see §3.3.4) were used to fit the near–infrared FP; the FP fit for these 182 galaxies is $r_{\rm eff} \propto \sigma_0^{1.45}\langle\Sigma_K\rangle_{\rm eff}^{-0.79}$. A correlation due to the measurement errors of $\log\sigma_0$ would act in the direction of the vectors in the lower–right of the panel labeled $\Delta\sigma_0$. If a galaxy had a starburst involving 10% of its mass at 5 Gyr before the present day, this would produce an offset as shown for the Bruzual (1983; B83) and Worthey (1994; W94) models. Since there is no such correlation along these model vectors between the two sets of residuals, this implies that there is no age effect, as traced by the Mg_2–σ_0 relation, which is the sole cause of the intrinsic scatter of the near–infrared FP.

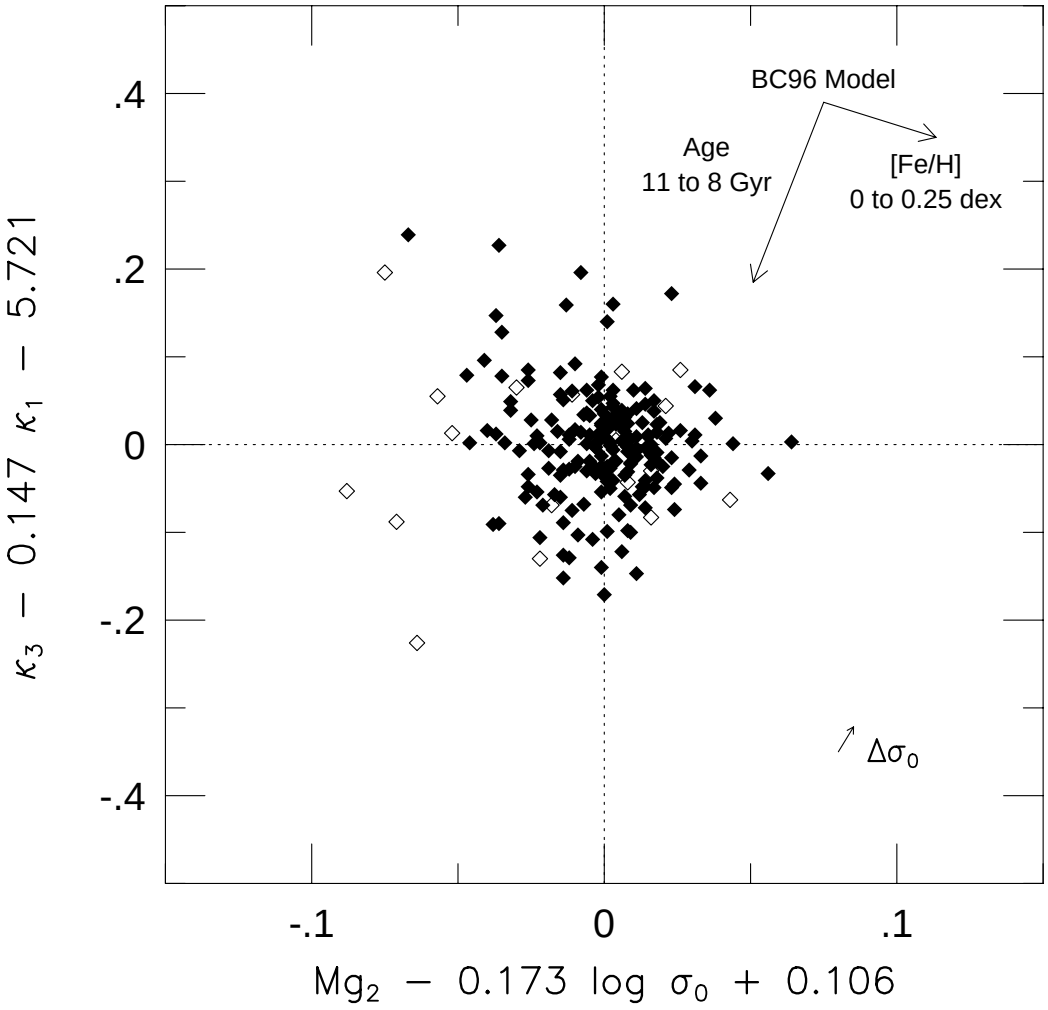

Figure 3.9: The residuals from the Mg_2–σ_0 relation (Equation 3.10) plotted against the residuals from the κ_3–κ_1 relation (Equation 3.6). Both relations show significant intrinsic scatter which could be due to variations in stellar populations at any given point on either relation. As shown by the vectors in the upper part of the figure, the Bruzual & Charlot (1996) models show that this diagram is a powerful diagnostic for separating the effects of age and metallicity. These models show the effect for changing the age from 11 to 8 Gyr for a solar metallicity population, and for changing [Fe/H] from 0 to 0.25 dex in a 11 Gyr old population. The effect of correlated errors in σ_0 are shown in the lower–right of the figure. Variations in both age and metallicity at any given mass or luminosity appear to be necessary to explain the intrinsic scatter in this diagram and the lack of correlation along either vector in the upper right of the figure.

effects, since Mg_2 decreases for younger stellar populations while it increases for higher metallicities, but (M/L_K) decreases for both. [If the vertical axis was $\Delta(M/L)$, measured at any optical wavelength, then age and metallicity would instead act nearly parallel.] The lack of any preferred correlation along either the age or metallicity vectors in Figure 3.9, while at the same time having a substantial intrinsic scatter for both relations, strongly indicates that both age and metallicity variations exist at any given point on both the Mg_2 and κ_3–κ_1 relations.

The Hβ index is expected to be a good indicator of the presence of a young stellar component, and either the Mg_2 or $\log\langle Fe\rangle$ indices should be good indicators of the mean metallicity of the stellar content. The large intrinsic scatter between the Hβ and Mg_2 indices, the lack of a correlation altogether between Hβ and $\log\langle Fe\rangle$, the strong correlation between Mg_2 and σ_0, and the weak correlation between $\log\langle Fe\rangle$ and σ_0 all indicate that there exist significant variations in both age and metallicity for any given value of σ_0 (Jørgensen 1997). This is fully consistent with the argument above based on the residuals of the Mg_2–σ_0 and κ_3–κ_1 relations.

3.3.6 The Faber–Jackson Relation

The correlation between luminosity and central velocity dispersion for elliptical galaxies was first noticed by Faber & Jackson (1976). If we fit the relation $L \propto \sigma_0^a$, this is equivalent to fitting $K_{\rm tot} = -2.5a \log \sigma_0 + b$. The best fitting Faber–Jackson relation for the K–band data is

$$M_K = K_{\rm tot} - 34.91 + 5\log h_{75} \;=\; -10.35\log\sigma_0 \qquad N = 252 \quad \mathrm{rms} = 0.93 \text{ mag} \\ \pm 0.55 \tag{3.11}$$

assuming $H_0 = 75$ km s^{-1} and that the Coma cluster ($cz = 7200$ km s^{-1}) is at rest with respect to the Hubble flow. The relation is plotted in Figure 3.10. The scatter of this relation is significantly smaller in the Coma cluster alone (rms= 0.72 mag).

3.3.7 The Modified Faber–Jackson Form of the FP

Since there is substantial scatter in the Faber–Jackson relation due to variations in surface brightness among galaxies at a given luminosity and central velocity dispersion, an alternate

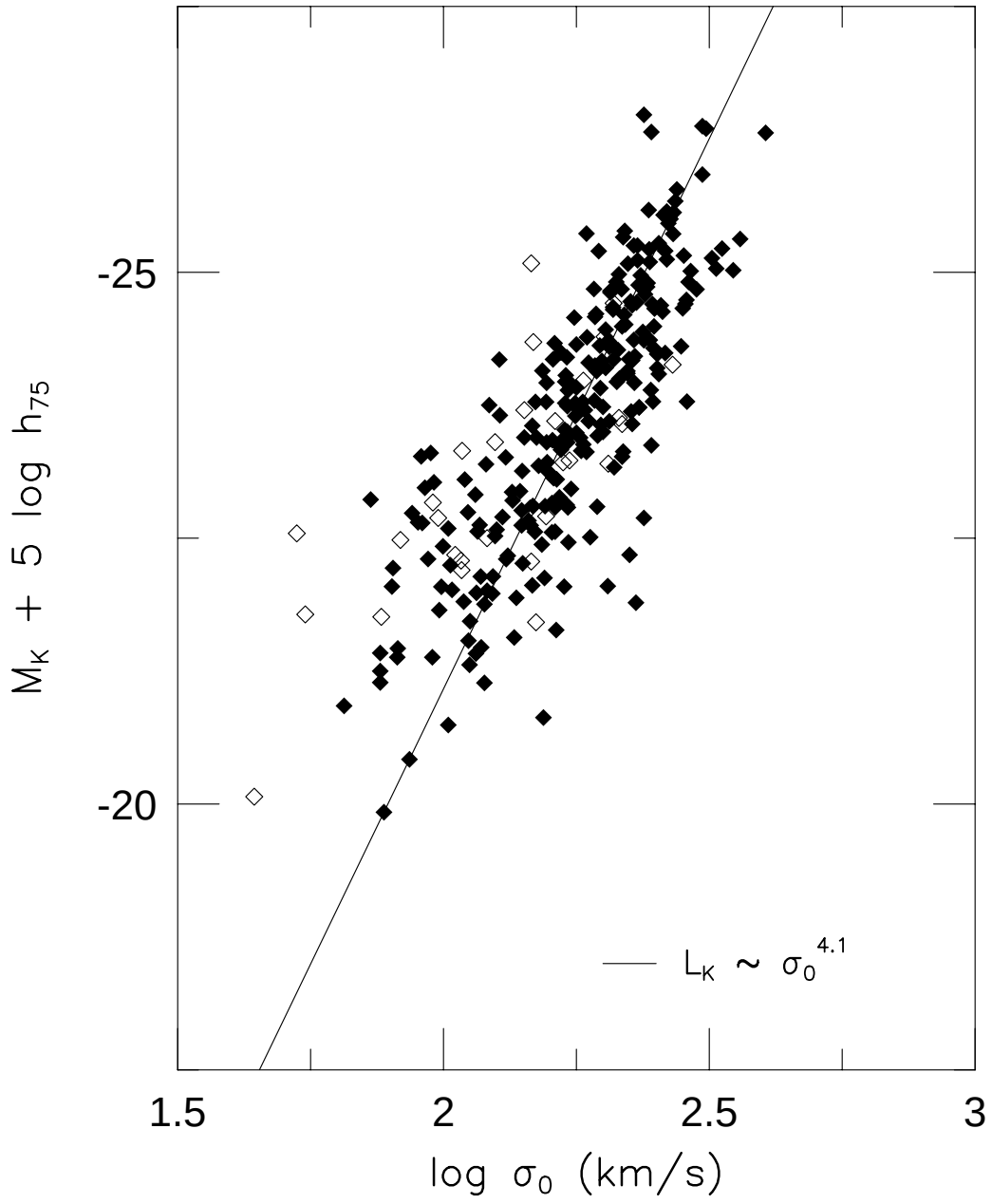

Figure 3.10: The Faber–Jackson relation between luminosity and central velocity dispersion. The best–fitting relation is $L_K \propto \sigma_0^{4.14\pm0.22}$ with a large scatter of 0.93 mag. The scatter is significantly smaller in the Coma cluster at 0.72 mag.

form of the FP is to substitute $K_{\rm tot}$ for $r_{\rm eff}$. This will be referred to as the "modified Faber–Jackson" relation, as it adds the additional $\langle\mu\rangle_{\rm eff}$ term to the Faber–Jackson relation. The form of this equation is

$$K_{\rm tot} = a' \log \sigma_0 ({\rm km\ s^{-1}}) + b' \langle\mu\rangle_{\rm eff} ({\rm mag\ arcsec^{-2}}) + c_i' \tag{3.12}$$

where the primed coefficients are used here for the modified Faber–Jackson relation. Since in the case of a pure de Vaucouleurs profile $K_{\rm tot}({\rm mag}) = -5 \log r_{\rm eff} + \langle\mu_K\rangle_{\rm eff} - 1.995$, the value $\log r_{\rm eff} = a \log \sigma_0 + b\langle\mu_K\rangle_{\rm eff} +$ constant can be substituted for $r_{\rm eff}$ resulting in $a = -5a'$ and $b = 0.2(1 - b')$, thereby relating Equations 3.1 and 3.12 to each other. The best–fitting relation of the modified Faber–Jackson form of the FP is:

$$\begin{array}{rcrrl} M_K + 5\log h_{75} & = & -8.16\log\sigma_0 - & 0.585\langle\mu_K\rangle_{\rm eff} + c_i & N = 251 \quad {\rm rms} = 0.51\ {\rm mag} \\ & & \pm 0.47 & \pm 0.062 & \end{array} \tag{3.13}$$

which has a scatter only 10% larger than the standard form of the near–infrared FP given in Equation 3.2. This equation represents the scaling relation $L_K \propto \sigma_0^{3.26\pm0.19} \langle\Sigma_K\rangle_{\rm eff}^{-0.59\pm0.06}$, which is fully equivalent within the uncertainties to the standard form of the near–infrared FP. Since the uncertainty on $K_{\rm tot} + 0.60\langle\mu_K\rangle_{\rm eff}$ is 0.068 mag, the total observational uncertainties in Equation 3.2 and 3.13 are similar. Hence Equation 3.13 also shows substantial intrinsic scatter in the properties of elliptical galaxies at any point along the FP.

3.3.8 The Kormendy Relation

Effective radius and mean surface brightness, which are two of the three terms in the FP, are correlated with each other (Kormendy 1977). The best fitting Kormendy relation for the K–band data is

$$\begin{array}{rcrl} \log R_{\rm eff} h_{75}^{-1} & = & 0.244\langle\mu_K\rangle_{\rm eff} - 3.637 & N = 269 \quad {\rm rms} = 0.227\ {\rm dex} \\ & & \pm 0.029 & \end{array} \tag{3.14}$$

assuming $H_0 = 75$ km s^{-1} and that the Coma cluster ($cz = 7200$ km s^{-1}) is at rest with respect to the Hubble flow. The relation is plotted in Figure 3.12. The scatter of this relation is significantly smaller in the Coma cluster alone (rms= 0.198 dex). Measurement

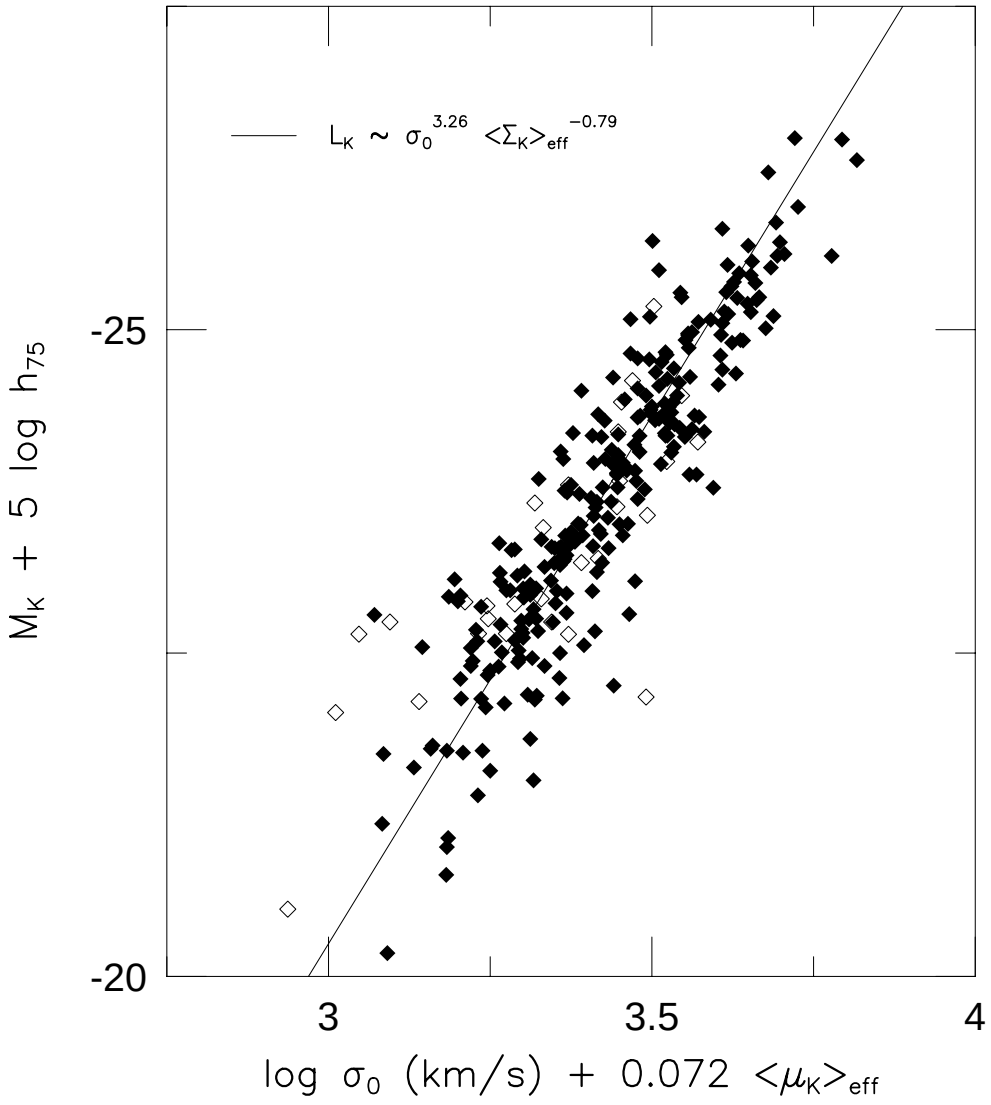

Figure 3.11: The "modified Faber–Jackson" form of the FP. The best–fitting relation is $L_K \propto \sigma_0^{3.26\pm0.19}\langle\Sigma_K\rangle_{\rm eff}^{-0.59\pm0.06}$ with a scatter of 0.51 mag. This form of the FP is nearly identical to that of Figure 3.2 and Equation 3.2, although it shows 10% larger scatter primarily due to larger observational uncertainties.

errors in $r_{\rm eff}$ and $\langle\mu\rangle_{\rm eff}$ are correlated and act in a direction nearly parallel to the Kormendy relation, but are not nearly large enough to account for the spread in galaxy properties along the relation. Changes in luminosity are skewed to this relation and shown in Figure 3.12. For this reason it is necessary that a magnitude–limited sample be defined in a consistent way for all clusters studied before conclusions based on changes in the zero–point (due to distances for nearby clusters or evolutionary brightening for higher redshifts) can be made.

3.3.9 The Radius–Luminosity Relation

The correlation between the effective radius and total magnitude for elliptical galaxies has long been used for distance scale work and especially cosmological tests (see Sandage & Perelmuter 1990 and references therein). The best fitting radius–luminosity relation for the K–band data is

$$\begin{aligned} M_K + 5\log h_{75} &= -4.40R_{\rm eff} - 22.31 \quad N = 269 \quad {\rm rms} = 0.88 \text{ mag} \\ &\quad \pm 0.26 \end{aligned} \tag{3.15}$$

assuming $H_0 = 75$ km s^{-1} and that the Coma cluster ($cz = 7200$ km s^{-1}) is at rest with respect to the Hubble flow. The relation is plotted as Figure 3.13. There is intrinsic scatter to this relation that is a result of the variation in surface brightness at a given radius and luminosity; lines of constant surface brightness are plotted in the figure to demonstrate this effect.

3.4 Exploring Simple Models for the Origins of the Elliptical Galaxy Scaling Relations in the Near–Infrared

The near–infrared FP has been shown in §3.3.1 to be represented by the scaling relation $r_{\rm eff} \propto \sigma_0^{1.53\pm0.08}\langle\Sigma_K\rangle_{\rm eff}^{-0.79\pm0.03}$. This relation shows a significant deviation from the optical forms of the FP: $r_{\rm eff} \propto \sigma_0^{1.24\pm0.07}\langle\Sigma\rangle_{\rm eff}^{-0.82\pm0.02}$ (Jørgensen, Franx, & Kjærgaard 1996) and $r_{\rm eff} \propto \sigma_0^{1.38\pm0.04}\langle\Sigma\rangle_{\rm eff}^{-0.82\pm0.03}$ (Hudson *et al.* 1997) in the R–band; or $r_{\rm eff} \propto \sigma_0^{1.13}\langle\Sigma\rangle_{\rm eff}^{-0.79}$ in the V–band (Guzmán, Lucey, & Bower 1993). There are two simple conclusions to draw from these data: (1) the slope of the near–infrared FP deviates from the virial expectation of $r_{\rm eff} \propto \sigma_0^2\langle\Sigma\rangle_{\rm eff}^{-1}$, and (2) the slope of the FP increases with wavelength. A third insight

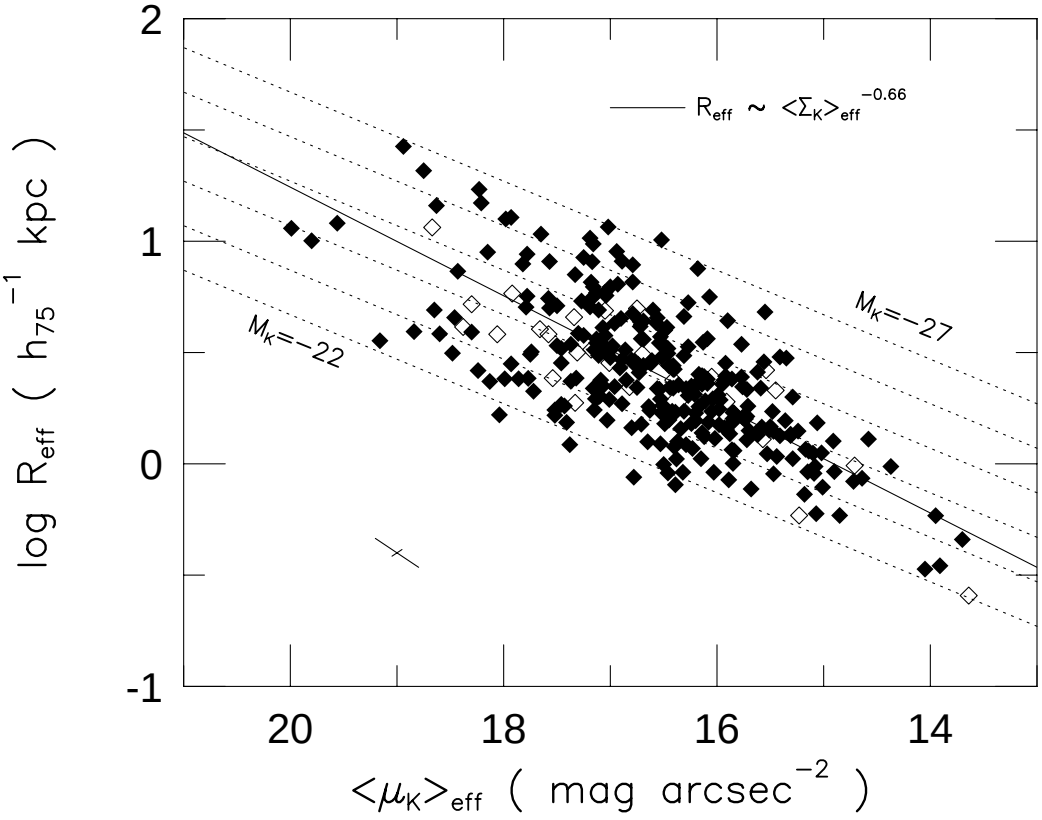

Figure 3.12: The Kormendy relation between effective radius and mean surface brightness. The best–fitting relation is $R_{\rm eff} \propto \langle\mu_k\rangle_{\rm eff}^{-0.61\pm0.07}$ with a scatter of 0.227 dex in $\log R_{\rm eff}$, which is 2.4 times worse than the scatter of the FP (which has the additional σ_0 term). The scatter is significantly smaller in the Coma cluster at 0.198 dex. Measurement errors in $R_{\rm eff}$ and $\langle\mu\rangle_{\rm eff}$ are correlated nearly along the relation, as shown by the representative error bars in the lower–left of the figure. The measurement uncertainties perpendicular to the relation are only 0.015 dex in $\log R_{\rm eff} - 0.32\langle\mu_K\rangle_{\rm eff}$. Luminosity changes act perpendicular to the relation, and representative lines of $M_K = -22$ mag to $M_K = -27$ mag are shown as dotted lines.

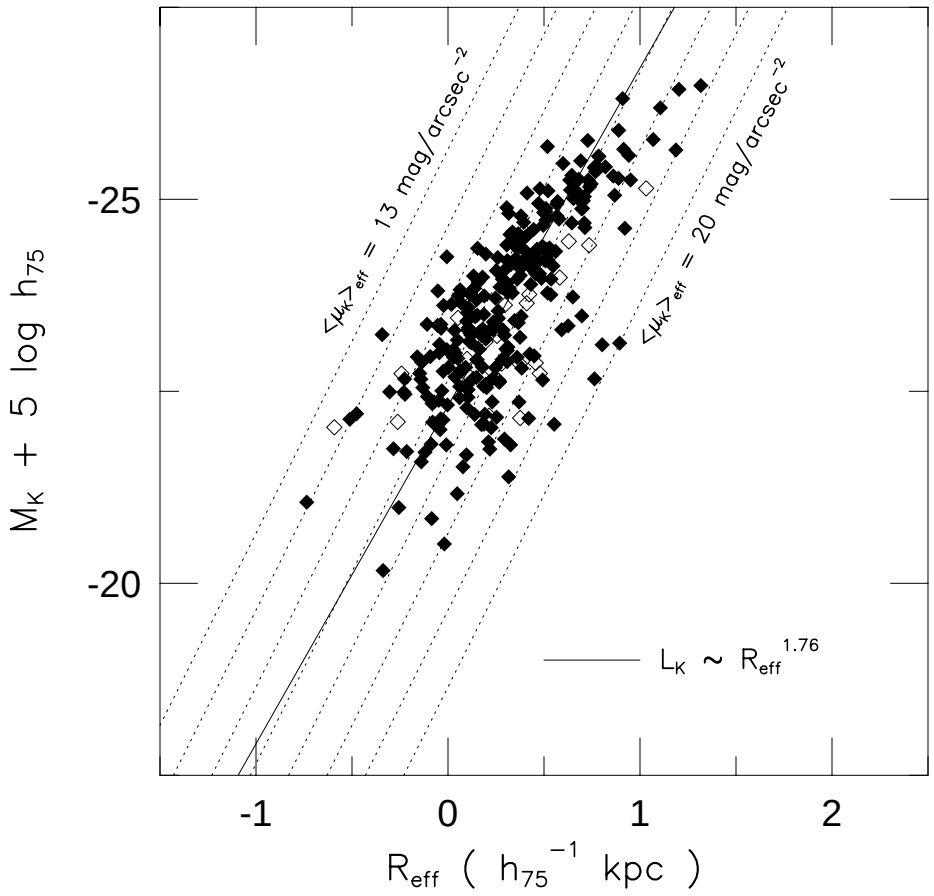

Figure 3.13: The relation between K–band total luminosity and effective radius given by $L_K \propto R_{\rm eff}^{1.76\pm0.10}$. There is substantial intrinsic scatter in this relation due to variations in surface brightness. The dotted lines each represent the variation of M_K and $R_{\rm eff}$ at constant surface brightness.

derives from the fact that the scatter of the FP is very similar at all wavelengths. These three points are sufficient to discuss several simple models for the physical origins of the FP.

The age–metallicity model of Worthey, Trager, & Faber (1995)—based on the form of the FP in the optical, various line indices, and simple stellar populations model comparisons—incorrectly predicts that the near–infrared FP should follow the virial form. Another model, that the FP slope is caused by deviations of the velocity distributions of elliptical galaxies from a homologous scaling family (Capelato, de Carvalho, & Carlberg 1995), incorrectly predicts that the slope of the FP should be independent of wavelength. If this breaking of homology has its origin in dissipationless merging, then this effect also cannot explain the correlation between Mg_2 and σ_0. A final model, which suggests that deviations of the light distributions of elliptical galaxies from the de Vaucouleurs $r^{1/4}$ form is the cause of the FP slope, is unable to account for the slope of the FP in the optical (Graham & Colless 1997), and for the same reasons it cannot explain the near–infrared FP slope.

The deviation of the slope of the near–infrared FP from the virial expectation, assuming homology and constant M/L among ellipticals, is a very significant result. This requires a breakdown of one or both assumptions: either M/L is systematically varying along the FP, or elliptical galaxies are systematically deviating from a homologous scaling family. If age is the stellar populations parameter which causes variations in the slope of the FP with wavelength, then age alone might possibly produce the slope of the K–band FP. This conclusion, however, is severely limited by the possibility of homology breaking along the elliptical galaxy sequence.

Allowing for structural deviations from homology, in the form of a Sersic $r^{1/n}$ profile, does not appear to cause significant changes to the slope of the FP for high S/N, V–band data in the Virgo cluster (Graham & Colless 1997). Instead, allowing for dynamical deviations from homology, via galaxy to galaxy variations in the mapping from σ_0 to $\sigma_{\rm eff}$, appears to cause significant changes in the slope of the FP (Busarello *et al.* 1997; cf. Graham & Colless 1997). Busarello *et al.* found a relationship between the velocity dispersions to be $\log \sigma_0 = (1.28 \pm 0.11) \log \sigma_{\rm eff} - 0.58$. Substituting for $\log \sigma_0$ into the K–band FP solution

in Equation 3.2 produces

$$\begin{array}{rcccc} \log r_{\rm eff} & = & 1.96 \log \sigma_{\rm eff} + & 0.314 \langle \mu_K \rangle_{\rm eff} + & \text{constant} \\ & & \pm 0.20 & \pm 0.011 & \end{array} \tag{3.16}$$

which is statistically consistent with the virial expectation of $r_{\rm eff} \propto \sigma^2$. This argument suggests that the deviation of the near–infrared FP from the virial expectation can be fully explained by systematic deviations of the velocity structure of elliptical galaxies from a homologous family, removing the requirement of large age spreads among elliptical galaxies.

Since either dynamical non-homology or large age spreads could produce the slope of the near–infrared FP, it is impossible to distinguish between these two simple models without further analysis. In addition, any model which incorporates either age or dynamical deviations from a homology along with metallicity variations cannot be excluded in this simple analysis, either. This strongly suggests that a much more detailed analysis, along with a more complicated model with several different variables, is necessary to explain the global properties of elliptical galaxies.

One last *ad hoc* model can be constructed in which there is a *conspiracy* between metallicity and age effects that act in a manner to keep the FP thin. In this model, there can be a large spread in age and metallicity at any given point of the FP—under the constraint that the two effects of age and metallicity work opposite to each other and thereby cancel out to maintain a small scatter. While this model would work at optical wavelengths, the independence of near–infrared light to metallicity would cause the thinness of the optical FP to break down into a thick, near–infrared FP. Since the near–infrared FP has similar observed and intrinsic thicknesses when compared to the optical FP, especially when considering the additional observational uncertainties on $r_{\rm eff}$ caused by σ_0 for the steeper slope of the near–infrared FP, this model can be excluded.

3.5 Discussion

The near–infrared FP that has been constructed in this paper has several important properties: (1) it deviates from the virial expectation (assuming constant M/L and homology); (2) it is steeper than the optical FP relations; (3) it has a similarly small scatter when compared to the optical FP relations; and (4) it has a small, but significantly resolved, intrinsic

scatter. These observational constraints are sufficient to exclude a number of simple models for the origin of the FP, but they do not provide unique discrimination between composite models which include either age, systematic deviations from dynamical homology, or both. Small additional contributions due to metallicity variations are also possible.

Better insight is gained by including the Mg_2 index into the analysis. The Mg_2 form of the FP has much larger scatter than the standard form, which argues that Mg_2 does not uniquely specify the depth of the potential well for each galaxy. This is entirely consistent with the resolved intrinsic scatter of the Mg_2–σ_0 relation. If some physical process like galactic winds (Yoshii & Arimoto 1987) caused the metallicity and potential well for all elliptical galaxies to behave like a one–parameter family, then some other physical property, such as dissipationless mergers or a large scatter in formation times, would be required to produce the small intrinsic scatter of the Mg_2–σ_0 relation and the large intrinsic scatter of the Mg_2 form of the FP.

The near–infrared FP has the unique property that the K–band light is virtually independent of metallicity. For this reason, residuals of the K–band FP (or the K–band relationship between κ_1 and κ_3) and the Mg_2–σ_0 relations could provide a strong discrimination between age and metallicity effects. The lack of any clear correlation between these residuals implies that neither age nor metallicity is a unique contributor to the intrinsic scatter of the FP or the Mg_2–σ_0 relations.

The Fundamental Plane is not just a simple correlation of the observed properties of elliptical galaxies, but rather a unique tool for studying the intrinsic physical properties spanned by these galaxies. The remarkable homogeneity of properties of elliptical galaxies that is implied by the regularity and thinness of the optical FP is clearly reproduced by their similarly regular properties in the near–infrared bandpass.

Acknowledgments

J. Blakeslee and J. Tonry are thanked for providing their SBF distance moduli in electronic form. This research has made use of the NASA/IPAC Extragalactic Database (NED) which is operated by the Jet Propulsion Laboratory, California Institute of Technology, under contract with the National Aeronautics and Space Administration. During the course of this project, M. A. P. received financial support from Jesse Greenstein and Kingsley Fellowships,

the Bressler Foundation; S. G. D. was supported in part by NSF grants AST–9123646 and AST–9157412.

References

Baum, W. A. 1959, PASP, 71, 106

Bender, R., Burstein, D., & Faber, S. M. 1992, ApJ, 399, 462

Bower, R. G., Lucey, J. R., & Ellis, R. S. 1992, MNRAS, 254, 601

Bruzual, A. G. 1983, ApJ, 273, 105

Bruzual, A. G., & Charlot, S. 1996, in preparation; see also Leitherer *et al.* (1996)

Busarello, G., Capaccioli, M., Capozziello, S., Longo, G., & Puddu, E. 1997, A&A, 320, 415

Capelato, H. V., de Carvalho, R. R., & Carlberg, R. G. 1995, ApJ, 451, 525

Capelato, H. V., de Carvalho, R. R., & Carlberg, R. G. 1997, in Galaxy Scaling Relations: Origins, Evolution, and Applications, Proceedings of the Third ESO–VLT Workshop, eds. L. N. da Costa & A. Renzini (Springer–Verlag: Berlin), 331

de Carvalho, R. R., & Djorgovski, S. 1989, ApJ, 341, L37

Charlot, S., Worthey, G., & Bressan, A. 1996, ApJ, 457, 625

Ciotti, L., Lanzoni, B., & Renzini, A. 1996, MNRAS, 282, 1

Djorgovski, S., & Davis, M. 1987, ApJ, 313, 59

Djorgovski, S., & Santiago, B. X. 1993, in Proceedings of the ESO/EIPC Workshop on Structure, Dynamics, and Chemical Evolution of Early–Type Galaxies, ed. J. Danziger, *et al.*, ESO publication No. 45, 59

Dressler, A. 1984, ApJ, 281, 512

Dressler, A., Lynden-Bell, D., Burstein, D., Davies, R. L., Faber, S. M., Terlevich, R. J., & Wegner, G. 1987, ApJ, 313, 42

Faber, S. M., & Jackson, R. E. 1976, ApJ, 204, 668

Faber, S. M., Wegner, G., Burstein, D., Davies, R. L., Dressler, A., Lynden-Bell, D., & Terlevich, R. J. 1989, ApJS, 69, 763

Franx, M., Illingworth, G., & Heckman, T. 1989, AJ, 98, 538

Graham, A., & Colless, M. 1997, MNRAS, 287, 221

Guzmán, R., Lucey, J. R., & Bower, R. G. 1993, MNRAS, 265, 731

Guzmán, R. 1995, in Proceedings of the Heron Island Workshop on Peculiar Velocities in the Universe, `http://qso.lanl.gov/~heron/`

Hudson, M. J., Lucey, J. R., Smith, R. J., & Steel, J. 1997, MNRAS, in press

Jørgensen, I. 1997, MNRAS, in press

Jørgensen, I., Franx, M., & Kjærgaard, P. 1995a, MNRAS, 273, 1097

Jørgensen, I., Franx, M., & Kjærgaard, P. 1995b, MNRAS, 276, 1341

Jørgensen, I., Franx, M., & Kjærgaard, P. 1996, MNRAS, 280, 167

Kormendy, J. 1977, ApJ, 218, 333

Lucey, J. R., & Carter, D. 1988, MNRAS, 235, 1177

Lynden–Bell, D., Faber, S. M., Burstein, D., Davies, R. L., Dressler, A., Terlevich, R. J., & Wegner, G. 1988, ApJ, 326, 19

Mould, J. R. 1978, ApJ, 220, 434

Murphy, D. C., Persson, S. E., Pahre, M. A., Sivaramakrishnan, A., & Djorgovski, S. G. 1995, PASP, 107, 1234

Pahre, M. A., Djorgovski, S. G., & de Carvalho, R. R. 1995, ApJ, 453, L17

Pahre, M. A., & Djorgovski, S. G. 1997, in The Nature of Elliptical Galaxies, Proceedings of the Second Stromlo Symposium, eds. M. Arnaboldi, G. S. Da Costa, & P. Saha, ASP Conf. Ser. Vol. 116, (San Francisco: ASP), 154

Pahre, M. A., Djorgovski, S. G., & de Carvalho, R. R. 1997, in Galaxy Scaling Relations: Origins, Evolution, and Applications, Proceedings of the Third ESO–VLT Workshop, eds. L. N. da Costa & A. Renzini (Springer–Verlag: Berlin), 197

Pahre, M. A. 1998, in preparation [Chapter 2 of this thesis]

Pahre, M. A., de Carvalho, R. R., & Djorgovski, S. G. 1998, in preparation [Chapter 4 of this thesis]

Peletier, R. F., Davies, R. L., Illingworth, G. D., Davis, L. E., & Cawson, M. 1990a, AJ, 100, 1091

Peletier, R. F., Valentijn, E. A., & Jameson, R. F. 1990b, A&A, 233, 62

Persson, S. E., Frogel, J. A., & Aaronson, M. 1979, ApJS, 39, 61

Prugniel, P., & Simien, F. 1996, A&A, 309, 749

Recillas-Cruz, E., Carrasco, L., Serrano, P. G., & Cruz-González, I. 1990, A&A, 229, 64

Recillas-Cruz, E., Carrasco, L., Serrano, P. G., & Cruz-González, I. 1991, A&A, 249, 312

Sandage, A. 1972, ApJ, 176, 21

Sandage, A., & Visvanathan, N. 1978, ApJ, 223, 707

Sandage, A., & Visvanathan, N. 1978, ApJ, 228, 81

Sandage, A., & Perelmuter, J.-M. 1990, ApJ, 361, 1

Smith, R. J., Lucey, J. R., Hudson, M. J., & Steel, J. 1997, MNRAS, in press

Terlevich, R. J., Davies, R. L., Faber, S. M., & Burstein, D. 1981, MNRAS, 196, 381

Tonry, J. L., & Davis, J. 1981, ApJ, 246, 680

Tonry, J. L., Blakeslee, J. P., Ajhar, E. A., & Dressler, A. 1997, ApJ, 475, 399

Visvanathan, N., & Sandage, A. 1977, ApJ, 216, 214

Worthey, G. 1994, ApJS, 95, 107

Worthey, G., González, J. J., & Faber, S. M. 1992, ApJS, 398, 69

Worthey, G., Trager, S. C., & Faber, S. M. 1995, in Fresh Views of Elliptical Galaxies, ASP Conf. Ser. Vol. 86, eds. A. Buzzoni & A. Renzini (San Francisco: ASP) 203

Yoshii, Y., & Arimoto, N. 1987, A&A, 188, 13

Chapter 4

The Physical Origins of the Fundamental Plane Scaling Relations for Early–Type Galaxies

Abstract

The physical origins of the Fundamental Plane (FP) scaling relations are investigated using large samples of early–type galaxies observed at optical and near–infrared wavelengths. The slope a in the FP relation $r_{\rm eff} \propto \sigma_0^a \langle\Sigma\rangle_{\rm eff}^b$ is shown to increase systematically with wavelength from the U–band ($\lambda \sim 0.35\mu$m) through the K–band ($\lambda \sim 2.2\mu$m). A distance–independent construction of the observables is described which provides an accurate measurement of the change in the FP slope between any pair of bandpasses. The variation of the FP slope with wavelength is strong evidence of systematic variations in stellar content along the elliptical galaxy sequence, but is insufficient to discriminate between a number of simple models for possible physical origins of the FP. Several other constraints on the properties of early–type galaxies—the slope of the Mg_2–σ_0 relation, the slope of the FP in the K–band, the effects of stellar populations gradients, and the effects of deviations of early–type galaxies from a dynamically homologous family—are then included to construct an empirical, self–consistent model which provides a complete picture of the underlying physical properties which are varying along the early–type galaxy sequence. The fundamental limitations to providing accurate constraints on the individual model parameters (variations in age and metallicity, and the size of the homology breaking) appear to be subtle variations between different stellar populations synthesis models and poorly constrained velocity dispersion aperture effects. This empirical approach nonetheless demonstrates that there are significant systematic variations in both age and metallicity along the elliptical galaxy sequence, and that a small, but systematic, breaking of dynamical homology is required. The intrinsic thickness of the FP can then be easily understood as small variations in age, metallicity, and deviations from a homology at any particular point along the FP. The model parameters will be better constrained by measurements of the change of the slope of the FP with redshift; predictions for this evolution with redshift are described.

This model for the underlying physical properties that produce the FP scaling relations provides a comprehensive framework for future investigations of the global properties of early–type galaxies.

4.1 Introduction

It was immediately recognized by Dressler *et al.* (1987) and Djorgovski & Davis (1987) that the existence of the bivariate Fundamental Plane (FP) correlations implied a strong regularity of the mass–to–light ratios (M/L) among elliptical galaxies. They further noticed that the exact form of the dependence of the observable measuring the size of the galaxy (the half–light radius $r_{\rm eff}$) and the observable measuring the dynamics of the internal stellar motions (the velocity dispersion σ) required M/L to vary slowly, but systematically, with the galaxy luminosity L. If the virial theorem is combined with the assumptions that elliptical galaxies form a homologous family and have a constant M/L, then the predicted dependence is $r_{\rm eff} \propto \sigma_0^2$. The observed power–law "slope" of this correlation (at optical wavelengths), however, ranges from $r_{\rm eff} \propto \sigma_0^{1.2}$ to $r_{\rm eff} \propto \sigma_0^{1.4}$. The difference between the predicted and observed correlations was taken as evidence that the assumption of constant M/L was in error: elliptical galaxies would then have $M/L \propto L^{0.25}$. The physical origin of this effect was unknown at the time, but later studies suggested it could be a result of variations in their stellar (Renzini & Ciotti 1993; Djorgovski & Santiago 1993; Worthey, Trager, & Faber 1996; Zepf & Silk; Prugniel & Simien 1996) or dark matter (Ciotti, Lanzoni, & Renzini 1996) content. The latter explanation, however, would be in contradiction to galactic wind models (Arimoto & Yoshii 1987) which can successfully account for the Mg_2–σ_0 relation (Ciotti, Lanzoni, & Renzini 1996). Velocity anisotropy could also contribute to this effect (Djorgovski & Santiago 1993; Ciotti, Lanzoni, & Renzini 1996) since more luminous ellipticals tend to be more anisotropic (Davies *et al.* 1983), but this effect has not been explored in much detail.

The difference between the predicted and observed FP correlations might not be a result of variations in the mass–to–light ratios among elliptical galaxies, but could instead be a systematic breakdown of homology along the galaxy sequence. These deviations from a homologous family could take a structural form in that the galaxies deviate from a pure de Vaucouleurs $r^{1/4}$ light profile: if the distribution of galaxy light follows a Sersic $r^{1/n}$ profile

(Sersic 1968), then a systematic variation of n as a function of luminosity could also be implied by the FP. It is known that not all elliptical galaxies follow a strict $r^{1/4}$ light profile (Caon, Capaccioli, & D'Onofrio 1993; Burkert 1993), but an investigation of galaxies in the Virgo cluster suggests that this effect is not sufficient to explain fully the departure of the observed FP correlations from the predictions (Graham & Colless 1997). Alternatively, the breakdown of homology could be of a dynamical nature, in the sense that the stellar velocity distributions vary systematically along the elliptical galaxy sequence. This effect appears to follow directly from dissipationless merging (Capelato, de Carvalho, & Carlberg 1995) when the orbital kinetic energy of the pre–merger galaxies relative to each other is redistributed into the internal velocity distribution of the merger product. The FP correlations would be affected because the central velocity dispersion σ_0 then does not map in a homologous way to the half–light velocity dispersion. Since the global photometric parameters are typically evaluated at the half–light radius, the exact details of the mapping of velocity dispersion from the core to the half–light radius are essential. An investigation of this effect on the FP by using velocity dispersion profiles from the literature suggests that it can contribute as much as one–half of the difference between the observed optical FP correlations and the virial expectation assuming constant M/L (Busarello *et al.* 1997).

The purpose of the present paper is to explore in detail the properties of early–type galaxies as a means of elucidating which underlying physical properties (and their systematic variations within the family of early–type galaxies) are the origins of the FP and other global correlations. The two major classes of physical properties that will be explored here are stellar populations (age and metallicity) and deviations from a homologous family.

The large catalogs of data used in the present paper will be summarized in §4.2, although more complete descriptions can be found in Pahre (1998; Chapter 2 of this thesis). As will be shown in §4.3, the scaling radius changes *systematically* from the optical to the near–infrared signifying the presence of color gradients, hence the use of $r_{\rm eff}(\lambda)$ in studying the variations of the FP with wavelength is an important new element of this work. The change of the slope of the FP between the optical and near–infrared bandpasses will be described in §4.4 and §4.5 using a methodology that is both distance independent and minimizes the cumulative effects of observational measurement uncertainties. It will be shown in those sections that the slope of the FP increases systematically with wavelength. The global, observed constraints on the properties of elliptical galaxies are enumerated in §4.6, thereby

providing a list of properties that any viable model for the origins of the FP must explain. A detailed and self–consistent model will be constructed in §4.7 which simultaneously accounts for the changes of the slope of the FP with wavelength, the absolute value of the slope in the K–band, the Mg_2–σ_0 relation, stellar populations gradients, and deviations of ellipticals from a dynamically homologous family.

4.2 Description of the Data

The data used for this paper were compiled by Pahre (1998, Chapter 2 of this thesis). The photometric data are global parameters taken from recent surveys from the U to K bandpasses: effective radii $r_{\rm eff}$, mean surface brightnesses $\langle\mu\rangle_{\rm eff}$ within those radii, total magnitudes $m_{\rm tot}$, global colors, and the D_n parameter (Dressler *et al.* 1987) defined in a self–consistent manner in all bandpasses. All global photometric parameters (including in the K–band) were derived independently from *imaging* data with two exceptions: the large survey of Faber *et al.* (1989) in the B and V bands utilized photo-electric photometry to derive the parameters; and the study of Prugniel & Simien (1996) only provide $r_{\rm eff}$ in the B–band, but provide colors ranging from U to $I_{\rm C}$ that were evaluated at the B–band $r_{\rm eff}$.

The spectroscopic data are taken from the literature using the aperture correction methodology of Jørgensen *et al.* (1995b) and the small offsets between data sets derived by Smith *et al.* (1997). The derived parameters are central velocity dispersion σ_0 and Mg_2 index, both normalized to a physical scale of diameter $1.53h_{75}^{-1}$ kpc corresponding to an angular diameter of 3.4 arcsec at the distance of the Coma cluster.

4.3 Comparing Optical and Near–Infrared Effective Radii

The comparison between radii and diameters, as measured independently in the optical and near–infrared, are plotted in Figure 4.1. There is a clear systematic difference between $\log r_{\rm eff,K}$ and $\log r_{\rm eff,opt}$, in the sense that the infrared effective radii are smaller than the optical ones. The $r_{\rm eff,opt}$ from the literature were not corrected for wavelength effects (as they should be due to the presence of color gradients), hence it is necessary to use subsamples for individual filters to make a meaningful comparison between optical and near–infrared effective radii. For example, comparing $r_{\rm eff,V}$ from Lucey *et al.* (1991b, 1997) with $r_{\rm eff,K}$

shows a median offset of $\log r_{\rm eff,V} - \log r_{\rm eff,K} = +0.08$ dex ($N = 94$). This can be understood most simply as a change in scale length between the optical and near–infrared. Using the formalism of Sparks & Jørgensen (1993), the change in scale length implied by a color gradient is $\Delta s = \Delta r_{\rm eff}/r_{\rm eff} = 0.18$, which is converted into an isophotal color gradient of $\Delta(\mu_V - \mu_K) = \beta \Delta \log r$ with $\beta \sim s = -0.18$ mag arcsec^{-2} dex^{-1}. This is similar to $\beta = -0.16$ mag arcsec^{-2} dex^{-1} found by Peletier *et al.* (1990b), albeit for a small sample (12 galaxies) with a small FOV detector. If the color gradient were due to a metallicity gradient, a simple change from [Fe/H]= 0 to -0.25 dex would produce a change in color of $\Delta(V-K) = 0.38$ mag, $\Delta(B-V) = 0.07$ mag, $\Delta(U-R) = 0.25$ mag, $\Delta(B-R) = 0.11$ mag (Worthey 1994). Thus, a metallicity gradient of Δ [Fe/H] $/\Delta \log r = -0.12$ would be consistent with the observed $\log r_{\rm eff,opt} - \log r_{\rm eff,K} = +0.08$ dex and the observed optical color gradients from the literature (Sandage & Visvanathan 1978a; Franx, Illingworth, & Heckman 1989; Peletier *et al.* 1990a; Jørgensen, Franx, & Kjærgaard 1995). If the trend of $\log r_{\rm eff,opt} - \log r_{\rm eff,K}$ with $\log r_{\rm eff,K}$ is real, then this would also be consistent with the size of the color gradients correlating with galaxy size and hence luminosity.

It is also apparent that there is no systematic offset between $\log D_V$ and $\log D_K$, which is due to the good match between the assumed mean galaxy colors of $(V-K) = 3.2$ mag used in the definition of D_K and the true mean galaxy color. The rms of this difference is 0.048 dex, which is significantly larger than the uncertainties in both measurements added in quadrature. Part of this effect is due to the change in the slope of the FP between the optical and near–infrared which causes a correlation of $\log D_K - \log D_V$ with $\log \sigma_0$. This effect will be discussed in §4.4.

There is a systematic offset of the quantity $(\log r_{\rm eff,K} - 0.32\langle\mu_K\rangle_{\rm eff}) - (\log r_{\rm eff,V} - 0.32\langle\mu_V\rangle_{\rm eff})$ in Figure 4.1 which is primarily due to the mean color in $(V-K)$, but some of this effect is also due to the correlation with σ_0 due to the change in the slope of the FP between the optical and near–infrared.

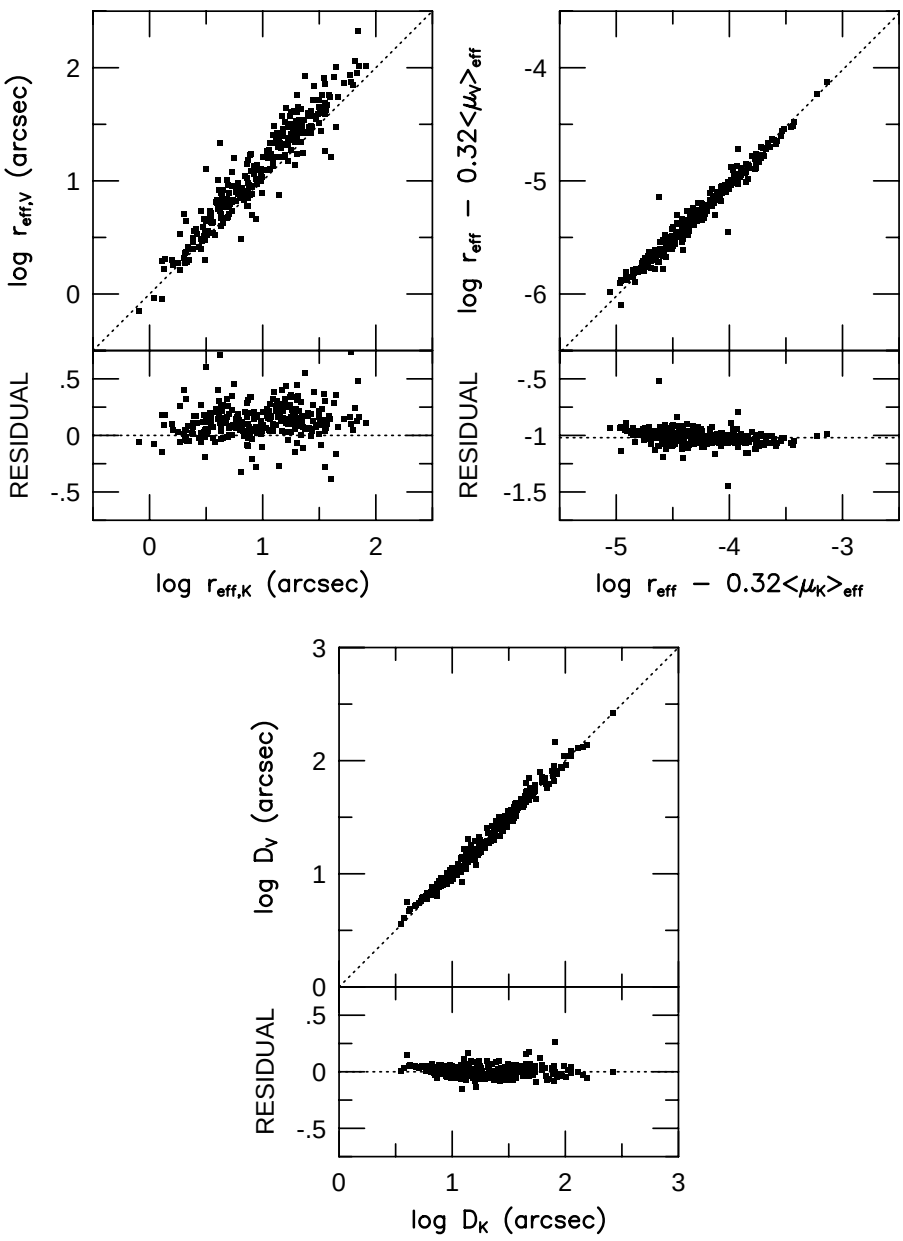

Figure 4.1: Comparison between the estimates of the effective radius $r_{\rm eff}$ and diameter D (i.e., D_V for the V–band, D_K for the K–band). The quantity $r_{\rm eff}$ differs between the optical and near–infrared. The median offset for the comparison with the data of Lucey *et al.* (1991b, 1997) is $\log r_{\rm eff,V} - \log r_{\rm eff,K} = 0.08$ dex. This systematic variation is consistent with a color gradient of $\Delta(\mu_V - \mu_K)/\Delta \log r_{\rm eff} = -0.18$ mag dex^{-1}, which is a good match to the observed color gradients in $(B-R)$ and $(U-R)$ if their origin is in radial variations in [Fe/H] (see text).

4.4 The Difference in Slope Between the Optical and Near–Infrared FP

4.4.1 The Traditional Method to Measure the Change in Slope of the FP

The near–infrared FP has been shown in Pahre *et al.* (1998a, Chapter 3 of this thesis) to be represented by the scaling relation $r_{\rm eff} \propto \sigma_0^{1.53\pm0.08}\langle\Sigma_K\rangle_{\rm eff}^{-0.79\pm0.03}$. This relation shows a significant deviation from the optical forms of the FP: $r_{\rm eff} \propto \sigma_0^{1.24\pm0.07}\langle\Sigma\rangle_{\rm eff}^{-0.82\pm0.02}$ (Jørgensen, Franx, & Kjærgaard 1996) and $r_{\rm eff} \propto \sigma_0^{1.38\pm0.04}\langle\Sigma\rangle_{\rm eff}^{-0.82\pm0.03}$ (Hudson *et al.* 1997) in the R–band; or $r_{\rm eff} \propto \sigma_0^{1.13}\langle\Sigma\rangle_{\rm eff}^{-0.79}$ in the V–band (Guzmán, Lucey, & Bower 1993). A simple conclusion can be drawn from these data: the slope of the FP increases with wavelength. While the trend appears clear in all these comparisons, the statistical significance of any one comparison is not overwhelming. For example, the change in slope from r–band to K–band is $+0.29 \pm 0.11$, which is at the $< 3\,\sigma$ confidence level (CL).

4.4.2 The New, Distance–Independent Method to Measure the Change in Slope of the FP

A more direct comparison will be made in this section between the optical and near–infrared FP relations by explicitly fitting the difference in slope for only those galaxies in common between a given optical survey and the near–infrared survey *using the same central velocity dispersions for both.* This will provide reasonable estimates of both the change in slope and its uncertainty.[1]

The method used here takes advantage of the observation that the quantity $\log r_{\rm eff} - b\langle\mu\rangle_{\rm eff}$ in the FP has a value of $b \sim 0.32$ that is independent of the wavelength studied or fitting method adopted. Note, for example, that $b = 0.326 \pm 0.011$ for the $R_{\rm C}$–band (Hudson *et al.* 1997), $b = 0.328 \pm 0.008$ for the r–band (Jørgensen, Franx, & Kjærgaard 1996), $b = 0.320 \pm 0.012$ for the $I_{\rm C}$–band (Scodeggio, Giovanelli, & Haynes 1997), and $b = 0.314 \pm 0.011$ for the K–band (Pahre, Djorgovski, & de Carvalho 1998a, Chapter 3 of this thesis). This agreement occurs despite the different fitting methods employed in each

[1] Jørgensen *et al.* (1996) fit their data in U, B, and g bandpasses by assuming the cluster distances from the r–band solution. While this is certainly an improvement over the free fitting method because it offers an additional constraint on the problem, we consider that the method which follows to be more elegant due to its independence from assumptions of distance.

study.[2] By assuming $b \equiv 0.32$, the optical and near–infrared forms of the FP reduce to

$$\begin{aligned} \log r_{\rm eff,K}({\rm arcsec}) &= a_K \log \sigma_0 + 0.32\langle\mu_K\rangle_{\rm eff} + c_{i,K} \\ \log r_{\rm eff,opt}({\rm arcsec}) &= a_{\rm opt} \log \sigma_0 + 0.32\langle\mu_{\rm opt}\rangle_{\rm eff} + c_{i,{\rm opt}} \end{aligned} \tag{4.1}$$

Taking the difference of these equations produces

$$(\log r_{\rm eff,K} - 0.32\langle\mu_K\rangle_{\rm eff}) - (\log r_{\rm eff,opt} - 0.32\langle\mu_{\rm opt}\rangle_{\rm eff}) = \Delta a \times \log \sigma_0 + c_{K,{\rm opt}} \tag{4.2}$$

where $\Delta a = a_K - a_{\rm opt}$ is the difference in FP slope between the near–infrared and optical, and the constants have been combined into $c_{K,{\rm opt}}$. There is no distance dependence on either the left–hand or right–hand sides of Equation 4.2, assuming that seeing corrections have been applied to $r_{\rm eff}$ and $\langle\mu\rangle_{\rm eff}$, and aperture corrections to σ_0. Therefore, all galaxies, both in clusters and the field, can be studied. When the optical FP is subtracted from the near–infrared FP, as has been done for Equation 4.2, then the left–hand side of the equation is related to the mean color offset between the two bandpasses—albeit corrected for a small, but systematic, reduction in effective radius from the optical to the near–infrared bandpasses.

Some literature sources measure a D_n parameter instead of $r_{\rm eff}$ and $\langle\mu\rangle_{\rm eff}$, hence an equivalent equation for the change in slope of the D_n–σ_0 relation is

$$\log D_K - \log D_{\rm opt} = \Delta a \times \log \sigma_0 + c_{K,{\rm opt}}. \tag{4.3}$$

All of the galaxies in the K–band sample with companion optical measurements of $r_{\rm eff}$ and $\langle\mu\rangle_{\rm eff}$ or D_n were fit to Equations 4.2 or 4.3, respectively. The sum of the absolute value of the residuals was minimized in a direction orthogonal to the relation, and the uncertainties on a and $c_{K,{\rm opt}}$ were determined from bootstrap resampling of the data. This combined sample used mean colors to convert data in the B, r, $R_{\rm C}$, or $I_{\rm C}$ bands into the V–band, with the exception of the Faber *et al.* (1989) data set, for which the observed

[2]Prugniel & Simien (1996) constructed a form of the FP (their Equation 3) which is equivalent to the modified Faber–Jackson relation (Pahre, Djorgovski, & de Carvalho 1998a, Chapter 3 of this thesis) in our notation. They argued that γ in $(1 + 2\gamma)/(1 + 2\beta) = -b'$ (using their notation for β and γ), where $2/(1 + 2\beta) = a'$, was poorly constrained but consistent with zero, and hence set $\gamma = 0$. This assumption causes the power law index b' for the surface brightness to vary with β and hence to vary with wavelength, *in contradiction to all of the studies quoted in the text* (for a range in wavelengths).

$(B-V)_0$ were used. The problem with using mean colors is that no account is made for the color–magnitude relation between the observed and V bandpasses, hence the slope of the FP does not change *by construction*. For this reason, separate comparisons are made for each literature source for those galaxies in common, but keeping the data in the original bandpass. All of these fits are listed in Table 4.1. Note that the catalogs prepared for the purpose of this comparison have been put onto a common extinction scale as described by Pahre (1998, Chapter 2 of this thesis). Several outlier data points were excluded from these fits: D45 in Klemola 44, PER199 in Perseus, and D27 in Coma from the comparison with Faber *et al.* (1989); E160G23 and NGC 4841A/B in Coma from the comparison with Scodeggio *et al.* (1997); and NGC 6482 from all comparisons.

The fits for each of the subsamples are plotted in Figures 4.2 and 4.3 for the comparisons of $\log r_{\rm eff} - 0.32\langle\mu\rangle_{\rm eff}$ and D_n, respectively. If the optical and near–infrared FP relations had the same slope, then all points would lie on a horizontal line in these figures; this is clearly not the case. The statistical significance of each regression for the comparison of $\log r_{\rm eff} - 0.32\langle\mu\rangle_{\rm eff}$ is at the 2–6 σ confidence level (CL), while the significance for the $\log D_K - \log D_{\rm opt}$ comparison is at the 3–10 σ CL. As a demonstration of how the method adopted here is superior to the alternate method of fitting the optical and near–infrared FP relations independently and then comparing their slopes, notice that the 0.06 dex uncertainty in Table 4.1 for the Jørgensen *et al.* (1996) r–band subsample is nearly a factor of two smaller than the 0.11 dex uncertainty derived when the independently fitted slopes were compared in §4.4.1, despite the fact that one–fourth the number of galaxies were used in this newer method. The difference is most likely due to several factors: an identical sample of galaxies is studied simultaneously in both the optical and near–infrared; the velocity dispersion term used is identical for both FP relations; there is no assumption about the distance to a given galaxy or its cluster; and the uncertainties in the velocity dispersion are not applied twice in the estimation of uncertainties.

All of the optical to near–infrared comparisons of $\log r_{\rm eff} - 0.32\langle\mu\rangle_{\rm eff}$, with the exception of the U–band comparison with Jørgensen *et al.* (1995a), are statistically indistinguishable. The uncertainties, however, are large enough that small but real trends with wavelength in the optical are not excluded. While the D_n–σ_0 relations show no statistical difference between the B and V bandpasses, there is a change in the slope between the optical to near–infrared data (significant at the 2–3 σ CL) from the V to the R (or r) bandpasses,

Table 4.1: Comparison of the Slope of the FP in the Optical and Near–Infrared

Literature Source	λ	Fundamental Plane						D_n–σ_0					
		Δa	$\pm$	$c_{K,opt}$	$\pm$	rms (dex)	N	Δa	$\pm$	$c_{K,opt}$	$\pm$	rms	N (dex)
All Data	$V^{\dagger}$	0.18	0.03	0.60	0.07	0.05	239	0.18	0.02	-0.41	0.06	0.04	249
Jørgensen *et al.* (1996)	U	0.51	0.13	0.28	0.30	0.03	20	0.38	0.05	-0.88	0.10	0.03	20
Jørgensen *et al.* (1996)	B	0.32	0.08	0.57	0.17	0.03	25	0.30	0.08	-0.70	0.18	0.03	26
Faber *et al.* (1989)	B	0.19	0.04	0.91	0.10	0.06	145	0.17	0.05	-0.37	0.12	0.05	149
Jørgensen *et al.* (1996)	g	0.21	0.12	0.59	0.28	0.04	26	0.23	0.06	-0.52	0.15	0.03	27
Lucey *et al.*‡	V	0.23	0.04	0.50	0.10	0.05	83	0.21	0.02	-0.48	0.05	0.03	135
Jørgensen *et al.* (1996)	r	0.17	0.06	0.54	0.14	0.04	55	0.12	0.02	-0.28	0.06	0.03	56
Smith *et al.* (1997)	$R_{\rm C}$	0.17	0.07	0.45	0.16	0.05	44	0.14	0.02	-0.32	0.04	0.02	44
Scodeggio *et al.* (1997)	$I_{\rm C}$	0.22	0.10	0.04	0.24	0.04	43	...	...	...	...	...	...

Notes: †The complete sample uses data from B to $I_{\rm C}$ bandpasses that have been converted to V assuming mean colors, except for the data of Faber *et al.* (1989) which have been converted from B to V using their measurements of $(B-V)$. ‡Lucey *et al.* refers to the combined sample of Lucey & Carter (1988), Lucey *et al.* (1991a,b), and Lucey *et al.* (1997).

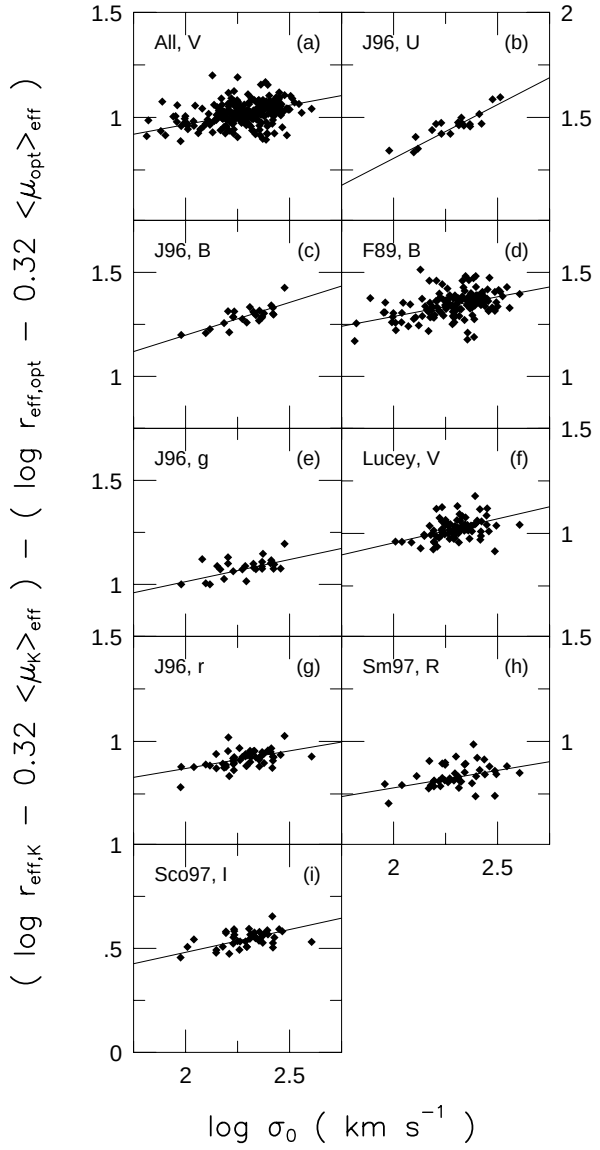

Figure 4.2: Comparison of the slope of the optical and near–infrared FP relations. Plotted as the vertical axis is the difference in $\log r_{\rm eff} - 0.32\langle\mu\rangle_{\rm eff}$ in the sense of K–band minus optical, while velocity dispersion is the horizontal axis. If the optical and near–infrared FP relations had identical slopes, then the points would lie on a horizontal line. The positive value of the linear regression in each case signifies a steepening of the FP as the wavelength moves from the optical to the near–infrared. The slopes and intercepts of these comparisons are listed in Table 4.1. The literature comparisons are: Faber *et al.* (1989; F89); Lucey & Carter (1988), Lucey *et al.* (1991a,b), and Lucey *et al.* (1997); Jørgensen *et al.* (1996; J96); Smith *et al.* (1997; Sm97); and Scodeggio *et al.* (1997; Sco97).

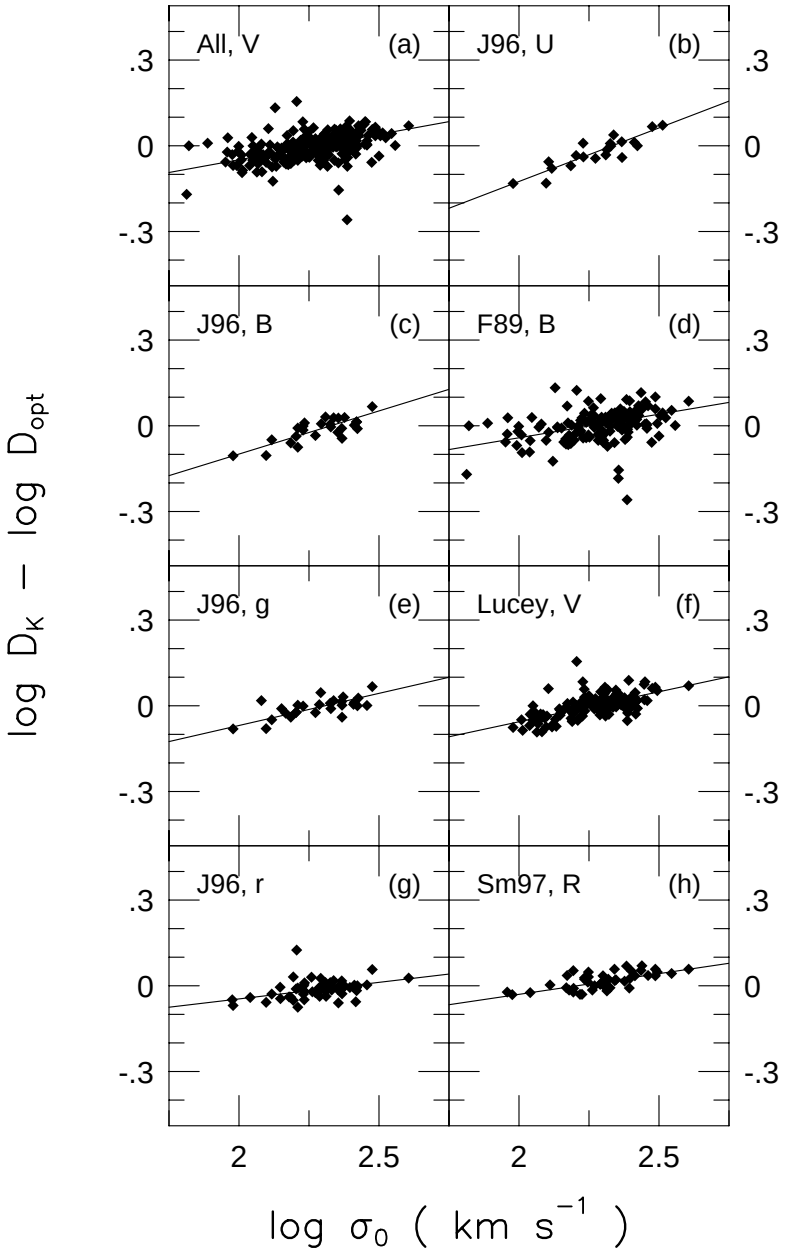

Figure 4.3: Comparison of the slope of the optical and near–infrared D_n–σ_0 relations. Plotted as the vertical axis is the difference in $\log D_K - \log D_{\rm opt}$, while velocity dispersion is the horizontal axis. If the optical and near–infrared FP relations had identical slopes, then the points would lie on a horizontal line. The positive value of the linear regression in each case signifies a steepening of the FP as the wavelength moves from the optical to the near–infrared. The literature comparisons are the same as in Figure 4.2.

or from the U to any other bandpass. The reason that the B band does not match this trend, or that the $\log r_{\rm eff} - 0.32\langle\mu\rangle_{\rm eff}$ comparison did not show the effect, is that these other comparisons have substantially larger observational measurement uncertainties. The D_n parameter can be measured 10–50% more reliably than $\log r_{\rm eff} - 0.32\langle\mu\rangle_{\rm eff}$, whether in the optical (Jørgensen, Franx, & Kjærgaard 1996; Smith *et al.* 1997; Lucey *et al.* 1997) or near–infrared (Pahre 1998a, Chapter 2 of this thesis).

4.4.3 Possible Environmental Effects on the FP

A significant offset in the relationship between $\log D_K - \log D_V$ and $\log \sigma_0$, as measured separately in the Coma cluster and the Hydra–Centaurus Region, was identified by by Guzmán (1995). If this were the case, it would suggest that there are significant environmental effects on the elliptical galaxy correlations, thereby preventing their utility as accurate distance indicators. The present paper includes larger samples of galaxies both in Coma and Hydra–Centaurus, as well as other rich clusters and low density environments, hence this effect can be re–analyzed. The data were broken down into six regions of the sky or similar density environments, compared to the overall solution (as listed in Table 4.1), and are displayed in Figure 4.4.

Guzmán (1995) found that $\log D_K - \log D_V$ at a given $\log \sigma_0$ was ~ 0.05 dex larger in Hydra–Centaurus region than in Coma, but panel (d) of Figure 4.4 shows that it is ~ 0.02 dex *smaller*. The entire difference between the results of Guzmán and the present work can be explained by different assumptions of Galactic extinction: he apparently used Burstein & Heiles (1982) maps (which are based on galaxy number counts and neutral gas emission) as the estimator of A_B, while this work used the 100μm emission (as measured by IRAS) as the estimator of A_B. While the two estimates agree fairly well in a global sense, they disagree by 0.1–0.2 mag in Hydra–Centaurus, in the sense that Burstein & Heiles (1982) underestimates A_B. Nonetheless, the formal error on A_B due to the uncertainties of the IRAS conversion in Laureijs, Helou, & Clark (1994), are sufficient to bring all the galaxies in this region into agreement with the global relation between $\log D_K - \log D_V$ and $\log \sigma_0$. Furthermore, the somewhat larger scatter of the galaxy properties found in this region, compared to the cluster subsamples in the other panels, also argues for significant, patchy dust extinction. It is interesting to note that by increasing A_B in Hydra–Centaurus, the distance estimations of Lynden–Bell *et al.* (1988) would place these galaxies closer to us,

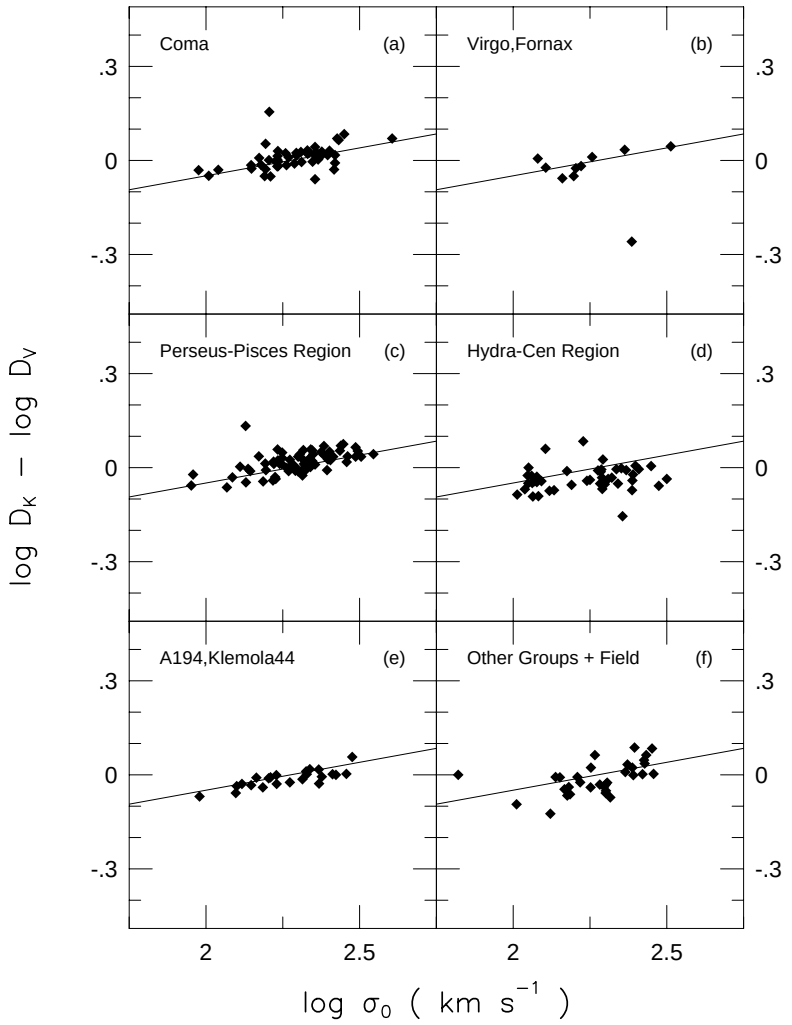

Figure 4.4: Comparison of the difference in slope and intercept of the D_V–σ_0 and D_K–σ_0 relations in various regions and density environments. The same straight line fit to the entire sample is displayed in each panel to ease comparison. Note how there is little or no difference between the slope or intercept in any panel and the mean relation. The largest possible offset is in the Hydra–Centaurus region, but this effect is smaller and *of opposite sign* when compared to the effect found by Guzmán (1995). The large difference between Guzmán (1995) and the present work is fully explained by different assumptions of Galactic extinction in the Hydra–Centaurus region; the formal uncertainty on the IRAS 100μm to A_B extinction conversion adopted here is consistent with there being no offset between the mean relation and the Hydra–Centaurus galaxy subsample. This figure provides evidence that there are no significant environmental effects on the D_n–σ_0 relation.

thereby strengthening the statistical evidence for a Great Attractor causing bulk motions of the galaxies in this region.

Inspection of Figure 4.4 therefore leads to the conclusion that there is no evidence that either the slope or intercept of the elliptical galaxy correlations are dependent on environment. The difference in FP intercept and scatter between galaxies in clusters and the general field (de Carvalho & Djorgovski 1992) would be naturally explained by errors in estimating dust extinction, and not by any intrinsic differences in the stellar populations (or other physical property) among elliptical galaxies that correlates with their environment. Difficulties in estimating Galactic dust extinction therefore appear to be the limiting factor for *optical* distance scale work using the elliptical galaxy correlations.

4.5 Comparing the Fundamental Plane Among Various Optical Bandpasses

When comparing the optical and near–infrared FP in §4.4, there were hints that the differences might be larger for the U–band than for, say, the $R_{\rm C}$–band. Small changes of the slope of the FP between U and r, for example, were reported by Jørgensen *et al.* (1996) and Djorgovski & Santiago (1993) in the sense that the U–band FP has the shallowest slope. Although the differences determined in this manner were of small significance, it should be possible to improve the significance by removing the distance assumptions and using the method described above. Catalogs of optical global photometric parameters and velocity dispersions were compiled from the literature in the same manner as for the near–infrared catalogs (see Pahre 1998a, Chapter 2 of this thesis). An additional catalog consisting of $(U-B)$, $(B-V)$, $(V-R_{\rm C})$, and $(V-I_{\rm C})$ colors and velocity dispersion was constructed from Prugniel & Simien (1996) without modification. Since Prugniel & Simien do not measure $r_{\rm eff}$ and $\langle\mu\rangle_{\rm eff}$ independently for each of the five bandpasses, the differences in $\log r_{\rm eff} - 0.32\langle\mu\rangle_{\rm eff}$ were taken to be 0.32 multiplied by the color. This approach is only partially correct since it does not account for the presence of color gradients, but the systematic errors resulting from this simplification are small.

All comparisons demonstrate that the redder bandpass has a steeper slope for the FP as evidenced by a positive Δa, although in several cases Δa is statistically indistinguishable from zero. The comparisons derived from surface photometry are displayed in Figures 4.5

Table 4.2: Comparison of the Slope of the FP Among Various Optical Bandpasses

Literature Source 1	λ_1	Literature Source 2	λ_2	Fundamental Plane						D_n–σ_0					
				Δa	$\pm$	c_{λ_1,λ_2}	$\pm$	rms (dex)	N	Δa	$\pm$	c_{λ_1,λ_2}	$\pm$	rms	N (dex)
JFK96	r	JFK96	U	0.22	0.03	0.01	0.07	0.03	45	0.17	0.03	-0.42	0.08	0.02	45
JFK96	B	JFK96	U	0.13	0.04	-0.15	0.09	0.02	46	0.09	0.03	-0.22	0.07	0.02	46
P96	B	P96	U	0.13	0.01	-0.13	0.02	0.03	353	...	...	...	...	...	...
P96	V	P96	B	0.05	0.01	0.19	0.01	0.02	406	...	...	...	...	...	...
JFK96	r	JFK96	B	0.18	0.04	-0.06	0.10	0.03	36	0.10	0.04	-0.23	0.08	0.02	37
JFK96	r	F89	B	0.18	0.08	0.00	0.18	0.09	50	0.06	0.04	-0.13	0.09	0.08	52
JFK96	r	JFK96	g	0.08	0.02	-0.04	0.05	0.02	79	0.09	0.01	-0.20	0.03	0.02	80
JFK96	r	L91/97	V	0.02	0.03	0.05	0.07	0.02	54	0.03	0.02	-0.04	0.05	0.02	73
P96	R_C	P96	V	0.03	0.01	0.10	0.02	0.01	256	...	...	...	...	...	...
Smi97	R_C	L91/97	V	0.00	0.04	0.18	0.08	0.02	23	0.01	0.02	-0.02	0.04	0.01	24
Sco97	I_C	L91/97	V	0.10	0.06	0.25	0.14	0.04	61	...	...	...	...	...	...
P96	I_C	P96	R_C	0.06	0.01	0.24	0.03	0.02	256	...	...	...	...	...	...
Sco97	I_C	JFK96	r	0.17	0.07	-0.00	0.15	0.04	45	...	...	...	...	...	...

Notes: The literature sources referenced in this table are as follows. F89: Faber *et al.* (1989). L91/97: Lucey & Carter (1988), Lucey *et al.* (1991a,b), and Lucey *et al.* (1997) J96: Jørgensen *et al.* (1996). P96: Prugniel & Simien (1996). Smi97: Smith *et al.* (1997). Sco97: Scodeggio *et al.* (1997).

and 4.6, while those derived from color information alone (i.e., Prugniel & Simien 1996) are displayed in Figure 4.7.

In several comparisons where the two bandpasses differ only slightly in wavelength—such as between the r–band and V–band—there is no significant variation of the slope of the FP. In most cases, however, there is a statistically significant 3–13 σ CL positive regression, and in no case is there a negative regression, in the analysis listed in Table 4.2.

4.6 General Constraints from the Elliptical Galaxy Scaling Relations

The preceding section, and a number of earlier papers, describe a series of global properties of early–type galaxies that are elucidated from the exact forms of the scaling relations in various bandpasses. These can be summarized as:

1. Early–type galaxies are well–described by a Fundamental Plane correlation corresponding to the scaling relation $r_{\rm eff} \propto \sigma_0^{1.53\pm0.08} \langle \Sigma_K \rangle_{\rm eff}^{-0.79\pm0.03}$ (Pahre, Djorgovski, & de Carvalho 1998a, Chapter 3 of this thesis).

2. As has been shown in §4.4, the slope of the FP (the exponent for the σ_0 term) steepens significantly between the optical and near–infrared. As shown in §4.5, the slope of the FP steepens with wavelength even among the optical bandpasses.

3. The slope of the FP at all wavelengths is inconsistent with the relation $r_{\rm eff} \propto \sigma_0^2 \langle \Sigma \rangle_{\rm eff}^{-1}$ which is expected from the virial theorem under the assumptions of constant mass–to–light ratio and homology within the family of elliptical galaxies.

4. The FP and Mg_2–σ_0 relations may be thin, but they have significant, resolved intrinsic scatter which cannot be explained by the observational uncertainties and does not have a clear correlation with any particular indicator of metallicity or age (Jørgensen, Franx, & Kjærgaard 1996; Pahre, Djorgovski, & de Carvalho 1998a, Chapter 3 of this thesis).

5. The effective radius of early–type galaxies was shown in §4.3 to be systematically smaller at longer wavelengths, which is basically equivalent to the existence (and size)

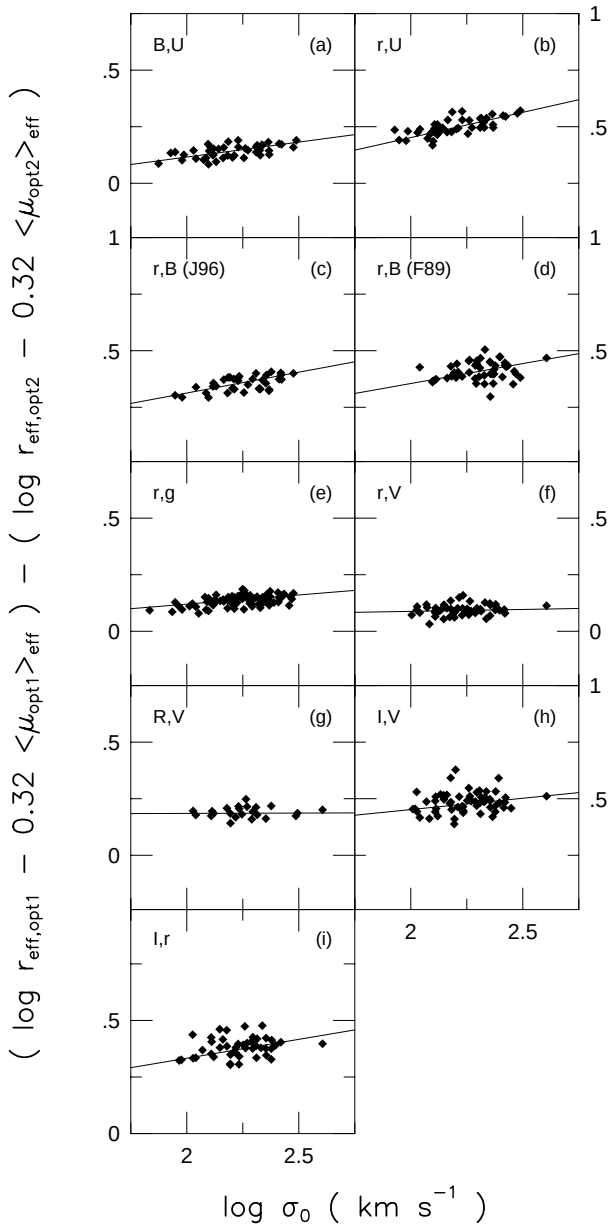

Figure 4.5: Comparison of the slope of the FP relations among various optical bandpasses from U to I_C. In each panel, the vertical axis is the difference in $r_{\rm eff} - 0.32\langle\mu\rangle_{\rm eff}$ measured in each of the pair of bandpasses; the bandpasses are identified in the upper–left corner of each panel, and the difference is in the sense of the first bandpass minus the second. The FP slope is steeper in redder bandpasses as is evidenced by the positive correlation in nearly every panel. Literature sources and regressions are taken from Table 4.2.

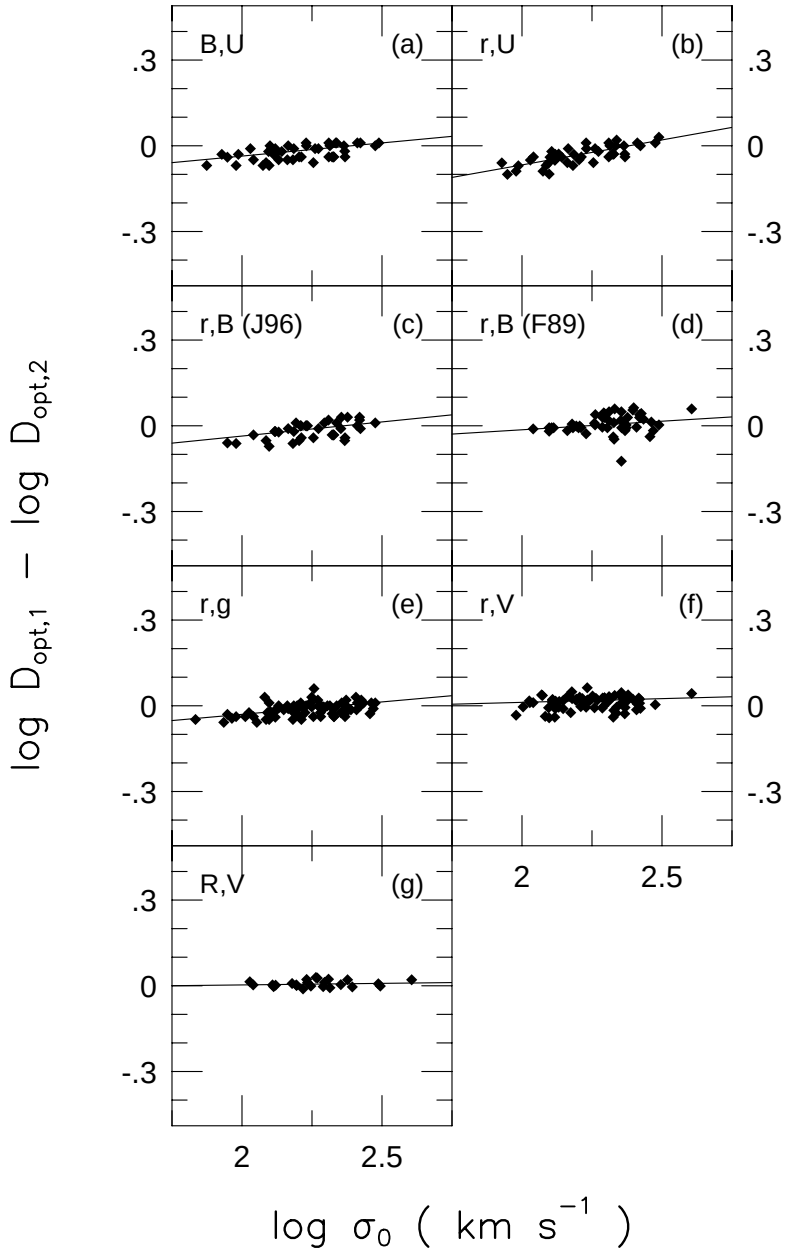

Figure 4.6: Comparison of the slope of the D_n–σ_0 relation among various optical bandpasses from U to I_C. In each panel, the vertical axis is the difference in $\log D_n$ measured in each of the pair of bandpasses; the bandpasses are identified in the upper–left corner of each panel, and the difference is in the sense of the first bandpass minus the second. The slope of the D_n–σ_0 relation is steeper in redder bandpasses as is evidenced by the positive correlation in nearly every panel. Literature sources and regressions are taken from Table 4.2.

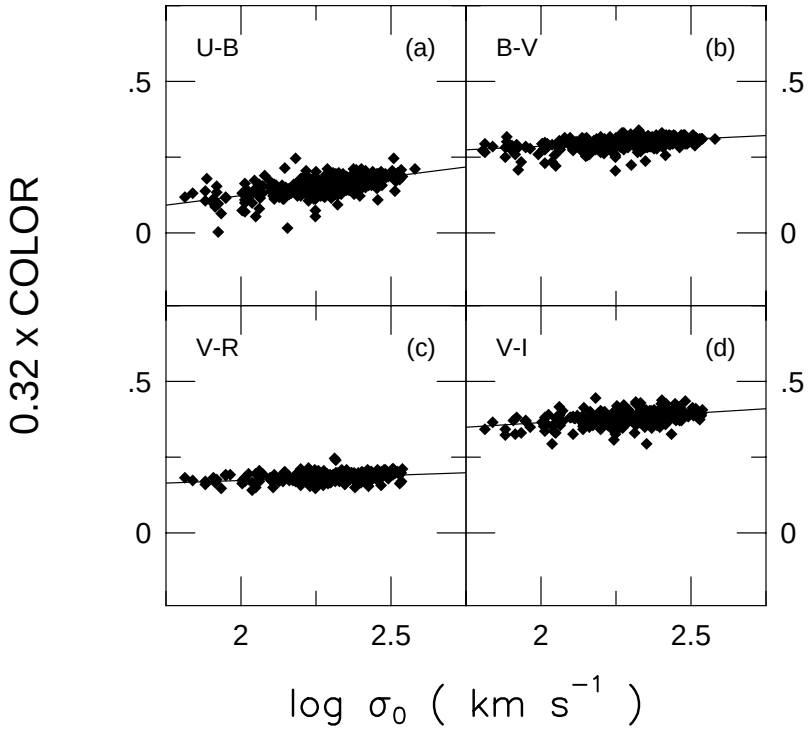

Figure 4.7: Approximate comparison of the slope of the FP relations between various optical bandpasses using the color information from Prugniel & Simien (1996). Since those authors did not measure $r_{\rm eff}$ and $\langle\mu\rangle_{\rm eff}$ independently for each bandpass, the quantity 0.32 times the color was substituted for the difference in $r_{\rm eff} - 0.32\langle\mu\rangle_{\rm eff}$ between each pair of bandpasses. This approach is reasonably similar to Figure 4.5, although it does not fully account for the effects of color gradients on the slope of the FP. Regressions are taken from Table 4.2. Notice that all panels show a regression with positive slope, once again indicating that the slope of the FP steepens with wavelength.

of color gradients in these galaxies if they result from metallicity gradients (Peletier 1993).

There are several other relevant properties of early–type galaxies that can be added to the above list but were not directly shown in this paper:

6. The velocity dispersion measured in an aperture decreases with the increasing size of this aperture according to a power law; the exponent of this power law appears to show a correlation with the luminosity or size of the galaxy (Jørgensen, Franx, & Kjærgaard 1995; Busarello *et al.* 1997).

7. The ratio of magnesium to iron appears to be overproduced in early–type galaxies relative to the solar value (Worthey, González, & Faber 1992), albeit with a significant spread in [Mg/Fe], implying the importance of type II supernovae chemical enrichment and rapid massive star formation in the galaxy formation process, particularly for the most luminous elliptical galaxies.

8. The correlation of Mg_2 with σ_0 implies a connection between the chemical enrichment of a galaxy and the depth of its potential well.

9. Optical and near–infrared color gradients in elliptical galaxies imply isophotal populations gradients of the order 0.16 to 0.30 dex in [Fe/H] (or 1.5 times this in log age) per decade of radius (Franx *et al.* 1989; Peletier *et al.* 1990a,b; Peletier 1993).

10. There is no know correlation between the size of the measured color gradient and the luminosity of the host galaxy (Peletier *et al.* 1990a), although some of the smallest galaxies show no gradients altogether.

Any viable model to explain the global properties of early–type galaxies must be able to account for all of these effects.

4.7 A Self–Consistent Model for the Underlying Physical Parameters Which Produce the FP Correlations

In this section, a series of models will be constructed and explored in order to determine if all the observational constraints in §4.6 can be explained in a fully consistent manner.

4.7.1 Modeling the Changes in the Slope of the FP Between Bandpasses

The effects on broadband color of the change in slope of the FP with wavelength can be expressed in a simple manner. Starting with the definition of total magnitude for a de Vaucouleurs profile,

$$m_{\rm tot} = -5 \log r_{\rm eff} + \langle \mu \rangle_{\rm eff} - 2.5 \log 2\pi \tag{4.4}$$

and the definition of the change in slope $\Delta a_{j,i}$ of the FP from bandpass j to bandpass i (Equation 4.2), the change in the global color $\Delta C_{i,j}$ between bandpass i and j is then

$$\begin{aligned} \Delta C_{i,j} &= 3.125 \left[(\log r_{\rm eff,j} - 0.32 \langle \mu_j \rangle_{\rm eff}) - (\log r_{\rm eff,i} - 0.32 \langle \mu_i \rangle_{\rm eff}) \right] \\ &\quad -1.875 \left(\log r_{\rm eff,i} - \log r_{\rm eff,j} \right) \\ &= 3.125 \Delta a_{j,i} \Delta \log \sigma_0 - 1.875 \Delta r_{\rm eff,i,j} \end{aligned} \tag{4.5}$$

where $\Delta r_{\rm eff,i,j}$ is the change of $\log r_{\rm eff}$ from bandpass i to bandpass j, and $\Delta \log \sigma_0 \sim 0.6$ dex is the change in $\log \sigma_0$ from one end of the FP to the other (a range within which $> 90\%$ of the galaxies lie). The two terms on the right–hand side in Equation 4.5 show the effects of the change in slope of the FP and the presence of color gradients, respectively.

In multi–color studies of isophotal color gradients in elliptical galaxies, Peletier *et al.* (1990a,b) and Franx *et al.* (1989) found consistent results if the underlying cause were metallicity gradients of -0.20, -0.16, and -0.3 dex, respectively. A simple stellar populations model can then be used to convert these estimates into any broadband isophotal color gradient β between U and K. The conversion from isophotal color gradient to $\Delta \log r_{\rm eff}$ is accomplished using Equation 21 of Sparks & Jørgensen, such that $\Delta \log r_{\rm eff} = \beta / (2.3 \times 1.20)$. Hence, only one parameter to represent the global mean metallicity gradient is introduced into the sets of equations described by Equation 4.5 for the 22 observed $\Delta a_{j,i}$ from Tables 4.1 and 4.2.

There is a significant difference in M/L even among the most sophisticated of simple stellar populations models (Charlot, Worthey, & Bressan 1996). Nonetheless, use of such models in a *differential* sense shows far less variation among the models. An example of this is given in Figure 4.8, where the mass–to–light ratio in the V–band and K–band is

compared for four such models. For large ages $t \geq 10$ Gyr, both the Vazdekis *et al.* (1996) and the Bruzual & Charlot (1996, as provided in Leitherer *et al.* 1996) models show similar behavior with M/L_K independent of [Fe/H], while the Worthey (1994) models have M/L_K *inversely* dependent on [Fe/H] and the Fritz-V. Alvensleben & Burkert (1995) models are inconclusive. In fact, Charlot, Worthey, & Bressan (1996) showed in detail how three models differ strongly in their near–infrared properties. From the inspection of the near–infrared portion of Figure 4.8, we have chosen only to make detailed comparisons with the Vazdekis *et al.* and Bruzual & Charlot models.

An additional question could be posed based on Figure 4.8: given that there are significant spreads in M/L between the four models at any wavelength, are the *changes* in M/L (by varying the age and/or metal abundance) more consistent between the models? This was addressed by Charlot *et al.* (1996) who showed that the variations among three models was of order $\delta(B-V)/\delta t \sim 0.004$ mag Gyr^{-1}, $\delta(V-K)/\delta t \sim 0.015$ mag Gyr^{-1}, and $\delta(M/L_V)/\delta t \sim 0.1$ M$_\odot$ L$_\odot^{-1}$ Gyr^{-1} at $t \sim 10$ Gyr. Hence a given model can be used to measure differential age or metallicity effects for an old stellar population while not providing an accurate absolute measure of either quantity.

The variations in magnitude as a function of changing [Fe/H] from -0.4 dex to $+0.4$ dex at $t = 11$ Gyr, and separately as a function of changing age from 2 to 17 Gyr (at intervals of 1 Gyr) at [Fe/H] $= 0$ dex, were calculated using the Bruzual & Charlot models for the $UBVR_{\rm C}I_{\rm C}K$ bandpasses. The same calculations were made for the Vazdekis *et al.* (1996) models. For the modeling below, the Gunn r–band will be assumed identical (for differential effects) to the Cousins $R_{\rm C}$–band, the Gunn g–band will be assumed identical to the V–band, and the K_s–band assumed identical to the K–band. These calculations are summarized in Table 4.3.

4.7.2 Additional Equations of Constraint

The fit to the Mg$_2$–σ_0 relation (Pahre, Djorgovski, & de Carvalho 1998a, Chapter 3 of this thesis) provides an additional equation of constraint derived from the Bruzual & Charlot models (using the variations specified in Table 4.3), namely

$$0.173 \pm 0.010 = \left[0.174\Delta \log t + 0.278 \left(\Delta\ [\mathrm{Fe/H}] + \left(\frac{\Delta\ [\mathrm{Fe/H}]}{1.2 \times 1.6 \Delta \log r}\right)\right)\right] \Delta \log \sigma_0 \tag{4.6}$$

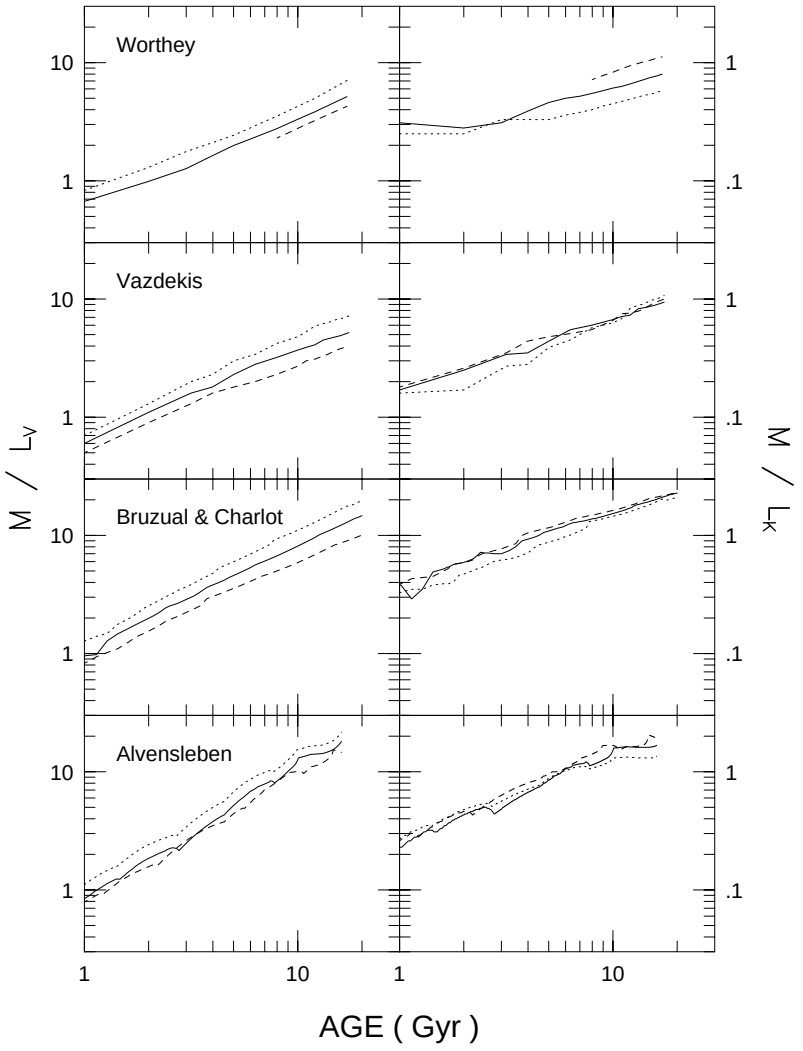

Figure 4.8: Comparison of M/L_V (left) and M/L_K (right) for four different stellar populations models from Worthey (1994), Vazdekis *et al.* (1996), Bruzual & Charlot (1996, in preparation; as provided in Leitherer *et al.* 1996), and Fritz-V. Alvensleben & Burkert (1995). Iron abundances of [Fe/H]= -0.4 (dashed line), 0.0 (solid line), and $+0.4$ dex (dotted line) are shown, except for the Fritze-v. Alvensleben & Burkert 1995 models which have the $+0.3$ dex model substituted for $+0.4$ dex. All models show similar variations in M/L_V with both time and abundance, but not M/L_K. In particular, the Worthey (1994) models show a dependence of M/L_K on [Fe/H]—such that metal–rich systems have small M/L_K—while the Vazdekis *et al.* and Bruzual & Charlot models have M/L_K independent of metal abundance.

Table 4.3: Variations in Magnitude for Various Bandpasses for the Bruzual & Charlot (1996) and Vazdekis *et al.* (1996) Models

Bandpass	Bruzual & Charlot (1996)		Vazdekis *et al.* (1996)	
	$\partial m/\partial \log t$ (mag dex^{-1})	$\partial m/\partial$[Fe/H] (mag dex^{-1})	$\partial m/\partial \log t$ (mag dex^{-1})	$\partial m/\partial$[Fe/H] (mag dex^{-1})
U	+2.934	+1.79	+2.480	+1.50
B	+2.428	+1.12	+2.010	+1.04
V	+2.165	+0.86	+1.755	+0.78
$R_{\rm C}$	+2.033	+0.73	+1.629	+0.63
$I_{\rm C}$	+1.925	+0.65	+1.540	+0.45
K	+1.480	−0.16	+1.566	−0.13
Mg_2	+0.174	+0.278	+0.119	+0.199

The factor of 1.2 in the denominator converts the isophotal gradients into linear changes in $r_{\rm eff}$ (from Equation 21 of Sparks & Jørgensen 1993), while the factor of 1.6 converts this change in $r_{\rm eff}$ into an aperture populations gradient (Sparks & Jørgensen 1993, Equation 18). This latter point is essential to recognize since Mg_2 is typically measured in an aperture of fixed physical size—and has been corrected to a fixed physical size using the methodology of Jørgensen *et al.* (1995b).

In all cases, an isophotal populations gradient of $\beta = \Delta(\mu_i - \mu_j)/\Delta \log r$ between bandpasses i and j is converted to an equivalent change in effective radius $\Delta r_{\rm eff,i,j} = \beta/(1.2\times 2.3)$, where the factor of 2.3 comes from converting the linear change in $r_{\rm eff}$ to logarithmic and the factor of 1.2 derives from Equation 21 of Sparks & Jørgensen (1993).

The slope of the FP in the K–band provides another equation of constraint, as its slope can be affected by age and deviations from homology, but virtually not by metallicity. From the fit to the Faber–Jackson relation in the K–band (Pahre, Djorgovski, & de Carvalho 1998a, Chapter 3 of this thesis), $\Delta K_{\rm tot} = 10.35\Delta\sigma_0$, from Table 4.3 $\Delta K_{\rm tot}({\rm mag}) = +1.48\Delta \log t - 0.16\Delta$[Fe/H] (dex), so the luminosity along the sequence varies as

$$\gamma = \frac{+1.48\Delta \log t - 0.16\Delta \text{ [Fe/H] (dex)}}{10.35\Delta \log \sigma_0} \tag{4.7}$$

In this way the slope of the K–band FP (i.e., a in $r_{\rm eff} \propto \sigma_0^a$; Pahre, Djorgovski, & de

Carvalho 1998a, Chapter 3 of this thesis) provides the equation of constraint

$$1.528 \pm 0.083 = \frac{1}{1+d}\left(\frac{2}{2\gamma+1}\right) \tag{4.8}$$

where a new model parameter d was introduced to represent the deviations of the family of ellipticals from a homologous family in dynamical structures. In this notation, the mapping of velocity dispersions is $\log\sigma_0 = (1+d)\log\sigma_{\rm eff} +$ const. to provide a systematic variation of $\log\sigma_0 - \log\sigma_{\rm eff}$ along the elliptical galaxy sequence. Introduction of the model parameter d also allows for an additional equation of constraint from the measurement of this mapping by Busarello *et al.* (1997), who found $d = 0.28 \pm 0.11$.

In summary, there are 22 equations of constraint represented by Equation 4.5 from the comparisons of the optical and near–infrared FP between pairs of bandpasses (where $\Delta a_{j,i}$ are provided in Tables 4.1 and 4.2), and one equation of constraint each from the Mg_2–σ_0 relation, the slope of the K–band FP relation, and the dynamical non-homology measurement. There are four free parameters: (1) the variation in age $\Delta\log t$ from one end of the FP to the other; (2) the variation in metallicity Δ[Fe/H] along the same sequence; (3) the size of the stellar populations gradient (equal for all elliptical galaxies), expressed for convenience as a metallicity gradient, which produces a color gradient $\beta = \Delta(\mu_i - \mu_j)/\Delta\log r$; and (4) the size of the dynamical non-homology contribution d to the mapping from σ_0 to $\sigma_{\rm eff}$.

4.7.3 Solutions to the Physical Quantities in the Model for the Scaling Relations

The variance was minimized orthogonal to the fit and the uncertainties for each measurement were included in the construction of the Chi–squared statistic. The uncertainties for the four measurements of the change in slope of the optical FP for the Prugniel & Simien (1996) data set were intentionally doubled to account for the systematic effect that these data do not explicitly account for the effects of color gradients. The parameter $\Delta\log\sigma_0$ was set to 0.6 dex to account for the range of velocity dispersion occupied by nearly all the elliptical galaxies; this number merely scales up the model parameters (except for d) without changing the significance of any parameter. The least–squares solution was for the

following values of the model parameters

$$\begin{aligned} \Delta \log t &= +0.38 \pm 0.20 \text{ dex} \\ \Delta \text{ [Fe/H]} &= +0.28 \pm 0.14 \text{ dex} \\ \frac{\Delta \text{ [Fe/H]}}{\Delta \log r} &= -0.26 \pm 0.28 \text{ dex} \\ d &= +0.17 \pm 0.10 \end{aligned} \tag{4.9}$$

The uncertainty estimates are taken from the covariance matrix. The reduced Chi–square for this fit is close to unity at 1.33, suggesting that the combination of the model and the uncertainty estimates in each of the observables is a reasonable description of the properties of elliptical galaxies along their sequence.

The results given in Equation 4.9 for the first time describe the underlying physical origin of the elliptical galaxy scaling relations using a self–consistent model that accounts for population gradients, wavelength effects on the FP, systematic deviations from homology, and a metal line–strength indicator. The formal significance of the results in Equation 4.9, however, appear to suffer from low significance for any given parameter: $\Delta \log t$, Δ[Fe/H], and d are all only significant at the 2 σ CL, while the populations gradient is virtually unconstrained and even consistent with zero. There is significant correlation between the model parameters which is the underlying cause of the reasonably large uncertainties on each parameter; the largest correlation coefficient is -0.7 between d and $\Delta \log t$, which is not surprising since either parameter (or a combination of both) is essential for satisfying constraint from the slope of the near–infrared FP (Equation 4.8).

The inability to constrain the populations gradients should not be considered a problem, since this model is actually only an indirect way of measuring populations gradients in ellipticals; far better are direct measurements of Mg_2 line strength or color gradients. For all of the following fits, an additional equation of constraint will be included to represent the populations gradients: Δ [Fe/H]$/\Delta \log r = -0.22 \pm 0.01$ dex per decade of radius, as this is the mean of color and line–strength gradients from the literature in the analysis of

Peletier (1993). The least–squares solution then becomes:

$$\begin{aligned} \Delta \log t &= +0.36 \pm 0.15 \text{ dex} \\ \Delta \text{ [Fe/H]} &= +0.26 \pm 0.11 \text{ dex} \\ \frac{\Delta \text{ [Fe/H]}}{\Delta \log r} &\equiv -0.22 \pm 0.01 \text{ dex} \\ d &= +0.17 \pm 0.09 \end{aligned} \tag{4.10}$$

with $\chi^2/\nu = 1.27$. When one or more parameters are set to zero, then the following series of solutions $(\Delta \log t, \Delta \text{ [Fe/H]}, d, \chi^2/\nu)$ are obtained:

$$\begin{array}{llll} \Delta \log t = +0.73 & \Delta \text{ [Fe/H]} = 0 & d = 0 & \chi^2/\nu = 1.47 \\ \Delta \log t = 0 & \Delta \text{ [Fe/H]} = +0.50 & d = 0 & \chi^2/\nu = 3.20 \\ \Delta \log t = 0 & \Delta \text{ [Fe/H]} = 0 & d = 0.30 & \chi^2/\nu = 41 \\ \Delta \log t = +0.73 & \Delta \text{ [Fe/H]} = 0 & d = 0.05 & \chi^2/\nu = 1.50 \\ \Delta \log t = +0.58 & \Delta \text{ [Fe/H]} = +0.11 & d = 0 & \chi^2/\nu = 1.44 \\ \Delta \log t = 0 & \Delta \text{ [Fe/H]} = +0.51 & d = 0.32 & \chi^2/\nu = 1.52 \end{array} \tag{4.11}$$

In all cases, there is a significant or substantial increase in χ^2/ν by factors between 1.13 to 40, suggesting that the full set of model parameters is required to provide an accurate representation of the observables.

Using the Vazdekis *et al.* (1996) models instead of the Bruzual & Charlot (1996) models, but still keeping $\Delta \text{ [Fe/H]}/\Delta \log r = -0.22 \pm 0.01$ dex per decade of radius, produces the solution:

$$\begin{aligned} \Delta \log t &= +0.14 \pm 0.07 \text{ dex} \\ \Delta \text{ [Fe/H]} &= +0.53 \pm 0.05 \text{ dex} \\ \frac{\Delta \text{ [Fe/H]}}{\Delta \log r} &\equiv -0.22 \pm 0.01 \text{ dex} \\ d &= +0.26 \pm 0.07 \end{aligned} \tag{4.12}$$

with $\chi^2/\nu = 1.04$. Since the model uncertainties have not been included in the χ^2 statistic, this reduction of 20% in χ^2/ν for the Vazdekis *et al.* (1996) models over the Bruzual & Charlot (1996) models suggests that the former have a subtle improvement over the latter in their treatment of the photometric properties of old stellar populations. Contours of joint probability between pairs of the model parameters are plotted in Figure 4.9 for this

solution.

If the differences in slope $\Delta a_{j,i}$ derived from the D_n–σ_0 relation are used instead of those from the quantity $\log r_{\rm eff} - 0.32\langle\mu\rangle_{\rm eff}$, then the solution is

$$\begin{aligned} \Delta \log t &= +0.16 \pm 0.09 \text{ dex} \\ \Delta\ [\mathrm{Fe/H}] &= +0.50 \pm 0.05 \text{ dex} \\ \frac{\Delta\ [\mathrm{Fe/H}]}{\Delta \log r} &\equiv -0.22 \pm 0.01 \text{ dex} \\ d &= +0.25 \pm 0.11 \end{aligned} \tag{4.13}$$

with a much poorer $\chi^2/\nu = 3.04$. The difference in χ^2/ν between this solution (using the differences in D_n) and the previous solution (using the differences in $\log r_{\rm eff} - 0.32\langle\mu\rangle_{\rm eff}$) can be directly attributed to the significantly smaller uncertainties in the measurements of $\Delta a_{j,i}$ from the D_n–σ_0 relation in Tables 4.1 and 4.2. The same effect in χ^2/ν is found when the Bruzual & Charlot models are used instead. We suspect that these small formal uncertainties arise due to a poor sensitivity of the D_n parameter to the subtle effects of color gradients, despite the apparent homogeneity and repeatability in measuring this quantity. On the other hand, the difference could point to overall limitations of the model if these small uncertainties in $\Delta a_{j,i}$ are real.

4.7.4 The Relative Roles of Various Constraints on the Model Solution

Several remarks need to be made about the contribution of the various equations of constraint towards the self–consistent solutions described above. Broadband colors are notoriously poor at discriminating between age and metallicity effects, which has been summarized elegantly by Worthey (1994) as the "3/2 Rule": changes in $\Delta \log t$ are virtually indistinguishable from changes in metallicity $\Delta[\mathrm{Fe/H}] \approx \frac{3}{2}\Delta \log t$. Note that all solutions for this model have $\Delta \log t + \frac{3}{2}\Delta[\mathrm{Fe/H}] \sim 0.75$ dex (Bruzual & Charlot models) or 0.95 dex (Vazdekis *et al.* models). The comparisons of the FP slopes in various optical and near–infrared bandpasses (represented by the $\Delta a_{j,i}$ terms) thus provide extremely good constraints on the joint contribution of age and metallicity to producing the slope of the FP at all bandpasses, but they do not provide a unique discrimination between age and metallicity effects as the dominant cause of the sequence.

A similar argument can be made as to the limitation of the Mg_2 index (in the Mg_2–σ_0

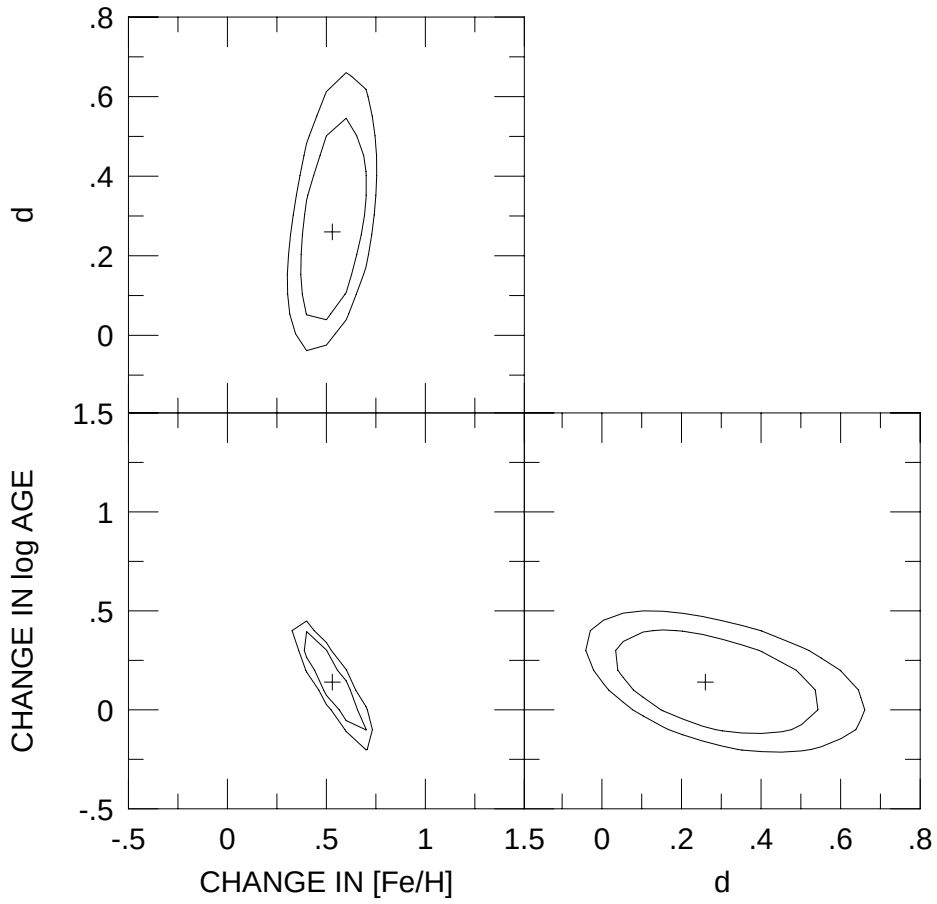

Figure 4.9: Contour plots of χ^2/ν for the self–consistent model described in the text using the stellar population synthesis models of Vazdekis *et al.* (1996) as an illustration of the joint confidence of pairs of parameters. In each figure, the χ^2 minimum is identified, and two contours delimiting the 95% and 99.7% confidence regions are shown. While age and metallicity have a well–determined joint contribution specified by the "3/2 rule" (as is apparent by their χ^2/ν valley with slope 3/2), the model parameter d, which describes the non-homology contribution, is poorly constrained by the observations. Since age and d are jointly constrained by the slope of the K–band FP (Equation 4.12), better independent constraints on d will further limit the allowed parameter space for age and thus further break the age–metallicity degeneracy.

relation) in dealing with this age–metallicity degeneracy. In our experience, however, this additional equation of constraint due to the Mg_2–σ_0 relation is essential to narrow the large parameter space that the populations gradients could occupy, since Δ[Fe/H] and the color gradient β enter into the $\Delta a_{j,i}$ equations in a fixed ratio *for all colors* but in a different ratio for the Mg_2–σ_0 relation. Virtually all metal absorption line indices will have similar age–metallicity degeneracy problems, but not the Balmer absorption lines of atomic hydrogen since they are quite sensitive to recent star formation activity. Future modeling work along these lines could reduce this degeneracy by including Balmer line measurements.

The introduction of the *absolute* slope of the near–infrared FP as an additional equation of constraint provides what is effectively a breaking of the age–metallicity degeneracy, since metallicity effects are unimportant at K while age effects are significant. The wrinkle caused by introducing the absolute slope of the near–infrared FP into the model is that there can be an additional effect caused by deviations from dynamical homology which can, in part or in whole, explain the deviation of the near–infrared FP from its virial expectation. It was therefore necessary to introduce one more parameter to represent this dynamical non-homology, and to include an additional equation of constraint governing it (as measured by Busarello *et al.* 1997), even though that constraint is not highly significant at the 2 σ CL. The large uncertainties in each model parameter in the simultaneous fit given by Equation 4.10 can be directly traced back to the poor constraint provided by the Busarello *et al.* (1997) measurement of d. This is clearly the portion of the entire set of observables that needs substantial more work in the future in order to narrow the space occupied by all the model parameters.

4.8 Discussion

The global scaling relations provide a unique tool for investigating the underlying physical properties which give rise to the sequence of elliptical galaxies. While these correlations have significant and resolved intrinsic dispersion, they are still quite thin and portray a remarkable homogeneity of galaxy properties from the U–band to the K–band.

The elliptical galaxy scaling relations in the near–infrared, with the exception of the K–band Faber–Jackson relation, do not follow the predictions of the virial theorem under the assumptions of constant M/L and homology. This is an important clue as to the physical

origins of these relations, which can immediately exclude a number of simple models (Pahre, Djorgovski, & de Carvalho 1998a, Chapter 3 of this thesis) to explain the elliptical galaxy sequence.

The global properties of elliptical galaxies that are enumerated in §4.6 provide a large set of observables which should be accounted for by any viable model for the physical properties which underlie and produce the elliptical galaxy sequence. There are certainly more properties from X–ray, far–infrared, and radio wavelengths which were not included in this list but ought to be in a more general discussion of the fundamental nature of elliptical galaxies.

The parameter space occupied by variations in age and metallicity, the size of the mean populations gradients, and the deviations from a dynamically homologous family has been shown in §4.7 to be limited significantly by a large and homogeneous sample of global optical and near–infrared photometric parameters and global spectroscopic parameters. While the degeneracy of age and metallicity is difficult to overcome with such data, observations in the metallicity insensitive K–band narrow the range of possible models to age and/or dynamical non-homology causing the K–band FP slope, while still not excluding metallicity as a contributor to the optical FP slope. The explicit accounting of the effects of populations gradients on all relevant parameters, and the inclusion of the slope of the Mg_2–σ_0 relation, provide a further narrowing of the allowed parameter space within the model.

The modeling methodology that has been developed in §4.7 provides the first self–consistent exploration of the underlying physical origins of the elliptical galaxy scaling relations which can simultaneously account for the following observables: (1) the *changes* of the slope of the FP among the $UBVRIK$ bandpasses; (2) the absolute value of the slope of the FP; (3) the effects of color gradients on the global properties of ellipticals; (4) the slope of the Mg_2–σ_0 relation; and (5) the contribution of deviations from a dynamically homologous family to the slope of the FP.

The only observed property of elliptical galaxies that is not explicitly described by this model is the super–solar enrichment of Mg relative to Fe, although it could certainly be accommodated by the inclusion of recent studies of $\langle$Fe$\rangle$ (such as by Jørgensen 1998 or Trager *et al.* 1998) and attempts to model this enrichment (Weiss, Peletier, & Matteucci 1995). It may be important to reanalyze the galactic wind models (Arimoto & Yoshii 1987) with these recent super metal–rich, α–element enhanced, stellar populations models in a

way which embodies the ongoing research into the relative contributions of Type Ia and II supernovae to the chemical enrichment of the host galaxies.

The aperture color–magnitude relation[3] has not been explicitly included in the model developed in §4.7 since there are not colors for the entire galaxy sample that are measured in a self–consistent manner. Nonetheless, a check on the model solutions in §4.7.3 is to compare their predicted slope for the aperture color–magnitude relation with the slope from observational data in the literature. The solutions of Equations 4.10 and 4.12, where the former had the larger age spread and the latter had the larger metallicity spread, predict slopes for the $(U-V)_0$ versus $V_{\rm tot}$ of -0.11 and -0.09, respectively, while the slope in the Coma cluster is -0.08 ± 0.01 (Bower, Lucey, & Ellis 1992b), suggesting that the model with smaller a age spread is favored. There is some uncertainty in this comparison, however, since $\partial(U-V)_0/\partial \log t$ varies between the two models by 6% and there might be small, additional systematic effects in matching the precise U–band filter used by Bower *et al.* (1992b). Furthermore, taking the observed values of $\Delta a_{B,U}$ and $\Delta a_{V,B}$ from Table 4.2 and inserting their sum into Equation 4.5 produces an expected ratio of $(\Delta C_{U,V} - 1.875\Delta r_{\rm eff,i,j})/\Delta \log \sigma_0 = 0.56$, which is similar to the value of 0.54 in Bower *et al.* (1992b).

Since the derived model solutions in §4.7.3 have small variations in age along the early–type galaxy sequence, the slope of the color–magnitude relation is expected to evolve slowly with redshift. The model with a total age variation of 0.14 dex (Equation 4.12) predicts that the slope of the color–magnitude relation should increase by 0.01 by $z = 0.5$, which does not contradict the comparison of the observations of Bower *et al.* (1992b) at $z = 0$ and Ellis *et al.* (1997) at $z = 0.5$, especially considering the potential systematic errors associated with rejecting the lower luminosity outliers in the higher redshift data. The slope of the color–magnitude relation is measured to an accuracy of only 0.02–0.04 by Stanford, Eisenhardt, & Dickinson (1998) for 17 clusters at $0.3 < z < 0.9$, so a change of 0.01 in the slope to $z = 0.5$ could certainly exist, especially considering the small systematic uncertainties which could result from the variations in the rest–frame wavelengths sampled for each cluster. The model with a larger age variation of 0.36 dex (Equation 4.10), however, has a larger predicted change in the slope of the color–magnitude relation and may be marginally in

[3]The distinction is made here between a *global* color–magnitude relation, for which the color is measured globally within the effective radius, and an *aperture* color–magnitude relation, for which the color is measured within a fixed, metric aperture for all galaxies independent of their effective radii. These two methods of measuring colors differ due to the presence of color gradients through Equation 4.5, such that the aperture color–magnitude relation has a steeper slope.

conflict with those data. Direct visual inspection of the color–magnitude relations ("blue–K") in Stanford *et al.* for all clusters at $z > 0.55$, however, leaves the distinct impression that larger variations in the slope of the color–magnitude relation are allowed by the data (with the one exception being GHO 1603+4313). Furthermore, the large aperture sizes used by Stanford *et al.* for measuring colors reduces the predicted evolution of the slope of the color–magnitude relation due to the effects of color gradients in the larger galaxies. As a result, both the model solutions derived in §4.7.3 are probably consistent with the slope of the color–magnitude relation at intermediate redshifts.

The model constructed in §4.7 also makes specific predictions about the behavior of the FP relations with look-back time or redshift. Age appears to be a significant contributor to the slope of the FP, in the sense that the most luminous elliptical galaxies might be as much as twice as old as the least luminous galaxies. In this model, the slope of the FP should evolve with redshift in the sense that the slope a in $r_{\rm eff} \propto \sigma_0^a$ will *decrease* with redshift, since the youngest galaxies at one end of the FP will evolve more quickly than the oldest galaxies at the other end. The specific predictions for the solutions from the Bruzual & Charlot models (Equation 4.10) and the Vazdekis *et al.* models (Equation 4.12) are shown in Figure 4.10. The evolution of the slope of the FP due to the presence of a dynamical non-homology effect is more complicated. Numerical simulations of dissipationless merging (Capelato, de Carvalho, & Carlberg 1995) seem to suggest that second generation mergers produce a slightly steeper FP than the first generation mergers. Since viewing the FP slope at larger redshifts would then be looking at earlier generations of mergers, their interpretation leads to the prediction that the role of dynamical non-homology should increase with redshift, thereby increasing d and decreasing the slope a with redshift at all wavelengths. This prediction should be treated with caution, however, since it is not clear that the origin of dynamical non-homology effects are in the merging process studied in the numerical simulations.

Deviations of the model parameter d from zero were constructed to portray the effects of dynamical non-homology on the slope of the FP via the mapping from σ_0 to $\sigma_{\rm eff}$, but it is important to consider if the non-homology represented by $d > 0$ could be a result of structural non-homology. Graham & Colless (1997) showed that the effects on the FP are minimal for the breaking of structural homology, but this result may not be conclusive since distance (such as the resolved depth of the cluster) could systematically affect their Virgo

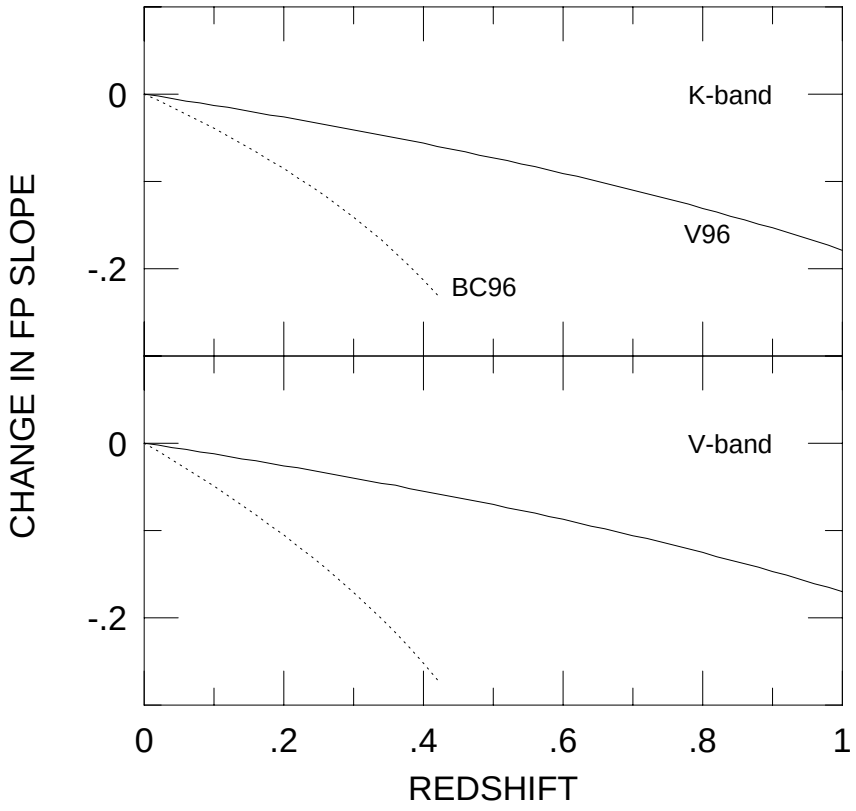

Figure 4.10: The evolution of the FP with redshift for the two self–consistent model solutions (Vazdekis *et al.* 1996, V96, Equation 4.12; Bruzual & Charlot 1996, BC96, Equation 4.10) which describe the intrinsic physical properties of the early–type galaxy sequence. The cosmology assumed is $(H_0, \Omega_0, \Lambda_0) = (75, 0.2, 0)$, and the oldest galaxies are taken to be the age of the universe in the present day. The models are arbitrarily cutoff when the youngest galaxies in the early–type galaxy sequence reach an age < 1 Gyr. The V96 model solution predicts a present–day age spread of 35% along the sequence, while the BC96 model solution predicts a present–day age spread of a factor of two.

cluster data, thereby hiding the structural homology breaking. The fundamental problem with invoking structural non-homology, as they pointed out, is that any increase in $r_{\rm eff}$ is compensated by a decrease in $\langle\mu\rangle_{\rm eff}$ (they actually found a slight over-compensation), which effectively nulls the result. This is basically a different way of thinking about the fact that only small uncertainties enter the FP through the quantity $\log r_{\rm eff} - 0.32\langle\mu\rangle_{\rm eff}$. In summary, since changes in $\langle\mu\rangle_{\rm eff}$ virtually compensate for changes in $r_{\rm eff}$ in the FP, there is no significant way that significant values of the non-homology parameter $d > 0$ can be traced back to systematic mismeasures of $r_{\rm eff}$.

One difficult problem that can be posed both by the Mg_2 version of the near–infrared FP (Pahre, Djorgovski, & de Carvalho 1998a, Chapter 3 of this thesis) and the optical FP in Jørgensen *et al.* (1996), is why this FP has much larger scatter than the standard σ_0 form of the FP. While the Mg_2 index is an indicator of variations in metallicity (Mould 1978), it can be affected by "filling" due to a younger stellar component and it reflects the existence of stellar populations gradients via Mg_2 line gradients (Couture & Hardy 1988; Gorgas, Efstathiou, & Aragón Salamanca 1990; Davies, Sadler, & Peletier 1993). But Mg_2 does not reflect the intrinsic *dynamical* effects which may vary along the elliptical sequence—or even at any given point in the sequence. Peletier (1993) argued that local velocity dispersion is not a universal predictor of Mg_2; this argument could be reversed to say that Mg_2 is not a universal predictor of velocity dispersion. While the Mg_2 FP is not explicitly described by the model in §4.7, its large scatter might reflect the real presence of a dynamical non-homology term $d > 0$ in the FP that is not accounted for in the Mg_2 FP.

The obvious limitation of this approach is that it still is an empirical description of the observations, not a theoretical construct based on first principles and galaxy formation theory. Nonetheless, it is a first step towards providing detailed, quantitative constraints on the properties that any viable theoretical model for galaxy formation and evolution needs to reproduce.

A more subtle limitation of this approach is its indirect inclusion of stellar populations gradients, such that the size of these gradients is virtually unconstrained by the model. Clearly, the optimal method of constraining stellar populations gradients is by directly observing them in various colors and line strengths. It is truly surprising that very few new observations have been reported since the review of Peletier (1993), despite the advent of large–format CCD and IR arrays, a sky–subtraction independent parameterization (Sparks

& Jørgensen 1993), and the wealth of photometry that has been obtained from the U to the K bandpasses (Bower, Lucey, & Ellis 1992a; Jørgensen, Franx, & Kjærgaard 1995; Smith *et al.* 1997; Lucey *et al.* 1997; Pahre 1998a, Chapter 2 of this thesis). Furthermore, comparing color gradient ratios (between different colors) will provide a strong tool to discriminate between stellar populations gradients and a diffuse component of dust (Wise & Silva 1996).

An unsolved problem underlying all interpretations of the intrinsic properties of elliptical galaxies using line strengths is the enhancement of Mg relative to Fe. This problem is not just a challenge for stellar populations synthesis models, but also for supernova nucleosynthesis, galaxy formation models, and galactic wind models.

The model parameters derived in §4.7 imply that age and metallicity are varying along the early–type galaxy sequence in the sense that the most luminous galaxies are the oldest and most metal rich. If there exists a mass–age sequence among early–type galaxies, this might be inconsistent with hierarchical models in which present day massive galaxies are built by successive mergers of smaller, sub–galactic units (cf. Kauffmann 1996). Furthermore, the sense of the metallicity variations is as expected if metallicity (and population gradients in metallicity, see §4.7.1) drives the color–magnitude relation (Kodama & Arimoto 1997) for elliptical galaxies.

The trend for more luminous galaxies to be more metal rich is in contradiction to the study of line indices of Trager (1997), who suggested that the most luminous galaxies are the oldest while also being the most metal poor. The correlation between age and metallicity in the Trager (1997) analysis, however, could be caused at least in part by the correlated errors in the derived parameters. Furthermore, there exists substantial scatter perpendicular to the correlation Trager proposes between age and metallicity which cannot be explained by correlated errors—this perpendicular scatter is exactly in the sense that age and metallicity are proposed to correlate in the present paper. Finally, the comparison of K–band surface brightness fluctuations measurements with $(V-I)$ color for 11 galaxies (Jensen 1997) also suggests that age variations of a factor of two to three are occurring along the elliptical galaxy sequence, further contradicting the large age spreads of Trager (1997).

4.9 Summary

The reduction of $r_{\rm eff}$ with increasing wavelength is an expected result of the presence of stellar population gradients. The fact that $r_{\rm eff}$ is a function of wavelength argues that any method of calculating intrinsic galaxy masses using the observables $r_{\rm eff}$ and σ_0 will be systematically flawed (see the discussion in Pahre, Djorgovski, & de Carvalho 1998a, Chapter 3 of this thesis). It is an open issue how best to match the observed effective radii, which are luminosity weighted for a particular bandpass and hence affected by stellar populations gradients, to the half mass radius of galaxies. The latter quantity is the intrinsic property which is desired from the observations and readily calculated in theoretical calculations, but its connection with any optical or near–infrared observations is still problematical.

The Fundamental Plane slope has been shown to steepen in a systematic way from shorter to longer wavelengths. The methodology presented here shows that changes of the FP slope between bandpasses can be measured accurately by a distance independent construction of the observables. This method is robust and typically reduces the uncertainty of the comparison by a factor of two, thereby allowing for more detailed model comparisons.

This paper presents for the first time a comprehensive model of the changes in global properties of elliptical galaxies that simultaneously accounts for a wide range of observables, namely: (1) the changes in slope of the FP between bandpasses; (2) the slope of the near–infrared FP; (3) the slope of the $\rm Mg_2$–σ_0 relation; (4) the presence and effects of stellar populations gradients; and (5) the presence of systematic deviations of the internal dynamical structures of elliptical galaxies from a homologous family. The observational constraints imposed by the last element of this model is clearly the weakest point and should be substantially improved upon in the future by obtaining velocity dispersion profiles for large samples of galaxies, such as in a rich cluster. Due to this observational shortcoming, this model does not yet provide highly significant measurements of the individual model parameters defining the variations in age and metallicity from one end of the FP to the other. The model, however, does provide a framework to re-evaluate these parameters as soon as newer and higher quality data become available.

Acknowledgments

This research has made use of the NASA/IPAC Extragalactic Database (NED) which is operated by the Jet Propulsion Laboratory, California Institute of Technology, under contract with the National Aeronautics and Space Administration. During the course of this project, M. A. P. received financial support from Jesse Greenstein and Kingsley Fellowships, the Bressler Foundation; S. G. D. was supported in part by NSF grants AST–9123646 and AST–9157412.

References

Arimoto, N., & Yoshii, Y. 1987, A&A, 173, 23

Baum, W. A. 1959, PASP, 71, 106

1992, ApJ, 399, 462

Bower, R. G., Lucey, J. R., & Ellis, R. S. 1992a, MNRAS, 254, 589

Bower, R. G., Lucey, J. R., & Ellis, R. S. 1992b, MNRAS, 254, 601

Bruzual, A. G. 1983, ApJ, 273, 105

Bruzual, A. G., & Charlot, S. 1996, in preparation

Burkert, A. 1993, A&A, 278, 23

Burstein, D., & Heiles, C. 1982, AJ, 87, 1165

Busarello, G., Capaccioli, M., Capozziello, S., Longo, G., & Puddu, E. 1997, A&A, 320, 415

Caon, N., Capaccioli, M., & D'Onofrio, M. 1993, MNRAS, 265, 1013

Capelato, H. V., de Carvalho, R. R., & Carlberg, R. G. 1995, ApJ, 451, 525

Capelato, H. V., de Carvalho, R. R., & Carlberg, R. G. 1997, in Galaxy Scaling Relations: Origins, Evolution, and Applications, Proceedings of the Third ESO–VLT Workshop, eds. L. N. da Costa & A. Renzini (Springer–Verlag: Berlin), 331

de Carvalho, R. R., & Djorgovski, S. 1992, ApJ, 389, L49

Charlot, S., Worthey, G., & Bressan, A. 1996, ApJ, 457, 625

Ciotti, L., Lanzoni, B., & Renzini, A. 1996, MNRAS, 282, 1

Couture, J., & Hardy, E. 1988, AJ, 96, 867

Davies, R. L., Efstathiou, G., Fall, S. M., Illingworth, G., & Schechter, P. L. 1983, ApJ, 266, 41

Davies, R. L., Sadler, E. M., & Peletier, R. F. 1993, MNRAS, 262, 650

Djorgovski, S., & Davis, M. 1987, ApJ, 313, 59

Djorgovski, S., & Santiago, B. X. 1993, in proceedings of the ESO/EIPC Workshop on Structure, Dynamics, and Chemical Evolution of Early–Type Galaxies, ed. J. Danziger, *et al.*, ESO publication No. 45, 59

Dressler, A. 1984, ApJ, 281, 512

Dressler, A., Lynden-Bell, D., Burstein, D., Davies, R. L., Faber, S. M., Terlevich, R. J., & Wegner, G. 1987, ApJ, 313, 42

Ellis, R. S., Smail, I., Dressler, A., Couch, W. J., Oemler, A., Jr., Butcher, H., & Sharples, R. M. 1997, ApJ, 483, 582

Faber, S. M., & Jackson, R. E. 1976, ApJ, 204, 668

Faber, S. M., Wegner, G., Burstein, D., Davies, R. L., Dressler, A., Lynden-Bell, D., & Terlevich, R. J. 1989, ApJS, 69, 763

Franx, M., Illingworth, G., & Heckman, T. 1989, AJ, 98, 538

Fritze-v. Alvensleben, U., & Burkert, A. 1995, A&A, 300, 58

Gorgas, J., Efstathiou, G., & Aragón Salamanca, A. 1990, MNRAS, 245, 217

Graham, A., & Colless, M. 1997, MNRAS, 287, 221

Guzmán, R. 1995, in proceedings of the Heron Island Workshop on Peculiar Velocities in the Universe, `http://qso.lanl.gov/~heron/`

Guzmán, R., & Lucey, J. R. 1993, MNRAS, 263, L47

Guzmán, R., Lucey, J. R., & Bower, R. G. 1993, MNRAS, 265, 731

Hudson, M. J., Lucey, J. R., Smith, R. J., & Steel, J. 1997, MNRAS, in press

Jensen, J. B. 1997, Ph.D. Thesis, University of Hawaii

Jørgensen, I. 1998, MNRAS, in press

Jørgensen, I., Franx, M., & Kjærgaard, P. 1995a, MNRAS, 273, 1097

Jørgensen, I., Franx, M., & Kjærgaard, P. 1995b, MNRAS, 276, 1341

Jørgensen, I., Franx, M., & Kjærgaard, P. 1996, MNRAS, 280, 167

Kauffmann, G. 1996, MNRAS, 281, 487

Kodama, T., & Arimoto, N. 1997, A&A, 320, 41

Kormendy, J. 1977, ApJ, 218, 333

Laureijs, R. J., Helou, G., & Clark, F. O. 1994, in Proceedings of The First Symposium on the Infrared Cirrus and Diffuse Interstellar Clouds, ASP Conf. Ser. Vol. 58, eds. R. M.

Cutri & W. B. Latter (San Francisco, ASP), 133

Leitherer, C., *et al.* 1996, PASP, 108, 996

Lucey, J. R., & Carter, D. 1988, MNRAS, 235, 1177

Lucey, J. R., Gray, P. M., Carter, D., & Terlevich, R. J. 1991a, MNRAS, 248, 804

Lucey, J. R., Guzmán, R., Carter, D., & Terlevich, R. J. 1991b, MNRAS, 253, 584

Lucey, J. R., Guzmán, R., Steel, J., & Carter, D. 1997, MNRAS, 287, 899

Lynden–Bell, D., Faber, S. M., Burstein, D., Davies, R. L., Dressler, A., Terlevich, R. J., & Wegner, G. 1988, ApJ, 326, 19

Mould, J. R. 1978, ApJ, 220, 434

Murphy, D. C., Persson, S. E., Pahre, M. A., Sivaramakrishnan, A., & Djorgovski, S. G. 1995, PASP, 107, 1234

Pahre, M. A. 1998, in preparation [Chapter 2 of this thesis]

Pahre, M. A., & Djorgovski, S. G. 1997, in The Nature of Elliptical Galaxies, Proceedings of the Second Stromlo Symposium, eds. M. Arnaboldi, G. S. Da Costa, & P. Saha, ASP Conf. Ser. Vol. 116, (San Francisco: ASP), 154

Pahre, M. A., Djorgovski, S. G., & de Carvalho, R. R. 1995, ApJ, 453, L17

Pahre, M. A., Djorgovski, S. G., & de Carvalho, R. R. 1997, in Galaxy Scaling Relations: Origins, Evolution, and Applications, Proceedings of the Third ESO–VLT Workshop, eds. L. N. da Costa & A. Renzini (Springer–Verlag: Berlin), 197

Pahre, M. A., Djorgovski, S. G., & de Carvalho, R. R. 1998, in preparation [Chapter 3 of this thesis]

Peletier, R. F. 1993, in proceedings of the ESO/EIPC Workshop on Structure, Dynamics, and Chemical Evolution of Early–Type Galaxies, ed. J. Danziger, *et al.*, ESO publication No. 45, 409

Peletier, R. F., Davies, R. L., Illingworth, G. D., Davis, L. E., & Cawson, M. 1990a, AJ, 100, 1091

Peletier, R. F., Valentijn, E. A., & Jameson, R. F. 1990b, A&A, 233, 62

Prugniel, P., & Simien, F. 1996, A&A, 309, 749

Recillas-Cruz, E., Carrasco, L., Serrano, P. G., & Cruz-González, I. 1990, A&A, 229, 64

Recillas-Cruz, E., Carrasco, L., Serrano, P. G., & Cruz-González, I. 1991, A&A, 249, 312

Renzini, A., & Ciotti, L. 1993, ApJ, 416, L49

Sandage, A. 1972, ApJ, 176, 21

Sandage, A., & Visvanathan, N. 1978, ApJ, 223, 707

Sandage, A., & Visvanathan, N. 1978, ApJ, 228, 81

Sandage, A., & Perelmuter, J.-M. 1990, ApJ, 361, 1

Scodeggio, M., Giovanelli, R., & Haynes, M. P. 1997, AJ, 113, 101

Sersic, J. L. 1968, Atlas de Galaxias Australes, Cordoba: Observatorio Astronomico

Smith, R. J., Lucey, J. R., Hudson, M. J., & Steel, J. 1997, MNRAS, in press

Sparks, W. B., & Jørgensen, I. 1993, AJ, 105, 1753

Stanford, S. A., Eisenhardt, P. R., & Dickinson, M. 1998, ApJ, 492, 461

Terlevich, R. J., Davies, R. L., Faber, S. M., & Burstein, D. 1981, MNRAS, 196, 381

Tonry, J. L., & Davis, J. 1981, ApJ, 246, 680

Tonry, J. L., Blakeslee, J. P., Ajhar, E. A., & Dressler, A. 1997, ApJ, 475, 399

Trager, S. C. 1997, Ph.D. Thesis, University of California (Santa Cruz)

Trager, S. C., Worthey, G., Faber, S. M., Burstein, D., & González, J. J. 1998, ApJS, in press

Vazdekis, A., Casuso, E., Peletier, R., & Beckman, J. E. 1996, ApJS, 106, 307

Visvanathan, N., & Sandage, A. 1977, ApJ, 216, 214

Weiss, A., Peletier, R. F., & Matteucci, F. 1995, A&A, 296, 73

Wise, M. W., & Silva, D. R. 1996, ApJ, 461, 155

Worthey, G. 1994, ApJS, 95, 107

Worthey, G., González, J. J., & Faber, S. M. 1992, ApJS, 398, 69

Worthey, G., Trager, S. C., & Faber, S. M. 1996, in Fresh Views of Elliptical Galaxies, ASP Conf. Ser. Vol. 86, eds. A. Buzzoni & A. Renzini (San Francisco: ASP) 203

Zepf, S. E., & Silk, J. 1996, ApJ, 466, 114

Chapter 5

Color Evolution in the Early–Type Galaxy Population in Rich Clusters at $0 < z < 0.6$

Abstract

The rate of evolution of the spectral energy distributions of coeval stellar systems is an important indicator of their mean age. The depression of the 4000 Å break is a strong feature in early–type galaxies that is expected to vary strongly with the age of the population; the broadband color $(U-V)_0$ spans this feature, and hence is a good indicator of the mean age of the early–type galaxy population. Many investigations of the color evolution of early–type galaxies have been limited by small sample sizes, possible field contamination (especially at higher redshifts), possible changes in the morphological mix with redshift, systematic uncertainties in modeling the effects of redshift on the broadband colors, and difficulties in making comparisons to nearby galaxy samples. In this paper, a new study of color evolution is described which uses two broadband colors (three filter observations) and a morphology indicator (concentration index) as the selection criteria to identify systematically the early–type galaxy population in 26 rich clusters of galaxies in the redshift range $0 < z < 0.6$, with one color is chosen to approximately sample $(U-V)_0$ for the appropriate cluster redshift. The second color is necessary to eliminate higher redshift field spiral galaxy contamination, and to minimize possible biases introduced by selecting on only a single color. The early–type galaxies selected in this way are shown to follow much tighter color–magnitude relations than the allowed range in color from a single color. Typically 50–200 galaxies are identified per cluster to comprise the complete sample. Limited comparisons of these quantitatively identified galaxies with spectroscopic redshifts and spectral classifications demonstrate that early–type, cluster member galaxies are identified at better than 90% efficiency.

The color intercept at fixed luminosity of the aperture color–magnitude relation is used as the measure of the mean evolution of the cluster early–type galaxy population with redshift. Corrections for the effects of seeing, redshift, and color gradients are described. The early–type galaxy population in these 26 rich clusters of galaxies shows

a systematic bluing trend in $(U-V)_0$ with redshift of $\Delta(U-V)_0 \approx -\log(1+z)$; the total internal uncertainties in $(U-V)_0$ are typically 0.05 mag for each cluster measurement, although the scatter of the final results suggests that this may be underestimated by a factor of up to two. Color evolution is detected here, albeit weakly, for the first time at $z \sim 0.2$, thereby demonstrating the power of the method. Comparisons of the color evolution with simple, synthesized stellar populations models implies that the mean stellar content of cluster early–type galaxies formed at $1 < z_f < 5$.

5.1 Introduction

Observations of the spectral energy distributions (SED) of galaxies are an important tool for understanding both their stellar content and evolutionary state. Large samples of high S/N spectra for galaxies at a range of redshifts, however, are not in general available to study galaxy populations in this way. The recent technological advances of high quantum efficiency, large format imaging detectors allows the study of galaxy SEDs with large samples, albeit with lower spectral resolution through broadband filters. Thus it is now possible to obtain detailed multicolor imaging data from the UV through the infrared for a large number of galaxies and hence study their color distributions and evolution.

Studies of the colors and luminosities of galaxies in the field have proliferated recently (Lilly *et al.* 1995; Songaila *et al.* 1994; Pahre *et al.* 1998a), especially with the Hubble Deep Field (Williams *et al.* 1996). The faint field galaxy population, however, is a difficult one to study systematically because of the lack of knowledge of the distances of the individual galaxies without pursuing an extensive redshift survey. Rich clusters of galaxies, on the other hand, provide an opportunity to observe simultaneously a large number of galaxies which are likely to be at the same distance and may also be coeval. Field subtraction of the interloper galaxies can be performed which substantially improves the statistical quality of such cluster galaxy samples, providing a powerful method to study the cluster galaxy population.

The measurement of color evolution for the cluster galaxy population has remained an elusive goal. The difficulties lie in very accurate photometric calibration, which entails the minimization of systematic effects due to seeing, aperture size, detector linearity, color gradients in the galaxy, color terms in observed detector + filter systems, etc. The problems are compounded by the difficulty of separating different galaxy populations within a single

cluster, as morphological information may be poor or lacking altogether.

Accurately distinguishing between the different cluster galaxy populations is a crucial step towards the measurement of evolution of a particular galaxy type. Doing this in a way that is uniform at a range of redshifts is further necessary to ensure that the same population of galaxies is being traced at all redshifts studied.

Elliptical galaxies in clusters may be the population with the simplest evolutionary history. They are thought to form at high redshift in a massive burst of star formation during a short period of time. The star formation then stops and the galaxies evolve passively until the present. Whether or not such a population of galaxies really exist, however, is still a topic of considerable current interest.

Luminosity evolution appears to be small and consistent with passive evolution out to $z \sim 0.4$ in the cluster elliptical galaxy population (Dickinson 1995; Barrientos, Schade, & López-Cruz 1996; van Dokkum & Franx 1996; Pahre, Djorgovski, & de Carvalho 1996; Schade, Barrientos, & Lopez–Cruz 1997). For example, evolution of 0.36 ± 0.14 mag was found between $z \sim 0$ and $z = 0.41$ in the K–band by Pahre *et al.* (1996). Color evolution should be a far more subtle effect of order 0.15 mag in rest-frame $(U - V)$ over the same redshift range (Bruzual & Charlot 1996), but provides complementary information to luminosity evolution by their different sensitivities to the stellar populations age, metallicity, and IMF.

Recent observations of the Fundamental Plane of elliptical galaxies at high redshift (Franx 1993; van Dokkum & Franx 1996; Kelson *et al.* 1997; Pahre, Djorgovski, & de Carvalho 1998c, Chapter 7 of this thesis) are demonstrating that it is possible to measure the global properties of ellipticals very accurately. As such, it is now a crucial time to address the issue of how the galaxies are selected for such studies, as this issue will have a significant bearing on the final results and their interpretation.

Ground–breaking work done by Koo (1981), who used three–color photometry (photographic u, g, r, i) to show that there existed a significant population of red galaxies in CL0016+16 ($z = 0.55$) that show little or no evolution. Ellis *et al.* (1985) used five color, intermediate bandwidth filters to demonstrate the early–type galaxies in the same cluster are somewhat bluer than the present–day equivalents. Hamilton (1985) used three–color (u, g, r, i) imaging to identify the reddest field galaxies for $0 < z < 0.8$ to demonstrate that there has been little or no evolution in the 4000 Å break for these galaxies across that

range in redshift. Finally, Fiala, Rakos, & Stockton (1986) demonstrated the use of redshift Strömgren photometry for the two–color identification of the cluster early–type population, and Rakos & Schombert (1995) have utilized this approach to track a reddening trend to $z = 0.4$ (which is expected in their filter system), followed by a bluing trend for $0.4 < z < 1$. All studies are notable for their use of multicolor imaging data to identify the early–type galaxy population in a reasonable, statistically–accurate manner.

While the Ellis *et al.* and Fiala *et al.* methods might appear to be well suited to further utilization, their use of nonstandard filters restrict their utility for large–scale surveys of clusters or investigators with resources too limited to purchase a set of filters specific to each redshift of interest. Furthermore, the calibration of such data can be quite challenging: Fiala *et al.* noted the necessity of a spectrophotometric standard galaxy in each cluster in order to establish the zero–point. Developing a simple method to utilize broadband data in a standard filter system (like $UBVR_{\rm C}I_{\rm C}$ as defined by Landolt 1992) is the goal of this paper.

A careful study was reported by Aragón–Salamanca *et al.* (1993) in which they utilized a K–selected, magnitude–limited sample of galaxies in the cores of rich clusters for $0.5 < z < 0.9$. This near–infrared selection was a significant advance, as it ensures a roughly equal mix of galaxy types throughout the relevant redshift range. The problem with near–infrared selection, however, is that it identifies a composite population of galaxies that is not limited to those of early–type. Thus subtle effects due to a different evolutionary history for the different morphological types can make their interpretation difficult. Field galaxy subtraction is still a significant issue for such studies, especially as fainter magnitudes are observed for the most distant clusters, due to the nature of a magnitude–limited survey at any wavelength. The K–selected approach has also been used by Stanford, Eisenhardt, & Dickinson (1995, 1998) in their study of the cluster galaxy population at $0.3 < z < 0.9$, although they also required a morphological selection using HST data.

This paper will develop a different method to identify the elliptical galaxy population in a robust, reliable, and quantitative manner using two–color and morphological information. The depth of the 4000 Å break is a strong feature by which to distinguish between old and star–forming galaxies, hence one color, $(U - V)_0$, is selected which spans this feature. The second color is useful for distinguishing between low redshift elliptical and high redshift star–forming galaxies that might happen to have identical values of the first color. These

two criteria work very effectively because cluster elliptical galaxies occupy a limited locus in color–color space. Morphological information is included in the selection criteria via the concentration index of Abraham *et al.* (1994).

It might seem circular to utilize color information if the eventual goals is to measure the color evolution of the elliptical galaxy population. The key portion of this method is the utilization of *multiple* selection criteria such that each criterion is applied weakly. The allowed range in each color of a given criterion is so large compared to the intrinsic scatter of the colors of ellipticals (and the photometric measurement errors) that the use of two–color selection criteria like the ones described here do not significantly bias the final color evolution measurement. As the selection criteria are fully quantitative, Monte Carlo simulations could be constructed to explore in detail the size of possible selection biases.

The null hypothesis to be explored in this paper is that early–type galaxies formed early in the universe's history in a synchronized epoch of star formation, and then evolved passively since that time. Any deviations of the color evolution of early–type galaxies from this null hypothesis will signal a departure from this simple model.

The previous, large–scale studies of color evolution in the early–type galaxy population in distant clusters concentrated on the redshift range $0.3 < z < 0.9$ (Aragón–Salamanca *et al.* 1993; Stanford *et al.* 1995, 1998), with the exception of the work of Fiala *et al.* (1986) using Strömgren photometry for $z < 0.4$. A major challenge is to compare the high redshift galaxies to their low redshift counterparts. This requires: (1) continuously sampling redshifts all the way down to $z = 0$; (2) utilizing a uniform selection criteria at all redshifts; (3) sampling similar rest–frame wavelengths at all redshifts; and (4) utilizing uniform photometric measurement techniques at all redshifts. One example of this difficulty in comparing distant and nearby galaxies is the difficulty Stanford *et al.* (1998) had in trying to tie in the colors of early–type galaxies in the Coma cluster with the colors of the $z > 0.3$ cluster galaxies (see their Figure 7); the Coma cluster galaxies appear to be 0.1–0.2 mag too blue. There is clearly a need for measurements of the colors of cluster early–type galaxies in the redshift range $0.1 < z < 0.3$.

A carefully-selected set of object criteria will be useful for a number of different investigations of galaxies in clusters at redshifts $z < 1$: the fraction of blue galaxies; color evolution in the elliptical galaxy sequence; the Fundamental Plane of elliptical galaxies and its various projections; and so on. Observations in UVI bands at $z < 0.15$, BRI bands at

$0.15 < z < 0.5$, and VIJ bands at $z = 0.55$ will be described in §5.2, the object detection and measurement of colors will be discussed in §5.3, and then these data will be used to demonstrate the color-morphology selection methodology in §5.4. The effectiveness of the method in identifying cluster, early–type galaxies will be discussed in §5.5 using reference to follow–up spectroscopic observations of > 100 galaxies in six clusters. Finally, the color evolution of early–type galaxies will be presented in §5.6 for 26 rich clusters of galaxies at $0 < z < 0.6$ which have utilized this two–color selection method to identify the galaxy samples.

5.2 Observations

Most of the observations for this paper were obtained at the Palomar Observatory 60–inch telescope (P60) between 1994 November and 1997 April using the facility's 2048×2048 pixel thinned, Tektronix CCD array (identified as "CCD 13"). This detector has excellent quantum efficiency ($\sim 80\%$) that is nearly flat in the wavelength range $4200 < \lambda < 7500$ Å. Its 24μm pixels project to a measured scale of 0.3717 arcsec with little distortion across the entire field-of-view. The I filter used between 1994 November and 1996 August did not have a red cutoff, hence the combined response of the detector and filter has an extended red response reaching beyond $\lambda = 1.0\mu$m. After 1996 August, a Gunn i interference filter was used, although it was still calibrated onto the Cousins $I_{\rm C}$ photometric system as defined by Landolt (1992).

Additional data were acquired for CL160134+4254 ($z = 0.539$) at V and i using the re-imaged mode of the COSMIC instrument mounted at the prime focus of the Palomar 200–inch Hale Telescope (Dressler, Kells, & Sivaramakrishnan 1998) in 1997 April. These COSMIC data used a Gunn i interference filter, a thinned, 2048×2048 pixel^2 CCD detector virtually identical to that at P60, producing 0.399 arcsec.

Observations in the J–band of CL160134+4254 were made using the Palomar 60–inch telescope's near–infrared camera (Murphy *et al.* 1995), which is based on a 256×256 pixel^2 NICMOS–3 array re-imaged at $1:1$ to produce a projected pixel size of $0.620''$ arcsec. Additional J–band observations of CL0016+16 were also made using the Palomar 200–inch telescope's near–infrared camera built by T. Jarrett and N. Gautier for the f/3.3 prime focus, which also uses a NICMOS–3 array and has a 0.494 arcsec projected pixel size.

All of the observations are summarized in Table 5.1.

Clusters at the lowest redshifts ($z < 0.15$) were observed in $UVI_{\rm C}$, those at higher redshifts ($0.15 < z < 0.5$) were observed in $BR_{\rm C}I_{\rm C}$, and those at the highest redshifts ($z > 0.5$) were observed in $V, I_{\rm C}, J$, thereby allowing similar wavelengths in the cluster rest-frame. Several of the clusters at $z \sim 0.2$ were also imaged in UV as an independent check of the systematic effects due to the k–corrections. All observations were made at least in part during photometric conditions, so that those taken under non–photometric conditions could be normalized onto the photometric data. Total exposure times were typically 5400 s in the bluest bandpass (sampling the rest-frame U–band), 3600 s in the middle wavelength, and 2700 s in the reddest wavelength. The integration time was usually divided into three or four separate exposures, and the telescope moved 15–30 arcsec between exposures to improve the flattening. Shorter exposure times of 500–2000 s were used for the P200 and Keck observations, although these data are deeper due to the increased telescope collecting area. Several other "blank" fields were selected in order to investigate the effects of the faint field galaxy population as interlopers to the cluster early–type galaxy selection criteria. The fields at J 0053+1234 were chosen to overlap with the deep, pencil beam redshift surveys of the Caltech group (Cohen *et al.* 1996; Pahre *et al.* 1998a), while the field at J 0237-0248 was chosen to be near to Abell 370, and hence sample a similar Galactic latitude.

All of the data were reduced in a standard manner. The optical data used dome and twilight flats for B, V, R, I, but only twilight flats for U. Dark sky flats were constructed from the medians of all background–limited observations for a given night in a given filter. As the telescope had been dithered by $30''$ between exposures, the images were re-registered, combined, and trimmed. The near–infrared data were dithered by $15''$ between exposures so that the sky frame could be constructed from the sigma–rejected average of all the exposures.

Table 5.1: Summary of Observations

Telescope	UT Dates	Cluster	RA (J2000)	Dec (J2000)	Filters
			hh mm ss	dd mm ss	
P60	1994 Nov 26–27	Blank J 0237-0248	02 37 18	-02 48 00	B,R,I
		Perseus	03 19 49	+41 27 51	U,B,I
		Abell 665	08 30 44	+65 50 28	B,V,R,I
P60	1995 Mar 7–8	Abell 688	08 37 31	+15 51 29	U,V,I
		Abell 851	09 43 03	+46 56 10	R
		Abell 1035	10 32 07	+40 12 33	U,V,I
		Abell 1689	13 11 25	-01 20 23	B,R,I
P60	1995 Apr 3–4	Abell 655	08 25 20	+47 07 12	U,V,I
		Abell 851	09 43 03	+46 56 10	B,R,I
		Abell 1689	13 11 25	-01 20 23	B,R,I
		Abell 2218	16 35 56	+66 12 37	B,R,I
P60	1995 Aug 22–25	Abell 24	00 22 30	+23 17 38	U,V,I
		Blank J 0053+1234	00 53 25	+12 34 11	B,R,I
		Abell 175	01 19 33	+14 52 44	U,V,I
		Abell 370	02 39 54	-01 34 24	B,R,I
		Blank J 1722+4950	17 22 25	+49 49 47	B,R,I
		Abell 2390	21 53 37	+17 41 46	B,R,I
		Abell 2443	22 26 01	+17 22 10	U,V,I
P60	1995 Oct 16–17	ZwCl0024+1652	00 26 32	+17 09 55	B,R,I
		Abell 98	00 46 27	+20 29 23	U,V,I
		Blank J 0053+1234	00 53 25	+12 34 11	U,V
		CL0303+1707	03 06 09	+17 18 50	B,R,I
P60	1995 Oct 24	MS0015.9+1609	00 18 33	+16 25 42	(U,)V,I
		CL0303+1707	03 06 09	+17 18 50	B,R
P60	1996 Mar 31 – Apr 1	CL160134+4254	16 03 10	+42 45 39	J
P60	1996 Apr 19	CL160134+4254	16 03 10	+42 45 39	V,I
P60	1996 Jul 13 – Aug 2	CL160134+4254	16 03 10	+42 45 39	J
P60	1996 Aug 10–13	Abell 2744	00 14 19	-30 23 25	B,R,I
		Blank J 0053+1234	00 53 25	+12 34 11	B,R,I
		CL005431-2756	00 56 55	-27 40 31	V,I
		CL140933+52	14 11 20	+52 12 21	B,R,I
		CL160134+4254	16 03 10	+42 45 39	V,I
		Abell 2218	16 35 56	+66 12 37	U,V
		Blank J 1722+4950	17 22 25	+49 49 47	U,V

Table 5.1—*Continued*

Telescope	UT Dates	Cluster	RA (J2000)	Dec (J2000)	Filters
			hh mm ss	dd mm ss	
		Abell 2390	21 53 37	+17 41 46	U,V
P60 (COSMIC CCD)	1996 Sep 13	MS0015.9+1609	00 18 33	+16 25 42	V,i
P60	1997 Apr 8–11	CL0952+44	09 49 50	+44 08 57	B,R,i
		Coma	12 59 00	+27 58 00	U,B,V,R,i
		Abell 1689	13 11 25	-01 20 23	U,V
		Abell 1795	13 49 00	+26 35 07	U,V,i
		CL1358+62	13 59 30	+62 30 06	B,R,i
		CL1446+2621	14 49 28	+26 07 57	B,R,i
		MS1512.4+3647	15 14 20	+36 36 04	B,R,i
		Abell 2065	15 22 49	+27 43 22	U,V,i
		Abell 2219	16 40 24	+46 42 54	B,R,i
P200	1997 Apr 11–12	CL160134+4254	16 03 10	+42 45 39	V,i
P200	1997 Jul 11–13	MS0015.9+1609	00 18 33	+16 25 42	J

5.2.1 Calibration

Optical photometric calibration was done using the standard star fields of Landolt (1992), which were chosen to have a large number of stars per field with a wide range of colors. Near–infrared calibration utilized the new HST standard stars of E. Persson (private communication). Standard star fields were observed up to large airmasses each night in order to measure the extinction coefficient in all bandpasses.

Photometric calibration for the optical imaging was performed interactively by fitting the extinction coefficient, zero–point, and first and second order color terms. None of the data required a second order color term to reduce the scatter significantly. The near–infrared data were calibrated the same way but without the use of a color term, as those standard stars are all of the same type (G dwarfs).

5.2.2 k–corrections

Observed magnitudes were converted to rest–frame U, V, and I magnitudes by calculating k–corrections. In the low redshift cases where the bluest filter were taken in the U–band, this k–correction takes the usual form of $U_0 = U_z - k_{z,U}$ for a redshift z. At higher redshifts, observations were made through longer wavelength filters in order to sample close to the rest–frame U–band light, so the k–correction must include the difference in zero–points between the observed bandpass and the U bandpass. For observations in V–band, for example, that are to be converted to the rest–frame U–band, the calculation is of the form $U_0 = V_z - k_{z,U,V}$. This latter calculation was shown by Aragón–Salamanca *et al.* (1993) to be robust for a wide variety of SEDs. Those authors derived these relative k–corrections as functions of the rest–frame SED color in order to account for the amount of mismatch between the observed and rest–frame bandpasses for each individual galaxy along the color–magnitude diagram. Since the data here will be used only to measure the variation of color given by the intercept of the color–magnitude relation at a fixed luminosity, it is only necessary to calculate the k–corrections appropriate to the "average" elliptical represented by that fiducial luminosity. All filter magnitudes are relative to αLyr under the assumption that it has zero color between all bandpasses.

The computation of $k_{z,B}$ and $k_{z,V}$ using the Bruzual & Charlot (1996, as provided in Leitherer *et al.* 1996) solar metallicity model has been checked against the empirical k–

corrections of Oke & Sandage (1968) and show agreement < 0.05 mag at both B and V. Small differences like these are to be expected for differences between the assumed filter shape and detector response between the two studies. The computation of $k_{z,U,V} - k_{z,V,I}$ has been checked against those calculations given in Aragón–Salamanca *et al.* (1993), with a similarly good agreement, although there are small differences (up to 0.1 mag at $z = 0.895$) which depend strongly on the exact shape of the I–band (or i–band) filter response assumed.

Various spectral energy distributions were taken from recent studies in the literature to estimate the k–corrections and their uncertainties. The assumed cosmology of $H_0 = 75$ km s^{-1} Mpc^{-1}, $\Omega_0 = 0.2$, and $\Lambda_0 = 0$ produce a universe with age ~ 11 Gyr, so models with near to this age were chosen to correspond to the "no evolution" k–corrections. The following models were used: Bruzual & Charlot (1996, as provided in Leitherer *et al.* 1996) with [Fe/H]$= -0.4$ dex, 0 dex, and $+0.4$ dex (Salpeter IMF), 0 dex (Scalo IMF); the solar metallicity model of Fioc & Rocca–Volmerange (1996), in which the Padova evolutionary tracks, Salpeter IMF, and those author's stellar library were chosen; the Worthey (1994) models with [Fe/H]$= -0.5$ dex, -0.25 dex, 0 dex, and $+0.5$ dex; and the Bressan, Chiosi, & Tantalo (1996) models with [Fe/H]$= -0.4$ dex, 0 dex, and $+0.4$ dex. The derived k–corrections are shown in Figure 5.1; the k–corrections for the four solar metallicity models only are plotted in Figure 5.2 for ease of comparison.

The k–corrections show good agreement among these different models despite the different modeling approaches, stellar libraries, and evolutionary tracks that went into each model. Only at redshifts corresponding to the extreme for each observed color do the k–corrections begin to show significant dispersion: the rms scatter is 0.07 mag at $z = 0.23$ for observed $(U - V)_z$, 0.06 mag at $z = 0.17$ for observed $(B - R)_z$, 0.04 mag at $z = 0.46$ for observed $(B - R)_z$, 0.10 mag at $z = 0.90$ for observed $(V - I)_z$, and 0.07 mag at $z = 0.90$ for observed $(V - i)_z$. Since the range of model metallicities is probably substantially larger than the true variations in metallicity among early–type galaxies at a fixed luminosity on the color–magnitude relation—or even along a significant extent of the color–magnitude relation—the uncertainty contributed to the final results from the k–corrections would be smaller than even these small variations among models. The Bruzual & Charlot (1996) solar metallicity and Salpeter IMF models are adopted for the remainder of this paper as representative of these various model SEDs.

The mean surface brightness within the isophotal detection aperture, which is used in

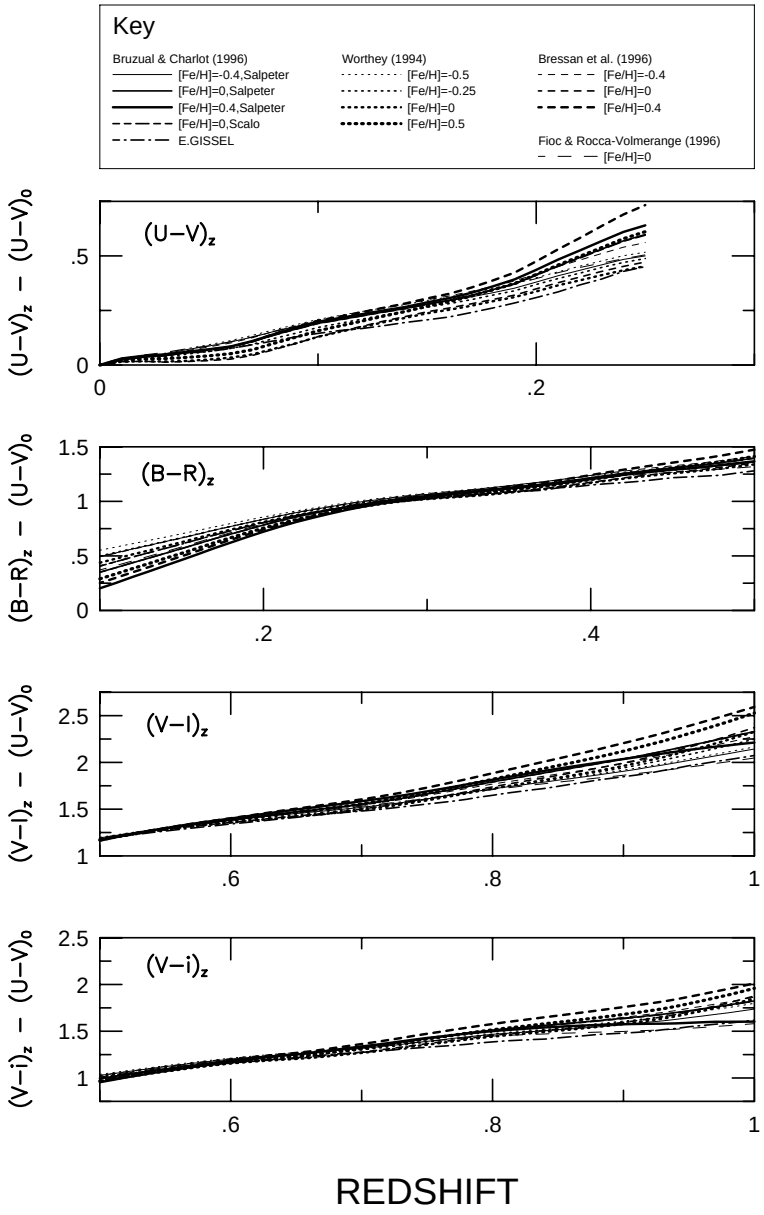

Figure 5.1: Comparison of k–corrections of the observed bandpasses $(U-V)_z$ $(0 < z < 0.23)$, $(B-R)_z$ $(0.17 < z < 0.46)$, $(V-I)_z$ $(0.51 < z < 0.895$, Cousins I filter), and $(V-i)_z$ $(0.51 < z < 0.895$, Gunn i filter) into rest–frame $(U-V)_0$. The observed color corresponding to each panel is given in the upper left of that panel; the key in the top panel identifies the various model SEDs used in the calculations. The k–corrections show good agreement in the redshift range for which they are employed. The k–corrections for the Bruzual & Charlot (1996) solar metallicity and Salpeter IMF are used for the remainder of this paper as their derived k–corrections are typical for this wide range of SEDs.

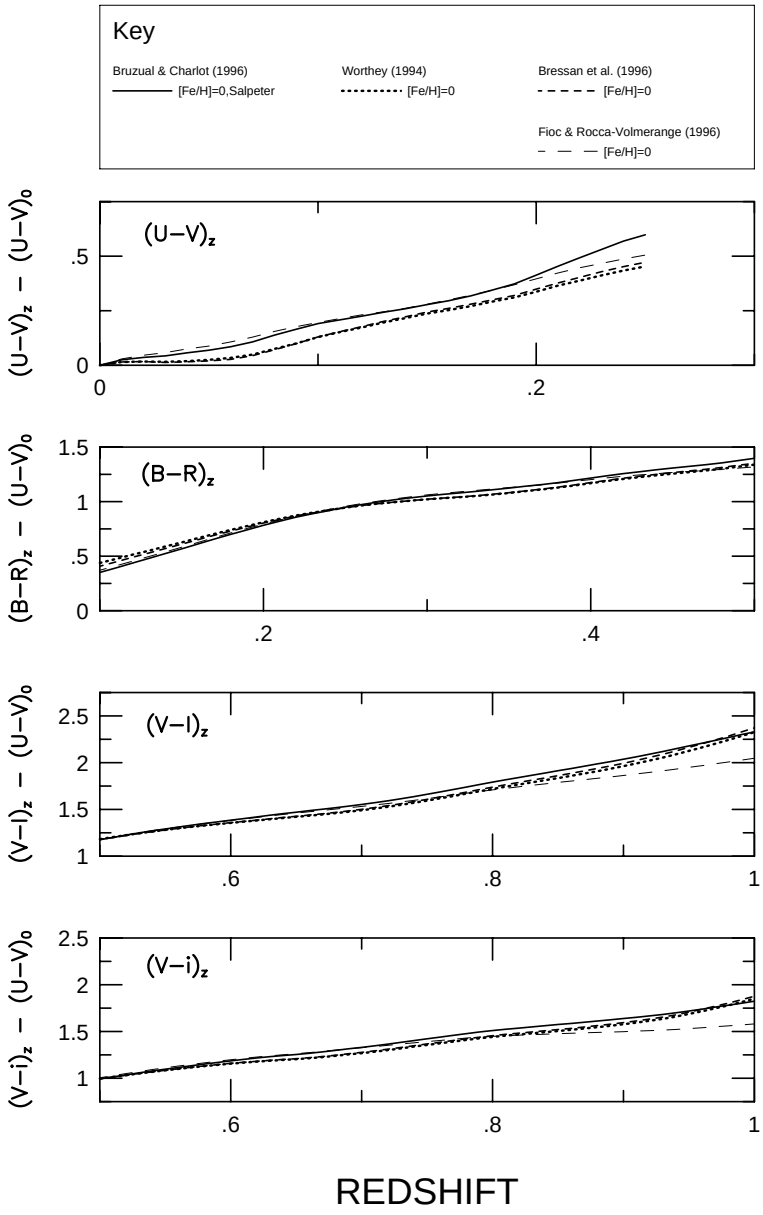

Figure 5.2: Comparison of k–corrections of the observed bandpasses for solar metallicity models only. Otherwise, this figure is identical to Figure 5.1. There is broad agreement between the models in all panels, with the exception of the top panel for observed $(U-V)_z$ at the highest redshifts.

the concentration index (Abraham *et al.*1994) discussed below, has evolutionary, surface brightness dimming, and k–corrections applied to place galaxies at very different redshifts onto a common scale for the galaxy selection criteria. The evolutionary correction at V from the Vazdekis *et al.* (1996) and Bruzual & Charlot (1996) models is ~ 2 mag $/\Delta \log t$ (see Pahre, de Carvalho, & Djorgovski 1998b, Chapter 4 of this thesis). This correction is very close to the value $2.5 \log(1+z)$ mag (see the discussion in Sandage 1988), so the latter correction is adopted for simplicity.

There should be a similar evolutionary correction to the total magnitude. This is an important point since the total magnitude will affect the color via the slope of the color–magnitude relation. Since the slope of this relation is $\Delta(U-V)_0 < 0.1 \Delta V_{\rm tot,0}$, this effect is < 0.04 mag for the highest redshift cluster ($z = 0.55$) in the entire survey; in the same redshift interval, on the other hand, the color evolution in $(U-V)_0$ should be ~ 0.25 mag from the Bruzual & Charlot (1996) models, so the effect of luminosity brightening will be a minor contribution to the color evolution. Since the amount of luminosity evolution could vary between models—in the simple stellar populations models, the cosmology, or formation redshift—this correction for evolutionary brightening will be included as part of the models that are constructed to explain the color evolution, and will not be applied directly to the total magnitudes.

Since elliptical galaxies in general have color gradients, it is necessary to measure the color in a homogeneous manner. The color–magnitude relation is usually expressed in terms of a correlation between the color measured in a fixed metric aperture and the total magnitude. The study of Bower *et al.* (1992b) in the Coma cluster utilized an aperture of 11 arcsec diameter, which is too small for comparisons with elliptical galaxies at high redshifts. Hence, it is necessary to choose a larger aperture for the higher redshifts, and to estimate a correction to the Bower *et al.* measurements. Color gradients will cause a larger aperture to have a bluer color. The color gradients in the literature (Peletier *et al.* 1990a; Franx, Illingworth, & Heckman 1989), if due to metallicity gradients in the underlying stellar populations, are consistent with a $(U-V)$ isophotal color gradient of ~ -0.16 mag arcsec^{-2} dex^{-1}. This translates to an aperture color gradient of $\sim -0.16/1.6 \approx -0.10$ mag dex^{-1} (Sparks & Jørgensen 1993). An aperture of 30 arcsec at the distance of the Coma cluster, corresponding to $6.7 h_{75}^{-1}$ kpc, is adopted here. Thus, the Bower *et al.* measurements in $(U-V)$ need to be changed by -0.044 mag to account for these color

gradients.

Images of the Coma cluster in U and V in photometric conditions were obtained as part of this study to determine if these corrections to account for color gradients are accurate. These images were obtained under poor seeing conditions (3 arcsec), and only cover a limited 12×12 arcsec^2 field, but are of sufficient quality to provide an estimate of the change in $(U-V)$ between apertures of 11 arcsec and 30 arcsec. Since these galaxies are very large, the algorithm FOCAS is not well–suited to measuring total magnitudes; instead, the values of $V_{\rm tot}$ from Lucey *et al.* (1997), based on their measurements of the half–light radii and half–light mean surface brightnesses, are adopted. There is a mean offset from the smaller to the larger aperture of $\Delta(U-V) = -0.035 \pm 0.008$ mag, which shows good agreement with the estimate based on color gradients from the literature, even though this is based on a small sample of 10 galaxies. Furthermore, the smaller aperture data show an agreement to within 0.01 mag in the intercept of the $(U-V)$ versus $V_{\rm tot}$ color–magnitude relation of Bower *et al.* when the slope of the relation is fixed to the Bower *et al.* slope of -0.0819. Hence, the $(U-V)$ data from the Coma cluster in Bower *et al.* can be put onto a common scale with the high redshift clusters, after accounting for color gradients, to an uncertainty of 0.01 mag. The empirically–derived correction of -0.035 mag will be adopted here.

5.2.3 Galactic Extinction

Galactic extinction was estimated using two different methods: (1) using the maps of Burstein & Heiles (1982), which are based on a combination of neutral hydrogen column density and extragalactic number counts; and (2) using the IRAS $\lambda = 100\mu$m maps, which primarily trace dust emission, and the conversion from S_{100} to A_B of Laureijs, Helou, & Clark (1994). The individual measurements for each cluster and blank field are provided in Table 5.2 and compared in Figure 5.3.

There is a systematic trend in the sense that the IRAS 100μm maps imply a larger amount of Galactic extinction; the formal linear regression has slope 1.64 ± 0.18, intercept -0.00 ± 0.02, and rms in the ordinate of 0.08 mag. If this uncertainty is shared equally between each measurement, it implies an uncertainty of 0.056 mag per measurement of A_B. The *a priori* assertion is that dust emission should be a better tracer of dust absorption, especially since there might be significant systematic variations in the dust–to–gas ratio in the Galaxy. It is for this reason that we have adopted the IRAS estimates; readers who

Table 5.2: Measurements of $(U-V)_0$ by Cluster

Cluster	A_B BH82 (mag)	A_B IRAS (mag)	z	Bandpasses Observed	Fixed Slope $(U-V)_0$ (mag)	Fixed Slope ± (mag)	Free Slope $(U-V)_0$ (mag)	Free Slope ± (mag)
Coma=A1656	0.05	-0.02	0.024	UVI	1.456	0.026	1.456	0.026
Abell 1795	0.00	0.01	0.062	UVI	1.469	0.041	1.496	0.041
Abell 2065	0.07	0.10	0.072	UVI	1.481	0.039	1.479	0.039
Abell 1035	0.00	0.03	0.080	UVI	1.145	0.039	1.140	0.039
Abell 98	0.06	0.16	0.105	UVI	1.830	0.042	1.894	0.043
Abell 2443	0.21	0.21	0.108	UVI	1.298	0.040	1.336	0.040
Abell 655	0.12	0.10	0.125	UVI	1.364	0.040	1.370	0.040
Abell 175	0.08	0.26	0.129	UVI	1.148	0.044	1.230	0.046
Abell 24	0.06	0.18	0.134	UVI	1.357	0.041	1.394	0.042
Abell 2218	0.08	0.07	0.171	UVI	1.425	0.041	1.420	0.039
Abell 2218	0.08	0.07	0.171	BRI	1.413	0.039	1.415	0.041
Abell 1689	0.02	0.21	0.181	UVI	1.318	0.045	1.381	0.039
Abell 1689	0.02	0.21	0.181	BRI	1.393	0.038	1.437	0.038
Abell 1689	0.02	0.21	0.181	BRI	1.431	0.038	1.480	0.044
Abell 665	0.13	0.12	0.182	BRI	1.488	0.039	1.538	0.039
Abell 2219	0.00	0.03	0.228	BRI	1.454	0.041	1.548	0.042
Abell 2390	0.33	0.37	0.231	UVI	1.428	0.050	1.442	0.047
Abell 2390	0.33	0.37	0.231	BRI	1.530	0.041	1.518	0.041
Abell 2744	···	0.01	0.308	BRI	1.333	0.043	1.439	0.042
MS1358.4+6245	0.04	0.04	0.328	BRI	1.447	0.042	1.481	0.042
CL1446+2621	0.08	0.08	0.37	BRI	1.448	0.053	1.516	0.055
MS1512.4+3647	0.03	0.03	0.372	BRI	1.438	0.054	1.632	0.070
Abell 370	0.06	0.19	0.373	BRI	1.272	0.041	1.352	0.041
CL0952+44	0.00	0.00	0.377	BRI	1.011	0.131	0.677	0.117
ZwCL0024+1652	0.14	0.20	0.390	BRI	1.462	0.046	1.568	0.046
Abell 851	0.02	0.00	0.402	BRI	1.379	0.050	1.418	0.047
CL0303+1706	0.36	0.54	0.418	BRI	1.209	0.047	1.262	0.052
CL140933+52	0.00	0.01	0.460	BRI	1.013	0.095	1.237	0.097
CL1601+4253	0.00	0.00	0.539	VIJ	1.228	0.042	1.238	0.041
MS0015.9+1609	0.09	0.24	0.541	VIJ	1.073	0.049	1.058	0.049
Binned by redshift:								
$0.062 \leq z \leq 0.134$	···	···	0.100	UVI	1.415	0.025	1.429	0.025
$0.171 \leq z \leq 0.231$	···	···	0.201	UBVRI	1.407	0.023	1.438	0.023
$0.308 \leq z \leq 0.328$	···	···	0.318	BRI	1.430	0.041	1.480	0.040
$0.370 \leq z \leq 0.460$	···	···	0.415	BRI	1.338	0.027	1.422	0.025
$0.539 \leq z \leq 0.541$	···	···	0.543	VIJ	1.226	0.043	1.238	0.042
Blank fields:								
J0237-0248	0.02	0.16	···	BRI	···	···	···	···
J0053+1234	0.19	0.30	···	UBVRI	···	···	···	···
J1722+4950	0.08	0.03	···	UBVRI	···	···	···	···

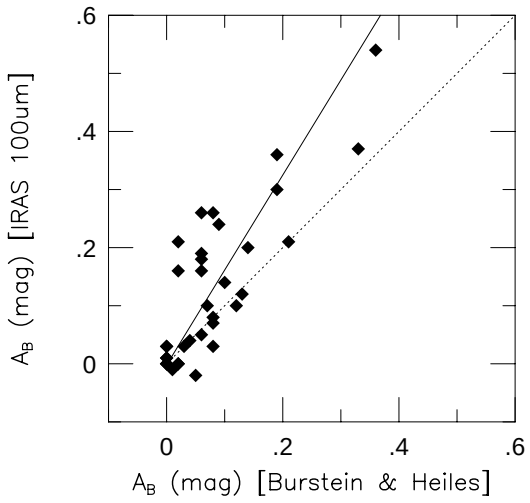

Figure 5.3: Comparison of Galactic extinction estimates A_B from the Burstein & Heiles (1982) HI maps and the IRAS $\lambda = 100\mu$m emission maps using the conversion of Laureijs, Helou, & Clark (1994) for the clusters and blank fields in the survey. The IRAS measure of Galactic extinction appears to be systematically larger than the HI measure; the linear regression (solid line) has slope 1.64, while the dotted line shows the relationship that would occur if both measurements were identical. If the residuals are shared equally between the two measurements, then this implies an uncertainty in Galactic extinction of 0.06 mag per measurement.

wish to use the Burstein & Heiles measurement (or an average of the two) may use the information in Table 5.3 to modify the measurements of color.

The Galactic extinction curve of Cardelli, Clayton, & Mathis (1989) with $R_V = 3.1$ was assumed to convert A_B into other wavelengths, producing $E(U-V) = 0.43A_B$, $E(B-R_C) = 0.38A_B$, and $E(V-I_C) = 0.30A_B$. The random uncertainties of $\Delta A_B = 0.056$ mag therefore result in $\Delta E(U-V) = 0.024$ mag. The largest difference between the estimates of A_B is 0.20 mag, which implies that the systematic errors of estimating Galactic extinction are < 0.09 mag in $(U-V)$ for the survey and even smaller at the longer observed wavelengths.

5.3 Object Detection and Measurement of Colors

The algorithm FOCAS (Jarvis & Tyson 1981) was used to detect objects and generate the original galaxy lists and measure total magnitudes. Only objects classified as galaxies ("g") or fuzzy–stars ("sf") by FOCAS were generally included in the subsequent galaxy lists. The exceptions were a few clusters at $z > 0.5$ with data from the Palomar 60–inch telescope in mediocre seeing; in these cases, star/galaxy classification was judged poor at the faintest magnitudes, so objects classified as stars ("s") were added to the list. Colors were measured using aperture photometry from the PHOT task in the DAOPHOT package of IRAF on images that had been smoothed to an identical resolution. All objects were required to have 3–σ detections in FOCAS.

The total magnitudes calculated in FOCAS are, in general, fainter than the true total magnitudes of the galaxies since the isophotal area used to calculate the total magnitude (which is an area twice the size as that encompassed by the detection isophote) does not extend to infinity. Simulated elliptical galaxies were constructed using the package ARTDATA in IRAF, using typical physical sizes, magnitudes, and noise characteristics for the optical imaging data. Object detection was performed on these images using FOCAS. The recovered total magnitude was typically ~ 0.3 mag fainter than the input total magnitude, although this effect varies weakly with input magnitude between ~ 0.2 mag for the brighter galaxies and ~ 0.4 mag for the faintest galaxies. This factor of 0.3 mag was applied to all total magnitudes, and the uncertainty in this correction is taken to be ± 0.1 mag. Since the slope of the color–magnitude relation is < 0.1 mag in color per 1 mag in luminosity, this correction of 0.3 ± 0.1 mag corresponds to a correction in color of only $< 0.03 \pm 0.01$ mag.

5.4 The Color–Morphology Selection Criteria to Identify Cluster Ellipticals

5.4.1 Summary of Selection Criteria Used

In summary, there are four different selection criteria used in identifying the sample of early–type galaxies in Figure 5.4: (1) the $(U-V)_0$ versus $V_{\rm tot,0}$ color–magnitude relation; (2) the $(V-I)_0$ versus $V_{\rm tot,0}$ color–magnitude relation; (3) $(U-V)_0$ versus $(V-I)_0$ color–color space; and (4) concentration index. These four selection criteria show substantial, but not complete, overlap in the galaxies which they select. For example, a high redshift field spiral galaxy might mimic the observed color $(B-R)$ but will not simultaneously mimic the observed color $(R-I)$. Likewise, a background or foreground early–type galaxy might mimic the concentration index of a cluster early–type, but will not match the observed colors. Finally, a cluster late–type galaxy may have a similar observed $(R-I)$ color as a cluster early–type galaxy, but will have a much younger mean age for its stellar content and hence a shallower 4000 Å break and bluer observed $(B-R)$ color. More than one of these four selection criteria is needed to exclude each of these undesired interloper galaxies.

5.4.2 Abell 665 ($z = 0.182$) as a Worked Example

The early–type population in clusters is easily identified by its position in a color–magnitude or color–color diagram. A good example of this for clusters at a range of redshifts is to be found in Dressler & Gunn (1992) for their *gri* imaging. Displayed in Figure 5.4 are a series of such color–magnitude, color–color, and concentration index–isophotal surface brightness diagrams for Abell 665 ($z = 0.182$). A clear color–magnitude relation is seen for this cluster in both $(U-V)_0$ versus $V_{\rm tot,0}$ and $(V-I)_0$ versus $V_{\rm tot,0}$, in which the most luminous early–type galaxies are the reddest. The two–color diagram of Figure 5.4 [$(U-V)_0$ versus $(V-I)_0$] demonstrates that the locus occupied by the early–type population lies at the red end of the cluster galaxy sequence.

The quantitative identification of the early–type galaxy sequence was done by iteratively fitting a linear color–magnitude relation to both colors $(U-V)_0$ and $(V-I)_0$ simultaneously as functions of $V_{\rm tot,0}$. The first iteration limited galaxies by their position in the color–color locus and concentration index–isophotal surface brightness diagrams; the subsequent

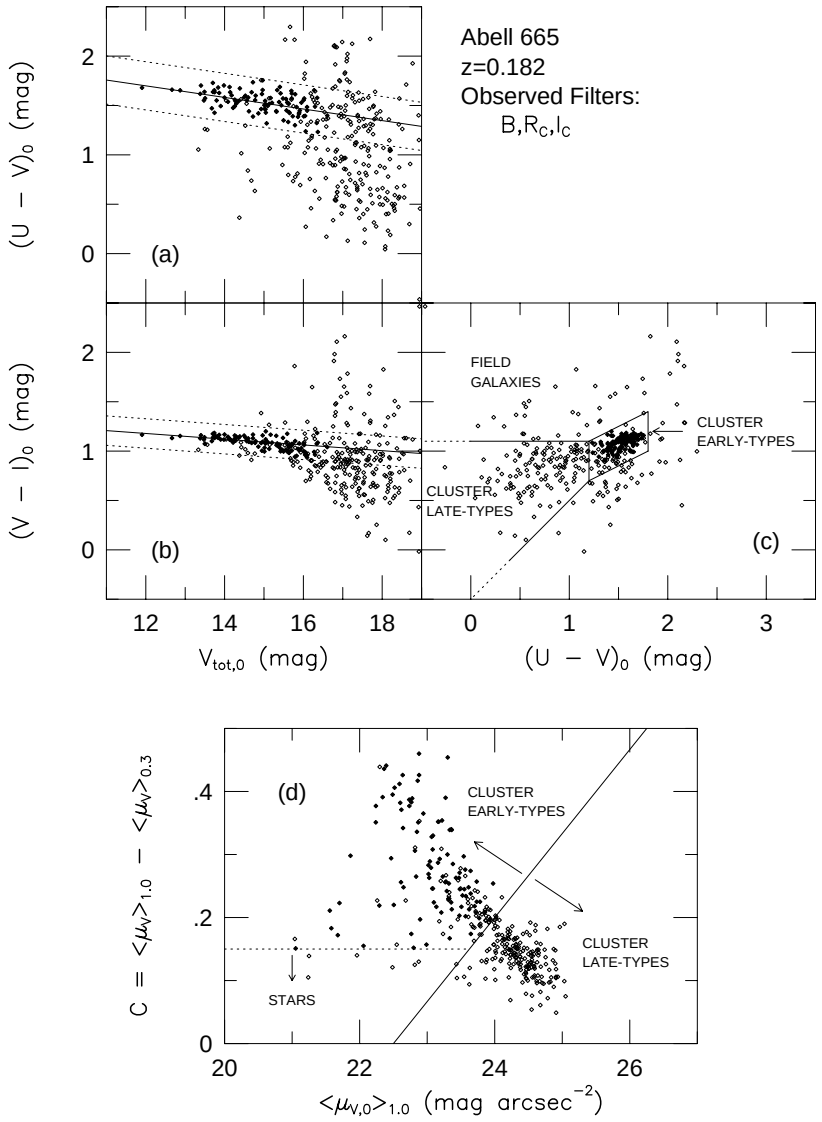

Figure 5.4: Identification of the early–type galaxy sequence in Abell 665 ($z = 0.182$). Only galaxies within the core region of the cluster ($r < 600$ kpc, $H_0 = 75$ km s Mpc^{-1}, $\Omega_0 = 0.2$) are included. Galaxies identified by the multi–color and concentration index selection criteria are identified with filled symbols; other galaxies are identified with open symbols. The fitted color–magnitude relations are plotted in panels (a) and (b) with solid lines with $\pm 2.5\sigma$ bounds plotted as dotted lines. The selection criteria for concentration index is plotted in panel (d) as a solid line (to differentiate early–type from late–type galaxies) and as a dotted line (to exclude misclassified stars that can enter the galaxy catalog).

iterations removed the color–color requirement, instead rejecting galaxies which lie outside of a certain range of $N\sigma$ from the color–magnitude relations obtained in the previous iteration. The scatter σ was estimated using the quartiles of the residual distribution, under the assumption that the uncertainties have a Gaussian distribution, which is a more robust measure of the scatter in the presence of a substantial interloper population (from field galaxies and cluster late–type galaxies). The number N of σ used for rejection is typically 3.5 on the second pass, and 2.5 on the third. There is little statistically–significant change in the color–magnitude relations between the iterations, suggesting that the procedure is robust.

5.4.3 Comparing the Effects of Each of the Selection Criteria

An illustration of the effects of each of the selection criteria is given in Figures 5.5 to 5.8. In each figure, only one of the selection criteria is applied, thereby demonstrating which galaxies in this parameter space are selected. It is clear that selection by the color–magnitude relation in Figures 5.5 and 5.6 shows excellent correlation with location on the concentration index diagram, selection by concentration index in 5.7 shows an excellent correlation with location in color–color space, selection by one color–magnitude relation shows an excellent correlation with the other color–magnitude relation, and so on.

5.4.4 The Field Galaxy Contamination as Measured from Blank Fields

One of the main goals of applying selection criteria based on color, total magnitude, and concentration index is to exclude field galaxies in a robust manner. Three "blank" fields were imaged as part of this study in order to quantify the effects of field galaxy contamination on the results. Two of these fields were imaged at $UBVRI$, while the third was imaged at BRI only. The integration times on these fields was very similar to that for the clusters themselves, so that a direct comparison could be made to the same limiting depths in apparent magnitude. The data for the field at J0053+1234 was also used as part of the pencil beam redshift survey described by Pahre *et al.* (1998).

The "blank" fields can be processed in the same manner as any of the cluster fields, i.e., applying the same k–correction for the appropriate filters at the cluster redshift. The combined field galaxy sample for observed BRI filters at $z = 0.182$, for use in estimating the contamination in Abell 665, is displayed in Figure 5.9. The total area covered by the "blank"

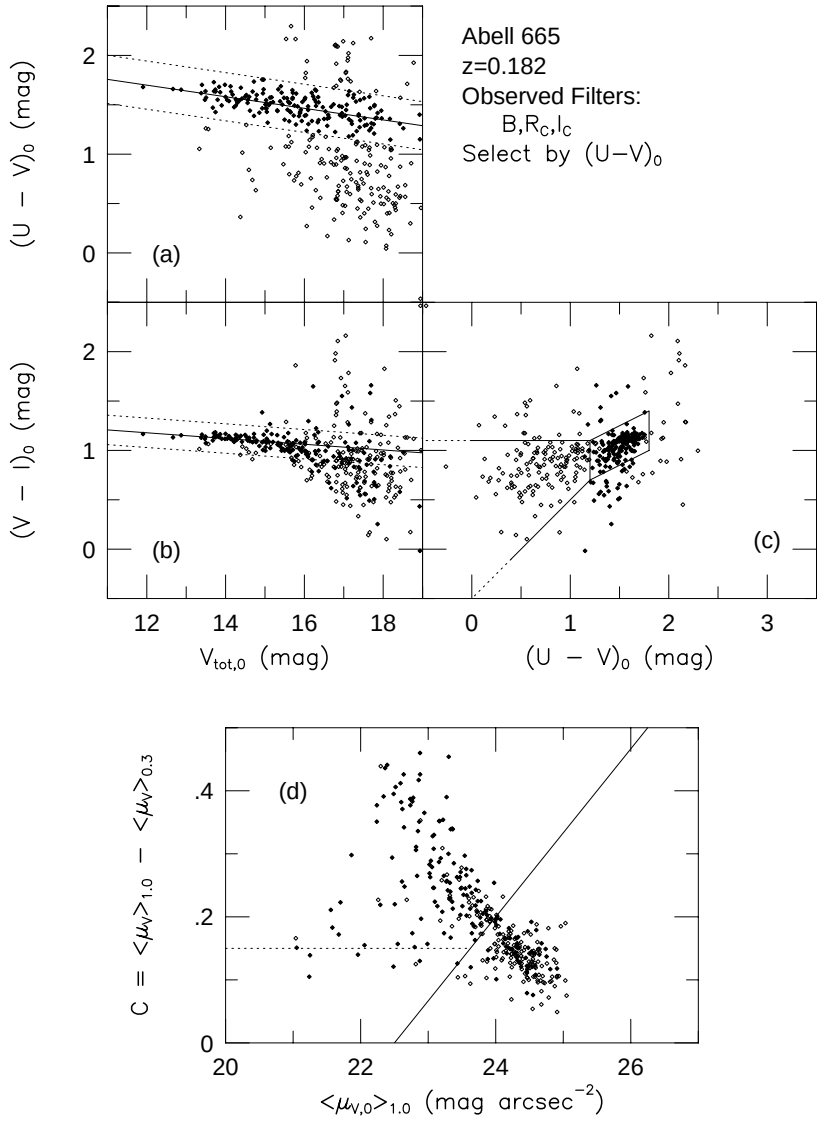

Figure 5.5: Effects of selection due to the $(U-V)_0$ versus $V_{\rm tot,0}$ color–magnitude relation in Abell 665. The same lines plotted in Figure 5.4 are plotted in each panel to assist in comparing the relative effects. The galaxies selected with this criterion [panel (a)] show an excellent correlation with the selection lines in the other panels (b)–(d).

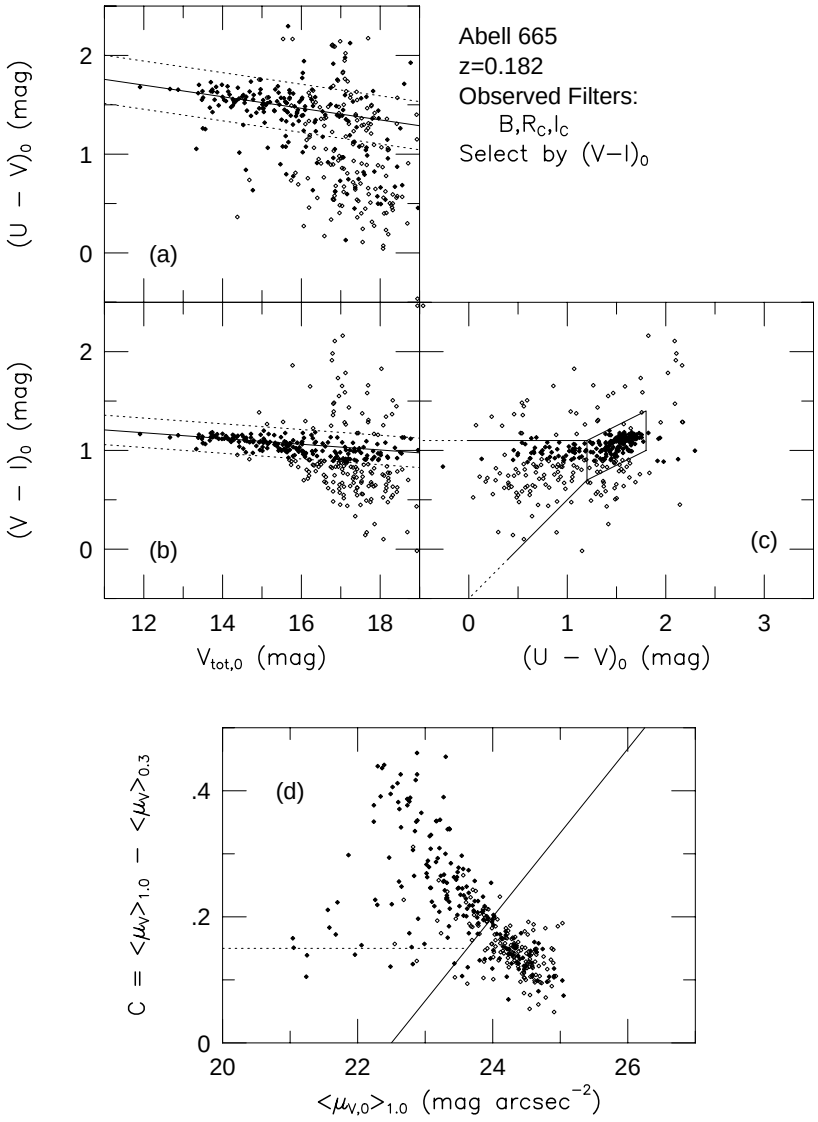

Figure 5.6: Effects of selection due to the $(V-I)_0$ versus $V_{\rm tot,0}$ color–magnitude relation in Abell 665. The same lines plotted in Figure 5.4 are plotted in each panel to assist in comparing the relative effects. The galaxies selected with this criterion [panel (b)] show an excellent correlation with the selection lines in the other panels [(a), (c), and (d)].

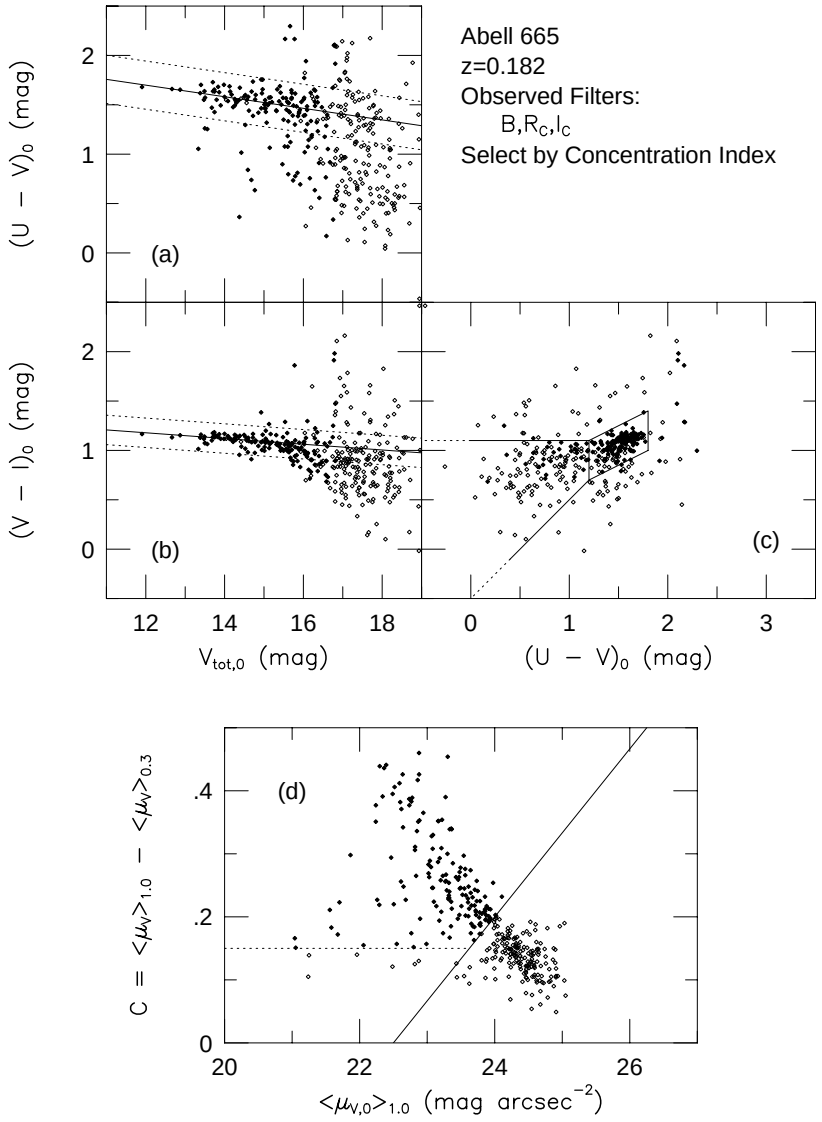

Figure 5.7: Effects of selection due to the concentration index in Abell 665. The same lines plotted in Figure 5.4 are plotted in each panel to assist in comparing the relative effects. The galaxies selected with this criterion [panel (d)] show an excellent correlation with the selection lines in the other panels (a)–(c).

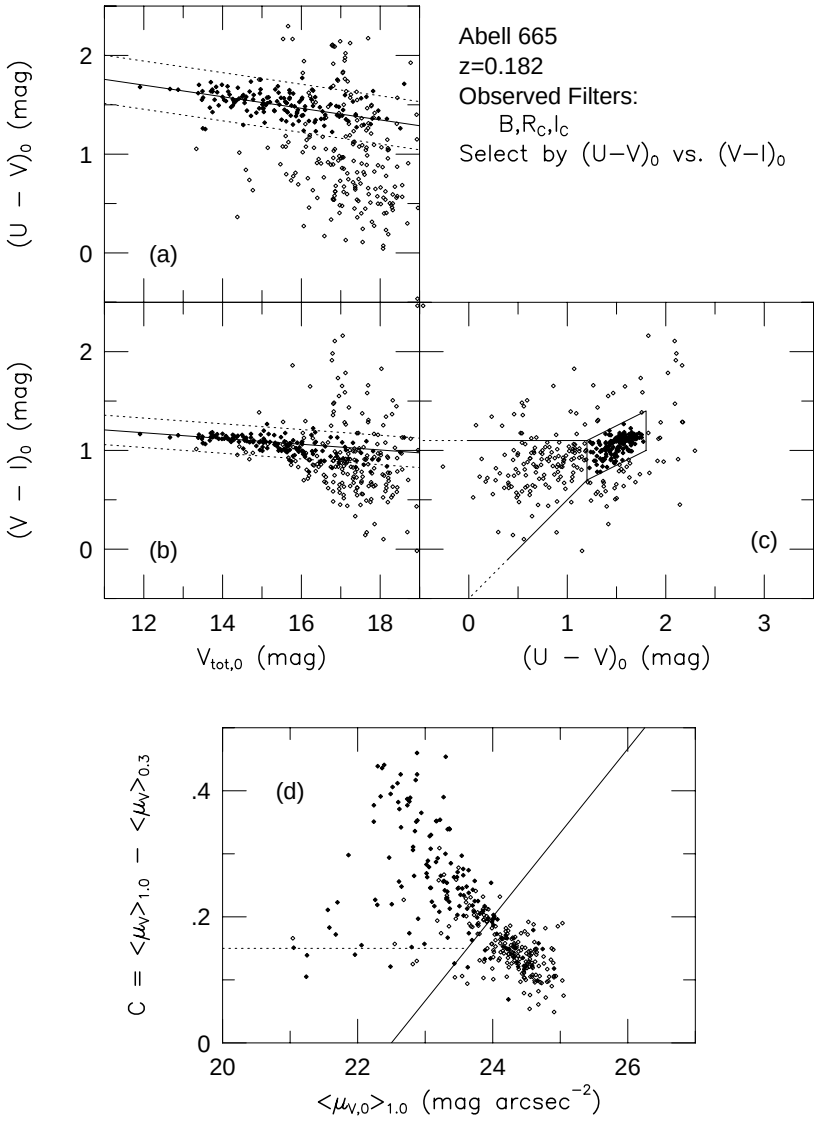

Figure 5.8: Effects of selection due to the two colors $(U-V)_0$ versus $(V-I)_0$ in Abell 665. The same lines plotted in Figure 5.4 are plotted in each panel to assist in comparing the relative effects. The galaxies selected with this criterion [panel (c)] show an excellent correlation with the selection lines in the other panels [(a), (b), and (d)].

fields is much larger than that for $r < 900 h_{75}^{-1}$ kpc for each cluster, so field contamination can be estimated by randomly drawing a subset of galaxies from the combined "blank" field sample. In the case of Abell 665, the area studied for the cluster galaxies is one–tenth of the area for the combined "blank" field sample, so 10% of the galaxies were drawn at random. One such Monte Carlo realization for Abell 665 is displayed in Figure 5.10. As can be seen in that figure, there are only six field galaxies expected to contaminate the Abell 665 cluster early–type galaxy sample of 105 galaxies. Hence the two–color and concentration index selection criteria are robust at excluding field galaxies at $z = 0.182$.

The median redshift for clusters imaged at UVI is $z = 0.12$, while the median redshift for clusters imaged at BRI is $z = 0.37$. The total field galaxy sample is plotted for each of these two redshifts in Figures 5.11 and 5.12, respectively. The area covered by the "blank" fields at $z = 0.12$ is three times the cluster areas at that redshift, so the contamination of two galaxies in the entire sample predicts that there should be less than one galaxy contaminating the cluster samples at $z = 0.12$. Hence, field galaxy contamination is unimportant at this redshift. The area covered by the "blank" fields at $z = 0.12$ is ~ 1.3 times the cluster areas at that redshift, so the contamination of two galaxies in the entire sample predicts that there should be ~ 1.5 galaxies contaminating each cluster sample at $z = 0.12$. The area covered by the "blank" fields at $z = 0.37$ is ~ 10 times the cluster areas at that redshift, so the contamination of 49 galaxies in the entire sample predicts that there should be ~ 4 galaxies contaminating each cluster sample at $z = 0.37$. The number of early–type galaxies per cluster selected using these criteria ranges from ~ 20 to ~ 200 depending on cluster richness, so field galaxy contamination is always $< 25\%$ and typically $< 10\%$.

Since the field galaxy contamination is so small for the entire cluster sample, no attempt has been made to apply statistical field galaxy subtraction.

5.5 Comparison of Color-Morphology Selection Results with Spectroscopic Information

5.5.1 New Spectroscopy of Galaxies from These Complete Samples

The original purpose of this study was to identify cluster early–type galaxies in a robust manner to exclude field galaxies and cluster late–type galaxies. A subset of these galaxies

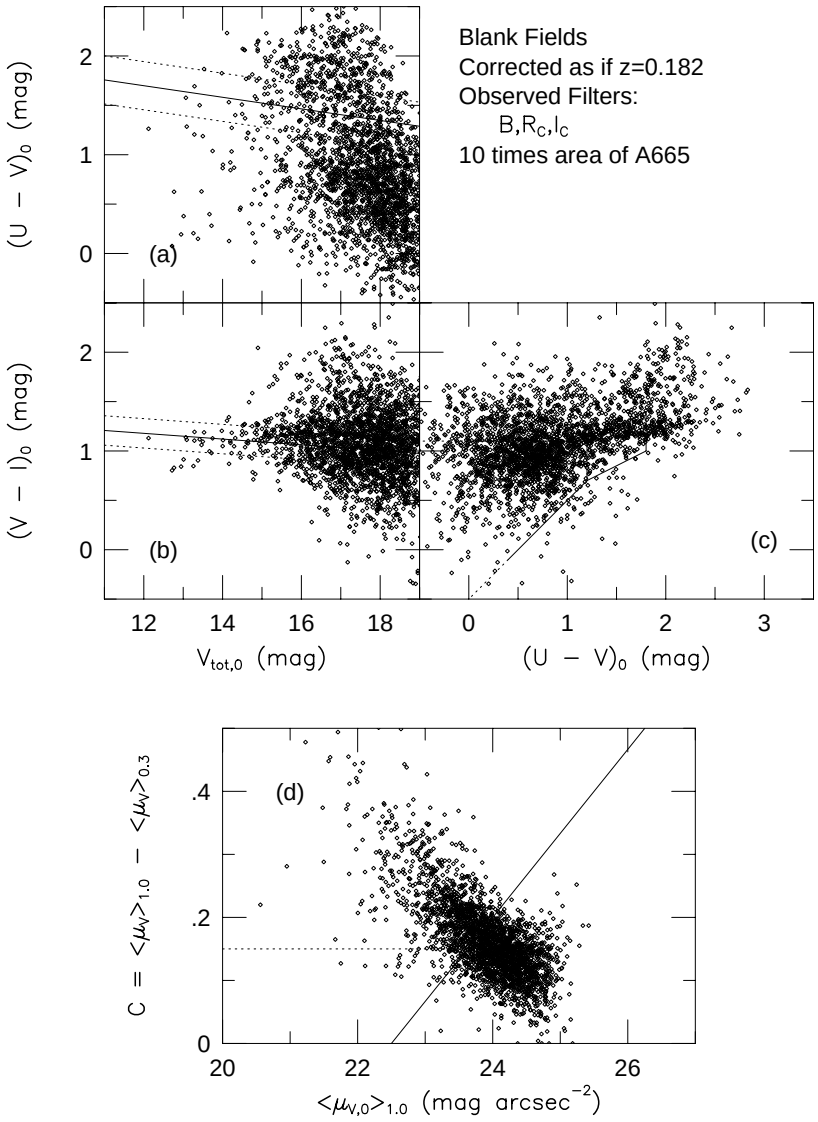

Figure 5.9: Field galaxy contamination estimated from three "blank" fields observed in the BR_CI_C bandpasses. The data derived from three 11.8×11.8 arcmin^2 fields which have been corrected in the same manner as for Abell 665 ($z = 0.182$). The area covered by the sum of these fields is ten times that of Abell 665. Note how only very few field galaxies scatter into the two color selection range of panel (c), showing that this plot alone is a strong method to discriminate between field early–type galaxies and the general field. This large database of field galaxies can be used to estimate statistically the field galaxy contamination for any cluster observations in the BR_CI_C bandpasses.

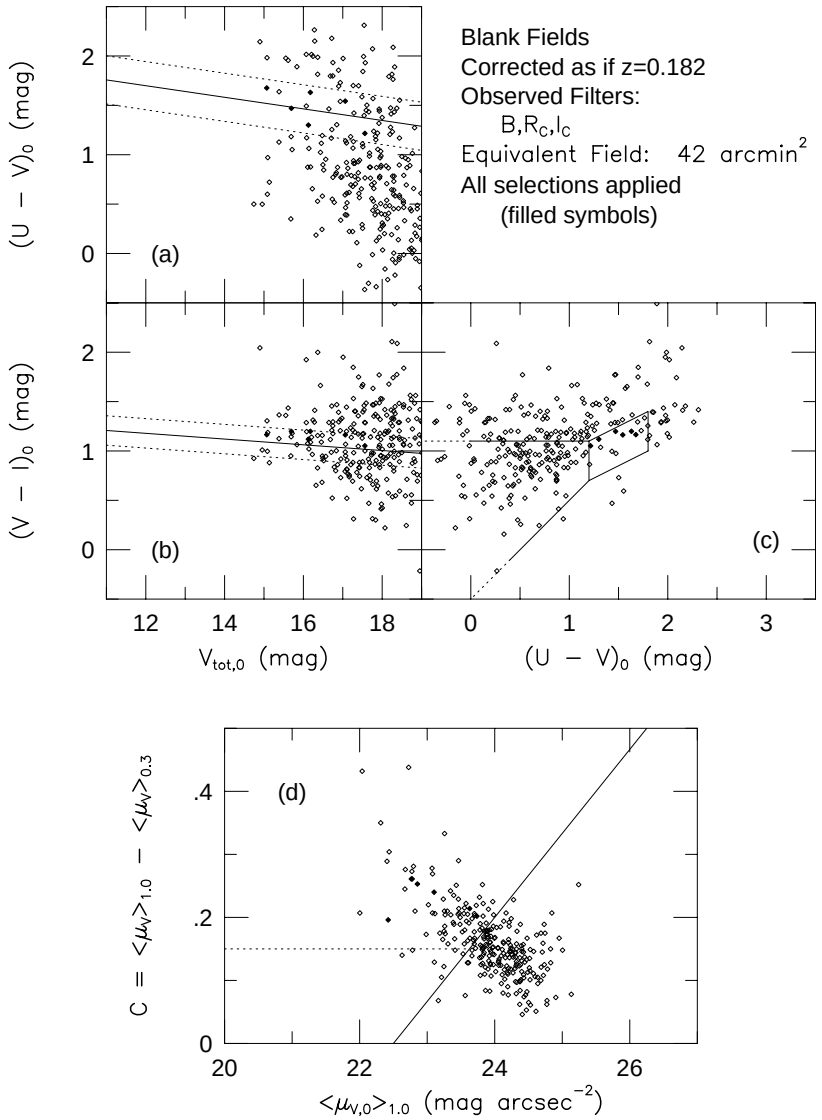

Figure 5.10: Field galaxy contamination in Abell 665 as estimated from three "blank" fields. Only 10% of the field galaxy sample has been randomly selected to match the field–of–view of the Abell 665 sample. The same selection criteria used for Abell 665 (Figure 5.4) have been applied to this field galaxy sample; the galaxies satisfying all the selection criteria are plotted as filled symbols, while the remainder of the randomly selected galaxies are plotted as open symbols. Only six field galaxies satisfy these selection criteria, while 105 probable early–type galaxies are found in Abell 665 (Figure 5.4), demonstrating the small field galaxy contamination in this method of selecting early–type galaxies in clusters.

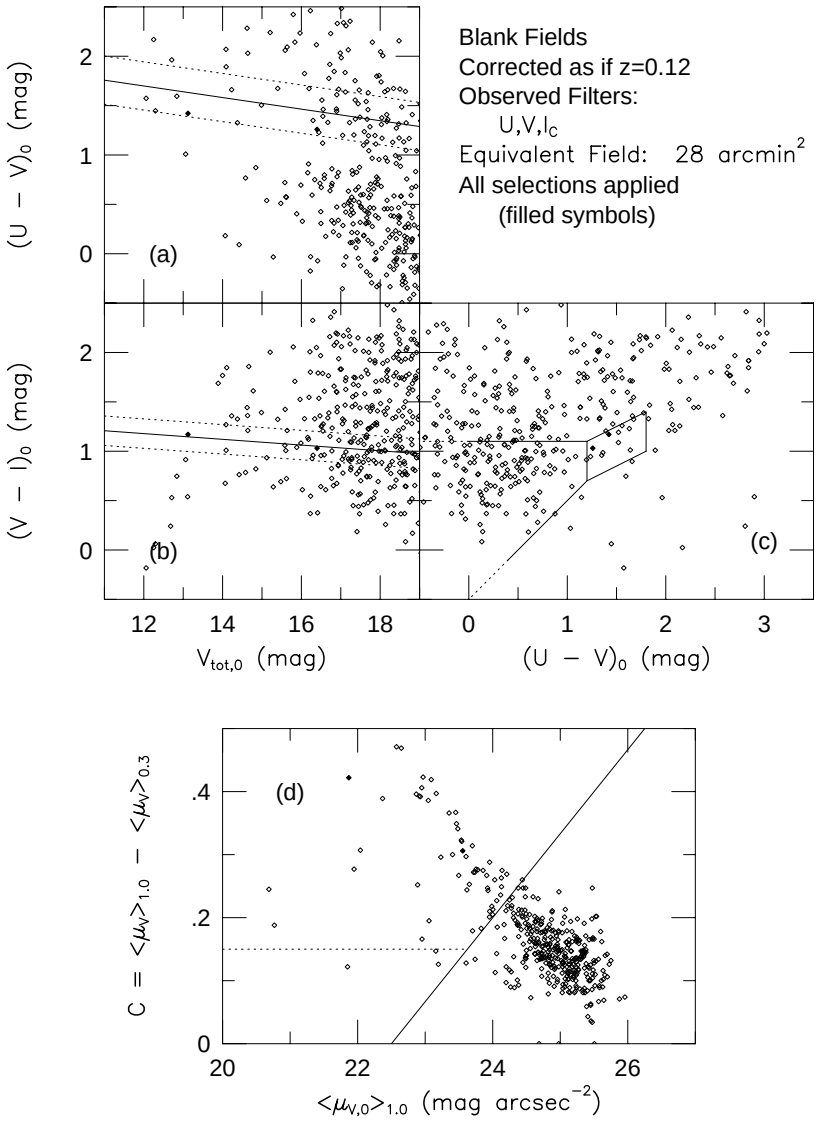

Figure 5.11: Field galaxy contamination at $z = 0.12$ from two "blank" fields observed in UVI filters. Of the 413 galaxies in these two fields covering 28 arcmin^2, there are only two galaxies which satisfy the selection criteria. Hence there is virtually no field galaxy contamination for observations of cluster early–type galaxies in UVI at $z < 0.15$.

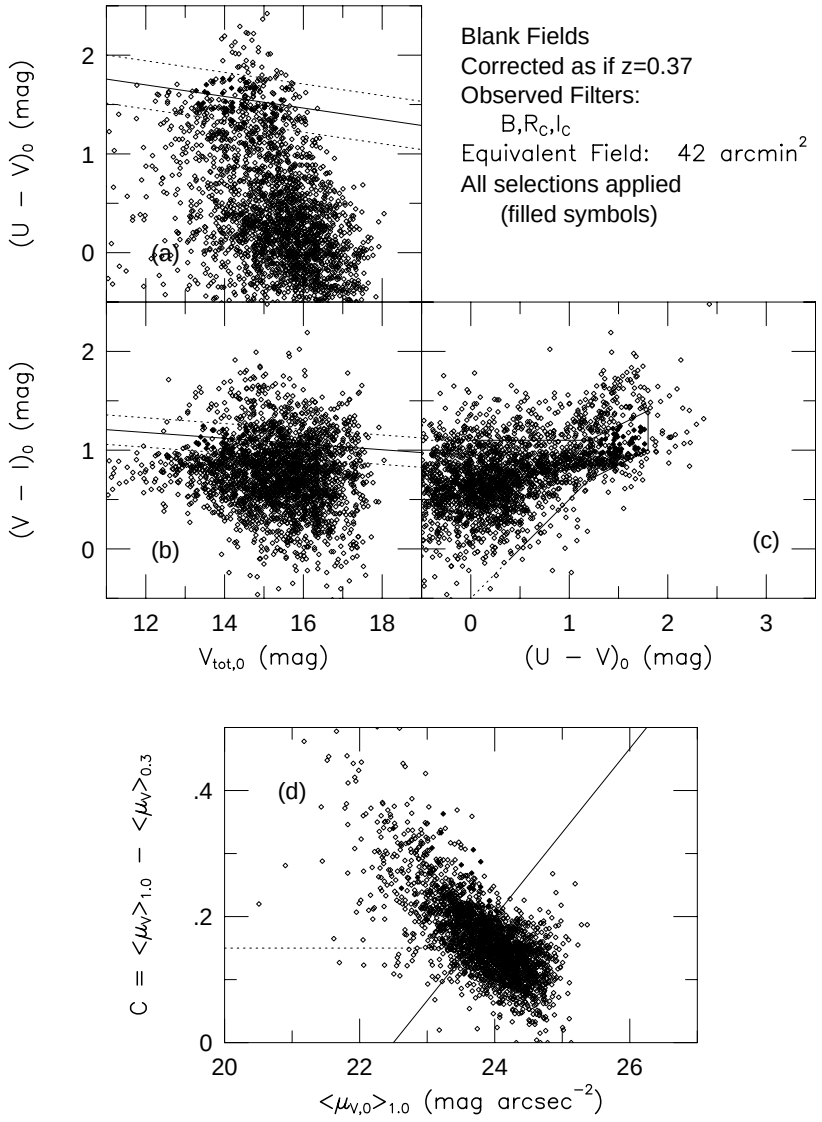

Figure 5.12: Field galaxy contamination at $z = 0.37$ from two "blank" fields observed in BRI filters. Of the 2602 galaxies in these three fields covering 42 arcmin^2, there are 49 galaxies which satisfy the selection criteria (filled symbols). Since the region studied for each cluster at this redshift is $\sim 1/10$ of this solid angle, there are only ~ 5 interloper galaxies expected at $z \sim 0.4$ per cluster.

were then chosen effectively at random for studying the evolution of the elliptical galaxy global scaling relations at these intermediate redshifts. As a result, there is a significant amount of followup spectroscopy that has been performed; these data will be presented in detail elsewhere (Pahre, Djorgovski, & de Carvalho 1998c, Chapter 7 of this thesis). A summary of the redshifts and spectral classification, however, will be given here in order to demonstrate the effectiveness of this method in identifying cluster early–type galaxies at intermediate redshifts.

The cluster samples were defined in a preliminary manner using similar methods to those described in this paper in preparation for the spectroscopy. Due to the field of view of the multi-object spectrographs employed, however, at the higher redshifts there was no selection by distance from the cluster center. Hence there might be additional field galaxy contamination due to the practical consideration that larger areas were studied, and this contamination would be expected to increase with redshift.

For 27 galaxies observed in cluster Abell 655 ($z = 0.129$), all 27 have velocities within ± 3000 km s^{-1} of the nominal cluster redshift and all have early–type absorption line spectra with no emission lines detected. For 19 galaxies observed in cluster Abell 665 ($z = 0.182$), all 19 have velocities within ± 2500 km s^{-1} of the nominal cluster redshift and all have early–type absorption line spectra with no emission lines detected. For 15 galaxies observed in cluster Abell 2390 ($z = 0.231$), one is a late–type star while the other 14 all have early–type absorption line spectra with no emission lines and velocities within ± 4000 km s^{-1} of the nominal cluster redshift. For 16 galaxies observed in cluster Abell 370 ($z = 0.372$), one has an early type spectrum but is in the foreground ($z \sim 0.32$), while the other 15 all have early–type absorption line spectra with no emission lines and velocities within ± 3500 km s^{-1} of the nominal cluster redshift. For 19 galaxies observed in cluster Abell 851 ($z = 0.402$), 4 have early–type spectra but are part of a foreground redshift structure ($z \sim 0.3$), one is a background emission line galaxy, one has weak emission lines with an early–type underlying absorption spectrum, while the other 13 are early–type galaxies at the cluster redshift. Two of the foreground galaxies are not located near to the cluster core, and therefore might have been excluded from the sample if there were a radial selection cut. For the 25 galaxies observed in cluster CL0016+16 ($z = 0.546$), 15 have early–type spectra at the cluster redshift, two are "K+A" galaxies at the cluster redshift, two are background "K+A" galaxies at $z = 0.656$, four are Galactic stars, and two are unknown

(but still consistent with being cluster early–type galaxies). The poor success in the latter cluster can be traced directly back to the poor quality photometry (compare to the other clusters) that was available for that cluster at the time of defining the spectroscopic sample, including the poor classification (using FOCAS) of the faint objects into stars and galaxies.

In summary, for the six clusters studied, 103/119 (87%) galaxies are early–type cluster members, 5/119 (4%) are foreground early–type galaxies (two of which would be excluded from the sample by a radial selection criterion), 5/119 (4%) are Galactic stars, 1/119 (1%) has both absorption lines and emission lines in its spectrum and is at the cluster redshift, 2/119 (2%) are "K+A" cluster members, and 3/119 (2.5%) are background galaxies. If cluster CL0016+16 were excluded, the success rate would be 92%, suggesting that for clusters with accurate photometry the method is $> 90\%$ in identifying cluster early–type galaxies. This is fully consistent with the estimates of $< 10\%$ field galaxy contamination based on the "blank" fields in §5.4.4.

5.5.2 Comparison to Redshift Surveys from the Literature

Redshift surveys in clusters at these redshifts typically rely on magnitude limited samples without any color or morphology (such as the concentration index) selection criteria. The Abraham *et al.* (1997) study of Abell 2390 ($z = 0.231$) had a 67% success rate in identifying cluster members in an r–band magnitude limited survey. That survey used a much longer strip ($6 \times 1h^{-2}$ Mpc^2); for a more restricted field of view, their success rate was $\sim 84\%$ in identifying cluster members (both early and late types). Dressler & Gunn (1992) studied seven clusters at $0.35 < z < 0.55$ and obtained a 66% success rate in identifying cluster members, although this study was not strictly magnitude limited. Ellis *et al.* (1997) constructed a morphologically identified sample of early–type galaxies in the cores of three clusters at $z \sim 0.55$ using HST/WFPC–2 images; from their derived color–magnitude relations, they had an 82% success rate in identifying early–type cluster members. Hence, the method described in this paper exceeds the efficiency of identifying early–type cluster members of any other method, even morphological classification from HST images.

5.5.3 The Exclusion of K+A Type Galaxies

At intermediate redshifts, there is a significant population of "K+A" galaxies[1] in rich clusters. While the intrinsic nature of these galaxies is still a topic of discussion, it appears that most of these galaxies are disk–dominated (Franx *et al.* 1997), such that they could be a significant contaminating population.

The cluster Abell 851 is probably the best–studied to date, with six K+A galaxies identified by Dressler & Gunn (1992) from spectra and 35 K+A galaxies identified by Belloni *et al.* (1995) from narrowband imaging. None of the Dressler & Gunn galaxies, and only 4/35 of the Belloni *et al.* galaxies, are part of the 97 early–type galaxies in the sample identified using the methodology and data in the present paper. For this reason, K+A galaxies are not expected to comprise a significant contaminating population of early–type galaxies identified with this method.

5.6 Color Evolution in the Early–Type Galaxy Population in Rich Clusters of Galaxies

The large data set that has been collected for the purpose of studying the early–type galaxy population for $0 < z < 0.6$ is summarized in Table 5.2. There are 35 different sets of observations, where a data set is comprised of set of images taken through three different filters (UVI, BRI, or VIJ), of 26 different clusters (including the Coma cluster).

The galaxies in each cluster were identified in the manner described above in §5.4. An original pass was made to select the galaxies using colors and magnitudes expected for a non–evolving population, and fit their color–magnitude relations in $(U-V)_0$ versus V and $(V-I_C)_0$ versus V. In a second pass, the fit from the first pass was used to select the galaxies from the original list which are consistent with the new color–magnitude, and color–color, relations. A 2.5–3 σ clipping algorithm was used for both iterations. The galaxies from the final pass are identified as "cluster early–types," and their mean color–magnitude relation, evaluated at the fiducial magnitude of $V_{\rm tot} = 14$ mag at the distance of the Coma cluster. The color–magnitude relations were fit in two different ways: (1) fixing the slope to the

[1]This terminology has been adopted to identify the presence of both K–giant stellar features (Ca II H and K, G band at $\lambda = 4000$ Å, MgH, and Mg_2 triplet) and A star features (strong Balmer lines of hydrogen) in the spectrum of such a galaxy. This type was previously called "E+A" by Dressler & Gunn (1992, and references therein), but is now generally called "K+A" (Dressler, private communication).

Bower *et al.* (1992b) color–magnitude relation in $(U-V)_0 = -0.08$, and a corresponding slope of -0.04 in $(V-I_C)_0$; and (2) allowing the slopes of both color–magnitude relations to be a free parameter. The results of these fits are displayed in Figures 5.13 to 5.17.

The data were also grouped into redshift bins of width 0.1 and fit in the same manner. This allows for the small sample sizes of some clusters to be averaged, thereby obtaining a more secure result. These binned results are displayed in Figure 5.18.

The intercepts of the $(U-V)$ color–magnitude relation are plotted as a function of redshift in Figure 5.19 for both the free fits to the slope of the relation and the constrained fits. There appears to be a small trend for the color to become bluer with redshift in a manner that is as expected for an evolving population of galaxies. The uncertainty estimates are the quadrature sum of the scatter about the relation (divided by $\sqrt{N-1}$), one–third of the expected luminosity evolution of $2.5\log(1+z)$ times the slope of the color–magnitude relation (to account for uncertainties in removing this effect), 0.02 mag as an uncertainty in $E(U-V)$, $E(B-R_C)$, or $E(V-I_C)$, 0.03 mag as a random uncertainty in the calibration, and 0.01 mag for the uncertainty in the correction for the effects of color gradients. The minimum uncertainty in $(U-V)_0$ per cluster for a typical redshift of $z = 0.3$ is then 0.038 mag, while the typical uncertainty is 0.047 mag. The data plotted in Figure 5.19 show a scatter of approximately 0.1 mag, suggesting that either the measurement uncertainties are underestimated or there are significant variations in $(U-V)_0$ among clusters. The latter we consider unlikely, given the small scatter shown by Smail *et al.* (1997) based on higher quality data on 10 clusters at $z \sim 0.25$.

Comparison is made in Figure 5.19 with models from Bruzual & Charlot (1996; as provided in Leitherer *et al.* 1996) having solar metallicity, a Salpeter initial mass function (IMF), and formation redshifts of $z_f = 1$ and 5. Only 0.21 mag of color of evolution is expected from the model between $z = 0$ and $z = 0.5$ for the highest formation redshift. There appears to be a small trend in the data which is consistent with this passively evolving galaxy model, but it is not a strong detection of color evolution.

The measurements of $(U-V)_0$ for the data which are binned in redshift are plotted in Figure 5.20. The fits allowing the slope to be a free parameter are expected to show larger systematic errors in their results. The fixed slope results, however, show that a small amount of color evolution appears to have been detected, even at the lower redshifts of the study. Two of the redshift bins, at $z \sim 0.3$ and 0.55, only include two clusters each, hence

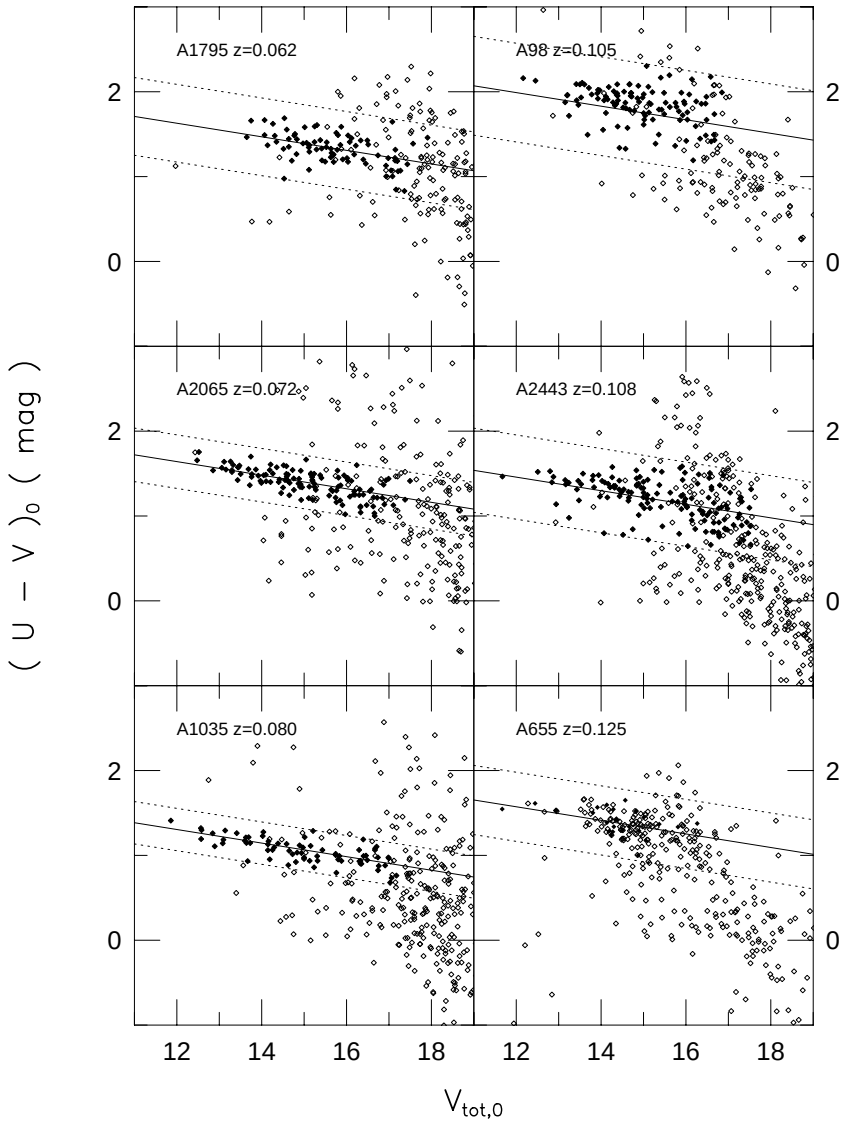

Figure 5.13: Color–magnitude relations for clusters observed in $(U - V)$ at $0.062 < z < 0.125$. The galaxies identified using the color–color, concentration index, and color–magnitude selection criteria are identified with filled symbols; other galaxies have open symbols. The individual cluster fits for the intercept of the color–magnitude relation with a fixed slope of -0.08 are displayed as a solid line in each panel, while the dotted lines indicate the $\pm 3\,\sigma$ limits based on the scatter of the galaxies from that relation.

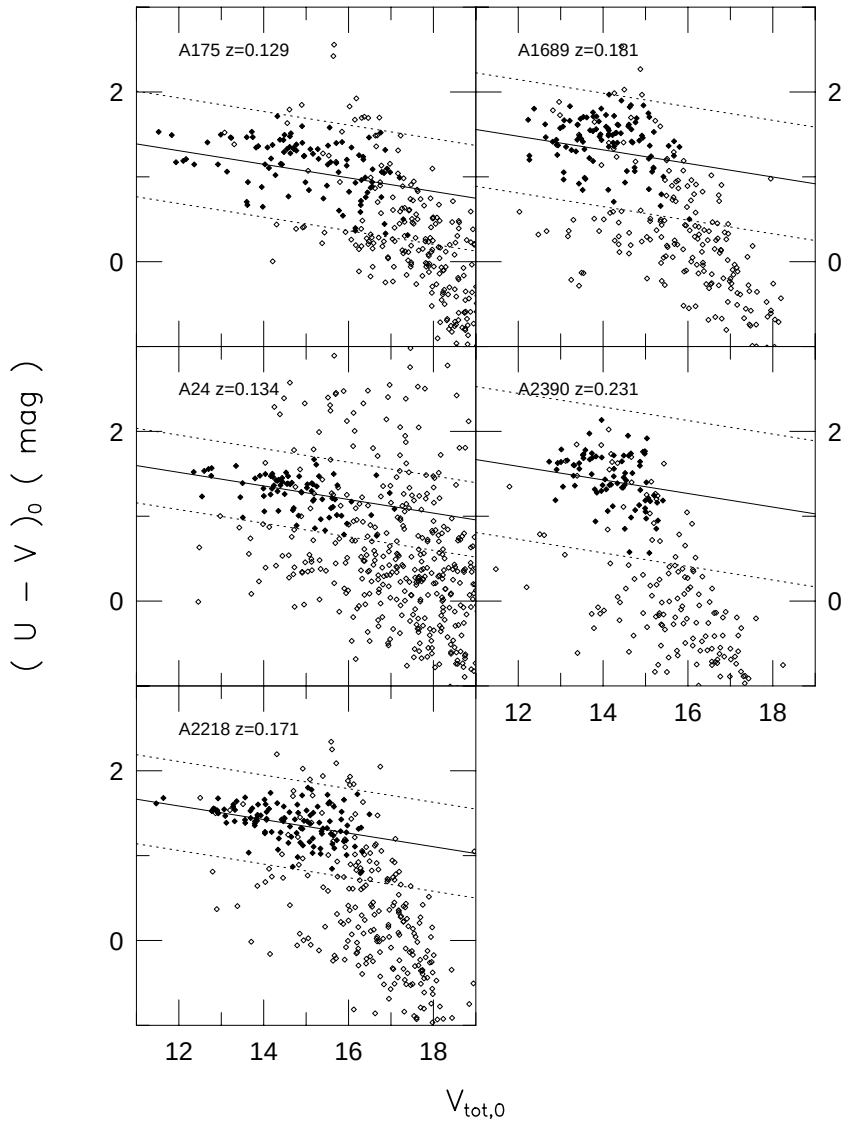

Figure 5.14: Color–magnitude relations for clusters observed in $(U-V)$ at $0.129 < z < 0.231$. Lines and symbols are the same as for Figure 5.13.

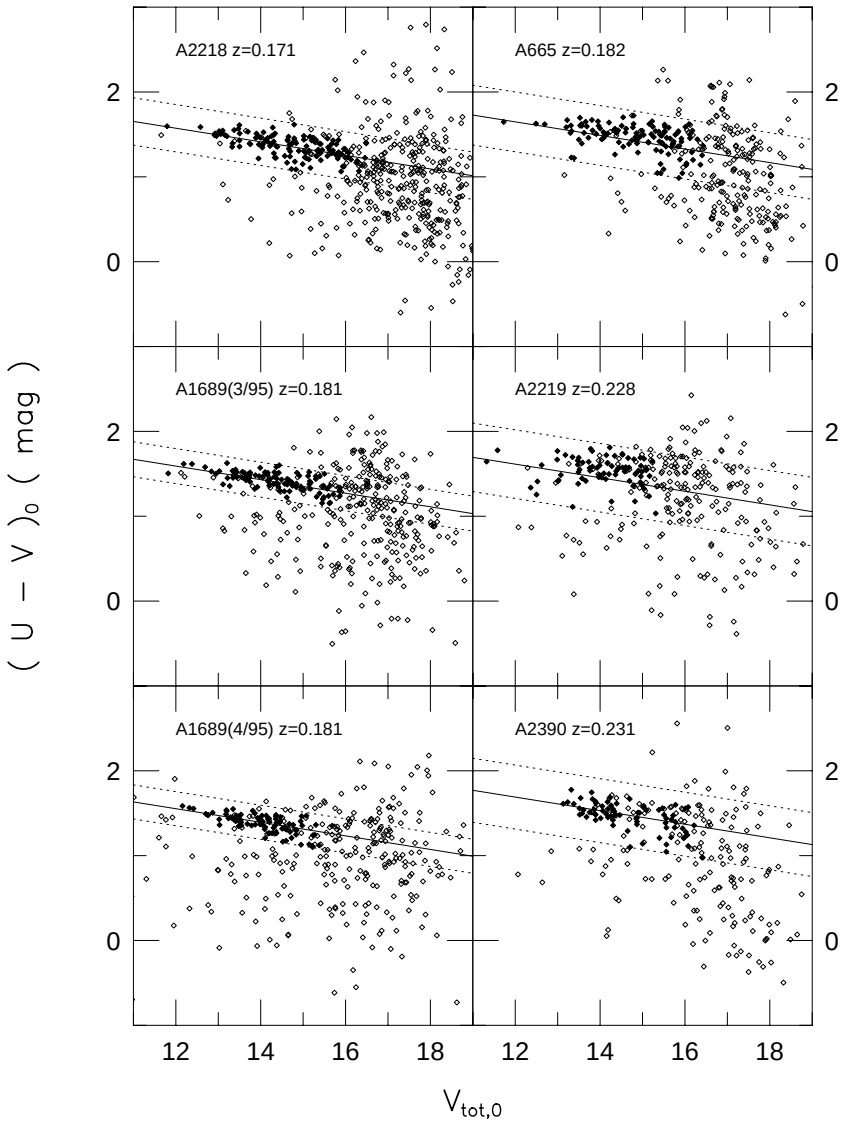

Figure 5.15: Color–magnitude relations for clusters observed in $(B-R)$ at $0.171 < z < 0.231$. Lines and symbols are the same as for Figure 5.13.

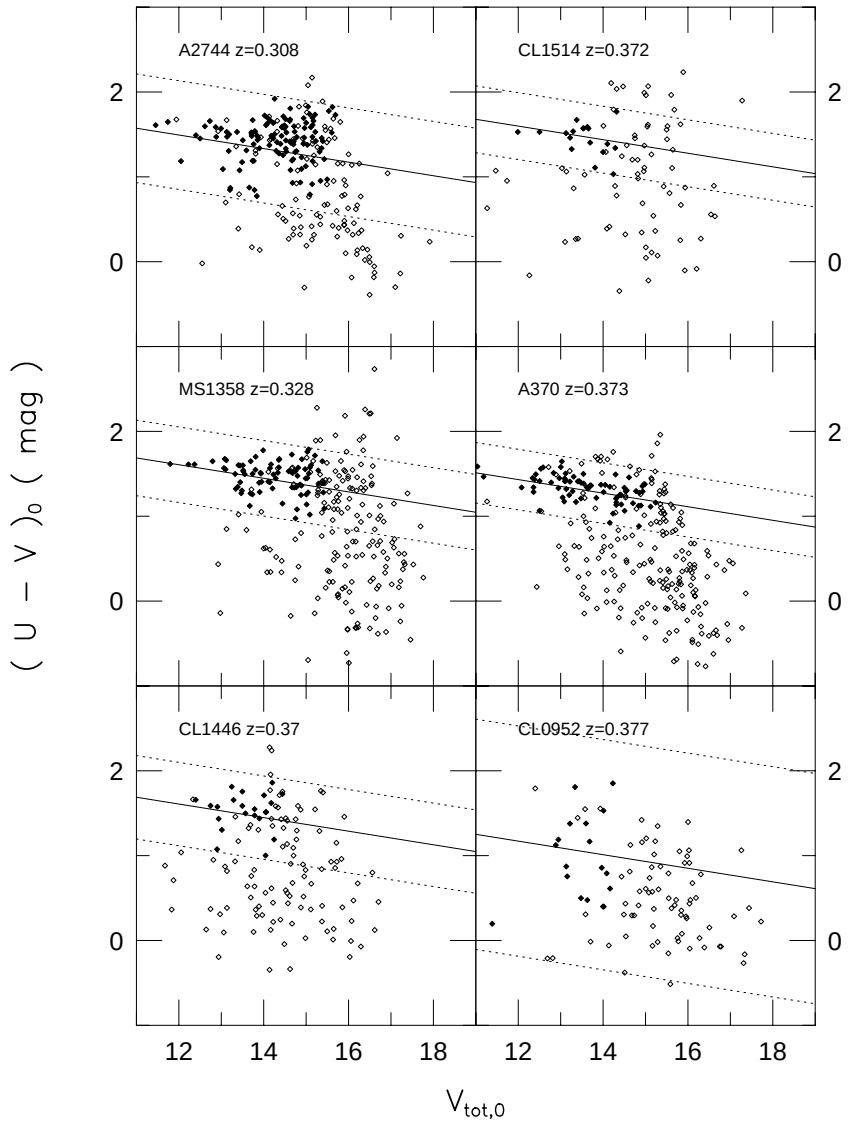

Figure 5.16: Color–magnitude relations for clusters observed in $(B-R)$ at $0.308 < z < 0.390$. Lines and symbols are the same as for Figure 5.13.

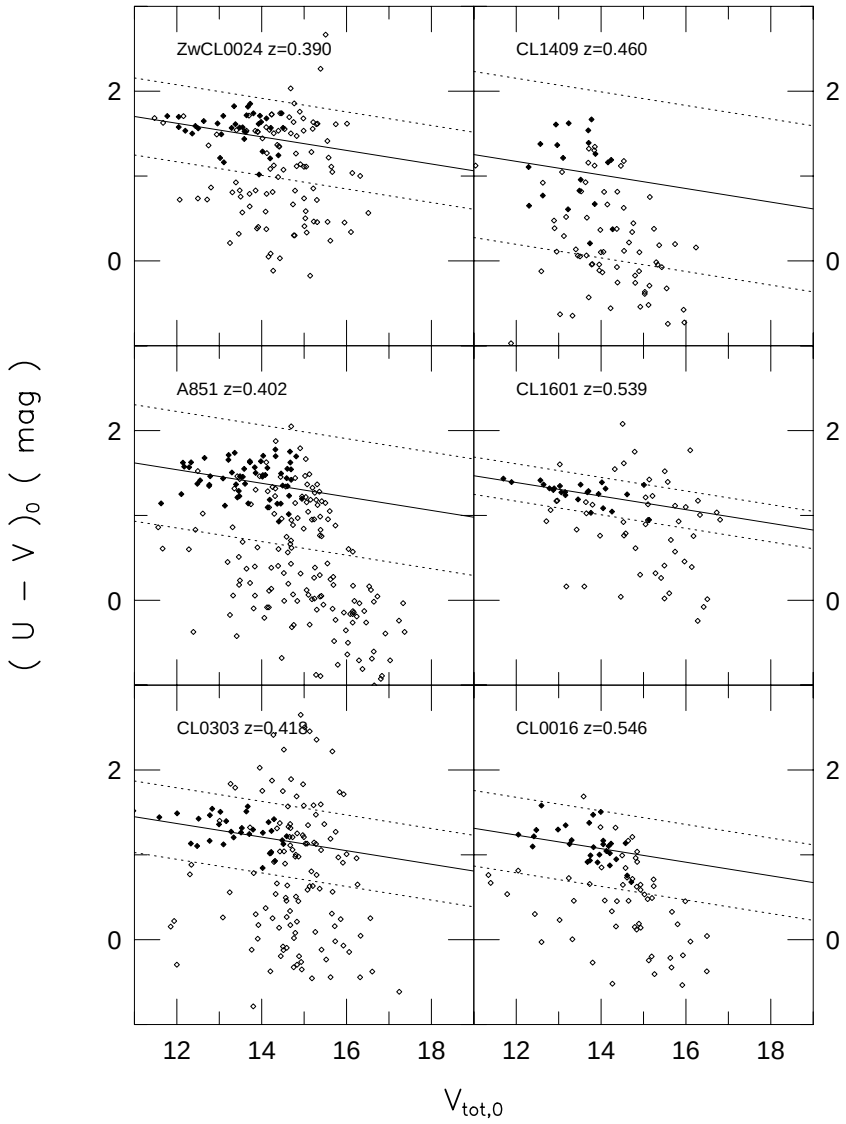

Figure 5.17: Color–magnitude relations for clusters observed in $(B-R)$ at $0.402 < z < 0.460$ and in $(V-I)$ at $0.539 < z < 0.546$. Lines and symbols are the same as for Figure 5.13.

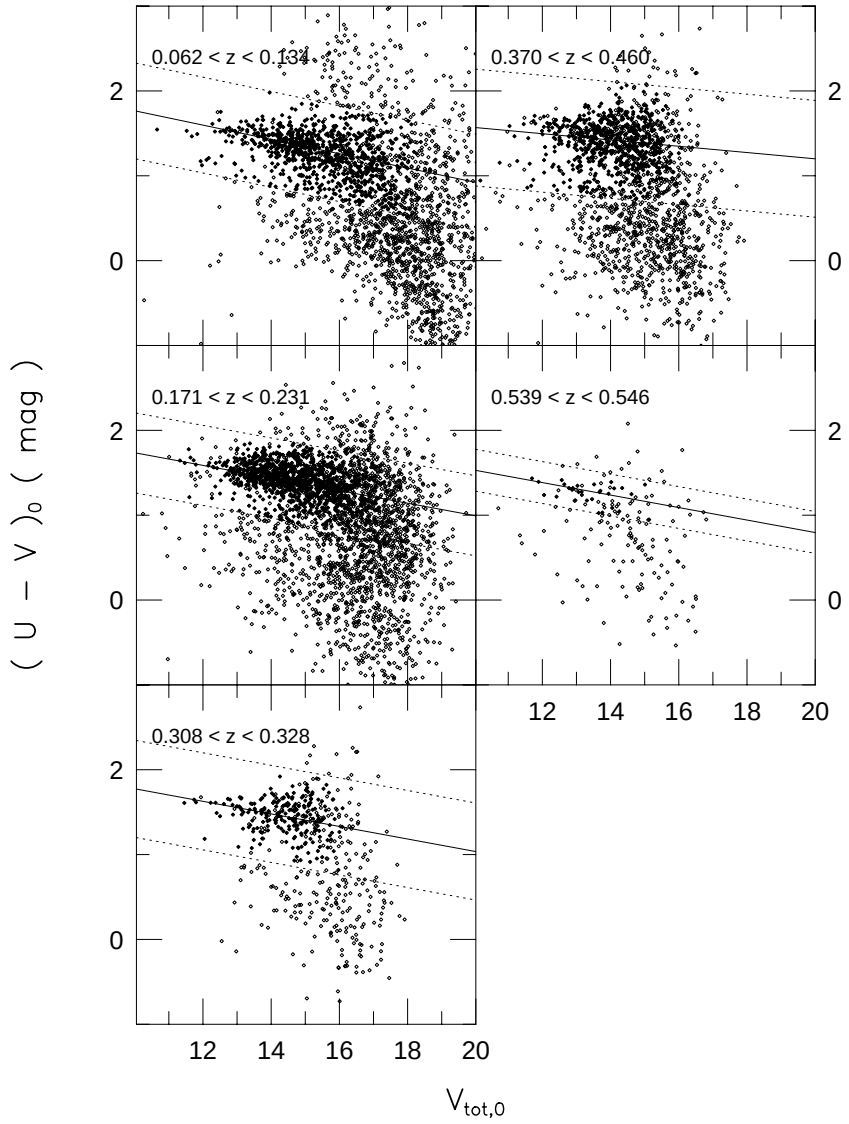

Figure 5.18: Color–magnitude relations binned by redshift. The slope and intercept of the color–magnitude relation is left as a free parameter in each fit. Lines and symbols are the same as for Figure 5.13.

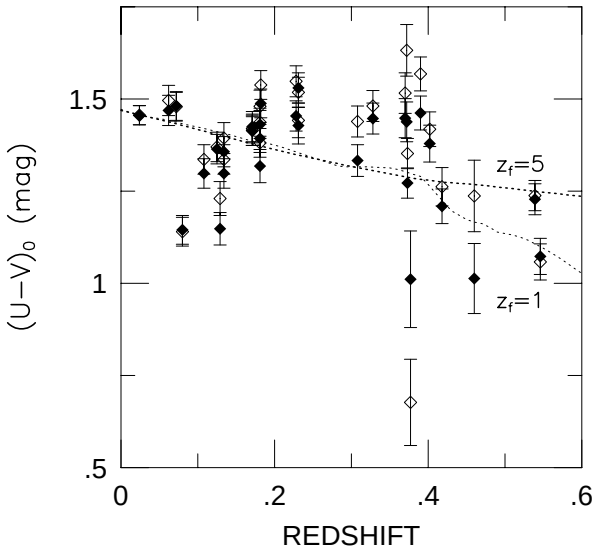

Figure 5.19: Color evolution $(U-V)_0$ for the individual cluster color–magnitude relations at $0.024 < z < 0.546$. The intercepts are taken at $V_{\rm tot,0} = 14$ mag (corrected to a redshift of $z = 0.024$) in the color–magnitude relations plotted in Figure 5.18. The solid symbols are for a fixed slope for the relation, while the open symbols are for the fitted value of the slope. Color evolution might be detected here, but the scatter of the individual cluster fits may mask the effect. Also plotted are Bruzual & Charlot (1996) models with solar metallicity and Salpeter IMF, with two different formation redshifts $z_f = 5$ and 1. The models have been zero–pointed to the Coma cluster at $z = 0.024$.

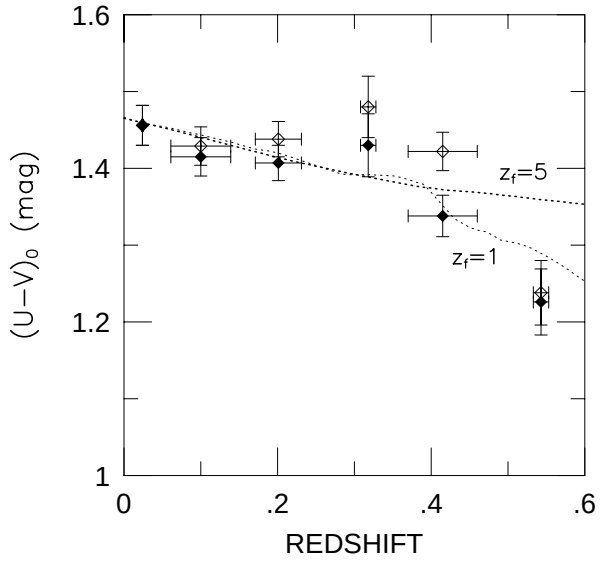

Figure 5.20: Color evolution $(U-V)_0$ for the binned data at $0.024 < z < 0.546$. The intercepts are taken at $V_{\rm tot,0} = 14$ mag (corrected to a redshift of $z = 0.024$) in the color–magnitude relations plotted in Figure 5.18. The solid symbols are for a fixed slope for the relation, while the open symbols are for the fitted value of the slope. The fits using a fixed slope of the color–magnitude relation are least susceptible to systematic errors, and hence are more reliable. A small amount of color evolution appears to be detected from these fits [filled symbols] even at low redshifts. Also plotted are Bruzual & Charlot (1996) models with solar metallicity and Salpeter IMF, with two different formation redshifts $z_f = 5$ and 1. The models have been zero–pointed to the Coma cluster at $z = 0.024$. Note that the data points at $z \sim 0.3$ and 0.55 only included two clusters each, and hence are less reliable as noted by their larger error bars in $(U-V)_0$.

their uncertainties are larger.

5.7 Summary

This paper presents a method by which early–type galaxies can be identified from two color (three bandpass) imaging data in a quantitative and reliable manner. The method utilizes the simple properties of this population of galaxies in their colors, color–magnitude relations, and morphology (from the concentration index of Abraham *et al.*1994). There is considerable overlap between the galaxies selected on the basis of each of these properties

taken separately, suggesting that no one criterion is dominating the possible selection effects.

The galaxies identified in this manner have a better than 90% probability that they lie at the cluster redshift and have an early–type spectral classification. The "K+A" galaxies appear to be easily excluded by this method thereby preventing contamination of the early–type population from galaxies that appear to be disks in HST images (Franx *et al.* 1997). Contamination by the general field appears to be extremely small and easily quantifiable using a limited number of "blank" fields.

This method has been applied to the statistical identification of early–type galaxies in 26 rich clusters of galaxies at $0 < z < 0.6$. A small amount of color evolution appears to have been detected from the data across this redshift range, and is consistent with moderate to high formation redshifts for the stellar content of the early–type galaxy population.

Acknowledgments

Many thanks to I. R. Smail, R. R. de Carvalho, and S. G. Djorgovski for discussions and suggestions regarding this project. Roy Gal is thanked for doing some of the CCD observing, and Tom Jarrett and Nick Gautier for building the P200 Prime Focus IR Camera.

References

Abraham, R. G., Valdes, F., Yee, H. K. C., & van den Bergh, S. 1994, ApJ, 432, 75

Aragón–Salamanca, A., Ellis, R. S., Couch, W. J., & Carter, D. 1993, MNRAS, 262, 764

Barrientos, L. F., Schade, D., & López–Cruz, O. 1996, ApJ, 460, L89

Bruzual, A. G., & Charlot, S. 1996, in preparation

Burstein, D., & Heiles, C. 1982, AJ, 87, 1165

Cohen, J. G., Hogg, D. W., Pahre, M. A., & Blandford, R. 1996, ApJ, 462, L9

Dickinson, M. 1995, in ASP Conf. Ser., Fresh Views on Elliptical Galaxies, eds. A. Buzzoni, A. Renzini, & A. Serrano (San Francisco: ASP), 283

van Dokkum, P. G., & Franx, M. 1996, MNRAS, 281, 985

Dressler, A., & Gunn, J. E. 1992, ApJS, 78, 1

Dressler, A., Kells, W., & Sivaramakrishnan, A. 1998, in preparation

Ellis, R. S., Couch, W. J., MacLaren, I., & Koo, D. C. 1985, MNRAS, 217, 239

Ellis, R. S., Smail, I., Dressler, A., Couch, W. J., Oemler, A., Jr., Butcher, H., & Sharples, R. M. 1997, ApJ, 483, 582

Fiala, N., Rakos, K. D., & Stockton, A. 1986, PASP, 98, 70

Franx, M. 1993, ApJ, 407, 5

Franx, M., Illingworth, G., & Heckman, T. 1989, AJ, 98, 538

Franx, M., Kelson, D., van Dokkum, P., Illingworth, G., & Fabricant, D. 1997, in The Nature of Elliptical Galaxies, Proceedings of the Second Stromlo Symposium, eds. M. Arnaboldi, G. S. Da Costa, & P. Saha, ASP Conf. Ser. Vol. 116, (San Francisco: ASP), 512

Fukugita, M., Doi, M., Dressler, A., & Gunn, J. E. 1995, ApJ, 439, 584

Hamilton, D. 1985, ApJ, 297, 371

Jarvis, J. F., & Tyson, J. A. 1981, AJ, 86, 476

Kelson, D. D., Dokkum, P. G., Franx, M., Illingworth, G. D., & Fabricant, D. 1997, ApJ, 478, L13

Koo, D. C. 1981, ApJ, 251, L75

Landolt, A. U. 1992, AJ, 104, 340

Laureijs, R. J., Helou, G., & Clark, F. O. 1994, in Proceedings of The First Symposium on the Infrared Cirrus and Diffuse Interstellar Clouds, ASP Conf. Ser. Vol. 58, eds. R. M.

Cutri & W. B. Latter (San Francisco, ASP), 133

Leitherer, C., *et al.* 1996, PASP, 108, 996

Lilly, S. J., Le Fevre, O., Crampton, D., Hammer, F., & Tresse, L. 1995, ApJ, 455, 50

Murphy, D. M., Persson, S. E., Pahre, M. A., Sivaramakrishnan, A., & Djorgovski, S. G. 1995, PASP, 107, 1234

Pahre, M. A., Djorgovski, S. G., & de Carvalho, R. R. 1996, ApJ, 456, L79

Pahre, M. A., *et al.* 1998a, ApJS, submitted

Pahre, M. A., de Carvalho, R. R., & Djorgovski, S. G. 1998b, in preparation [Chapter 4 of this thesis]

Pahre, M. A., Djorgovski, S. G., & de Carvalho, R. R. 1998c, in preparation [Chapter 7 of this thesis]

Peletier, R. F., Davies, R. L., Illingworth, G. D., Davis, L. E., & Cawson, M. 1990a, AJ, 100, 1091

Rakos, K. D., & Schombert, J. M. 1995, ApJ, 439, 47

Sandage, A. 1988, ARA&A, 26, 561

Schade, D., Barrientos, L. Felipe, & López–Cruz, O. 1997, ApJ, 477, L17

Smail, I., Edge, A. C., Ellis, R. S., & Blandford, R. D. 1998, MNRAS, 293, 124

Songaila, A., Cowie, L. L., Hu, E. M., & Gardner, J. P. 1994, ApJS, 94, 461

Sparks, W. B., & Jørgensen, I. 1993, AJ, 105, 1753

Stanford, S. A., Eisenhardt, P. R., & Dickinson, M. 1995, ApJ, 450, 512

Stanford, S. A., Eisenhardt, P. R., & Dickinson, M. 1998, ApJ, 492, 461

Williams, R. E., *et al.* 1996, AJ, 112, 1335

Chapter 6

Global Spectroscopic and Photometric Properties of Early–Type Galaxies in Eight Clusters at $0.1 < z < 0.6$

Abstract

An imaging and spectroscopy survey of early–type galaxies in eight clusters at $0.1 < z < 0.6$ is described. The galaxy sample has been selected quantitatively using two–color (three bandpass) information and a morphological indicator (the concentration index). The data indicate that the method is $> 90\%$ effective at identifying early–type galaxies which are cluster members. The spectroscopic data on 110 early–type galaxies are at moderate dispersion ($\sigma_{inst} \sim 60$ km s^{-1}) and excellent S/N allowing for the measurement of central velocity dispersions and line strengths for each of the galaxies. The use of small apertures for the spectroscopy minimize the aperture corrections, thereby ensuring that both local and high redshift galaxies are observed similarly. Central velocity dispersions and line strengths have been drawn from the literature for 18 additional galaxies. Near–infrared imaging in the K–band has been obtained for the combined 128 galaxy sample. Two–dimensional, seeing–convolved models have been fit to each galaxy image in order to measure the effective radii $r_{\rm eff}$ and mean surface brightnesses $\langle \mu_K \rangle_{\rm eff}$ within those radii. These data more than quadruple the number of early–type galaxies with both spectroscopic and photometric properties available to study the evolution of their properties to intermediate redshifts.

6.1 Introduction

Studies of galaxy evolution in rich clusters of galaxies have proliferated recently with the high quality data resulting from the refurbished Hubble Space Telescope. The photometric properties of early–type galaxies (Dickinson 1995; Barrientos, Schade, & López-Cruz 1996; Pahre, Djorgovski, & de Carvalho 1996; Ellis *et al.* 1997; Kelson *et al.* 1997; Stanford,

Eisenhardt, & Dickinson 1998; Barger *et al.* 1998; Bender *et al.* 1998) and the morphological fractions of various galaxy types (Dressler *et al.* 1997, Couch *et al.* 1998, and references therein) have particularly benefitted from HST imaging data. The problems with interpreting these purely photometric data, however, are the following: (1) there can be significant numbers of interloper galaxies from the general field; (2) the masses of the galaxies are poorly constrained (although note the novel technique of Natarajan *et al.* 1998, who use galaxy lensing to probe statistically the dark halos of cluster galaxies); and (3) the photometric correlations that can be used to study luminosity evolution have large scatter.

The Fundamental Plane (FP; Dressler *et al.* 1987; Djorgovski & Davis 1987) bivariate correlations are, by construction, the optimal tool for exploring the global properties of elliptical galaxies. The standard construction of the FP is a correlation between the effective radius $r_{\rm eff}$, the mean surface brightness $\langle\mu\rangle_{\rm eff}$ enclosed within that radius, and the central velocity dispersion σ_0. While a purely photometric Fundamental Plane correlation exists which could use HST data alone (de Carvalho & Djorgovski 1992), it is marred by potential systematic errors which limit its utility (Scodeggio, Giovanelli, & Haynes 1997).

The FP correlations and their projections onto two of the three axes can be used to study the evolution of early–type galaxies. The intercept on the $\langle\mu\rangle_{\rm eff}$ axis provides a direct measure of the mean luminosity evolution of the early–type galaxy population as a whole by measuring its brightening on top of the Tolman surface brightness dimming signal (Dickinson 1995; Barrientos *et al.* 1996; Pahre *et al.* 1996; van Dokkum & Franx 1996; Kelson *et al.* 1997; Barger *et al.* 1998). This evolution of the mean surface brightness at some fiducial effective radius (defined in physical units like kpc) and central velocity dispersion is sometimes referred to as an evolution of the mean M/L for the stellar content of the galaxies (van Dokkum & Franx 1996; Kelson *et al.* 1997), a practice which we will attempt to avoid due to the wavelength–dependent difficulties of relating the observables $(r_{\rm eff}, \sigma_0)$ to a galaxy's mass (Pahre, de Carvalho, & Djorgovski 1998b, Chapter 4 of this thesis).

A more important and subtle effect, however, is the possibility that the slope of the FP correlations—i.e., the power law index a in the scaling relation $r_{\rm eff} \propto \sigma_0^a \langle\Sigma\rangle_{\rm eff}^b$—might be evolving with redshift, thus implying a systematic variation in the global properties of elliptical galaxies along the FP. If less luminous elliptical galaxies have a stellar content which is younger on average than more luminous elliptical galaxies, then this could produce

such an evolution in the slope of the FP. Such an effect has not yet been observed since there have not been large enough samples of elliptical galaxies with measured global properties ($r_{\rm eff}, \langle\mu\rangle_{\rm eff}, \sigma_0$) at higher redshifts (van Dokkum & Franx 1996; Kelson *et al.* 1997; Bender *et al.* 1998). The purpose of the present paper is to contribute towards changing this situation by substantially enlarging the sample of elliptical galaxies in clusters with measurements of global parameters that will constrain potential evolution of the slope of the FP correlations with redshift.

The first step of studying galaxies at high redshifts is to construct a homogeneous, statistically complete, and unbiased sample. This point will be addressed in §6.2. A subsample of these galaxies were then observed spectroscopically, to measure central velocity dispersions and line strengths, and photometrically, to measure effective radii and mean surface brightnesses. These two sets of data will be discussed in §6.3 and 6.4, respectively. A small sample of galaxies, previously observed spectroscopically and documented in the literature, will be drawn together to supplement the new data in this paper.

This paper adds a total of 110 spectroscopic observations (two of which repeat measurements in the literature), and 128 near–infrared photometric observations (all of which are new), of galaxies in distant clusters that are suitable for studies of the evolution of the global scaling relations. When including other literature observations, this brings the total number of the available spectroscopic measurements from 42 to 150, and the total number of photometric observations from 30 to 138. Since both spectroscopic and photometric parameters are required for the construction of the FP, this paper more than quadruples the number of galaxies at high redshift with observations suitable for studying the evolution of the FP correlations. The observations currently available in the literature, and those for the present paper, are summarized in Table 6.1.

6.2 Selection of Galaxy Sample in Each Cluster

No attempt was made to select the clusters studied here in any methodical fashion; instead, the criteria were that each cluster must be rich, lie at high Galactic latitude, and have HST/WFPC–2 imaging available (or scheduled at the time of selection) for at least one pointing in the cluster. At $z \sim 0.1$, there is a dearth of such HST/WFPC–2 images of rich clusters: since the cluster angular extents are too large for the WFPC–2 field–of–

Table 6.1: Summary of All Available Data Appropriate for Studying the Evolution of the Early–Type Galaxy Scaling Relations

Cluster	z	This Paper		Literature				
		N_{spec}	N_{phot}	N_{spec}	$N_{spec,repeat}$	N_{phot}	Filters	Reference
Abell 655	0.129	27	27	···	···	···	···	···
Abell 665	0.181	19	19	[6]†	?†	[6]†	$R_{\rm C}^{\dagger}$	F93
Abell 2390	0.228	14	14	···	···	···	···	
MS1358.4+6245	0.328	···	···	8*	···	8*	F606W,F814W	K97
Abell 370	0.372	16	21	9	2	7	F675W	Z97,B98
MS1512.4+3647	0.372	···	···	6	···	2	F675W	Z97,B98
CL0949+44	0.377	···	···	6	···	···	···	Z97
ZwCL0024+1652	0.391	···	8	9‡	···	9‡	F702W,$R_{\rm C}$,$I_{\rm C}$	vD96
Abell 851	0.407	14	14	···	···	···	···	···
MS0015.9+1609=CL0016+16	0.546	15	15	···	···	···	···	···
MS2053.7-0447	0.583	···	5	5	···	5	F702W,F814W	K97
Interlopers	~ 0.3	5	5	···	···	···	···	···
Sum	$0.129 \leq z \leq 0.583$	110	128	42	2	30	···	···

Notes: The quantity N_{spec} is the number of spectroscopic observations (central velocity dispersions; also line indices in the case of Ziegler & Bender 1997), N_{phot} is the number of photometric measurements of $r_{\rm eff}$ and $\langle\mu\rangle_{\rm eff}$, and $N_{spec,repeat}$ is the number of spectroscopic observations in common between that particular literature source and the present paper. †The photometric and spectroscopic data for Abell 665 of Franx (1993) are not fully documented in the literature, and hence are not included in the totals at the bottom of the table. One "K+A" galaxy has been excluded from this number. *Two "K+A" galaxies have been excluded from this number. †One of these galaxies, DGS 218, appears not to be fully documented in the literature (Schneider, Dressler, & Gunn 1986) and hence is not included in the totals. All of the remaining 8 galaxies are included in the totals, although some of these galaxies do not actually have elliptical morphologies (van Dokkum & Franx 1996). References: Franx (1993, F93); van Dokkum & Franx (1996, vD96); Kelson *et al.* (1997, K97; Ziegler & Bender (1997, Z97); and Bender *et al.* (1998, B98).

view (FOV), and the galaxies are reasonably resolved by ground–based imaging in modest conditions, there has been no HST cluster imaging program at $z \sim 0.1$. The cluster Abell 655 ($z = 0.129$) was selected to have high richness in the Abell (1958) catalog, be with a redshift range ($0.08 < z < 0.15$), and lie high Galactic latitude.

All clusters were imaged in two broadband colors (three bandpasses) selected to sample the rest–frame wavelengths corresponding to the U ($\lambda \sim 3600$ Å), V ($\lambda \sim 5500$ Å), and $I_{\rm C}$ ($\lambda \sim 8000$ Å) bandpasses. These CCD $UBVRI$ and near–infrared J observations, and others of similar intermediate redshift clusters, are presented and discussed elsewhere (Pahre 1998b, Chapter 5 of this thesis). For each cluster, a number of selection criteria were employed to isolate the early–type, cluster member galaxy population from the contamination from field galaxies and late–type cluster member galaxies. These criteria were: location in the $(U-V)_0$ versus $(V-I_{\rm C})$ color–color space; color within $\pm$0.3–0.5 mag (depending on data quality and cluster properties) of the two color–magnitude relations in $(U-V)_0$ and $(V-I_{\rm C})$ versus V; concentration index (Abraham *et al.*1994); and 5 σ detection in all three bandpasses.[1] Having more than one color allowed the color windows chosen to be large, since the second color effectively selects against background field spiral galaxies—which can be red in one pair of bandpasses by nature of their redshift, but will not match the photometric properties of an early–type cluster member in the other bandpass. The use of the concentration index effectively provides a morphological selection criterion to further exclude galaxies with significant disks as well as misclassified Galactic stars.

These selection criteria are excellent at identifying a sample of galaxies with high probability that they are both cluster members and have early–type spectra. The spectroscopic data in the present paper which will be discussed in §6.3 show that for high quality photometric data the method produces $> 90\%$ success rate.

Within these complete samples of galaxies for each cluster, a subsample was chosen which would fit onto a multi–slit mask for spectroscopic observations. If the cluster had an obvious cD galaxy, that galaxy was excluded from the list by inspection since those galaxies may follow different scaling relations and also have a higher probability of harboring an active nucleus; the exception was the cD galaxy in Abell 655. The mask was constrained to include the position of the HST/WFPC–2 data, although the available FOV for multi–slits

[1]The samples for each cluster discussed in Pahre (1998b; Chapter 5 of this thesis) were actually limited at 3 σ. A higher threshold was adopted here in order to ensure the accuracy of the photometric parameters in choosing objects for follow–up spectroscopy.

is three times larger than the FOV of WFPC–2. Hence, only one–third of the galaxies typically lie within the WFPC–2 FOV. Morphological selection criteria could have been applied instead based on the WFPC–2 images, but would only provide information on that subset of one–third of the data for which spectroscopy could be obtained; it was for this reason that we opted to use the two–color and concentration index selection criteria instead. The properties of the galaxies as derived from these WFPC–2 data will be provided in a future contribution.

The issue could be raised that the adopted selection criteria bias the sample towards passively evolving early–type galaxies, and away from galaxies which are currently forming, or recently forming (within the previous several Gyr), stars. Three points can be made to address such concerns. First, the color window is large at $\pm$0.3–0.5 mag, thereby allowing for a wide range of star formation histories. If passively evolving galaxies formed 10 Gyr ago (the age of the universe is $\sim$ 11 Gyr in a $H_0 = 75$ km s^{-1} Mpc^{-1}, $\Omega_0 = 0.2$, $\Lambda_0 = 0$ cosmology), then at $z \sim 0.5$ these galaxies were $\sim$ 6 Gyr old and have $(U-V)_0 = 1.46$ mag in the Bruzual & Charlot (1996, as provided in Leitherer *et al.* 1996) models of solar metallicity. If the mean galaxy color were somewhat bluer, as would occur if there were a distribution of galaxy formation times, then the allowed ages would be even younger. The limit of $\pm$0.5 mag from the color–magnitude relation allows galaxies that are as little as 1 Gyr old at $z = 0.5$ to fall into the sample, therefore *age spreads of at least a factor of six* are allowed by these color selection criteria. Post star–burst galaxies are not excluded from the sample *a priori*.

Second, the spectroscopic galaxy class of "K+A" galaxies,[2] as identified by their superposition of the spectra of old K giant stars and A stars from a recent burst of star formation, appear to correspond to disk galaxy morphologies in HST images (Franx *et al.* 1997). Even if a velocity dispersion could be measured from the spectrum of a disk galaxy, the measurement is probably physically meaningless since disk galaxies are dynamically "cold" (supported by bulk rotation), not dynamically "hot" like elliptical galaxies. Hence, there appears to be no good reason to want to include "K+A" galaxies in a sample of "elliptical" or "early–type" galaxies that is intended to study the FP. Note that a morphological

[2]This terminology has been adopted to identify the presence of both K–giant stellar features (Ca II H and K, G band at $\lambda = 4000$ Å, MgH, and Mg_2 triplet) and A star features (strong Balmer lines of hydrogen) in the spectrum of such a galaxy. This type was previously called "E+A" by Dressler & Gunn (1992, and references therein), but is now generally called "K+A" (Dressler, private communication).

selection criterion (say, from HST images) would therefore *also* exclude "K+A" galaxies, hence the color selection criteria is no worse.

Finally, it was shown by Pahre (1998, Chapter 5 of this thesis) that various color–magnitude, color–color, and concentration index selection criteria mostly identify the same galaxy population. Hence the selection criteria adopted here produce very similar galaxy lists to selection by an alternate method.

The finding charts identifying the galaxies studied in the present paper are provided in Figures 6.1 to 6.6. The object coordinates are provided in Tables 6.2 through 6.7. The astrometry is zero–pointed to the Digitized Sky Survey, and the distortion at the instrument focal plane has been kindly model-led by J. Cohen using images of globular clusters with accurate plate solutions from K. Cudworth. The relative accuracy of these coordinates is 0.1 arcsec, while the absolute accuracy may approach 0.5–1.0 arcsec as a result of the general limitations of the overall, absolute astrometric solution in the Digitized Sky Survey. Total magnitudes from FOCAS (Jarvis & Tyson 1981) are also tabulated with a -0.3 mag offset applied to account for the flux missed by that algorithm (see Pahre 1998b, Chapter 5 of this thesis).

6.3 Spectroscopy

6.3.1 Observations

Spectra of a subsample of the galaxy sample for each cluster were obtained with the Low Resolution Imaging Spectrograph (LRIS; Oke *et al.* 1995) in multi–slit mode on the W. M. Keck I 10 m Telescope between 1995 September and 1996 September. This instrument has a 4×7.3 arcmin^2 usable field–of–view available for multi–slits, where the longer dimension corresponds to the spatial direction of the spectra. In placing slits on galaxies, it was decided not to use all of the field available perpendicular to the slits in order to provide more uniform spectral coverage for all slits. The slits were machine punched out of aluminum sheet metal, and then mounted in the focal plane using an assembly which bends the sheets to approximately match the curved focal plane of the telescope at the Cassegrain focus.

The slit width was chosen to be 0.7 arcsec in order to minimize aperture corrections which can become quite large at $z \sim 0.5$ for wider slits. The pixel scale for the instrument

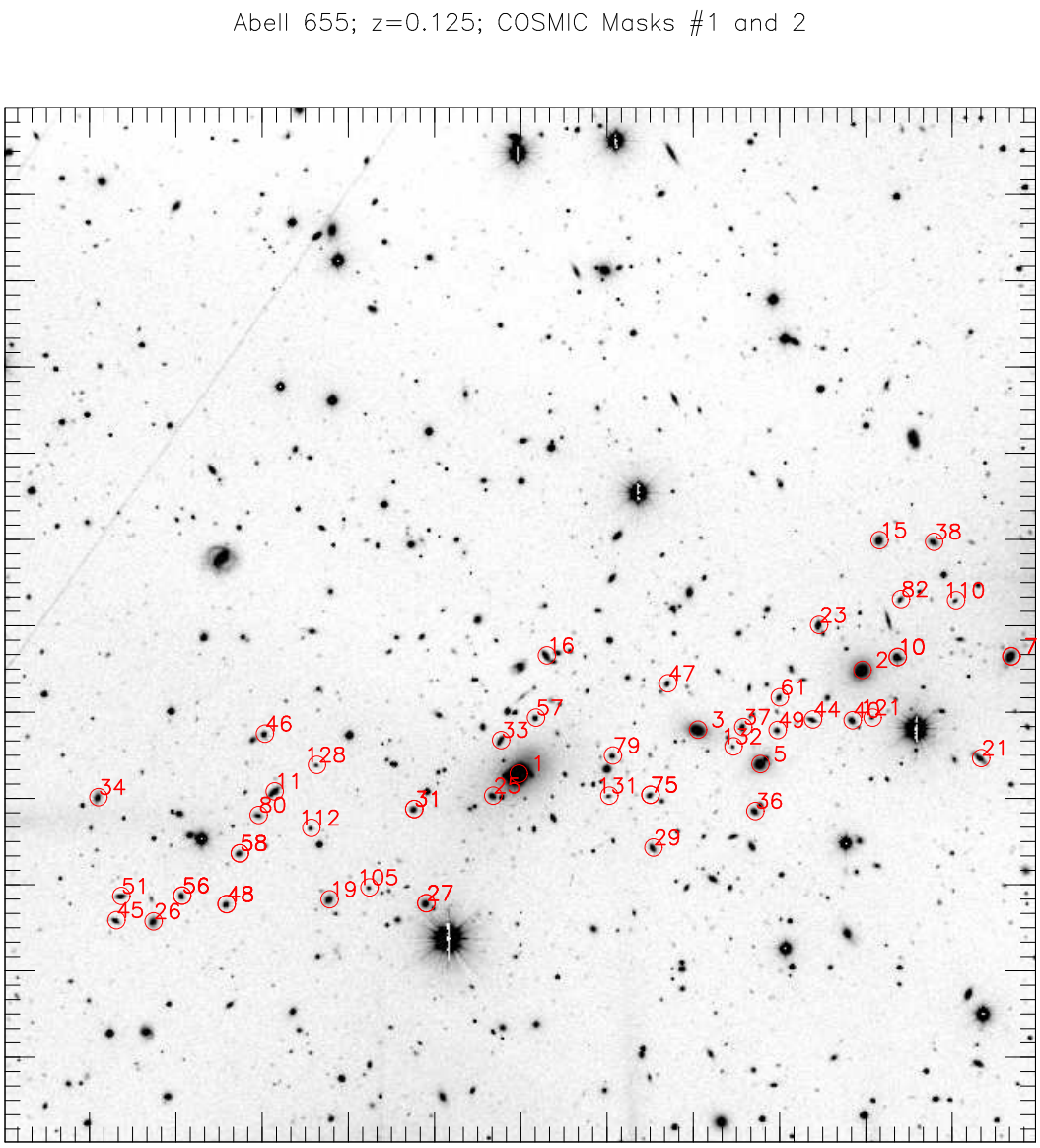

Figure 6.1: Finding chart for galaxies in Abell 655. The image was taken in the V–band with a CCD on the Palomar 60–inch Telescope. North is up and east to the left. The small tick marks on each axis correspond to 10 arcsec, while the large tick marks are 1 arcmin.

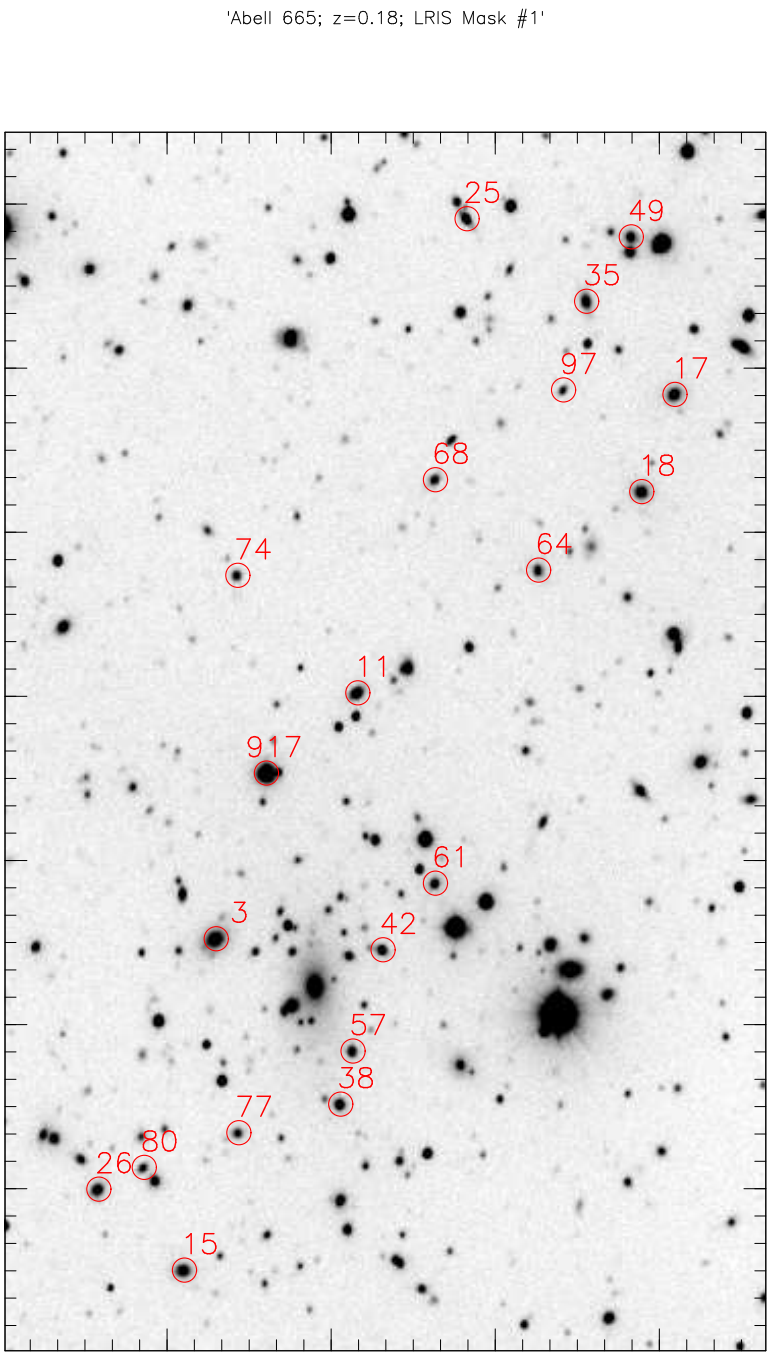

Figure 6.2: Finding chart for galaxies in Abell 665. The image was taken in the R_C–band with a CCD on the Palomar 60–inch Telescope. North is up and east to the left. The small tick marks on each axis correspond to 10 arcsec, while the large tick marks are 1 arcmin.

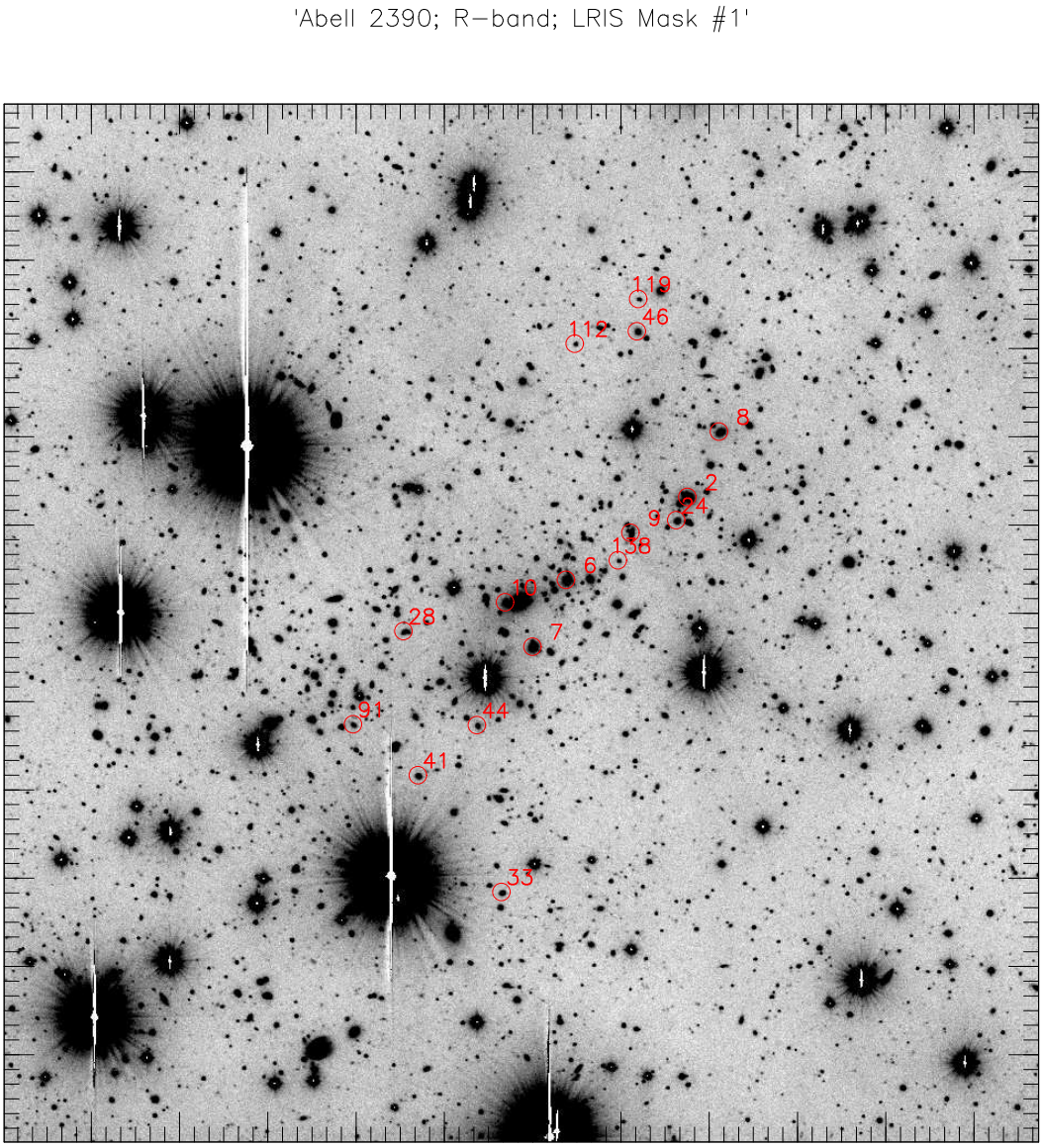

Figure 6.3: Finding chart for galaxies in Abell 2390. The image was taken in the R_C–band with a CCD on the Palomar 60–inch Telescope. North is up and east to the left. The small tick marks on each axis correspond to 10 arcsec, while the large tick marks are 1 arcmin.

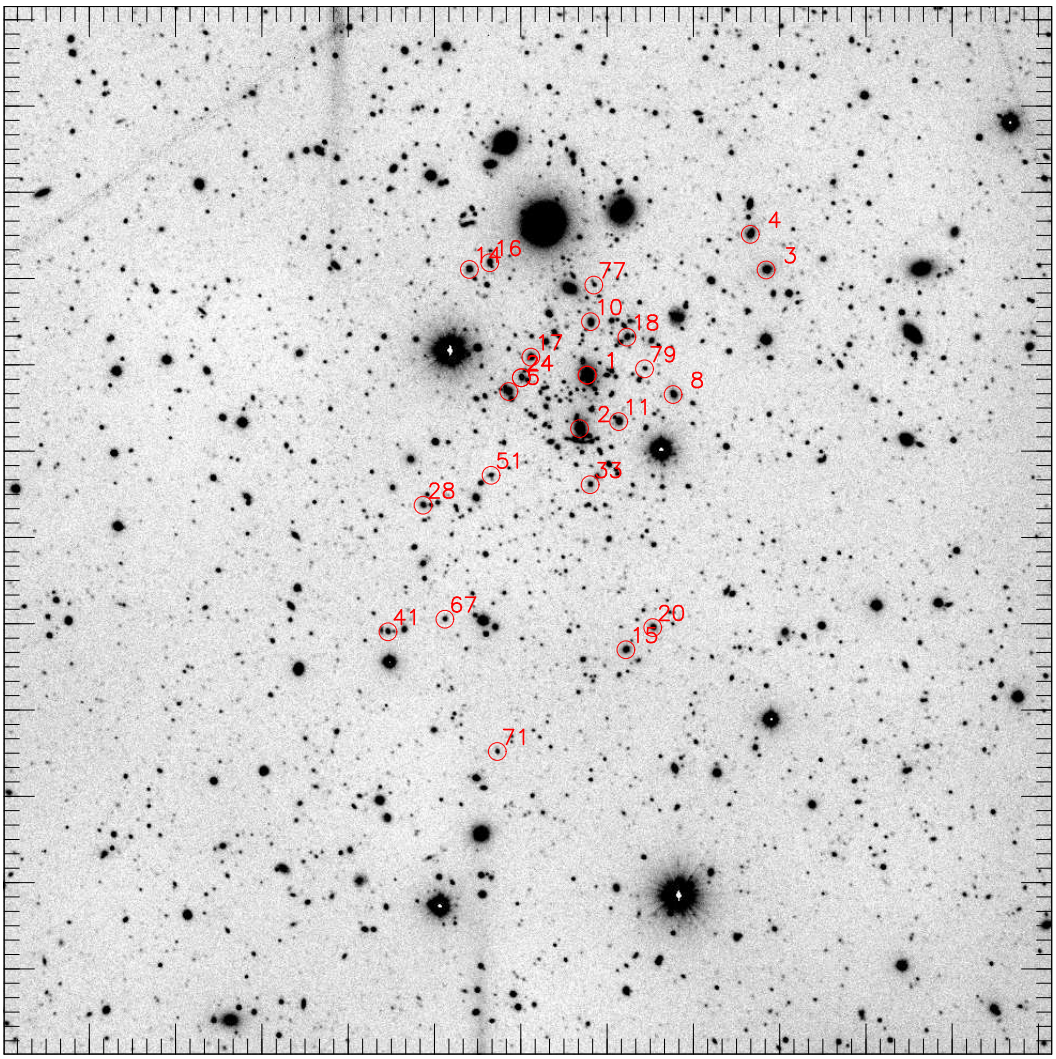

Figure 6.4: Finding chart for galaxies in Abell 370. The image was taken in the R_C–band with a CCD on the Palomar 60–inch Telescope. North is up and east to the left. The small tick marks on each axis correspond to 10 arcsec, while the large tick marks are 1 arcmin. The two serendipitously observed sources are not identified here, although coordinates are provided in Table 6.5. Galaxies from Ziegler & Bender (1997) are also identified in this figure using our object identification numbers; cross–references are also given in Table 6.5.

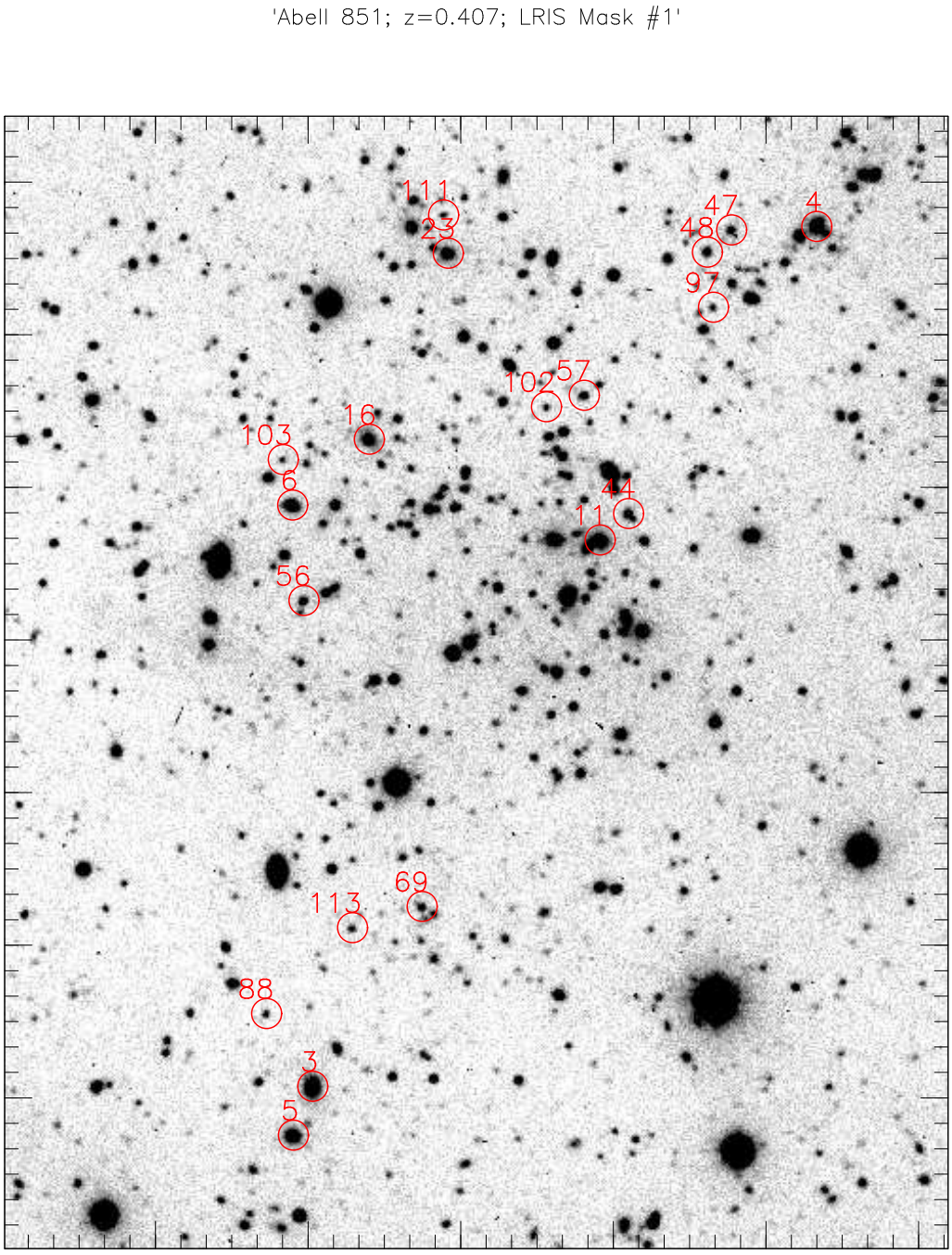

Figure 6.5: Finding chart for galaxies in Abell 851. The image was taken in the R_C–band with a CCD on the Palomar 60–inch Telescope. North is up and east to the left. The small tick marks on each axis correspond to 10 arcsec, while the large tick marks are 1 arcmin.

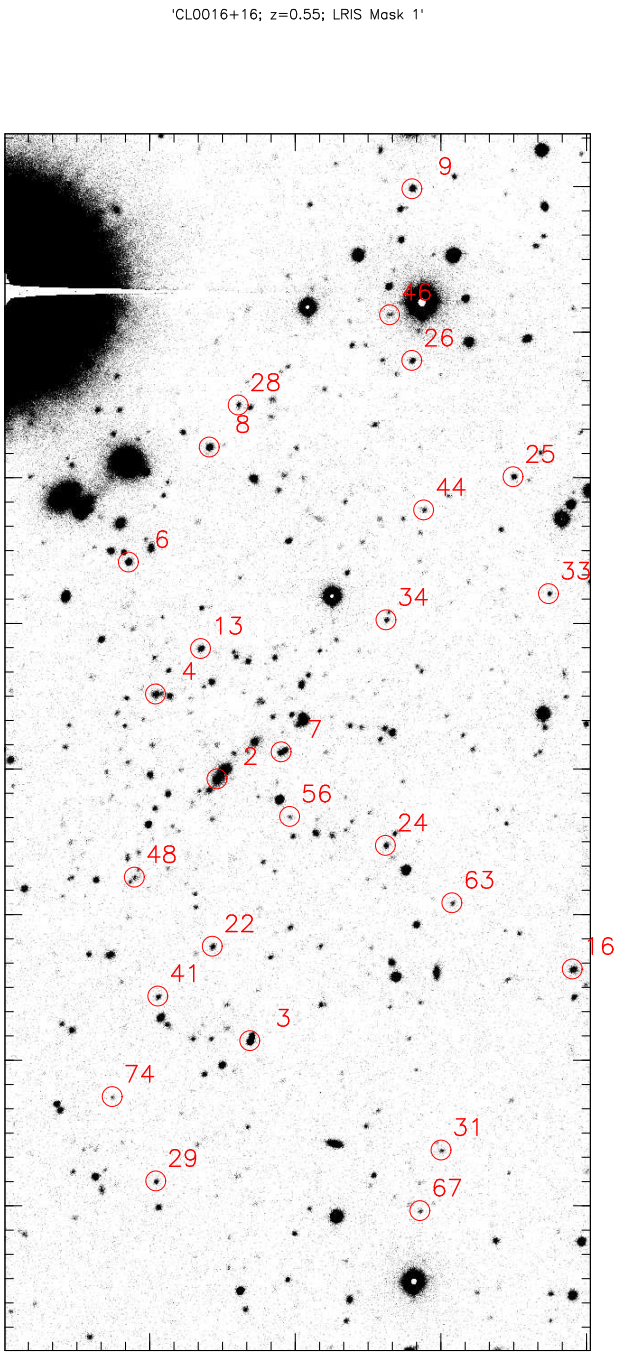

Figure 6.6: Finding chart for galaxies in MS0015.9+1609. The image was taken in the I_C–band with a CCD on the Palomar 60–inch Telescope. Note that north is to the left and east down. The small tick marks on each axis correspond to 10 arcsec, while the large tick marks are 1 arcmin.

Table 6.2: Photometric Properties for Galaxies in Abell 655

Galaxy ID	Right Ascension (J2000)	Declination (J2000)	$\log r_{\rm eff}$ (arcsec)	$\log r_{\rm eff}$ (kpc)	$\pm$	$\langle\mu_{K_s}\rangle_{\rm eff}$ (mag/$''$)	$\langle\mu_K\rangle_{\rm eff}^{corr}$ (mag/$''$)	$\pm$	V_{tot} (mag)	$\langle\mu_V\rangle_{\rm eff}^{corr}$ (mag/$''$)	$\pm$
1	08 25 29.10	+47 08 00.5	1.116	1.433	0.009	18.41	18.15	0.05	14.65	21.44	0.07
2	08 25 05.74	+47 09 16.0	0.949	1.266	0.021	18.50	18.25	0.07	16.27	22.24	0.12
3	08 25 16.91	+47 08 32.8	-0.144	0.165	0.292	18.24	18.00	0.05	16.66	17.20	0.71
5	08 25 12.61	+47 08 09.5	0.295	0.590	0.027	16.78	16.53	0.05	16.93	19.64	0.14
7	08 24 55.59	+47 09 26.9	0.416	0.721	0.027	17.54	17.29	0.05	17.14	20.45	0.14
10	08 25 03.34	+47 09 25.3	0.428	0.733	0.032	17.89	17.64	0.05	17.63	21.00	0.17
11	08 25 45.75	+47 07 46.0	0.394	0.702	0.054	18.11	17.85	0.11	17.67	20.84	0.27
19	08 25 41.89	+47 06 31.3	0.374	0.695	0.047	17.84	17.58	0.05	17.85	20.90	0.24
23	08 25 08.74	+47 09 46.8	0.609	0.937	0.032	18.95	18.68	0.07	17.98	22.17	0.17
25	08 25 30.83	+47 07 45.0	0.410	0.753	0.044	18.05	17.79	0.05	17.59	20.84	0.23
26	08 25 53.89	+47 06 14.3	0.383	0.704	0.047	18.12	17.86	0.10	18.08	21.20	0.24
27	08 25 35.30	+47 06 29.5	0.440	0.758	0.037	18.04	17.78	0.08	18.04	21.43	0.19
31	08 25 36.20	+47 07 34.9	0.231	0.554	0.042	17.48	17.22	0.06	18.18	20.51	0.22
33	08 25 30.33	+47 08 23.7	0.441	0.769	0.041	18.24	17.99	0.07	18.21	21.66	0.21
44	08 25 09.07	+47 08 40.9	0.432	0.731	0.078	18.87	18.61	0.05	18.48	21.83	0.39
45	08 25 56.43	+47 06 14.8	0.353	0.677	0.054	18.43	18.18	0.05	18.41	21.41	0.27
48	08 25 48.92	+47 06 27.0	0.340	0.643	0.082	18.29	18.03	0.06	18.53	21.43	0.41
49	08 25 11.47	+47 08 33.3	0.384	0.705	0.056	18.62	18.37	0.05	18.50	21.66	0.28
56	08 25 51.96	+47 06 32.5	0.411	0.715	0.064	18.83	18.57	0.09	18.67	21.92	0.32
57	08 25 27.98	+47 08 39.6	0.370	0.691	0.054	18.53	18.27	0.09	18.72	21.77	0.27
58	08 25 48.06	+47 07 02.5	0.447	0.768	0.064	19.00	18.74	0.05	18.65	22.08	0.32
75	08 25 20.09	+47 07 47.0	0.070	0.390	0.087	17.86	17.60	0.05	18.86	20.39	0.44
79	08 25 22.69	+47 08 14.0	0.232	0.559	0.080	18.12	17.85	0.08	18.93	21.25	0.40
82	08 25 03.18	+47 10 05.6	0.438	0.773	0.171	20.06	19.81	0.50	18.93	22.34	0.66
105	08 25 39.19	+47 06 39.9	0.160	0.469	0.105	18.51	18.24	0.11	19.45	21.41	0.53
110	08 24 59.42	+47 10 05.3	0.215	0.551	0.171	19.40	19.15	0.05	19.74	22.05	0.66
132	08 25 14.47	+47 08 21.5	0.356	0.661	0.271	19.89	19.64	0.16	19.98	22.99	0.76

Table 6.3: Photometric Properties for Galaxies in Abell 665

Galaxy ID	Right Ascension (J2000)	Declination (J2000)	$\log r_{\rm eff}$ (arcsec)	$\log r_{\rm eff}$ (kpc)	$\pm$	$\langle\mu_{K_s}\rangle_{\rm eff}$ (mag/$''$)	$\langle\mu_K\rangle_{\rm eff}^{corr}$ (mag/$''$)	$\pm$	R_{tot} (mag)	$\langle\mu_V\rangle_{\rm eff}^{corr}$ (mag/$''$)	$\pm$
3	08 31 03.21	+65 50 48.4	0.578	1.008	0.009	18.20	17.87	0.05	16.76	21.29	0.07
11	08 30 54.60	+65 52 17.7	0.196	0.626	0.030	16.90	16.57	0.05	17.49	20.10	0.16
15	08 31 05.33	+65 48 47.3	0.263	0.696	0.035	17.47	17.13	0.05	17.58	20.50	0.18
17	08 30 35.49	+65 54 05.5	0.003	0.444	0.031	16.17	15.83	0.05	17.53	19.16	0.16
18	08 30 37.54	+65 53 30.1	0.229	0.666	0.036	17.23	16.89	0.05	17.57	20.32	0.19
25	08 30 47.77	+65 55 10.7	0.142	0.585	0.100	17.35	17.01	0.05	17.71	20.03	0.50
26	08 31 10.38	+65 49 17.3	0.235	0.675	0.054	17.51	17.16	0.05	17.80	20.55	0.27
35	08 30 40.69	+65 54 40.0	0.038	0.489	0.054	16.92	16.57	0.05	17.85	19.62	0.27
38	08 30 55.90	+65 49 47.4	-0.198	0.253	0.049	15.69	15.35	0.05	17.93	18.54	0.25
42	08 30 53.27	+65 50 43.6	-0.152	0.293	0.127	16.17	15.83	0.05	18.08	18.92	0.64
49	08 30 37.99	+65 55 03.3	0.250	0.693	0.047	17.84	17.51	0.05	18.09	20.96	0.24
57	08 30 55.13	+65 50 06.7	-0.051	0.384	0.083	16.77	16.43	0.07	18.35	19.68	0.42
61	08 30 50.10	+65 51 07.7	-0.231	0.217	0.058	15.95	15.63	0.05	18.35	18.86	0.29
64	08 30 43.74	+65 53 01.8	0.078	0.497	0.065	17.53	17.21	0.05	18.31	20.37	0.33
68	08 30 49.83	+65 53 35.3	-0.051	0.366	0.059	16.78	16.44	0.05	18.39	19.75	0.30
74	08 31 01.68	+65 53 01.2	-0.075	0.362	0.077	17.15	16.83	0.05	18.62	19.92	0.39
77	08 31 02.00	+65 49 37.3	0.054	0.470	0.107	17.55	17.21	0.05	18.62	20.51	0.54
80	08 31 07.66	+65 49 25.1	0.135	0.573	0.077	17.85	17.51	0.05	18.69	20.98	0.39
97	08 30 42.13	+65 54 07.6	-0.341	0.097	0.108	16.09	15.75	0.05	18.97	18.86	0.54

Table 6.4: Photometric Properties for Galaxies in Abell 2390

Galaxy ID	Right Ascension (J2000)	Declination (J2000)	$\log r_{\rm eff}$ (arcsec)	$\log r_{\rm eff}$ (kpc)	$\pm$	$\langle\mu_K\rangle_{\rm eff}$ (mag/″)	$\langle\mu_K\rangle_{\rm eff}^{corr}$ (mag/″)	$\pm$	R_{tot} (mag)	$\langle\mu_V\rangle_{\rm eff}^{corr}$ (mag/″)	$\pm$
2	21 53 28.69	+17 42 51.3	0.486	0.995	0.002	18.35	17.97	0.05	18.18	22.00	0.05
6	21 53 34.54	+17 41 56.5	0.616	1.125	0.002	19.19	18.81	0.05	18.57	23.03	0.05
7	21 53 36.19	+17 41 11.6	0.415	0.927	0.003	18.31	17.90	0.05	18.92	22.29	0.05
9	21 53 31.42	+17 42 27.8	0.471	1.004	0.003	18.56	18.20	0.05	18.66	22.45	0.05
10	21 53 37.45	+17 41 42.2	-0.043	0.453	0.004	14.96	14.58	0.05	18.10	19.27	0.05
24	21 53 29.24	+17 42 35.7	0.084	0.593	0.002	17.11	16.73	0.05	18.95	20.75	0.05
28	21 53 42.32	+17 41 23.9	-0.252	0.258	0.008	16.57	16.20	0.05	19.43	19.57	0.06
33	21 53 37.89	+17 38 25.2	-0.006	0.501	0.006	17.10	16.73	0.05	19.28	20.66	0.06
41	21 53 41.77	+17 39 45.6	-0.092	0.413	0.012	17.25	16.88	0.05	19.24	20.19	0.08
44	21 53 38.91	+17 40 18.9	-0.049	0.453	0.008	17.61	17.24	0.05	19.84	20.99	0.06
46	21 53 30.94	+17 44 44.7	-0.016	0.492	0.017	17.59	17.21	0.05	19.83	21.12	0.10
91	21 53 44.80	+17 40 21.2	-0.203	0.312	0.040	17.58	17.19	0.05	20.07	20.40	0.21
112	21 53 33.91	+17 44 37.1	-0.199	0.322	0.025	17.62	17.24	0.05	19.93	20.32	0.13
119	21 53 30.85	+17 45 06.7	-0.213	0.486	0.020	17.64	17.64	0.05	19.98	20.91	0.11
138	21 53 32.05	+17 42 09.1	-0.394	0.115	0.033	17.41	17.03	0.05	20.27	19.67	0.17
8	21 53 27.13	+17 43 35.4	...	...	...	...	...	...	18.29	...	...

Notes to table: Object # 8 is identified as a Galactic star.

Table 6.5: Photometric Properties for Galaxies in Abell 370

Galaxy ID	Right Ascension (J2000)	Declination (J2000)	$\log r_{\rm eff}$ (arcsec)	$\log r_{\rm eff}$ (kpc)	$\pm$	$\langle\mu_K\rangle_{\rm eff}$ (mag/$''$)	$\langle\mu_K\rangle_{\rm eff}^{corr}$ (mag/$''$)	$\pm$	R_{tot} (mag)	$\langle\mu_V\rangle_{\rm eff}^{corr}$ (mag/$''$)	$\pm$
1	02 39 52.67	-01 34 18.6	0.244	0.897	0.004	17.58	16.88	0.05	17.45	19.23	0.05
2	02 39 53.07	-01 34 55.8	0.695	1.348	0.007	19.14	18.45	0.05	17.45	21.52	0.06
3	02 39 44.28	-01 33 07.9	-0.206	0.443	0.006	15.73	15.06	0.05	17.59	17.18	0.06
4	02 39 44.98	-01 32 43.0	-0.063	0.582	0.008	16.69	16.02	0.05	18.27	18.59	0.06
10	02 39 52.47	-01 33 41.5	-0.059	0.585	0.014	17.37	16.67	0.05	18.36	18.64	0.09
15	02 39 51.12	-01 37 30.3	0.037	0.688	0.009	17.21	16.49	0.05	18.49	19.20	0.07
20	02 39 49.85	-01 37 15.2	-0.475	0.182	0.014	15.50	14.82	0.05	18.75	16.97	0.09
24	02 39 55.73	-01 34 19.6	-0.356	0.292	0.011	15.65	14.95	0.05	18.79	17.58	0.07
28	02 40 00.40	-01 35 47.0	-0.361	0.291	0.015	16.17	15.47	0.05	18.77	17.52	0.09
33	02 39 52.63	-01 35 35.0	-0.574	0.079	0.021	15.33	14.81	0.05	18.77	16.89	0.12
41	02 40 02.14	-01 37 14.6	-0.204	0.391	0.012	16.57	15.89	0.05	18.97	18.56	0.08
51	02 39 57.22	-01 35 27.1	-0.786	-0.139	0.069	14.22	13.51	0.05	18.91	15.52	0.35
67	02 39 59.49	-01 37 06.6	-0.115	0.541	0.020	17.57	16.88	0.05	18.99	19.00	0.11
71	02 39 57.18	-01 38 39.4	-0.330	0.320	0.030	16.78	16.08	0.05	18.82	17.73	0.16
77	02 39 52.28	-01 33 16.0	-0.342	0.311	0.033	17.18	16.51	0.05	19.28	18.19	0.17
79	02 39 50.00	-01 34 15.1	-0.658	-0.013	0.064	15.41	14.75	0.05	19.24	16.60	0.32
SER1	02 40 00.21	-01 35 39.9	···	···	0.000	···	···	···	···	16.60	0.32
SER2	02 39 44.94	-01 32 40.9	-0.566	0.049	0.048	16.11	15.44	0.09	···	16.60	0.32
16=A02	02 39 57.10	-01 32 59.1	···	···	0.000	···	···	···	19.24	···	0.05
14=A03	02 39 58.04	-01 33 03.5	···	···	0.000	···	···	···	19.35	···	0.05
18=A13	02 39 50.79	-01 33 52.8	···	···	0.000	···	···	···	19.45	···	0.05
17=A17	02 39 55.27	-01 34 05.4	-0.088	0.564	0.013	17.16	16.45	0.05	19.51	19.61	0.08
8=A23	02 39 48.71	-01 34 33.4	0.122	0.774	0.011	17.71	17.04	0.05	20.18	21.41	0.07
11=A28	02 39 51.25	-01 34 51.5	-0.059	0.587	0.004	16.85	16.17	0.05	20.25	20.56	0.05
5=A32	02 39 56.32	-01 34 29.0	0.140	0.788	0.011	17.94	17.27	0.05	20.36	21.68	0.07

Notes to table: Galaxy identifications are for the present study, with the exception of those labeled "A," which are from Ziegler & Bender (1997).

Table 6.6: Photometric Properties for Galaxies in Abell 851

Galaxy ID	Right Ascension (J2000)	Declination (J2000)	$\log r_{\rm eff}$ (arcsec)	$\log r_{\rm eff}$ (kpc)	$\pm$	$\langle\mu_{K_s}\rangle_{\rm eff}$ (mag/$''$)	$\langle\mu_K\rangle_{\rm eff}^{corr}$ (mag/$''$)	$\pm$	R_{tot} (mag)	$\langle\mu_V\rangle_{\rm eff}^{corr}$ (mag/$''$)	$\pm$
4	09 42 48.05	+47 01 16.9	-0.117	0.555	0.049	16.23	15.32	0.05	18.37	18.17	0.25
11	09 42 56.20	+46 59 12.3	0.321	0.993	0.067	18.41	17.52	0.05	18.84	20.87	0.34
16	09 43 05.13	+46 59 50.5	0.307	0.976	0.058	18.46	17.56	0.05	18.88	20.82	0.29
23	09 43 02.20	+47 01 04.2	-0.057	0.614	0.063	17.29	16.43	0.66	19.10	19.29	0.32
44	09 42 55.12	+46 59 22.8	0.142	0.805	0.161	19.20	18.30	0.11	20.02	21.13	0.61
47	09 42 51.32	+47 01 15.0	0.160	0.830	0.227	19.50	18.61	0.05	20.15	21.37	0.74
48	09 42 52.24	+47 01 06.2	-0.736	-0.068	0.293	14.91	13.99	0.05	19.85	16.53	0.77
56	09 43 07.55	+46 58 46.8	-0.148	0.526	0.287	18.09	17.18	0.08	20.15	19.80	0.74
57	09 42 56.89	+47 00 09.1	-0.313	0.359	0.252	17.38	16.48	0.05	20.02	18.86	0.66
69	09 43 02.83	+46 56 47.0	-0.010	0.661	0.120	18.67	17.79	0.27	20.41	20.79	0.60
88	09 43 08.75	+46 56 04.0	-0.223	0.444	0.252	19.13	18.22	0.80	21.04	20.32	0.61
97	09 42 51.98	+47 00 44.5	-0.659	0.013	0.256	17.58	16.70	0.73	21.18	18.33	0.78
102	09 42 58.34	+47 00 04.4	-0.520	0.146	0.259	17.86	16.98	0.05	21.02	18.87	0.65
111	09 43 02.40	+47 01 19.3	-0.604	0.062	0.294	18.16	17.31	0.05	21.29	18.75	0.67
113	09 43 05.50	+46 56 38.3	-0.015	0.647	0.262	18.92	17.85	0.62	21.18	21.17	0.61
3	09 43 06.93	+46 55 35.6	0.113	0.684	0.045	17.07	16.55	0.05	18.02	19.71	0.23
5	09 43 07.65	+46 55 16.3	0.169	0.740	0.088	17.91	17.39	0.06	18.56	20.52	0.44
6	09 43 08.04	+46 59 24.2	-0.094	0.478	0.069	16.78	16.26	0.05	18.65	19.30	0.35
103	09 43 08.43	+46 59 42.1	-0.127	0.444	0.285	19.68	19.16	0.79	21.54	22.02	0.73

Notes to table: The galaxies # 3, 5, 6, and 103 correspond to a foreground redshift structure at $z = 0.285$ (see Table 6.12).

Table 6.7: Photometric Properties for Galaxies in MS0015.9+1609

Galaxy ID	Right Ascension (J2000)	Declination (J2000)	$\log r_{\rm eff}$ (arcsec)	$\log r_{\rm eff}$ (kpc)	$\pm$	$\langle\mu_K\rangle_{\rm eff}$ (mag/″)	$\langle\mu_K\rangle_{\rm eff}^{corr}$ (mag/″)	$\pm$	I_{tot} (mag)	$\langle\mu_V\rangle_{\rm eff}^{corr}$ (mag/″)	$\pm$
2	00 18 33.51	+16 26 16.5	0.731	1.466	0.010	20.01	18.82	0.05	18.29	22.95	0.07
3	00 18 41.03	+16 26 05.0	···	···	0.000	···	···	···	18.49	···	0.05
4	00 18 31.04	+16 26 41.3	···	···	0.000	···	···	···	18.79	···	0.05
6	00 18 27.25	+16 26 51.4	···	···	0.000	···	···	···	18.96	···	0.05
7	00 18 32.77	+16 25 49.9	-0.094	0.641	0.086	17.49	16.15	0.05	18.92	19.41	0.43
8	00 18 23.99	+16 26 17.2	0.185	0.924	0.014	18.81	17.60	0.05	19.06	20.97	0.09
9	00 18 16.70	+16 24 51.7	···	···	0.000	···	···	···	19.45	···	0.05
13	00 18 29.76	+16 26 22.3	0.123	0.860	0.017	18.83	17.62	0.05	19.61	21.21	0.10
16	00 18 39.14	+16 23 51.4	0.182	0.919	0.015	18.94	17.71	0.05	19.50	21.36	0.09
22	00 18 38.30	+16 26 19.7	-0.525	0.215	0.171	16.45	15.16	0.08	20.18	18.58	0.66
24	00 18 35.50	+16 25 07.6	···	···	0.000	···	···	···	20.12	···	0.05
25	00 18 25.00	+16 24 12.2	-0.148	0.585	0.016	17.83	16.65	0.05	19.88	20.17	0.09
26	00 18 21.62	+16 24 53.1	0.077	0.810	0.020	18.95	17.79	0.05	19.89	21.34	0.11
28	00 18 22.81	+16 26 04.9	0.024	0.753	0.027	19.01	17.79	0.05	20.44	21.52	0.14
29	00 18 45.00	+16 26 44.8	···	···	0.000	···	···	···	20.36	···	0.05
31	00 18 44.26	+16 24 46.9	-0.302	0.437	0.036	18.24	17.05	0.05	20.14	19.64	0.19
33	00 18 28.37	+16 23 58.4	···	···	0.000	···	···	···	20.20	···	0.05
34	00 18 29.04	+16 25 05.7	···	···	0.000	···	···	···	19.68	···	0.05
41	00 18 39.70	+16 26 42.6	···	···	0.000	···	···	···	20.35	···	0.05
44	00 18 25.91	+16 24 49.3	-0.177	0.558	0.023	18.18	16.98	0.05	20.40	20.51	0.13
46	00 18 20.30	+16 25 01.9	···	···	0.000	···	···	···	20.92	···	0.05
48	00 18 36.28	+16 26 51.4	-0.566	0.170	0.276	16.60	15.27	0.05	20.42	18.56	0.78
56	00 18 34.62	+16 25 46.9	-0.920	-0.182	0.281	16.01	14.70	0.70	20.94	17.34	0.61
63	00 18 37.18	+16 24 40.6	-0.392	0.344	0.299	17.82	16.48	0.62	20.57	19.57	0.70
67	00 18 45.98	+16 24 56.2	···	···	0.000	···	···	···	20.95	···	0.05
74	00 18 42.56	+16 27 02.2	-0.101	0.638	0.057	19.43	18.23	0.06	21.09	21.58	0.29
Ser1	00 18 19.47	+16 25 01.9	···	···	0.000	···	···	···	···	···	0.05
Ser2	00 18 40.86	+16 26 04.0	···	···	0.000	···	···	···	···	···	0.05

Notes to table: Near–infrared $r_{\rm eff}$ and $\langle\mu\rangle_{\rm eff}$ were derived only for those galaxies having an early–type spectrum at the cluster redshift (see Table 6.13). [a]These values of $\langle\mu_K\rangle_{\rm eff}$ were measured through a K_s filter; the remaining galaxies were observed through a K filter. The k–corrections applied to convert $\langle\mu_K\rangle_{\rm eff}$ to $\langle\mu_K\rangle_{\rm eff}^{corr}$ account for the filter distinction.

is ~ 0.215 arcsec, hence the slit width is oversampled. Moderate dispersion gratings were used and produced the following measured spectral resolutions: 0.85 Å pixel^{-1} for Abell 665, Abell 2390, and Abell 370 (using the 900 l/mm grating blazed at 5500 Å); 0.93 Å pixel^{-1} for Abell 851 (831 l/mm grating blazed at 8200 Å); and 1.25 Å pixel^{-1} for MS0015.9+1609 (600 l/mm grating blazed at 7500 Å). The 831/8200 grating was not available for the 1995 September observations, hence the Abell 370 observations were made with the 900/5500 grating instead. The central wavelength was chosen to cover the redshifted lines of Hβ ($\lambda = 4861$ Å), Mg$_2$ ($\lambda \sim 5175$ Å), Fe5270, and Fe5335. In the case of MS0015.9+1609 ($z = 0.546$), the Mg$_2$ line would fall in a portion of the night sky dominated by emission lines, so the redshifted G–band ($\lambda \sim 4306$ Å) was targeted instead. For this reason, Mg$_2$ and Fe indices are only observed for the clusters at $z < 0.5$; likewise, the 4000 Å break and O II ($\lambda = 3727$ Å) are only observed for MS0015.9+1609.

The seeing was typically 0.7 to 1.0 arcsec as measured on the setup images; typical slit-mask alignment uncertainties are ~ 0.1 arcsec, which is similar to the accuracy of the astrometry both of the input coordinates (obtained from CCD frames taken at the Palomar 60–inch Telescope; see §6.2 above) and the distortion map for the focal plane of the LRIS instrument. In some cases the telescope drifted slightly during an exposure, as determined by a loss of flux from one exposure to the next, which resulted in a second slit-mask alignment procedure. Exposures of an internal halogen lamp for flat–fielding, and of arc lamps (Hg+Kr, Ne, and/or Ar) were taken after each sequence of spectra. The total exposure times were 5000 s for Abell 665, 11200 s for Abell 2390, 14800 s for Abell 370, 14400 s for Abell 851, and 19200 s for MS0015.9+1609. The exposure times do not necessarily scale with galaxy redshift since some data were taken through thin cirrus and hence required longer exposures. The inverse gain and read noise for the LRIS CCD and readout electronics were measured to be 2.1 e$^-$ DN^{-1} and 6.1 e$^-$, respectively.

Spectra of Abell 655 were obtained in 1996 November and 1997 April with the COSMIC instrument (Dressler, Kells, & Sivaramakrishnan 1998) in re-imaged mode mounted at the prime focus of the Hale 5 m Telescope at Palomar Observatory. Multi–slits of 0.8 arcsec width were constructed using photographic film mounted at the focal plane. The slit width corresponds to ~ 2 pixel at the re-imaged scale of 0.399 arcsec pixel^{-1}. The field available for multi–slits is $\sim 8 \times 12$ arcmin^2, with the long dimension corresponding to the spatial direction for the spectra. A different mask was constructed for each of the two observations,

although there is a small number of galaxies common between the two masks. A constant pixel scale across the focal plane was assumed for the fabrication of the multi–slit masks (i.e., without inclusion of a distortion map). This created the requirement that the multi–slits not span more than ~ 3 arcmin in the direction perpendicular to the slits.

A transmission grism with 600 l/mm, blazed at 4800 Å and having a central wavelength of 5000 Å, was used which produces a dispersion of 1.46 Å pixel^{-1} at 5000 Å. Since the dispersing element was a grism, no tilts are possible to change the central wavelength; instead, the multi–slits as a whole were moved within the focal plane in the dispersion direction to produce a change in effective central wavelength to $\sim$ 5500 Å. Due to the lower dispersion, these spectra span a significantly larger wavelength range than the Keck data, typically from slightly bluewards of the 4000 Å break (in the rest–frame for the $z = 0.129$ cluster) nearly to the red–shifted Na lines (5890 Å in the rest–frame). The inverse gain and read noise for the COSMIC CCD and readout electronics were measured to be 3.2 e$^-$ DN^{-1} and 13 e$^-$, respectively. The combination of the somewhat high read noise for this instrument, narrow slit widths, and moderate spectral resolution resulted in a minimum exposure time for each individual spectrum of 2400 seconds for the spectra to be background limited. The total exposure time was 11200 s for the 1996 November observations, and 16800 s in 1997 April. While the latter data were of a longer integration, the seeing was considerably worse at $\sim$ 2.0 arcsec (instead of $\sim$ 1.0 arcsec for the 1996 November observations) and the spectrograph itself appeared to be in poor focus (possibly due to the heating element in the spectrograph being unable to keep up with the large and rapid temperature changes during the two nights of observations), hence the 1997 April data are of a substantially poorer quality. Only three spectra from the latter data set (galaxies # 1, 7, and 10) have S/N and quality similar to that of the 1996 November data; galaxy # 1 is the only one that is not a repeat observation, and hence only it is presented here.

6.3.2 Data Reductions

Data reductions and analysis were done using the IRAF package, with additional scripts and programs written by one of the authors (M. A. P.). The spectra were over-scan subtracted and then flattened using the internal halogen lamp (Keck) or an external halogen lamp (Palomar) reflected against the inside of the telescope dome. This flat–field frame was normalized by a smooth running median in the spectral direction in order to remove the

wavelength response of the lamp.

The Keck multi–slit spectra show substantial distortion across the full FOV which appears as a tilt of the sky lines along the slits at either end of the mask. The galaxies are extended, so the sky must be subtracted from pixels located a significant distance from the galaxy along the slit. This distortion must therefore be corrected for accurate sky subtraction. A multi–slit mask was fabricated which consisted of a series of slits at the same spatial position, but extended the full length of the mask FOV.[3] Exposures of arc lamps were taken through this mask in order to map out the spectrograph distortion pattern. The distortion map was constrained only to modify the light distribution in the spectral direction (i.e., the spatial direction was unaffected by construction) in order to straighten the sky lines. This distortion solution successfully corrects tilts as large as 10% for the extreme slits in all cases except for MS0015.9+1609. It was discovered later that the MS0015.9+1609 observations were obtained with a new CCD dewar field flattening window, so the distortion map obtained on a subsequent run (after the instrument had been moved to Keck II) was only moderately successful in removing the distortion pattern. This resulted in poor sky subtraction for the slits furthest from the optical axis of the instrument.

After application of the distortion correction, an illumination correction was made to each slit using spectra of the twilight sky. Since the Keck multi–slit mask fabrication utilizes a machine punch of an aluminum sheet, there are significant variations (nearly reaching 5% in the worst cases) in the throughput along a given slit even after manual filing of the slits prior to installation in the instrument. The film used for the Palomar multi–slit masks was somewhat more uniform, although there were still some significant variations in width for these narrow (0.8 arcsec) slits. The illumination correction from the twilight spectra appears to reduce this variation to $< 1\%$, as judged by a comparison of the night sky line flux along a given slit. This effect of variable slit width is the limiting factor for accurate sky subtraction of these multi–slit spectra (with the exception of MS0015.9+1609, as described above, which was limited by the poorly known distortion map).

Cosmic ray removal was performed using the SZAP task (written by M. Dickinson) on each individual two–dimensional spectrum. The night sky emission was removed by subtraction in the spatial direction performed directly on the two–dimensional images for each individual slit using median filtering with sigma clipping in the task BACKGROUND.

[3] A single long slit could not be used as it would be susceptible to flexure of the mask assembly.

The order chosen of the fit to the sky along the spatial direction for each slit was determined from a series of tests in which the S/N ratio was measured for each extracted spectrum. The order varied between first and fourth, depending on the length of the slit (with longer slits allowing higher orders) and the brightness of the object (with brighter objects requiring lower orders since there is less available region of sky along the slit). The optimal order of the fitting function, however, was found to be roughly constant for each multi–slit mask. The trace of the spectrum was fit for each individual slit observation, since the objects are relatively bright ($16 < R_{\rm C} < 20$ mag was typical) and the trace can vary somewhat depending on the altitude and azimuth of the telescope during the time of each observation. Spectra were extracted for 4 pixel widths along the slit ($\sim$ 0.9 arcsec for Keck/LRIS; $\sim$ 1.6 arcsec for P200/COSMIC), with the narrow extractions being motivated by the desire to minimize the aperture corrections to the final velocity dispersion measurements. It is an indication of the excellent throughput of the LRIS instrument that the spectra described here show high S/N (nearly all spectra have S/N$>$ 20; a significant number have S/N$>$ 50) despite the narrow slit size (0.7×0.9 arcsec^2) and moderate spectral dispersion ($\lambda/\Delta\lambda \sim 7000$ pixel^{-1}).

The spectra were individually wavelength calibrated using the night sky lines, which are typically split even at $\lambda > 7000$ Å due to the moderate dispersion of the spectrographs in these configurations. The final spectrum for each object was then obtained by combining the individually extracted and wavelength–calibrated spectra, thereby allowing for changes in the overall flux of each spectrum (due to varying airmass or cirrus) and providing a final pass to reject cosmic rays and bad pixels (using a sigma clipping algorithm in the task SCOMBINE) that may have been missed earlier. Tests were done to ensure that this entire data reduction procedure produced the optimal S/N and instrumental resolution for the output spectra while minimizing the sky subtraction artifacts.

Spectra of arcs (a combination of Hg, Kr, Ar, and/or Ne, depending on the wavelength of the observations) were obtained immediately after each set of spectra. The spectra were checked to ensure that the instrumental resolution of the arc spectra matched them accurately, since it is possible that the sky spectra (and hence the galaxy spectra) could be degraded due to instrument flexure or drift. One test performed was to slew the telescope during the afternoon to various positions in the dome to mimic the pointing of the telescope during the observations, taking arc spectra at each position. No significant differences were

found between the instrumental resolution of the arc lines obtained in this manner, the sky lines obtained during the course of the observations, or the arc lines obtained immediately following the observations. For this reason, the arc lines can be used below in §6.3.4 and 6.3.5 to define the instrumental resolution for the modeling necessary to measure central velocity dispersions and line indices.

The final spectra for the five clusters are displayed in Figures 6.7 to 6.12. The quality of the spectral extractions are excellent, with the only exception being the several objects with extreme slit positions in MS0015.9+1609; see the discussion on distortion above. A worthwhile comparison can be made between the spectra of Figure 6.12 and Kelson *et al.* (1997, where only two bright galaxy spectra are shown) or Ziegler & Bender (1997) at similar redshifts: the spectra in the present paper show excellent sky subtraction and S/N even for the faintest galaxies.

6.3.3 Stellar Template Spectra

High resolution spectra of Galactic giant stars ranging from early F to late K types were obtained with the HIRES cross–dispersed echelle spectrograph (Vogt *et al.* 1994) on the Keck I 10 m Telescope by J. K. McCarthy as part of a separate observing program (Djorgovski *et al.* 1997). L. Lu acquired additional observations to cover a large spectral range for two stars of K0 III spectral type. Both sets of data were kindly reduced by those individuals and provided electronically to the authors. These observations are at a far higher resolution ($\sigma_{\rm inst} \sim 1$ km s^{-1}) than the galaxy observations ($\sigma_{\rm inst} \sim 60$ to 120 km s^{-1}) and have essentially infinite S/N for these bright stars. The difficulty of using these observations lies in "stitching" together the different spectral orders, since there can be significant response variations at the ends of each order. Fits to the continuum were used to normalize the individual spectral orders, but this method is not particularly successful for orders having an absorption line at one end, or for broad wavelength regions with many metal line features, particularly around Mg_2 at $\lambda \sim 5170$ Å, or for the reddest orders of the McCarthy *et al.* data which have small gaps between successive orders. Flux calibration of the spectra does not significantly improve these effects, for reasons that are not yet fully understood (L. Lu, private communication). As will be shown below, these template spectra show excellent fits to the galaxy spectra despite these minor problems.

A separate collection of stellar spectra was obtained from the study of Jones (1996)

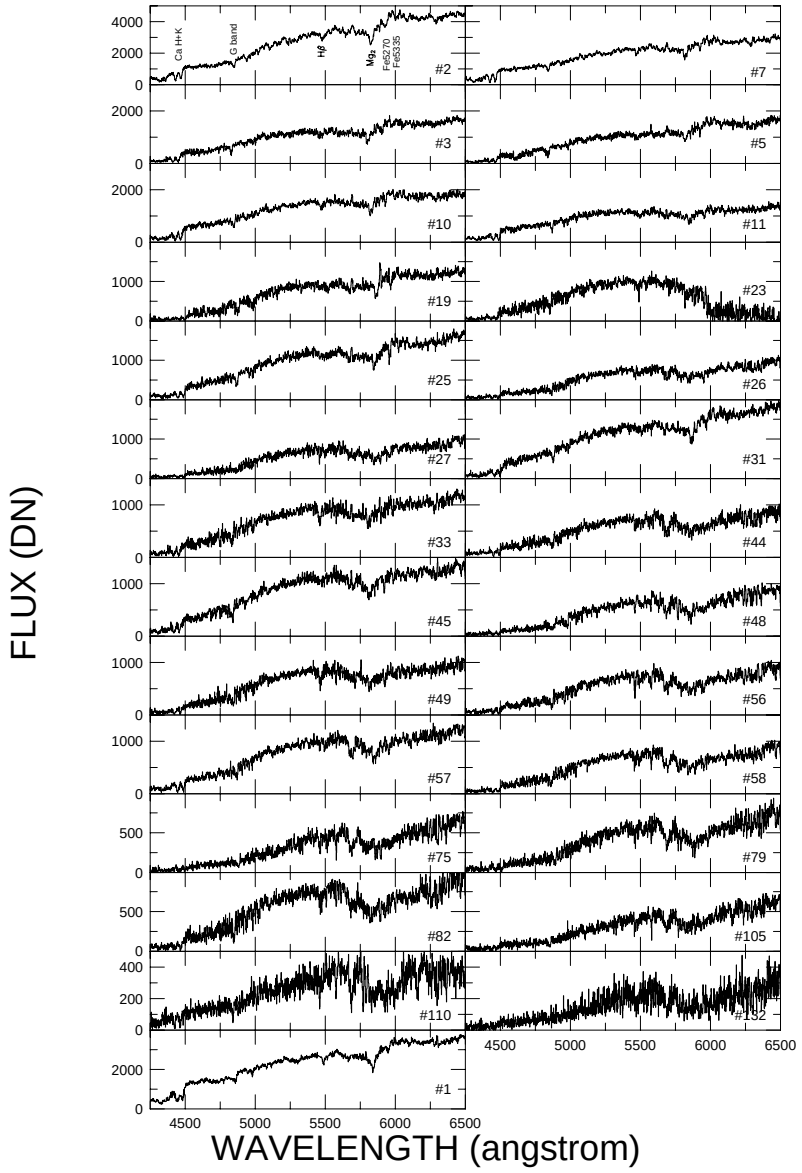

Figure 6.7: Spectra of galaxies in Abell 655 ($z = 0.129$) obtained with the COSMIC instrument on the Palomar 200–inch telescope. All galaxies have early–type spectra within ± 2600 km s^{-1} of the mean cluster redshift. Prominent absorption–line features are identified in the upper–left panel. The bottom panel (galaxy # 1) was the only unique spectrum with sufficient S/N obtained from the second mask; observations of galaxies # 7 and 10 with sufficient S/N were obtained with both masks, but are not included here as their quality is poorer than the first mask.

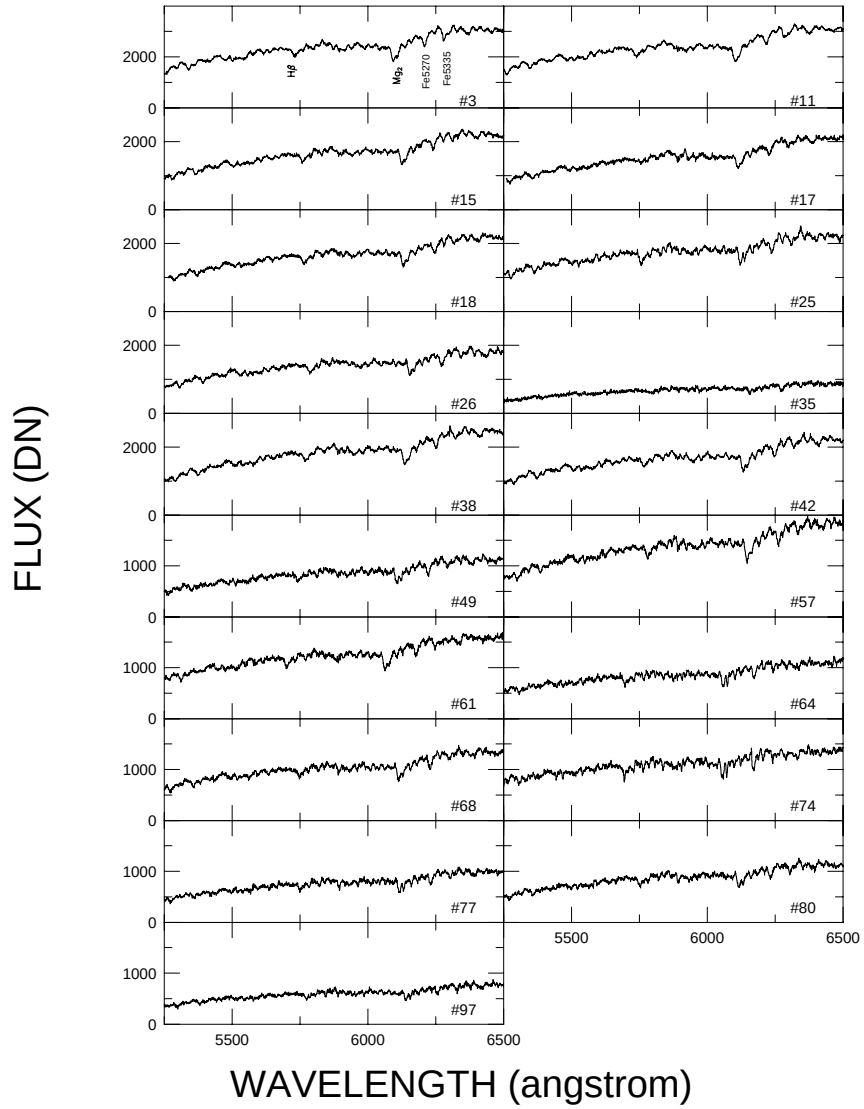

Figure 6.8: Spectra of galaxies in Abell 665 ($z = 0.181$) obtained with the LRIS instrument on the Keck I telescope. All galaxies have early–type spectra within ± 2500 km s^{-1} of the cluster redshift. Prominent absorption–line features are identified in the upper–left panel.

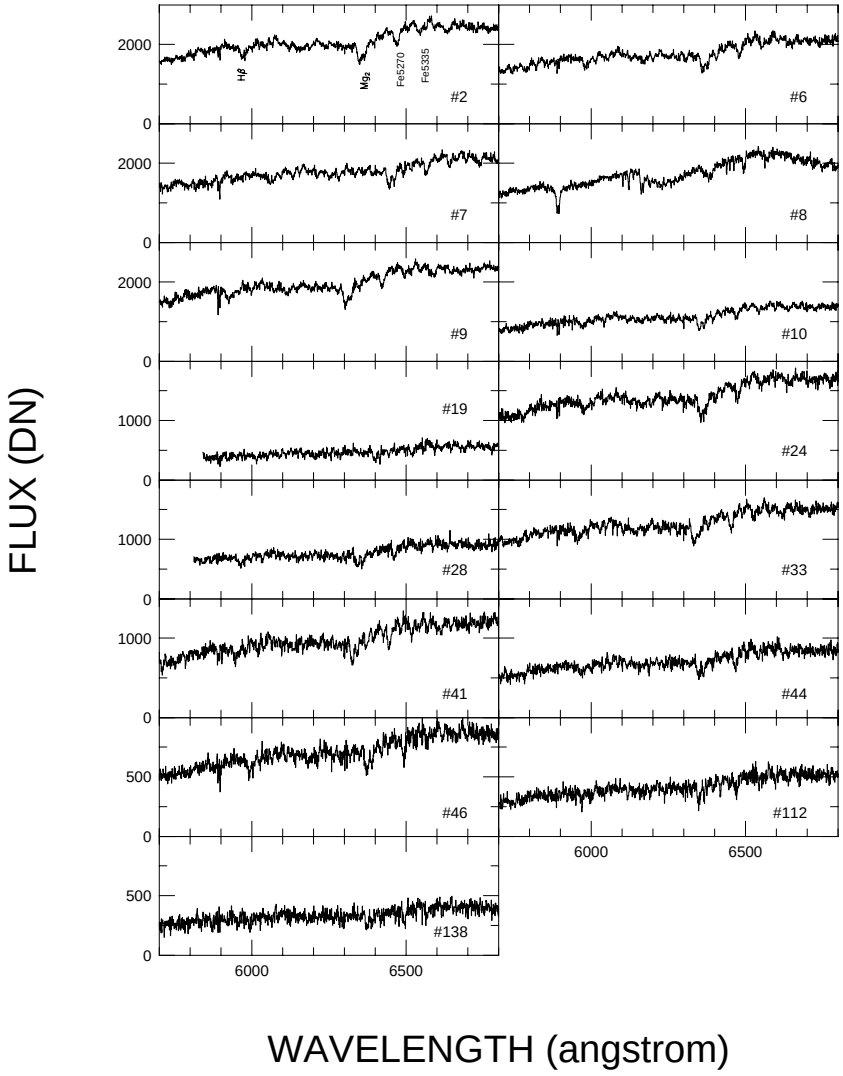

Figure 6.9: Spectra of galaxies in Abell 2390 ($z = 0.228$) obtained with the LRIS instrument on the Keck I telescope. Object #8 is a Galactic star, while the other 14 galaxies all have early–type spectra within ± 4500 km s^{-1} of the cluster redshift. Prominent absorption–line features are identified in the upper–left panel.

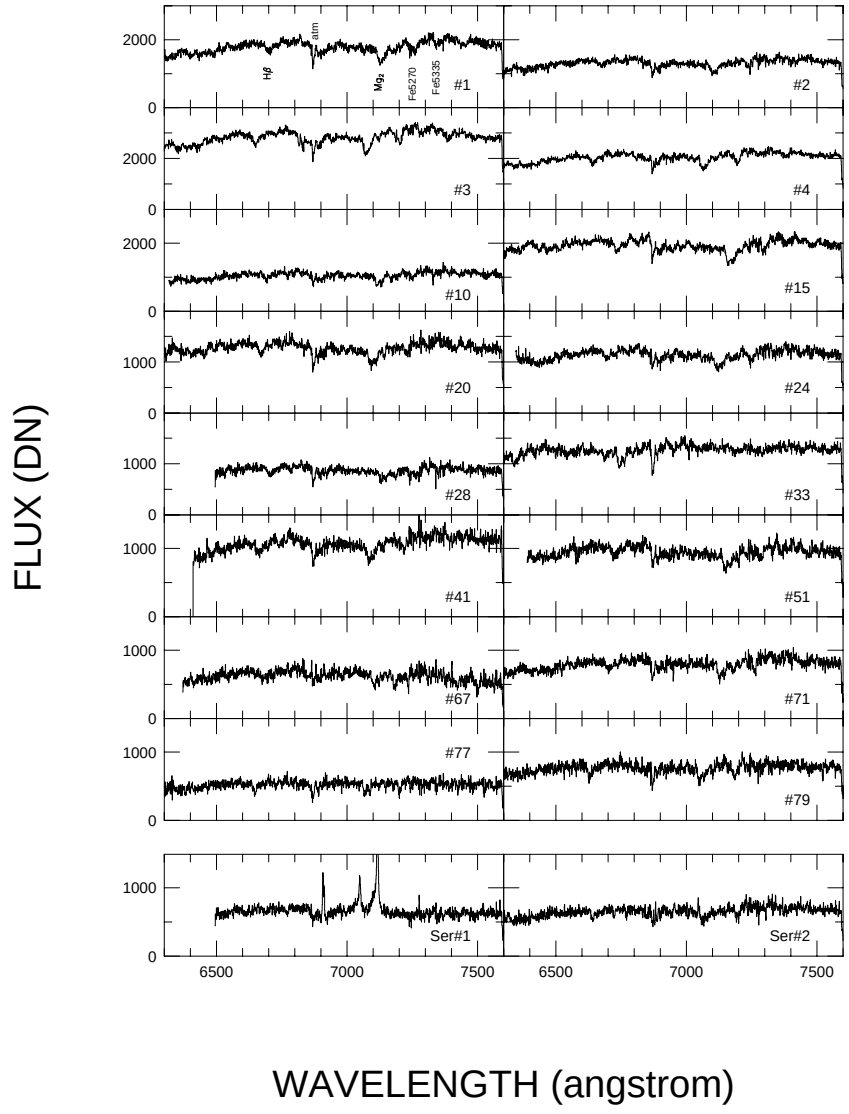

Figure 6.10: Spectra of galaxies in Abell 370 ($z = 0.372$) obtained with the LRIS instrument on the Keck I telescope. Two serendipitous objects (Ser 1 and 2), which landed on slits targeting other objects, are identified in the bottom panels; the first is a background emission–line galaxy at $z = 0.423$, while the other is of early–type at the cluster redshift. All 16 target galaxies, all have early–type spectra; one galaxy (# 33) lies 7300 km s^{-1} behind the mean cluster redshift, while the others are all within $\pm$2500 km s^{-1} of the mean cluster redshift. Prominent absorption–line features are identified in the upper–left panel.

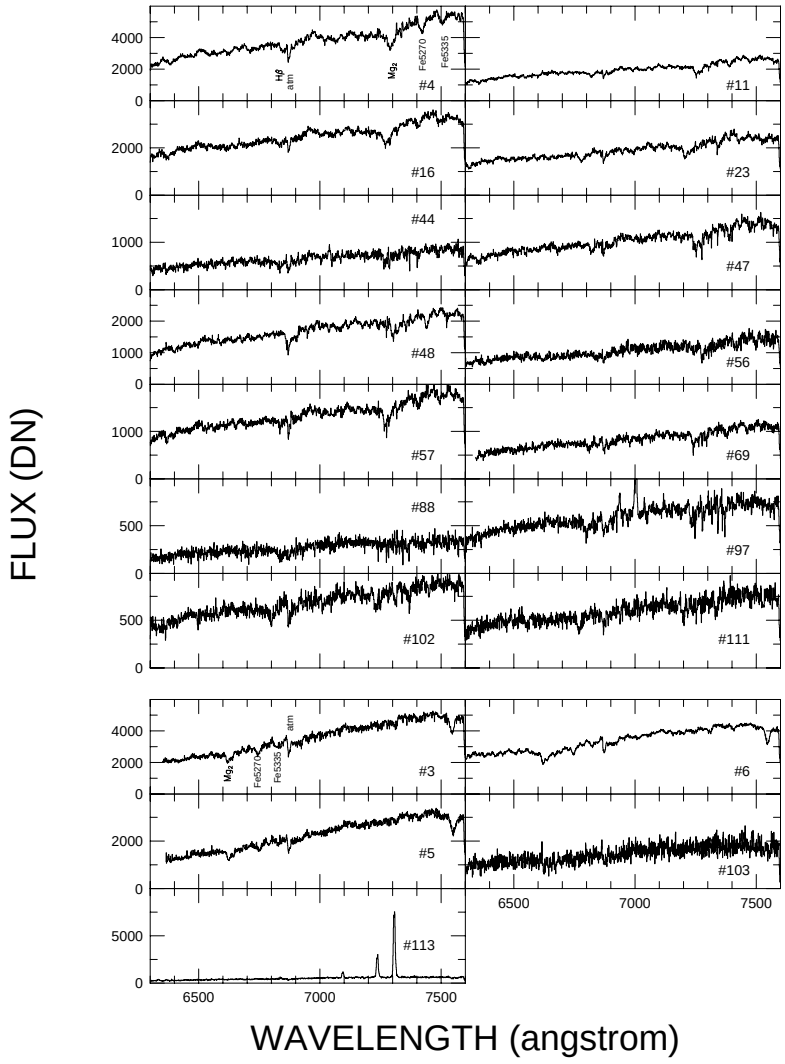

Figure 6.11: Spectra of galaxies in Abell 851 ($z = 0.405$) obtained with the LRIS instrument on the Keck I telescope. Five target galaxies which do not lie at the cluster redshift are identified separately in the bottom panels of the figure. Four have early–type spectra and lie in a foreground redshift structure at $z \sim 0.285$, while object # 113 is a background emission–line galaxy at $z = 0.46$. Prominent absorption–line features at $z = 0.285$ are identified in the panel for object # 3. One other target galaxy (# 97) has weak emission lines superimposed on an early–type spectrum at the cluster redshift. The other 13 target galaxies have early–type spectra within ± 2500 km s^{-1} of the cluster redshift. Prominent absorption–line features at $z = 0.407$ are identified in the upper–left panel. Also labeled is a prominent atmospheric absorption feature ("atm").

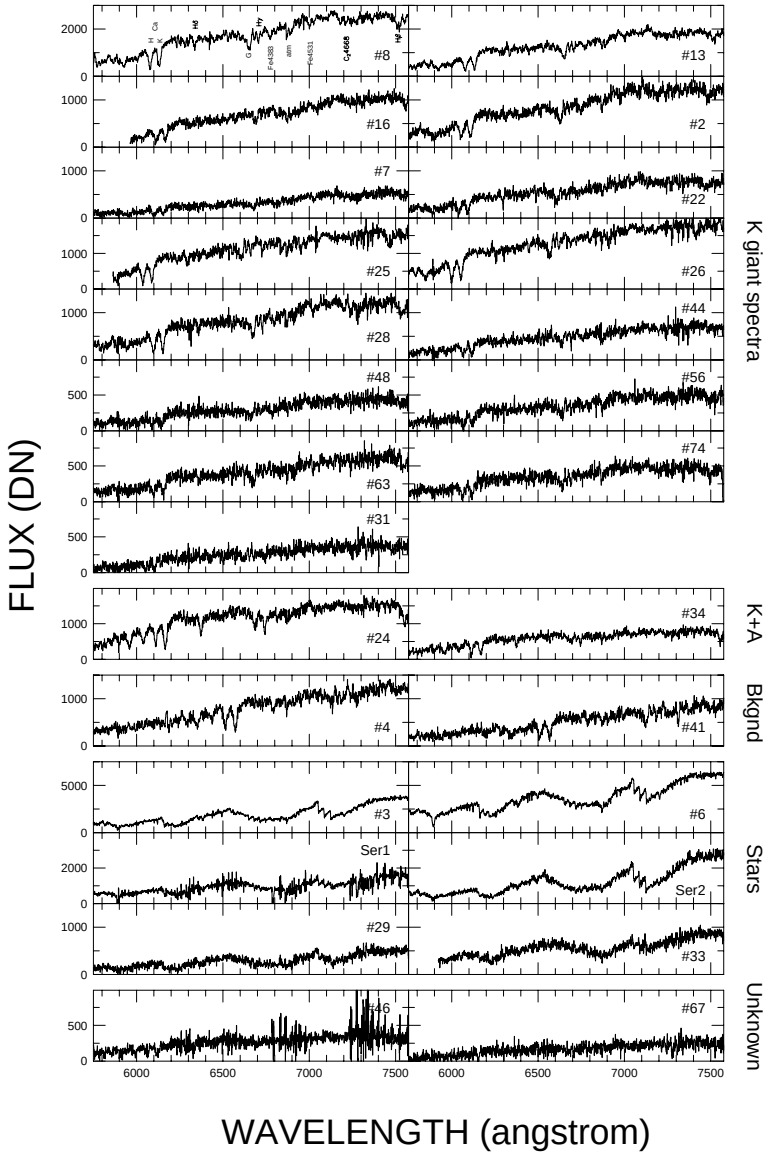

Figure 6.12: Spectra of galaxies in MS0015.9+1609 ($z = 0.546$) obtained with the LRIS instrument on the Keck I telescope. Of the 27 spectra obtained (25 target objects and two serendipitous sources which fell on two of the slits), 15 are at the cluster redshift and have spectra resembling a K giant, two are at the cluster redshift but have a superposition of K giant and A star spectra ("K+A" galaxies), two are in the background at $z \sim 0.66$, six (including the two serendipitous objects) are Galactic stars, and two lack identifiable spectral features ("unknown"). The high contamination rate for this mask is a direct result of the poor quality of the $VI_{\rm C}J$ photometry—the images were neither deep nor obtained in good seeing—which had been obtained in time to select the spectroscopic sample. Prominent absorption features (and an atmospheric band, labeled "atm"), are identified in the upper–left panel.

in electronic form from the compilation of Leitherer *et al.* (1996). This is a very large sample of 684 stars, spanning a wide range of spectral type, luminosity class, and metal abundance. The spectra were obtained in two wavelength ranges, $3820 < \lambda < 4500$ Å and $4780 < \lambda < 5460$ Å, which sample the wavelength regions around the G–band ($\lambda \sim 4300$ Å) and Mg_2 ($\lambda \sim 5170$ Å), respectively. The resolution of these spectra is only modest at 1.8 Å, but this is somewhat better than the rest–frame resolution for all the galaxy observations in the present paper except Abell 370.

6.3.4 Measurement of Velocities and Velocity Dispersions

There are three standard methods to measure velocity dispersions in early–type galaxies using the absorption lines and stellar templates. The first measures the width of the peak in the cross–correlation (CC) between the galaxy and template spectra (Tonry & Davis 1979); the position of the cross–correlation peak is the measure of the redshift. The second method performs a Gaussian fit to the ratio of the Fourier transform (FT) of the galaxy spectrum to the FT of the redshifted template spectrum, and is therefore referred to as the Fourier Quotient (FQ) method (Sargent *et al.* 1977). The third method is similar to the Fourier Quotient method in that it compares the FTs of the galaxy and redshifted template spectra, but instead fits FT of the galaxy spectrum with the FT of the stellar template convolved (multiplied in Fourier space) with the Gaussian broadening. In this Fourier Fitting (FF) method (Franx, Illingworth, & Heckman 1989), the error analysis for the least–squares minimization is simpler than the FQ case since the χ^2 statistic in Fourier space has been constructed in such a way that it is proportional to the χ^2 statistic for the original spectra. For this reason the FF method is preferred over the FQ method. In this paper, we will compare the FF and CC methods, since these two methods are largely independent in a computational sense.

For nearby early–type galaxies, the template stars are observed with the same observational setup used for the galaxies in order to measure the instrumental resolution under the assumption that the stars have zero velocity dispersion (or rotation). For virtually all observational setups to measure galaxy velocity dispersions, the instrumental resolution is much greater than the rotation (or upper observed upper limits to the rotation) for typical stars of late spectral type. This method works for nearby galaxies primarily because the wavelength of the galaxy absorption features is very close to that of the template stars,

hence the instrumental resolution is effectively the same for both star and galaxy observations. For early–type galaxies at significant redshifts, however, the instrumental resolution can vary significantly between the wavelength of a given line for the template star and the redshifted wavelength of that line for the observations of the galaxy. The empirical reason is that most spectrographs have instrumental resolutions which are constant in $\Delta\lambda$, not $\Delta\lambda/\lambda$. The result of this effect is that the effective instrumental resolution for the galaxy will be somewhat smaller than that for the template star, leading to an underestimate of the galaxy velocity dispersion. An additional complication is that the grating tilt must be changed between observations of star and galaxy to sample the same wavelength range in the rest–frame. Depending on the dispersing element, the instrumental resolution might increase significantly at bluer wavelengths causing an additional difficulty in matching the template and galaxy instrumental resolutions.

Several approaches can be used to measure velocity dispersions for early–type galaxies at significant redshifts. One approach is to narrow the slit width for the stellar observations, and change the grating tilt, in order to sample the same wavelength range as the galaxy and provide the same instrumental resolution. This approach was used by Ziegler & Bender (1997) for observations of ellipticals at $z = 0.37$. The advantage of this approach is that the same spectrograph is used for both galaxy and template spectra; the disadvantages are that some spectrographs do not allow for continuously variable slit widths, the instrumental resolution might increase significantly below a certain wavelength, the template stars must be re-observed for each target galaxy redshift, and the difficulty in modifying the grating tilt in some spectrographs (or impossibility if a transmission grism is used, as we have done here for the Palomar 200–inch observations). An alternate approach is to obtain higher resolution template spectra from elsewhere, redshift these template spectra to match the target galaxy of interest, and then broaden the template spectra to the instrumental resolution appropriate for the galaxy observations (which can be measured from arc or night sky lines). This approach was used by van Dokkum & Franx (1996) at $z = 0.39$ and Kelson *et al.* (1997) at $z = 0.33$ and $z = 0.58$. The advantages of this method are that no telescope time (at least on the large telescopes needed for the observations of distant galaxies) is used observing bright template stars, a given set of template spectra can be used for any desired redshift for the galaxies, the instrumental resolution for the galaxy observations need not be measured accurately prior to obtaining the template spectra,

additional stars can be added to the sample later, and full control of the template spectral broadening is reserved for later data analysis; the disadvantages are that the instrumental response could deviate significantly from the functional form chosen for the broadening of the template spectra since the template and galaxy spectra are typically obtained with completely different spectrographs, and that additional observations are necessary at higher resolution for the template spectra.

In the second method, there are basically two different procedures for smoothing the template spectra to the galaxy instrumental resolution: (1) if the template spectra have essentially infinite resolution compared to the galaxy spectra, then an arc line can be used to convolve the template spectra to the appropriate resolution; or (2) if the template spectra have only somewhat better resolution than the galaxy spectra, then a functional form must be assumed to broaden the stellar spectra the appropriate amount to match the resolution of the galaxy observations. The first method is more elegant in that no assumption is made about the shape of the instrumental response, but rather the true response is used for the convolution. The second method is more practical in that stellar template observations available (or feasible with short exposure times on a modest aperture telescope) are typically of only moderate resolution. The studies of van Dokkum & Franx (1996) and Kelson *et al.* (1997) both utilized the latter approach. Both of these approaches will be explored here—the first utilizing the high resolution spectra from Keck/HIRES, the second utilizing the moderate resolution spectra from Jones (1996)—as independent checks on the methodology. Since the instrumental resolution varies with position within the multi–slit mask, with the highest resolution for the spectra near the center of the mask, the broadening of the stellar template spectra must be performed separately for each galaxy spectrum.

The IRAF task FXCOR was used to measure the redshift and velocity dispersion for each galaxy with the CC method. For the 1996 November P200/COSMIC observations of Abell 655, the large wavelength range allowed for the galaxy spectra to be divided into blue and red portions to cross–correlate independently with the Jones (1996) blue and red template observations. One galaxy (# 48) showed a significant difference of 460 km s^{-1} between the two redshift measurements, but the other 25 galaxies as a whole showed no systematic offset within the 1 σ CL uncertainty of 4 km s^{-1}. The internal uncertainty implied by this comparison is 14 km s^{-1} per redshift measurement.

A contributed IRAF task FFFQ was used to measure the velocity dispersion for each

galaxy using the FF method. The redshift of each galaxy was fixed to the measurement derived from the CC method, since those measurements have excellent internal accuracy. A range of template stars were fit using the highest S/N observations—Abell 665 ($z = 0.18$) observations from Keck/LRIS. The results were compared to determine which provided the minimum residual from the fit to velocity dispersion and line strength. A clear minimum was found for both the Keck/HIRES and Jones (1996) stellar templates around spectral type G7–9 III. An additional improvement was found by using stars with one–half solar metallicity (i.e., [Fe/H]~ -0.3 dex) in the Jones (1996) spectra.[4] Using only the Jones (1996) templates between G5 and K2, the scatter in velocity dispersions using the FF method is only 0.01 dex, suggesting that small mismatches between template and galaxy are only a minor contribution to the overall uncertainties in the measurement of velocity dispersion. The star HD134190 (G7.5 III; [Fe/H]~ -0.3 dex) showed the smallest scatter, and was used for all final results. Fits to four galaxy spectra in Abell 665 using this template spectrum are shown in Figure 6.13.

Comparison of the CC and FF methods show a small, but marginally significant, offset in their measured velocity dispersions of $\Delta \log \sigma_0 = 0.016 \pm 0.007$, in the sense that the CC velocity dispersions are slightly larger. Half of this difference will be adopted as a potential systematic error in the velocity dispersions. The scatter between the two measurements is 0.028 dex which corresponds to an internal uncertainty of 0.020 dex per measurement if the uncertainties are evenly distributed between the CC and FF methods. The internal fitting uncertainties are typically 0.010 dex for the FF method, and 0.012 dex for the CC method, suggesting that these internal uncertainties are underestimated by a factor of two. The quoted internal uncertainties in this paper will therefore be doubled to account for this effect.

Comparison of the velocity dispersions using the Keck/HIRES templates and the Jones (1996) templates yields small offset of 0.008 ± 0.003 dex for the FF method, in the sense that the Keck/HIRES template spectra result in slightly larger velocity dispersions. Comparison of the velocity dispersions using the Keck/HIRES templates and the Jones (1996)

[4]We expect *a priori* that observations of galaxies at higher redshifts should show a best fit for increasingly earlier spectral type as the mean age of their stellar content is observed at progressively earlier epochs, hence it is not surprising that the best fit was obtained with a slightly earlier spectral type than G9–K1 III than is typical for local galaxies (cf. van Dokkum & Franx 1996). The slow change with redshift of mean spectral type for early–type galaxies can be used as an indicator of the mean age of the galaxy population and hence galaxy evolution. To our knowledge this property has never been measured with such Fourier techniques, but pursuing this topic is beyond the scope of the present paper.

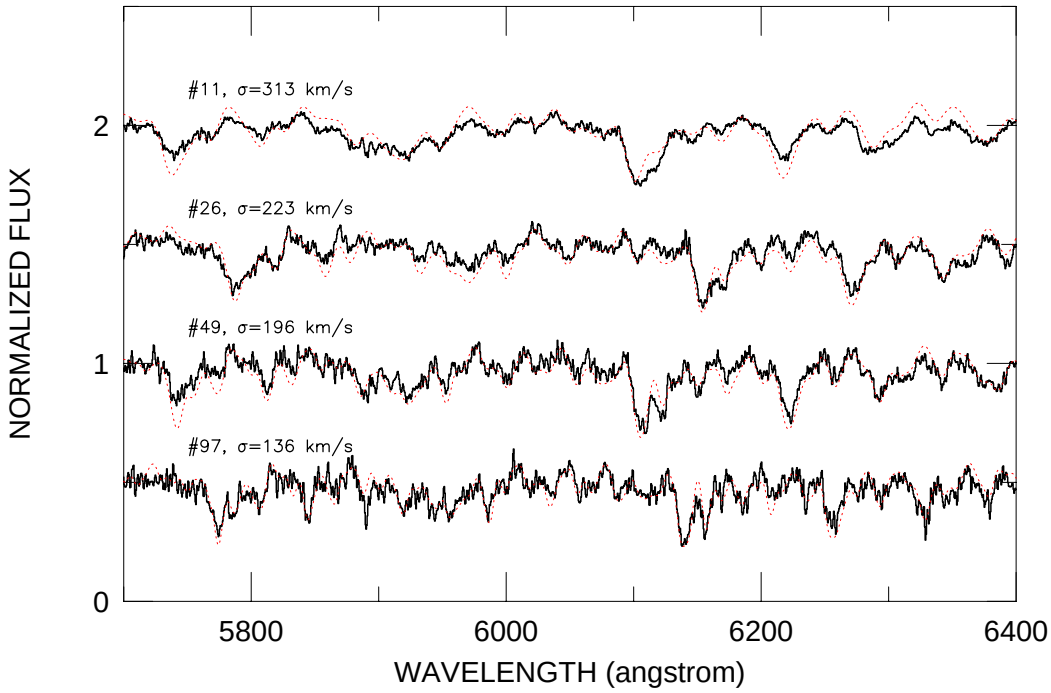

Figure 6.13: Fits to several galaxy spectra for Abell 665 using stellar template HD134190 (G7.5 III, [Fe/H]~ -0.3 dex). The galaxy spectra are plotted as solid, thick lines, while the broadened template fits are plotted as dashed lines. All spectra are normalized by their continuum to unity, then offset vertically for clarity. The fitted values of the velocity dispersions were taken from the Fourier fitting method of Franx *et al.* (1989).

templates yields small and statistically insignificant offsets of 0.002 ± 0.002 dex for the CC method, in the sense that the Keck/HIRES template spectra result in slightly smaller velocity dispersions. We will adopt 0.005 dex as a possible systematic error on the velocity dispersions due to difference in the manner of broadening the stellar template spectra.

The velocity dispersions have been measured in small apertures—0.7×0.9 arcsec^2 for the Keck/LRIS spectra at $0.18 < z < 0.55$, 0.8×1.6 arcsec^2 for the P200/COSMIC data at $z = 0.13$—in order to minimize aperture corrections. This is in direct contrast to the observations of Ziegler & Bender (1997), who used apertures of 3.6×3.6 arcsec^2, which presumably extend to radii larger than $r_{\rm eff}$ for most of their galaxies at $z = 0.37$. The aperture is also somewhat smaller than that used by van Dokkum & Franx (1996), who used apertures of 1.6×1.8 arcsec^2 in observing galaxies at $z = 0.39$.[5] Jørgensen *et al.* (1995b) used velocity dispersion profiles from the literature to construct empirical dynamical models for elliptical galaxies and study the effects of aperture size on the velocity dispersion. They showed that the velocity dispersion $\sigma(r)$ measured within a radius r scales as $-0.04 \log r$. They proceeded to correct nearby galaxies to a common fiducial scale of $2r = 3.4$ arcsec at the distance of the Coma cluster, a practice which has been subsequently widely adopted (van Dokkum & Franx 1996; Smith *et al.* 1997; Lucey *et al.* 1997; Kelson *et al.* 1997; Pahre 1998a, Chapter 2 of this thesis; cf. Ziegler & Bender 1997). A circular aperture used in the normalization of Jørgensen *et al.* can be obtained from the rectangular apertures used in the present paper by the the conversion formula $r_{ap} \sim 1.025 d \sqrt{xy/\pi}$ (Smith *et al.* 1997), where d is the distance to the galaxy. The aperture corrections adopted here (using the cosmology $H_0 = 75$ km s^{-1} Mpc^{-1}, $\Omega_0 = 0.2$, $\Lambda_0 = 0$) for the velocity dispersions are then the following: $\Delta\sigma = 0.010$ dex for Abell 655 ($z = 0.129$); $\Delta\sigma = 0.008$ dex for Abell 665 ($z = 0.181$); $\Delta\sigma = 0.012$ dex for Abell 2390 ($z = 0.228$); $\Delta\sigma = 0.017$ dex for Abell 370 ($z = 0.372$); $\Delta\sigma = 0.018$ dex for Abell 851 ($z = 0.407$); $\Delta\sigma = 0.014$ dex for four galaxies in the foreground of Abell 851 ($z = 0.285$); and $\Delta\sigma = 0.021$ dex for MS0015.9+1609 ($z = 0.546$). Jørgensen *et al.* also found a weak dependence of the factor -0.04 in the aperture correction on galaxy luminosity, in the sense that it varied from -0.02 in the smallest galaxies to -0.06 in the largest. We adopt a systematic error contribution of 25% of the aperture correction such that this systematic error scales with redshift as $\sim 0.01z$ dex

[5] It is not clear what aperture sizes were used by Kelson *et al.* (1997), who may have used a similar setup as our Keck/LRIS data.

for an aperture that is fixed in angular size.

In summary, for Abell 665 ($z = 0.181$) the internal uncertainties on the velocity dispersions are 0.02 dex per measurement due to variations among template spectra, the fitting uncertainties, and the uncertainties in the small aperture corrections, all added in quadrature. These internal uncertainties increase with redshift since the S/N typically decreases with redshift, such that the uncertainties are $\sim$ 0.04 dex for the lower S/N spectra at $z = 0.55$. The possible systematic errors rise to 0.011 dex at $z = 0.5$ due to the effects of analysis methodology (FF or CC), broadening methodology, and aperture corrections added in quadrature. These random uncertainties and systematic errors compare favorably with recent high quality velocity dispersion measurements for nearby galaxies (Jørgensen, Franx, & Kjærgaard 1995; Smith *et al.* 1997). The observations described here, however, do not have any significant overlap with other studies, hence the external random uncertainties and possible systematic errors are not constrained.

The redshifts and central velocity dispersions are provided in Tables 6.8 to 6.13.

6.3.5 Measurement of Line Indices

The most common set of line indices that are measured for early–type galaxies are those defined by the Lick group (see Trager *et al.* 1998 for a summary), which are based on a series of observations between 1972 and 1984 of Galactic stars and nearby galaxies with the Image Dissector Scanner at the Lick 3 m Shane Telescope. This study is noteworthy for its large size and wide variety of objects studied with a common instrumental setup; the stellar populations models of Worthey (1994), and more recent studies such as Worthey & Ottaviani (1997), have been constructed to exploit fully these data by direct comparisons with models. An additional large sample of index measurements has been made by Jørgensen (1998) onto this system, thereby supplementing the largely field galaxy sample of Trager *et al.* (1998) with many early–type galaxies in rich clusters of galaxies. The major drawbacks of the IDS, however, are its low resolution and peculiar noise properties. Nonetheless, the galaxy observations acquired and published with this setup over many years provide a good baseline with which to compare other observations of early–type galaxies, both nearby and at high redshifts.

Some of the definitions for the Lick IDS indices have changed over the years. The definitions that are adopted here are taken from Trager *et al.* (1998) for all indices except:

Table 6.8: Spectroscopic Properties for Galaxies in Abell 655

Galaxy ID	z	$\log \sigma_0$ (km s^{-1})	$\pm$	Hδ_F (Å)	G4300 (Å)	Hγ_F (Å)	C$_2$4668 (Å)	Hβ_G (Å)	Mg$_2$ (mag)	Mg$_b$ (Å)	Mg$_2^*$ (mag)	$\langle$Fe$\rangle$ (Å)
1	0.1291	2.582	0.005	-0.32	4.05	-1.71	4.76	2.07	0.379	4.17	0.262	1.40
2	0.1263	2.417	0.010	0.09	4.87	-1.47	7.97	1.94	0.369	5.32	0.330	2.79
3	0.1213	2.213	0.011	0.88	5.71	-1.68	5.60	1.33	0.422	6.21	0.373	3.56
5	0.1248	2.451	0.006	6.62	9.04	-2.06	6.91	1.77	0.372	5.19	0.323	3.13
7	0.1248	2.366	0.011	0.45	4.87	-0.72	7.23	2.12	0.328	5.50	0.339	3.15
10	0.1257	2.330	0.012	0.60	4.99	-1.35	5.09	2.39	0.346	6.03	0.365	2.44
11	0.1306	2.162	0.024	0.60	5.08	-0.91	3.30	1.99	0.360	4.75	0.299	3.23
19	0.1329	2.315	0.009	2.99	10.30	-2.84	3.69	0.53	0.374	10.33	0.514	3.79
23	0.1387	2.259	0.005	-3.19	-1.18	0.35	-0.37	-0.20	-0.271	3.21	0.191	···
25	0.1306	2.396	0.011	1.25	6.87	-1.82	4.50	0.73	0.382	4.81	0.302	3.65
26	0.1294	2.103	0.007	2.82	7.90	-1.00	5.53	1.49	0.344	4.74	0.298	2.65
27	0.1312	2.320	0.004	2.67	5.11	-2.17	4.83	1.11	0.501	4.57	0.288	4.83
31	0.1332	2.443	0.006	-0.15	5.62	-1.11	4.80	1.32	0.379	5.48	0.338	3.33
33	0.1227	1.982	0.019	-0.64	7.17	-0.77	4.39	4.08	0.326	4.39	0.277	3.82
44	0.1315	1.954	0.010	5.12	6.10	2.17	3.00	0.81	0.356	4.34	0.274	1.45
45	0.1240	2.182	0.018	2.35	7.44	-1.53	4.51	1.11	0.366	3.64	0.225	2.90
48	0.1304	2.211	0.005	1.01	7.56	-3.87	5.23	0.50	0.502	7.14	0.412	2.40
49	0.1244	2.050	0.016	2.76	7.60	0.85	1.71	4.51	0.341	3.78	0.235	2.49
56	0.1303	2.063	0.008	4.64	9.21	-2.21	6.11	0.95	0.417	4.19	0.264	3.91
57	0.1303	2.192	0.011	1.46	4.71	-0.98	4.17	1.51	0.393	4.71	0.297	3.03
58	0.1300	2.291	0.005	2.54	10.32	-2.22	4.55	1.81	0.380	4.26	0.269	2.38
75	0.1328	2.225	0.005	-0.31	7.98	0.30	9.05	0.57	0.415	3.49	0.213	2.96
79	0.1357	2.151	0.013	0.06	4.97	0.90	6.81	1.34	0.508	4.84	0.304	2.61
82	0.1261	1.924	0.011	0.73	9.40	-2.02	4.37	3.22	0.471	4.04	0.254	1.67
105	0.1362	1.993	0.063	-2.97	-5.53	2.00	-2.63	-2.71	0.326	0.67	-0.243	0.99
110	0.1249	1.988	0.064	2.13	6.26	0.58	1.88	4.50	0.197	0.36	-0.419	···
132	0.1248	1.673	0.000	-1.62	3.76	-0.05	8.09	5.57	0.312	2.85	0.157	···

Table 6.9: Spectroscopic Properties for Galaxies in Abell 665

Galaxy ID	z	$\log \sigma_0$ (km s^{-1})	$\pm$	Hβ_G (Å)	Mg$_2$ (mag)	Mg$_b$ (Å)	Mg$_2^*$ (mag)	$\langle$Fe$\rangle$ (Å)
3	0.1786	2.439	0.013	1.90	0.304	5.02	0.314	3.32
11	0.1803	2.515	0.011	2.21	0.323	5.38	0.333	3.44
15	0.1847	2.414	0.021	2.16	0.288	4.73	0.298	2.12
17	0.1823	2.448	0.009	1.11	0.288	4.83	0.303	2.84
18	0.1857	2.412	0.021	2.22	0.273	4.31	0.272	2.36
25	0.1842	2.279	0.028	2.57	0.244	3.85	0.240	2.87
26	0.1905	2.355	0.024	2.52	0.268	4.44	0.280	3.38
35	0.1907	2.303	0.018	1.78	0.194	2.79	0.151	2.60
38	0.1867	2.461	0.012	2.07	0.296	4.89	0.307	2.50
42	0.1861	2.395	0.018	2.04	0.313	4.94	0.310	2.84
49	0.1812	2.264	0.029	2.14	0.263	4.38	0.276	3.30
57	0.1888	2.325	0.021	2.06	0.268	4.52	0.285	2.66
61	0.1727	2.358	0.012	2.06	0.255	4.62	0.291	2.27
64	0.1719	2.080	0.037	2.33	0.254	4.08	0.256	2.44
68	0.1825	2.306	0.026	2.09	0.280	4.45	0.280	2.31
74	0.1714	1.976	0.047	2.54	0.203	3.17	0.187	1.92
77	0.1830	2.173	0.030	1.88	0.251	3.98	0.250	2.34
80	0.1831	2.276	0.028	2.44	0.252	4.37	0.276	2.64
97	0.1878	2.208	0.033	2.31	0.241	3.49	0.213	2.30

Table 6.10: Spectroscopic Properties for Galaxies in Abell 2390

Galaxy ID	z	$\log \sigma_0$ (km s^{-1})	$\pm$	Hβ_G (Å)	Mg$_2$ (mag)	Mg$_b$ (Å)	Mg$_2^*$ (mag)	$\langle$Fe$\rangle$ (Å)
2	0.2281	2.425	0.013	2.05	0.289	4.75	0.298	2.91
6	0.2303	2.313	0.017	1.94	0.272	4.26	0.269	2.85
7	0.2466	2.277	0.019	1.81	0.220	4.06	0.255	2.43
9	0.2192	2.371	0.011	1.94	0.296	4.67	0.294	2.64
10	0.2282	2.250	0.020	2.26	0.288	4.42	0.279	2.57
24	0.2293	2.461	0.015	1.97	0.294	4.80	0.302	2.94
28	0.2266	2.157	0.025	2.61	0.271	4.49	0.283	2.27
33	0.2250	2.305	0.022	2.21	0.273	4.56	0.287	3.05
41	0.2235	2.166	0.030	1.82	0.258	3.52	0.216	3.05
44	0.2277	2.139	0.026	2.18	0.264	4.18	0.264	2.90
46	0.2326	2.208	0.022	2.54	0.226	4.30	0.271	2.25
91	0.2376	1.804	0.042	1.62	0.223	3.83	0.239	3.00
112	0.2281	1.966	0.039	1.89	0.226	3.94	0.247	2.49
138	0.2327	2.029	0.017	1.72	0.238	4.42	0.279	3.48
Galactic Star								
8	0.0000	...	...	...	...	...	...	...

Table 6.11: Spectroscopic Properties for Galaxies in Abell 370

Galaxy ID	z	$\log \sigma_0$ (km s^{-1})	$\pm$	Hβ_G (Å)	Mg$_2$ (mag)	Mg$_b$ (Å)	Mg$_2^*$ (mag)	$\langle$Fe$\rangle$ (Å)
1	0.3781	2.519	0.005	2.07	0.294	4.99	0.312	3.96
2	0.3728	2.404	0.007	1.73	0.258	4.42	0.279	2.06
3	0.3674	2.500	0.006	2.05	0.252	5.29	0.328	3.03
4	0.3658	2.463	0.006	2.18	0.240	4.44	0.280	3.21
10	0.3761	2.291	0.009	2.02	0.266	5.22	0.325	2.94
15	0.3848	2.463	0.006	2.21	0.328	5.20	0.324	2.94
20	0.3717	2.430	0.010	2.23	0.302	4.79	0.301	1.82
24	0.3766	2.399	0.007	1.86	0.274	4.60	0.290	2.95
28	0.3790	2.345	0.008	2.36	0.231	3.25	0.194	3.80
41	0.3699	2.467	0.009	1.96	0.261	4.81	0.302	2.94
51	0.3826	2.279	0.010	1.93	0.289	3.88	0.243	2.50
67	0.3738	2.207	0.011	2.35	0.188	4.07	0.256	1.29
71	0.3785	2.242	0.016	2.12	0.260	4.09	0.257	2.76
77	0.3673	1.976	0.019	2.82	0.166	4.38	0.276	2.75
79	0.3636	2.227	0.011	2.54	0.214	3.97	0.249	3.02
SER2	0.3660	2.074	0.015	1.85	0.205	3.57	0.220	2.53
16=A02	0.3633	2.432	0.040	1.51	···	4.98	0.312	···
14=A03	0.3601	2.432	0.040	2.87	···	4.81	0.302	···
18=A13	0.3774	2.399	0.040	1.25	···	4.66	0.293	···
17=A17	0.3818	2.333	0.040	1.94	···	4.12	0.259	···
8=A23	0.3680	2.448	0.040	2.17	···	4.81	0.302	···
11=A28	0.3709	2.390	0.040	1.87	···	4.73	0.298	···
5=A32	0.3686	2.268	0.040	1.80	···	3.79	0.236	···
Foreground Early–Type Galaxy								
33	0.3045	2.325	0.013	2.31	0.215	4.50	0.284	4.09
Background Emission Line Galaxy								
SER1	0.4213	···	···	···	···	···	···	···

Table 6.12: Spectroscopic Properties for Galaxies in Abell 851

Galaxy ID	z	$\log \sigma_0$ (km s^{-1})	$\pm$	Hβ_G (Å)	Mg$_2$ (mag)	Mg$_b$ (Å)	Mg$_2^*$ (mag)	$\langle$Fe$\rangle$ (Å)
4	0.4091	2.407	0.011	2.01	0.275	4.46	0.281	2.65
11	0.4028	2.423	0.014	1.97	0.259	5.03	0.315	2.87
16	0.4061	2.396	0.011	1.39	0.267	4.35	0.275	2.10
23	0.3942	2.273	0.019	2.38	0.233	3.75	0.233	2.33
44	0.4058	···	···	3.16	0.181	3.26	0.194	1.71
47	0.4027	2.328	0.013	1.75	0.283	5.75	0.352	2.85
48	0.4124	2.243	0.031	2.65	0.201	3.69	0.228	2.50
56	0.4078	2.090	0.022	2.06	0.239	3.38	0.204	2.51
57	0.4062	2.299	0.018	1.54	0.261	4.86	0.305	2.45
69	0.4008	2.288	0.014	1.88	0.204	4.12	0.259	2.55
88	0.4080	1.633	0.010	4.42	0.042	0.67	0.042[a]	1.87
97	0.3987	1.750	0.016	2.54	0.101	2.60	0.132	2.37
102	0.3985	2.173	0.018	2.93	0.129	3.04	0.175	2.14
111	0.3925	1.766	0.031	3.27	0.115	1.33	0.115[a]	1.74
Foreground Early–Type Galaxies								
3	0.2805	2.352	0.008	···	0.235	3.80	0.237	3.15
5	0.2813	2.328	0.008	···	0.284	4.54	0.286	1.10
6	0.2807	2.276	0.014	2.06	0.291	4.54	0.286	2.36
103	0.2816	1.722	0.017	1.13	0.183	2.34	0.102	1.06
Background Emission Line Galaxy								
113	0.4594	···	···	···	···	···	···	···

Table 6.13: Spectroscopic Properties for Galaxies in MS0015.9+1609

Galaxy ID	z	$\log \sigma_0$ (km s^{-1})	$\pm$	Hδ_F (Å)	G4300 (Å)	Hγ_F (Å)	C$_2$4668 (Å)	Hβ_G (Å)
2	0.5392	2.412	0.018	0.65	5.84	-1.77	7.33	2.24
7	0.5511	2.291	0.009	0.67	6.05	-2.01	9.64	1.61
8	0.5450	2.318	0.013	1.49	5.36	0.14	8.93	2.54
13	0.5449	2.422	0.017	0.81	6.63	-0.81	8.60	2.30
16	0.5540	2.339	0.017	0.67	4.05	-0.74	6.13	-0.53
22	0.5352	2.269	0.020	2.26	5.54	0.13	7.74	2.45
25	0.5342	2.317	0.026	2.40	4.58	0.15	4.60	3.29
26	0.5254	2.494	0.018	1.21	5.50	-0.42	4.24	2.23
28	0.5503	2.333	0.013	1.06	5.82	-0.11	9.14	2.63
31	0.5384	2.200	0.023	1.05	4.75	-1.11	8.24	2.51
44	0.5416	2.200	0.023	1.05	5.35	-0.21	8.16	0.92
48	0.5480	2.315	0.013	-1.19	6.74	-1.15	5.35	1.60
56	0.5418	2.337	0.017	0.43	6.60	0.28	6.94	1.62
63	0.5505	2.297	0.018	1.34	7.35	-1.81	5.98	1.99
74	0.5416	2.220	0.022	2.27	6.15	-0.45	8.03	3.19
"K+A" Galaxies								
24	0.5536	...	...	...	...	...	...	...
34	0.5542	...	...	...	...	...	...	...
Background "K+A" Galaxies								
4	0.6559	...	...	...	...	...	...	...
41	0.6550	...	...	...	...	...	...	...
Galactic Stars								
3	0.0000	...	...	...	...	...	...	...
6	0.0000	...	...	...	...	...	...	...
29	0.0000	...	...	...	...	...	...	...
33	0.0000	...	...	...	...	...	...	...
Ser1	0.0000	...	...	...	...	...	...	...
Ser2	0.0000	...	...	...	...	...	...	...
Unknown								
46	...	...	...	...	...	...	...	...
67	...	...	...	...	...	...	...	...

Hβ_G was taken from Jørgensen (1998), and Hδ_F and Hγ_F were taken from Worthey & Ottaviani (1997). These latter two indices are narrower than most Lick IDS indices, and were constructed in order to provide a stronger dependence on age than metallicity. The index name "$C_2$4668" (Trager *et al.* 1998) is adopted here rather than the more historical name "Fe4668." An additional composite index was also added: $\langle \mathrm{Fe} \rangle$ = (Fe5270+Fe5335)/2.

Since the IDS data have poor instrumental resolution compared to all of the data described in this paper, it is necessary to smooth these high redshift data to the IDS resolution. For some data sets, such as Abell 370 ($z = 0.37$) which has < 1.5 Å FWHM resolution in the rest–frame, this procedure is quite draconian. As shown by Worthey & Ottaviani (1997), the IDS resolution is 8.6 Å FWHM at $\lambda \sim 5000$ Å, and deteriorates to ~ 10.0 Å at $\lambda \sim 4300$ Å and $\lambda \sim 6000$ Å. Since all of the clusters, with the exception of MS0015.9+1609, were observed at rest–frame $\lambda_0 \sim 5000$ Å, these data have been smoothed to 8.6 Å FWHM. The data for MS0015.9+1609 were centered at the G–band ($\lambda \sim 4306$ Å), so they were smoothed to ~ 10.0 Å FWHM.

The Lick indices are defined for the Galactic stars observed with the IDS instrumental setup, hence the velocity dispersions of other galaxies must be accounted for since this effect will broaden light beyond the width of the absorption features. A series of tests in which the high redshift galaxy spectra, already broadened once to bring them to the nominal IDS instrumental resolution, were further broadened to simulate the effects of various velocity dispersions. These tests showed that the corrections for each index for the effects of velocity dispersion were effectively identical to those found by Trager *et al.* (1998). For this reason, the corrections in Trager *et al.* were adopted. Two of the bluest absorption features, Hδ_F and Hγ_F, which were subsequently defined by Worthey & Ottaviani (1997), are not included in the Trager *et al.* corrections, so new corrections were derived for these indices:

$$\begin{aligned} \mathrm{H}\delta_F^{\mathrm{corr}} &= \mathrm{H}\delta_F^{\mathrm{obs}}(1 - 5.88 \times 10^{-7}\sigma^2) \\ \mathrm{H}\gamma_F^{\mathrm{corr}} &= \mathrm{H}\gamma_F^{\mathrm{obs}}(1 + 1.04 \times 10^{-7}\sigma^2) \end{aligned} \tag{6.1}$$

where Hγ_F is particularly insensitive to velocity dispersion effects, reaching only $\sim 2\%$ for σ as large as 450 km s^{-1}.

Significant line strength gradients exist in many galaxies and in many line indices, with the possible exception of Hβ (Davies, Sadler, & Peletier 1993). This property affects the

line strengths measured in a fixed aperture, much like velocity dispersion gradients cause $\sigma(r)$ to be smaller than σ_0 as r increases. Following Jørgensen (1998), aperture corrections are made to the line indices in the same manner as for velocity dispersions, although their relative sizes vary slightly. In particular, Mg_2 is corrected by $\alpha \log(r_{ap}/r_{norm})$, where r_{norm} is defined as 1.7 arcsec at the distance of the Coma cluster and $\alpha = 0.04$. The other indices are defined differently, so their corrections are of the form $\log(\mathrm{index})_{norm} = \log(\mathrm{index})_{ap} + \alpha \log(r_{ap}/r_{norm})$; for Mg_b and all Fe indices $\alpha = 0.05$, while for $C_2 4668$ $\alpha = 0.08$. The Hβ_G index has no aperture correction applied, since line–strength gradients in this index are either small or consistent with no gradient (Davies *et al.* 1993).

Note that for the same reasons mentioned above in §6.3.4, the use of small observed apertures in the present study result in only very small aperture corrections being applied to the data. Once again, this is in direct contrast to the measurements of Ziegler & Bender (1997), many of whose Mg_b measurements at $z = 0.37$ are possibly suspect due to the fact that the least luminous galaxies—those probably having $r_{\mathrm{eff}} \ll 1$ arcsec—were observed through an extremely large aperture of 3.6×3.6 arcsec^2. Furthermore, the exact form of the aperture correction is important for the Ziegler & Bender data: their correction to Mg_b could vary substantially and systematically along the galaxy sequence if different assumptions for r_{eff} were made (i.e., see their Equation 19), therefore possibly changing the conclusions reached on the basis of such data.

The presence of a small amount of emission can be superimposed on the Hβ_G index, thereby reducing its line strength. One way to estimate this effect is by looking at the strength of [O III] line at $\lambda = 5007$ Å, assuming an emission line ratio between [O III] and Hβ_G, and then correcting the observed values of Hβ_G for the effect. Any galaxies with strong emission lines have been excluded from the sample in the present paper, as have galaxies exhibiting "K+A" spectra. There is no direct evidence for [O III] emission from inspection of the spectra, hence no correction has been applied to the Hβ_G indices. Jørgensen (1998) also applied no Hβ_G emission correction to the indices measured for that nearby galaxy sample, although both Gonzalez (1993) and Trager *et al.* (1998) did.

We have selected several key line indices for inclusion in the tables. For the clusters at $0.18 < z < 0.41$, the rest–frame wavelength studied spanned Hβ_G to Fe5335, so the indices tabulated are Hβ_G, Mg_2, Mg_b, and $\langle \mathrm{Fe} \rangle$. For MS0015.9+1609 at $z = 0.546$, the spectra were centered on the G–band $\lambda \sim 4306$ Å in the rest–frame, so the indices tabulated are

Hδ_F, G4300, Hγ_F, $C_2$4668, and Hβ_G. For Abell 655 at $z = 0.129$, the larger wavelength coverage allows for all of the above indices to be measured.

The Lick indices were measured from IDS spectra that were not flux calibrated. Measurements with other instruments, however, typically flux calibrate their spectra prior to measuring the indices. Worthey & Ottaviani (1997) compared two different data sets—data from the MDM observatory which were not flux calibrated, and other data from Jones (1996) that were flux calibrated—and showed that there were only very small median shifts for both data sets in the zero–points for the atomic line indices such as Mg_b and Fe. The broad molecular line indices such as Mg_1 and Mg_2, however, show a significant offset (0.05 mag for Mg_2) between the MDM data set that was not flux calibrated and the Lick IDS line indices, as indicated by stars observed in common between the two samples.

The relationship between the Mg_2 and Mg_b indices is a good check on systematics in measuring both quantities, in particular in identifying if the lack of flux calibration affects the measurements of the broad Mg_2 index. This relation between the two indices for nearby galaxies (from Jørgensen 1998), and the data from this paper for the high redshifts galaxies, are plotted in Figure 6.14. The Abell 665 and Abell 2390 data show little or no offset, the Abell 370 and Abell 851 data have Mg_2 that is somewhat too small for their Mg_b, and the Abell 655 data have Mg_2 significantly larger for their Mg_b. The Mg_b indices will be adopted here; all subsequent references to Mg_2 will be calculated from the Mg_b measurements using the Jørgensen (1998) conversion

$$Mg_2^* = 0.638 \log\ Mg_b - 0.133. \tag{6.2}$$

We note that Ziegler & Bender (1997) also measured Mg_b at $z = 0.37$—for reasons of lower instrumental resolution and problematical sky subtraction—which they compared to Mg_2 measurements of nearby elliptical galaxies.

Since the spectra in the present paper are not spectrophotometric, there are atmospheric absorption features which remain in the spectra. The absorption for $\lambda > 7590$ Å contaminates the sideband for the Hβ_G index for $z > 0.54$, and the Fe5335 index (used in the $\langle$Fe$\rangle$) for $z > 0.412$. The latter only affects one galaxy, but the former systematically affects MS0015.9+1609 since the mean redshift of the cluster if $z = 0.546$. Hence, for MS0015.9+1609 the standard absorption feature Hβ, as is used by Trager *et al.* (1998), was

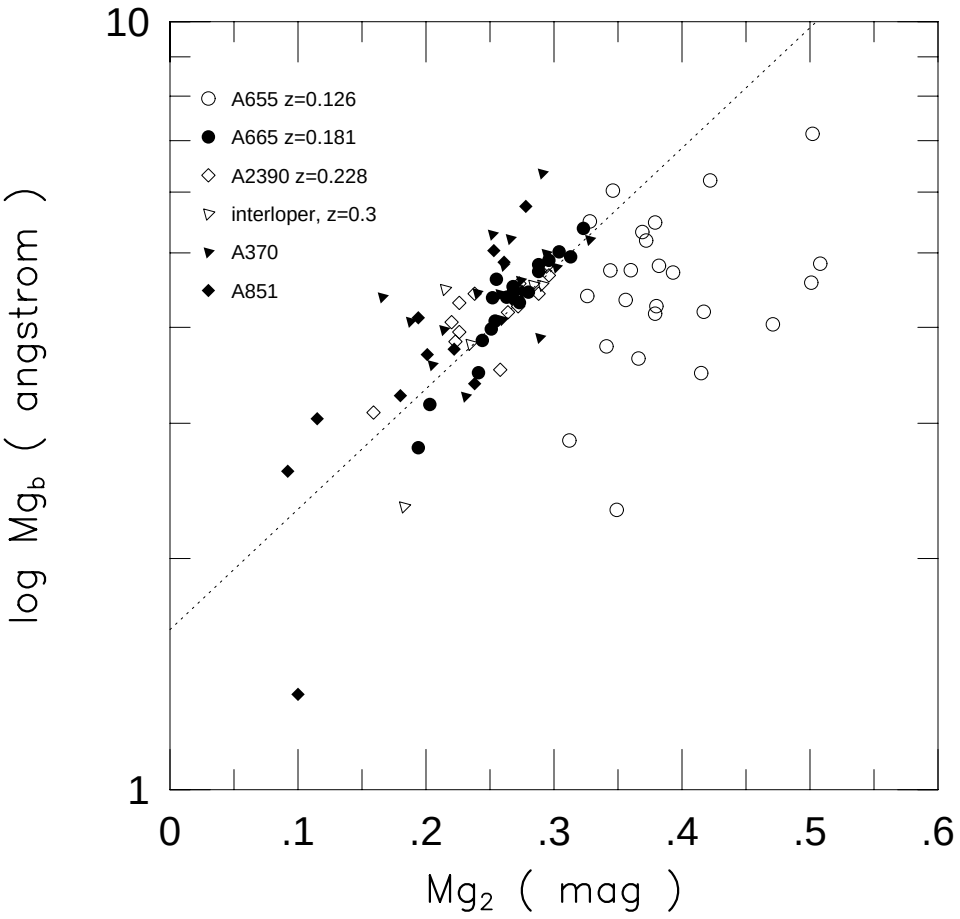

Figure 6.14: Comparison of Mg_2 and Mg_b for high redshift galaxies observed. Since the observations were not flux calibrated, this diagram is a useful diagnostic for possible systematic shifts between the narrow Mg_b index, which should be relatively unaffected, and the broadband Mg_2 index, which might be significantly affected. The dotted line is the relationship between the two indices from Jørgensen (1998). The Abell 665 and Abell 2390 data show little or no offset, the Abell 370 and Abell 851 data have Mg_2 that is somewhat too small for their Mg_b, and the Abell 655 data have Mg_2 significantly larger for their Mg_b.

adopted and converted to Hβ_G using the relationship from Jørgensen (1997):

$$\mathrm{H}\beta_G = 0.866\mathrm{H}\beta + 0.485. \tag{6.3}$$

Another atmospheric line absorbs $6865 < \lambda < 6885$ Å, therefore affecting Hβ_G sidebands at $0.392 < z < 0.427$ and Hβ sidebands at $0.404 < z < 0.426$. It only affects the Hβ_G line itself for $0.409 < z < 0.419$. This is an issue for Abell 851 at a mean cluster redshift of $z = 0.404$, for which two galaxies (# 4 and 48) are affected. For Abell 851 this narrow atmospheric line was interpolated across interactively and caution must be exercised when using these Hβ_G measurements. This atmospheric line also affects the $\langle$Fe$\rangle$ sidebands for galaxies at $0.280 < z < 0.316$, but since only interloper galaxies were found in this survey within this redshift range, no attempt was made at correction.

The line indices are provided in Tables 6.8 to 6.13.

6.3.6 Spectroscopic Parameters From the Literature

There have only been a few measurements of velocity dispersions and line indices for early–type galaxies at redshifts $0.1 < z < 0.6$ that could supplement the present study or provide external consistency checks on galaxies observed in common. In all of the studies in the literature to date (see Table 6.1) which are appropriate to investigations of the elliptical galaxy scaling relations, there have been only 51 measurements of velocity dispersions. While Franx (1993) pioneered the field with observations of Abell 665 ($z = 0.181$), the seven galaxy observations (one of which has "K+A" spectral type) are neither tabulated nor identified in finding charts, hence there is no possible comparison with those data. Two of the galaxies observed by Kelson *et al.* are also of "K+A" spectral type. Accounting for both of these issues reduces the total number of galaxies with velocity dispersions in the literature to 42. The present study will add an additional 110 galaxies (two of which are in common with previous observations in the literature) to more than triple the total number available.

Observations of central velocity dispersions nine galaxies in ZwCL0024+1652 at $z = 0.39$ were presented by van Dokkum & Franx (1996), although only seven appear to have early–type spectra and three of those are morphologically problematical (one has a triple nucleus, another is a probable spiral galaxy, and the third is SB0 morphological type). Since they

Table 6.14: Photometric and Spectroscopic Properties for Galaxies in ZwCL0024+1652

Galaxy ID	$\log r_{\rm eff}$ (arcsec)	$\log r_{\rm eff}$ (kpc)	$\pm$	$\langle\mu_{K_s}\rangle_{\rm eff}$ (mag/$''$)	$\langle\mu_K\rangle_{\rm eff}^{corr}$ (mag/$''$)	$\pm$	$\langle\mu_V\rangle_{\rm eff}^{corr}$ (mag/$''$)	$\pm$	$\log\sigma_0$ (km s^{-1})	$\pm$
DGS111	0.078	0.738	0.095	18.08	17.24	0.05	22.61	0.20	2.193	0.040
DGS130	-0.142	0.518	0.039	16.79	15.95	0.05	20.91	0.20	2.386	0.040
DGS158	0.606	1.266	0.028	19.23	18.39	0.05	23.21	0.20	2.501	0.040
DGS161	0.674	1.334	0.077	19.29	18.45	0.12	22.72	0.20	2.439	0.040
DGS162	-0.035	0.625	0.156	17.32	16.48	0.05	23.18	0.20	2.223	0.040
DGS169	0.598	1.258	0.057	19.04	18.20	0.05	22.10	0.20	2.534	0.040
DGS186	-0.023	0.637	0.056	16.86	16.02	0.05	22.77	0.20	2.582	0.040
DGS202	0.690	1.350	0.069	19.67	18.83	0.09	23.51	0.20	2.394	0.040

Note: Galaxy identifications (DGS) are from Dressler, Gunn, & Schneider (1985) and Schneider, Dressler, & Gunn (1986).

have corrected for aperture effects in the same manner as the present paper, no further corrections are needed.[6] These data are provided in Table 6.14. It is not clear what the selection criteria were for constructing this sample, as a significant percentage of the objects observed (14 in all) showed features that were inconsistent with an early–type galaxy at the cluster redshift. It is unclear whether they used selection criteria other than brightness and how easily the objects could be fit onto a single multi–slit mask.

The study of Ziegler & Bender (1997) observed 21 galaxies in three clusters at $z = 0.37$, one of which is cluster Abell 370. The Ziegler & Bender measurements for Abell 370 are included in Table 6.11. They provide central velocity dispersions σ_0, Mg$_b$ indices, and Hβ indices. The aperture corrections are modified to be consistent with our method: $\Delta\log\sigma_0 = 0.043$ dex (instead of 0.042 dex), and $\Delta\log{\rm Mg}_b({\rm mag}) = 0.054$ dex (instead of the constant offset $\Delta{\rm Mg}_b = 0.60$ mag). Their Hβ indices are converted to Hβ_G using the relation from Jørgensen (1998) of H$\beta_G = 0.866{\rm H}\beta + 0.485$, and we do not apply their correction for emission possibly contaminating Hβ measurements. There are two galaxies in common: galaxy # 1 (corresponding to their ID=A20) is measured here to have $\log\sigma_0 = 2.519$ and Mg$_b = 4.99$ mag while they find $\log\sigma_0 = 2.478$ and Mg$_b = 4.51$ mag; and galaxy # 24 (their ID=A18) for which we measure $\log\sigma_0 = 2.399$ and Mg$_b = 4.60$ mag while they measure $\log\sigma_0 = 2.363$ and Mg$_b = 4.33$ mag. The velocity dispersion measurements individually

[6]Object # 218 on the list of van Dokkum & Franx (1996) does not appear on the lists of Dressler, Gunn, & Schneider (1985) or Schneider, Dressler, & Gunn (1985). The identification of this source is currently unknown, and hence not included here.

agree to < 0.05 dex with no statistically significant mean offset, while the Mg_b measurements differ by a mean offset of 0.38 mag, with only $\sim 20\%$ of that offset being explainable by the differences in assumed aperture corrections. Ziegler & Bender used selection by a single color in constructing their sample, so their selection criteria are similar to those employed by the present paper. Furthermore, all of their galaxies in Abell 370 satisfy the selection criteria adopted in the present paper (see §6.2 and Pahre 1998b, Chapter 5 of this thesis), so there is probably little or no practical difference between the two different approaches.

Kelson *et al.* (1997) measured central velocity dispersions for ten galaxies (two of which are of "K+A" spectral type) in cluster MS1358.4+6245 at $z = 0.33$ and five galaxies in cluster MS2053.7-0447 at $z = 0.58$.[7] As described below in §6.4, the present paper includes near–infrared imaging observations of galaxies in the latter cluster, and hence only those central velocity dispersions from Kelson *et al.* for MS2053.7-0447 are relevant to this paper. Since their method of aperture correction is similar to the one adopted in the present paper, no additional corrections need to be applied. Kelson *et al.* used a color selection in an attempt to exclude blue field galaxies, but the size of the color window adopted is not specified. All five galaxies in MS2053.7-0447 satisfy the $(V - I_{\mathrm{C}})$ color–magnitude constraints adopted in the present paper (see §6.2 and Pahre 1998b, Chapter 5 of this thesis), hence there is probably little practical difference between the two selection methods. We will assume that their selection criteria are similar to those of the present paper, since the color window adopted in our selection criteria (see §6.2 and Pahre 1998b, Chapter 5 of this thesis) typically allowed a large color range of ±0.3–0.5 mag from the mean color–magnitude relation in $(U - V)_0$ versus V_0. Their velocity dispersions are provided in Table 6.15.

6.4 Photometry

6.4.1 K–band Imaging

Near–infrared imaging using a K_s filter of Abell 655, Abell 665, ZwCL0024+1652, Abell 851, MS0015.9+1609=CL0016+16, and MS2053.7-0447 was obtained using the Prime Focus Infra-Red Camera (PFIRCam) with a NICMOS–3 256×256 pixel^2 HgCdTe array (produced

[7] While Kelson *et al.* used the same instrument (Keck/LRIS) as the present paper, and hence most certainly observed many more galaxies on each multi–slit mask, they have narrowed their sample presented to include only those galaxies also within the FOV of the HST/WFPC–2 images available at that time. This is no doubt the reason why the number of galaxies in their sample is small at each redshift.

Table 6.15: Photometric and Spectroscopic Properties for Galaxies in MS2053.7-0447

Galaxy ID	$\log r_{\rm eff}$ (arcsec)	$\log r_{\rm eff}$ (kpc)	$\pm$	$\langle\mu_{K_s}\rangle_{\rm eff}$ (mag/$''$)	$\langle\mu_K\rangle_{\rm eff}^{corr}$ (mag/$''$)	$\pm$	$\langle\mu_V\rangle_{\rm eff}^{corr}$ (mag/$''$)	$\pm$	$\log\sigma_0$ (km s^{-1})	$\pm$
K311	-0.482	0.268	0.226	16.87	15.46	0.05	20.52	0.20	2.348	0.049
K197	0.412	1.162	0.081	19.23	17.82	0.20	22.03	0.20	2.504	0.025
K422	-0.075	0.675	0.226	18.71	17.30	0.37	20.68	0.20	2.199	0.061
K551	-0.459	0.291	0.269	17.39	15.98	0.19	19.05	0.20	2.336	0.038
K432	-0.365	0.385	0.289	17.47	16.06	0.28	20.82	0.20	2.207	0.054

Note: Object identifications (K) are from Kelson *et al.* (1997).

by Rockwell International) on the Palomar 5 m Hale Telescope in 1997 March and July. This instrument re-images the focal plane at 1:1 to produce a 0.494 arcsec projected pixel scale and 126×126 arcsec^2 field–of–view (FOV). Due to the large projected size of the pixels and the large aperture of the telescope, the sky background per pixel is quite high—even through a K_s filter—limiting exposures to 3 seconds to fill the pixel wells halfway to saturation. Six exposures were coadded in the readout electronics before writing to disk. The telescope was dithered ~ 10 arcsec in a random direction (and distance) between each set of six exposures. Since the galaxies observed spectroscopically in §6.3.1 were typically distributed across fields of size 2×7.3 arcmin^2 (Keck/LRIS) or 4×12 arcmin^2 (P200/COSMIC), it was necessary to mosaic three or four separate, overlapping pointings of the PFIRCam. Only one pointing was obtained for ZwCL0024+1652. Each of these individual pointings was 486 seconds for Abell 655 and Abell 665, 972 seconds for both ZwCL0024+1652 and Abell 851, and 1296 seconds for both MS0015.9+1609 and MS2053.7-0447. The seeing was typically 0.9 to 1.5 arcsec, such that the images marginally sampled, or slightly undersampled, the seeing. Since the instantaneous FOV is large for this instrument, there were usually many stars on the images to define the instrumental PSF.

Additional imaging using a K filter of Abell 2390, Abell 370, and MS0015.9+1609 was obtained with the Near–Infra-Red Camera (NIRC; Matthews & Soifer 1994) on the Keck I 10 m Telescope in 1994 October, 1995 June and October, and 1996 September and October. This instrument is located at the forward Cassegrain focus of the telescope and re-images the focal plane to produce a projected pixel scale of 0.15 arcsec on a InSb 256×256 pixel^2 array produced by the Santa Barbara Research Corporation. Six exposures of 10 seconds each were coadded in the readout electronics before writing an image to disk. The telescope was

dithered by 5–10 arcsec between exposures. Since the FOV of this instrument is small at 38× 38 arcsec^2, only 1–3 target galaxies could be imaged at a time. Typical exposure times were 660 seconds for Abell 2390 and Abell 370, and 1200 seconds for MS0015.9+1609. The seeing for these data ranged from 0.3 arcsec (MS0015.9+1609 observations in 1996 September) to 0.6 arcsec (some of the Abell 2390 and Abell 370 observations in 1995 October). Additional observations of a few galaxies in MS0015.9+1609 were obtained in 1996 October with $\sim$ 1 arcsec and variable seeing which were only used for galaxy # 74 (for which no other observations were available). Since the instantaneous FOV is small for this instrument (38×38 arcsec^2) there were usually few stars, if any, suitable for defining the instrumental PSF on the images (with the exception being Abell 2390, which is at moderately low Galactic latitude). Most of the observations were taken in continuous sequences, however, such that the PSF defined in one field could be used for other images taken near to the same time.

Data were reduced in the IRAF package using scripts written by one of the authors (M. A. P.) or with the package DIMSUM (written by P. Eisenhardt, M. Dickinson, and A. Stanford). The first step was to subtract a dark frame taken with the same exposure time. Flat fields were constructed from the data frames themselves, and sky frames were constructed from running medians of nine frames taken in time immediately before and after a given target frame. The frames were then registered using bright objects and integer pixel shifts, and averaged using a 3 σ clip to reject cosmic rays and warm pixels. Calibration was obtained by observations of the HST (E. Persson, private communication) or UKIRT (Casali & Hawarden 1992) faint standard stars, with the latter being used only for the Keck/NIRC observations of 1994 October. The Palomar data reach $K = 20$ mag at better than 5 σ confidence level (CL), while the Keck data reach $K = 21$ mag at the same CL.

The models of Worthey (1994) and Bruzual & Charlot (1996, as provided in Leitherer *et al.* 1996) were used to calculate k–corrections separately for the K and K_s filters. The solar metallicity and 11 Gyr old models were used in both cases. The agreement is better than 0.04 mag between the two models for all redshifts. The k–corrections are plotted as a function of redshift in Figure 6.15. At $z = 0.55$, the Worthey model predicts a difference of $k_{K_s} - k_K = 0.13$ mag, while the Bruzual & Charlot model predicts a difference of 0.11 mag.

The photometry was corrected for Galactic extinction using the values derived from the IRAS maps by Pahre (1998b, Chapter 5 of this thesis) for each cluster. The value of $A_B = 0.36$ mag was adopted for MS2053.7-0447. Extinction in the near–infrared K–band

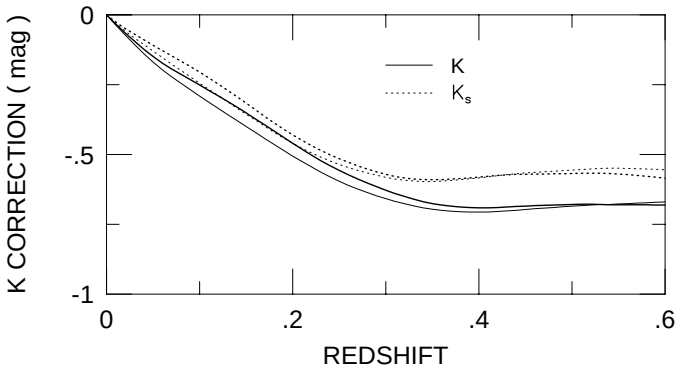

Figure 6.15: K–corrections for the K and K_s filters, in the sense that the value on the vertical axis should be subtracted from all observed magnitudes to correct them to zero redshift assuming no evolution. The K_s filter was used for the Palomar/PFIRCam data, while the K filter was used for the Keck/NIRC data. Two different spectral energy distributions were used to derive these corrections: Worthey (1994; thin line) and Bruzual & Charlot (1996, as provided in Leitherer *et al.* 1996; thick line). Data from both telescopes were acquired for MS0015.9+1609 at $z = 0.546$, which are predicted to show a 0.11 mag offset due to the different filter responses.

was taken to be $A_K = 0.085 A_B$.

6.4.2 Measuring Global Photometric Parameters

Two–dimensional elliptical galaxy models convolved with the instrumental PSF were fit directly to the pixel data $I_{x,y}$ in the final, reduced images. This procedure is similar to that found by van Dokkum & Franx (1996). This procedure typically required two steps: first, the stars were fit by various functional forms to determine the best fitting model to the PSF; and second, the target galaxies were fit by de Vaucouleurs models convolved with the PSF determined in the first step. The model forms used for the PSF were taken from IRAF package DAOPHOT (Lorentzian, Moffat, Gaussian, Penny, etc.). For all of these ground–based data, a Moffat function with $\beta = 2.5$ produced the smallest reduced chi–squared

χ^2/ν. The model for the galaxies was the de Vaucouleurs form

$$\begin{aligned} \Sigma_{x,y} &= \Sigma_{\rm e} \exp\left[-7.67\left(\tfrac{a}{a_{\rm e}}-1\right)^{0.25}\right] \\ a &= \sqrt{x_*^2+y_*^2} \\ x_* &= (x-x_0)\cos\theta + (y-y_0)\sin\theta \\ y_* &= \left[(y-y_0)\cos\theta - (x-x_0)\sin\theta\right]/(1-\epsilon) \end{aligned} \tag{6.4}$$

where a is the semi–major axis length, $a_{\rm e}$ is the half–light semimajor length, ϵ is the ellipticity, (x_0, y_0) is the centroid for a given star or galaxy, $\Sigma_{\rm e}$ is the isophotal surface brightness at $a = a_{\rm e}$, and (x_*, y_*) are transformed coordinates [from (x, y)] for position angle θ that places the semi–major axis parallel to the x_* axis. Using these equations, the effective radius $r_{\rm eff}$ and mean surface brightness $\langle\mu\rangle_{\rm eff}$ within the effective radius are

$$\begin{aligned} r_{\rm eff} &= a_{\rm e}\sqrt{(1-\epsilon)} \\ \langle\mu\rangle_{\rm eff} &= -2.5\log\Sigma_{\rm e} + 5\log s - 1.393 + \text{zeropoint} \end{aligned} \tag{6.5}$$

which provides $\langle\mu\rangle_{\rm eff}$ in units of mag arcsec^{-2} given the pixel scale s. A constant term to account for sky could be added to the model in Equation 6.4, but since this procedure will be used for measuring model parameters from near–infrared imaging data for which the sky has already been subtracted, we chose to assume the sky value is exactly zero. Tests done for several galaxy images demonstrated that the fitted value of the sky was usually very close to zero.

Minimization was done using the Levenberg–Marquardt algorithm using a program modified from Press *et al.* (1986) by one of the authors (M. A. P.) to handle two–dimensional arrays of data. The χ^2 statistic used was

$$\chi^2 = \sum_{x=1}^{i}\sum_{y=1}^{j} w_{x,y}\left[I_{x,y} - (\Sigma_{x,y}\circ P_{x,y})\right]^2/\sigma_{x,y}^2 \tag{6.6}$$

where $I_{x,y}$ is the pixel data, $\Sigma_{x,y}$ is the model of the galaxy (defined in Equation 6.4), $P_{x,y}$ is the model of the PSF, the galaxy image has size $i \times j$, $\sigma_{x,y}$ is the noise in each pixel, and $\circ$ denotes convolution. The model value $\Sigma_{x,y}$ for a given pixel was calculated using subpixellation of a factor of five in each dimension both to integrate across each pixel smoothly and to avoid spikes at small radii. A weighting function $w_{x,y}$ suggested in the IRAF package

DAOPHOT was applied that falls off as

$$w_{x,y} = \left(\frac{5}{5 + r'^2 / \left(1 - r'^2\right)} \right)^2 \tag{6.7}$$

where $r = \sqrt{(x - x_0)^2 + (y - y_0)^2}$ is the radius from the center of the object, $r' = r/r_{max}$, and r_{max} is the maximum fitting radius. The maximum fitting radius was typically chosen to be r_{max} =5–10 arcsec depending on the size of the galaxy and the seeing FWHM of the image. The computer program takes several seconds per iteration on a Sun Ultra 1/170 computer to fit a seeing–convolved model to a galaxy in a $\sim 50 \times 50$ pixel^2 image with the model sub-sampled 5×5 in each pixel. Between three and 20 iterations are required for good convergence, depending on the accuracy of the initial parameter estimates. Most of the computational time is spent on calculating the partial derivatives at each pixel for each iteration of the non–linear least squares algorithm.

As is well known, unique minimization of the parameters $\log r_{\rm eff}$ and $\langle\mu\rangle_{\rm eff}$ is often not achieved in practice since there is an extended valley with a χ^2 minimum. The quantity $\log r_{\rm eff} - 0.32\langle\mu\rangle_{\rm eff}$ is perpendicular to the direction of this χ^2 minimum valley, and hence this quantity can be measured in a highly accurate and robust manner. This is an extremely useful property of such model fitting, as this is the photometric quantity that enters the FP. For this reason, there is very little systematic error associated with the quantity $\log r_{\rm eff} - 0.32\langle\mu\rangle_{\rm eff}$ in the FP that is due to the extent of this χ^2 minimum valley.

Multiple galaxies and stars which are overlapping in their light distributions can be fit simultaneously using this procedure. While it might be simpler to fit all objects in a given image simultaneously, the number of model parameters and pixels requires substantial computer memory and computational requirements. A faster way, which was taken here, is to fit only those objects in each pass which overlap with each other, a step which is similar to the DAOPHOT package's GROUP task, and then repeat for a new set of overlapping objects.

Simulated stars and galaxies convolved with PSFs were constructed using the IRAF package ARTDATA and fit with the two–dimensional models using this procedure. The reduced chi–squared χ^2/ν was typically between 0.3 and 2.5, demonstrating that the models fitted to the data, as well as the noise model, are reasonable representations of the

properties of the simulated images. These simulations show that the model fitting typically underestimates $r_{\rm eff}$ by 5–35%, with the largest underestimations occurring for the smallest model galaxies explored (i.e., for $r_{\rm eff}$ less than the PSF FWHM). As expected, the quantity $\log r_{\rm eff} - 0.32\langle\mu\rangle_{\rm eff}$ showed a small scatter and no mean offset between the model fits and the input galaxy parameters. In order to rectify the underestimation of $r_{\rm eff}$, 20% has been added to all measurements of $r_{\rm eff}$ and $\Delta \log r_{\rm eff}/0.32 = 0.25$ mag arcsec^{-2} has been subtracted from all measurements of $\langle\mu\rangle_{\rm eff}$. We emphasize that this correction does not influence the photometric parameters entering the FP, but merely provides measurements of $r_{\rm eff}$ which can be more easily compared to measurements by other methods.

Tests were performed to estimate the effects of a bad estimate of the PSF on the model measurements of $r_{\rm eff}$ and $\langle\mu\rangle_{\rm eff}$. While $r_{\rm eff}$ varies systematically with the PSF width, in the sense that an underestimate of the PSF width yields an overestimate of $r_{\rm eff}$, the quantity $\log r_{\rm eff} - 0.32\langle\mu\rangle_{\rm eff}$ shows no systematic effects at the level of the internal uncertainties. The difficulty of estimating the PSF accurately (to better than 20%) for the Keck/NIRC observations, since not all the images have stars in the small FOV, therefore does not contribute to systematic errors in the model parameters that can affect the FP.

The model fits to the real data have $\chi^2/\nu \sim 0.5$ to 6, suggesting that the models are reasonable approximations to the light distributions of the early–type galaxies, and that the noise model is adequate. It is important to note that these values of χ^2/ν for fitting de Vaucouleurs models to elliptical galaxies are not unusual: even the best photometry and most detailed analysis produces similar χ^2/ν (Saglia *et al.* 1997). There are no doubt important structural effects in real ellipticals which deviate from even a bulge plus disk model for observations at any S/N (Saglia *et al.* 1997).

There are repeat observations available for eight galaxies in MS0015.9+1609, albeit taken through different filters. The k–correction models, as shown above in §6.4.1, predict a mean offset of 0.12 mag between the two filters at $z = 0.55$. The comparisons, expressed as differences in $(\log r_{\rm eff} - 0.32\langle\mu\rangle_{\rm eff})$, are shown in Figure 6.16. The model prediction for the offset is $0.32 \times 0.12 = 0.04$, while the mean observed offset is 0.07 ± 0.03. Excluding the most discrepant point, the scatter implies that the quantity $\log r_{\rm eff} - \langle\mu\rangle_{\rm eff}$ is measured to an accuracy of 0.05 dex, worse than for nearby galaxies. The internal uncertainties on the fits for the MS0015.9+1609 galaxies in the P200 data are ~ 0.1 dex in $\log r_{\rm eff}$, or even worse, since many of the galaxies have effective diameters very similar to the seeing FWHM

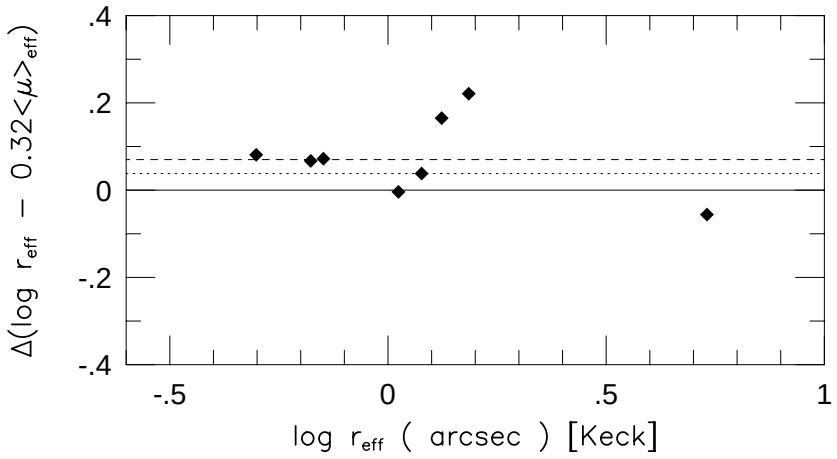

Figure 6.16: Comparison of model photometric fits in K and K_s filters for eight galaxies in MS0015.9+1609. The ordinate is in the sense of the P200 K_s quantity $\log r_{\rm eff} - \langle\mu_{K_s}\rangle_{\rm eff}$ minus the Keck K quantity $\log r_{\rm eff} - \langle\mu_K\rangle_{\rm eff}$. The model prediction for the offset is $0.32 \times 0.12 = 0.04$ mag (dotted line), while the mean observed offset is 0.07 ± 0.03 mag (dashed line). Excluding the most discrepant point, the scatter implies that the quantity $(\log r_{\rm eff} - \langle\mu_K\rangle_{\rm eff})$ is measured to an accuracy of 0.05 dex, which is significantly worse than for nearby galaxies.

of 1.2 arcsec. On the other hand, the internal uncertainties on the Keck data for the same cluster are all 0.01 to 0.06 dex, since the seeing for these data was 0.45 arcsec FWHM. So it is not surprising that there is a significant scatter between the two different measurements; it is actually quite remarkable that the systematic photometric offset in the fitted model parameters between the two data sets is consistent within the uncertainties to the prediction from the k–corrections.

The near–infrared measurements of $r_{\rm eff}$, $\langle\mu_K\rangle_{\rm eff}$, and $\langle\mu_K\rangle_{\rm eff}^{corr}$ (the latter has the surface brightness dimming and k–corrections applied) are provided in Tables 6.2 to 6.7 for the six clusters with new velocity dispersions, and in Tables 6.14 and 6.15 for the two clusters, ZwCL0024+1652 and MS2053.7-0447, with velocity dispersions taken from the literature.

6.4.3 Optical Global Photometric Parameters

Optical total magnitudes approximately sampling the rest–frame V–band were obtained by Pahre (1998b, Chapter 5 of this thesis) as part of the construction of the galaxy sample in each cluster. Total magnitudes are taken from that study for each of the galaxies, which

are corrected by -0.3 mag to account for the flux missed by FOCAS in estimating the total magnitude; this correction was derived using simulated images of galaxies. Under the assumption that $r_{\rm eff}$ is the same in the optical and the near–infrared, which is not strictly true but can be used operationally for this purpose, then the mean surface brightness $\langle\mu_V\rangle_{\rm eff}$ evaluated at the effective radius is

$$\langle\mu_V\rangle_{\rm eff} = m_{\rm tot} + 5\log r_{\rm eff} + 2.5\log 2\pi. \tag{6.8}$$

Calculations of k–corrections from the observed filter into rest–frame V–band were also done by Pahre (1998b, Chapter 5 of this thesis), which are applied here. Finally, these surface brightnesses are corrected for dimming with redshift. An uncertainty of 0.2 mag is adopted for $\langle\mu_V\rangle_{\rm eff}^{corr}$ calculated in this manner.

For the cases where there are no total magnitudes from Pahre (1998b, Chapter 5 of this thesis), as is the case for both ZwCL0024+1652 and MS2053.7-0447, then the value of $\langle\mu_V\rangle_{\rm eff}$ is adopted from van Dokkum & Franx (1996) or Kelson *et al.* (1997), respectively. These values are corrected for the difference between the optical and near–infrared measurements of $r_{\rm eff}$ using $\Delta\langle\mu_V\rangle_{\rm eff} = 0.32(\log r_{\rm eff,K} - \log r_{\rm eff,V})$.

These optical photometric parameters are included in Tables 6.2 to 6.7, Table 6.14, and 6.15.

6.5 Summary

This paper presents spectroscopy of 110 early–type galaxies, and near–infrared photometry of 128 early–type galaxies in six distant clusters at $0.1 < z < 0.6$. This large sample more than quadruples the number of galaxy observations available in the literature which are suitable for investigations of the Fundamental Plane correlations at high redshift.

This sample of data is ideally suited for follow–up studies of the early–type galaxy correlations (the Fundamental Plane), their evolution, and the investigation of the Tolman surface brightness dimming cosmological test. The data also provide line strength measures that may indicate the stellar content of distant, early–type galaxies. All of these aspects will be investigated in a future contribution (Pahre, Djorgovski, & de Carvalho 1998c, Chapter 7 of this thesis).

Acknowledgments

Many thanks are due to Roy Gal, Limin Lu, and Tom Barlow for providing the high resolution velocity standards used in this paper. This research has made use of the NASA/IPAC Extragalactic Database (NED) which is operated by the Jet Propulsion Laboratory, California Institute of Technology, under contract with the National Aeronautics and Space Administration. During the course of this project, M. A. P. and S. G. D. were supported in part by NSF grants AST–9123646 and AST–9157412 and the Bressler Foundation.

References

Abell, G. O. 1958, ApJS, 3, 211

Abraham, R. G., Valdes, F., Yee, H. K. C., & van den Bergh, S. 1994, ApJ, 432, 75

Barger, A. J., Aragón-Salamanca, A., Smail, I., Ellis, R. S., Couch, W. J., Dressler, A., Oemler, A., Jr., Poggianti, B. M., & Sharples, R. M. 1998, ApJ, in press

Barrientos, L. F., Schade, D., & López–Cruz, O. 1996, ApJ, 460, L89

Bender, R., Saglia, R. P., Ziegler, B., Belloni, P., Greggio, L., Hopp, U., & Bruzual, G. 1998, ApJ, in press

de Carvalho, R. R., & Djorgovski, S. 1992, ApJ, 389, L49

Casali, M. M., & Hawarden, T. G. 1992, JCMT-UKIRT Newsletter, 3, 33

Couch, W. J., Barger, A. J., Smail, I., Ellis, R. S., & Sharples, R. M. 1998, ApJ, in press

Davies, R. L., Sadler, E. M., & Peletier, R. F. 1993, MNRAS, 262, 650

Dickinson, M. 1995, in ASP Conf. Ser., Fresh Views on Elliptical Galaxies, eds. A. Buzzoni, A. Renzini, & A. Serrano (San Francisco: ASP), 283

Djorgovski, S., & Davis, M. 1987, ApJ, 313, 59

Djorgovski, S. G., Gal, R. R., McCarthy, J. K., Cohen, J. G., de Carvalho, R. R., Meylan, G., Bendinelli, O., & Parmeggiani, G. 1997, ApJ, 474, 19

van Dokkum, P. G., & Franx, M. 1996, MNRAS, 281, 985

Dressler, A., Gunn, J. E., & Schneider, D. P. 1985, ApJ, 294, 70

Dressler, A., Kells, W., & Sivaramakrishnan, A. 1998, in preparation

Dressler, A., Lynden-Bell, D., Burstein, D., Davies, R. L., Faber, S. M., Terlevich, R. J., & Wegner, G. 1987, ApJ, 313, 42

Dressler, A., Oemler, A., Jr., Couch, W. J., Smail, I., Ellis, R. S., Barger, A., Butcher, H., Poggianti, B. M., & Sharples, R. M. 1997, ApJ, 490, 577

Ellis, R. S., Smail, I., Dressler, A., Couch, W. J., Oemler, A., Jr., Butcher, H., & Sharples, R. M. 1997, ApJ, 483, 582

Franx, M. 1993, ApJ, 407, 5

Franx, M., Illingworth, G., & Heckman, T. 1989, AJ, 98, 538

Franx, M., Kelson, D., van Dokkum, P., Illingworth, G., & Fabricant, D. 1997, in The Nature of Elliptical Galaxies, Proceedings of the Second Stromlo Symposium, eds. M. Arnaboldi, G. S. Da Costa, & P. Saha, ASP Conf. Ser. Vol. 116, (San Francisco: ASP), 512

Gonzalez, J. J. 1993, Ph.D. thesis, University of California (Santa Cruz)

Jarvis, J. F., & Tyson, J. A. 1981, AJ, 86, 476

Jones, L. 1996, Ph.D. thesis, University of North Carolina at Chapel Hill

Jørgensen, I. 1998, MNRAS, in press

Jørgensen, I., Franx, M., & Kjærgaard, P. 1995a, MNRAS, 273, 1097

Jørgensen, I., Franx, M., & Kjærgaard, P. 1995b, MNRAS, 276, 1341

Kelson, D. D., Dokkum, P. G., Franx, M., Illingworth, G. D., & Fabricant, D. 1997, ApJ, 478, L13

Leitherer, C., *et al.* 1996, PASP, 108, 996

Lucey, J. R., Guzmán, R., Steel, J., & Carter, D. 1997, MNRAS, 287, 899

Matthews, K., & Soifer, B. T. 1994, in Infrared Astronomy with Arrays, ed. I. McLean (Dordrecht: Kluwer), 239

Natarajan, P., Kneib, J. P., Smail, I., & Ellis, R. S. 1998, ApJ, submitted

Oke, J. B., *et al.* 1995, PASP, 107, 375

Pahre, M. A. 1998a, in preparation [Chapter 2 of this thesis]

Pahre, M. A. 1998b, in preparation [Chapter 5 of this thesis]

Pahre, M. A., Djorgovski, S. G., & de Carvalho, R. R. 1996, ApJ, 456, L79

Pahre, M. A., de Carvalho, R. R., & Djorgovski, S. G. 1998a, in preparation [Chapter 4 of this thesis]

Pahre, M. A., Djorgovski, S. G., & de Carvalho, R. R. 1998b, in preparation [Chapter 7 of this thesis]

Press, W. H., Flannery, B. P., Teukolsky, S. A., & Vetterling, W. T. 1986, Numerical Recipes

(Cambridge: Cambridge University Press)

Saglia, R. P., Bertschinger, E., Baggley, G., Burstein, D., Colless, M., Davies, R. L., McMahan, R. K., Jr., & Wegner, G. 1997, ApJS, 109, 79

Sargent, W. L. W., Schechter, P. L., Boksenberg, A., & Shortridge, K. 1977, ApJ, 212, 326

Schneider, D. P., Dressler, A., & Gunn, J. E. 1986, AJ, 92, 523

Scodeggio, M., Giovanelli, R., & Haynes, M. P. 1997, AJ, 113, 2087

Smith, R. J., Lucey, J. R., Hudson, M. J., & Steel, J. 1997, MNRAS, in press

Stanford, S. A., Eisenhardt, P. R., & Dickinson, M. 1998, ApJ, 492, 461

Tonry, J., & Davis, M. 1979, AJ, 84, 1511

Trager, S. C., Worthey, G., Faber, S. M., Burstein, D., & González, J. J. 1998, ApJS, in press

Vogt, S., *et al.* 1994, Proc. SPIE, 2198, 362

Worthey, G., & Ottaviani, D. L. 1997, ApJS, 111, 377

Ziegler, B. L., & Bender, R. 1997, MNRAS, 291, 527

Chapter 7

The Evolution of the Fundamental Plane of Early–Type Galaxies for $0 < z < 0.6$

Abstract

Results are presented for a study of the global photometric and spectroscopic parameters of more than 100 early–type galaxies in eight rich clusters of galaxies at $0.1 < z < 0.6$. The parameters used include central velocity dispersions, line strengths, and effective radii and mean surface brightnesses in the near–infrared K–band. This wavelength was chosen for its near independence of metallicity effects, thereby allowing for a separation of age and metallicity effects as the galaxies are observed at higher redshifts. The slope of the near–infrared K–band Fundamental Plane (FP) correlations is found for the first time to flatten with increasing redshift, implying that lower luminosity early–type galaxies are evolving faster, and thus have younger mean stellar content, than more luminous galaxies. Age spreads of up to a factor of two are allowed among early–type galaxies. The intercept of the FP on the mean surface brightness axis demonstrates the Tolman surface brightness dimming effect that is expected in an expanding world model. After correcting for this cosmological dimming, luminosity evolution at fixed galaxy mass is detected at a rate of $\Delta K \approx -2.5\log(1+z)$ mag to $z \sim 0.6$. The Hβ_G line index is found to increase by 0.067 ± 0.034 dex to $z = 0.55$, the Mg_2 index decreases by 0.023 ± 0.004 mag to $z = 0.4$, and the $\langle$Fe$\rangle$ index decreases by 0.036 ± 0.011 dex to $z = 0.4$, when compared to nearby galaxy samples at fixed central velocity dispersion. The evolution of the K–band luminosity and the line strengths are consistent with a mean formation redshift of $3 \lesssim z \lesssim 5$ for the stellar content of the early–type galaxy population in rich clusters of galaxies, while the evolution of the slope of the FP implies that the lowest luminosity galaxies could have formed at $z_f \sim 1$.

7.1 Introduction

Since the pioneering work by Faber (1973) on the colors, luminosities, and line strengths of elliptical galaxies, it has been generally accepted that the systematic variations among this galaxy population is primarily one of metallicity. Metal line strengths are the strongest, and colors the reddest, for the most luminous galaxies. There is, however, a degeneracy between age and metallicity effects on most color and metal line indices that is elegantly summarized by the "3/2 rule" (Worthey 1994): changes in age are virtually indistinguishable from changes in metallicity via the relation $\Delta \log \mathrm{age} = \frac{3}{2}\Delta[\mathrm{Fe/H}]$. While recent work comparing the line strengths of the Balmer series of hydrogen appear promising due to an increased sensitivity to age instead of metallicity (Worthey & Ottaviani 1997), the available data for nearby galaxies do not yet provide a strong case for significant variations in the ages among elliptical galaxies due to substantial, correlated errors in the determination of the derived age and metallicity of each individual galaxy (Trager 1997).

An alternate approach is to observe the Fundamental Plane (FP) and other correlations among the properties of early–type galaxies in order to elucidate which underlying physical parameters are varying along the galaxy sequence. When data on nearby galaxies in bandpasses ranging from the U–band ($\lambda \sim 0.36\mu$m) to the K–band ($\lambda = 2.2\mu$m) are combined with central velocity dispersions, Mg_2 line indices, color gradients, and possible deviations of the family of early–type galaxies from a homologous family, there is a narrowing of the parameter space among the underlying physical parameters (Pahre, de Carvalho, & Djorgovski 1998b, Chapter 4 of this thesis). Nonetheless, the limited knowledge of the dynamics of elliptical galaxies at large radii and the age–metallicity degeneracy still prevent such models from specifying uniquely the variations in age and metallicity that are implied.

A compatible method to break the age–metallicity degeneracy is to observe similar early–type galaxies at higher redshifts, thereby observing the rate at which they evolve with redshift. Fast rates of evolution with redshift can be directly associated with young mean ages for the stellar content of the galaxy population. The difficulty with this approach is that these distant galaxies are faint while high S/N is required to measure the central velocity dispersions. Pioneering work by Franx and collaborators (Franx 1993; van Dokkum & Franx 1996; Kelson *et al.* 1997) has demonstrated the feasibility of measuring central velocity dispersions, effective radii, and mean surface brightnesses for galaxies at redshifts

of nearly $z = 0.6$. The small number of galaxies in all of those studies, even when *combined*, limits the amount of information that can be deduced. In particular, the slope a of the FP scaling relation $R_{\rm eff} \propto \sigma_0^a \langle\Sigma\rangle_{\rm eff}^b$ is an important indicator of the relative ages of galaxies along the early–type galaxy sequence (Pahre, de Carvalho, & Djorgovski 1998b, Chapter 4 of this thesis), but can be measured only to an accuracy of ± 0.3 or worse for similarly small galaxy samples in the nearby universe (Jørgensen, Franx, & Kjærgaard 1996; Pahre, Djorgovski, & de Carvalho 1998a, Chapter 3 of this thesis).

The K–band window at 2.2μm is an important wavelength for studying the global properties of early–type galaxies since near–infrared light is an excellent tracer of bolometric luminosity and hence nearly independent of metallicity effects. The FP correlations at this wavelength are not a function of mean age alone since systematic deviations from a dynamically homologous family (Capelato, de Carvalho, & Carlberg 1995; Busarello *et al.* 1997) could play a significant role in the K–band (Pahre, Djorgovski, & de Carvalho 1995; Pahre & Djorgovski 1997). It is important to note, however, that the dynamical effect will contribute *at all wavelengths* equally. Observations of the K–band FP correlations at high redshifts can thus place a crucial role in separating the effects of age, metallicity, and homology breaking along the early–type galaxy sequence. This approach is adopted for the present paper.

Observing the strengths of the metal lines of Mg_2 at high redshifts can also be a method of measuring the rate of evolution along the early–type galaxy sequence. As the mean age of the stellar content becomes younger a higher fraction of its light is emitted by hot stars, the continuum emission of which increasingly "fill" the Mg_2 absorption feature from the cooler stars in the observed composite spectrum. Early work on the Mg_2 index at $z = 0.37$ was done by Bender, Ziegler, & Bruzual (1996). The Mg_2 index, however, is much more sensitive to metallicity effects than it is to age effects (Mould 1978), which makes the interpretation of such data problematical without additional constraints.

A more robust approach than observing Mg_2 at high redshifts would be to study other line indices which can better separate the effects of age and metallicity. The Balmer lines of hydrogen are very sensitive to age effects (Worthey & Ottaviani 1997) which can then be coupled with metal absorptions lines such as Mg_2 and $\langle$Fe$\rangle$ to discriminate between age and metallicity. The difficulty of drawing conclusions from measurements of these line indices at high redshifts is that their strength varies systematically along the early–type sequence

with galaxy luminosity or velocity dispersion (Faber 1973; Jørgensen 1998). Hence it is important to measure the central velocity dispersions for each galaxy, thereby comparing nearby and distant galaxies at fixed velocity dispersion. This is the approach adopted for the present paper, which will draw upon central velocity dispersions and the line strengths of Hβ_G, Mg$_2$, and $\langle$Fe$\rangle$.

The data used in this paper are at redshifts $0.1 < z < 0.6$, are mostly new observations, were presented in a previous paper in this series (Pahre, Djorgovski, & de Carvalho 1998c, Chapter 6 of this thesis), and will be summarized in §7.2. The near–infrared FP correlations and their evolution in both slope and intercept will be described in §7.3 and §7.4, respectively. The evolution of the line strengths will be presented in §7.5.

7.2 Summary of Data

The data used in this paper are moderate dispersion spectroscopy and near–infrared imaging of early–type galaxies in eight clusters at $0.1 < z < 0.6$, and are described elsewhere (Pahre, Djorgovski, & de Carvalho 1998c, Chapter 6 of this thesis). The galaxies in each cluster were identified in a systematic and homogeneous manner using two color and morphological information (Pahre 1998b, Chapter 5 of this thesis) that does not bias the sample against post star–burst galaxies with ages of ~ 1 Gyr (see the discussion in Pahre, Djorgovski, & de Carvalho 1998c, Chapter 6 of this thesis). Central velocity dispersions and line strengths, the latter calculated on the Lick/IDS system of indices (Trager *et al.* 1998, with Hβ_G added using the definition of Jørgensen 1998), have been determined from the new spectra in six clusters. The Mg$_2^*$ index has been calculated from measurements of Mg$_b$, using the relation of Jørgensen (1998), since the new spectra are not flux calibrated and therefore suffer systematic effects in the measurement of broadband indices like Mg$_2$. Central velocity dispersions and line strengths were drawn from Ziegler & Bender (1997) to complement the new spectra in Abell 370; central velocity dispersions (line strengths are unavailable) were drawn from van Dokkum & Franx (1996) and Kelson *et al.* (1997) for two additional clusters. Aperture corrections were applied in the manner described by Jørgensen, Franx, & Kjærgaard (1995). Near–infrared effective radii $r_{\rm eff}$ and mean surface brightnesses $\langle\mu\rangle_{\rm eff}$ have been derived from K–band imaging data for galaxies in all eight clusters by fitting model images convolved with the PSF directly to the imaging pixel data.

The following two comparison samples of nearby early–type galaxies in clusters are also discussed in this paper: (1) line strengths and central velocity dispersions from Jørgensen (1998), along with the scaling relations among these variables that were derived in that paper; and (2) new effective radii $r_{\rm eff}$ and mean surface brightnesses $\langle\mu\rangle_{\rm eff}$ that were obtained in the K–band using imaging data (Pahre 1998a, Chapter 2 of this thesis), central velocity dispersions and Mg_2 line strengths drawn from the literature for each galaxy, and the Fundamental Plane scaling relations among these variables (Pahre, Djorgovski, & de Carvalho 1998a, Chapter 3 of this thesis).

7.3 Evolution of the Surface Brightness Intercept of the FP

The bivariate correlation between the parameters of effective radius $r_{\rm eff}$, mean surface brightness $\langle\mu\rangle_{\rm eff}$ enclosed within that radius, and central velocity dispersion σ_0 for galaxies at $z \sim 0$ is

$$\log R_{\rm eff}(h_{75}^{-1}\ {\rm kpc}) = 1.528 \log \sigma_0 + 0.314 \langle\mu_K\rangle_{\rm eff} - 8.298, \tag{7.1}$$

which was determined for more than 200 early–type galaxies in rich clusters (Pahre, Djorgovski, & de Carvalho 1998a, Chapter 3 of this thesis). In Figure 7.1, this relation is plotted for both the nearby and high redshift galaxies after the k–correction has been applied but *without having applied a correction for surface brightness dimming to* $\langle\mu_K\rangle_{\rm eff}$. As the redshift increases, there is a clear trend in which the galaxies systematically move to the right of the local relation. Nearly all of this effect is due to the Tolman surface brightness dimming (Tolman 1934; Hubble & Tolman 1935) for an expanding world model.

In Figure 7.2, this relation is plotted for both the nearby and high redshift galaxies *after having applied a correction for surface brightness dimming and a k–correction to* $\langle\mu_K\rangle_{\rm eff}$. As the redshift increases, there is a clear trend in which the galaxies systematically move to the left of the local relation. This is the signal of luminosity evolution in the early–type galaxy population.

The evolution of the surface brightness intercept of the K–band Fundamental Plane, obtained by fixing the local relation slope and evaluating the median intercept, is plotted in Figure 7.3. The passive evolution of the early–type population is inconsistent with formation

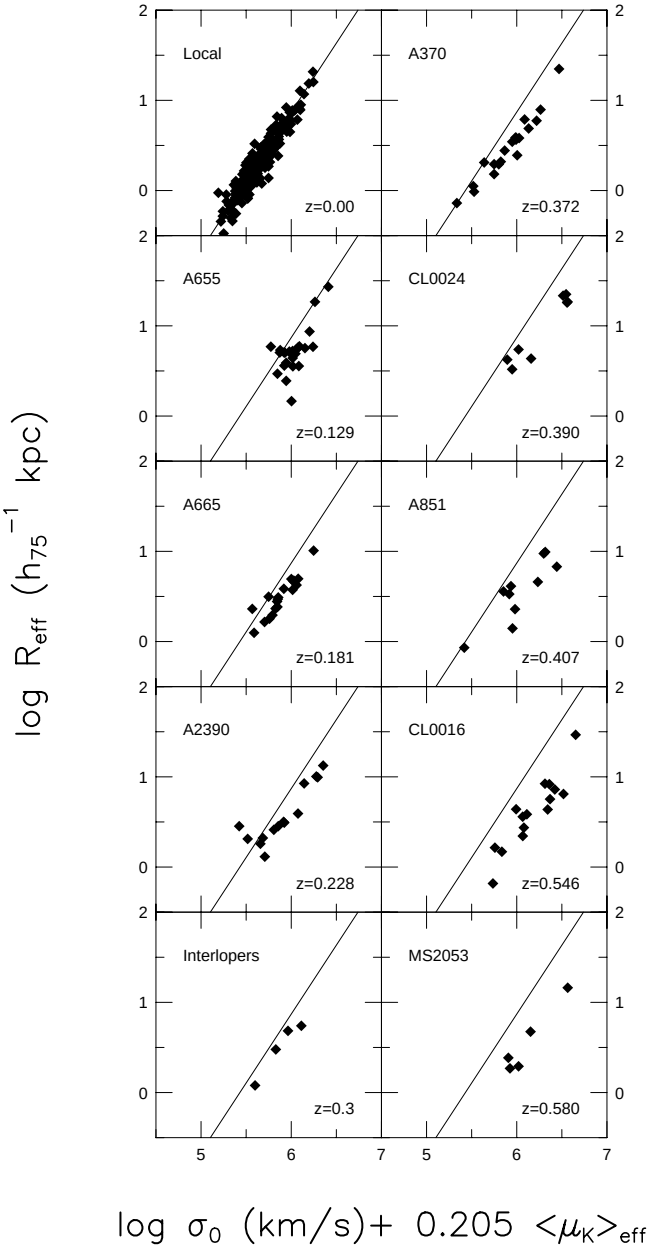

Figure 7.1: The Fundamental Plane at low and high redshift demonstrating the Tolman surface brightness dimming signal. The local relation is plotted as a line in all the panels. There is a systematic effect in that the galaxies move further to the right of the relation as the redshift increases, which is due to the SB dimming (Tolman 1934; Hubble & Tolman 1935) in the $\langle \mu_K \rangle_{\rm eff}$ term in the quantity plotted on the horizontal axis.

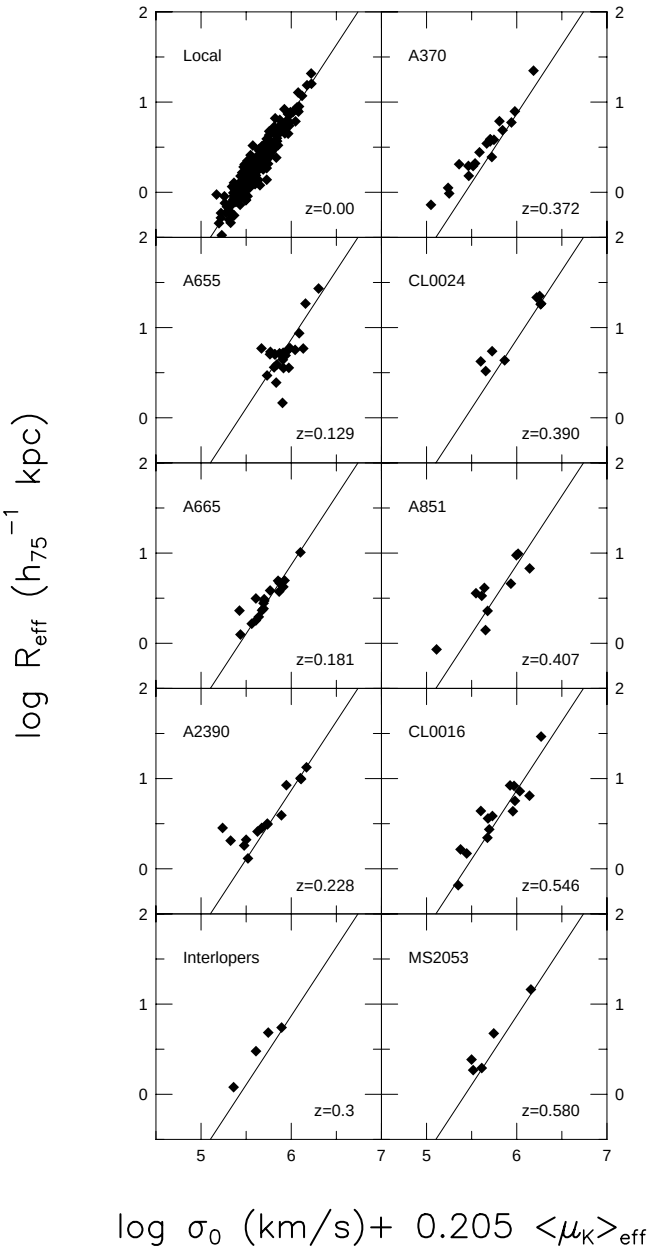

Figure 7.2: Detection of luminosity evolution from the near–infrared Fundamental Plane. In contrast to Figure 7.1, the surface brightness dimming signal has been corrected for each galaxy. The local relation is plotted as a line in all the panels. Now the data can be seen to move systematically towards the left of the local relation, which is the sign of luminosity evolution in the parameter $\langle \mu_K \rangle_{\rm eff}$ plotted on the horizontal axis. Note also how the data suggest that the slope of the FP relation appears to become shallower with redshift.

redshifts of $z_f = 1$, instead implying that the stellar content in these galaxies formed at a mean redshift of $3 < z_f < 5$. The rate of evolution of the K–band light appears to be consistent with the simple relation $\Delta K \approx -2.5 \log(1+z)$ mag.

7.4 Evolution of the Slope of the FP

This is the first study to contain a galaxy sample that is large enough to measure the slope of the Fundamental Plane at $z > 0.1$. For example, the combined samples of van Dokkum & Franx (1996) and Kelson *et al.* (1997) have observations of only 21 early–type galaxies divided amongst three clusters at $z = 0.33$, 0.39, and 0.58. Furthermore, the full extent of the FP was not well sampled in any of these three clusters. It is clear from studies of the FP slope with nearby cluster galaxy samples (Jørgensen, Franx, & Kjærgaard 1996; Pahre, Djorgovski, & de Carvalho 1998a, Chapter 3 of this thesis) that large uncertainties result from small sample sizes.

The present paper contains a large combined sample of more than 100 galaxies in eight rich clusters at $0.1 < z < 0.6$. This large number allows both for the slope of the FP to be determined to better accuracy and for a few clearly outlying data points to be identified and excluded. The fits to the FP are of the form

$$\log R_{\rm eff} = a \log \sigma_0 + b \langle \mu_K \rangle_{\rm eff}^{corr} + c \tag{7.2}$$

where the mean surface brightness $\langle \mu_K \rangle_{\rm eff}^{corr}$ has a surface brightness dimming and k–correction applied, and $R_{\rm eff}$ is in units of h_{75}^{-1} kpc assuming $\Omega_0 = 0.2$ and $\Lambda_0 = 0$. Since virtually every study of the FP for nearby clusters has found that $b = 0.32$, independent of wavelength or environment, we have chosen to fix $b = 0.32$ to improve the convergence. The parameter a in Equation 7.2 is referred to as the slope of the FP. A few data points were excluded from the fits by inspecting their residuals. The fit for one of the clusters, MS0015.9+1609 ($z = 0.546$), did not converge to a solution, hence results for it will not be presented here. The clusters Abell 370 ($z = 0.372$), ZwCL0024+1652 ($z = 0.391$), and Abell 851 ($z = 0.407$) have been combined together to improve the quality of their fit; differential luminosity evolution across $\Delta z = 0.03$ is expected to be $\Delta K < 0.03$ mag, so no correction for this effect was applied. A fit is reported here for MS2053 ($z = 0.58$), although

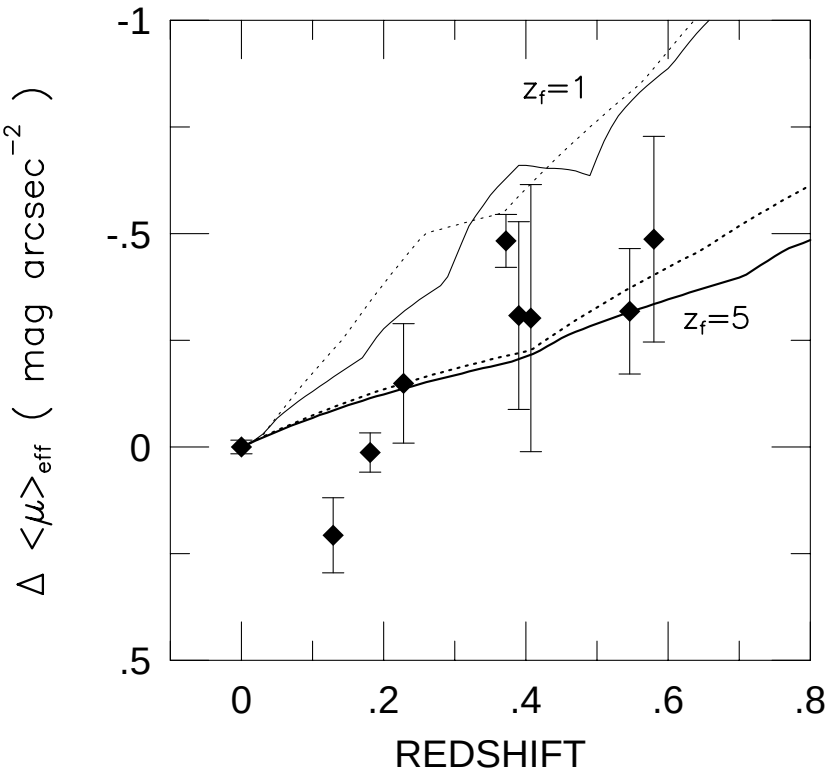

Figure 7.3: Evolution of the surface brightness intercept of the Fundamental Plane in the K–band. The median offset of each cluster from the local relation in Figure 7.2 is plotted here. The lines are the model evolution for early–type galaxies in a $(H_0, \Omega_0, \Lambda_0) = (75, 0.2, 0)$ cosmology for a formation redshift $z_f = 1$ (light lines) or 5 (heavy lines), zero–pointed to the local galaxies. The solid lines are for the Bruzual & Charlot (1996) models of solar metallicity and Salpeter IMF, while the dotted lines are for the Vazdekis *et al.* (1996) models of solar metallicity and bimodal IMF. The luminosity evolution of the K–band FP implies high redshift formation for the cluster early–type galaxies.

Table 7.1: Individual Fits to the K–band Fundamental Plane Slope

Cluster	z	a	$\pm$	$\langle\mu_K\rangle_{\rm eff}^{corr}$ (mag arcsec^{-2})	$\pm$	rms (dex)	N_{fit}
Local	0.000	1.528	0.043	16.749	0.020	0.102	253
A655	0.129	1.455	0.198	16.994	0.089	0.130	22
A665	0.181	1.310	0.141	16.746	0.039	0.050	17
A2390	0.228	1.191	0.160	16.714	0.071	0.075	12
A370,CL0024,A851	0.390	1.007	0.116	16.212	0.049	0.088	33
MS2053	0.583	1.015	0.345	16.330	0.112	0.072	5

Notes: (1) The rms is expressed in units of $\log R_{\rm eff}$. (2) The uncertainties for a are the formal uncertainties from the FP fit. (3) The uncertainties for $\langle\mu_K\rangle_{\rm eff}^{corr}$ are taken from the random uncertainties of each fit, a systematic photometric calibration error of 0.05 mag per cluster (to account for zero–point, k–correction, and corrections applied after the two–dimensional, seeing–convolved model fitting), and a systematic error of 0.02 dex in $\log\sigma_0$, all added in quadrature.

its statistical significance is small as a direct result of there only being five galaxies observed.

The individual cluster fits to the K–band FP are provided in Table 7.1, and plotted in Figure 7.4. While the cluster Abell 655 ($z = 0.129$) appears to have large scatter, the other clusters have statistically significant fits to the FP slope with small scatter.

The slope of the near–infrared K–band FP shows a systematic flattening with redshift, in the sense that the value of a decreases with z. The effect appears to be strong, changing the scaling relation from $R_{\rm eff} \propto \sigma_0^{1.5}$ seen locally to $R_{\rm eff} \propto \sigma_0^{1.0}$ at $0.4 < z < 0.6$. The slopes of the K–band FP as a function of redshift are plotted in Figure 7.5. Also plotted is the variation of the intercept on the $\langle\mu_K\rangle_{\rm eff}^{corr}$ axis, calculated at the standard condition of $R_{\rm eff} = 3h_{75}^{-1}$ kpc and $\sigma_0 = 200$ km s^{-1}, that is derived from these fits which allow the slope of the FP to be a free parameter.

The discovery here that the slope of the K–band FP is changing with redshift is a direct indication that there exist systematic, differential age effects along the full extent of the FP. These age variations are in the sense that the galaxies at the low–luminosity (or low central velocity dispersion, or small effective radius) end of the FP are evolving faster with redshift than the galaxies at the high luminosity end of the FP. One issue that is not clear is whether the complete nearby galaxy sample from Pahre *et al.* (1998a, Chapter 3 of this thesis), or only the richest clusters like Coma, should be compared to the high redshift

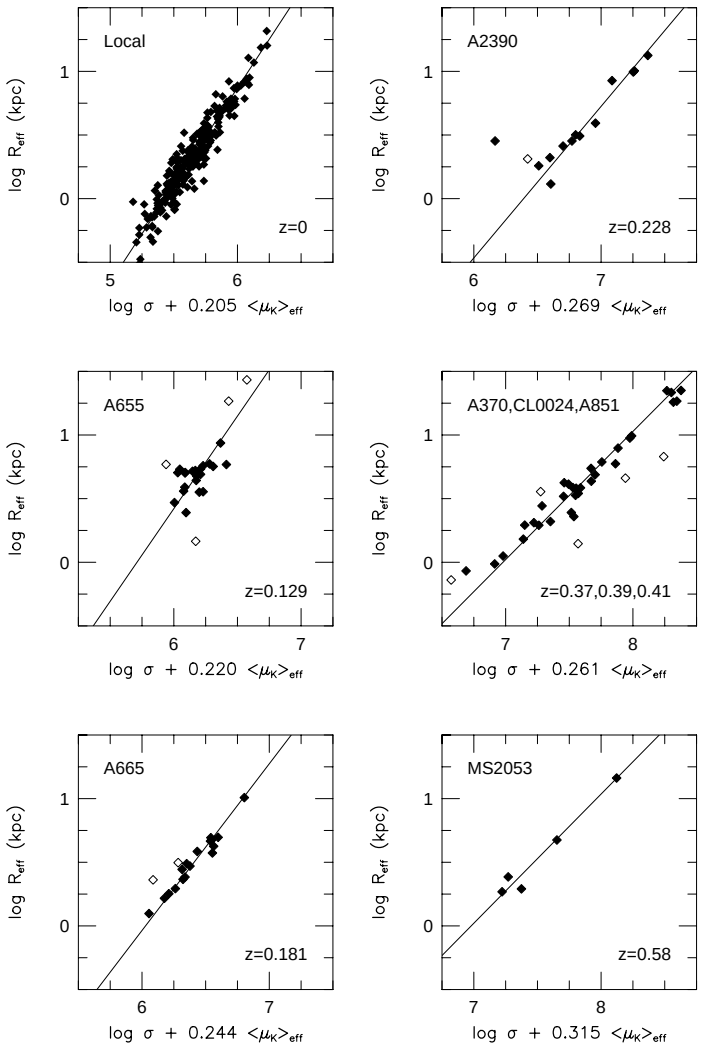

Figure 7.4: The individual fits to the slope of the K–band Fundamental Plane for clusters in the survey at $0 < z < 0.6$. One cluster (MS0015.9+1609) is not plotted as its FP fit did not converge. All panels are plotted with the same relative scale for the vertical and horizontal axes, hence the visual effect of the slope of the FP flattening with increasing redshift is apparent. This shows that the power–law coefficient a in $R_{\rm eff} \propto \sigma_0^a$ is systematically decreasing with redshift. Galaxies included in each cluster fit are plotted as filled symbols, while those that are excluded from the fit are plotted as open symbols. The data in cluster Abell 655 appear to have large scatter despite the fact that the fit is formally significant.

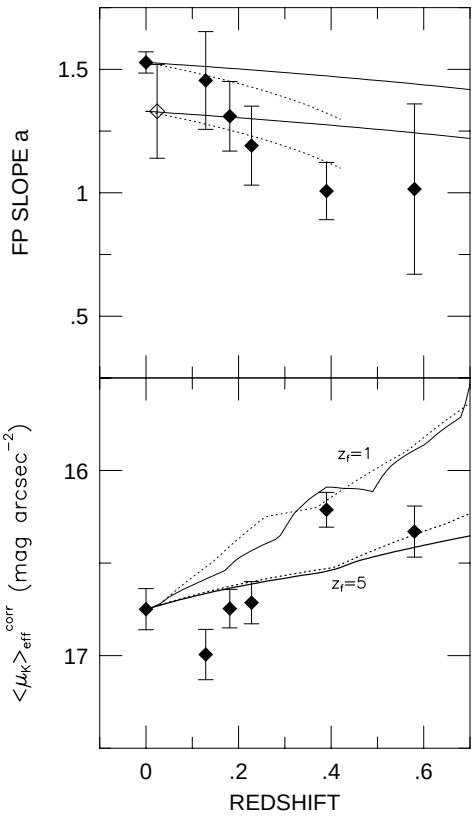

Figure 7.5: The evolution with redshift of the slope [top] and intercept [bottom] of the K–band Fundamental Plane. The individual cluster fits are taken from Table 7.1. [top] The slope of the FP appears to evolve with redshift. The entire local galaxy cluster sample (from Pahre, Djorgovski, & de Carvalho 1998a, Chapter 3 of this thesis) is plotted as a filled symbol at $z = 0$, while the Coma cluster alone is plotted as an open symbol at $z = 0.024$. Comparison is made to models constructed by Pahre *et al.* (1998b, Chapter 4 of this thesis) which attempt to describe the global properties of nearby early–type galaxies in clusters: the solid line is a model in which the early–type galaxy sequence is primarily a metallicity sequence, while the dotted line is a model in which age effects dominate the sequence. The latter model is cut–off when the galaxies at the bottom end of the sequence reach an age of 1 Gyr in the assumed cosmology, at which point they may begin to drop out of the sample. The models are plotted twice: the upper lines are zero–pointed to the complete nearby galaxy sample while the lower lines are zero–pointed to the Coma cluster sample alone. The model comparisons with the data suggest that age spreads of up to a factor of two may exist along the early–type galaxy sequence. [bottom] The evolution of mean surface brightness with redshift is compared to the same models plotted in Figure 7.3, implying slow and passive evolution for a galaxy population whose *mean* formation redshift appears to be $1 < z_f < 5$. The intercept of the FP on the $\langle\mu_K\rangle_{\rm eff}^{corr}$ axis is calculated at the standard condition $R_{\rm eff} = 3h_{75}^{-1}$ kpc and $\sigma_0 = 200$ km s^{-1}.

observations of early–type galaxies in rich clusters. The amount of evolution of the slope of the FP decreases by 40% if the Coma cluster is used for the comparison, although there is still a detection of significant evolution in the slope in both cases.

This effect was predicted in a model by Pahre *et al.* (1998b, Chapter 4 of this thesis) on the basis of the global properties of nearby elliptical galaxies. The predictions of two versions of the Pahre *et al.* model—one in which age variations dominate over metallicity variations, the other in which metallicity variations dominate over age variations—are plotted in Figure 7.5 for direct comparison. It is apparent that these models can fit the data if the Coma cluster is used for the nearby comparison sample, but not if the entire nearby galaxy sample of Pahre *et al.* (1998a, Chapter 3 of this thesis) is used. In the latter case, the systematic age variations along the FP would be a factor of two to four for present day ellipticals; in the former case, the age variations are a factor of two or less.

If there were an age spread of a factor of ten among present–day early–type galaxies (as advocated by Trager 1997), then the large age spreads would cause the FP to change slope with redshift much faster than is observed. In particular, the model of Pahre *et al.* (1998b, Chapter 4 of this thesis) in which an age spread of a factor of two ($\Delta \log t = 0.3$ dex) causes a change in the slope of the FP of ~ -0.25 dex by $z = 0.4$. Changing the age spread to a factor of ten ($\Delta \log t = 1$ dex) causes a change in the slope of the FP of ~ -0.8 dex, which is much more than the data allow; the disagreement becomes even worse at $z = 0.58$. It appears as though *the existence of an FP correlation at all at $z > 0.5$ probably excludes age variations of a factor of ten* as advocated by Trager (1997).

7.5 Evolution of the Line Strengths

The line of Hβ_G and the central velocity dispersion was measured in six clusters at $0.1 < z < 0.6$, while the lines of Mg_2 and $\langle Fe \rangle$ were only measured for five clusters at $0.1 < z < 0.4$. The data are compared to early–type galaxies in nearby, rich clusters from Jørgensen (1998) in Figure 7.6 as a function of central velocity dispersion.

The data for Abell 655 at $z = 0.129$ are of the lowest quality in the sample, and show considerable scatter in their properties. The higher redshifts, however, show systematic trends with redshift in their line strengths: the Mg_2 and $\langle Fe \rangle$ indices are somewhat weaker at $0.2 < z < 0.4$ than the nearby galaxies, while the Hβ_G index at $0.2 < z < 0.6$ is

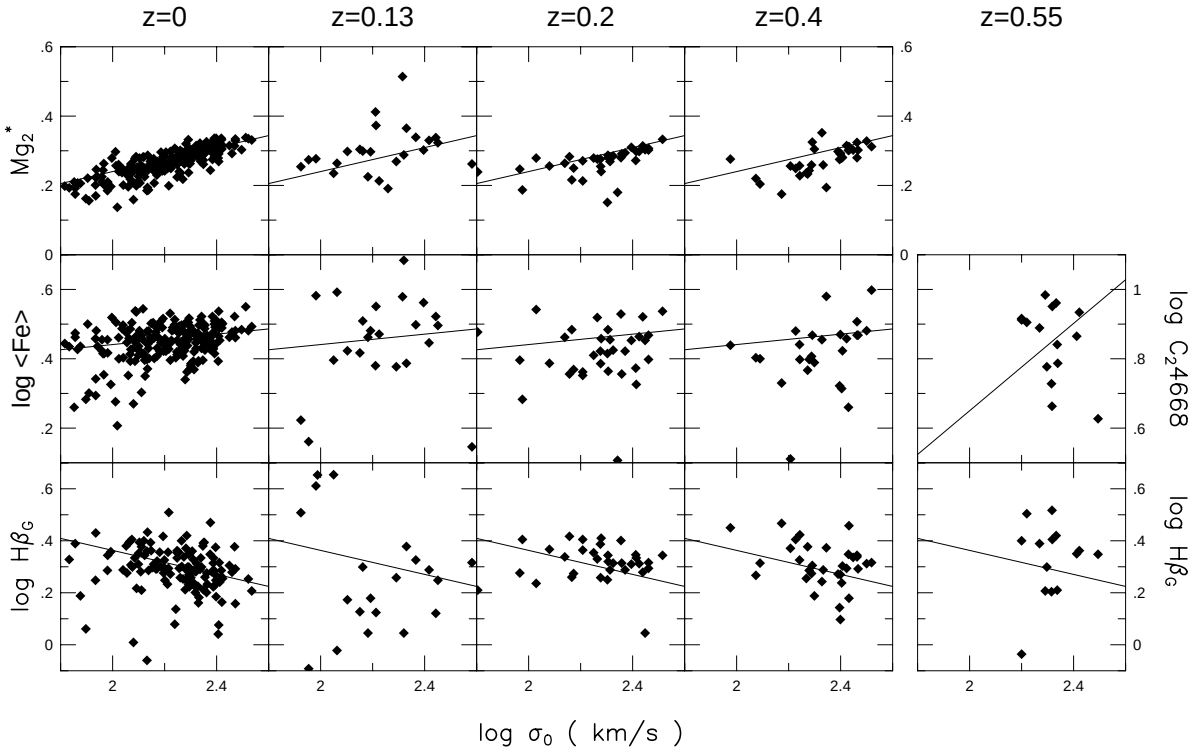

Figure 7.6: The relations between line strength and central velocity dispersion. The data have been binned with redshift, and data for $z \sim 0$ early–type galaxies in clusters from Jørgensen (1998) are shown for comparison. In each panel, the solid line is the relation between the plotted parameters for early–type galaxies in nearby, rich clusters from Jørgensen (1998), with the exception of the Mg_2–σ_0 relation which is taken from Pahre *et al.* (1998a, Chapter 3 of this thesis). While the $z = 0.13$ data for Abell 655 are noisy, there are trends for the Mg_2 and $\langle Fe \rangle$ indices weakening with redshift at fixed central velocity dispersion. The Hβ_G index appears to show a small strengthening with redshift, despite the fact that the index measurements were not corrected for emission which could partly fill in this line. At $z = 0.55$, the different rest–frame wavelength coverage still allows Hβ to be measured, but not Mg_2 or $\langle Fe \rangle$; $C_2$4668 has been substituted. All of these index variations with redshift are in the sense expected for a passively evolving, old stellar population.

Table 7.2: Evolution of the Line Strengths With Redshift

	log H β_G Index				Mg_2 Index				log⟨Fe⟩ Index			
$\overline{z}$	Δ (Å)	$\pm$	rms	N	Δ (mag)	$\pm$	rms	N	Δ (Å)	$\pm$	rms	N
0.00	0.000	0.003	0.041	187	0.000	0.001	0.023	290	0.000	0.003	0.041	187
0.13	-0.012	0.047	0.195	18	0.013	0.008	0.037	23	0.006	0.022	0.101	22
0.21	0.014	0.011	0.063	33	-0.016	0.003	0.016	33	-0.034	0.014	0.078	33
0.39	0.021	0.015	0.083	33	-0.023	0.004	0.025	33	-0.036	0.011	0.052	25
0.55	0.067	0.034	0.119	13	...	...	...	...	...	...	...	...

somewhat stronger. There is no clear trend in the Mg_2–σ_0 relation changing slope with redshift, although small variations in slope cannot be excluded by these data. If the slope of these relations are fixed to the values of Jørgensen (1998) for ⟨Fe⟩ and Hβ_G, and to the value of Pahre *et al.* (1998a, Chapter 3 of this thesis) for Mg_2, then the mean intercept from the local relation can be calculated. These offsets of the high redshift cluster galaxies relative to the low redshift ones are listed in Table 7.2 and shown as a function of redshift in Figure 7.7. The uncertainty estimates are the standard deviations of the mean, which might underestimate the true errors if there are significant systematic effects. The line indices, however, are narrow,[1] observed at moderate dispersion (∼2–3 Å resolution FWHM in the observed frame) and excellent S/N (> 20 per Å for most galaxies, > 50 per Å for a significant number of galaxies), and have been put onto the Lick/IDS system in a standard manner (see Pahre, Djorgovski, & de Carvalho 1998c, Chapter 6 of this thesis, for details). These spectral data are not spectrophotometric, but tests done by Worthey & Ottaviani (1997) suggest that there will not be significant systematic effects in the measurement of these narrow line indices. Hence, systematic errors are probably equal to, or smaller than, the random uncertainties quoted in Table 7.2.

There is a signature of evolution in all three line indices with redshift. The scatter about all three relations is similar to the scatter at low redshifts, implying a similar homogeneity of galaxy properties at any point along the early–type galaxy sequence at all redshifts. Simple stellar populations models from Bruzual & Charlot (1996, as provided in Leitherer *et al.* 1996) and Vazdekis *et al.* (1996) are plotted for comparison by assuming a $(H_0, \Omega_0, \Lambda_0) = (75, 0.2, 0)$ cosmology and that the galaxies form at redshifts $z_f = 1$ or 5. The metal line indices of Mg_2 and ⟨Fe⟩ for $z \leq 0.4$ cannot discriminate between the different formation

[1]The Mg$_b$ index was observed, rather than the extremely broadband Mg_2 index. The conversion between the two was calculated using the transformation of Jørgensen (1998) based on a nearby galaxy sample.

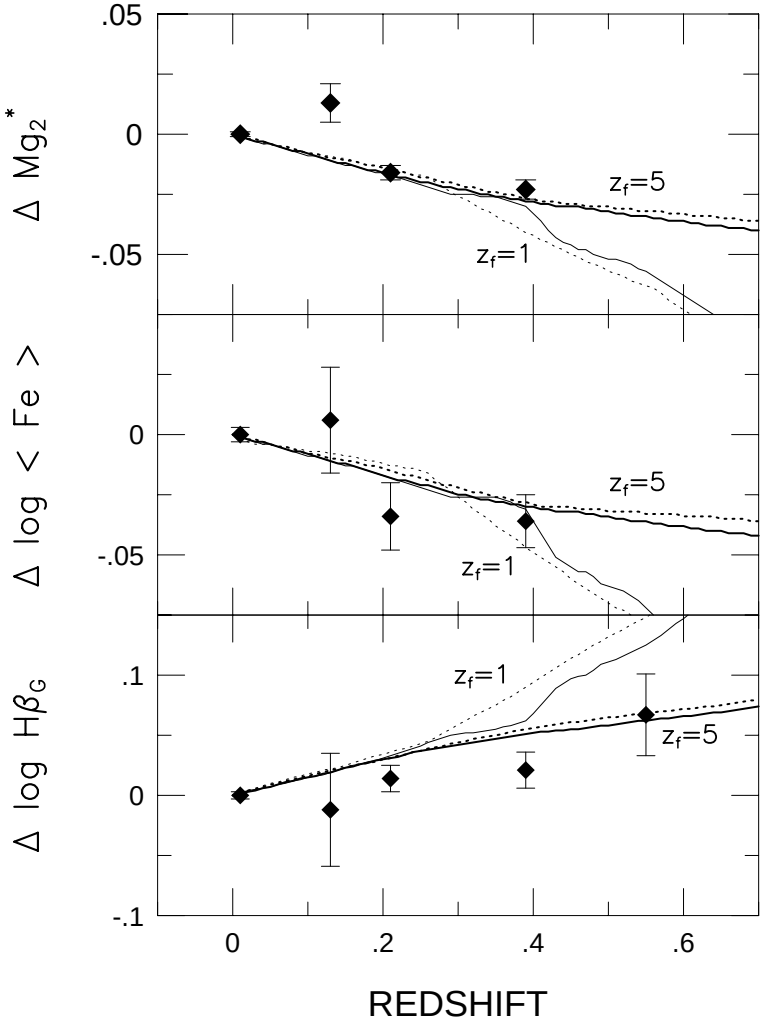

Figure 7.7: The evolution of the mean line strengths with redshift. Each plotted point is the mean offset of the intercept of the data points in Figure 7.6 from the nearby galaxy relation (Jørgensen 1998); the error bars are the standard deviation of the mean. The lines are the model evolution for early–type galaxies in a $(H_0, \Omega_0, \Lambda_0) = (75, 0.2, 0)$ cosmology for a formation redshift $z_f = 1$ (light lines) or 5 (heavy lines), zero–pointed to the local galaxies. The solid lines are for the Bruzual & Charlot (1996) models of solar metallicity and Salpeter IMF, while the dotted lines are for the Vazdekis *et al.* (1996) models of solar metallicity and bimodal IMF. The evolution of Mg_2 and $\langle Fe \rangle$ cannot discriminate among formation redshifts $1 < z_f < 5$, but the evolution of the Balmer line $H\beta_G$, which is sensitive to the presence of hot stars in a younger stellar population, demonstrates that the galaxies formed at $z_f \sim 5$.

redshifts, but the Hβ_G index shows clearly that a higher formation redshift is significantly more compatible with the data.

One point needs to be addressed regarding the Hβ_G indices. Neither the high (Pahre, Djorgovski, & de Carvalho 1998c, Chapter 6 of this thesis) nor the low (Jørgensen 1998) redshift galaxies were corrected for possible Hβ emission that can partially fill the absorption feature. Both Gonzalez (1993) and Trager *et al.* (1998) apply corrections for Hβ emission to their samples of nearby galaxies based on measurements of possible [O III] emission at $\lambda = 5007$ Å. These corrections can often be quite substantial, although it is not clear if this correction is warranted. Applying any such corrections will always lead to estimates of younger ages since Hβ is sensitive to the mean age of a stellar population. The data in this paper are directly compared only to the nearby galaxy sample of Jørgensen (1998), who also did not apply a correction to Hβ_G line strengths, so any systematic error caused by this effect is probably small and possibly cancels out in the comparison. We note that both Jørgensen (1998) and Pahre *et al.* (1998c, Chapter 6 of this thesis) excluded from their sample any galaxy that had significant emission of [O III].

7.6 Discussion

This paper describes the results from a large study of more than 100 early–type galaxies in eight rich clusters of galaxies at $0.1 < z < 0.6$. Direct comparisons of the FP correlations and the line strengths at fixed central velocity dispersion have been made to large, homogeneous samples of early–type galaxies in nearby, rich clusters of galaxies.

All of the correlations studied are fully consistent with a population of early–type galaxies which formed early in the universe's history at $z_f \geq 3$ and evolved passively since that time. The slope of the K–band FP, however, shows a systematic flattening with redshift which appears to suggest that the lowest luminosity galaxies are evolving somewhat faster than the highest luminosity galaxies. This can be expected if there exists an age spread of as much as a factor of two among early–type galaxies that is systematic from one end of the FP to the other. The age effects are lessened, however, if comparison is only made to the Coma cluster at $z = 0.024$, which shows a marginally shallower slope but could be more similar to the rich clusters observed at the higher redshifts. These high redshift galaxy observations show a modest agreement with the model predictions of Pahre *et al.* (1998b), which were

based on an analysis of many different photometric, dynamical, and line strength properties of nearby galaxies. The evolution of the slope of the FP with redshift could, however, be caused by evolving dynamical homology breaking, although we note that the details of such an effect, which might be caused by the changing merging rates with redshift, are currently unconstrained in the models.

A naive interpretation of the hierarchical merging picture in standard Cold, Dark Matter (CDM) models is that the most massive galaxies formed at the latest epochs, and are hence the youngest. More sophisticated, semi–analytical techniques (Kauffmann 1996) suggest that while this picture is the model prediction for elliptical galaxies in the low density environments of the general field, elliptical galaxies in the cores of rich clusters should show no correlation between mass and age. This prediction of the CDM model appears to be directly contradicted by the evolving slope of the FP in §7.4 and the comprehensive model describing the global properties of nearby elliptical galaxies (Pahre, de Carvalho, & Djorgovski 1998b, Chapter 4 of this thesis), both of which imply that more massive elliptical galaxies are older than less massive galaxies. The CDM model predicts the same mass–to–light ratio for all elliptical galaxies independent of wavelength (Kauffmann & Charlot 1997), while the slope of the FP in various bandpasses shows a significant dependence of M/L on mass, even in a complete model separating stellar populations and homology breaking (or dark matter) effects (Pahre, de Carvalho, & Djorgovski 1998b, Chapter 4 of this thesis). Finally, the CDM model predicts that elliptical galaxies in the field are 4 Gyr younger than those in rich clusters (Kauffmann 1996), which is contradicted by the similar evolutionary rate with redshift found for both field and cluster elliptical galaxies (Schade *et al.* 1996) and the similarity of the D_n–σ_0 relation at V and K in both rich clusters and low density environments (Pahre, de Carvalho, & Djorgovski 1998b, Chapter 4 of this thesis). While the CDM models in their semi–analytical formalism have been successful at reproducing the slope of the Mg_2–σ_0 relation (Kauffmann & Charlot 1997), the morphology–density relation (Kauffmann 1995; Baugh, Cole, & Frenk 1996), and the small scatter (but *not* the slope)[2] of the aperture color–magnitude relation (Kauffmann 1996; Baugh, Cole, & Frenk 1996), there appear to be other substantial contradictions between the standard CDM model predictions and the observed global properties of elliptical galaxies. These serious problems call into

[2]While the model of Kauffmann & Charlot (1997) appears to be successful at producing the slope of the color–magnitude relation this is probably accidental since adding the effects of color gradients into the CDM models probably causes the model slope to be significantly larger than the observed one.

question the fundamental assertion of the semi–analytical modeling technique that elliptical galaxies are formed solely from the merger of two spiral galaxies of similar mass.

The small scatter of the FP that is seen both locally (Jørgensen, Franx, & Kjærgaard 1996; Hudson *et al.* 1997; Pahre, Djorgovski, & de Carvalho 1998a, Chapter 3 of this thesis) and at high redshifts (van Dokkum & Franx 1996; Kelson *et al.* 1997; and Table 7.1 of this paper), as well as the small scatter of the Mg_2 and $\langle Fe \rangle$ line indices as a function of central velocity dispersion that is seen both locally (Jørgensen 1998) and at $0.1 < z < 0.4$ in §7.5, implies that the intrinsic physical properties of elliptical galaxies are tightly constrained for any given luminosity or mass. It is an open challenge to reproduce this small scatter, especially at intermediate redshifts, in any model. Not only does there appear to be a significant synchronicity in galaxy formation along the FP such that massive ellipticals form first, but there must be an additional synchronicity in that galaxies at any given mass must form within an extremely small time frame of one another.

The K–band FP and its evolution appears to be an excellent tool with which to probe the evolution of early–type galaxies in clusters with excellent accuracy. Future work will consist in expanding this sample dramatically at high redshifts in order to determine in far better detail how the slopes of the FP and line strength correlations evolve with redshift. Such observations will prove essential for precise measurements of the variations allowed in the stellar populations parameters along the full extent of the early–type galaxy sequence.

Acknowledgments

The authors thank I. Jørgensen for providing her line index strengths for nearby galaxies in electronic form prior to publication. During the course of this project, M. A. P. received partial financial support from the Bressler Foundation; M. A. P. and S. G. D. were supported in part by NSF grants AST–9123646 and AST–9157412.

References

Bender, R., Ziegler, B., & Bruzual, G. 1996, ApJ, 463, L51

Bruzual, A. G., & Charlot, S. 1996, in preparation

Busarello, G., Capaccioli, M., Capozziello, S., Longo, G., & Puddu, E. 1997, A&A, 320, 415

Capelato, H. V., de Carvalho, R. R., & Carlberg, R. G. 1995, ApJ, 451, 525

van Dokkum, P. G., & Franx, M. 1996, MNRAS, 281, 985

Faber, S. M. 1973, ApJ, 179, 731

Franx, M. 1993, ApJ, 407, 5

Gonzalez, J. J. 1993, Ph.D. thesis, University of California (Santa Cruz)

Hubble, E., & Tolman, R. C. 1935, ApJ, 82, 302

Hudson, M. J., Lucey, J. R., Smith, R. J., & Steel, J. 1997, MNRAS, in press

Jørgensen, I., Franx, M., & Kjærgaard, P. 1995, MNRAS, 273, 1097

Jørgensen, I., Franx, M., & Kjærgaard, P. 1996, MNRAS, 280, 167

Jørgensen, I. 1998, MNRAS, in press

Kauffmann, G. 1996, MNRAS, 281, 487

Kauffmann, G., & Charlot, S. 1997, MNRAS, submitted

Kelson, D. D., Dokkum, P. G., Franx, M., Illingworth, G. D., & Fabricant, D. 1997, ApJ, 478, L13

Leitherer, C., *et al.* 1996, PASP, 108, 996

Mould, J. R. 1978, ApJ, 220, 434

Pahre, M. A., Djorgovski, S. G., & de Carvalho, R. R. 1995, ApJ, 453, L17

Pahre, M. A., & Djorgovski, S. G. 1997, in The Nature of Elliptical Galaxies, Proceedings of the Second Stromlo Symposium, eds. M. Arnaboldi, G. S. Da Costa, & P. Saha, ASP Conf. Ser. Vol. 116, (San Francisco: ASP), 154

Pahre, M. A. 1998a, in preparation [Chapter 2 of this thesis]

Pahre, M. A. 1998b, in preparation [Chapter 5 of this thesis]

Pahre, M. A., Djorgovski, S. G., & de Carvalho, R. R. 1998a, in preparation [Chapter 3 of this thesis]

Pahre, M. A., de Carvalho, R. R., & Djorgovski, S. G. 1998b, in preparation [Chapter 4 of this thesis]

Pahre, M. A., Djorgovski, S. G., & de Carvalho, R. R. 1998c, in preparation [Chapter 7 of this thesis]

Schade, D., Carlberg, R. G., Yee, H. K. C., López-Cruz, O., & Ellingson, E. 1996, ApJ, 464, L63

Tolman, R. C. 1934, Relativity, Thermodynamics and Cosmology (Oxford: Oxford Univ. Press)

Trager, S. C. 1997, Ph.D. Thesis, University of California (Santa Cruz)

Trager, S. C., Worthey, G., Faber, S. M., Burstein, D., & González, J. J. 1998, ApJS, in press

Vazdekis, A., Casuso, E., Peletier, R., & Beckman, J. E. 1996, ApJS, 106, 307

Worthey, G. 1994, ApJS, 95, 107

Worthey, G., & Ottaviani, D. L. 1997, ApJS, 111, 377

Ziegler, B. L., & Bender, R. 1997, MNRAS, 291, 527

Chapter 8

Summary: The Physical Properties Underlying the Sequence of Elliptical Galaxies

8.1 The Sequence of Elliptical Galaxies

This thesis has attempted to address the following question: What are the underlying physical properties that vary along the sequence of elliptical galaxies? There are a number of different properties which were investigated: metallicity, age, and systematic homology breaking. Other properties, such as initial mass function (IMF), dark matter content, dynamical anisotropy, and multiple episodes of star formation, may also vary along the galaxy sequence.

Since only some properties were investigated, it may be argued that the conclusions drawn from this work are not unique. To this there are several responses. One, while some of the models not addressed in this thesis can provide a reasonable explanation as to why the slope of the FP does not match the virial expectation (under the assumptions of constant mass–to–light ratio and homology), the systematic steepening of the slope of the FP with wavelength (shown in Chapter 4) can only be addressed by the stellar populations parameters of age, metallicity, and the IMF.

Two, the exclusion of the IMF from consideration for the models in Chapter 4 was a result of the limited constraints available for the shape of the IMF in the extreme environment that existed during the presumably high rate of star formation during elliptical galaxy formation. A limitation of the empirical model in Chapter 4 is that the physical properties are constructed so as to be varying smoothly along the galaxy sequence; a sudden transition to a completely different IMF shape (like one that varies piece–wise) cannot be accommodated in this model.

Three, variations in the dark matter content of elliptical galaxies might certainly be playing a role, but addressing this issue requires very high S/N spectra which can typically

only be obtained for a few galaxies at a time. As time progresses and these galaxy samples increase to critical mass, this issue will be addressed. Nonetheless, the inclusion of a wavelength–independent contributor to the slope of the FP in the models of Chapter 4 could be recast as a constraint on systematic dark matter variations among elliptical galaxies.

Four, dynamical anisotropy could be relevant, but it might already have been addressed in an indirect manner through the treatment of the systematic breaking of homology among the dynamical structures of elliptical galaxies (see Ciotti 1997 for how the two are connected). It was merely an observer's bias to call this effect "dynamical non-homology," since operationally that is the effect which appears as systematic variations in the function $\sigma(r/r_{\rm eff})$ which correlate with luminosity along the galaxy sequence.

Finally, since the slope of the K–band FP itself appears to be varying with redshift (Chapter 7), there now appears to be strong evidence that age must be playing a role along the galaxy sequence.

In summary, while some of the models that have been proposed to explain the slope of the FP have not been dealt with in this thesis, the *class* of stellar populations models that were discussed (Chapter 4) *must* be included in any comprehensive picture for the origins of the FP since the slope of the FP has now been shown to vary with wavelength (Chapters 3 and 4) and redshift (Chapter 7). As a result, models for variations in dark matter or dynamical anisotropy can only be discussed as possible effects in addition to the required stellar populations effects.

8.2 Summary of Results in This Thesis

This thesis has presented a number of different kinds of new data, and has drawn upon additional data from the literature, all of which were used to probe the underlying physical properties of elliptical galaxies which vary along the galaxy sequence. The major sets of data presented and conclusions reached in this thesis are:

- Near–infrared imaging data in the K–band atmospheric window at $\lambda = 2.2\mu$m were described for 341 early–type galaxies, which were mostly drawn from rich clusters of galaxies in the local universe. This is the first large–scale, near–infrared imaging survey of early–type galaxies.

- These data were used to construct the first large, homogeneous set of global photometric parameters derived from near–infrared imaging data (Chapter 2).

- These global photometric parameters were supplemented by global spectroscopic parameters (central velocity dispersions and Mg_2 indices, Chapter 2), and then used to construct the near–infrared Fundamental Plane (FP) of elliptical galaxies and its related correlations and projections (Chapter 3). These correlations were shown to have a small scatter that is similar to the optical FP correlations, and to deviate strongly from the virial expectation under the assumptions of homology and constant mass–to–light ratio.

- The near–infrared and spectroscopic data were supplemented by optical global photometric parameters (Chapter 2), which were then used to show for the first time, in a distance independent manner (Chapter 4), that the slope of the FP correlations systematically increase with wavelength.

- A complete and self–consistent model was developed (Chapter 4) which, for the first time, could simultaneously account for

  - the variations in the slope of the FP from the U–band ($\lambda = 0.36\mu$m) to the K–band ($\lambda = 2.2\mu$m),
  - the slope of the Mg_2–σ_0 relation,
  - the effects of populations gradients on the global scaling relations, and
  - the effects of systematic deviations of the dynamical structures of elliptical galaxies from a homologous family.

  This model generated a probability distribution for the variations in both age and metallicity along the sequence of elliptical galaxies, as well as for the extent that dynamical non–homology contributes to the sequence.

- Predictions were made (Chapter 4) based on this model for the variations in the slope of the FP with redshift both at optical and near–infrared wavelengths. This model has a modest agreement with observations of the slope of the FP at high redshift (Chapter 7).

- A new approach was described (Chapter 5) that uses two–color imaging data and a quantitative measure of morphology to identify a statistically complete and robust sample of early–type galaxies in distant clusters. This method proved to be $> 90\%$ effective in identifying galaxies with both an early–type spectral classification and a redshift placing them in the target cluster (Chapter 6).

- The galaxy samples identified in 26 clusters at $0 < z < 0.6$ were used to measure the color evolution in rest–frame $(U - V)_0$ (Chapter 5); the galaxies become bluer only slowly with redshift, with the effect being only $\lesssim 0.25$ mag between $z = 0$ and $z = 0.55$.

- Moderate dispersion spectroscopy of more than 100 early–type galaxies in six clusters at $0.1 < z < 0.6$ was described, which allowed for the measurement of central velocity dispersions and line strengths for each galaxy (Chapter 6). This galaxy sample more than tripled the number of previously available data in the literature on velocity dispersions of early–type galaxies at intermediate redshifts.

- Near–infrared imaging was described for the same galaxy sample, as well as 18 galaxies which have measurements of central velocity dispersions in the literature (Chapter 6). Model galaxies, convolved with the instrumental PSF, were fit directly to the pixel data in order to measure the global photometric parameters of each galaxy. The combination of imaging and spectroscopic data more than quadruples the available data in the literature suitable for studying the elliptical galaxy scaling relations at high redshift.

- The near–infrared FP at high redshift was constructed for the first time (Chapter 7). The Tolman surface brightness dimming effect in an expanding world model was detected easily from these data, and small, but significant, luminosity evolution was detected on top of the dimming effect. The luminosity evolution is consistent with a high formation redshift for the mean stellar content of elliptical galaxies.

- The FP was shown for the first time to change slope with redshift (Chapter 7), despite the fact that the galaxy sample in this thesis is still quite small. Since the near–infrared light is virtually independent of metallicity, this is strong evidence that there exist significant and systematic age spreads of up to a factor of two along the FP sequence.

- The line strengths of Mg_2, $H\beta_G$, and $\langle Fe \rangle$, measured at fixed central velocity dispersion, were shown to evolve slowly with redshift in a manner which is fully consistent with passive evolution of a stellar content which formed at high redshift (Chapter 7). The Mg_2 evolutionary effect had been shown previously, but the evolution of the other two indices are shown here for the first time. The $H\beta_G$ index evolution is important, as it appears to be a good indicator of stellar age.

8.3 A Picture for the History of Elliptical Galaxies

It now appears that elliptical galaxies in rich clusters formed at high redshift for the following reasons:

- the evolution in $(U-V)_0$ color as a function of redshift for $0 < z < 0.6$ (Chapter 5) and $0 < z < 0.9$ (Rakos & Schombert 1995; Stanford, Eisenhardt, & Dickinson 1998),
- the evolution of the SB intercept of the FP for $0 < z < 0.6$ (Chapter 7; van Dokkum & Franx 1996; Kelson *et al.* 1997), and
- the evolution of the line indices Mg_2, $\langle Fe \rangle$, and especially $H\beta_G$ for $0 < z < 0.6$ (Chapter 7).[1]

It further appears as though there was a systematic variation in formation redshift $1 < z_f < 5$, with the most massive galaxies having formed at the highest redshifts, for the following reasons:

- the slope of the FP varies with wavelength for nearby galaxies (Chapter 4) in a manner which appears to require a small, but significant, age spread among elliptical galaxies,
- the evolution of the slope of the FP for $0 < z < 0.6$ (Chapter 7), and
- the surface brightness fluctuations magnitudes in the K–band correlate with $(V-I)$ color (Jensen 1997).

[1]Note that while evolution of Mg_2 has been described by Bender, Ziegler, & Bruzual (1996), the model comparisons shown in Chapter 7 in Figure 7.7 suggest that no distinction between formation redshifts $z_f = 1$ and $z_f = 5$ can be drawn on the basis of Mg_2 measurements at $z \sim 0.4$. For this reason their work on Mg_2 at $z = 0.37$ is not included here as a constraint on the formation redshift.

8.3.1 Can These Results be Reconciled with the Line Index Measurements of Trager (1997)?

The results presented in this thesis (Chapters 4 and 7) show that age, and probably also metallicity, are varying along the sequence such that the most luminous galaxies are both the oldest and the most metal rich. While this may sound like vindication for the currently popular idea that age is an important contributor to the variations in physical properties along the elliptical galaxy sequence (Worthey, Trager, & Faber 1995; Trager 1997), the results in this thesis directly contradict both the *sense* in which metallicity is varying in those other models and the *size* of the age variations from one end of the galaxy sequence to the other. The latter point is crucial, since the variations of the FP correlations with wavelength (Chapter 4) and redshift (Chapter 7) can allow up to a factor of two in total age spread, while the age spreads implied by the nearby galaxy samples of Gonzalez (1993) and Trager (1997), when compared to the models of Worthey (1994), seem to imply age spreads of approximately a factor of ten.

If the age variations were a factor of ten, then the slope of the near–infrared FP (Chapter 3) would have to be *shallower* than the optical FP if the most luminous galaxies were actually old and metal poor.[2] This is in direct contrast to the effect seen in Chapter 4. It is also extremely difficult to allow such large age spreads within the modest change in the slope of the FP with redshift (Chapter 7).

How might the results of Trager (1997)—which imply an age spread of a factor of ten based on observations of line indices and comparisons with models for nearby elliptical galaxies—be reconciled with the results presented in this thesis?

The answer may lie in the subtle issue of correlated errors on the model–derived ages and metallicities in the Trager (1997) analysis. In that work, for example, measurements of Hβ and MgFe were compared with the Worthey (1994) models to derive an age and metallicity

[2]While Worthey *et al.* (1995) argue that the near–infrared FP in their model ought to be much *steeper* than the optical FP, their interpretation is probably flawed due to their reliance on the near–infrared models of Worthey (1994). As shown in Chapter 4, those models show a strong, inverse dependence of $(M/L)_K$ on metallicity, while both the Bruzual & Charlot (1996) and Vazdekis *et al.* (1996) models show virtually no dependence of $(M/L)_K$ on metallicity. This near–infrared property of the Worthey (1994) models is most likely wrong for a number of fundamental reasons (see Charlot, Worthey, & Bressan 1996). If there is a large age spread and a modest metallicity spread among elliptical galaxies, with the most luminous galaxies being both the oldest and most metal poor, then the age effect will make the optical FP shallower while the metallicity effect will partially offset by making the optical slightly steeper. Removal of metallicity effects in the near–infrared will then make that FP even shallower than the optical FP *in direct contrast to the data and FP correlations of Chapters 3 and 4.*

for each galaxy. A set of such derived ages and metallicities, taken directly from Trager (1997), is plotted in Figure 8.1. The problem with this method is that age and metallicity do not act parallel to either of the axes defined by the observables Hβ and Mg_2. A measurement error in either quantity therefore results in a *correlated* error in both age and metallicity. The *sense* of this correlated error in the model–derived parameters is exactly along the direction of the suggested correlation between age and metallicity of Trager (1997), which immediately raises a suspicion as to whether this correlation is real or an artifact of the analysis. This effect was clearly identified by Trager (1997), who constructed a series of Monte Carlo simulations in an attempt to assess quantitatively these effects. Inspection of the results of these simulations suggests that an underestimation of the uncertainties in the measurement of Hβ, Mg_2, and $\langle$Fe$\rangle$ in the Gonzalez (1993) data is all that is necessary to erase the suggested correlation between age and metallicity. This modest underestimation of the uncertainties might be somewhat troubling, but it is a possibility that should be entertained.[3]

If the correlation of age and metallicity favored by Trager (1997)—where older elliptical galaxies are more metal poor—were actually a result of correlated measurement errors, then how would the modest age and metallicity variations suggested in the present thesis appear in the data of Trager (1997)? The answer is simple: a correlation where the oldest elliptical galaxies are also the most metal rich would appear as a scatter *perpendicular* to the correlation claimed by Trager (1997). The Monte Carlo simulations provide strong evidence that there is very little correlated error in this perpendicular direction, while the data show a substantially larger scatter than the simulations. This scatter in the perpendicular direction cannot be ascribed to the correlated errors on the derived age and metallicity values, and hence the scatter appears real and intrinsic to the population of elliptical galaxies—only in a sense which differs from the interpretation of Trager (1997). The models from Chapter 4 lie in this perpendicular direction and are plotted in Figure 8.1, implying that this is the true sense of the correlation of age and metallicity along the elliptical galaxy sequence. In summary, this interpretation suggests that the data of Gonzalez (1993), as well as the calculation of age and metallicity in the analysis of Trager (1997) based on the Worthey

[3]Looking at the comparison of the extent of the Trager (1997) correlation between age and metallicity and the extent of the same correlation derived from the Monte Carlo simulations (which represent the effects of measurement uncertainties in producing correlated errors in the derived age and metallicity values), the correlation suggested by Trager (1997) could alternatively be called a "two sigma result."

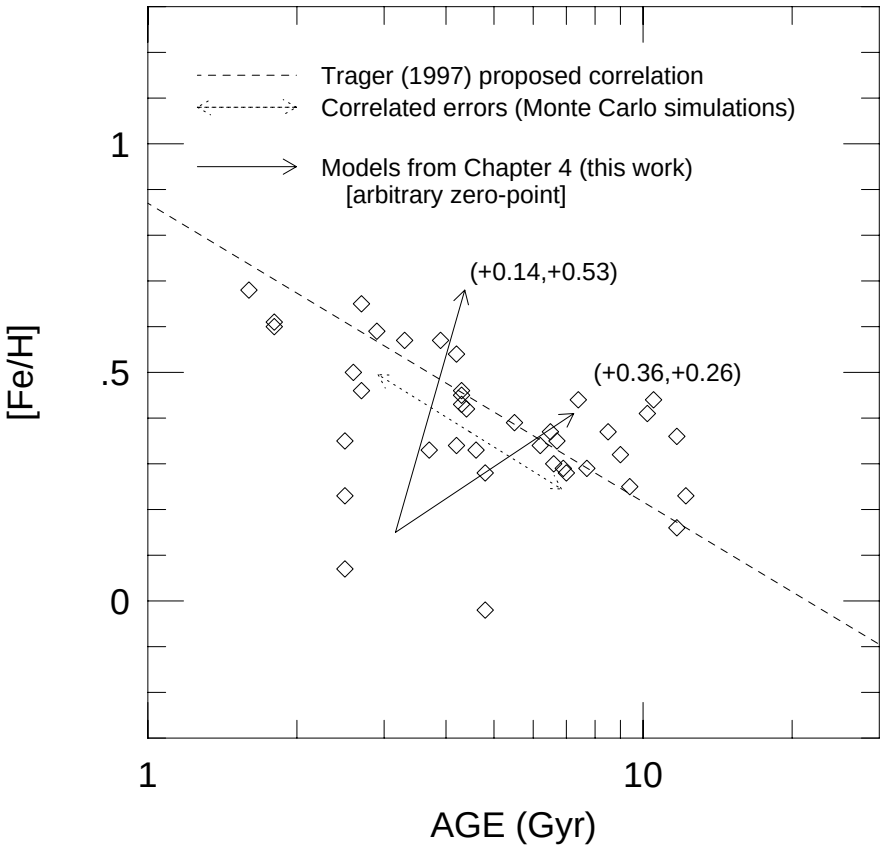

Figure 8.1: Comparison of the models from this thesis (Chapter 4) with the ages and metallicities derived by Trager (1997) from the Hβ and MgFe data of Gonzalez (1993, open symbols) using the models of Worthey (1994). The correlation suggested by Trager (1997, dashed line), in which the most luminous galaxies are both the oldest and the most metal *poor*, lies parallel to the direction of the correlated measurement errors in age and metallicity (dotted line vectors) based on the Monte Carlo simulations of Trager (1997). The errors perpendicular to this line, however, are extremely small and are suggested here to portray the true intrinsic variations along the elliptical galaxy sequence. The models proposed in this thesis (Chapter 4)—based on the optical and near–infrared FP, Mg_2–σ_0 relation, color gradients, and dynamical non–homology—are plotted as solid line vectors and represent variations across the full sequence of elliptical galaxies of $(\Delta \log t, \Delta[\mathrm{Fe/H}]) = (+0.36, +0.26)$ [Equation 4.10] and $(+0.14, +0.53)$ [Equation 4.12]. These models are broadly consistent with the evolution of the line indices and the slope of the FP with redshift (Chapter 7) and imply that the most luminous elliptical galaxies are both the oldest and the most metal *rich*. It is clearly difficult to interpret diagrams such as this one which have a strong correlation of errors in the derived parameters of age and metallicity.

(1994) models, are fully consistent with the conclusions reached in the present thesis—while the *interpretation* of Trager (1997) based on those same data and analysis is inconsistent.

While some investigators have insisted that the combination of a metallicity sensitive line index (like Mg_2 or $\langle Fe \rangle$) with a Balmer series line index (like Hβ) is an excellent way to separate the effects of age and metallicity in the stellar populations of elliptical galaxies, the strongly correlated errors between the derived ages and metallicities suggest that this approach is fundamentally problematical. This point is emphasized by the large uncertainties involved in interpreting a diagram such as Figure 8.1. The approach taken in this thesis, on the other hand, uses subtle but significant variations in the global scaling relations as a function of wavelength for nearby galaxies (Chapter 4) and as a function of redshift for distant galaxies (Chapter 7).

8.3.2 The Formation Epoch for Elliptical Galaxies

While the average elliptical galaxy appears to have formed at redshifts of $z_f \sim 3$, the changing slope of the FP with redshift implies that this formation redshift correlates with position on the FP, and hence with luminosity. In a $(H_0, \Omega_0, \Lambda_0) = (75, 0.2, 0)$ cosmology the age of the universe is ~ 11 Gyr. Formation of the most massive and luminous galaxies at $z_f = 5$ results in a present age for these galaxies of 10 Gyr; observations of the FP at $z \sim 0.5$ describes the properties of these galaxies when they were ~ 5 Gyr old. If the least massive galaxies formed at $z_f = 1$, then their present age is 6 Gyr which provides nearly the factor of two variation in the present–day ages of these galaxies that one model in Chapter 4 (Equation 4.10) required; observations of the FP at $z \sim 0.5$ describes the properties of these lowest luminosity galaxies when they were ~ 2 Gyr old. The range in formation redshift of $1 < z_f < 5$, with the "average" elliptical galaxy forming at $z \sim 3$, fits all available data and models for nearby and intermediate redshift elliptical galaxies. The data at $0 < z < 0.6$ therefore imply that $1 < z_f < 5$ was the epoch of elliptical galaxy formation.

One of the most exciting discoveries to come from the Keck Telescopes is the spectroscopic identification of a population of star forming galaxies at $z \sim 3$ (Steidel *et al.* 1996). This population has been argued to match the approximate comoving number density of nearby elliptical galaxies, it appears to have the star formation rates necessary to create massive galaxies (Steidel *et al.* 1996), and the galaxies have morphologies which are similar to present–day spheroids (Giavalisco, Steidel, & Macchetto 1996). Furthermore, the clus-

tering properties of these galaxies (Steidel *et al.* 1998) suggest that many of these "Lyman break" galaxies belong to massive structures which will collapse at later epochs to form the rich clusters in which elliptical galaxies are often found at low redshift. Nonetheless, while the connection of $z \sim 3$ star forming galaxies to local elliptical galaxies appears significant—possibly even strong—the nature of the evidence connecting the two is still primarily circumstantial.

One method of connecting nearby galaxies with their star forming progenitors at high redshifts is effectively the approach adopted in this thesis: observe elliptical galaxies progressively back in redshift for $0 < z < 0.6$ using their global properties as the indicator of their history. The obvious hope is that future observations of the elliptical galaxy scaling relations at $z > 0.6$ will eventually find a closer link in redshift with future observations of star forming galaxies at $1 < z < 2$. Such observations would provide a much stronger connection between the low and high redshift populations of galaxies.

8.3.3 Hierarchical Structure Formation and Elliptical Galaxies

The Cold, Dark Matter (CDM) cosmological model has enjoyed a number of stunning successes in the last two decades, particularly in the predictions regarding the cosmic microwave background radiation and its anisotropy. Detailed numerical simulations of CDM models imply that the formation of large structures, such as rich clusters, should occur late in the universe's history. Likewise, the most massive galaxies should also form late in the CDM model through a hierarchical series of mergers of disk galaxies: large amounts of dissipation accompany a given merger which can increase the luminosity density to the values commonly found for elliptical galaxies, and the supernova winds from a massive burst of star formation following the merger can blow away the gas to stop future star formation. The consequences of hierarchical structure formation in the CDM model should be directly testable by a number of observed properties of elliptical galaxies both nearby and at higher redshifts since these galaxies have well–constrained properties and provide a significant baseline in mass.

A naive picture of hierarchical structure formation suggests that the largest galaxies formed last, hence the elliptical galaxies sequence should have an anti–correlation between age and luminosity. More sophisticated, semi–analytical models suggest that while this naive picture is a reasonable representation of the CDM model for the low density environment

of the general field, in rich clusters the models predict no correlation between age and luminosity for elliptical galaxies (Kauffmann 1996). The reason for this modification is that even in a CDM model the mergers in the cores of rich clusters occur at early epochs, while the mergers in the field occur quite at late epochs virtually up to the present day. This prediction for the age sequence is directly contradicted by the implied age sequence of the models developed in Chapter 4 (based on the scaling relations for nearby early–type galaxies, Equations 4.10 and 4.12) and the evolution of the slope of the FP with redshift in Chapter 7 (Figure 7.5).

The present–day age of an elliptical galaxy in the field is predicted in a CDM model to be 4 Gyr younger than an elliptical galaxy in a rich cluster (Kauffmann 1996). This effect is contradicted by the comparison of relations between ($\log D_K - \log D_V$ and $\log \sigma_0$ (Chapter 4) for many different environments ranging from rich clusters to loose groups and the general field (Figure 4.4). Field and cluster elliptical galaxies at intermediate redshifts were also found to follow similar scaling relations and have a similar evolutionary history (Schade *et al.* 1996), further contradicting the CDM prediction of Kauffmann (1996).

The mass–to–light ratio for elliptical galaxies is predicted in a CDM model to be roughly constant with mass both in the optical and near–infrared (Kauffmann & Charlot 1997). The difficulty of making a comparison between this model prediction (which only includes the stellar M/L and total stellar mass for each galaxy) and the observations is that other effects may enter, such as non–homology and variations in dark matter content. The model constructed in Chapter 4, however, explicitly separates the stellar populations effects from the non–homology (or dark matter content) effects, and hence a direct comparison is made with the Kauffmann & Charlot prediction. The intrinsic properties of the stellar populations in the model of Chapter 4 still have a significant dependence of M/L on mass at every wavelength, thus contradicting the CDM model.

It should be noted that the CDM model is successful at producing a small scatter for the color–magnitude relation in rich clusters up to $z \sim 1$ (Kauffmann 1996; Baugh, Cole, & Frenk 1996). The model of Kauffmann & Charlot (1997) can also match the slope of the Mg_2–σ_0 relation, although this is achieved through an assumption of constant v_c/σ. The morphology density relation is reproduced by the models (Kauffmann 1995; Baugh, Cole, & Frenk 1996). On the other hand, while the model of Kauffmann & Charlot (1997) appears to be successful at producing the slope of the color–magnitude relation this is probably

accidental since adding the effects of color gradients into the CDM models probably causes the model slope to be significantly larger than the observed one.

It appears as though the CDM, semi–analytical models have been only partially successful in describing the properties of real elliptical galaxies. Both of the major classes of these models (Kauffmann, or Baugh and collaborators) rely on dividing galaxies between elliptical and spiral based on a threshold mass fraction in the merger process. Thus elliptical galaxies in such a model can *only* form through mergers of two disk galaxies of similar mass *by construction*. While these semi–analytical CDM models seem to be capable of producing the required comoving number density and bias properties of $z \sim 3$ star forming galaxies (Frenk *et al.* 1997), the implied stellar masses for those galaxies is only a few times $10^9 M_\odot$ ($10^{10} M_\odot$ for a Λ CDM model) and the results are highly sensitive to the IMF and the linear density fluctuation spectrum σ_8. This stellar mass appears to be unreasonably small: at a star formation rate of $\sim 10 M_\odot$ yr^{-1} the population would be observed as Lyman break galaxies for only $\Delta z \sim 0.2$, implying comoving number densities of these objects (which the models themselves imply are associated with $10^{12} M_\odot$ dark halos) far in excess of local densities.

In order to match the local space densities of massive galaxies associated with $10^{12} M_\odot$ dark halos, the Lyman break galaxies at $z \sim 3$ must then have substantially larger stellar masses than a few times $10^9 M_\odot$ in order to prolong their star formation time-scale and thus reduce their comoving number density. In that case, much more massive stellar populations are formed at $z \sim 3$, implying that the stellar content of massive elliptical galaxies can be assembled in a manner which is more akin to "monolithic collapse" at early epochs, thereby avoiding the hierarchical merging formation route.

Perhaps the inconsistencies between the CDM model predictions and the actual global properties of elliptical galaxies could be repaired by a model in which massive elliptical galaxies can form early—possibly then virtually no elliptical galaxies form through hierarchical, dissipational merging. This might be accomplished in the cosmological models by significant variations in the mass density of the universe (i.e., repeating the semi–analytical calculations for $\Omega_0 < 1$), increasing the bias parameter for elliptical galaxies at the high redshifts at which they are forming, and expanding the histories or formation processes that can produce elliptical galaxies. Furthermore, the fact that the semi–analytical CDM models can predict a mass–metallicity relation (the Mg_2–σ_0 relation) and a color–magnitude

relation (within a factor of two in slope), while they are unable to produce a stellar M/L systematic variation as a function of stellar L, suggests that there are serious problems in the semi–analytical treatment of how to associate stellar mass with total mass.

8.4 Future Work

The most glaring limitation to the accuracy of the model for the elliptical galaxy scaling relations in Chapter 4 is the poor understanding of the effects of aperture on measured, line–of–sight velocity dispersions. While Jørgensen, Franx, & Kjærgaard (1995) showed that there was a simple, power–law relation between $\sigma(r)$ and σ_0, they also noted that there appeared to be a weak, but systematic variation of this power–law index of a factor of three along the galaxy sequence. Busarello *et al.* (1997) have showed that there is a marginally significant relation between $\log \sigma_0$ (the central velocity dispersion) and $\log \sigma_{\rm eff}$ (the velocity dispersion at the effective radius) that, if true, would contradict the assumption that elliptical galaxies form a homologous family. de Carvalho, Capelato, & Carlberg (private communication) appear to be able to reproduce this effect with the first generation of mergers of dissipationless systems in their numerical simulations. If this effect could be quantified much more accurately in an empirical manner, specifically by measuring velocity dispersions as a function of aperture size for many galaxies, then the combination of this new constraint with the slope of the FP in the K–band (Chapter 3) would determine far more accurately the variations in age that are allowed along the early–type galaxy sequence for the model constructed here (Chapter 4). Who would have thought that measurements of velocity dispersions in various aperture sizes could help break the age–metallicity degeneracy?

The other limitation of this model for the galaxy sequence is that it does not constrain color gradients. Combining the K–band galaxy photometry (Chapter 2) with the larger body of surface photometry at optical wavelengths that is already available in the literature is an obvious project which could provide far better constraints on the size of color gradients in elliptical galaxies. The ratios of optical–optical and optical–infrared color gradients should, once and for all, also discriminate between stellar populations gradients (Peletier 1993) and diffuse distributions of dust (Wise & Silva 1996) as the primary cause of color gradients in elliptical galaxies.

At high redshifts, it is clear that the astronomical community is only now, with the advent of the 10 m class telescopes like Keck, beginning to assemble significant sample sizes of early–type galaxies at intermediate redshifts. A number of different groups, including competitors within certain other institutions, are currently attacking this problem. It would not be surprising if the data at $0.1 < z < 0.6$ in this thesis are dwarfed several years from now. The challenges for the future investigators will be: (1) to determine the variations of the FP slope with redshift to much higher accuracy than has been achieved here, thereby directly determining the effects of age on the elliptical galaxy sequence; (2) to begin to duplicate observations of some galaxies between research groups, and within a research group, since velocity dispersion measurements for local galaxies often show significant and systematic variations from run to run, telescope to telescope, month to month, and observer to observer; (3) to develop a new set of high resolution stellar template spectra, spanning a significant range of metallicity and spectral type, which can be used to measure velocity dispersions more accurately at high redshifts; (4) to devise a new set of line indices which are much more appropriate in resolution to the spectroscopy that is now typically obtained—the indices based on the Lick/IDS data, at 8–10 Å resolution, do not fully exploit the wealth of information in moderate dispersion spectra at high redshifts; (5) to construct a catalog of photometry *at many wavelengths* for a sample of galaxies, which can then be used to examine the variations of the FP correlations with wavelength using the method developed in Chapter 4; (6) to determine what effects different galaxy selection criteria have on the properties measured by the FP correlations; and (7) to investigate possible variations in the FP correlations for galaxies in X–ray, optical, or CMBR (via the Sunyaev–Zeldovich effect) selected clusters.

Achieving all of these goals would be an impressive maturation of the study of the elliptical galaxy correlations.

References

Baugh, C. M., Cole, S., & Frenk, C. S. 1996, MNRAS, 283, 1361

Bender, R., Ziegler, B., & Bruzual, G. 1996, ApJ, 463, L51

Bruzual, A. G., & Charlot, S. 1996, in preparation

Busarello, G., Capaccioli, M., Capozziello, S., Longo, G., & Puddu, E. 1997, A&A, 320, 415

Charlot, S., Worthey, G., & Bressan, A. 1996, ApJ, 457, 625

Ciotti, L. 1997, in Galaxy Scaling Relations: Origins, Evolution, and Applications, Proceedings of the Third ESO–VLT Workshop, eds. L. N. da Costa & A. Renzini (Springer–Verlag: Berlin), 38

van Dokkum, P. G., & Franx, M. 1996, MNRAS, 281, 985

Frenk, C. S., Baugh, C. M., Cole, S., & Lacey, C. 1997, in Dark Matter 1996: Dark and Visible Matter in Galaxies and Cosmological Implications, eds. M. Persic, & P. Salucci, in press

Giavalisco, M., Steidel, C. C., & Macchetto, F. D. 1996, ApJ, 470, 189

Gonzalez, J. J. 1993, Ph.D. thesis, University of California (Santa Cruz)

Jensen, J. B. 1997, Ph.D. Thesis, University of Hawaii

Jørgensen, I., Franx, M., & Kjærgaard, P. 1995, MNRAS, 276, 1341

Kauffmann, G. 1995, MNRAS, 274, 153

Kauffmann, G. 1996, MNRAS, 281, 487

Kauffmann, G., & Charlot, S. 1997, MNRAS, submitted

Kelson, D. D., Dokkum, P. G., Franx, M., Illingworth, G. D., & Fabricant, D. 1997, ApJ, 478, L13

Peletier, R. F. 1993, in proceedings of the ESO/EIPC Workshop on Structure, Dynamics, and Chemical Evolution of Early–Type Galaxies, ed. J. Danziger, *et al.*, ESO publication No. 45, 409

Rakos, K. D., & Schombert, J. M. 1995, ApJ, 439, 47

Schade, D., Carlberg, R. G., Yee, H. K. C., López-Cruz, O., & Ellingson, E. 1996, ApJ, 464, L63

Stanford, S. A., Eisenhardt, P. R., & Dickinson, M. 1998, ApJ, 492, 461

Steidel, C. C., Giavalisco, M., Pettini, M., Dickinson, M., & Adelberger, K. L. 1996, ApJ, 462, L17

Steidel, C. C., Adelberger, K. L., Dickinson, M., Giavalisco, M., Pettini, M., & Kellogg, M. 1998, ApJ, 492, 428

Trager, S. C. 1997, Ph.D. Thesis, University of California (Santa Cruz)

Vazdekis, A., Casuso, E., Peletier, R., & Beckman, J. E. 1996, ApJS, 106, 307

Wise, M. W., & Silva, D. R. 1996, ApJ, 461, 155

Worthey, G. 1994, ApJS, 95, 107

Worthey, G., Trager, S. C., & Faber, S. M. 1995, in Fresh Views of Elliptical Galaxies, ASP Conf. Ser. Vol. 86, eds. A. Buzzoni & A. Renzini (San Francisco: ASP) 203

Appendix A Tables of Global Photometric and Spectroscopic Parameters for Nearby Early–Type Galaxy Surveys

This appendix includes catalogs of data that were compiled in Chapter 2 and used in Chapters 3, 4, and 7 in constructing the Fundamental Plane and other correlations.

The global photometric parameters for the 454 individual measurements in the K–band are tabulated in Table A.1. The circular aperture photometry was used to measure half–light effective radii $r_{\rm eff}$ and mean surface brightnesses $\langle\mu\rangle_{\rm eff}$, total magnitude $K_{\rm tot}$, and D_K. The isophotal, elliptical surface photometry was used to measure half–light semimajor axis lengths $a_{\rm e}$, mean surface brightnesses $\langle\mu\rangle_{\rm e}$, ellipticity $\epsilon_{\rm e}$ evaluated at the half–light semimajor axis length, total magnitude $K_{\rm tot}$, and effective radius $r_{\rm e} = a_{\rm e}\sqrt{1-\epsilon_{\rm e}}$.

Multiple observations from the circular aperture photometry were averaged (using logarithmic quantities) to create a combined, final K–band data set in Table A.2 of the 341 galaxies studied. Also listed in that table are the optical global photometric parameters and the spectroscopic parameters drawn from the literature using the methods described in §2.9. The spectroscopic quantities are corrected to a physical aperture diameter of 1.53 kpc, corresponding to an angular size of 3.4 arcsec at the distance of the Coma cluster ($H_0 = 75$ km s^{-1} Mpc^{-1}). When a $(V-K)$ color is not calculated using matched aperture magnitudes it is identified with a colon.

A series of catalogs were created for the comparison between the K–band photometric quantities and the optical photometric quantities from each literature source (or collection of studies by a similar group of authors). These are tabulated as Tables A.3 through A.13. All of the spectroscopic quantities and morphological types are taken as the same values from the final catalog (Table A.2), but are reproduced in the individual comparison catalogs for ease of inspection.

An additional series of catalogs were created for the comparison of photometric quantities among optical bandpasses. Some of these galaxies overlap with the K–band survey,

while others do not. Hence the spectroscopic quantities are listed for each galaxy in each catalog. These catalogs are included as Tables A.14 through A.21.

Table A.1: All Measurements of K–Band Global Photometric Parameters

Name	Cluster/ Group	Tel	Circular Aperture Photometry					Surface Photometry			
			$\log r_{\rm eff}$ ($''$)	$\langle\mu\rangle_{\rm eff}$ (mag/$''$)	$K_{\rm tot}$ (mag)	$\log D_K$ ($''$)	K_{20} (mag)	$\log r_{\rm e}$ ($''$)	ϵ_e	$\langle\mu\rangle_{\rm e}$ (mag/$''$)	$K_{\rm tot}$ (mag)
(1)	(2)	(3)	(4)	(5)	(6)	(7)	(8)	(9)	(10)	(11)	(12)
D22	A194	P60	0.890	18.480	12.032	0.667	12.609	1.147	0.214	19.615	11.885
D28	A194	P60	0.775	17.861	11.991	0.692	12.449	0.591	0.379	16.881	11.929
D29	A194	P60	0.519	15.412	10.827	1.142	11.067	0.726	0.577	16.186	10.561
D30	A194	P60	0.663	16.218	10.909	1.080	11.259	1.012	0.493	17.828	10.773
D33	A194	P60	0.592	15.743	10.788	1.131	11.072	0.486	0.393	14.650	10.227
D44	A194	P60	0.738	16.816	11.131	1.001	11.551	0.484	0.493	15.620	11.203
D45	A194	P60	0.625	16.388	11.266	1.000	11.573	0.806	0.297	17.134	11.111
D50	A194	P60	0.558	15.576	10.791	1.144	11.064	0.790	0.399	16.691	10.743
D52	A194	P60	0.555	16.796	12.025	0.818	12.292	0.127	0.433	14.529	11.894
D53	A194	P60	0.520	15.313	10.721	1.170	10.967	0.675	0.448	15.766	10.399
D55	A194	P60	0.479	17.378	12.993	0.554	13.212	0.565	0.496	17.540	12.723
D57	A194	P60	0.660	17.460	12.164	0.665	12.514	0.493	0.167	16.302	11.844
D62	A194	P60	0.778	17.539	11.655	0.832	12.115	1.190	0.333	19.225	11.280
I1696	A194	P60	0.680	15.972	10.576	1.166	10.951	0.752	0.098	16.265	10.511
N0533	A194	P60	1.301	17.171	8.671	1.460	9.880	1.284	0.250	16.983	8.565
N0538	A194	P60	0.860	16.502	10.206	1.188	10.784	1.001	0.568	16.893	9.891
N0541	A194	P60	1.209	17.181	9.141	1.359	10.190	1.417	0.201	18.126	9.047
N0545	A194	P60	1.425	17.648	8.527	1.424	9.990	1.704	0.323	18.714	8.201
N0547	A194	P60	0.939	16.134	9.444	1.408	10.082	0.951	0.148	16.037	9.286
N0548	A194	P60	0.924	17.503	10.887	0.979	11.514	0.854	0.184	17.076	10.809
N0564	A194	P60	0.919	16.269	9.678	1.329	10.291	0.754	0.253	15.382	9.618
FCOM	A2199	P60	0.288	16.319	12.889	0.683	13.054	0.241	0.605	15.930	12.731
FCOM	A2199	P60	0.354	16.663	12.897	0.662	13.048	0.117	0.709	15.922	13.336
L111	A2199	P60	0.799	17.342	11.349	0.928	11.825	0.581	0.404	16.492	11.595
L112	A2199	P60	0.188	15.097	12.169	0.898	12.255	0.446	0.170	15.954	11.734
L113	A2199	P60	0.199	15.844	12.856	0.720	12.973	-0.046	0.140	14.026	12.254
L114	A2199	P60	0.270	15.617	12.280	0.854	12.390	0.107	0.581	14.813	12.285
L118	A2199	P60	0.717	17.252	11.672	0.866	12.079	0.758	0.225	17.406	11.619
L136	A2199	P60	0.286	15.470	12.042	0.907	12.166	0.433	0.172	15.903	11.746
L1381	A2199	P60	0.004	14.468	12.454	0.872	12.469	-0.004	0.605	14.701	12.733
L1381	A2199	P60	0.117	14.976	12.396	0.860	12.443	0.134	0.340	14.908	12.245
L139	A2199	P60	0.258	16.921	13.631	0.473	13.723	0.616	0.425	19.346	14.272
L139	A2199	P60	0.301	17.107	13.607	0.467	13.813	0.236	0.444	15.954	12.783
L139	A2199	P60	0.638	18.255	13.068	0.452	13.417	0.152	0.455	15.032	12.281
L143	A2199	P60	0.324	15.060	11.438	1.118	11.575	0.663	0.273	16.268	10.961
L145	A2199	P60	0.826	17.655	11.530	0.863	12.028	0.393	0.450	15.360	11.403
L145	A2199	P60	0.915	17.946	11.374	0.871	11.986	0.176	0.447	13.850	10.977
L145	A2199	P60	0.975	18.161	11.293	0.854	11.979	0.435	0.435	15.462	11.293
L150	A2199	P60	0.193	16.234	13.267	0.618	13.374	0.420	0.429	16.983	12.886
L150	A2199	P60	0.444	17.184	12.970	0.633	13.179	0.524	0.580	17.496	12.882
L151	A2199	P60	0.358	17.519	13.732	0.447	13.875	0.057	0.139	15.489	13.214
L152	A2199	P60	1.094	18.353	10.888	0.894	11.751	1.077	0.176	18.142	10.760
L152	A2199	P60	1.311	18.989	10.439	0.883	11.663	1.333	0.104	18.939	10.281
L153	A2199	P60	0.522	16.744	12.134	0.806	12.372	0.823	0.698	18.019	11.908
L153	A2199	P60	0.664	17.268	11.953	0.799	12.297	0.568	0.638	16.132	11.296
L158	A2199	P60	0.580	16.455	11.558	0.955	11.836	0.856	0.192	17.778	11.502
N6158	A2199	P60	0.990	17.329	10.384	1.112	11.104	1.086	0.244	17.700	10.273
N6158COMP	A2199	P60	0.479	17.158	12.769	0.652	12.993	0.591	0.540	17.505	12.555
N6166	A2199	P60	1.326	18.150	9.523	1.243	10.790	1.263	0.256	17.511	9.199
N6166	A2199	P60	1.419	18.302	9.212	1.276	10.675	1.578	0.361	18.581	8.696
NCOM	A2199	P60	-0.155	14.990	13.782	0.572	13.786	-0.481	0.152	11.974	12.390

Table A.1—*Continued*

Name	Group	Tel	Circular Aperture Photometry					Surface Photometry			
			$\log r_{\rm eff}$	$\langle\mu\rangle_{\rm eff}$	$K_{\rm tot}$	$\log D_K$	K_{20}	$\log r_{\rm e}$	ϵ_e	$\langle\mu\rangle_{\rm e}$	$K_{\rm tot}$
			($''$)	(mag/$''$)	(mag)	($''$)	(mag)	($''$)		(mag/$''$)	(mag)
(1)	(2)	(3)	(4)	(5)	(6)	(7)	(8)	(9)	(10)	(11)	(12)
NCOM	A2199	P60	-0.027	15.476	13.617	0.584	13.702	-0.347	0.112	12.774	12.525
S18	A2199	P60	0.418	15.857	11.773	0.958	11.957	0.637	0.110	16.586	11.406
S18	A2199	P60	0.577	16.414	11.531	0.959	11.816	0.588	0.087	16.319	11.383
S26	A2199	P60	0.883	17.581	11.169	0.937	11.757	0.960	0.167	17.925	11.127
S30	A2199	P60	0.243	15.236	12.031	0.923	12.147	-0.097	0.673	13.855	12.339
S30	A2199	P60	0.350	15.685	11.942	0.922	12.102	0.405	0.152	15.715	11.698
S30	A2199	P60	0.520	16.400	11.804	0.922	12.070	0.833	0.251	18.057	11.897
S30	A2199	P60	0.839	17.625	12.071	0.925	12.074	0.839	0.279	18.262	12.071
S33	A2199	P60	0.281	15.383	11.988	0.924	12.122	0.167	0.146	14.485	11.656
S33	A2199	P60	0.286	15.368	11.943	0.933	12.089	0.299	0.091	15.251	11.761
S33	A2199	P60	0.358	15.747	11.962	0.911	12.129	0.297	0.094	15.173	11.693
S34	A2199	P60	0.307	16.092	12.560	0.774	12.711	0.188	0.052	15.075	12.140
S34	A2199	P60	0.360	16.304	12.508	0.767	12.686	0.111	0.078	14.587	12.045
S43	A2199	P60	0.480	16.406	12.011	0.843	12.228	0.225	0.394	14.538	11.414
S44	A2199	P60	0.452	16.206	11.953	0.885	12.159	0.428	0.009	15.855	11.721
Z34A	A2199	P60	0.871	17.267	10.916	1.017	11.487	1.109	0.288	18.309	10.769
L102	A2634	P60	0.705	16.687	11.167	1.012	11.550	0.643	0.190	16.233	11.021
L106	A2634	P60	0.377	15.849	11.970	0.903	12.131	0.444	0.329	16.044	11.825
L107	A2634	P60	0.728	18.063	12.429	0.621	12.840	0.560	0.149	17.066	12.271
L108	A2634	P60	0.104	14.971	12.457	0.836	12.536	-0.060	0.401	13.485	11.797
L108	A2634	P60	0.161	15.197	12.389	0.844	12.475	-0.022	0.330	13.591	11.707
L109	A2634	P60	0.083	14.753	12.338	0.873	12.406	-0.310	0.543	11.602	11.143
L109	A2634	P60	0.140	15.057	12.357	0.856	12.442	-0.066	0.338	12.960	11.289
L111	A2634	P60	0.565	18.236	13.419	0.436	13.754	0.856	0.069	19.216	12.941
L113	A2634	P60	0.403	16.645	12.630	0.709	12.820	-0.022	0.635	13.816	11.925
L1201	A2634	P60	0.465	16.474	12.149	0.829	12.358	0.535	0.299	16.559	11.889
L1201	A2634	P60	0.470	16.491	12.147	0.822	12.358	0.494	0.219	16.218	11.751
L121	A2634	P60	0.314	15.927	12.362	0.821	12.495	0.334	0.063	15.786	12.114
L121	A2634	P60	0.330	16.026	12.376	0.810	12.521	0.117	0.244	14.664	12.090
L124	A2634	P60	0.334	15.900	12.237	0.839	12.390	0.053	0.238	13.793	11.535
L124	A2634	P60	0.360	15.971	12.175	0.852	12.339	0.314	0.203	15.421	11.859
L124	A2634	P60	0.364	15.962	12.146	0.857	12.299	0.143	0.331	14.497	11.791
L124	A2634	P60	0.467	16.360	12.027	0.859	12.242	0.336	0.212	15.357	11.679
L1261	A2634	P60	0.041	15.009	12.808	0.773	12.845	-0.060	0.391	14.191	12.502
L129	A2634	P60	0.539	16.134	11.444	0.993	11.698	0.834	0.555	17.362	11.197
L129	A2634	P60	0.545	16.154	11.434	0.993	11.691	0.730	0.508	16.775	11.128
L134	A2634	P60	0.639	16.377	11.183	1.031	11.517	0.512	0.216	15.586	11.034
L134	A2634	P60	0.688	16.550	11.115	1.034	11.490	0.729	0.171	16.689	11.047
L135	A2634	P60	0.489	16.442	12.003	0.852	12.226	0.537	0.422	16.400	11.722
L138	A2634	P60	0.777	16.957	11.080	1.008	11.537	0.785	0.049	16.895	10.978
L139	A2634	P60	0.763	16.719	10.911	1.059	11.350	0.658	0.075	16.041	10.755
L140	A2634	P60	0.248	14.912	11.680	1.005	11.789	0.279	0.230	14.782	11.392
N7720	A2634	P60	0.985	16.622	9.701	1.318	10.404	1.116	0.278	17.087	9.511
N7720	A2634	P60	1.335	17.765	9.095	1.332	10.364	1.508	0.381	18.502	8.966
N7720A	A2634	P60	0.334	15.310	11.640	1.000	11.799	0.137	0.270	13.723	11.046
N7720A	A2634	P60	0.348	15.405	11.671	0.991	11.839	0.281	0.073	14.437	11.038
D20	CEN45	C40old	1.044	17.060	9.847	1.234	10.703	1.292	0.303	18.143	9.687
D20	CEN45	C40old	1.090	17.203	9.757	1.239	10.684	1.352	0.244	18.297	9.544
D23	CEN45	C40old	0.934	16.730	10.062	1.215	10.762	0.966	0.553	16.643	9.819
D24	CEN45	C40old	1.105	17.572	10.052	1.107	11.025	0.841	0.554	16.047	9.850
D24	CEN45	C40old	1.153	17.755	9.994	1.101	11.039	0.845	0.537	16.044	9.822

Table A.1—*Continued*

Name	Group	Tel	Circular Aperture Photometry					Surface Photometry			
			$\log r_{\rm eff}$	$\langle\mu\rangle_{\rm eff}$	$K_{\rm tot}$	$\log D_K$	K_{20}	$\log r_{\rm e}$	ϵ_e	$\langle\mu\rangle_{\rm e}$	$K_{\rm tot}$
			($''$)	(mag/$''$)	(mag)	($''$)	(mag)	($''$)		(mag/$''$)	(mag)
(1)	(2)	(3)	(4)	(5)	(6)	(7)	(8)	(9)	(10)	(11)	(12)
D27	CEN45	C40old	0.815	16.527	10.458	1.152	11.003	0.415	0.374	14.464	10.396
D45	CEN45	C40old	1.061	15.771	8.470	1.615	9.350	1.147	0.426	15.956	8.227
N4616	CEN45	C40old	1.136	17.072	9.396	1.319	10.403	1.214	0.057	17.334	9.269
N4709	CEN45	C40old	1.451	17.250	7.999	1.612	9.556	1.550	0.098	17.489	7.745
D19	CEN30	C40old	0.719	15.021	9.428	1.438	9.863	0.832	0.258	15.233	9.080
D22	CEN30	C40old	0.959	17.012	10.220	1.167	10.955	1.166	0.462	18.013	10.189
D29	CEN30	C40old	1.020	17.072	9.978	1.204	10.789	1.342	0.645	18.497	9.794
D49	CEN30	C40old	0.693	16.153	10.694	1.128	11.110	0.554	0.041	15.267	10.505
D50	CEN30	C40old	0.974	17.101	10.237	1.146	10.980	0.880	0.074	16.539	10.142
D56	CEN30	C40old	0.747	16.399	10.665	1.118	11.154	0.820	0.052	16.687	10.593
D58	CEN30	C40old	0.782	16.029	10.124	1.245	10.646	0.531	0.516	14.484	9.835
D58	CEN30	C40old	0.836	16.243	10.068	1.246	10.645	0.607	0.486	14.875	9.844
D9	CEN30	C40old	0.912	17.146	10.593	1.074	11.275	1.092	0.135	17.992	10.534
J316	CEN30	C40old	0.905	15.479	8.960	1.513	9.618	0.984	0.248	15.664	8.748
N4645	CEN30	C40old	1.122	15.916	8.313	1.614	9.285	1.156	0.323	16.051	8.274
N4661	CEN30	C40old	1.041	17.374	10.171	1.128	11.033	0.883	0.623	16.349	9.940
N4696	CEN30	C100	1.810	18.197	7.152	1.663	9.531	1.947	0.057	18.431	6.699
N4696	CEN30	C100	1.838	18.253	7.070	1.668	9.525	1.967	0.099	18.502	6.672
N4696	CEN30	C40old	1.878	18.187	6.800	1.722	9.509	1.979	0.369	18.564	6.676
N4706	CEN30	C40old	1.423	17.778	9.059	1.434	9.934	1.423	0.506	18.169	9.059
N4729	CEN30	C40old	1.149	16.522	8.784	1.497	9.797	1.193	0.022	16.627	8.669
N4767	CEN30	C40old	1.283	16.468	8.056	1.649	9.324	1.425	0.446	16.992	7.874
D106	COMA	P60	0.438	16.529	12.345	0.776	12.548	0.334	0.109	15.687	12.015
D125	COMA	P60	0.124	15.067	12.448	0.836	12.539	0.009	0.145	14.063	12.028
D149	COMA	P60	-0.125	14.530	13.148	0.582	13.170	-0.268	0.662	11.547	10.872
D149	COMA	P60	0.742	18.382	12.675	0.516	13.095	0.479	0.696	16.791	12.405
D173	COMA	P60	0.417	16.227	12.150	0.846	12.324	0.666	0.418	17.383	12.058
D210	COMA	P60	0.559	16.467	11.675	0.926	11.956	0.576	0.252	16.587	11.711
D24	COMA	P60	0.631	16.106	10.953	1.089	11.281	0.486	0.275	15.421	10.994
D27	COMA	P60	0.544	17.034	12.321	0.736	12.583	0.258	0.198	15.196	11.915
D32	COMA	P60	0.310	16.315	12.769	0.709	12.911	0.164	0.556	15.627	12.808
D80	COMA	P60	0.797	17.934	11.951	0.747	12.434	0.763	0.317	17.723	11.916
D81	COMA	P60	0.732	17.767	12.109	0.744	12.541	1.084	0.238	19.330	11.915
D96	COMA	P60	0.529	16.237	11.597	0.957	11.856	0.870	0.080	17.902	11.558
E159G43	COMA	P60	0.702	16.190	10.682	1.137	11.066	0.758	0.322	16.398	10.612
E159G63	COMA	P60	0.866	17.462	11.134	0.947	11.682	0.954	0.148	17.796	11.031
E159G83	COMA	P60	0.728	16.088	10.452	1.205	10.889	0.960	0.177	17.200	10.405
E159G89	COMA	P60	0.825	17.000	10.880	1.043	11.410	0.896	0.057	17.243	10.769
E160G159	COMA	P60	0.869	17.035	10.697	1.071	11.251	0.953	0.176	17.368	10.606
E160G22	COMA	P60	0.607	15.705	10.671	1.162	10.978	0.853	0.371	16.733	10.474
E160G23	COMA	P60	0.452	15.790	11.538	0.992	11.744	0.516	0.248	15.877	11.300
E160G23	COMA	P60	0.547	16.034	11.308	1.024	11.574	0.369	0.054	14.716	10.871
E160G27	COMA	P60	0.611	16.510	11.459	0.960	11.768	0.467	0.044	15.505	11.177
I0832	COMA	P60	0.814	16.797	10.730	1.085	11.228	0.857	0.075	16.934	10.653
I0843	COMA	P60	0.742	15.919	10.212	1.247	10.639	0.744	0.475	15.723	10.009
I3900	COMA	P60	0.627	15.914	10.781	1.172	11.114	0.634	0.236	15.754	10.588
I3947	COMA	P60	0.470	16.123	11.779	0.926	11.999	0.348	0.345	15.144	11.409
I3957	COMA	P60	0.418	15.968	11.884	0.908	12.059	0.638	0.004	16.933	11.743
I3957	COMA	P60	0.672	16.926	11.572	0.915	11.961	1.055	0.047	18.697	11.427
I3959	COMA	P60	0.605	16.080	11.059	1.069	11.365	0.465	0.179	15.252	10.931
I3959	COMA	P60	0.706	16.464	10.939	1.070	11.345	0.597	0.162	15.866	10.888

Table A.1—*Continued*

Name	Group	Tel	Circular Aperture Photometry					Surface Photometry			
			$\log r_{\rm eff}$	$\langle\mu\rangle_{\rm eff}$	$K_{\rm tot}$	$\log D_K$	K_{20}	$\log r_{\rm e}$	ϵ_e	$\langle\mu\rangle_{\rm e}$	$K_{\rm tot}$
			($''$)	(mag/$''$)	(mag)	($''$)	(mag)	($''$)		(mag/$''$)	(mag)
(1)	(2)	(3)	(4)	(5)	(6)	(7)	(8)	(9)	(10)	(11)	(12)
I4011	COMA	P60	0.634	17.065	11.896	0.827	12.222	0.544	0.111	16.461	11.745
I4011	COMA	P60	0.667	17.158	11.829	0.833	12.198	0.438	0.245	16.028	11.846
I4012	COMA	P60	0.312	15.146	11.593	1.011	11.748	0.111	0.105	13.636	11.095
I4021	COMA	P60	0.809	16.774	10.735	1.086	11.225	0.849	0.088	16.891	10.650
I4045	COMA	P60	0.481	15.315	10.911	1.136	11.126	0.301	0.414	14.110	10.610
I4051	COMA	P60	1.058	17.505	10.221	1.118	11.018	1.061	0.190	17.423	10.120
I4133	COMA	P60	0.535	16.079	11.408	1.000	11.663	0.764	0.041	17.207	11.390
N4673	COMA	P60	0.760	15.619	9.827	1.340	10.269	0.756	0.124	15.435	9.659
N4692	COMA	P60	1.117	17.133	9.554	1.290	10.446	1.137	0.205	17.149	9.467
N4789	COMA	P60	1.039	16.604	9.414	1.372	10.202	1.277	0.317	17.511	9.133
N4807	COMA	P60	0.740	16.117	10.419	1.195	10.843	0.835	0.182	16.443	10.273
N4816	COMA	P60	1.299	18.150	9.661	1.163	10.875	1.516	0.191	18.990	9.415
N4824	COMA	P60	0.695	16.963	11.495	0.925	11.877	0.740	0.157	17.100	11.404
N4827	COMA	P60	1.001	16.899	9.898	1.245	10.631	1.081	0.192	17.217	9.819
N4839	COMA	P60	1.290	17.783	9.340	1.264	10.525	1.486	0.410	18.584	9.160
N4840	COMA	P60	0.709	16.093	10.552	1.169	10.941	0.638	0.197	15.641	10.451
N4841A	COMA	P60	1.094	17.172	9.705	1.255	10.571	1.127	0.182	17.261	9.632
N4841B	COMA	P60	0.790	16.687	10.740	1.091	11.210	0.755	0.015	16.397	10.626
N4850	COMA	P60	0.537	15.845	11.170	1.062	11.430	0.364	0.044	14.534	10.720
N4854	COMA	P60	0.930	17.579	10.931	0.975	11.570	1.187	0.353	18.762	10.831
N4860	COMA	P60	0.706	15.948	10.424	1.205	10.807	0.674	0.149	15.607	10.241
N4864	COMA	P60	0.878	16.983	10.597	1.138	11.196	0.819	0.100	16.415	10.324
N4867	COMA	P60	0.497	15.700	11.223	1.058	11.453	0.562	0.061	15.881	11.076
N4869	COMA	P60	0.812	16.610	10.557	1.152	11.057	0.664	0.186	15.732	10.420
N4871	COMA	P60	0.694	16.597	11.133	1.045	11.509	0.891	0.457	17.267	10.816
N4871	COMA	P60	0.865	17.220	10.904	1.017	11.459	0.777	0.425	16.699	10.819
N4872	COMA	P60	0.458	15.560	11.278	1.055	11.483	0.642	0.053	16.206	11.000
N4872	COMA	P60	0.462	15.587	11.281	1.052	11.491	0.646	0.038	16.184	10.958
N4873	COMA	P60	0.584	16.424	11.505	1.042	11.791	0.813	0.263	16.985	10.926
N4874	COMA	P60	1.646	18.695	8.469	1.311	10.371	1.690	0.100	18.815	8.372
N4874	COMA	P60	1.684	18.808	8.391	1.309	10.378	1.666	0.129	18.725	8.402
N4876	COMA	P60	0.683	16.543	11.132	1.020	11.491	0.562	0.256	15.587	10.783
N4881	COMA	P60	0.860	16.855	10.561	1.114	11.107	0.801	0.041	16.483	10.481
N4886	COMA	P60	0.865	17.299	10.977	0.990	11.525	0.943	0.062	17.576	10.863
N4886	COMA	P60	0.875	17.319	10.947	0.996	11.508	0.902	0.028	17.363	10.858
N4886	COMA	P60	0.914	17.489	10.922	0.985	11.538	1.045	0.054	18.020	10.799
N4889	COMA	P60	1.053	16.260	8.999	1.563	9.767	1.345	0.347	17.097	8.375
N4889	COMA	P60	1.343	17.147	8.435	1.527	9.703	1.410	0.358	17.292	8.247
N4889	COMA	P60	1.377	17.247	8.366	1.524	9.704	1.412	0.351	17.292	8.234
N4894	COMA	P60	0.940	18.304	11.609	0.812	12.264	0.823	0.599	17.816	11.709
N4898E	COMA	P60	0.350	15.845	12.096	0.882	12.262	0.204	0.130	14.605	11.585
N4898W	COMA	P60	0.657	15.986	10.705	1.174	11.062	0.637	0.332	15.618	10.436
N4906	COMA	P60	0.835	17.109	10.939	1.016	11.450	0.772	0.135	16.699	10.845
N4923	COMA	P60	0.640	16.041	10.844	1.114	11.177	0.647	0.177	15.910	10.679
N4926	COMA	P60	0.986	16.717	9.791	1.275	10.515	1.021	0.108	16.839	9.740
N4927	COMA	P60	0.844	16.461	10.248	1.205	10.787	0.890	0.251	16.618	10.172
N4952	COMA	P60	0.982	16.571	9.665	1.313	10.372	1.003	0.312	16.608	9.597
N4957	COMA	P60	1.053	17.187	9.926	1.211	10.729	1.041	0.256	17.046	9.849
N4971	COMA	P60	0.909	17.128	10.589	1.095	11.210	0.747	0.398	16.615	10.882
N5004	COMA	P60	0.919	16.530	9.941	1.267	10.557	1.033	0.287	16.968	9.805
RB40	COMA	P60	-0.678	11.489	12.894	0.735	12.880	-0.796	0.573	7.003	8.967

Table A.1—*Continued*

Name	Group	Tel	Circular Aperture Photometry					Surface Photometry			
			$\log r_{\rm eff}$	$\langle\mu\rangle_{\rm eff}$	$K_{\rm tot}$	$\log D_K$	K_{20}	$\log r_{\rm e}$	ϵ_e	$\langle\mu\rangle_{\rm e}$	$K_{\rm tot}$
			($''$)	(mag/$''$)	(mag)	($''$)	(mag)	($''$)		(mag/$''$)	(mag)
(1)	(2)	(3)	(4)	(5)	(6)	(7)	(8)	(9)	(10)	(11)	(12)
RB40	COMA	P60	0.185	15.787	12.864	0.726	12.992	0.375	0.571	16.461	12.596
RB42	COMA	P60	0.480	17.226	12.833	0.625	13.066	0.683	0.415	18.026	12.617
RB42	COMA	P60	0.955	19.030	12.261	0.634	12.921	0.915	0.563	18.884	12.311
RB55	COMA	P60	0.901	19.161	12.838	0.551	13.343	0.901	0.410	19.339	12.838
I2006	FORNAX	C100	1.191	16.380	8.432	1.571	9.493	1.453	0.216	17.313	8.052
I2006	FORNAX	C100	1.324	16.825	8.209	1.577	9.499	1.459	0.140	17.267	7.976
I2006	FORNAX	C40new	1.420	17.137	8.041	1.574	9.524	1.440	0.119	17.197	8.002
N1316	FORNAX	C100	1.425	15.173	6.053	1.653	7.570	1.591	0.324	15.645	5.696
N1316	FORNAX	C40new	1.662	15.934	5.629	2.166	7.634	1.707	0.275	15.957	5.424
N1336	FORNAX	C40new	1.103	17.525	10.012	1.150	10.955	1.249	0.149	18.115	9.873
N1339	FORNAX	C100	0.760	14.860	9.063	1.521	9.511	0.966	0.286	15.718	8.894
N1339	FORNAX	C40new	1.009	15.714	8.677	1.566	9.447	1.179	0.311	16.471	8.580
N1344	FORNAX	C100	1.467	16.580	7.248	1.792	8.837	1.531	0.370	16.794	7.142
N1344	FORNAX	C40new	1.538	16.805	7.119	1.789	8.854	1.604	0.379	17.071	7.058
N1351	FORNAX	C40new	0.995	15.909	8.941	1.489	9.697	1.061	0.392	16.150	8.851
N1351	FORNAX	C100	1.183	16.484	8.573	1.514	9.639	1.258	0.371	16.790	8.504
N1366	FORNAX	C40new	0.894	15.442	8.979	1.504	9.607	1.189	0.546	16.923	8.984
N1374	FORNAX	C100	1.259	16.312	8.023	1.647	9.217	1.349	0.083	16.667	7.929
N1374	FORNAX	C100	1.286	16.402	7.974	1.648	9.222	1.365	0.101	16.714	7.893
N1374	FORNAX	C40new	1.313	16.499	7.937	1.652	9.228	1.380	0.103	16.771	7.874
N1375	FORNAX	C100	1.431	18.194	9.045	1.238	10.574	1.738	0.554	19.101	8.416
N1375	FORNAX	C40new	1.604	18.725	8.708	1.240	10.573	1.706	0.543	18.988	8.462
N1379	FORNAX	C100	1.529	17.484	7.845	1.605	9.580	1.671	0.126	17.962	7.613
N1379	FORNAX	C40new	1.592	17.657	7.700	1.605	9.557	1.656	0.076	17.884	7.608
N1380	FORNAX	C100	1.519	16.281	6.689	1.978	8.394	1.741	0.402	16.991	6.289
N1380	FORNAX	C40new	1.526	16.345	6.717	1.923	8.425	1.659	0.527	16.939	6.650
N1380A	FORNAX	C40new	1.445	18.603	9.385	1.118	10.892	1.582	0.717	19.151	9.248
N1380B	FORNAX	C40new	1.919	19.987	8.397	1.048	10.978	2.052	0.192	20.304	8.049
N1381	FORNAX	C40new	1.074	15.719	8.356	1.611	9.220	1.226	0.576	16.385	8.261
N1387	FORNAX	C100	0.846	14.142	7.917	1.856	8.403	1.026	0.132	14.684	7.557
N1387	FORNAX	C40new	1.098	15.016	7.528	1.803	8.410	1.098	0.193	15.002	7.519
N1389	FORNAX	C40new	1.035	15.800	8.628	1.570	9.421	1.022	0.293	15.550	8.442
N1389	FORNAX	C100	1.072	15.814	8.461	1.609	9.335	1.268	0.398	16.519	8.183
N1389	FORNAX	C100	1.086	15.924	8.499	1.589	9.368	1.139	0.307	15.973	8.283
N1399	FORNAX	C100	1.418	15.627	6.544	2.017	8.005	1.396	0.109	15.402	6.429
N1399	FORNAX	C40new	1.504	15.901	6.389	2.003	8.017	1.438	0.107	15.548	6.364
N1404	FORNAX	C40new	1.341	15.409	6.710	1.972	8.026	1.292	0.121	15.085	6.632
N1404	FORNAX	C100	1.360	15.458	6.660	2.012	8.006	1.330	0.123	15.206	6.562
N1427	FORNAX	C40new	1.173	16.232	8.371	1.598	9.403	1.275	0.319	16.641	8.270
N1427	FORNAX	C100	1.226	16.356	8.233	1.619	9.365	1.375	0.314	16.933	8.062
N1428	FORNAX	C40new	1.243	17.992	9.780	1.185	10.897	1.126	0.430	17.360	9.733
E501G21	HYDRA	C40old	0.885	16.702	10.280	1.176	10.916	1.262	0.687	18.416	10.113
E501G47	HYDRA	C40old	1.551	18.629	8.878	1.226	10.693	1.937	0.423	19.717	8.039
E501G49	HYDRA	C40old	0.891	17.312	10.861	1.003	11.524	1.227	0.544	18.722	10.591
N3305	HYDRA	C40old	0.953	16.091	9.330	1.407	10.053	0.897	0.068	15.744	9.267
N3308	HYDRA	C40old	1.498	17.932	8.448	1.419	10.155	1.621	0.289	18.432	8.332
N3309	HYDRA	C100	1.258	16.695	8.409	1.550	9.554	1.169	0.154	16.261	8.422
N3309	HYDRA	C40old	1.290	16.833	8.387	1.546	9.656	1.253	0.166	16.616	8.356
N3309	HYDRA	C40old	1.308	16.853	8.319	1.555	9.616	1.288	0.195	16.710	8.278
N3311	HYDRA	C40old	1.709	18.634	8.095	1.388	10.259	1.526	0.107	17.866	8.243
N3311	HYDRA	C100	1.710	18.669	8.123	1.389	10.211	1.647	0.093	18.284	8.053

Table A.1—*Continued*

Name	Group	Tel	Circular Aperture Photometry					Surface Photometry			
			$\log r_{\rm eff}$	$\langle\mu\rangle_{\rm eff}$	$K_{\rm tot}$	$\log D_K$	K_{20}	$\log r_{\rm e}$	ϵ_e	$\langle\mu\rangle_{\rm e}$	$K_{\rm tot}$
			($''$)	(mag/$''$)	(mag)	($''$)	(mag)	($''$)		(mag/$''$)	(mag)
(1)	(2)	(3)	(4)	(5)	(6)	(7)	(8)	(9)	(10)	(11)	(12)
N3311	HYDRA	C100	1.735	18.731	8.059	1.392	10.202	1.708	0.079	18.464	7.930
N3311	HYDRA	C100	1.747	18.873	8.145	1.351	10.310	1.678	0.084	18.491	8.105
N3311	HYDRA	C100	1.850	19.039	7.794	1.371	10.259	1.707	0.012	18.401	7.871
N3311	HYDRA	C100	1.890	19.132	7.688	1.372	10.256	1.627	0.180	18.277	8.146
N3311	HYDRA	C40old	2.075	19.474	7.105	1.407	10.252	2.016	0.076	19.200	7.125
N3312	HYDRA	C40old	1.208	16.793	8.760	1.476	9.859	1.421	0.346	17.587	8.488
N3315	HYDRA	C40old	0.991	16.490	9.541	1.420	10.319	1.373	0.100	17.920	9.061
N3316	HYDRA	C40old	1.089	16.745	9.305	1.362	10.233	1.299	0.209	17.616	9.126
R253	HYDRA	C40old	1.240	19.291	11.097	0.591	12.252	1.163	0.338	18.867	11.058
R253	HYDRA	C40old	1.368	19.791	10.953	0.551	12.368	0.932	0.171	17.909	11.254
R253	HYDRA	C40old	1.571	20.322	10.469	0.583	12.317	1.270	0.204	19.023	10.677
R293	HYDRA	C40old	0.611	18.036	12.988	0.505	13.500	0.810	0.104	18.443	12.400
S135	HYDRA	C40old	0.346	15.474	11.750	0.954	11.930	0.367	0.175	14.900	11.072
S154	HYDRA	C40old	0.382	15.882	11.972	0.877	12.161	0.041	0.320	13.614	11.407
S154	HYDRA	C40old	0.486	16.347	11.926	0.868	12.169	0.212	0.172	14.500	11.448
S154	HYDRA	C40old	0.607	16.890	11.855	0.853	12.236	0.117	0.213	13.698	11.121
S201	HYDRA	C40old	1.006	18.383	11.354	0.833	12.230	1.420	0.201	19.909	10.813
S23	HYDRA	C40old	1.256	18.427	10.151	1.006	11.384	1.595	0.422	19.457	9.486
S37	HYDRA	C40old	0.729	16.564	10.923	1.047	11.381	1.006	0.615	17.688	10.664
S46	HYDRA	C40old	1.065	18.178	10.857	0.881	11.738	0.976	0.451	17.688	10.814
S46	HYDRA	C40old	1.150	18.427	10.679	0.882	11.696	1.009	0.430	17.686	10.648
S53	HYDRA	C40old	0.480	14.981	10.584	1.210	10.821	0.455	0.514	14.626	10.359
S53	HYDRA	C40old	0.597	15.490	10.509	1.202	10.847	0.493	0.490	14.733	10.278
S61	HYDRA	C40old	0.320	14.622	11.022	1.133	11.177	0.173	0.311	13.748	10.892
S61	HYDRA	C40old	0.332	14.653	10.996	1.135	11.165	0.326	0.113	14.350	10.723
S68	HYDRA	C40old	0.731	16.802	11.151	0.996	11.565	1.010	0.381	17.757	10.709
S68	HYDRA	C40old	0.737	16.695	11.014	1.018	11.475	0.767	0.234	16.622	10.793
S83	HYDRA	C40old	0.883	17.750	11.339	0.859	11.980	1.049	0.407	17.905	10.665
S96	HYDRA	C40old	0.627	16.309	11.177	1.024	11.541	0.639	0.520	16.309	11.114
D32	KLEM44	C40new	0.638	15.771	10.583	1.188	10.927	0.667	0.198	15.790	10.462
D34	KLEM44	C40new	0.522	17.334	12.727	0.600	13.010	0.079	0.229	14.515	12.120
D42	KLEM44	C40new	1.146	17.819	10.091	1.119	11.120	1.558	0.401	19.435	9.649
D43	KLEM44	C40new	0.696	16.744	11.266	0.987	11.663	0.702	0.302	16.615	11.110
D44	KLEM44	C40new	0.090	15.153	12.711	0.787	12.780	-0.056	0.481	14.216	12.502
D44	KLEM44	C40new	0.134	15.202	12.543	0.820	12.554	0.111	0.232	14.513	11.969
D45	KLEM44	C40new	0.633	17.323	12.160	0.772	12.502	0.739	0.067	17.557	11.869
D51	KLEM44	C40new	0.210	16.032	12.984	0.681	13.134	0.380	0.324	16.509	12.611
D55	KLEM44	C40new	0.505	16.174	11.650	0.950	11.923	0.520	0.394	15.986	11.392
D56	KLEM44	C40new	1.043	17.163	9.955	1.211	10.790	1.073	0.199	17.262	9.901
D58	KLEM44	C40new	0.594	15.761	10.793	1.153	11.114	0.729	0.449	16.100	10.461
D59	KLEM44	C40new	0.624	17.081	11.963	0.823	12.302	0.697	0.189	17.375	11.894
D59	KLEM44	C40new	0.625	17.108	11.986	0.822	12.333	0.791	0.120	17.857	11.907
D77	KLEM44	C40new	0.778	16.494	10.609	1.137	11.084	0.787	0.156	16.457	10.528
N7562	PEGASUS	P60	1.228	16.362	8.225	1.630	9.297	1.324	0.310	16.682	8.065
N7617	PEGASUS	P60	0.870	16.500	10.151	1.211	10.711	0.875	0.355	16.471	10.101
N7619	PEGASUS	P60	1.239	16.138	7.948	1.683	9.045	1.234	0.223	16.061	7.897
N7626	PEGASUS	P60	1.449	17.048	7.810	1.632	9.303	1.540	0.170	17.421	7.726
BGP110	PERSEUS	P60	0.688	17.407	11.968	0.744	12.342	0.723	0.527	17.281	11.673
BGP63	PERSEUS	P60	0.588	16.294	11.358	1.060	11.666	0.757	0.075	16.753	10.975
BGP65	PERSEUS	P60	1.193	18.649	10.689	0.921	11.708	1.363	0.377	19.296	10.485
CR32	PERSEUS	P60	0.869	16.335	9.996	1.284	10.541	0.849	0.104	15.954	9.711

Table A.1—*Continued*

Name	Group	Tel	Circular Aperture Photometry					Surface Photometry			
			$\log r_{\rm eff}$	$\langle\mu\rangle_{\rm eff}$	$K_{\rm tot}$	$\log D_K$	K_{20}	$\log r_{\rm e}$	ϵ_e	$\langle\mu\rangle_{\rm e}$	$K_{\rm tot}$
			($''$)	(mag/$''$)	(mag)	($''$)	(mag)	($''$)		(mag/$''$)	(mag)
(1)	(2)	(3)	(4)	(5)	(6)	(7)	(8)	(9)	(10)	(11)	(12)
CR32	PERSEUS	P60	1.037	16.907	9.727	1.293	10.505	1.059	0.151	16.847	9.556
CR36	PERSEUS	P60	0.637	15.878	10.698	1.148	11.030	0.615	0.271	15.635	10.568
I0310	PERSEUS	P60	1.177	16.788	8.909	1.442	9.916	1.314	0.037	17.302	8.738
N1260	PERSEUS	P60	0.892	16.074	9.621	1.370	10.200	0.820	0.551	15.512	9.419
N1260	PERSEUS	P60	0.895	16.035	9.562	1.367	10.158	0.818	0.541	15.459	9.376
N1270	PERSEUS	P60	0.802	15.285	9.279	1.458	9.774	0.766	0.306	15.092	9.265
N1272	PERSEUS	P60	1.381	17.464	8.566	1.491	9.901	1.468	0.047	17.653	8.318
N1272	PERSEUS	P60	1.442	17.674	8.470	1.473	9.929	1.487	0.043	17.717	8.288
N1273	PERSEUS	P60	0.904	16.170	9.655	1.373	10.272	1.110	0.193	17.035	9.488
N1274	PERSEUS	P60	0.559	15.145	10.354	1.250	10.616	0.760	0.355	15.949	10.152
N1275	PERSEUS	P60	1.602	17.982	7.978	1.531	9.829	1.687	0.188	18.155	7.723
N1277	PERSEUS	P60	0.490	14.352	9.905	1.374	10.117	0.515	0.455	14.181	9.616
N1277	PERSEUS	P60	0.491	14.392	9.942	1.372	10.152	0.507	0.449	14.139	9.612
N1278	PERSEUS	P60	1.258	17.040	8.756	1.458	9.882	1.250	0.146	16.879	8.632
N1282	PERSEUS	P60	1.061	16.670	9.370	1.358	10.190	1.263	0.225	17.507	9.194
N1282	PERSEUS	P60	1.067	16.743	9.411	1.345	10.238	1.204	0.175	17.291	9.276
N1283	PERSEUS	P60	0.653	15.511	10.250	1.260	10.576	0.766	0.125	15.885	10.059
N1293	PERSEUS	P60	0.820	15.974	9.880	1.306	10.377	0.772	0.146	15.688	9.832
N1293	PERSEUS	P60	0.929	16.346	9.703	1.316	10.340	0.965	0.127	16.497	9.678
PER101	PERSEUS	P60	0.601	16.650	11.651	0.903	11.950	0.193	0.380	14.289	11.330
PER152	PERSEUS	P60	0.380	15.644	11.750	0.949	11.913	0.422	0.078	15.742	11.641
PER152	PERSEUS	P60	0.398	15.722	11.739	0.947	11.913	0.358	0.102	15.400	11.612
PER153	PERSEUS	P60	0.408	16.386	12.347	0.779	12.530	0.079	0.441	14.503	12.115
PER153	PERSEUS	P60	0.408	16.405	12.366	0.772	12.572	0.049	0.460	14.368	12.129
PER163	PERSEUS	P60	0.260	14.780	11.490	1.056	11.598	0.076	0.547	13.722	11.353
PER163	PERSEUS	P60	0.281	14.924	11.525	1.055	11.643	0.246	0.378	14.419	11.193
PER164	PERSEUS	P60	0.614	16.011	10.946	1.091	11.249	0.647	0.399	15.856	10.623
PER164	PERSEUS	P60	0.618	16.027	10.942	1.090	11.242	0.701	0.404	16.125	10.627
PER195	PERSEUS	P60	0.731	16.521	10.874	1.099	11.276	0.732	0.117	16.223	10.571
PER199	PERSEUS	P60	0.459	15.089	10.800	1.172	11.007	0.520	0.265	15.276	10.685
N0379	PISCES	P60	0.899	15.720	9.232	1.451	9.816	0.688	0.457	14.387	8.955
N0380	PISCES	P60	0.942	15.928	9.223	1.429	9.899	0.879	0.131	15.605	9.214
N0382	PISCES	P60	0.673	15.723	10.361	1.225	10.718	0.428	0.081	14.312	10.179
N0383	PISCES	P60	1.221	16.556	8.456	1.545	9.514	1.176	0.136	16.308	8.433
N0384	PISCES	P60	0.630	15.173	10.028	1.339	10.338	0.816	0.374	15.899	9.822
N0385	PISCES	P60	1.033	16.895	9.736	1.263	10.522	1.018	0.113	16.782	9.698
N0386	PISCES	P60	0.857	17.141	10.860	1.020	11.392	0.766	0.279	16.592	10.769
N0392	PISCES	P60	0.989	16.413	9.472	1.381	10.207	1.089	0.270	16.775	9.334
N0394	PISCES	P60	0.610	15.527	10.482	1.236	10.781	0.624	0.526	15.378	10.263
N0410	PISCES	P60	1.360	17.003	8.209	1.561	9.532	1.463	0.286	17.416	8.104
Z01047	PISCES	P60	0.493	15.893	11.433	1.000	11.659	0.569	0.090	16.207	11.367
N4168	VIRGO	P60	1.517	17.641	8.061	1.524	9.687	1.450	0.105	17.289	8.045
N4239	VIRGO	P60	1.171	17.721	9.870	1.141	10.842	1.067	0.451	17.116	9.784
N4261	VIRGO	P60	1.491	16.460	7.009	1.834	8.587	1.423	0.171	16.117	7.009
N4318	VIRGO	P60	0.867	16.383	10.053	1.236	10.600	0.797	0.212	15.769	9.792
N4339	VIRGO	P60	1.431	17.298	8.147	1.536	9.590	1.456	0.051	17.398	8.122
N4342	VIRGO	P60	0.612	13.953	8.900	1.567	9.209	0.365	0.473	11.899	8.074
N4365	VIRGO	P60	1.582	16.529	6.622	1.912	8.389	1.566	0.240	16.434	6.607
N4365	VIRGO	C100	1.584	16.549	6.634	1.937	8.468	1.583	0.221	16.458	6.549
N4371	VIRGO	P60	1.533	17.050	7.389	1.717	9.054	1.509	0.187	16.748	7.208
N4374	VIRGO	C100	1.391	15.528	6.577	2.082	7.962	1.430	0.168	15.499	6.354

Table A.1—*Continued*

Name	Group	Tel	Circular Aperture Photometry					Surface Photometry			
			$\log r_{\rm eff}$	$\langle\mu\rangle_{\rm eff}$	$K_{\rm tot}$	$\log D_K$	K_{20}	$\log r_{\rm e}$	ϵ_e	$\langle\mu\rangle_{\rm e}$	$K_{\rm tot}$
			($''$)	(mag/$''$)	(mag)	($''$)	(mag)	($''$)		(mag/$''$)	(mag)
(1)	(2)	(3)	(4)	(5)	(6)	(7)	(8)	(9)	(10)	(11)	(12)
N4374	VIRGO	P60	1.585	16.022	6.104	2.051	7.853	1.560	0.119	15.876	6.080
N4374	VIRGO	P60	1.606	16.114	6.087	2.047	7.877	1.607	0.116	16.086	6.054
N4377	VIRGO	P60	1.091	15.983	8.534	1.584	9.410	1.334	0.171	17.069	8.401
N4382	VIRGO	P60	1.799	16.939	5.951	2.016	8.196	1.904	0.310	17.393	5.876
N4387	VIRGO	P60	1.221	16.849	8.748	1.472	9.789	1.175	0.434	16.551	8.679
N4406	VIRGO	P60	1.833	17.157	5.996	1.990	8.315	1.953	0.290	17.610	5.852
N4434	VIRGO	P60	1.549	17.787	8.046	1.487	9.714	1.805	0.034	18.703	7.683
N4435	VIRGO	P60	1.175	15.453	7.582	1.785	8.570	1.160	0.480	15.433	7.637
N4442	VIRGO	P60	1.266	15.542	7.218	1.853	8.368	1.406	0.431	16.104	7.081
N4458	VIRGO	P60	1.298	17.458	8.974	1.352	10.182	1.374	0.104	17.742	8.878
N4464	VIRGO	P60	0.908	15.861	9.323	1.413	9.927	0.818	0.287	15.389	9.303
N4467	VIRGO	P60	0.785	16.783	10.866	1.037	11.331	0.316	0.378	14.383	10.809
N4468	VIRGO	P60	1.439	18.839	9.648	1.031	11.124	1.547	0.325	19.232	9.500
N4472	VIRGO	P60	1.851	16.521	5.268	2.189	7.685	1.876	0.189	16.580	5.203
N4472	VIRGO	C100	1.952	16.813	5.057	2.448	7.787	1.915	0.090	16.642	5.074
N4473	VIRGO	P60	1.303	15.560	7.047	1.879	8.233	1.351	0.445	15.792	7.041
N4476	VIRGO	P60	1.003	16.336	9.326	1.384	10.047	0.549	0.539	14.122	9.385
N4478	VIRGO	P60	1.254	16.278	8.011	1.667	9.134	1.152	0.199	15.652	7.899
N4478	VIRGO	C100	1.317	16.551	7.968	1.660	9.224	1.380	0.176	16.639	7.742
N4486	VIRGO	P60	1.909	17.021	5.479	2.109	8.152	1.759	0.103	16.349	5.559
N4486B	VIRGO	P60	0.387	13.909	9.981	1.350	10.146	0.029	0.285	11.759	9.620
N4489	VIRGO	C100	1.300	17.597	9.104	1.300	10.393	1.458	0.092	18.239	8.954
N4489	VIRGO	P60	1.396	17.883	8.907	1.316	10.298	1.568	0.072	18.577	8.744
N4550	VIRGO	P60	1.221	16.414	8.312	1.583	9.394	0.977	0.639	15.038	8.159
N4551	VIRGO	P60	1.357	17.148	8.367	1.513	9.676	1.320	0.322	16.929	8.334
N4552	VIRGO	C100	1.256	15.201	6.925	2.072	8.083	1.336	0.085	15.443	6.766
N4552	VIRGO	P60	1.320	15.347	6.751	1.965	7.983	1.369	0.068	15.525	6.683
N4564	VIRGO	P60	1.226	15.858	7.735	1.725	8.789	1.384	0.594	16.631	7.715
N4621	VIRGO	C100	1.381	15.741	6.840	2.036	8.272	1.716	0.314	16.844	6.268
N4621	VIRGO	P60	1.569	16.273	6.435	1.958	8.148	1.700	0.402	16.852	6.359
N4636	VIRGO	C100	1.592	16.816	6.862	1.927	8.678	1.660	0.176	16.989	6.692
N4636	VIRGO	P60	1.712	17.041	6.486	1.894	8.561	1.780	0.257	17.398	6.502
N4649	VIRGO	P60	1.722	16.175	5.569	2.152	7.663	1.695	0.209	16.042	5.570
N4660	VIRGO	C100	1.015	15.118	8.045	1.704	8.846	1.115	0.465	15.606	8.038
N4660	VIRGO	P60	1.089	15.369	7.928	1.721	8.763	1.094	0.442	15.447	7.980
N4697	VIRGO	P60	1.778	16.826	5.943	2.024	8.127	1.863	0.310	16.984	5.674
N4733	VIRGO	P60	1.926	19.557	7.932	1.199	10.557	1.874	0.016	19.220	7.857
N0584	CETUS	P60	1.325	15.888	7.266	1.820	8.509	1.389	0.372	16.173	7.235
N0596	CETUS	P60	1.347	16.567	7.836	1.655	9.127	1.438	0.156	17.021	7.836
N0636	CETUS	P60	1.249	16.524	8.284	1.566	9.408	1.357	0.155	17.050	8.270
N1395	ERIDANUS	C40new	1.496	16.313	6.836	1.891	8.489	1.514	0.201	16.346	6.781
N1400	ERIDANUS	C40new	1.238	15.840	7.653	1.744	8.794	1.248	0.113	15.880	7.645
N1407	ERIDANUS	C40new	1.553	16.537	6.777	1.901	8.542	1.540	0.048	16.395	6.697
N1426	ERIDANUS	C40new	1.250	16.631	8.383	1.546	9.547	1.316	0.388	16.945	8.368
N1439	ERIDANUS	C40new	1.280	16.890	8.495	1.498	9.757	1.443	0.094	17.570	8.361
N3377	LEO	P60	1.294	15.927	7.460	1.778	8.647	1.400	0.497	16.403	7.410
N3379	LEO	C100	1.400	15.397	6.404	2.230	7.828	1.424	0.131	15.439	6.323
N3379	LEO	P60	1.472	15.588	6.231	2.047	7.738	1.458	0.125	15.538	6.255
N3384	LEO	P60	1.124	14.709	7.094	1.911	7.993	1.326	0.131	15.449	6.823
N3412	LEO	P60	1.645	17.177	6.955	1.752	8.803	1.948	0.463	18.469	6.734
N3489	LEO	P60	1.341	15.757	7.057	1.861	8.293	1.502	0.478	16.647	7.143

Table A.1—*Continued*

Name	Group	Tel	Circular Aperture Photometry					Surface Photometry			
			$\log r_{\rm eff}$ ($''$)	$\langle\mu\rangle_{\rm eff}$ (mag/$''$)	$K_{\rm tot}$ (mag)	$\log D_K$ ($''$)	K_{20} (mag)	$\log r_{\rm e}$ ($''$)	ϵ_e	$\langle\mu\rangle_{\rm e}$ (mag/$''$)	$K_{\rm tot}$ (mag)
(1)	(2)	(3)	(4)	(5)	(6)	(7)	(8)	(9)	(10)	(11)	(12)
I3370	N4373grp	C100	1.333	16.455	7.795	1.700	9.109	1.339	0.150	16.354	7.662
I3370	N4373grp	C40old	1.473	16.896	7.533	1.711	9.158	1.412	0.150	16.559	7.503
N4373	N4373grp	C40old	1.362	16.441	7.634	1.734	9.022	1.481	0.287	16.874	7.475
N5813	N5846grp	P60	1.551	17.107	7.357	1.707	9.049	1.749	0.279	17.969	7.228
N5831	N5846grp	P60	1.371	16.995	8.144	1.564	9.479	1.346	0.112	16.814	8.089
N5845	N5846grp	P60	0.520	13.696	9.102	1.530	9.345	0.511	0.150	13.257	8.706
N5846	N5846grp	P60	1.630	17.050	6.905	1.854	8.814	1.678	0.073	17.110	6.726
N5846A	N5846grp	P60	0.387	14.055	10.126	1.320	10.287	-0.013	0.437	11.512	9.588
ARK66	N741grp	P60	0.615	16.070	11.000	1.077	11.315	0.895	0.365	17.438	10.968
I2311	FIELD	C100	1.057	15.571	8.293	1.661	9.144	1.088	0.047	15.627	8.190
I4296	HG22grp	C100	1.238	16.083	7.898	1.697	9.026	1.198	0.104	15.867	7.882
I4296	HG22grp	C100	1.330	16.309	7.661	1.729	8.971	1.315	0.100	16.211	7.641
I4296	HG22grp	C100	1.353	16.431	7.672	1.717	9.027	1.343	0.097	16.357	7.645
M32	LOCALgrp	P60	1.549	14.642	4.902	2.418	6.627	1.455	0.216	14.207	4.937
N0661	GH18	P60	1.066	16.255	8.929	1.469	9.757	1.055	0.297	16.164	8.893
N0680	GH20	P60	1.037	15.790	8.609	1.558	9.399	1.142	0.205	16.245	8.540
N0720	FIELD	P60	1.397	16.141	7.159	1.831	8.542	1.400	0.433	16.091	7.098
N0741	N741grp	P60	1.499	17.609	8.119	1.529	9.728	1.517	0.164	17.612	8.034
N0742	N741grp	P60	1.013	17.211	10.601	1.180	10.898	1.013	0.159	17.660	10.601
N0821	FIELD	P60	1.310	16.308	7.761	1.691	8.999	1.367	0.367	16.526	7.697
N2325	FIELD	C100	1.774	18.279	7.411	1.582	9.663	1.890	0.259	18.475	7.028
N2434	HG1grp	C100	1.212	16.061	8.003	1.685	9.097	1.288	0.103	16.289	7.854
N2434	HG1grp	C100	1.291	16.347	7.898	1.683	9.133	1.331	0.117	16.470	7.820
N2986	HG36grp	C100	1.290	16.256	7.809	1.700	9.061	1.295	0.124	16.197	7.725
N2986	HG36grp	C100	1.570	17.019	7.171	1.768	9.010	1.698	0.154	17.366	6.881
N3258	ANTLIA	C100	1.146	16.180	8.453	1.580	9.421	1.053	0.122	15.676	8.417
N3258	ANTLIA	C100	1.205	16.357	8.336	1.589	9.419	1.141	0.104	15.984	8.282
N3557	FIELD	C100	1.136	15.342	7.668	1.789	8.620	1.146	0.251	15.251	7.528
N3557	FIELD	C100	1.212	15.606	7.553	1.800	8.629	1.193	0.247	15.430	7.469
N4946	N5011grp	C40old	1.195	16.684	8.715	1.490	9.812	1.140	0.114	16.352	8.655
N5061	HG31+35grp	C100	1.132	15.154	7.498	1.900	8.478	1.367	0.116	16.090	7.260
N5128	N5128grp	C40old	1.671	15.405	5.057	2.196	7.152	1.489	0.094	14.696	5.254
N5128	N5128grp	C100	1.892	15.873	4.415	1.895	6.991	1.857	0.168	15.796	4.515
N5812	FIELD	P60	1.117	15.575	7.993	1.695	8.886	1.087	0.043	15.393	7.960
N5898	FABER71grp	C100	1.104	15.737	8.221	1.641	9.123	0.992	0.056	15.175	8.222
N5898	FABER71grp	C100	1.136	15.830	8.155	1.659	9.121	1.086	0.067	15.542	8.115
N5982	GH158	P60	1.183	16.031	8.121	1.657	9.126	1.184	0.309	15.977	8.061
N6411	FIELD	P60	1.124	16.742	9.128	1.407	10.012	1.134	0.303	16.692	9.026
N6482	FIELD	P60	1.148	15.852	8.118	1.675	9.044	1.092	0.269	15.475	8.022
N6702	FIELD	P60	1.176	16.859	8.985	1.419	9.975	1.173	0.224	16.770	8.909
N6703	FIELD	P60	1.146	15.924	8.197	1.644	9.120	1.175	0.016	15.978	8.108
N7236	FABER86grp	P60	0.687	15.906	10.476	1.198	10.839	0.143	0.382	12.749	10.046
N7237	FABER86grp	P60	1.323	18.490	9.880	1.076	11.154	1.573	0.273	19.418	9.556
N7385	FIELD	P60	1.342	17.601	8.895	1.382	10.168	1.351	0.121	17.519	8.768
N7454	GH163	P60	1.262	17.233	8.926	1.411	10.038	1.520	0.289	17.967	8.372
N7768	A2666	P60	1.230	17.300	9.154	1.370	10.234	1.261	0.265	17.337	9.038

Table A.2: Combined Catalog of Global Parameters for All Program Galaxies

Name	Cluster/ Group	Type	K–band				V–band					
			$\log r_{\rm eff}$ ($''$)	$\langle\mu\rangle_{\rm eff}$ (mag/$''$)	$K_{\rm tot}$ (mag)	$\log D_K$ ($''$)	$\log r_{\rm eff}$ ($''$)	$\langle\mu\rangle_{\rm eff}$ (mag/$''$)	$\log D_V$ ($''$)	$V-K$ (mag)	$\log\sigma_0$ (km s^{-1})	Mg_2 (mag)
(1)	(2)	(3)	(4)	(5)	(6)	(7)	(8)	(9)	(10)	(11)	(12)	(13)
D22	A194	S0	0.890	18.48	12.03	0.667	···	···	···	···	1.913	···
D28	A194	S0	0.775	17.86	11.99	0.692	···	···	···	···	1.881	···
D29	A194	S0	0.519	15.41	10.83	1.142	···	···	1.178	···	2.100	···
D30	A194	S0/a	0.663	16.22	10.91	1.080	···	···	1.139	···	2.082	···
D33	A194	S0	0.592	15.74	10.79	1.131	···	···	1.164	···	2.147	···
D44	A194	S0/a	0.738	16.82	11.13	1.001	···	···	1.034	···	2.165	···
D45	A194	S0	0.625	16.39	11.27	1.000	1.337	20.24	1.050	1.28:	2.093	···
D50	A194	S0	0.558	15.58	10.79	1.144	···	···	1.153	···	2.164	···
D52	A194	E	0.555	16.80	12.03	0.818	0.630	20.03	0.887	2.96:	1.979	0.204
D53	A194	S0	0.520	15.31	10.72	1.170	···	···	1.176	···	2.377	···
D55	A194	S0	0.479	17.38	12.99	0.554	···	···	···	···	1.936	···
D57	A194	E	0.660	17.46	12.16	0.665	···	···	···	···	1.881	···
D62	A194	Sa/0	0.778	17.54	11.65	0.832	···	···	···	···	1.883	···
I1696	A194	E	0.680	15.97	10.58	1.166	0.840	19.70	1.177	3.15:	2.204	0.295
N0533	A194	E3	1.301	17.17	8.67	1.460	1.610	21.31	1.457	2.98	2.457	0.317
N0538	A194	Sa	0.860	16.50	10.21	1.188	1.150	20.64	1.207	3.09:	2.310	···
N0541	A194	S0	1.209	17.18	9.14	1.359	1.330	20.78	1.357	3.16:	2.328	0.312
N0545	A194	S0	1.425	17.65	8.53	1.424	1.420	20.80	1.407	3.17:	2.367	0.314
N0547	A194	E1	0.939	16.13	9.44	1.408	1.100	19.86	1.397	3.14:	2.326	0.319
N0548	A194	E	0.924	17.50	10.89	0.979	1.100	21.08	1.037	2.94:	2.097	0.246
N0564	A194	E	0.919	16.27	9.68	1.329	1.130	20.10	1.357	3.07:	2.368	0.298
FCOM	A2199	E/S0	0.320	16.49	12.89	0.672	0.303	19.34	0.719	2.91:	2.130	0.264
L111	A2199	S0/a	0.799	17.34	11.35	0.928	···	···	0.931	···	2.303	···
L112	A2199	E/S0	0.188	15.10	12.17	0.898	···	···	0.888	···	2.355	···
L113	A2199	E	0.199	15.84	12.86	0.720	0.302	19.22	0.761	3.00	2.218	0.268
L114	A2199	S0	0.270	15.62	12.28	0.854	0.208	18.47	0.852	3.08	2.290	0.301
L118	A2199	E	0.717	17.25	11.67	0.866	···	···	0.910	···	2.186	···
L136	A2199	S0	0.286	15.47	12.04	0.907	···	···	···	···	2.266	···
L1381	A2199	S0	0.061	14.72	12.43	0.866	···	···	0.836	···	2.338	···
L139	A2199	E	0.400	17.43	13.44	0.464	···	···	···	···	1.971	···
L143	A2199	S0	0.324	15.06	11.44	1.118	0.644	19.45	1.043	3.23:	2.447	0.325
L145	A2199	S0/a	0.905	17.92	11.40	0.863	0.942	21.05	0.873	3.00	2.169	0.285
L150	A2199	S0	0.318	16.71	13.12	0.625	···	···	0.688	···	2.068	···
L151	A2199	S0	0.358	17.52	13.73	0.447	···	···	···	···	2.016	···
L152	A2199	S0/a	1.202	18.67	10.66	0.888	1.315	22.02	0.902	2.94:	2.165	0.312
L153	A2199	S0/a	0.593	17.01	12.04	0.802	0.800	20.76	0.819	3.01:	2.152	0.274
L158	A2199	S0	0.580	16.45	11.56	0.955	0.524	19.46	0.912	3.21:	2.349	0.305
N6158	A2199	E	0.990	17.33	10.38	1.112	1.030	20.50	1.123	3.03:	2.269	0.275
N6158COMP	A2199	U	0.479	17.16	12.77	0.652	···	···	···	···	1.965	0.230
N6166	A2199	E2	1.373	18.23	9.37	1.259	1.927	22.82	1.194	2.59	2.487	0.323
NCOM	A2199	E	-0.092	15.23	13.70	0.577	-0.152	17.97	0.613	2.96:	2.227	0.285
S18	A2199	E	0.498	16.14	11.65	0.959	0.641	19.70	0.969	3.05:	2.291	0.304
S26	A2199	E	0.883	17.58	11.17	0.937	0.959	20.93	0.925	3.07	2.246	0.286
S30	A2199	E	0.489	16.24	11.96	0.923	0.300	18.53	0.931	3.18	2.394	0.261
S33	A2199	E	0.307	15.50	11.96	0.923	0.318	18.69	0.905	3.15:	2.458	0.309
S34	A2199	E	0.334	16.20	12.53	0.770	0.283	19.03	0.778	3.02	2.195	0.273
S43	A2199	E	0.480	16.41	12.01	0.843	0.510	19.63	0.855	3.12:	2.300	0.300
S44	A2199	E	0.452	16.21	11.95	0.885	0.395	19.10	0.880	3.10:	2.284	0.300
Z34A	A2199	E	0.871	17.27	10.92	1.017	0.909	20.38	1.042	2.98	2.314	0.285
L102	A2634	E	0.705	16.69	11.17	1.012	0.773	20.05	1.004	3.11:	2.285	0.265

Table A.2—*Continued*

Name	Cluster/ Group	Type	K–band				V–band					
			$\log r_{\rm eff}$ ($''$)	$\langle\mu\rangle_{\rm eff}$ (mag/$''$)	$K_{\rm tot}$ (mag)	$\log D_K$ ($''$)	$\log r_{\rm eff}$ ($''$)	$\langle\mu\rangle_{\rm eff}$ (mag/$''$)	$\log D_V$ ($''$)	$V-K$ (mag)	$\log\sigma_0$ (km s^{-1})	Mg$_2$ (mag)
(1)	(2)	(3)	(4)	(5)	(6)	(7)	(8)	(9)	(10)	(11)	(12)	(13)
L106	A2634	S0	0.377	15.85	11.97	0.903	0.397	19.08	0.890	3.15:	2.193	0.285
L107	A2634	SBO/a	0.728	18.06	12.43	0.621	0.735	21.00	0.672	2.91:	2.035	0.216
L108	A2634	S0	0.134	15.08	12.42	0.839	0.311	18.99	0.827	3.26:	2.221	0.279
L109	A2634	S0	0.111	14.90	12.35	0.865	0.288	18.97	0.807	3.42:	2.233	0.263
L111	A2634	U	0.565	18.24	13.42	0.436	...	...	...	...	...	...
L113	A2634	U	0.403	16.64	12.63	0.709	...	...	...	...	...	...
L1201	A2634	S0/a	0.467	16.48	12.15	0.825	0.469	19.60	0.824	3.11:	2.210	0.297
L121	A2634	E	0.322	15.98	12.37	0.815	0.369	19.25	0.816	3.11:	2.263	0.284
L124	A2634	E	0.382	16.05	12.15	0.852	0.458	19.55	0.827	3.22:	2.273	0.297
L1261	A2634	S0	0.041	15.01	12.81	0.773	-0.039	17.71	0.784	2.99:	2.144	0.258
L129	A2634	S0	0.542	16.14	11.44	0.993	0.720	20.11	0.937	3.32:	2.317	0.302
L134	A2634	E	0.664	16.46	11.15	1.032	0.787	20.01	1.030	3.10:	2.340	0.301
L135	A2634	S0	0.489	16.44	12.00	0.852	0.476	19.39	0.883	3.00:	2.086	0.263
L138	A2634	E	0.777	16.96	11.08	1.008	0.943	20.64	0.996	3.08:	2.319	0.309
L139	A2634	E	0.763	16.72	10.91	1.059	0.905	20.40	1.033	3.17:	2.335	0.324
L140	A2634	S0	0.248	14.91	11.68	1.005	0.276	18.36	0.950	3.35:	2.346	0.314
N7720	A2634	E	1.160	17.19	9.40	1.326	1.288	20.83	1.273	3.17	2.494	0.331
N7720A	A2634	E	0.340	15.36	11.65	0.995	0.419	18.93	0.953	3.29:	2.305	0.295
D20	CEN45	S0	1.067	17.13	9.80	1.236	...	...	1.328	...	2.064	...
D23	CEN45	S0	0.934	16.73	10.06	1.215	...	...	1.289	...	2.118	...
D24	CEN45	S0p	1.129	17.66	10.02	1.104	...	...	1.219	...	2.022	...
D27	CEN45	E	0.815	16.53	10.46	1.152	0.937	19.98	1.221	3.02:	2.038	0.264
D45	CEN45	U	1.061	15.77	8.47	1.615	1.337	19.93	1.637	3.16:	2.390	0.297
N4616	CEN45	E	1.136	17.07	9.40	1.319	1.297	20.73	1.361	3.07:	2.240	0.267
N4709	CEN45	E1	1.451	17.25	8.00	1.612	1.837	21.51	1.653	3.48:	2.388	0.324
D19	CEN30	S0	0.719	15.02	9.43	1.438	...	...	1.470	...	2.289	...
D22	CEN30	S0	0.959	17.01	10.22	1.167	...	...	1.258	...	2.082	...
D29	CEN30	S0	1.020	17.07	9.98	1.204	...	...	1.290	...	2.013	...
D49	CEN30	E	0.693	16.15	10.69	1.128	...	...	1.153	...	2.047	0.292
D50	CEN30	E	0.974	17.10	10.24	1.146	...	...	1.195	...	2.062	0.254
D56	CEN30	E	0.747	16.40	10.66	1.118	...	...	1.190	...	2.133	...
D58	CEN30	S0	0.809	16.14	10.10	1.246	...	...	1.301	...	2.190	...
D9	CEN30	U	0.912	17.15	10.59	1.074	...	...	...	...	2.212	0.210
J316	CEN30	S0	0.905	15.48	8.96	1.513	...	...	1.518	...	2.336	...
N4645	CEN30	E	1.122	15.92	8.31	1.614	1.337	19.83	1.653	3.31:	2.250	0.269
N4661	CEN30	E	1.041	17.37	10.17	1.128	...	...	...	...	2.167	0.256
N4696	CEN30	E1	1.842	18.21	7.01	1.684	2.327	22.52	1.756	3.02	2.387	0.267
N4706	CEN30	S0	1.423	17.78	9.06	1.434	...	...	1.466	3.47:	2.321	0.297
N4729	CEN30	E	1.149	16.52	8.78	1.497	1.337	20.42	1.508	3.50:	2.175	0.261
N4767	CEN30	E	1.283	16.47	8.06	1.649	1.487	20.24	1.702	3.30:	2.298	0.278
D106	COMA	S0	0.438	16.53	12.35	0.776	0.419	19.40	0.827	2.84	2.210	0.241
D125	COMA	E	0.124	15.07	12.45	0.836	0.219	18.50	0.854	3.09:	2.235	0.256
D149	COMA	S0	0.307	16.46	12.91	0.549	0.709	21.26	0.553	3.13	...	...
D173	COMA	S0	0.417	16.23	12.15	0.846	0.527	19.68	0.861	3.12	2.147	0.287
D210	COMA	Ep	0.559	16.47	11.68	0.926	0.539	19.39	0.949	2.99:	2.237	0.270
D24	COMA	E	0.631	16.11	10.95	1.089	0.599	19.18	1.063	3.19:	2.359	0.301
D27	COMA	E	0.544	17.03	12.32	0.736	0.674	20.44	0.785	2.63:	2.009	0.260
D32	COMA	S0	0.310	16.32	12.77	0.709	0.270	19.09	0.741	2.92:	...	...
D80	COMA	S0	0.797	17.93	11.95	0.747	...	...	...	...	...	...
D81	COMA	E	0.732	17.77	12.11	0.744	0.810	20.90	0.794	2.85:	2.191	0.265
D96	COMA	E	0.529	16.24	11.60	0.957	0.651	19.80	0.947	3.12:	2.269	0.285

Table A.2—*Continued*

Name	Cluster/ Group	Type	K–band				V–band					
			$\log r_{\rm eff}$ ($''$)	$\langle\mu\rangle_{\rm eff}$ (mag/$''$)	$K_{\rm tot}$ (mag)	$\log D_K$ ($''$)	$\log r_{\rm eff}$ ($''$)	$\langle\mu\rangle_{\rm eff}$ (mag/$''$)	$\log D_V$ ($''$)	$V-K$ (mag)	$\log\sigma_0$ (km s^{-1})	Mg_2 (mag)
(1)	(2)	(3)	(4)	(5)	(6)	(7)	(8)	(9)	(10)	(11)	(12)	(13)
E159G43	COMA	U	0.702	16.19	10.68	1.137	0.710	19.53	1.106	3.37	2.402	···
E159G63	COMA	U	0.866	17.46	11.13	0.947	0.902	20.81	0.939	3.21	2.173	···
E159G83	COMA	E	0.728	16.09	10.45	1.205	0.956	19.82	···	3.30	2.305	···
E159G89	COMA	E	0.825	17.00	10.88	1.043	0.867	20.02	···	3.07	2.230	···
E160G159	COMA	U	0.869	17.04	10.70	1.071	0.849	20.20	1.061	3.20	2.360	···
E160G22	COMA	E	0.607	15.71	10.67	1.162	1.009	20.17	···	3.33	2.417	···
E160G23	COMA	E	0.500	15.91	11.42	1.008	1.101	21.51	···	3.23	2.250	···
E160G27	COMA	E	0.611	16.51	11.46	0.960	0.766	20.15	0.963	3.04	2.235	0.282
I0832	COMA	E	0.814	16.80	10.73	1.085	0.890	19.97	···	2.90:	2.320	···
I0843	COMA	S0	0.742	15.92	10.21	1.247	1.198	20.34	···	3.42	2.393	···
I3900	COMA	SB0	0.627	15.91	10.78	1.172	0.704	18.76	···	3.10	2.431	···
I3947	COMA	S0	0.470	16.12	11.78	0.926	0.589	19.58	0.952	2.95	2.148	0.279
I3957	COMA	S0	0.545	16.45	11.73	0.912	0.637	19.84	0.926	3.15	2.179	0.292
I3959	COMA	E3	0.655	16.27	11.00	1.069	0.769	19.86	1.053	3.24	2.295	0.307
I4011	COMA	E	0.650	17.11	11.86	0.830	0.624	20.03	0.860	3.11	2.040	0.280
I4012	COMA	E	0.312	15.15	11.59	1.011	0.363	18.56	0.988	3.30	2.259	0.292
I4021	COMA	E	0.809	16.77	10.73	1.086	0.486	19.25	0.931	3.96	2.206	0.300
I4045	COMA	E4	0.481	15.31	10.91	1.136	0.660	19.25	1.115	3.26	2.331	0.306
I4051	COMA	E0	1.058	17.50	10.22	1.118	1.272	21.42	1.075	3.17	2.355	0.332
I4133	COMA	E	0.535	16.08	11.41	1.000	0.701	19.77	1.004	3.04	2.233	0.289
N4673	COMA	E1	0.760	15.62	9.83	1.340	0.824	19.06	1.344	3.17	2.347	···
N4692	COMA	E	1.117	17.13	9.55	1.290	1.207	20.76	1.225	3.22	2.432	0.307
N4789	COMA	S0	1.039	16.60	9.41	1.372	1.213	20.03	1.302	3.23	2.427	0.287
N4807	COMA	S0	0.740	16.12	10.42	1.195	0.831	19.28	1.169	3.13	2.336	0.275
N4816	COMA	S0	1.299	18.15	9.66	1.163	1.236	21.00	1.160	3.17	2.365	0.306
N4824	COMA	E	0.695	16.96	11.49	0.925	0.678	19.99	0.924	3.18	2.205	0.278
N4827	COMA	S0	1.001	16.90	9.90	1.245	1.094	20.17	···	3.27	2.465	···
N4839	COMA	E	1.290	17.78	9.34	1.264	1.425	21.29	1.272	3.21	2.420	0.313
N4840	COMA	E1	0.709	16.09	10.55	1.169	0.793	19.59	1.152	3.22	2.377	0.320
N4841A	COMA	E	1.094	17.17	9.71	1.255	1.170	20.44	1.284	3.10	2.417	0.320
N4841B	COMA	E	0.790	16.69	10.74	1.091	0.930	20.13	1.151	2.81	2.355	0.295
N4850	COMA	S0	0.537	15.85	11.17	1.062	0.738	19.78	1.048	3.17	2.233	0.269
N4854	COMA	SB0	0.930	17.58	10.93	0.975	1.102	21.22	0.969	3.09	2.263	0.311
N4860	COMA	E2	0.706	15.95	10.42	1.205	0.895	19.82	1.188	3.17	2.396	0.342
N4864	COMA	E2	0.878	16.98	10.60	1.138	0.880	20.04	1.114	3.00:	2.294	0.286
N4867	COMA	E3	0.497	15.70	11.22	1.058	0.553	19.11	1.038	3.16	2.353	0.308
N4869	COMA	E3	0.812	16.61	10.56	1.152	0.920	20.16	1.125	3.06	2.309	0.316
N4871	COMA	S0	0.779	16.91	11.02	1.031	0.919	20.54	1.001	3.06	2.234	0.281
N4872	COMA	SB0	0.459	15.57	11.28	1.053	0.482	18.84	1.036	3.25	2.330	0.301
N4873	COMA	S0	0.584	16.42	11.51	1.042	0.813	20.24	0.989	2.85	2.194	0.290
N4874	COMA	E0	1.665	18.75	8.43	1.310	1.743	22.15	1.282	3.31	2.377	0.323
N4876	COMA	E5	0.683	16.54	11.13	1.020	0.671	19.59	1.035	3.20	2.262	0.248
N4881	COMA	E	0.860	16.86	10.56	1.114	1.022	20.49	1.119	3.12	2.311	0.292
N4886	COMA	E0	0.885	17.37	10.95	0.990	0.874	20.34	1.018	3.13	2.194	0.252
N4889	COMA	E4	1.258	16.89	8.60	1.538	1.484	20.85	1.468	3.35	2.606	0.351
N4894	COMA	S0	0.940	18.30	11.61	0.812	0.664	20.21	0.843	3.09	1.976	0.233
N4898E	COMA	E	0.350	15.85	12.10	0.882	0.300	18.64	0.901	2.98:	2.232	0.266
N4898W	COMA	E	0.657	15.99	10.71	1.174	0.770	19.47	1.171	3.08:	2.232	0.266
N4906	COMA	E3	0.835	17.11	10.94	1.016	0.831	20.19	1.021	3.19	2.229	0.295
N4923	COMA	S0	0.640	16.04	10.84	1.114	0.865	19.93	1.124	2.99	2.288	0.307
N4926	COMA	S0	0.986	16.72	9.79	1.275	0.995	19.90	1.258	3.25	2.420	0.321

Table A.2—*Continued*

Name	Cluster/ Group	Type	K–band				V–band					
			$\log r_{\rm eff}$ ($''$)	$\langle\mu\rangle_{\rm eff}$ (mag/$''$)	$K_{\rm tot}$ (mag)	$\log D_K$ ($''$)	$\log r_{\rm eff}$ ($''$)	$\langle\mu\rangle_{\rm eff}$ (mag/$''$)	$\log D_V$ ($''$)	$V-K$ (mag)	$\log\sigma_0$ (km s^{-1})	Mg$_2$ (mag)
(1)	(2)	(3)	(4)	(5)	(6)	(7)	(8)	(9)	(10)	(11)	(12)	(13)
N4927	COMA	S0	0.844	16.46	10.25	1.205	1.047	20.59	1.121	3.44	2.450	0.354
N4952	COMA	E	0.982	16.57	9.66	1.313	1.106	19.82	···	3.20	2.358	···
N4957	COMA	E3	1.053	17.19	9.93	1.211	1.244	20.70	1.179	3.19	2.330	0.298
N4971	COMA	S0	0.909	17.13	10.59	1.095	0.880	19.87	···	3.29	2.250	···
N5004	COMA	S0	0.919	16.53	9.94	1.267	1.064	19.79	···	3.11	2.371	···
RB40	COMA	U	-0.244	13.64	12.88	0.730	···	···	···	···	···	···
RB42	COMA	U	0.718	18.13	12.55	0.629	···	···	···	···	···	···
RB55	COMA	U	0.901	19.16	12.84	0.551	···	···	···	···	···	···
I2006	FORNAX	S0	1.312	16.78	8.23	1.574	1.457	20.49	1.568	3.18:	2.080	0.268
N1316	FORNAX	S0	1.543	15.55	5.84	1.909	1.907	19.97	2.168	3.25:	2.386	···
N1336	FORNAX	U	1.103	17.52	10.01	1.150	1.487	21.61	···	2.70:	2.061	···
N1339	FORNAX	E	0.884	15.29	8.87	1.543	1.227	19.69	1.568	3.06	2.204	0.290
N1344	FORNAX	E5	1.503	16.69	7.18	1.790	1.597	20.18	1.808	3.16	2.221	0.242
N1351	FORNAX	S0	1.089	16.20	8.76	1.501	1.407	20.42	1.558	3.11	2.160	0.267
N1366	FORNAX	U	0.894	15.44	8.98	1.504	···	···	···	···	···	···
N1374	FORNAX	E	1.286	16.40	7.98	1.649	1.477	20.31	1.638	3.26	2.257	0.297
N1375	FORNAX	S0	1.518	18.46	8.88	1.239	1.437	21.22	···	3.07:	1.724	···
N1379	FORNAX	E	1.561	17.57	7.77	1.605	1.627	20.87	1.628	3.09	2.106	0.243
N1380	FORNAX	S0	1.523	16.31	6.70	1.950	1.755	20.42	···	3.36:	2.352	···
N1380A	FORNAX	U	1.445	18.60	9.38	1.118	1.711	22.29	···	2.72:	1.903	···
N1380B	FORNAX	U	1.919	19.99	8.40	1.048	···	···	···	3.12:	1.982	···
N1381	FORNAX	S0	1.074	15.72	8.36	1.611	1.235	19.51	···	3.12:	2.207	···
N1387	FORNAX	U	0.972	14.58	7.72	1.829	···	···	···	3.29:	···	···
N1389	FORNAX	U	1.064	15.85	8.53	1.589	1.207	20.82	1.618	3.08:	···	···
N1399	FORNAX	E1	1.504	15.90	6.39	2.003	1.627	19.69	1.958	3.46	2.513	0.327
N1404	FORNAX	E1	1.341	15.41	6.71	1.972	1.427	19.04	1.938	3.33	2.363	0.302
N1427	FORNAX	E	1.199	16.29	8.30	1.608	1.517	20.41	1.658	2.94	2.197	0.240
N1428	FORNAX	U	1.243	17.99	9.78	1.185	···	···	···	···	···	···
E501G21	HYDRA	S0/ap	0.885	16.70	10.28	1.176	···	···	1.196	···	2.163	···
E501G47	HYDRA	S0	1.551	18.63	8.88	1.226	···	···	1.166	···	2.105	···
E501G49	HYDRA	SB0	0.891	17.31	10.86	1.003	···	···	1.009	···	2.034	···
N3305	HYDRA	E0	0.953	16.09	9.33	1.407	0.970	19.36	1.415	3.23	2.368	···
N3308	HYDRA	S0	1.498	17.93	8.45	1.419	1.510	21.12	1.425	3.24	2.287	0.293
N3309	HYDRA	E3	1.285	16.79	8.37	1.550	1.340	20.18	1.555	3.24	2.409	0.329
N3311	HYDRA	E2	1.817	18.94	7.86	1.381	2.060	22.71	1.355	3.42	2.292	0.309
N3312	HYDRA	Sb	1.208	16.79	8.76	1.476	1.647	21.36	···	2.98:	2.312	···
N3315	HYDRA	S0	0.991	16.49	9.54	1.420	0.891	19.52	1.336	3.72	2.228	···
N3316	HYDRA	SB0	1.089	16.75	9.30	1.362	1.187	20.34	1.353	3.24:	2.247	···
R253	HYDRA	U	1.393	19.80	10.84	0.575	···	···	···	···	1.905	···
R293	HYDRA	U	0.611	18.04	12.99	0.505	···	···	···	···	1.644	···
S135	HYDRA	E	0.346	15.47	11.75	0.954	···	···	1.004	···	2.049	···
S154	HYDRA	E3	0.491	16.37	11.92	0.866	···	···	0.912	···	2.077	···
S201	HYDRA	SB	1.006	18.38	11.35	0.833	···	···	···	···	2.174	···
S23	HYDRA	S0	1.256	18.43	10.15	1.006	···	···	1.032	···	2.060	···
S37	HYDRA	S0/E7	0.729	16.56	10.92	1.047	···	···	1.090	···	2.070	···
S46	HYDRA	SB0	1.108	18.30	10.77	0.881	···	···	0.939	···	2.033	···
S53	HYDRA	S0	0.538	15.24	10.55	1.206	···	···	1.215	···	2.276	···
S61	HYDRA	E1	0.326	14.64	11.01	1.134	···	···	1.170	···	2.309	···
S68	HYDRA	S0:	0.734	16.75	11.08	1.007	···	···	1.050	···	2.092	···
S83	HYDRA	S0/S	0.883	17.75	11.34	0.859	···	···	0.859	···	2.050	···
S96	HYDRA	S0/S	0.627	16.31	11.18	1.024	···	···	1.053	···	2.077	···

Table A.2—*Continued*

Name	Cluster/ Group	Type	K–band				V–band					
			$\log r_{\rm eff}$ ($''$)	$\langle\mu\rangle_{\rm eff}$ (mag/$''$)	$K_{\rm tot}$ (mag)	$\log D_K$ ($''$)	$\log r_{\rm eff}$ ($''$)	$\langle\mu\rangle_{\rm eff}$ (mag/$''$)	$\log D_V$ ($''$)	$V-K$ (mag)	$\log\sigma_0$ (km s^{-1})	Mg_2 (mag)
(1)	(2)	(3)	(4)	(5)	(6)	(7)	(8)	(9)	(10)	(11)	(12)	(13)
D32	KLEM44	E	0.638	15.77	10.58	1.188	0.850	19.89	1.131	3.35:	2.476	0.331
D34	KLEM44	Ep	0.522	17.33	12.73	0.600	...	...	0.751	...	1.990	...
D42	KLEM44	D	1.146	17.82	10.09	1.119	1.320	21.50	1.101	3.05:	2.338	0.362
D43	KLEM44	S0	0.696	16.74	11.27	0.987	0.960	20.71	1.011	3.01:	2.273	...
D44	KLEM44	E	0.111	15.18	12.63	0.803	-0.040	17.62	0.811	2.99:	2.210	0.292
D45	KLEM44	E	0.633	17.32	12.16	0.772	0.670	20.45	0.801	2.99:	2.117	0.242
D51	KLEM44	S0	0.210	16.03	12.98	0.681	0.260	19.17	0.721	2.96:	2.185	...
D55	KLEM44	E	0.505	16.17	11.65	0.950	0.520	19.30	0.951	3.07:	2.229	0.304
D56	KLEM44	D	1.043	17.16	9.96	1.211	1.200	20.79	1.211	3.06:	2.423	0.310
D58	KLEM44	E	0.594	15.76	10.79	1.153	0.830	19.77	1.151	3.16:	2.412	0.292
D59	KLEM44	S0	0.624	17.09	11.97	0.822	0.730	20.46	0.851	2.98:	2.230	...
D77	KLEM44	S0	0.778	16.49	10.61	1.137	0.880	19.95	1.151	3.09:	2.314	...
N7562	PEGASUS	E2	1.228	16.36	8.22	1.630	1.377	20.14	1.589	3.18	2.383	0.280
N7617	PEGASUS	S0	0.870	16.50	10.15	1.211	1.187	21.24	1.078	3.56	2.129	0.216
N7619	PEGASUS	E	1.239	16.14	7.95	1.683	1.507	20.42	1.648	3.31:	2.505	0.331
N7626	PEGASUS	E	1.449	17.05	7.81	1.632	1.577	20.77	1.608	3.46	2.405	0.321
BGP110	PERSEUS	U	0.688	17.41	11.97	0.744	...	...	...	...	...	...
BGP63	PERSEUS	U	0.588	16.29	11.36	1.060	...	...	...	...	...	...
BGP65	PERSEUS	U	1.193	18.65	10.69	0.921	...	...	...	...	...	...
CR32	PERSEUS	U	0.953	16.62	9.86	1.288	1.137	20.56	1.238	3.27:	2.375	0.307
CR36	PERSEUS	E	0.637	15.88	10.70	1.148	0.794	19.54	1.157	3.19	2.312	0.300
I0310	PERSEUS	S0	1.177	16.79	8.91	1.442	1.327	20.61	1.384	3.46	2.341	0.261
N1260	PERSEUS	S0/a	0.893	16.05	9.59	1.368	1.087	20.11	1.330	3.36:	2.320	0.224
N1270	PERSEUS	E	0.802	15.29	9.28	1.458	0.848	18.76	1.415	3.41	2.545	0.365
N1272	PERSEUS	E	1.411	17.57	8.52	1.482	1.474	20.97	1.412	3.35	2.439	0.334
N1273	PERSEUS	S0	0.904	16.17	9.65	1.373	0.957	19.44	1.350	3.17	2.319	0.274
N1274	PERSEUS	E3	0.559	15.14	10.35	1.250	0.637	18.70	1.238	3.27:	2.240	0.293
N1275	PERSEUS	U	1.602	17.98	7.98	1.531	1.213	19.65	...	3.07:	2.391	...
N1277	PERSEUS	U	0.490	14.37	9.92	1.373	...	...	...	...	...	...
N1278	PERSEUS	E	1.258	17.04	8.76	1.458	1.360	20.63	1.423	3.38	2.414	0.307
N1282	PERSEUS	E	1.064	16.71	9.39	1.352	1.106	19.94	1.359	3.16	2.325	0.270
N1283	PERSEUS	E1	0.653	15.51	10.25	1.260	0.921	19.71	1.239	3.30	2.346	0.299
N1293	PERSEUS	E0	0.874	16.16	9.79	1.311	0.978	19.72	1.293	3.26	2.342	0.328
PER101	PERSEUS	U	0.601	16.65	11.65	0.903	0.747	20.25	0.960	3.07:	1.952	0.233
PER152	PERSEUS	E	0.389	15.68	11.74	0.948	0.560	19.62	0.912	3.22	2.172	0.308
PER153	PERSEUS	U	0.408	16.39	12.36	0.775	0.577	20.23	0.779	3.23:	2.137	0.227
PER163	PERSEUS	E	0.270	14.85	11.51	1.055	0.527	19.02	1.032	3.10	2.234	0.289
PER164	PERSEUS	U	0.616	16.02	10.94	1.090	0.917	20.37	1.071	3.26:	2.220	0.280
PER195	PERSEUS	E	0.731	16.52	10.87	1.099	1.080	20.64	1.129	2.97	2.225	0.290
PER199	PERSEUS	S0	0.459	15.09	10.80	1.172	0.731	19.41	1.137	3.27	2.300	0.289
N0379	PISCES	S0	0.899	15.72	9.23	1.451	1.241	20.44	1.382	3.54	2.384	0.305
N0380	PISCES	E2	0.942	15.93	9.22	1.429	1.018	19.49	1.393	3.38	2.461	0.337
N0382	PISCES	E	0.673	15.72	10.36	1.225	0.785	19.45	1.194	3.35	2.248	0.271
N0383	PISCES	S0	1.221	16.56	8.46	1.545	1.488	20.82	1.491	3.51	2.436	0.309
N0384	PISCES	E	0.630	15.17	10.03	1.339	0.889	19.43	1.288	3.33	2.402	0.310
N0385	PISCES	S0	1.033	16.89	9.74	1.263	1.095	20.23	1.263	3.24	2.270	0.287
N0386	PISCES	E3	0.857	17.14	10.86	1.020	0.774	19.94	1.042	3.18	1.958	0.242
N0392	PISCES	S0	0.989	16.41	9.47	1.381	1.073	19.85	1.355	3.23	2.397	0.294
N0394	PISCES	S0	0.610	15.53	10.48	1.236	0.751	19.32	1.188	3.28	2.248	0.269
N0410	PISCES	E	1.360	17.00	8.21	1.561	1.434	20.49	1.526	3.40	2.487	0.343
Z01047	PISCES	E	0.493	15.89	11.43	1.000	0.538	19.21	0.997	3.21	2.111	0.289

Table A.2—*Continued*

Name	Cluster/ Group	Type	K–band				V–band					
			$\log r_{\rm eff}$ ($''$)	$\langle\mu\rangle_{\rm eff}$ (mag/$''$)	$K_{\rm tot}$ (mag)	$\log D_K$ ($''$)	$\log r_{\rm eff}$ ($''$)	$\langle\mu\rangle_{\rm eff}$ (mag/$''$)	$\log D_V$ ($''$)	$V-K$ (mag)	$\log\sigma_0$ (km s^{-1})	Mg_2 (mag)
(1)	(2)	(3)	(4)	(5)	(6)	(7)	(8)	(9)	(10)	(11)	(12)	(13)
N4168	VIRGO	E2	1.517	17.64	8.06	1.524	1.657	21.26	1.561	3.11:	2.263	0.249
N4239	VIRGO	E	1.171	17.72	9.87	1.141	1.207	20.68	1.311	2.83:	1.813	0.151
N4261	VIRGO	E2	1.491	16.46	7.01	1.834	1.587	20.25	1.758	3.44:	2.461	0.323
N4318	VIRGO	E	0.867	16.38	10.05	1.236	0.777	19.13	1.268	3.07:	2.009	···
N4339	VIRGO	E0	1.431	17.30	8.15	1.536	1.487	20.78	1.508	3.10	1.960	0.238
N4342	VIRGO	U	0.612	13.95	8.90	1.567	0.787	18.11	1.508	3.52:	2.362	0.277
N4365	VIRGO	E3	1.583	16.54	6.63	1.924	1.757	20.43	1.878	3.20	2.392	0.304
N4371	VIRGO	SB0	1.533	17.05	7.39	1.717	1.627	20.61	···	3.15	2.097	···
N4374	VIRGO	E1	1.595	16.07	6.09	2.049	1.737	19.80	2.042	3.00	2.455	0.290
N4377	VIRGO	S0	1.091	15.98	8.53	1.584	1.129	19.26	···	2.97	2.149	···
N4382	VIRGO	S0	1.799	16.94	5.95	2.016	1.849	20.25	···	3.09	2.283	···
N4387	VIRGO	E	1.221	16.85	8.75	1.472	1.177	19.82	1.492	3.10	1.996	0.220
N4406	VIRGO	E3	1.833	17.16	6.00	1.990	1.957	20.69	2.038	3.15	2.379	0.294
N4434	VIRGO	E	1.549	17.79	8.05	1.487	1.267	20.21	1.458	3.44:	2.046	0.241
N4435	VIRGO	SB0	1.175	15.45	7.58	1.785	1.457	19.82	···	3.17	2.225	···
N4442	VIRGO	SB0	1.266	15.54	7.22	1.853	1.453	19.46	···	3.17	2.336	···
N4458	VIRGO	E0	1.298	17.46	8.97	1.352	1.427	20.90	1.421	2.91	1.992	0.204
N4464	VIRGO	S	0.908	15.86	9.32	1.413	0.697	18.15	1.418	3.08	2.071	0.220
N4467	VIRGO	E2	0.785	16.78	10.87	1.037	0.977	20.74	1.028	3.26:	1.888	0.244
N4468	VIRGO	S0	1.439	18.84	9.65	1.031	1.477	21.88	···	2.92	1.881	0.144
N4472	VIRGO	E2	1.851	16.52	5.27	2.189	2.017	20.42	2.138	3.18	2.425	0.292
N4473	VIRGO	E5	1.303	15.56	7.05	1.879	1.397	19.12	1.911	3.18	2.248	0.289
N4476	VIRGO	S0	1.003	16.34	9.33	1.384	1.207	20.12	1.468	2.88	1.553	0.137
N4478	VIRGO	E2	1.286	16.41	7.99	1.664	1.137	18.88	1.728	3.05	2.168	0.246
N4486	VIRGO	E0	1.909	17.02	5.48	2.109	2.017	20.55	2.108	3.21	2.558	0.296
N4486B	VIRGO	E0	0.387	13.91	9.98	1.350	0.397	17.15	1.348	3.21:	2.188	0.287
N4489	VIRGO	E	1.348	17.74	9.01	1.308	1.507	21.24	1.407	2.93:	1.740	0.173
N4550	VIRGO	SB0	1.221	16.41	8.31	1.583	1.321	19.89	···	3.06	1.919	···
N4551	VIRGO	E	1.357	17.15	8.37	1.513	1.247	19.95	1.515	3.22	1.999	0.242
N4552	VIRGO	E	1.320	15.35	6.75	1.965	1.477	19.22	1.939	3.17	2.405	0.309
N4564	VIRGO	E	1.226	15.86	7.74	1.725	1.337	19.55	1.724	3.21	2.213	0.333
N4621	VIRGO	E5	1.569	16.27	6.43	1.958	1.667	19.91	1.941	3.17	2.358	0.309
N4636	VIRGO	E0	1.652	16.93	6.67	1.911	2.007	21.15	1.910	2.97	2.285	0.297
N4649	VIRGO	E2	1.722	16.18	5.57	2.152	1.867	19.98	2.124	3.28:	2.524	0.328
N4660	VIRGO	E	1.052	15.24	7.99	1.713	1.097	18.70	1.688	3.07	2.280	0.276
N4697	VIRGO	E6	1.778	16.83	5.94	2.024	1.877	20.36	2.041	3.16	2.228	0.279
N4733	VIRGO	E	1.926	19.56	7.93	1.199	···	···	···	···	1.863	0.164
N0584	CETUS	E4	1.325	15.89	7.27	1.820	1.437	19.47	1.851	3.20	2.301	0.268
N0596	CETUS	E	1.347	16.57	7.84	1.655	1.477	20.09	1.721	3.09	2.176	0.236
N0636	CETUS	E3	1.249	16.52	8.28	1.566	1.277	19.72	1.628	3.11	2.185	0.261
N1395	ERIDANUS	E2	1.496	16.31	6.84	1.891	1.657	20.18	1.868	3.39	2.388	0.310
N1400	ERIDANUS	S0	1.238	15.84	7.65	1.744	1.577	20.51	1.657	3.50	2.395	0.303
N1407	ERIDANUS	E0	1.553	16.54	6.78	1.901	1.857	20.91	1.817	3.45	2.452	0.322
N1426	ERIDANUS	E4	1.250	16.63	8.38	1.546	1.417	20.35	1.592	3.18	2.167	0.254
N1439	ERIDANUS	E1	1.280	16.89	8.49	1.498	1.617	21.22	1.506	3.12	2.152	0.267
N3377	LEO	E5	1.294	15.93	7.46	1.778	1.527	19.70	1.902	2.87	2.121	0.245
N3379	LEO	E1	1.472	15.59	6.23	2.047	1.547	19.02	2.085	3.08	2.296	0.295
N3384	LEO	SB0	1.124	14.71	7.09	1.911	1.397	18.89	···	3.00	2.193	0.289
N3412	LEO	SB0	1.645	17.18	6.96	1.752	1.479	19.79	···	3.00	1.980	0.219
N3489	LEO	S0	1.341	15.76	7.06	1.861	1.345	18.91	···	2.87	1.941	0.166
I3370	N4373grp	E2	1.403	16.68	7.66	1.705	1.577	20.42	1.718	3.19	2.285	0.249

Table A.2—*Continued*

Name	Cluster/ Group	Type	K–band				V–band					
			$\log r_{\rm eff}$ ($''$)	$\langle\mu\rangle_{\rm eff}$ (mag/$''$)	$K_{\rm tot}$ (mag)	$\log D_K$ ($''$)	$\log r_{\rm eff}$ ($''$)	$\langle\mu\rangle_{\rm eff}$ (mag/$''$)	$\log D_V$ ($''$)	$V-K$ (mag)	$\log\sigma_0$ (km s^{-1})	Mg$_2$ (mag)
(1)	(2)	(3)	(4)	(5)	(6)	(7)	(8)	(9)	(10)	(11)	(12)	(13)
N4373	N4373grp	S0	1.362	16.44	7.63	1.734	1.537	20.08	1.785	3.05	2.341	0.255
N5813	N5846grp	E1	1.551	17.11	7.36	1.707	1.687	20.83	1.698	3.23:	2.365	0.297
N5831	N5846grp	E3	1.371	17.00	8.14	1.564	1.427	20.41	1.571	3.21:	2.209	0.278
N5845	N5846grp	E	0.520	13.70	9.10	1.530	0.557	17.08	1.531	3.25:	2.391	0.293
N5846	N5846grp	E0	1.630	17.05	6.91	1.854	1.917	21.21	1.791	3.12:	2.433	0.312
N5846A	N5846grp	E2	0.387	14.05	10.13	1.320	0.495	17.47	···	3.03:	2.350	0.275
ARK66	N741grp	U	0.615	16.07	11.00	1.077	···	···	···	···	···	···
I2311	FIELD	E0	1.057	15.57	8.29	1.661	1.247	19.45	1.663	3.19:	2.352	0.238
I4296	HG22grp	E	1.307	16.27	7.74	1.714	1.757	20.92	1.750	3.11:	2.500	···
M32	LOCALgrp	U	1.549	14.64	4.90	2.418	1.587	17.84	2.418	3.06:	1.821	0.112
N0661	GH18	E	1.066	16.25	8.93	1.469	1.237	19.98	1.508	3.11:	2.181	0.291
N0680	GH20	E	1.037	15.79	8.61	1.558	1.267	19.73	1.616	3.11:	2.301	0.281
N0720	FIELD	E5	1.397	16.14	7.16	1.831	1.597	20.15	1.798	3.46	2.372	0.323
N0741	N741grp	E0	1.499	17.61	8.12	1.529	1.717	21.56	1.493	3.28	2.428	0.334
N0742	N741grp	E0	1.013	17.21	10.60	1.180	···	···	···	···	2.236	···
N0821	FIELD	E6	1.310	16.31	7.76	1.691	1.657	20.71	1.722	3.11	2.282	0.293
N2325	FIELD	E4	1.774	18.28	7.41	1.582	1.937	21.86	1.589	3.28	2.138	0.282
N2434	HG1grp	E0	1.252	16.20	7.95	1.684	1.607	20.46	1.756	3.10	2.316	0.247
N2986	HG36grp	E2	1.430	16.64	7.49	1.734	1.617	20.51	1.728	3.42	2.398	0.299
N3258	ANTLIA	E1	1.176	16.27	8.39	1.584	1.437	20.41	1.579	3.27	2.449	0.335
N3557	FIELD	E3	1.174	15.47	7.61	1.795	1.577	19.95	1.853	2.98	2.474	0.297
N4946	N5011grp	E	1.195	16.68	8.71	1.490	1.227	19.90	1.558	3.38:	2.290	0.290
N5061	HG31+35grp	E0	1.132	15.15	7.50	1.900	1.407	19.10	1.951	2.87	2.283	0.235
N5128	N5128grp	U	1.782	15.64	4.74	2.046	2.521	21.10	···	2.79:	2.164	···
N5812	FIELD	E0	1.117	15.57	7.99	1.695	1.377	19.72	1.746	3.21:	2.302	0.316
N5898	FABER71grp	E0	1.120	15.78	8.19	1.650	1.337	19.40	1.805	2.83	2.356	0.303
N5982	GH158	E3	1.183	16.03	8.12	1.657	1.397	20.02	1.655	3.37	2.421	0.289
N6411	FIELD	E	1.124	16.74	9.13	1.407	1.427	20.86	1.431	3.02:	2.218	0.268
N6482	FIELD	E	1.148	15.85	8.12	1.675	0.877	17.48	1.848	3.26	2.460	0.323
N6702	FIELD	E	1.176	16.86	8.98	1.419	1.457	21.09	1.396	3.29	2.253	0.271
N6703	FIELD	S0	1.146	15.92	8.20	1.644	1.377	19.86	1.684	3.00	2.252	0.269
N7236	FABER86grp	S0	0.687	15.91	10.48	1.198	1.007	20.26	1.223	3.20:	2.306	0.292
N7237	FABER86grp	S0	1.323	18.49	9.88	1.076	1.537	22.40	1.013	3.14:	2.266	0.323
N7385	FIELD	E	1.342	17.60	8.89	1.382	1.637	21.81	1.335	3.15:	2.426	0.325
N7454	GH163	E4	1.262	17.23	8.93	1.411	1.387	20.57	1.505	2.89:	2.011	0.191
N7768	A2666	E	1.230	17.30	9.15	1.370	1.477	21.31	1.367	3.12:	2.457	0.314

Table A.3: Comparisons of K–band Quantities with B–band Quantities from Faber *et al.* (1989)

Name	Cluster/ Group	Type	K–band				B–band					
			$\log r_{\rm eff}$ ($''$)	$\langle\mu\rangle_{\rm eff}$ (mag/$''$)	$K_{\rm tot}$ (mag)	$\log D_K$ ($''$)	$\log r_{\rm eff}$ ($''$)	$\langle\mu\rangle_{\rm eff}$ (mag/$''$)	$\log D_B$ ($''$)	$B-K$ (mag)	$\log\sigma_0$ (km s^{-1})	Mg_2 (mag)
(1)	(2)	(3)	(4)	(5)	(6)	(7)	(8)	(9)	(10)	(11)	(12)	(13)
D45	A194	U	0.625	16.39	11.27	1.000	1.337	21.24	1.504	2.28:	2.093	...
N0533	A194	E3	1.301	17.17	8.67	1.460	1.677	22.45	1.469	3.92:	2.457	0.317
N0541	A194	S0	1.209	17.18	9.14	1.359	1.627	22.76	1.320	4.07:	2.328	0.312
N0545	A194	S0	1.425	17.65	8.53	1.424	...	...	1.390	...	2.367	0.314
N0547	A194	E1	0.939	16.13	9.44	1.408	...	...	1.410	...	2.326	0.319
N0548	A194	E	0.924	17.50	10.89	0.979	1.277	22.59	1.030	3.81:	2.097	0.246
N0564	A194	E	0.919	16.27	9.68	1.329	1.307	21.73	1.344	4.06:	2.368	0.298
N6158	A2199	E	0.990	17.33	10.38	1.112	1.047	21.71	1.118	4.17:	2.269	0.275
N6166	A2199	E2	1.373	18.23	9.37	1.259	1.757	23.54	1.158	3.93:	2.487	0.323
N7720	A2634	E	1.160	17.19	9.40	1.326	1.407	22.20	1.318	4.11:	2.494	0.331
D27	CEN45	U	0.815	16.53	10.46	1.152	0.937	20.85	1.244	3.89:	2.038	0.264
D45	CEN45	U	1.061	15.77	8.47	1.615	1.337	20.82	1.637	4.06:	2.390	0.297
N4616	CEN45	E	1.136	17.07	9.40	1.319	1.297	21.61	1.361	3.96:	2.240	0.267
N4709	CEN45	E1	1.451	17.25	8.00	1.612	1.837	22.44	1.624	3.80:	2.388	0.324
N4645	CEN30	E	1.122	15.92	8.31	1.614	1.337	20.76	1.651	4.06:	2.250	0.269
N4696	CEN30	E1	1.842	18.21	7.01	1.684	2.327	23.44	1.724	3.47:	2.387	0.267
N4729	CEN30	E	1.149	16.52	8.78	1.497	1.337	21.34	1.487	4.13:	2.175	0.261
N4767	CEN30	E	1.283	16.47	8.06	1.649	1.487	21.14	1.700	3.93:	2.298	0.278
D27	COMA	U	0.544	17.03	12.32	0.736	0.937	21.52	1.031	3.07:	2.009	0.260
I3957	COMA	S0	0.545	16.45	11.73	0.912	0.647	20.91	0.945	4.10:	2.179	0.292
I3959	COMA	E3	0.655	16.27	11.00	1.069	0.757	20.93	1.039	4.29:	2.295	0.307
I4011	COMA	E	0.650	17.11	11.86	0.830	0.727	21.43	0.882	4.04:	2.040	0.280
I4012	COMA	E	0.312	15.15	11.59	1.011	0.477	20.11	0.972	4.37:	2.259	0.292
I4021	COMA	E	0.809	16.77	10.73	1.086	0.597	20.67	0.962	4.66:	2.206	0.300
I4045	COMA	E4	0.481	15.31	10.91	1.136	0.727	20.64	1.092	4.44:	2.331	0.306
I4051	COMA	E0	1.058	17.50	10.22	1.118	1.307	22.57	1.072	4.16:	2.355	0.332
N4692	COMA	E	1.117	17.13	9.55	1.290	1.207	21.74	1.225	4.28:	2.432	0.307
N4789	COMA	S0	1.039	16.60	9.41	1.372	1.377	22.05	1.302	4.22:	2.427	0.287
N4807	COMA	S0	0.740	16.12	10.42	1.195	0.947	21.23	1.169	4.37:	2.336	0.275
N4816	COMA	S0	1.299	18.15	9.66	1.163	1.327	22.44	1.159	4.19:	2.365	0.306
N4839	COMA	E	1.290	17.78	9.34	1.264	1.457	22.50	1.242	4.11:	2.420	0.313
N4841B	COMA	E	0.790	16.69	10.74	1.091	1.267	21.86	1.275	3.45:	2.355	0.295
N4854	COMA	SB0	0.930	17.58	10.93	0.975	1.257	23.11	0.879	4.35:	2.263	0.311
N4860	COMA	E2	0.706	15.95	10.42	1.205	0.927	21.11	1.156	4.36:	2.396	0.342
N4864	COMA	E2	0.878	16.98	10.60	1.138	0.927	21.28	1.112	4.12:	2.294	0.286
N4867	COMA	E3	0.497	15.70	11.22	1.058	0.577	20.21	1.052	4.22:	2.353	0.308
N4869	COMA	E3	0.812	16.61	10.56	1.152	0.917	21.18	1.122	4.19:	2.309	0.316
N4872	COMA	SB0	0.459	15.57	11.28	1.053	0.507	19.91	1.052	4.16:	2.330	0.301
N4874	COMA	E0	1.665	18.75	8.43	1.310	1.787	23.29	1.282	4.10:	2.377	0.323
N4876	COMA	E5	0.683	16.54	11.13	1.020	0.747	21.02	1.002	4.25:	2.262	0.248
N4881	COMA	E	0.860	16.86	10.56	1.114	1.047	21.72	1.102	4.19:	2.311	0.292
N4886	COMA	E0	0.885	17.37	10.95	0.990	0.957	21.60	1.042	3.97:	2.194	0.252
N4889	COMA	E4	1.258	16.89	8.60	1.538	1.497	22.00	1.452	4.25:	2.606	0.351
N4906	COMA	E3	0.835	17.11	10.94	1.016	0.887	21.35	1.059	4.05:	2.229	0.295
N4923	COMA	S0	0.640	16.04	10.84	1.114	0.917	21.20	1.122	4.16:	2.288	0.307
N4926	COMA	S0	0.986	16.72	9.79	1.275	1.047	21.21	1.252	4.27:	2.420	0.321
N4957	COMA	E3	1.053	17.19	9.93	1.211	1.157	21.84	1.179	4.28:	2.330	0.298
I2006	FORNAX	S0	1.312	16.78	8.23	1.574	1.457	21.44	1.568	4.13:	2.080	0.268
N1316	FORNAX	S0	1.543	15.55	5.84	1.909	1.907	20.93	2.168	4.06:	2.386	...

Table A.3—*Continued*

Name	Cluster/ Group	Type	K–band				B–band			$B-K$	$\log \sigma_0$	Mg_2
			$\log r_{\rm eff}$ ($''$)	$\langle\mu\rangle_{\rm eff}$ (mag/$''$)	$K_{\rm tot}$ (mag)	$\log D_K$ ($''$)	$\log r_{\rm eff}$ ($''$)	$\langle\mu\rangle_{\rm eff}$ (mag/$''$)	$\log D_B$ ($''$)	(mag)	(km s^{-1})	(mag)
(1)	(2)	(3)	(4)	(5)	(6)	(7)	(8)	(9)	(10)	(11)	(12)	(13)
N1339	FORNAX	E	0.884	15.29	8.87	1.543	1.227	20.62	1.568	4.09:	2.204	0.290
N1344	FORNAX	E5	1.503	16.69	7.18	1.790	1.597	21.09	1.808	4.06:	2.221	0.242
N1351	FORNAX	S0	1.089	16.20	8.76	1.501	1.407	21.32	1.558	3.97:	2.160	0.267
N1374	FORNAX	E	1.286	16.40	7.98	1.649	1.477	21.25	1.638	4.16:	2.257	0.297
N1379	FORNAX	E	1.561	17.57	7.77	1.605	1.627	21.79	1.628	3.98:	2.106	0.243
N1389	FORNAX	U	1.064	15.85	8.53	1.589	1.207	21.75	1.618	5.39:	...	...
N1399	FORNAX	E1	1.504	15.90	6.39	2.003	1.627	20.68	1.958	4.33:	2.513	0.327
N1404	FORNAX	E1	1.341	15.41	6.71	1.972	1.427	20.01	1.938	4.29:	2.363	0.302
N1427	FORNAX	E	1.199	16.29	8.30	1.608	1.517	21.33	1.658	3.89:	2.197	0.240
N3305	HYDRA	E0	0.953	16.09	9.33	1.407	0.977	20.31	1.408	4.13:	2.368	...
N3308	HYDRA	S0	1.498	17.93	8.45	1.419	1.517	22.14	1.406	4.14:	2.287	0.293
N3309	HYDRA	E3	1.285	16.79	8.37	1.550	1.497	21.69	1.536	4.13:	2.409	0.329
N3311	HYDRA	E2	1.817	18.94	7.86	1.381	2.227	24.16	1.286	3.74:	2.292	0.309
D45	KLEM44	U	0.633	17.32	12.16	0.772	1.337	21.45	1.437	1.59:	2.117	0.242
N7562	PEGASUS	E2	1.228	16.36	8.22	1.630	1.377	21.13	1.589	4.23:	2.383	0.280
N7617	PEGASUS	S0	0.870	16.50	10.15	1.211	1.187	22.22	1.078	4.57:	2.129	0.216
N7619	PEGASUS	E	1.239	16.14	7.95	1.683	1.507	21.40	1.648	4.29:	2.505	0.331
N7626	PEGASUS	E	1.449	17.05	7.81	1.632	1.577	21.74	1.608	4.22:	2.405	0.321
CR32	PERSEUS	U	0.953	16.62	9.86	1.288	1.137	21.55	1.238	4.27:	2.375	0.307
CR36	PERSEUS	U	0.637	15.88	10.70	1.148	0.817	20.74	1.138	4.22:	2.312	0.300
N1260	PERSEUS	S0/a	0.893	16.05	9.59	1.368	1.087	21.05	1.330	4.30:	2.320	0.224
N1270	PERSEUS	E	0.802	15.29	9.28	1.458	0.877	19.99	1.404	4.44:	2.545	0.365
N1272	PERSEUS	E	1.411	17.57	8.52	1.482	1.657	22.52	1.424	4.07:	2.439	0.334
N1273	PERSEUS	S0	0.904	16.17	9.65	1.373	1.017	20.66	1.368	4.08:	2.319	0.274
N1274	PERSEUS	E3	0.559	15.14	10.35	1.250	0.637	19.66	1.238	4.23:	2.240	0.293
N1278	PERSEUS	E	1.258	17.04	8.76	1.458	1.377	21.76	1.408	4.29:	2.414	0.307
N1282	PERSEUS	E	1.064	16.71	9.39	1.352	1.117	21.01	1.371	4.12:	2.325	0.270
N1283	PERSEUS	E1	0.653	15.51	10.25	1.260	1.177	21.78	1.216	4.38:	2.346	0.299
N1293	PERSEUS	E0	0.874	16.16	9.79	1.311	1.207	21.61	1.266	4.25:	2.342	0.328
PER101	PERSEUS	U	0.601	16.65	11.65	0.903	0.747	21.19	0.960	4.01:	1.952	0.233
PER152	PERSEUS	U	0.389	15.68	11.74	0.948	0.587	20.86	0.879	4.46:	2.172	0.308
PER153	PERSEUS	U	0.408	16.39	12.36	0.775	0.577	21.21	0.779	4.21:	2.137	0.227
PER163	PERSEUS	U	0.270	14.85	11.51	1.055	0.587	20.35	1.011	4.35:	2.234	0.289
PER164	PERSEUS	U	0.616	16.02	10.94	1.090	0.917	21.33	1.071	4.23:	2.220	0.280
PER195	PERSEUS	U	0.731	16.52	10.87	1.099	1.207	22.32	1.071	4.08:	2.225	0.290
PER199	PERSEUS	U	0.459	15.09	10.80	1.172	1.527	23.47	1.101	4.55:	2.300	0.289
N0379	PISCES	S0	0.899	15.72	9.23	1.451	1.027	20.72	1.359	4.53:	2.384	0.305
N0380	PISCES	E2	0.942	15.93	9.22	1.429	1.177	21.27	1.359	4.49:	2.461	0.337
N0382	PISCES	E	0.673	15.72	10.36	1.225	...	...	1.139	...	2.248	0.271
N0383	PISCES	S0	1.221	16.56	8.46	1.545	...	...	1.429	...	2.436	0.309
N0385	PISCES	S0	1.033	16.89	9.74	1.263	1.307	22.09	1.229	4.20:	2.270	0.287
N0386	PISCES	E3	0.857	17.14	10.86	1.020	0.807	21.07	1.049	4.11:	1.958	0.242
N0392	PISCES	S0	0.989	16.41	9.47	1.381	1.257	21.59	1.336	4.21:	2.397	0.294
N0410	PISCES	E	1.360	17.00	8.21	1.561	1.567	22.04	1.502	4.28:	2.487	0.343
N4168	VIRGO	E2	1.517	17.64	8.06	1.524	1.657	22.10	1.561	3.95:	2.263	0.249
N4239	VIRGO	E	1.171	17.72	9.87	1.141	1.207	21.49	1.311	3.64:	1.813	0.151
N4261	VIRGO	E2	1.491	16.46	7.01	1.834	1.587	21.24	1.758	4.43:	2.461	0.323
N4318	VIRGO	E	0.867	16.38	10.05	1.236	0.777	20.03	1.268	3.97:	2.009	...
N4339	VIRGO	E0	1.431	17.30	8.15	1.536	1.487	21.71	1.508	4.21:	1.960	0.238
N4342	VIRGO	U	0.612	13.95	8.90	1.567	0.787	19.07	1.508	4.48:	2.362	0.277
N4365	VIRGO	E3	1.583	16.54	6.63	1.924	1.757	21.42	1.878	4.25:	2.392	0.304

Table A.3—*Continued*

Name	Cluster/ Group	Type	K–band				B–band					
			$\log r_{\rm eff}$ ($''$)	$\langle\mu\rangle_{\rm eff}$ (mag/$''$)	$K_{\rm tot}$ (mag)	$\log D_K$ ($''$)	$\log r_{\rm eff}$ ($''$)	$\langle\mu\rangle_{\rm eff}$ (mag/$''$)	$\log D_B$ ($''$)	$B-K$ (mag)	$\log\sigma_0$ (km s^{-1})	Mg_2 (mag)
(1)	(2)	(3)	(4)	(5)	(6)	(7)	(8)	(9)	(10)	(11)	(12)	(13)
N4374	VIRGO	E1	1.595	16.07	6.09	2.049	1.737	20.77	2.042	4.19:	2.455	0.290
N4387	VIRGO	E	1.221	16.85	8.75	1.472	1.177	20.73	1.492	4.04:	1.996	0.220
N4406	VIRGO	E3	1.833	17.16	6.00	1.990	1.957	21.59	2.038	3.98:	2.379	0.294
N4434	VIRGO	E	1.549	17.79	8.05	1.487	1.267	21.14	1.458	4.37:	2.046	0.241
N4458	VIRGO	E0	1.298	17.46	8.97	1.352	1.427	21.80	1.421	3.87:	1.992	0.204
N4464	VIRGO	S	0.908	15.86	9.32	1.413	0.697	19.08	1.418	3.98:	2.071	0.220
N4467	VIRGO	E2	0.785	16.78	10.87	1.037	0.977	21.68	1.028	4.20:	1.888	0.244
N4472	VIRGO	E2	1.851	16.52	5.27	2.189	2.017	21.40	2.138	4.28:	2.425	0.292
N4473	VIRGO	E5	1.303	15.56	7.05	1.879	1.397	20.05	1.911	4.15:	2.248	0.289
N4476	VIRGO	S0	1.003	16.34	9.33	1.384	1.207	20.93	1.468	3.85:	1.553	0.137
N4478	VIRGO	E2	1.286	16.41	7.99	1.664	1.137	19.75	1.728	3.87:	2.168	0.246
N4486	VIRGO	E0	1.909	17.02	5.48	2.109	2.017	21.51	2.108	4.10:	2.558	0.296
N4486B	VIRGO	E0	0.387	13.91	9.98	1.350	0.397	18.11	1.348	4.16:	2.188	0.287
N4489	VIRGO	E	1.348	17.74	9.01	1.308	1.507	22.08	1.407	3.76:	1.740	0.173
N4551	VIRGO	E	1.357	17.15	8.37	1.513	1.247	20.88	1.515	4.13:	1.999	0.242
N4552	VIRGO	E	1.320	15.35	6.75	1.965	1.477	20.18	1.939	4.26:	2.405	0.309
N4564	VIRGO	E	1.226	15.86	7.74	1.725	1.337	20.48	1.724	4.22:	2.213	0.333
N4621	VIRGO	E5	1.569	16.27	6.43	1.958	1.667	20.88	1.941	4.25:	2.358	0.309
N4636	VIRGO	E0	1.652	16.93	6.67	1.911	2.007	22.07	1.910	3.86:	2.285	0.297
N4649	VIRGO	E2	1.722	16.18	5.57	2.152	1.867	20.96	2.124	4.26:	2.524	0.328
N4660	VIRGO	E	1.052	15.24	7.99	1.713	1.097	19.68	1.688	4.27:	2.280	0.276
N4697	VIRGO	E6	1.778	16.83	5.94	2.024	1.877	21.28	2.041	4.09:	2.228	0.279
N0584	CETUS	E4	1.325	15.89	7.27	1.820	1.437	20.39	1.851	4.10:	2.301	0.268
N0596	CETUS	E	1.347	16.57	7.84	1.655	1.477	20.99	1.721	3.95:	2.176	0.236
N0636	CETUS	E3	1.249	16.52	8.28	1.566	1.277	20.63	1.628	4.00:	2.185	0.261
N1395	ERIDANUS	E2	1.496	16.31	6.84	1.891	1.657	21.13	1.868	4.23:	2.388	0.310
N1400	ERIDANUS	S0	1.238	15.84	7.65	1.744	1.577	21.53	1.657	4.46:	2.395	0.303
N1407	ERIDANUS	E0	1.553	16.54	6.78	1.901	1.857	21.92	1.817	4.28:	2.452	0.322
N1426	ERIDANUS	E4	1.250	16.63	8.38	1.546	1.417	21.25	1.592	4.01:	2.167	0.254
N1439	ERIDANUS	E1	1.280	16.89	8.49	1.498	1.617	22.12	1.506	4.01:	2.152	0.267
N3377	LEO	E5	1.294	15.93	7.46	1.778	1.527	20.55	1.902	3.78:	2.121	0.245
N3379	LEO	E1	1.472	15.59	6.23	2.047	1.547	19.94	2.085	4.08:	2.296	0.295
I3370	N4373grp	E2	1.403	16.68	7.66	1.705	1.577	21.32	1.736	4.02:	2.285	0.249
N4373	N4373grp	S0	1.362	16.44	7.63	1.734	1.537	20.96	1.793	3.89:	2.341	0.255
N5813	N5846grp	E1	1.551	17.11	7.36	1.707	1.687	21.76	1.698	4.16:	2.365	0.297
N5831	N5846grp	E3	1.371	17.00	8.14	1.564	1.427	21.34	1.571	4.14:	2.209	0.278
N5845	N5846grp	E	0.520	13.70	9.10	1.530	0.557	18.04	1.531	4.21:	2.391	0.293
N5846	N5846grp	E0	1.630	17.05	6.91	1.854	1.917	22.18	1.791	4.09:	2.433	0.312
I2311	FIELD	E0	1.057	15.57	8.29	1.661	1.247	20.36	1.663	4.10:	2.352	0.238
I4296	HG22grp	E	1.307	16.27	7.74	1.714	1.757	21.85	1.750	3.95:	2.500	...
M32	LOCALgrp	U	1.549	14.64	4.90	2.418	1.587	18.68	2.418	3.90:	1.821	0.112
N0661	GH18	E	1.066	16.25	8.93	1.469	1.237	20.90	1.508	4.03:	2.181	0.291
N0680	GH20	E	1.037	15.79	8.61	1.558	1.267	20.63	1.616	4.01:	2.301	0.281
N0720	FIELD	E5	1.397	16.14	7.16	1.831	1.597	21.14	1.798	4.28:	2.372	0.323
N0741	N741grp	E0	1.499	17.61	8.12	1.529	1.717	22.52	1.493	4.12:	2.428	0.334
N0821	FIELD	E6	1.310	16.31	7.76	1.691	1.657	21.59	1.722	4.03:	2.282	0.293
N2325	FIELD	E4	1.774	18.28	7.41	1.582	1.937	22.82	1.589	3.95:	2.138	0.282
N2434	HG1grp	E0	1.252	16.20	7.95	1.684	1.607	21.34	1.756	3.85:	2.316	0.247
N2986	HG36grp	E2	1.430	16.64	7.49	1.734	1.617	21.47	1.728	4.15:	2.398	0.299
N3258	ANTLIA	E1	1.176	16.27	8.39	1.584	1.437	21.38	1.579	4.16:	2.449	0.335
N3557	FIELD	E3	1.174	15.47	7.61	1.795	1.577	20.89	1.853	3.96:	2.474	0.297

Table A.3—*Continued*

Name	Cluster/ Group	Type	K–band				B–band					
			$\log r_{\rm eff}$ ($''$)	$\langle\mu\rangle_{\rm eff}$ (mag/$''$)	$K_{\rm tot}$ (mag)	$\log D_K$ ($''$)	$\log r_{\rm eff}$ ($''$)	$\langle\mu\rangle_{\rm eff}$ (mag/$''$)	$\log D_B$ ($''$)	$B-K$ (mag)	$\log\sigma_0$ (km s^{-1})	Mg_2 (mag)
(1)	(2)	(3)	(4)	(5)	(6)	(7)	(8)	(9)	(10)	(11)	(12)	(13)
N4946	N5011grp	E	1.195	16.68	8.71	1.490	1.227	20.79	1.536	3.99:	2.290	0.290
N5061	HG31+35grp	E0	1.132	15.15	7.50	1.900	1.407	19.92	1.951	3.77:	2.283	0.235
N5812	FIELD	E0	1.117	15.57	7.99	1.695	1.377	20.59	1.746	4.08:	2.302	0.316
N5898	FABER71grp	E0	1.120	15.78	8.19	1.650	1.337	20.24	1.805	3.67:	2.356	0.303
N5982	GH158	E3	1.183	16.03	8.12	1.657	1.397	20.96	1.655	4.15:	2.421	0.289
N6411	FIELD	E	1.124	16.74	9.13	1.407	1.427	21.80	1.431	3.96:	2.218	0.268
N6482	FIELD	E	1.148	15.85	8.12	1.675	0.877	18.18	1.848	3.30:	2.460	0.323
N6702	FIELD	E	1.176	16.86	8.98	1.419	1.457	22.01	1.396	4.14:	2.253	0.271
N6703	FIELD	S0	1.146	15.92	8.20	1.644	1.377	20.78	1.684	4.02:	2.252	0.269
N7236	FABER86grp	S0	0.687	15.91	10.48	1.198	1.007	21.21	1.223	4.15:	2.306	0.292
N7237	FABER86grp	S0	1.323	18.49	9.88	1.076	1.537	23.36	1.013	4.10:	2.266	0.323
N7385	FIELD	E	1.342	17.60	8.89	1.382	1.637	22.77	1.335	4.11:	2.426	0.325
N7454	GH163	E4	1.262	17.23	8.93	1.411	1.387	21.44	1.505	3.75:	2.011	0.191
N7768	A2666	E	1.230	17.30	9.15	1.370	1.477	22.19	1.367	3.99:	2.457	0.314

Table A.4: Comparisons of K–band Quantities with B–band Quantities from Dressler *et al.* (1991)

Name	Cluster/ Group	Type	K–band				B–band			
			$\log r_{\rm eff}$ ($''$)	$\langle\mu\rangle_{\rm eff}$ (mag/$''$)	$K_{\rm tot}$ (mag)	$\log D_K$ ($''$)	$\log D_B$ ($''$)	$B-K$ (mag)	$\log\sigma_0$ (km s^{-1})	Mg_2 (mag)
(1)	(2)	(3)	(4)	(5)	(6)	(7)	(8)	(9)	(10)	(11)
N4709	CEN45	E1	1.451	17.25	8.00	1.612	1.653	4.42:	2.388	0.324
N4645	CEN30	E	1.122	15.92	8.31	1.614	1.653	4.26:	2.250	0.269
N4696	CEN30	E1	1.842	18.21	7.01	1.684	1.756	4.42:	2.387	0.267
N4706	CEN30	S0	1.423	17.78	9.06	1.434	1.466	4.42:	2.321	0.297
N4729	CEN30	E	1.149	16.52	8.78	1.497	1.508	4.45:	2.175	0.261
N4767	CEN30	E	1.283	16.47	8.06	1.649	1.702	4.25:	2.298	0.278
I3370	N4373grp	E2	1.403	16.68	7.66	1.705	1.718	4.26:	2.285	0.249
N4373	N4373grp	S0	1.362	16.44	7.63	1.734	1.785	4.07:	2.341	0.255
N4946	N5011grp	E	1.195	16.68	8.71	1.490	1.558	4.33:	2.290	0.290

Table A.5: Comparisons of K–band Quantities with V–band Quantities from Lucey & Carter (1988) and Lucey *et al.* (1991a, b; 1997)

Name	Cluster/ Group	Type	K–band				V–band					
			$\log r_{\rm eff}$ ($''$)	$\langle\mu\rangle_{\rm eff}$ (mag/$''$)	$K_{\rm tot}$ (mag)	$\log D_K$ ($''$)	$\log r_{\rm eff}$ ($''$)	$\langle\mu\rangle_{\rm eff}$ (mag/$''$)	$\log D_V$ ($''$)	$V-K$ (mag)	$\log\sigma_0$ (km s^{-1})	Mg_2 (mag)
(1)	(2)	(3)	(4)	(5)	(6)	(7)	(8)	(9)	(10)	(11)	(12)	(13)
D22	A194	S0	0.890	18.48	12.03	0.667	...	...	...	...	1.913	...
D28	A194	S0	0.775	17.86	11.99	0.692	...	...	...	...	1.881	...
D29	A194	S0	0.519	15.41	10.83	1.142	...	...	1.178	...	2.100	...
D30	A194	S0/a	0.663	16.22	10.91	1.080	...	...	1.139	...	2.082	...
D33	A194	S0	0.592	15.74	10.79	1.131	...	...	1.164	...	2.147	...
D44	A194	S0/a	0.738	16.82	11.13	1.001	...	...	1.034	...	2.165	...
D45	A194	S0	0.625	16.39	11.27	1.000	...	...	1.050	...	2.093	...
D50	A194	S0	0.558	15.58	10.79	1.144	...	...	1.153	...	2.164	...
D52	A194	E	0.555	16.80	12.03	0.818	...	...	0.894	...	1.979	0.204
D53	A194	S0	0.520	15.31	10.72	1.170	...	...	1.176	...	2.377	...
D55	A194	S0	0.479	17.38	12.99	0.554	...	...	...	...	1.936	...
D57	A194	E	0.660	17.46	12.16	0.665	...	...	...	...	1.881	...
D62	A194	Sa/0	0.778	17.54	11.65	0.832	...	...	...	...	1.883	...
N0538	A194	Sa	0.860	16.50	10.21	1.188	...	...	1.212	...	2.310	...
N0541	A194	S0	1.209	17.18	9.14	1.359	...	...	1.347	...	2.328	0.312
N0545	A194	S0	1.425	17.65	8.53	1.424	...	...	1.409	...	2.367	0.314
N0547	A194	E1	0.939	16.13	9.44	1.408	...	...	1.411	...	2.326	0.319
N0548	A194	E	0.924	17.50	10.89	0.979	...	...	1.053	...	2.097	0.246
FCOM	A2199	E/S0	0.320	16.49	12.89	0.672	0.303	19.34	0.719	2.91:	2.130	0.264
L111	A2199	S0/a	0.799	17.34	11.35	0.928	...	...	0.931	...	2.303	...
L112	A2199	E/S0	0.188	15.10	12.17	0.898	...	...	0.888	...	2.355	...
L113	A2199	E	0.199	15.84	12.86	0.720	0.302	19.22	0.761	3.00:	2.218	0.268
L114	A2199	S0	0.270	15.62	12.28	0.854	0.208	18.47	0.852	3.08:	2.290	0.301
L118	A2199	E	0.717	17.25	11.67	0.866	...	...	0.910	...	2.186	...
L136	A2199	S0	0.286	15.47	12.04	0.907	...	...	...	...	2.266	...
L1381	A2199	S0	0.061	14.72	12.43	0.866	...	...	0.836	...	2.338	...
L139	A2199	E	0.400	17.43	13.44	0.464	...	...	...	...	1.971	...
L143	A2199	S0	0.324	15.06	11.44	1.118	0.644	19.45	1.043	3.23:	2.447	0.325
L145	A2199	S0/a	0.905	17.92	11.40	0.863	0.942	21.05	0.873	3.00:	2.169	0.285
L150	A2199	S0	0.318	16.71	13.12	0.625	...	...	0.688	...	2.068	...
L151	A2199	S0	0.358	17.52	13.73	0.447	...	...	...	...	2.016	...
L152	A2199	S0/a	1.202	18.67	10.66	0.888	1.315	22.02	0.902	2.94:	2.165	0.312
L153	A2199	S0/a	0.593	17.01	12.04	0.802	0.800	20.76	0.819	3.01:	2.152	0.274
L158	A2199	S0	0.580	16.45	11.56	0.955	0.524	19.46	0.912	3.21:	2.349	0.305
N6158	A2199	E	0.990	17.33	10.38	1.112	1.030	20.50	1.123	3.03:	2.269	0.275
N6158COMP	A2199	U	0.479	17.16	12.77	0.652	...	...	...	...	1.965	0.230
N6166	A2199	E2	1.373	18.23	9.37	1.259	1.927	22.82	1.194	2.59:	2.487	0.323
NCOM	A2199	E	-0.092	15.23	13.70	0.577	-0.152	17.97	0.613	2.96:	2.227	0.285
S18	A2199	E	0.498	16.14	11.65	0.959	0.641	19.70	0.969	3.05:	2.291	0.304
S26	A2199	E	0.883	17.58	11.17	0.937	0.959	20.93	0.925	3.07:	2.246	0.286
S30	A2199	E	0.489	16.24	11.96	0.923	...	...	0.935	...	2.394	0.261
S33	A2199	E	0.307	15.50	11.96	0.923	0.318	18.69	0.905	3.15:	2.458	0.309
S34	A2199	E	0.334	16.20	12.53	0.770	0.283	19.03	0.778	3.02:	2.195	0.273
S43	A2199	E	0.480	16.41	12.01	0.843	0.510	19.63	0.855	3.12:	2.300	0.300
S44	A2199	E	0.452	16.21	11.95	0.885	0.395	19.10	0.880	3.10:	2.284	0.300
Z34A	A2199	E	0.871	17.27	10.92	1.017	0.909	20.38	1.042	2.98:	2.314	0.285
L102	A2634	E	0.705	16.69	11.17	1.012	0.773	20.05	1.004	3.11:	2.285	0.265
L106	A2634	S0	0.377	15.85	11.97	0.903	0.397	19.08	0.890	3.15:	2.193	0.285
L107	A2634	SBO/a	0.728	18.06	12.43	0.621	0.735	21.00	0.672	2.91:	2.035	0.216

Table A.5—*Continued*

Name	Cluster/ Group	Type	K–band				V–band					
			$\log r_{\rm eff}$ ($''$)	$\langle\mu\rangle_{\rm eff}$ (mag/$''$)	$K_{\rm tot}$ (mag)	$\log D_K$ ($''$)	$\log r_{\rm eff}$ ($''$)	$\langle\mu\rangle_{\rm eff}$ (mag/$''$)	$\log D_V$ ($''$)	$V-K$ (mag)	$\log\sigma_0$ (km s^{-1})	Mg_2 (mag)
(1)	(2)	(3)	(4)	(5)	(6)	(7)	(8)	(9)	(10)	(11)	(12)	(13)
L108	A2634	S0	0.134	15.08	12.42	0.839	0.311	18.99	0.827	3.26:	2.221	0.279
L109	A2634	S0	0.111	14.90	12.35	0.865	0.288	18.97	0.807	3.42:	2.233	0.263
L1201	A2634	S0/a	0.467	16.48	12.15	0.825	0.469	19.60	0.824	3.11:	2.210	0.297
L121	A2634	E	0.322	15.98	12.37	0.815	0.369	19.25	0.816	3.11:	2.263	0.284
L124	A2634	E	0.382	16.05	12.15	0.852	0.458	19.55	0.827	3.22:	2.273	0.297
L1261	A2634	S0	0.041	15.01	12.81	0.773	-0.039	17.71	0.784	2.99:	2.144	0.258
L129	A2634	S0	0.542	16.14	11.44	0.993	0.720	20.11	0.937	3.32:	2.317	0.302
L134	A2634	E	0.664	16.46	11.15	1.032	0.787	20.01	1.030	3.10:	2.340	0.301
L135	A2634	S0	0.489	16.44	12.00	0.852	0.476	19.39	0.883	3.00:	2.086	0.263
L138	A2634	E	0.777	16.96	11.08	1.008	0.943	20.64	0.996	3.08:	2.319	0.309
L139	A2634	E	0.763	16.72	10.91	1.059	0.905	20.40	1.033	3.17:	2.335	0.324
L140	A2634	S0	0.248	14.91	11.68	1.005	0.276	18.36	0.950	3.35:	2.346	0.314
N7720	A2634	E	1.160	17.19	9.40	1.326	1.288	20.83	1.273	3.17:	2.494	0.331
N7720A	A2634	E	0.340	15.36	11.65	0.995	0.419	18.93	0.953	3.29:	2.305	0.295
D20	CEN45	S0	1.067	17.13	9.80	1.236	···	···	1.328	···	2.064	···
D23	CEN45	S0	0.934	16.73	10.06	1.215	···	···	1.289	···	2.118	···
D24	CEN45	S0p	1.129	17.66	10.02	1.104	···	···	1.219	···	2.022	···
D27	CEN45	E	0.815	16.53	10.46	1.152	···	···	1.221	···	2.038	0.264
N4709	CEN45	E1	1.451	17.25	8.00	1.612	···	···	1.637	···	2.388	0.324
D19	CEN30	S0	0.719	15.02	9.43	1.438	···	···	1.470	···	2.289	···
D22	CEN30	S0	0.959	17.01	10.22	1.167	···	···	1.258	···	2.082	···
D29	CEN30	S0	1.020	17.07	9.98	1.204	···	···	1.290	···	2.013	···
D49	CEN30	E	0.693	16.15	10.69	1.128	···	···	1.153	···	2.047	0.292
D50	CEN30	E	0.974	17.10	10.24	1.146	···	···	1.195	···	2.062	0.254
D56	CEN30	E	0.747	16.40	10.66	1.118	···	···	1.190	···	2.133	···
D58	CEN30	S0	0.809	16.14	10.10	1.246	···	···	1.301	···	2.190	···
J316	CEN30	S0	0.905	15.48	8.96	1.513	···	···	1.518	···	2.336	···
N4696	CEN30	E1	1.842	18.21	7.01	1.684	···	···	1.736	···	2.387	0.267
N4706	CEN30	S0	1.423	17.78	9.06	1.434	···	···	1.464	···	2.321	0.297
D106	COMA	S0	0.438	16.53	12.35	0.776	0.419	19.40	0.827	2.94:	2.210	0.241
D125	COMA	E	0.124	15.07	12.45	0.836	0.219	18.50	0.854	3.09:	2.235	0.256
D173	COMA	S0	0.417	16.23	12.15	0.846	0.527	19.68	0.861	3.05:	2.147	0.287
D210	COMA	Ep	0.559	16.47	11.68	0.926	0.539	19.39	0.949	2.99:	2.237	0.270
D24	COMA	E	0.631	16.11	10.95	1.089	0.599	19.18	1.063	3.19:	2.359	0.301
D27	COMA	E	0.544	17.03	12.32	0.736	0.674	20.44	0.785	2.93:	2.009	0.260
D81	COMA	E	0.732	17.77	12.11	0.744	0.810	20.90	0.794	2.85:	2.191	0.265
D96	COMA	E	0.529	16.24	11.60	0.957	0.651	19.80	0.947	3.12:	2.269	0.285
E159G43	COMA	U	0.702	16.19	10.68	1.137	0.710	19.53	1.106	3.31:	2.402	···
E159G63	COMA	U	0.866	17.46	11.13	0.947	0.902	20.81	0.939	3.22:	2.173	···
E159G83	COMA	U	0.728	16.09	10.45	1.205	0.993	20.45	1.140	3.40:	2.307	···
E159G89	COMA	U	0.825	17.00	10.88	1.043	0.973	20.64	1.063	3.10:	2.231	···
E160G159	COMA	U	0.869	17.04	10.70	1.071	0.849	20.20	1.061	3.23:	2.360	···
E160G22	COMA	U	0.607	15.71	10.67	1.162	0.785	19.75	1.116	3.40:	2.415	···
E160G23	COMA	U	0.500	15.91	11.42	1.008	0.601	19.55	0.999	3.27:	2.250	···
E160G27	COMA	E	0.611	16.51	11.46	0.960	0.766	20.15	0.963	3.08:	2.235	0.282
I0832	COMA	E	0.814	16.80	10.73	1.085	0.981	20.63	1.069	3.23:	2.321	···
I0843	COMA	S0	0.742	15.92	10.21	1.247	0.978	20.34	1.158	3.57:	2.392	···
I3900	COMA	SB0	0.627	15.91	10.78	1.172	0.708	19.40	1.140	3.19:	2.432	···
I3947	COMA	S0	0.470	16.12	11.78	0.926	0.589	19.58	0.952	3.02:	2.148	0.279
I3957	COMA	S0	0.545	16.45	11.73	0.912	0.637	19.84	0.926	3.06:	2.179	0.292
I3959	COMA	E3	0.655	16.27	11.00	1.069	0.769	19.86	1.053	3.18:	2.295	0.307

Table A.5—*Continued*

Name	Cluster/ Group	Type	K–band				V–band					
			$\log r_{\rm eff}$ ($''$)	$\langle\mu\rangle_{\rm eff}$ (mag/$''$)	$K_{\rm tot}$ (mag)	$\log D_K$ ($''$)	$\log r_{\rm eff}$ ($''$)	$\langle\mu\rangle_{\rm eff}$ (mag/$''$)	$\log D_V$ ($''$)	$V-K$ (mag)	$\log\sigma_0$ (km s^{-1})	Mg_2 (mag)
(1)	(2)	(3)	(4)	(5)	(6)	(7)	(8)	(9)	(10)	(11)	(12)	(13)
I4011	COMA	E	0.650	17.11	11.86	0.830	0.624	20.03	0.860	3.01:	2.040	0.280
I4012	COMA	E	0.312	15.15	11.59	1.011	0.363	18.56	0.988	3.23:	2.259	0.292
I4021	COMA	E	0.809	16.77	10.73	1.086	0.486	19.25	0.931	3.64:	2.206	0.300
I4045	COMA	E4	0.481	15.31	10.91	1.136	0.660	19.25	1.115	3.29:	2.331	0.306
I4051	COMA	E0	1.058	17.50	10.22	1.118	1.272	21.42	1.075	3.14:	2.355	0.332
I4133	COMA	E	0.535	16.08	11.41	1.000	0.701	19.77	1.004	3.09:	2.233	0.289
N4673	COMA	E1	0.760	15.62	9.83	1.340	0.824	19.06	1.344	3.21:	2.347	···
N4692	COMA	E	1.117	17.13	9.55	1.290	1.210	20.70	1.281	3.23:	2.397	0.307
N4789	COMA	S0	1.039	16.60	9.41	1.372	1.188	20.37	1.353	3.22:	2.423	0.287
N4807	COMA	S0	0.740	16.12	10.42	1.195	0.835	19.65	1.197	3.19:	2.328	0.275
N4816	COMA	S0	1.299	18.15	9.66	1.163	1.236	21.00	1.160	3.08:	2.365	0.306
N4824	COMA	E	0.695	16.96	11.49	0.925	0.678	19.99	0.924	3.08:	2.205	0.278
N4827	COMA	S0	1.001	16.90	9.90	1.245	1.010	20.18	1.224	3.25:	2.448	···
N4839	COMA	E	1.290	17.78	9.34	1.264	1.425	21.29	1.272	3.01:	2.420	0.313
N4840	COMA	E1	0.709	16.09	10.55	1.169	0.793	19.59	1.152	3.19:	2.377	0.320
N4841A	COMA	E	1.094	17.17	9.71	1.255	1.170	20.44	1.284	2.99:	2.417	0.320
N4850	COMA	S0	0.537	15.85	11.17	1.062	0.738	19.78	1.048	3.20:	2.233	0.269
N4854	COMA	SB0	0.930	17.58	10.93	0.975	1.102	21.22	0.969	3.02:	2.263	0.311
N4860	COMA	E2	0.706	15.95	10.42	1.205	0.895	19.82	1.188	3.19:	2.396	0.342
N4864	COMA	E2	0.878	16.98	10.60	1.138	0.880	20.04	1.114	3.05:	2.294	0.286
N4867	COMA	E3	0.497	15.70	11.22	1.058	0.553	19.11	1.038	3.21:	2.353	0.308
N4869	COMA	E3	0.812	16.61	10.56	1.152	0.920	20.16	1.125	3.16:	2.309	0.316
N4871	COMA	S0	0.779	16.91	11.02	1.031	0.919	20.54	1.001	3.12:	2.234	0.281
N4872	COMA	SB0	0.459	15.57	11.28	1.053	0.482	18.84	1.036	3.18:	2.330	0.301
N4874	COMA	E0	1.665	18.75	8.43	1.310	1.743	22.15	1.282	3.11:	2.377	0.323
N4876	COMA	E5	0.683	16.54	11.13	1.020	0.689	19.82	1.015	3.25:	2.264	0.248
N4881	COMA	E	0.860	16.86	10.56	1.114	1.022	20.49	1.119	3.05:	2.311	0.292
N4886	COMA	E0	0.885	17.37	10.95	0.990	0.874	20.34	1.018	3.01:	2.194	0.252
N4889	COMA	E4	1.258	16.89	8.60	1.538	1.484	20.85	1.468	3.15:	2.606	0.351
N4906	COMA	E3	0.835	17.11	10.94	1.016	0.831	20.19	1.021	3.09:	2.229	0.295
N4923	COMA	S0	0.640	16.04	10.84	1.114	0.865	19.93	1.124	3.08:	2.288	0.307
N4926	COMA	S0	0.986	16.72	9.79	1.275	0.995	19.90	1.258	3.15:	2.420	0.321
N4927	COMA	S0	0.844	16.46	10.25	1.205	1.047	20.59	1.121	3.39:	2.450	0.354
N4952	COMA	E	0.982	16.57	9.66	1.313	1.014	19.93	1.295	3.24:	2.391	···
N4957	COMA	E3	1.053	17.19	9.93	1.211	1.149	20.75	1.200	3.21:	2.344	0.298
N4971	COMA	S0	0.909	17.13	10.59	1.095	0.863	20.24	1.060	3.28:	2.250	···
N5004	COMA	S0	0.919	16.53	9.94	1.267	1.018	20.08	1.263	3.19:	2.372	···
E501G21	HYDRA	S0/ap	0.885	16.70	10.28	1.176	···	···	1.196	···	2.163	···
E501G47	HYDRA	S0	1.551	18.63	8.88	1.226	···	···	1.166	···	2.105	···
E501G49	HYDRA	SB0	0.891	17.31	10.86	1.003	···	···	1.009	···	2.034	···
N3305	HYDRA	E0	0.953	16.09	9.33	1.407	···	···	1.397	···	2.368	···
N3308	HYDRA	S0	1.498	17.93	8.45	1.419	···	···	1.409	···	2.287	0.293
N3309	HYDRA	E3	1.285	16.79	8.37	1.550	···	···	1.545	···	2.409	0.329
N3311	HYDRA	E2	1.817	18.94	7.86	1.381	···	···	1.332	···	2.292	0.309
N3312	HYDRA	Sb	1.208	16.79	8.76	1.476	···	···	···	···	2.312	···
N3315	HYDRA	S0	0.991	16.49	9.54	1.420	···	···	1.336	···	2.228	···
N3316	HYDRA	SB0	1.089	16.75	9.30	1.362	···	···	1.353	···	2.247	···
S135	HYDRA	E	0.346	15.47	11.75	0.954	···	···	1.004	···	2.049	···
S154	HYDRA	E3	0.491	16.37	11.92	0.866	···	···	0.912	···	2.077	···
S201	HYDRA	SB	1.006	18.38	11.35	0.833	···	···	···	···	2.174	···
S23	HYDRA	S0	1.256	18.43	10.15	1.006	···	···	1.032	···	2.060	···

Table A.5—*Continued*

Name	Cluster/ Group	Type	K–band				V–band					
			$\log r_{\rm eff}$ ($''$)	$\langle\mu\rangle_{\rm eff}$ (mag/$''$)	$K_{\rm tot}$ (mag)	$\log D_K$ ($''$)	$\log r_{\rm eff}$ ($''$)	$\langle\mu\rangle_{\rm eff}$ (mag/$''$)	$\log D_V$ ($''$)	$V-K$ (mag)	$\log\sigma_0$ (km s^{-1})	Mg_2 (mag)
(1)	(2)	(3)	(4)	(5)	(6)	(7)	(8)	(9)	(10)	(11)	(12)	(13)
S37	HYDRA	S0/E7	0.729	16.56	10.92	1.047	···	···	1.090	···	2.070	···
S46	HYDRA	SB0	1.108	18.30	10.77	0.881	···	···	0.939	···	2.033	···
S53	HYDRA	S0	0.538	15.24	10.55	1.206	···	···	1.215	···	2.276	···
S61	HYDRA	E1	0.326	14.64	11.01	1.134	···	···	1.170	···	2.309	···
S68	HYDRA	S0:	0.734	16.75	11.08	1.007	···	···	1.050	···	2.092	···
S83	HYDRA	S0/S	0.883	17.75	11.34	0.859	···	···	0.859	···	2.050	···
S96	HYDRA	S0/S	0.627	16.31	11.18	1.024	···	···	1.053	···	2.077	···
D32	KLEM44	E	0.638	15.77	10.58	1.188	···	···	1.127	···	2.476	0.331
D34	KLEM44	Ep	0.522	17.33	12.73	0.600	···	···	0.751	···	1.990	···
D42	KLEM44	D	1.146	17.82	10.09	1.119	···	···	1.106	···	2.338	0.362
D43	KLEM44	S0	0.696	16.74	11.27	0.987	···	···	···	···	2.273	···
D44	KLEM44	E	0.111	15.18	12.63	0.803	···	···	0.814	···	2.210	0.292
D45	KLEM44	E	0.633	17.32	12.16	0.772	···	···	0.841	···	2.117	0.242
D51	KLEM44	S0	0.210	16.03	12.98	0.681	···	···	···	···	2.185	···
D55	KLEM44	E	0.505	16.17	11.65	0.950	···	···	0.956	···	2.229	0.304
D56	KLEM44	D	1.043	17.16	9.96	1.211	···	···	1.220	···	2.423	0.310
D58	KLEM44	E	0.594	15.76	10.79	1.153	···	···	1.145	···	2.412	0.292
D59	KLEM44	S0	0.624	17.09	11.97	0.822	···	···	···	···	2.230	···
D77	KLEM44	S0	0.778	16.49	10.61	1.137	···	···	···	···	2.314	···

Table A.6: Comparisons of K–band Quantities with R–band Quantities from Smith *et al.* (1997)

Name	Cluster/ Group	Type	K–band				R–band			$R-K$	$\log\sigma_0$	Mg_2
			$\log r_{\rm eff}$ ($''$)	$\langle\mu\rangle_{\rm eff}$ (mag/$''$)	$K_{\rm tot}$ (mag)	$\log D_K$ ($''$)	$\log r_{\rm eff}$ ($''$)	$\langle\mu\rangle_{\rm eff}$ (mag/$''$)	$\log D_R$ ($''$)	(mag)	(km s^{-1})	(mag)
(1)	(2)	(3)	(4)	(5)	(6)	(7)	(8)	(9)	(10)	(11)	(12)	(13)
L113	A2199	Q	0.199	15.84	12.86	0.720	0.316	18.74	0.750	2.44	2.218	0.268
L114	A2199	S0	0.270	15.62	12.28	0.854	0.266	18.15	0.849	2.68	2.290	0.301
L145	A2199	R	0.905	17.92	11.40	0.863	0.907	20.35	0.870	2.54	2.169	0.285
N6166	A2199	E2	1.373	18.23	9.37	1.259	1.893	22.17	1.201	2.62	2.487	0.323
S26	A2199	E	0.883	17.58	11.17	0.937	0.964	20.38	0.924	2.63	2.246	0.286
S30	A2199	E	0.489	16.24	11.96	0.923	0.300	17.96	0.931	2.61	2.394	0.261
S34	A2199	E	0.334	16.20	12.53	0.770	0.403	18.96	0.779	2.55	2.195	0.273
Z34A	A2199	E	0.871	17.27	10.92	1.017	0.950	19.95	1.035	2.55	2.314	0.285
N7720	A2634	E	1.160	17.19	9.40	1.326	1.279	20.20	1.278	2.81	2.494	0.331
D149	COMA	U	0.307	16.46	12.91	0.549	0.709	20.69	0.553	2.56	...	...
I3957	COMA	S0	0.545	16.45	11.73	0.912	0.573	19.01	0.927	2.52	2.179	0.292
I3959	COMA	E3	0.655	16.27	11.00	1.069	0.773	19.29	1.058	2.66	2.295	0.307
I4011	COMA	E	0.650	17.11	11.86	0.830	0.687	19.70	0.854	2.53	2.040	0.280
N4869	COMA	E3	0.812	16.61	10.56	1.152	0.914	19.51	1.139	2.62	2.309	0.316
N4871	COMA	U	0.779	16.91	11.02	1.031	0.843	19.69	1.003	2.64	2.234	0.281
N4872	COMA	SB0	0.459	15.57	11.28	1.053	0.508	18.36	1.041	2.68	2.330	0.301
N4873	COMA	U	0.584	16.42	11.51	1.042	0.813	19.67	0.989	2.38	2.194	0.290
N4874	COMA	E0	1.665	18.75	8.43	1.310	1.811	21.71	1.294	2.73	2.377	0.323
N4876	COMA	E5	0.683	16.54	11.13	1.020	0.671	19.02	1.035	2.60	2.262	0.248
N4886	COMA	E0	0.885	17.37	10.95	0.990	0.915	19.92	1.012	2.54	2.194	0.252
N4889	COMA	E4	1.258	16.89	8.60	1.538	1.509	20.33	1.480	2.79	2.606	0.351
N4894	COMA	U	0.940	18.30	11.61	0.812	0.664	19.64	0.843	2.50	1.976	0.233
CR36	PERSEUS	E	0.637	15.88	10.70	1.148	0.794	18.97	1.157	2.62	2.312	0.300
I0310	PERSEUS	S0	1.177	16.79	8.91	1.442	1.327	20.04	1.384	2.89	2.341	0.261
N1270	PERSEUS	E	0.802	15.29	9.28	1.458	0.848	18.19	1.415	2.84	2.545	0.365
N1272	PERSEUS	E	1.411	17.57	8.52	1.482	1.474	20.40	1.412	2.78	2.439	0.334
N1273	PERSEUS	S0	0.904	16.17	9.65	1.373	0.957	18.87	1.350	2.60	2.319	0.274
N1278	PERSEUS	E	1.258	17.04	8.76	1.458	1.360	20.06	1.423	2.81	2.414	0.307
N1282	PERSEUS	E	1.064	16.71	9.39	1.352	1.106	19.37	1.359	2.59	2.325	0.270
N1283	PERSEUS	E1	0.653	15.51	10.25	1.260	0.921	19.14	1.239	2.73	2.346	0.299
N1293	PERSEUS	E0	0.874	16.16	9.79	1.311	0.978	19.15	1.293	2.69	2.342	0.328
PER152	PERSEUS	E	0.389	15.68	11.74	0.948	0.560	19.05	0.912	2.65	2.172	0.308
PER163	PERSEUS	E	0.270	14.85	11.51	1.055	0.527	18.45	1.032	2.53	2.234	0.289
PER195	PERSEUS	E	0.731	16.52	10.87	1.099	1.080	20.07	1.129	2.40	2.225	0.290
PER199	PERSEUS	S0	0.459	15.09	10.80	1.172	0.731	18.84	1.137	2.70	2.300	0.289
N0379	PISCES	S0	0.899	15.72	9.23	1.451	1.241	19.87	1.382	2.97	2.384	0.305
N0380	PISCES	E2	0.942	15.93	9.22	1.429	1.018	18.92	1.393	2.81	2.461	0.337
N0382	PISCES	E	0.673	15.72	10.36	1.225	0.785	18.88	1.194	2.78	2.248	0.271
N0383	PISCES	S0	1.221	16.56	8.46	1.545	1.488	20.25	1.491	2.94	2.436	0.309
N0384	PISCES	E	0.630	15.17	10.03	1.339	0.889	18.86	1.288	2.76	2.402	0.310
N0385	PISCES	S0	1.033	16.89	9.74	1.263	1.095	19.66	1.263	2.67	2.270	0.287
N0386	PISCES	E3	0.857	17.14	10.86	1.020	0.774	19.37	1.042	2.61	1.958	0.242
N0392	PISCES	S0	0.989	16.41	9.47	1.381	1.073	19.28	1.355	2.66	2.397	0.294
N0394	PISCES	S0	0.610	15.53	10.48	1.236	0.751	18.75	1.188	2.71	2.248	0.269
N0410	PISCES	E	1.360	17.00	8.21	1.561	1.434	19.92	1.526	2.83	2.487	0.343
Z01047	PISCES	E	0.493	15.89	11.43	1.000	0.538	18.64	0.997	2.64	2.111	0.289

Table A.7: Comparisons of K–band Quantities with r–band Quantities from Jørgensen *et al.* (1995a)

Name	Cluster/ Group	Type	K–band				r–band			$r-K$	$\log\sigma_0$	Mg_2
			$\log r_{\rm eff}$ ($''$)	$\langle\mu\rangle_{\rm eff}$ (mag/$''$)	$K_{\rm tot}$ (mag)	$\log D_K$ ($''$)	$\log r_{\rm eff}$ ($''$)	$\langle\mu\rangle_{\rm eff}$ (mag/$''$)	$\log D_r$ ($''$)	(mag)	(km s^{-1})	(mag)
(1)	(2)	(3)	(4)	(5)	(6)	(7)	(8)	(9)	(10)	(11)	(12)	(13)
D52	A194	U	0.555	16.80	12.03	0.818	0.630	19.78	0.887	2.71:	1.979	0.204
I1696	A194	E	0.680	15.97	10.58	1.166	0.840	19.45	1.177	2.90:	2.204	0.295
N0533	A194	E3	1.301	17.17	8.67	1.460	1.610	21.06	1.457	2.77:	2.457	0.317
N0538	A194	U	0.860	16.50	10.21	1.188	1.150	20.39	1.207	2.84:	2.310	...
N0541	A194	S0	1.209	17.18	9.14	1.359	1.330	20.53	1.357	2.91:	2.328	0.312
N0545	A194	S0	1.425	17.65	8.53	1.424	1.420	20.55	1.407	2.92:	2.367	0.314
N0547	A194	E1	0.939	16.13	9.44	1.408	1.100	19.61	1.397	2.89:	2.326	0.319
N0548	A194	E	0.924	17.50	10.89	0.979	1.100	20.83	1.037	2.69:	2.097	0.246
N0564	A194	E	0.919	16.27	9.68	1.329	1.130	19.85	1.357	2.82:	2.368	0.298
D106	COMA	S0	0.438	16.53	12.35	0.776	0.390	18.99	0.851	2.63:	2.210	0.241
D173	COMA	S0	0.417	16.23	12.15	0.846	0.530	19.52	0.851	2.88:	2.147	0.287
D32	COMA	S0	0.310	16.32	12.77	0.709	0.270	18.84	0.741	2.67:	...	...
I3947	COMA	S0	0.470	16.12	11.78	0.926	0.520	19.00	0.971	2.70:	2.148	0.279
I3957	COMA	S0	0.545	16.45	11.73	0.912	0.630	19.51	0.951	2.76:	2.179	0.292
I3959	COMA	E3	0.655	16.27	11.00	1.069	0.730	19.42	1.081	2.88:	2.295	0.307
I4011	COMA	E	0.650	17.11	11.86	0.830	0.690	19.98	0.871	2.73:	2.040	0.280
I4012	COMA	E	0.312	15.15	11.59	1.011	0.330	18.23	0.981	3.02:	2.259	0.292
I4021	COMA	E	0.809	16.77	10.73	1.086	0.510	19.02	0.961	3.33:	2.206	0.300
I4045	COMA	E4	0.481	15.31	10.91	1.136	0.640	18.79	1.151	2.90:	2.331	0.306
I4051	COMA	E0	1.058	17.50	10.22	1.118	1.260	21.02	1.121	2.78:	2.355	0.332
N4839	COMA	E	1.290	17.78	9.34	1.264	1.470	21.18	1.281	2.75:	2.420	0.313
N4840	COMA	E1	0.709	16.09	10.55	1.169	0.810	19.35	1.171	2.89:	2.377	0.320
N4841A	COMA	E	1.094	17.17	9.71	1.255	1.250	20.39	1.311	2.65:	2.417	0.320
N4841B	COMA	E	0.790	16.69	10.74	1.091	0.930	19.88	1.151	2.69:	2.355	0.295
N4850	COMA	S0	0.537	15.85	11.17	1.062	0.670	19.07	1.111	2.74:	2.233	0.269
N4854	COMA	SB0	0.930	17.58	10.93	0.975	1.150	21.13	0.991	2.76:	2.263	0.311
N4860	COMA	E2	0.706	15.95	10.42	1.205	0.930	19.64	1.211	2.88:	2.396	0.342
N4864	COMA	E2	0.878	16.98	10.60	1.138	0.890	19.78	1.141	2.75:	2.294	0.286
N4867	COMA	E3	0.497	15.70	11.22	1.058	0.490	18.53	1.071	2.86:	2.353	0.308
N4869	COMA	E3	0.812	16.61	10.56	1.152	0.880	19.74	1.141	2.88:	2.309	0.316
N4871	COMA	S0	0.779	16.91	11.02	1.031	0.920	20.24	1.021	2.82:	2.234	0.281
N4872	COMA	SB0	0.459	15.57	11.28	1.053	0.480	18.53	1.061	2.88:	2.330	0.301
N4873	COMA	S0	0.584	16.42	11.51	1.042	0.870	20.09	1.011	2.63:	2.194	0.290
N4874	COMA	E0	1.665	18.75	8.43	1.310	1.850	22.13	1.311	2.71:	2.377	0.323
N4876	COMA	E5	0.683	16.54	11.13	1.020	0.710	19.47	1.041	2.83:	2.262	0.248
N4881	COMA	E	0.860	16.86	10.56	1.114	1.040	20.24	1.151	2.73:	2.311	0.292
N4886	COMA	E0	0.885	17.37	10.95	0.990	0.970	20.38	1.041	2.70:	2.194	0.252
N4889	COMA	E4	1.258	16.89	8.60	1.538	1.530	20.64	1.511	2.77:	2.606	0.351
N4894	COMA	S0	0.940	18.30	11.61	0.812	0.680	19.93	0.861	2.57:	1.976	0.233
N4898E	COMA	E	0.350	15.85	12.10	0.882	0.300	18.39	0.901	2.73:	2.232	0.266
N4898W	COMA	E	0.657	15.99	10.71	1.174	0.770	19.22	1.171	2.83:	2.232	0.266
N4906	COMA	E3	0.835	17.11	10.94	1.016	0.870	20.09	1.031	2.85:	2.229	0.295
N4923	COMA	S0	0.640	16.04	10.84	1.114	0.930	19.88	1.151	2.79:	2.288	0.307
N4926	COMA	S0	0.986	16.72	9.79	1.275	1.040	19.79	1.281	2.88:	2.420	0.321
N3305	HYDRA	E0	0.953	16.09	9.33	1.407	0.970	19.11	1.415	2.95:	2.368	...
N3308	HYDRA	S0	1.498	17.93	8.45	1.419	1.510	20.87	1.425	2.89:	2.287	0.293
N3309	HYDRA	E3	1.285	16.79	8.37	1.550	1.340	19.93	1.555	2.93:	2.409	0.329
N3311	HYDRA	E2	1.817	18.94	7.86	1.381	2.060	22.46	1.355	2.64:	2.292	0.309
D32	KLEM44	U	0.638	15.77	10.58	1.188	0.850	19.64	1.131	3.10:	2.476	0.331

Table A.7—*Continued*

Name	Cluster/ Group	Type	K–band				r–band					
			$\log r_{\rm eff}$ ($''$)	$\langle\mu\rangle_{\rm eff}$ (mag/$''$)	$K_{\rm tot}$ (mag)	$\log D_K$ ($''$)	$\log r_{\rm eff}$ ($''$)	$\langle\mu\rangle_{\rm eff}$ (mag/$''$)	$\log D_r$ ($''$)	$r-K$ (mag)	$\log\sigma_0$ (km s^{-1})	Mg_2 (mag)
(1)	(2)	(3)	(4)	(5)	(6)	(7)	(8)	(9)	(10)	(11)	(12)	(13)
D42	KLEM44	U	1.146	17.82	10.09	1.119	1.320	21.25	1.101	2.80:	2.338	0.362
D43	KLEM44	U	0.696	16.74	11.27	0.987	0.960	20.46	1.011	2.76:	2.273	···
D44	KLEM44	U	0.111	15.18	12.63	0.803	-0.040	17.37	0.811	2.74:	2.210	0.292
D45	KLEM44	U	0.633	17.32	12.16	0.772	0.670	20.20	0.801	2.74:	2.117	0.242
D51	KLEM44	U	0.210	16.03	12.98	0.681	0.260	18.92	0.721	2.71:	2.185	···
D55	KLEM44	U	0.505	16.17	11.65	0.950	0.520	19.05	0.951	2.82:	2.229	0.304
D56	KLEM44	U	1.043	17.16	9.96	1.211	1.200	20.54	1.211	2.81:	2.423	0.310
D58	KLEM44	U	0.594	15.76	10.79	1.153	0.830	19.52	1.151	2.91:	2.412	0.292
D59	KLEM44	U	0.624	17.09	11.97	0.822	0.730	20.21	0.851	2.73:	2.230	···
D77	KLEM44	U	0.778	16.49	10.61	1.137	0.880	19.70	1.151	2.84:	2.314	···

Table A.8: Comparisons of K–band Quantities with U–band Quantities from Jørgensen *et al.* (1996)

Name	Cluster/ Group	Type	K–band				U–band					
			$\log r_{\rm eff}$ ($''$)	$\langle\mu\rangle_{\rm eff}$ (mag/$''$)	$K_{\rm tot}$ (mag)	$\log D_K$ ($''$)	$\log r_{\rm eff}$ ($''$)	$\langle\mu\rangle_{\rm eff}$ (mag/$''$)	$\log D_U$ ($''$)	$U-K$ (mag)	$\log\sigma_0$ (km s^{-1})	Mg_2 (mag)
(1)	(2)	(3)	(4)	(5)	(6)	(7)	(8)	(9)	(10)	(11)	(12)	(13)
D52	A194	U	0.555	16.80	12.03	0.818	0.650	21.29	0.950	4.15:	1.979	0.204
I1696	A194	E	0.680	15.97	10.58	1.166	0.910	21.28	1.200	4.47:	2.204	0.295
N0538	A194	U	0.860	16.50	10.21	1.188	1.150	22.02	1.220	4.47:	2.310	···
N0541	A194	S0	1.209	17.18	9.14	1.359	1.410	22.41	1.360	4.50:	2.328	0.312
N0545	A194	S0	1.425	17.65	8.53	1.424	1.490	22.44	1.410	4.55:	2.367	0.314
N0547	A194	E1	0.939	16.13	9.44	1.408	1.210	21.66	1.400	4.54:	2.326	0.319
N0548	A194	E	0.924	17.50	10.89	0.979	1.200	22.53	1.110	4.03:	2.097	0.246
N0564	A194	E	0.919	16.27	9.68	1.329	1.200	21.70	1.370	4.41:	2.368	0.298
N1379	FORNAX	E	1.561	17.57	7.77	1.605	1.770	22.62	1.661	4.29:	2.106	0.243
N1399	FORNAX	E1	1.504	15.90	6.39	2.003	1.690	21.47	1.931	4.90:	2.513	0.327
D32	KLEM44	U	0.638	15.77	10.58	1.188	0.950	21.70	1.121	4.80:	2.476	0.331
D42	KLEM44	U	1.146	17.82	10.09	1.119	1.480	23.43	1.081	4.41:	2.338	0.362
D43	KLEM44	U	0.696	16.74	11.27	0.987	0.960	22.01	1.031	4.31:	2.273	···
D45	KLEM44	U	0.633	17.32	12.16	0.772	0.770	21.97	0.851	4.15:	2.117	0.242
D51	KLEM44	U	0.210	16.03	12.98	0.681	0.450	21.28	0.751	4.38:	2.185	···
D55	KLEM44	U	0.505	16.17	11.65	0.950	0.650	21.23	0.941	4.53:	2.229	0.304
D56	KLEM44	U	1.043	17.16	9.96	1.211	1.250	22.40	1.211	4.49:	2.423	0.310
D58	KLEM44	U	0.594	15.76	10.79	1.153	0.870	21.36	1.141	4.60:	2.412	0.292
D59	KLEM44	U	0.624	17.09	11.97	0.822	0.850	22.24	0.861	4.33:	2.230	···
D77	KLEM44	U	0.778	16.49	10.61	1.137	0.950	21.60	1.151	4.48:	2.314	···

Table A.9: Comparisons of K–band Quantities with B–band Quantities from Jørgensen *et al.* (1996)

Name	Cluster/ Group	Type	K–band				B–band			$B-K$	$\log \sigma_0$	Mg_2
			$\log r_{\rm eff}$ ($''$)	$\langle\mu\rangle_{\rm eff}$ (mag/$''$)	$K_{\rm tot}$ (mag)	$\log D_K$ ($''$)	$\log r_{\rm eff}$ ($''$)	$\langle\mu\rangle_{\rm eff}$ (mag/$''$)	$\log D_B$ ($''$)	(mag)	(km s^{-1})	(mag)
(1)	(2)	(3)	(4)	(5)	(6)	(7)	(8)	(9)	(10)	(11)	(12)	(13)
D52	A194	U	0.555	16.80	12.03	0.818	0.630	20.78	0.923	3.71:	1.979	0.204
I1696	A194	E	0.680	15.97	10.58	1.166	0.890	20.73	1.203	4.00:	2.204	0.295
N0541	A194	S0	1.209	17.18	9.14	1.359	1.390	21.83	1.363	3.99:	2.328	0.312
N0545	A194	S0	1.425	17.65	8.53	1.424	1.500	21.89	1.433	3.97:	2.367	0.314
N0547	A194	E1	0.939	16.13	9.44	1.408	1.100	20.73	1.403	4.01:	2.326	0.319
N0548	A194	E	0.924	17.50	10.89	0.979	1.140	21.95	1.083	3.67:	2.097	0.246
N0564	A194	E	0.919	16.27	9.68	1.329	1.170	21.08	1.373	3.90:	2.368	0.298
D106	COMA	U	0.438	16.53	12.35	0.776	0.420	20.26	0.851	3.80:	2.210	0.241
I4051	COMA	E0	1.058	17.50	10.22	1.118	1.300	22.37	1.091	3.99:	2.355	0.332
N4839	COMA	E	1.290	17.78	9.34	1.264	1.490	22.47	1.251	3.96:	2.420	0.313
N4864	COMA	E2	0.878	16.98	10.60	1.138	0.880	20.92	1.131	3.93:	2.294	0.286
N4867	COMA	E3	0.497	15.70	11.22	1.058	0.480	19.61	1.081	3.97:	2.353	0.308
N4869	COMA	E3	0.812	16.61	10.56	1.152	0.890	21.02	1.121	4.13:	2.309	0.316
N4871	COMA	U	0.779	16.91	11.02	1.031	0.920	21.45	1.021	4.03:	2.234	0.281
N4872	COMA	SB0	0.459	15.57	11.28	1.053	0.460	19.61	1.051	4.03:	2.330	0.301
N4874	COMA	E0	1.665	18.75	8.43	1.310	1.760	23.12	1.281	4.03:	2.377	0.323
N4906	COMA	E3	0.835	17.11	10.94	1.016	0.890	21.30	1.031	3.99:	2.229	0.295
N4926	COMA	S0	0.986	16.72	9.79	1.275	1.070	21.14	1.261	4.12:	2.420	0.321
D32	KLEM44	U	0.638	15.77	10.58	1.188	0.930	21.14	1.121	4.32:	2.476	0.331
D42	KLEM44	U	1.146	17.82	10.09	1.119	1.350	22.50	1.091	3.95:	2.338	0.362
D43	KLEM44	U	0.696	16.74	11.27	0.987	0.940	21.49	1.021	3.87:	2.273	...
D44	KLEM44	U	0.111	15.18	12.63	0.803	-0.020	18.60	0.811	3.89:	2.210	0.292
D45	KLEM44	U	0.633	17.32	12.16	0.772	0.670	21.27	0.821	3.81:	2.117	0.242
D51	KLEM44	U	0.210	16.03	12.98	0.681	0.320	20.30	0.741	3.87:	2.185	...
D55	KLEM44	U	0.505	16.17	11.65	0.950	0.570	20.39	0.951	3.98:	2.229	0.304
D56	KLEM44	U	1.043	17.16	9.96	1.211	1.240	21.83	1.221	3.95:	2.423	0.310
D58	KLEM44	U	0.594	15.76	10.79	1.153	0.850	20.75	1.151	4.07:	2.412	0.292

Table A.10: Comparisons of K–band Quantities with g–band Quantities from Jørgensen *et al.* (1996)

Name	Cluster/ Group	Type	K–band				g–band					
			$\log r_{\rm eff}$ ($''$)	$\langle\mu\rangle_{\rm eff}$ (mag/$''$)	$K_{\rm tot}$ (mag)	$\log D_K$ ($''$)	$\log r_{\rm eff}$ ($''$)	$\langle\mu\rangle_{\rm eff}$ (mag/$''$)	$\log D_g$ ($''$)	$g-K$ (mag)	$\log\sigma_0$ (km s^{-1})	Mg_2 (mag)
(1)	(2)	(3)	(4)	(5)	(6)	(7)	(8)	(9)	(10)	(11)	(12)	(13)
D52	A194	U	0.555	16.80	12.03	0.818	0.640	20.19	0.899	3.09:	1.979	0.204
I1696	A194	E	0.680	15.97	10.58	1.166	0.860	19.97	1.189	3.35:	2.204	0.295
N0533	A194	E3	1.301	17.17	8.67	1.460	1.630	21.56	1.459	3.20:	2.457	0.317
N0541	A194	S0	1.209	17.18	9.14	1.359	1.380	21.09	1.369	3.29:	2.328	0.312
N0545	A194	S0	1.425	17.65	8.53	1.424	1.440	21.09	1.409	3.39:	2.367	0.314
N0547	A194	E1	0.939	16.13	9.44	1.408	1.120	20.13	1.399	3.34:	2.326	0.319
N0548	A194	E	0.924	17.50	10.89	0.979	1.100	21.19	1.059	3.05:	2.097	0.246
N0564	A194	E	0.919	16.27	9.68	1.329	1.140	20.32	1.369	3.25:	2.368	0.298
I2006	FORNAX	S0	1.312	16.78	8.23	1.574	1.490	20.84	1.556	3.42:	2.080	0.268
N1339	FORNAX	E	0.884	15.29	8.87	1.543	1.210	19.84	1.566	3.38:	2.204	0.290
N3305	HYDRA	E0	0.953	16.09	9.33	1.407	1.000	19.70	1.405	3.44:	2.368	...
N3308	HYDRA	S0	1.498	17.93	8.45	1.419	1.520	21.40	1.415	3.39:	2.287	0.293
N3309	HYDRA	E3	1.285	16.79	8.37	1.550	1.390	20.56	1.545	3.39:	2.409	0.329
N3311	HYDRA	E2	1.817	18.94	7.86	1.381	2.120	23.06	1.335	3.03:	2.292	0.309
D32	KLEM44	U	0.638	15.77	10.58	1.188	0.880	20.26	1.121	3.62:	2.476	0.331
D42	KLEM44	U	1.146	17.82	10.09	1.119	1.420	22.03	1.101	3.22:	2.338	0.362
D43	KLEM44	U	0.696	16.74	11.27	0.987	1.070	21.26	1.011	3.17:	2.273	...
D44	KLEM44	U	0.111	15.18	12.63	0.803	-0.040	17.83	0.801	3.20:	2.210	0.292
D45	KLEM44	U	0.633	17.32	12.16	0.772	0.740	20.78	0.821	3.07:	2.117	0.242
D51	KLEM44	U	0.210	16.03	12.98	0.681	0.240	19.33	0.721	3.19:	2.185	...
D55	KLEM44	U	0.505	16.17	11.65	0.950	0.530	19.57	0.951	3.31:	2.229	0.304
D56	KLEM44	U	1.043	17.16	9.96	1.211	1.200	21.01	1.211	3.28:	2.423	0.310
D58	KLEM44	U	0.594	15.76	10.79	1.153	0.800	19.89	1.141	3.39:	2.412	0.292
N1426	ERIDANUS	E4	1.250	16.63	8.38	1.546	1.330	20.23	1.572	3.31:	2.167	0.254
N1439	ERIDANUS	E1	1.280	16.89	8.49	1.498	1.450	20.82	1.508	3.31:	2.152	0.267
N0720	FIELD	E5	1.397	16.14	7.16	1.831	1.530	20.14	1.800	3.52:	2.372	0.323
N7385	FIELD	E	1.342	17.60	8.89	1.382	1.520	21.58	1.355	3.33:	2.426	0.325

Table A.11: Comparisons of K–band Quantities with I–band Quantities from Scodeggio *et al.* (1997)

Name	Cluster/ Group	Type	K–band				I–band				
			$\log r_{\rm eff}$ ($''$)	$\langle\mu\rangle_{\rm eff}$ (mag/$''$)	$K_{\rm tot}$ (mag)	$\log D_K$ ($''$)	$\log r_{\rm eff}$ ($''$)	$\langle\mu\rangle_{\rm eff}$ (mag/$''$)	$I-K$ (mag)	$\log\sigma_0$ (km s^{-1})	Mg_2 (mag)
(1)	(2)	(3)	(4)	(5)	(6)	(7)	(8)	(9)	(10)	(11)	(12)
L102	A2634	E	0.705	16.69	11.17	1.012	···	···	2.05:	2.285	0.265
L129	A2634	S0	0.542	16.14	11.44	0.993	···	···	1.42:	2.317	0.302
L134	A2634	E	0.664	16.46	11.15	1.032	···	···	1.91:	2.340	0.301
L138	A2634	S0	0.777	16.96	11.08	1.008	···	···	1.93:	2.319	0.309
N7720	A2634	E	1.160	17.19	9.40	1.326	···	···	0.91:	2.494	0.331
N7720A	A2634	E	0.340	15.36	11.65	0.995	···	···	2.32:	2.305	0.295
D106	COMA	S0	0.438	16.53	12.35	0.776	0.540	18.33	1.43:	2.210	0.241
D173	COMA	S0	0.417	16.23	12.15	0.846	0.629	18.39	1.39:	2.147	0.287
D27	COMA	E	0.544	17.03	12.32	0.736	0.773	19.33	1.47:	2.009	0.260
E159G83	COMA	E	0.728	16.09	10.45	1.205	0.956	18.66	1.75:	2.305	···
E159G89	COMA	E	0.825	17.00	10.88	1.043	0.867	18.86	1.71:	2.230	···
E160G22	COMA	E	0.607	15.71	10.67	1.162	1.009	19.01	1.85:	2.417	···
E160G23	COMA	E	0.500	15.91	11.42	1.008	1.101	20.35	2.27:	2.250	···
E160G27	COMA	E	0.611	16.51	11.46	0.960	0.721	18.62	1.71:	2.235	0.282
I0832	COMA	E	0.814	16.80	10.73	1.085	0.890	18.81	1.74:	2.320	···
I0843	COMA	S0	0.742	15.92	10.21	1.247	1.198	19.18	1.62:	2.393	···
I3900	COMA	SB0	0.627	15.91	10.78	1.172	0.704	17.60	1.41:	2.431	···
I3947	COMA	S0	0.470	16.12	11.78	0.926	0.740	18.50	1.40:	2.148	0.279
I3957	COMA	S0	0.545	16.45	11.73	0.912	0.568	18.11	1.58:	2.179	0.292
I3959	COMA	E3	0.655	16.27	11.00	1.069	0.663	17.88	1.58:	2.295	0.307
I4011	COMA	E	0.650	17.11	11.86	0.830	0.750	19.12	1.65:	2.040	0.280
I4012	COMA	E	0.312	15.15	11.59	1.011	0.417	17.02	1.49:	2.259	0.292
I4045	COMA	E4	0.481	15.31	10.91	1.136	0.865	18.31	1.61:	2.331	0.306
I4051	COMA	E0	1.058	17.50	10.22	1.118	1.321	20.13	1.67:	2.355	0.332
N4789	COMA	S0	1.039	16.60	9.41	1.372	1.213	18.87	1.64:	2.427	0.287
N4807	COMA	S0	0.740	16.12	10.42	1.195	0.831	18.12	1.67:	2.336	0.275
N4816	COMA	S0	1.299	18.15	9.66	1.163	1.390	20.17	1.69:	2.365	0.306
N4827	COMA	S0	1.001	16.90	9.90	1.245	1.094	19.01	1.77:	2.465	···
N4839	COMA	E	1.290	17.78	9.34	1.264	1.519	20.07	1.46:	2.420	0.313
N4840	COMA	E1	0.709	16.09	10.55	1.169	0.823	18.22	1.72:	2.377	0.320
N4841A	COMA	E	1.094	17.17	9.71	1.255	0.834	18.57	2.34:	2.417	0.320
N4841B	COMA	E	0.790	16.69	10.74	1.091	1.199	19.18	1.02:	2.355	0.295
N4850	COMA	S0	0.537	15.85	11.17	1.062	0.774	18.44	1.74:	2.233	0.269
N4854	COMA	SB0	0.930	17.58	10.93	0.975	1.134	19.96	1.65:	2.263	0.311
N4860	COMA	E2	0.706	15.95	10.42	1.205	0.885	18.28	1.69:	2.396	0.342
N4864	COMA	E2	0.878	16.98	10.60	1.138	0.952	18.80	1.55:	2.294	0.286
N4867	COMA	E3	0.497	15.70	11.22	1.058	0.664	17.90	1.60:	2.353	0.308
N4869	COMA	E3	0.812	16.61	10.56	1.152	0.919	18.65	1.65:	2.309	0.316
N4871	COMA	S0	0.779	16.91	11.02	1.031	1.146	19.88	1.65:	2.234	0.281
N4872	COMA	SB0	0.459	15.57	11.28	1.053	0.512	17.38	1.62:	2.330	0.301
N4873	COMA	S0	0.584	16.42	11.51	1.042	1.136	19.96	1.54:	2.194	0.290
N4874	COMA	E0	1.665	18.75	8.43	1.310	1.724	20.71	1.75:	2.377	0.323
N4876	COMA	E5	0.683	16.54	11.13	1.020	0.915	18.93	1.55:	2.262	0.248
N4881	COMA	E	0.860	16.86	10.56	1.114	0.956	18.93	1.73:	2.311	0.292
N4886	COMA	E0	0.885	17.37	10.95	0.990	0.964	19.41	1.76:	2.194	0.252
N4889	COMA	E4	1.258	16.89	8.60	1.538	1.553	19.47	1.52:	2.606	0.351
N4894	COMA	S0	0.940	18.30	11.61	0.812	1.150	20.38	1.32:	1.976	0.233
N4906	COMA	E3	0.835	17.11	10.94	1.016	0.856	18.81	1.63:	2.229	0.295
N4923	COMA	S0	0.640	16.04	10.84	1.114	0.792	18.18	1.59:	2.288	0.307

Table A.11—*Continued*

Name	Cluster/ Group	Type	K–band				I–band				
			$\log r_{\rm eff}$ ($''$)	$\langle\mu\rangle_{\rm eff}$ (mag/$''$)	$K_{\rm tot}$ (mag)	$\log D_K$ ($''$)	$\log r_{\rm eff}$ ($''$)	$\langle\mu\rangle_{\rm eff}$ (mag/$''$)	$I-K$ (mag)	$\log\sigma_0$ (km s^{-1})	Mg_2 (mag)
(1)	(2)	(3)	(4)	(5)	(6)	(7)	(8)	(9)	(10)	(11)	(12)
N4926	COMA	S0	0.986	16.72	9.79	1.275	0.953	18.26	1.66:	2.420	0.321
N4927	COMA	S0	0.844	16.46	10.25	1.205	1.058	18.98	1.74:	2.450	0.354
N4952	COMA	E	0.982	16.57	9.66	1.313	1.106	18.66	1.64:	2.358	···
N4957	COMA	E3	1.053	17.19	9.93	1.211	1.244	19.54	1.66:	2.330	0.298
N4971	COMA	S0	0.909	17.13	10.59	1.095	0.880	18.71	1.69:	2.250	···
N5004	COMA	S0	0.919	16.53	9.94	1.267	1.064	18.63	1.58:	2.371	···

Table A.12: Comparisons of K–band Quantities with V–band Quantities from Bower *et al.* (1992a)

Name	Cluster/ Group	Type	K–band				$V-K$	$\log\sigma_0$	Mg_2
			$\log r_{\rm eff}$ ($''$)	$\langle\mu\rangle_{\rm eff}$ (mag/$''$)	$K_{\rm tot}$ (mag)	$\log D_K$ ($''$)	(mag)	(km s^{-1})	(mag)
(1)	(2)	(3)	(4)	(5)	(6)	(7)	(8)	(9)	(10)
D106	COMA	U	0.438	16.53	12.35	0.776	2.84	2.210	0.241
D173	COMA	U	0.417	16.23	12.15	0.846	3.12	2.147	0.287
E159G43	COMA	U	0.702	16.19	10.68	1.137	3.37	2.402	···
E159G63	COMA	U	0.866	17.46	11.13	0.947	3.21	2.173	···
E159G83	COMA	U	0.728	16.09	10.45	1.205	3.30	2.307	···
E159G89	COMA	U	0.825	17.00	10.88	1.043	3.07	2.231	···
E160G159	COMA	U	0.869	17.04	10.70	1.071	3.20	2.360	···
E160G22	COMA	U	0.607	15.71	10.67	1.162	3.33	2.415	···
E160G23	COMA	U	0.500	15.91	11.42	1.008	3.23	2.250	···
E160G27	COMA	U	0.611	16.51	11.46	0.960	3.04	2.235	0.282
I0843	COMA	S0	0.742	15.92	10.21	1.247	3.42	2.392	···
I3900	COMA	SB0	0.627	15.91	10.78	1.172	3.10	2.432	···
I3947	COMA	S0	0.470	16.12	11.78	0.926	2.95	2.150	0.279
I3957	COMA	S0	0.545	16.45	11.73	0.912	3.15	2.181	0.292
I3959	COMA	E3	0.655	16.27	11.00	1.069	3.24	2.294	0.307
I4011	COMA	E	0.650	17.11	11.86	0.830	3.11	2.039	0.280
I4012	COMA	E	0.312	15.15	11.59	1.011	3.30	2.260	0.292
I4021	COMA	E	0.809	16.77	10.73	1.086	3.96	2.207	0.300
I4045	COMA	E4	0.481	15.31	10.91	1.136	3.26	2.331	0.306
I4051	COMA	E0	1.058	17.50	10.22	1.118	3.17	2.360	0.332
I4133	COMA	E	0.535	16.08	11.41	1.000	3.04	2.223	0.289
N4673	COMA	E1	0.760	15.62	9.83	1.340	3.17	2.347	···
N4692	COMA	E	1.117	17.13	9.55	1.290	3.22	2.397	0.307
N4789	COMA	S0	1.039	16.60	9.41	1.372	3.23	2.423	0.287
N4807	COMA	S0	0.740	16.12	10.42	1.195	3.13	2.328	0.275
N4816	COMA	S0	1.299	18.15	9.66	1.163	3.17	2.346	0.306
N4824	COMA	U	0.695	16.96	11.49	0.925	3.18	2.202	0.278
N4827	COMA	S0	1.001	16.90	9.90	1.245	3.27	2.448	···
N4839	COMA	E	1.290	17.78	9.34	1.264	3.21	2.432	0.313
N4840	COMA	E1	0.709	16.09	10.55	1.169	3.22	2.379	0.320
N4841A	COMA	E	1.094	17.17	9.71	1.255	3.10	2.410	0.320
N4841B	COMA	E	0.790	16.69	10.74	1.091	2.81	2.355	0.295
N4850	COMA	S0	0.537	15.85	11.17	1.062	3.17	2.235	0.269
N4854	COMA	SB0	0.930	17.58	10.93	0.975	3.09	2.263	0.311
N4860	COMA	E2	0.706	15.95	10.42	1.205	3.17	2.395	0.342
N4867	COMA	E3	0.497	15.70	11.22	1.058	3.16	2.353	0.308
N4869	COMA	E3	0.812	16.61	10.56	1.152	3.06	2.306	0.316
N4871	COMA	U	0.779	16.91	11.02	1.031	3.06	2.234	0.281
N4872	COMA	SB0	0.459	15.57	11.28	1.053	3.25	2.331	0.301
N4873	COMA	U	0.584	16.42	11.51	1.042	2.85	2.194	0.290
N4874	COMA	E0	1.665	18.75	8.43	1.310	3.31	2.388	0.323
N4876	COMA	E5	0.683	16.54	11.13	1.020	3.20	2.264	0.248
N4881	COMA	E	0.860	16.86	10.56	1.114	3.12	2.304	0.292
N4886	COMA	E0	0.885	17.37	10.95	0.990	3.13	2.189	0.252
N4889	COMA	E4	1.258	16.89	8.60	1.538	3.35	2.603	0.351
N4894	COMA	U	0.940	18.30	11.61	0.812	3.09	1.976	0.233
N4906	COMA	E3	0.835	17.11	10.94	1.016	3.19	2.230	0.295
N4923	COMA	S0	0.640	16.04	10.84	1.114	2.99	2.292	0.307
N4926	COMA	S0	0.986	16.72	9.79	1.275	3.25	2.414	0.321

Table A.12—*Continued*

Name	Cluster/ Group	Type	K–band				$V-K$	$\log\sigma_0$	Mg_2
			$\log r_{\rm eff}$ ($''$)	$\langle\mu\rangle_{\rm eff}$ (mag/$''$)	$K_{\rm tot}$ (mag)	$\log D_K$ ($''$)	(mag)	(km s^{-1})	(mag)
(1)	(2)	(3)	(4)	(5)	(6)	(7)	(8)	(9)	(10)
N4927	COMA	S0	0.844	16.46	10.25	1.205	3.44	2.450	0.354
N4952	COMA	E	0.982	16.57	9.66	1.313	3.20	2.391	···
N4957	COMA	E3	1.053	17.19	9.93	1.211	3.19	2.344	0.298
N4971	COMA	S0	0.909	17.13	10.59	1.095	3.29	2.250	···
N5004	COMA	S0	0.919	16.53	9.94	1.267	3.11	2.372	···
N4339	VIRGO	E0	1.431	17.30	8.15	1.536	3.10	1.960	0.238
N4365	VIRGO	E3	1.583	16.54	6.63	1.924	3.20	2.392	0.304
N4371	VIRGO	SB0	1.533	17.05	7.39	1.717	3.15	2.097	···
N4374	VIRGO	E1	1.595	16.07	6.09	2.049	3.00	2.455	0.290
N4377	VIRGO	S0	1.091	15.98	8.53	1.584	2.97	2.149	···
N4382	VIRGO	S0	1.799	16.94	5.95	2.016	3.09	2.283	···
N4387	VIRGO	E	1.221	16.85	8.75	1.472	3.10	1.996	0.220
N4406	VIRGO	E3	1.833	17.16	6.00	1.990	3.15	2.379	0.294
N4435	VIRGO	SB0	1.175	15.45	7.58	1.785	3.17	2.225	···
N4442	VIRGO	SB0	1.266	15.54	7.22	1.853	3.17	2.336	···
N4458	VIRGO	E0	1.298	17.46	8.97	1.352	2.91	1.992	0.204
N4464	VIRGO	S	0.908	15.86	9.32	1.413	3.08	2.071	0.220
N4468	VIRGO	S0	1.439	18.84	9.65	1.031	2.92	1.881	0.144
N4472	VIRGO	E2	1.851	16.52	5.27	2.189	3.18	2.425	0.292
N4473	VIRGO	E5	1.303	15.56	7.05	1.879	3.18	2.248	0.289
N4476	VIRGO	S0	1.003	16.34	9.33	1.384	2.88	1.553	0.137
N4478	VIRGO	E2	1.286	16.41	7.99	1.664	3.05	2.168	0.246
N4486	VIRGO	E0	1.909	17.02	5.48	2.109	3.21	2.558	0.296
N4550	VIRGO	SB0	1.221	16.41	8.31	1.583	3.06	1.919	···
N4551	VIRGO	E	1.357	17.15	8.37	1.513	3.22	1.999	0.242
N4552	VIRGO	E	1.320	15.35	6.75	1.965	3.17	2.405	0.309
N4564	VIRGO	E	1.226	15.86	7.74	1.725	3.21	2.213	0.333
N4621	VIRGO	E5	1.569	16.27	6.43	1.958	3.17	2.358	0.309
N4636	VIRGO	E0	1.652	16.93	6.67	1.911	2.97	2.285	0.297
N4660	VIRGO	E	1.052	15.24	7.99	1.713	3.07	2.280	0.276
N4697	VIRGO	E6	1.778	16.83	5.94	2.024	3.16	2.228	0.279

Table A.13: Comparisons of K–band Quantities with V–band Quantities from Sandage & Visvanathan (1978) and Persson *et al.* (1979)

Name	Cluster/ Group	Type	K–band				$V-K$	$\log\sigma_0$	Mg_2
			$\log r_{\rm eff}$ ($''$)	$\langle\mu\rangle_{\rm eff}$ (mag/$''$)	$K_{\rm tot}$ (mag)	$\log D_K$ ($''$)	(mag)	(km s^{-1})	(mag)
(1)	(2)	(3)	(4)	(5)	(6)	(7)	(8)	(9)	(10)
N0533	A194	E3	1.301	17.17	8.67	1.460	2.98	2.457	0.317
N4696	CEN30	E1	1.842	18.21	7.01	1.684	3.02	2.387	0.267
I4011	COMA	E	0.650	17.11	11.86	0.830	2.85	2.039	0.280
I4012	COMA	E	0.312	15.15	11.59	1.011	3.66	2.260	0.292
N4873	COMA	U	0.584	16.42	11.51	1.042	3.01	2.194	0.290
N4874	COMA	E0	1.665	18.75	8.43	1.310	3.23	2.388	0.323
N4881	COMA	E	0.860	16.86	10.56	1.114	3.14	2.304	0.292
N4886	COMA	E0	0.885	17.37	10.95	0.990	2.86	2.189	0.252
N4889	COMA	E4	1.258	16.89	8.60	1.538	3.38	2.603	0.351
N4923	COMA	S0	0.640	16.04	10.84	1.114	3.16	2.292	0.307
N1316	FORNAX	S0	1.543	15.55	5.84	1.909	3.25:	2.386	···
N1339	FORNAX	E	0.884	15.29	8.87	1.543	3.06	2.204	0.290
N1344	FORNAX	E5	1.503	16.69	7.18	1.790	3.16	2.221	0.242
N1351	FORNAX	S0	1.089	16.20	8.76	1.501	3.11	2.160	0.267
N1374	FORNAX	E	1.286	16.40	7.98	1.649	3.26	2.257	0.297
N1375	FORNAX	S0	1.518	18.46	8.88	1.239	3.07:	1.724	···
N1379	FORNAX	E	1.561	17.57	7.77	1.605	3.09	2.106	0.243
N1380	FORNAX	S0	1.523	16.31	6.70	1.950	3.36:	2.352	···
N1380B	FORNAX	U	1.919	19.99	8.40	1.048	3.12:	1.982	···
N1381	FORNAX	S0	1.074	15.72	8.36	1.611	3.12:	2.207	···
N1387	FORNAX	U	0.972	14.58	7.72	1.829	3.29:	···	···
N1389	FORNAX	U	1.064	15.85	8.53	1.589	3.08:	···	···
N1399	FORNAX	E1	1.504	15.90	6.39	2.003	3.46	2.513	0.327
N1404	FORNAX	E1	1.341	15.41	6.71	1.972	3.33	2.363	0.302
N1427	FORNAX	E	1.199	16.29	8.30	1.608	2.94	2.197	0.240
N3305	HYDRA	E0	0.953	16.09	9.33	1.407	3.23	2.368	···
N3308	HYDRA	S0	1.498	17.93	8.45	1.419	3.24	2.287	0.293
N3309	HYDRA	E3	1.285	16.79	8.37	1.550	3.24	2.409	0.329
N3311	HYDRA	E2	1.817	18.94	7.86	1.381	3.42	2.292	0.309
N3315	HYDRA	S0	0.991	16.49	9.54	1.420	3.72	2.228	···
N7562	PEGASUS	E2	1.228	16.36	8.22	1.630	3.18	2.383	0.280
N7617	PEGASUS	S0	0.870	16.50	10.15	1.211	3.56	2.129	0.216
N7626	PEGASUS	E	1.449	17.05	7.81	1.632	3.46	2.405	0.321
N4365	VIRGO	E3	1.583	16.54	6.63	1.924	3.30	2.392	0.304
N4374	VIRGO	E1	1.595	16.07	6.09	2.049	3.30	2.455	0.290
N4406	VIRGO	E3	1.833	17.16	6.00	1.990	3.17	2.379	0.294
N4472	VIRGO	E2	1.851	16.52	5.27	2.189	3.27	2.425	0.292
N4478	VIRGO	E2	1.286	16.41	7.99	1.664	3.15	2.168	0.246
N4552	VIRGO	E	1.320	15.35	6.75	1.965	3.26	2.405	0.309
N4621	VIRGO	E5	1.569	16.27	6.43	1.958	3.27	2.358	0.309
N4636	VIRGO	E0	1.652	16.93	6.67	1.911	3.47	2.285	0.297
N4660	VIRGO	E	1.052	15.24	7.99	1.713	3.01	2.280	0.276
N4697	VIRGO	E6	1.778	16.83	5.94	2.024	3.24	2.228	0.279
N0584	CETUS	E4	1.325	15.89	7.27	1.820	3.20	2.301	0.268
N0596	CETUS	E	1.347	16.57	7.84	1.655	3.09	2.176	0.236
N0636	CETUS	E3	1.249	16.52	8.28	1.566	3.11	2.185	0.261
N1395	ERIDANUS	E2	1.496	16.31	6.84	1.891	3.39	2.388	0.310
N1400	ERIDANUS	S0	1.238	15.84	7.65	1.744	3.50	2.395	0.303
N1407	ERIDANUS	E0	1.553	16.54	6.78	1.901	3.45	2.452	0.322

Table A.13—*Continued*

Name	Cluster/ Group	Type	K–band				$V-K$	$\log \sigma_0$	Mg_2
			$\log r_{\rm eff}$ ($''$)	$\langle\mu\rangle_{\rm eff}$ (mag/$''$)	$K_{\rm tot}$ (mag)	$\log D_K$ ($''$)	(mag)	(km s^{-1})	(mag)
(1)	(2)	(3)	(4)	(5)	(6)	(7)	(8)	(9)	(10)
N1426	ERIDANUS	E4	1.250	16.63	8.38	1.546	3.18	2.167	0.254
N1439	ERIDANUS	E1	1.280	16.89	8.49	1.498	3.12	2.152	0.267
N3377	LEO	E5	1.294	15.93	7.46	1.778	2.87	2.121	0.245
N3379	LEO	E1	1.472	15.59	6.23	2.047	3.08	2.296	0.295
N3384	LEO	SB0	1.124	14.71	7.09	1.911	3.00	2.193	0.289
N3412	LEO	SB0	1.645	17.18	6.96	1.752	3.00	1.980	0.219
N3489	LEO	S0	1.341	15.76	7.06	1.861	2.87	1.941	0.166
I3370	N4373grp	E2	1.403	16.68	7.66	1.705	3.19	2.285	0.249
N4373	N4373grp	S0	1.362	16.44	7.63	1.734	3.05	2.341	0.255
I4296	HG22grp	E	1.307	16.27	7.74	1.714	3.11:	2.500	...
N0720	FIELD	E5	1.397	16.14	7.16	1.831	3.46	2.372	0.323
N0741	N741grp	E0	1.499	17.61	8.12	1.529	3.28	2.428	0.334
N0821	FIELD	E6	1.310	16.31	7.76	1.691	3.11	2.282	0.293
N2325	FIELD	E4	1.774	18.28	7.41	1.582	3.28	2.138	0.282
N2434	HG1grp	E0	1.252	16.20	7.95	1.684	3.10	2.316	0.247
N2986	HG36grp	E2	1.430	16.64	7.49	1.734	3.42	2.398	0.299
N3258	ANTLIA	E1	1.176	16.27	8.39	1.584	3.27	2.449	0.335
N3557	FIELD	E3	1.174	15.47	7.61	1.795	2.98	2.474	0.297
N5061	HG31+35grp	E0	1.132	15.15	7.50	1.900	2.87	2.283	0.235
N5898	FABER71grp	E0	1.120	15.78	8.19	1.650	2.83	2.356	0.303
N5982	GH158	E3	1.183	16.03	8.12	1.657	3.37	2.421	0.289
N6482	FIELD	E	1.148	15.85	8.12	1.675	3.26	2.460	0.323
N6702	FIELD	E	1.176	16.86	8.98	1.419	3.29	2.253	0.271
N6703	FIELD	S0	1.146	15.92	8.20	1.644	3.00	2.252	0.269

Table A.14: Comparisons of r–band and U–band Quantities from Jørgensen *et al.* (1995a; JFK95a)

Name	Cluster/ Group	Type	r–band				U–band					
			$\log r_{\rm eff}$ ($''$)	$\langle\mu\rangle_{\rm eff}$ (mag/$''$)	$r_{\rm tot}$ (mag)	$\log D_r$ ($''$)	$\log r_{\rm eff}$ ($''$)	$\langle\mu\rangle_{\rm eff}$ (mag/$''$)	$\log D_U$ ($''$)	$U-r$ (mag)	$\log\sigma_0$ (km s^{-1})	Mg_2 (mag)
(1)	(2)	(3)	(4)	(5)	(6)	(7)	(8)	(9)	(10)	(11)	(12)	(13)
D52	A194	U	0.630	19.86	14.71	0.861	0.650	21.29	0.950	1.36:	1.979	0.204
I0106	A194	U	1.310	20.63	12.09	1.301	1.370	22.39	1.320	1.54:	...	...
I0120	A194	U	0.900	20.21	13.71	1.001	1.150	22.52	1.040	1.40:	2.041	0.245
I1696	A194	E	0.840	19.53	13.34	1.151	0.910	21.28	1.200	1.49:	2.204	0.295
N0535	A194	S0	1.090	20.47	13.03	1.111	1.420	23.00	1.140	1.33:	2.131	0.240
N0538	A194	U	1.150	20.47	12.72	1.181	1.150	22.02	1.220	1.55:	2.310	...
N0541	A194	S0	1.330	20.61	11.96	1.331	1.410	22.41	1.360	1.51:	2.328	0.312
N0545	A194	S0	1.420	20.63	11.54	1.381	1.490	22.44	1.410	1.55:	2.367	0.314
N0547	A194	E1	1.100	19.69	12.20	1.371	1.210	21.66	1.400	1.57:	2.326	0.319
N0548	A194	E	1.100	20.91	13.41	1.011	1.200	22.53	1.110	1.25:	2.097	0.246
N0560	A194	U	1.010	19.53	12.48	1.311	1.130	21.37	1.370	1.40:	2.255	0.281
N0564	A194	E	1.130	19.93	12.29	1.331	1.200	21.70	1.370	1.51:	2.368	0.298
ZH05	A194	U	0.800	19.88	13.88	1.011	0.820	21.43	1.070	1.47:	2.162	...
ZH07	A194	U	0.700	18.98	13.48	1.141	0.770	20.69	1.210	1.45:	2.182	0.252
ZH08	A194	U	0.870	19.79	13.45	1.111	0.940	21.41	1.200	1.36:	2.075	...
ZH09	A194	U	0.750	19.69	13.95	1.021	0.830	21.40	1.090	1.42:	2.086	0.242
ZH10	A194	U	0.650	18.80	13.55	1.151	0.720	20.64	1.180	1.58:	2.322	0.313
ZH12	A194	U	0.760	19.28	13.48	1.141	0.800	20.95	1.180	1.52:	2.212	0.257
D32	KLEMOLA44	U	0.850	19.64	13.39	1.131	0.950	21.70	1.121	1.70:	2.476	0.331
D33	KLEMOLA44	U	0.670	20.83	15.48	0.581	0.690	22.41	0.641	1.51:	1.928	...
D37	KLEMOLA44	U	0.690	20.67	15.22	0.631	0.700	22.08	0.731	1.37:	1.948	...
D38	KLEMOLA44	U	0.511	19.13	14.59	0.931	0.640	21.19	0.941	1.59:	2.165	0.294
D39	KLEMOLA44	U	0.730	20.43	14.79	0.791	0.780	22.04	0.841	1.43:	2.118	...
D40	KLEMOLA44	U	0.700	20.98	15.48	0.531	0.790	22.76	0.601	1.45:	1.987	...
D42	KLEMOLA44	U	1.320	21.25	12.65	1.101	1.480	23.43	1.081	1.60:	2.338	0.362
D43	KLEMOLA44	U	0.960	20.46	13.66	1.011	0.960	22.01	1.031	1.55:	2.273	...
D45	KLEMOLA44	U	0.670	20.20	14.86	0.801	0.770	21.97	0.851	1.41:	2.117	0.242
D49	KLEMOLA44	U	0.439	19.62	15.43	0.731	0.310	20.58	0.771	1.43:	2.100	...
D50	KLEMOLA44	U	0.950	20.43	13.69	1.011	1.160	22.76	1.001	1.57:	2.310	...
D51	KLEMOLA44	U	0.260	18.92	15.62	0.721	0.450	21.28	0.751	1.67:	2.185	...
D55	KLEMOLA44	U	0.520	19.05	14.46	0.951	0.650	21.23	0.941	1.71:	2.229	0.304
D56	KLEMOLA44	U	1.200	20.54	12.54	1.211	1.250	22.40	1.211	1.68:	2.423	0.310
D58	KLEMOLA44	U	0.830	19.52	13.38	1.151	0.870	21.36	1.141	1.70:	2.412	0.292
D59	KLEMOLA44	U	0.730	20.21	14.56	0.851	0.850	22.24	0.861	1.60:	2.230	...
D60	KLEMOLA44	U	0.600	19.64	14.64	0.881	0.650	21.39	0.911	1.57:	2.119	0.251
D65	KLEMOLA44	U	1.030	20.48	13.34	1.071	1.080	22.30	1.071	1.64:	2.335	...
D66	KLEMOLA44	U	0.511	20.11	15.56	0.651	0.530	21.65	0.701	1.47:	2.030	...
D68	KLEMOLA44	U	0.230	19.25	16.11	0.631	0.310	20.99	0.691	1.45:	2.095	...
D76	KLEMOLA44	U	0.620	20.01	14.91	0.791	0.650	21.65	0.831	1.53:	2.142	...
D77	KLEMOLA44	U	0.880	19.70	13.30	1.151	0.950	21.60	1.151	1.65:	2.314	...
D83	KLEMOLA44	U	0.830	20.51	14.37	0.871	0.880	22.26	0.891	1.57:	2.106	...
N1379	OTHER	U	1.680	20.80	10.40	1.621	1.770	22.62	1.661	1.49:	2.106	0.243
N1399	OTHER	U	1.650	19.56	9.31	1.961	1.690	21.47	1.931	1.77:	2.489	0.325
N7144	OTHER	E0	1.470	20.09	10.74	1.621	1.560	22.02	1.631	1.60:	2.261	0.284
N7145	OTHER	E0	1.430	20.24	11.10	1.541	1.530	22.08	1.581	1.48:	2.113	0.252
N7507	OTHER	E0	1.420	19.14	10.04	1.841	1.530	21.22	1.841	1.68:	2.364	0.321

Table A.15: Comparisons of r–band and B–band Quantities from JFK95a

Name	Cluster/ Group	Type	r–band				B–band					
			$\log r_{\rm eff}$ ($''$)	$\langle\mu\rangle_{\rm eff}$ (mag/$''$)	$r_{\rm tot}$ (mag)	$\log D_r$ ($''$)	$\log r_{\rm eff}$ ($''$)	$\langle\mu\rangle_{\rm eff}$ (mag/$''$)	$\log D_B$ ($''$)	$B-r$ (mag)	$\log\sigma_0$ (km s^{-1})	Mg_2 (mag)
(1)	(2)	(3)	(4)	(5)	(6)	(7)	(8)	(9)	(10)	(11)	(12)	(13)
N4839	COMA	E	1.470	21.18	11.84	1.281	1.490	22.47	1.251	1.22:	2.420	0.313
N4926	COMA	S0	1.040	19.79	12.60	1.281	1.070	21.14	1.261	1.24:	2.420	0.321
N4869	COMA	E3	0.880	19.74	13.35	1.141	0.890	21.02	1.121	1.24:	2.309	0.316
D106	COMA	U	0.389	18.99	15.04	0.851	0.420	20.26	0.851	1.16:	2.210	0.241
N4906	COMA	E3	0.870	20.09	13.74	1.031	0.890	21.30	1.031	1.14:	2.229	0.295
N4874	COMA	E0	1.850	22.13	10.88	1.311	1.760	23.12	1.281	1.32:	2.377	0.323
N4872	COMA	SB0	0.480	18.53	14.13	1.061	0.460	19.61	1.051	1.15:	2.330	0.301
N4871	COMA	U	0.920	20.24	13.64	1.021	0.920	21.45	1.021	1.21:	2.234	0.281
N4867	COMA	E3	0.490	18.53	14.09	1.071	0.480	19.61	1.081	1.12:	2.353	0.308
RB257	COMA	U	0.170	17.99	15.14	0.871	0.150	19.12	0.861	1.20:	2.193	0.279
I4051	COMA	E0	1.260	21.02	12.72	1.121	1.300	22.37	1.091	1.21:	2.355	0.332
N4864	COMA	E2	0.890	19.78	13.34	1.141	0.880	20.92	1.131	1.18:	2.294	0.286
D52	A194	U	0.630	19.86	14.71	0.861	0.630	20.78	0.923	0.92:	1.979	0.204
I0120	A194	U	0.900	20.21	13.71	1.001	0.990	21.55	1.033	1.01:	2.041	0.245
I1696	A194	E	0.840	19.53	13.34	1.151	0.890	20.73	1.203	1.02:	2.204	0.295
N0535	A194	S0	1.090	20.47	13.03	1.111	1.240	22.01	1.133	1.00:	2.131	0.240
N0541	A194	S0	1.330	20.61	11.96	1.331	1.390	21.83	1.363	1.00:	2.328	0.312
N0545	A194	S0	1.420	20.63	11.54	1.381	1.500	21.89	1.433	0.97:	2.367	0.314
N0547	A194	E1	1.100	19.69	12.20	1.371	1.100	20.73	1.403	1.04:	2.326	0.319
N0548	A194	E	1.100	20.91	13.41	1.011	1.140	21.95	1.083	0.89:	2.097	0.246
N0560	A194	U	1.010	19.53	12.48	1.311	1.060	20.67	1.353	0.96:	2.255	0.281
N0564	A194	E	1.130	19.93	12.29	1.331	1.170	21.08	1.373	1.00:	2.368	0.298
ZH07	A194	U	0.700	18.98	13.48	1.141	0.720	20.02	1.203	0.97:	2.182	0.252
ZH09	A194	U	0.750	19.69	13.95	1.021	0.760	20.70	1.073	0.97:	2.086	0.242
ZH10	A194	U	0.650	18.80	13.55	1.151	0.660	19.87	1.183	1.03:	2.322	0.313
ZH12	A194	U	0.760	19.28	13.48	1.141	0.750	20.28	1.183	1.03:	2.212	0.257
W43	A3574	U	0.990	21.08	14.13	0.831	1.220	0.04	1.301	-9.99	...	...
D32	KLEMOLA44	U	0.850	19.64	13.39	1.131	0.930	21.14	1.121	1.21:	2.476	0.331
D37	KLEMOLA44	U	0.690	20.67	15.22	0.631	0.630	21.43	0.691	0.98:	1.948	...
D38	KLEMOLA44	U	0.511	19.13	14.59	0.931	0.590	20.54	0.941	1.12:	2.165	0.294
D42	KLEMOLA44	U	1.320	21.25	12.65	1.101	1.350	22.50	1.091	1.14:	2.338	0.362
D43	KLEMOLA44	U	0.960	20.46	13.66	1.011	0.940	21.49	1.021	1.10:	2.273	...
D44	KLEMOLA44	U	-0.041	17.37	15.57	0.811	-0.020	18.60	0.811	1.15:	2.210	0.292
D45	KLEMOLA44	U	0.670	20.20	14.86	0.801	0.670	21.27	0.821	1.07:	2.117	0.242
D51	KLEMOLA44	U	0.260	18.92	15.62	0.721	0.320	20.30	0.741	1.16:	2.185	...
D55	KLEMOLA44	U	0.520	19.05	14.46	0.951	0.570	20.39	0.951	1.16:	2.229	0.304
D56	KLEMOLA44	U	1.200	20.54	12.54	1.211	1.240	21.83	1.221	1.15:	2.423	0.310
D58	KLEMOLA44	U	0.830	19.52	13.38	1.151	0.850	20.75	1.151	1.16:	2.412	0.292
D60	KLEMOLA44	U	0.600	19.64	14.64	0.881	0.630	20.85	0.901	1.10:	2.119	0.251

Table A.16: Comparisons of r–band and g–band Quantities from JFK95a

Name	Cluster/ Group	Type	r–band				g–band					
			$\log r_{\rm eff}$ ($''$)	$\langle\mu\rangle_{\rm eff}$ (mag/$''$)	$r_{\rm tot}$ (mag)	$\log D_r$ ($''$)	$\log r_{\rm eff}$ ($''$)	$\langle\mu\rangle_{\rm eff}$ (mag/$''$)	$\log D_g$ ($''$)	$g-r$ (mag)	$\log\sigma_0$ (km s^{-1})	Mg_2 (mag)
(1)	(2)	(3)	(4)	(5)	(6)	(7)	(8)	(9)	(10)	(11)	(12)	(13)
D52	A194	U	0.630	19.86	14.71	0.861	0.640	20.19	0.899	0.30:	1.979	0.204
I0120	A194	U	0.900	20.21	13.71	1.001	0.990	20.83	1.039	0.30:	2.041	0.245
I1696	A194	E	0.840	19.53	13.34	1.151	0.860	19.97	1.189	0.37:	2.204	0.295
N0533	A194	E3	1.610	21.14	11.10	1.431	1.630	21.56	1.459	0.35:	2.457	0.317
N0535	A194	S0	1.090	20.47	13.03	1.111	1.130	21.01	1.119	0.40:	2.131	0.240
N0541	A194	S0	1.330	20.61	11.96	1.331	1.380	21.09	1.369	0.30:	2.328	0.312
N0545	A194	S0	1.420	20.63	11.54	1.381	1.440	21.09	1.409	0.39:	2.367	0.314
N0547	A194	E1	1.100	19.69	12.20	1.371	1.120	20.13	1.399	0.37:	2.326	0.319
N0548	A194	E	1.100	20.91	13.41	1.011	1.100	21.19	1.059	0.28:	2.097	0.246
N0560	A194	U	1.010	19.53	12.48	1.311	1.060	19.99	1.349	0.28:	2.255	0.281
N0564	A194	E	1.130	19.93	12.29	1.331	1.140	20.32	1.369	0.36:	2.368	0.298
ZH07	A194	U	0.700	18.98	13.48	1.141	0.710	19.33	1.189	0.31:	2.182	0.252
ZH09	A194	U	0.750	19.69	13.95	1.021	0.770	20.05	1.069	0.29:	2.086	0.242
ZH10	A194	U	0.650	18.80	13.55	1.151	0.680	19.27	1.179	0.36:	2.322	0.313
ZH12	A194	U	0.760	19.28	13.48	1.141	0.740	19.53	1.189	0.32:	2.212	0.257
ZH19	A194	U	0.920	19.81	13.21	1.111	0.870	19.90	1.169	0.27:	2.053	0.231
ZH31	A194	U	0.730	19.97	14.32	0.901	0.730	20.26	0.949	0.29:	1.834	0.191
ZH39	A194	U	0.800	19.50	13.51	1.121	0.850	20.04	1.159	0.36:	2.281	0.268
ZH52	A194	U	0.630	19.41	14.27	0.971	0.660	19.85	1.009	0.33:	2.012	0.295
ZH53	A194	U	0.950	20.65	13.90	0.931	0.950	20.92	0.989	0.27:	1.935	0.199
ZH56	A194	U	0.760	19.41	13.62	1.091	0.770	19.80	1.129	0.35:	2.329	0.306
ZH59	A194	U	1.190	21.29	13.35	0.861	1.350	22.26	0.769	0.39:	...	...
D32	KLEMOLA44	U	0.850	19.64	13.39	1.131	0.880	20.26	1.121	0.51:	2.476	0.331
D37	KLEMOLA44	U	0.690	20.67	15.22	0.631	0.690	21.07	0.661	0.40:	1.948	...
D38	KLEMOLA44	U	0.511	19.13	14.59	0.931	0.520	19.57	0.941	0.41:	2.165	0.294
D42	KLEMOLA44	U	1.320	21.25	12.65	1.101	1.420	22.03	1.101	0.42:	2.338	0.362
D43	KLEMOLA44	U	0.960	20.46	13.66	1.011	1.070	21.26	1.011	0.40:	2.273	...
D44	KLEMOLA44	U	-0.041	17.37	15.57	0.811	-0.040	17.83	0.801	0.46:	2.210	0.292
D45	KLEMOLA44	U	0.670	20.20	14.86	0.801	0.740	20.78	0.821	0.33:	2.117	0.242
D51	KLEMOLA44	U	0.260	18.92	15.62	0.721	0.240	19.33	0.721	0.48:	2.185	...
D55	KLEMOLA44	U	0.520	19.05	14.46	0.951	0.530	19.57	0.951	0.48:	2.229	0.304
D56	KLEMOLA44	U	1.200	20.54	12.54	1.211	1.200	21.01	1.211	0.47:	2.423	0.310
D58	KLEMOLA44	U	0.830	19.52	13.38	1.151	0.800	19.89	1.141	0.48:	2.412	0.292
D60	KLEMOLA44	U	0.600	19.64	14.64	0.881	0.610	20.04	0.921	0.36:	2.119	0.251
D70	KLEMOLA44	U	0.090	18.47	16.02	0.681	0.140	19.13	0.681	0.48:	2.131	0.286
A0426-54	DORADUS	U	1.540	22.28	12.59	0.871	1.460	22.36	0.981	0.37:	1.654	0.084
N1411	DORADUS	U	1.240	19.08	10.88	1.661	1.260	19.58	1.681	0.43:	2.100	0.211
N1527	DORADUS	U	1.450	19.65	10.40	1.721	1.470	20.16	1.731	0.44:	2.199	0.258
N1533	DORADUS	U	1.360	19.41	10.62	1.681	1.360	19.92	1.671	0.51:	2.244	0.280
N1543	DORADUS	SB0	1.450	19.60	10.36	1.741	1.480	20.16	1.741	0.45:	2.159	0.275
N1549	DORADUS	E0	1.540	19.33	9.63	1.921	1.570	19.88	1.921	0.44:	2.305	0.294
N1553	DORADUS	S0	1.810	19.85	8.80	2.041	1.840	20.40	2.041	0.44:	2.216	0.262
N1574	DORADUS	S0	1.320	18.76	10.16	1.831	1.340	19.30	1.831	0.47:	2.314	0.285
N1596	DORADUS	S0	1.320	19.29	10.70	1.691	1.350	19.83	1.691	0.43:	2.197	0.269
A1959-56	GRM15	U	1.530	20.35	10.71	1.601	1.530	20.83	1.591	0.48:	2.420	0.330
I4944	GRM15	U	1.260	21.20	12.90	1.051	1.330	21.89	1.021	0.44:	2.081	0.157
I4952	GRM15	U	1.220	20.41	12.31	1.271	1.280	21.03	1.281	0.40:	2.124	0.223
N6848	GRM15	U	1.610	21.38	11.34	1.311	1.670	22.13	1.251	0.53:	2.257	0.238
N6850	GRM15	U	1.220	20.01	11.91	1.391	1.360	21.03	1.361	0.51:	2.249	0.222
N6854	GRM15	U	1.450	21.07	11.82	1.291	1.480	21.59	1.301	0.41:	2.329	0.299

Table A.16—*Continued*

Name	Cluster/ Group	Type	r–band				g–band					
			$\log r_{\rm eff}$ ($''$)	$\langle\mu\rangle_{\rm eff}$ (mag/$''$)	$r_{\rm tot}$ (mag)	$\log D_r$ ($''$)	$\log r_{\rm eff}$ ($''$)	$\langle\mu\rangle_{\rm eff}$ (mag/$''$)	$\log D_g$ ($''$)	$g-r$ (mag)	$\log\sigma_0$ (km s^{-1})	Mg_2 (mag)
(1)	(2)	(3)	(4)	(5)	(6)	(7)	(8)	(9)	(10)	(11)	(12)	(13)
N6854B	GRM15	U	0.130	17.58	14.94	0.941	0.140	18.00	0.951	0.39:	···	···
N6855	GRM15	U	1.230	20.46	12.31	1.261	1.260	21.05	1.261	0.48:	2.283	0.318
E436G42	HYDRA	U	0.520	18.47	13.88	1.111	0.580	18.85	1.195	0.16:	···	···
E436G44	HYDRA	U	0.980	19.37	12.47	1.341	1.000	19.80	1.375	0.36:	2.214	0.256
E436G45	HYDRA	U	0.459	18.17	13.88	1.131	0.530	18.81	1.155	0.39:	2.280	0.266
E437G11	HYDRA	U	0.920	19.33	12.73	1.281	0.980	19.99	1.285	0.45:	2.276	···
E437G13	HYDRA	U	0.800	19.00	13.01	1.251	0.820	19.46	1.275	0.39:	2.225	···
E437G21	HYDRA	U	1.060	19.84	12.54	1.291	1.130	20.51	1.295	0.42:	2.249	0.281
E437G38	HYDRA	U	0.960	19.72	12.93	1.221	1.030	20.39	1.235	0.42:	···	···
E437G45	HYDRA	U	1.090	20.18	12.73	1.221	1.220	20.99	1.245	0.34:	2.104	0.277
E501G13	HYDRA	U	0.950	19.23	12.48	1.341	0.980	19.73	1.365	0.39:	2.353	0.304
I2597	HYDRA	U	1.360	20.07	11.28	1.521	1.380	20.53	1.535	0.39:	2.389	0.316
N3305	HYDRA	E0	0.970	19.18	12.34	1.391	1.000	19.70	1.405	0.41:	2.368	···
N3308	HYDRA	S0	1.510	20.94	11.39	1.401	1.520	21.40	1.415	0.43:	2.287	0.293
N3309	HYDRA	E3	1.340	20.00	11.30	1.531	1.390	20.56	1.545	0.38:	2.409	0.329
N3311	HYDRA	E2	2.060	22.53	10.23	1.331	2.120	23.06	1.335	0.32:	2.292	0.309
R154	HYDRA	U	0.630	18.92	13.78	1.111	0.640	19.33	1.125	0.38:	···	···
R338	HYDRA	U	0.630	19.07	13.93	1.041	0.620	19.39	1.075	0.36:	1.751	···
RMH26	HYDRA	U	0.890	20.27	13.82	0.991	0.870	20.59	1.015	0.39:	2.025	···
RMH28	HYDRA	U	0.790	19.75	13.80	1.051	0.800	20.20	1.065	0.42:	2.149	0.271
RMH29	HYDRA	U	0.610	18.43	13.38	1.201	0.630	18.93	1.225	0.43:	2.185	···
RMH30	HYDRA	U	1.160	20.99	13.20	1.051	1.200	21.50	1.065	0.37:	2.287	0.270
RMH35	HYDRA	U	0.800	19.62	13.62	1.071	0.820	20.09	1.095	0.40:	2.091	···
RMH50	HYDRA	U	0.820	20.62	14.53	0.831	0.850	21.06	0.875	0.33:	1.964	···
RMH63	HYDRA	U	1.080	21.05	13.65	0.921	1.130	21.43	1.005	0.20:	···	···
RMH64	HYDRA	U	1.230	21.26	13.12	0.981	1.140	21.24	1.055	0.31:	···	···
E318G21	OTHER	U	1.150	19.83	12.09	1.371	1.170	20.36	1.371	0.46:	2.211	0.250
E462G15	OTHER	U	1.320	19.95	11.36	1.511	1.340	20.46	1.521	0.44:	2.469	0.289
E553G02	OTHER	U	1.260	20.31	12.02	1.351	1.310	21.00	1.321	0.51:	2.407	0.277
I2006	OTHER	U	1.460	20.31	11.02	1.561	1.490	20.86	1.551	0.44:	2.097	···
I5157	OTHER	U	1.220	20.03	11.94	1.391	1.260	20.64	1.381	0.47:	···	···
N0720	OTHER	E5	1.520	19.66	10.06	1.791	1.530	20.17	1.791	0.47:	2.372	0.323
N1339	OTHER	U	1.170	19.25	11.40	1.561	1.210	19.86	1.561	0.47:	2.202	0.285
N1426	OTHER	U	1.300	19.77	11.28	1.551	1.330	20.30	1.551	0.42:	2.162	0.259
N1439	OTHER	U	1.390	20.22	11.28	1.491	1.450	20.84	1.501	0.40:	2.182	0.253
N1726	OTHER	S0	1.340	19.96	11.27	1.531	1.380	20.59	1.521	0.49:	2.356	0.297
N1794	OTHER	U	1.210	20.28	12.23	1.311	1.230	20.83	1.291	0.48:	2.271	0.216
N2513	OTHER	E	1.350	20.14	11.39	1.481	1.380	20.75	1.471	0.50:	2.434	0.314
N2974	OTHER	E4	1.370	19.35	10.51	1.731	1.420	20.06	1.711	0.53:	2.372	0.290
N6849	OTHER	SB0	1.520	21.21	11.62	1.311	1.550	21.69	1.331	0.37:	2.293	0.262
N7385	OTHER	E	1.500	21.12	11.62	1.341	1.520	21.68	1.321	0.49:	2.426	0.325
N7785	OTHER	E5	1.340	19.88	11.19	1.561	1.350	20.39	1.551	0.47:	2.462	0.292

Table A.17: Comparisons of r–band Quantities from Jørgensen *et al.* (1995a) and B–band Quantities from Faber *et al.* (1989)

Name	Cluster/ Group	Type	r–band				B–band			$B-r$	$\log\sigma_0$	Mg_2
			$\log r_{\rm eff}$ ($''$)	$\langle\mu\rangle_{\rm eff}$ (mag/$''$)	$r_{\rm tot}$ (mag)	$\log D_r$ ($''$)	$\log r_{\rm eff}$ ($''$)	$\langle\mu\rangle_{\rm eff}$ (mag/$''$)	$\log D_B$ ($''$)	(mag)	(km s^{-1})	(mag)
(1)	(2)	(3)	(4)	(5)	(6)	(7)	(8)	(9)	(10)	(11)	(12)	(13)
N4839	COMA	E	1.470	21.18	11.84	1.281	1.457	22.50	1.242	1.37:	2.420	0.313
N4926	COMA	S0	1.040	19.79	12.60	1.281	1.047	21.21	1.252	1.39:	2.420	0.321
N4854	COMA	SB0	1.150	21.13	13.38	0.991	1.257	23.11	0.879	1.59:	2.263	0.311
I3959	COMA	E3	0.730	19.42	13.78	1.081	0.757	20.93	1.039	1.41:	2.295	0.307
I3957	COMA	S0	0.630	19.51	14.37	0.951	0.647	20.91	0.945	1.34:	2.179	0.292
N4923	COMA	S0	0.930	19.88	13.23	1.151	0.917	21.20	1.122	1.37:	2.288	0.307
N4869	COMA	E3	0.880	19.74	13.35	1.141	0.917	21.18	1.122	1.31:	2.309	0.316
N4906	COMA	E3	0.870	20.09	13.74	1.031	0.887	21.35	1.059	1.20:	2.229	0.295
N4876	COMA	E5	0.710	19.47	13.93	1.041	0.747	21.02	1.002	1.42:	2.262	0.248
N4874	COMA	E0	1.850	22.13	10.88	1.311	1.787	23.29	1.282	1.39:	2.377	0.323
N4872	COMA	SB0	0.480	18.53	14.13	1.061	0.507	19.91	1.052	1.28:	2.330	0.301
N4867	COMA	E3	0.490	18.53	14.09	1.071	0.577	20.21	1.052	1.36:	2.353	0.308
I4051	COMA	E0	1.260	21.02	12.72	1.121	1.307	22.57	1.072	1.38:	2.355	0.332
N4889	COMA	E4	1.530	20.64	10.99	1.511	1.497	22.00	1.452	1.48:	2.606	0.351
I4011	COMA	E	0.690	19.98	14.54	0.871	0.727	21.43	0.882	1.32:	2.040	0.280
N4886	COMA	E0	0.970	20.38	13.54	1.041	0.957	21.60	1.042	1.27:	2.194	0.252
N4864	COMA	E2	0.890	19.78	13.34	1.141	0.927	21.28	1.112	1.37:	2.294	0.286
I4045	COMA	E4	0.640	18.79	13.60	1.151	0.727	20.64	1.092	1.54:	2.331	0.306
I4021	COMA	E	0.511	19.02	14.47	0.961	0.597	20.67	0.962	1.34:	2.206	0.300
I4012	COMA	E	0.330	18.23	14.59	0.981	0.477	20.11	0.972	1.35:	2.259	0.292
N4860	COMA	E2	0.930	19.64	12.99	1.211	0.927	21.11	1.156	1.48:	2.396	0.342
N4881	COMA	E	1.040	20.24	13.04	1.151	1.047	21.72	1.102	1.45:	2.311	0.292
N4841B	COMA	E	0.930	19.88	13.23	1.151	1.267	21.86	1.275	0.76:	2.355	0.295
N0533	A194	E3	1.610	21.14	11.10	1.431	1.677	22.45	1.469	1.07:	2.457	0.317
N0541	A194	S0	1.330	20.61	11.96	1.331	1.627	22.76	1.320	1.08:	2.328	0.312
N0545	A194	S0	1.420	20.63	11.54	1.381	···	-9.99	1.390	-9.99	2.367	0.314
N0547	A194	E1	1.100	19.69	12.20	1.371	···	-9.99	1.410	-9.99	2.326	0.319
N0548	A194	E	1.100	20.91	13.41	1.011	1.277	22.59	1.030	1.04:	2.097	0.246
N0564	A194	E	1.130	19.93	12.29	1.331	1.307	21.73	1.344	1.16:	2.368	0.298
D45	A539	U	0.780	19.71	13.81	1.051	1.337	21.04	1.568	-9.99	2.355	0.314
E264G31	S639	U	1.270	20.28	11.94	1.371	1.447	22.31	1.308	1.39:	2.399	0.276
D45	KLEMOLA44	U	0.670	20.20	14.86	0.801	1.337	21.45	1.437	-9.99	2.117	0.242
N1549	DORADUS	E0	1.540	19.33	9.63	1.921	1.677	20.96	1.928	1.13:	2.305	0.294
N6854	GRM15	U	1.450	21.07	11.82	1.291	1.497	22.32	1.338	1.08:	2.329	0.299
N3305	HYDRA	E0	0.970	19.18	12.34	1.391	0.977	20.31	1.408	1.10:	2.368	···
N3308	HYDRA	S0	1.510	20.94	11.39	1.401	1.517	22.14	1.406	1.18:	2.287	0.293
N3309	HYDRA	E3	1.340	20.00	11.30	1.531	1.497	21.69	1.536	1.12:	2.409	0.329
N3311	HYDRA	E2	2.060	22.53	10.23	1.331	2.227	24.16	1.286	1.03:	2.292	0.309
E318G21	OTHER	U	1.150	19.83	12.09	1.371	1.237	21.37	1.378	1.23:	2.211	0.250
E462G15	OTHER	U	1.320	19.95	11.36	1.511	1.367	21.34	1.528	1.22:	2.469	0.289
I2006	OTHER	U	1.460	20.31	11.02	1.561	1.457	21.44	1.568	1.14:	2.097	···
I5157	OTHER	U	1.220	20.03	11.94	1.391	1.447	22.92	1.078	2.07:	···	···
N0720	OTHER	E5	1.520	19.66	10.06	1.791	1.597	21.14	1.798	1.20:	2.372	0.323
N1339	OTHER	U	1.170	19.25	11.40	1.561	1.227	20.62	1.568	1.16:	2.202	0.285
N1379	OTHER	U	1.680	20.80	10.40	1.621	1.627	21.79	1.628	1.18:	2.106	0.243
N1399	OTHER	U	1.650	19.56	9.31	1.961	1.627	20.68	1.958	1.20:	2.489	0.325
N1426	OTHER	U	1.300	19.77	11.28	1.551	1.417	21.32	1.568	1.13:	2.162	0.259
N1439	OTHER	U	1.390	20.22	11.28	1.491	1.617	22.14	1.498	1.10:	2.182	0.253
N1726	OTHER	S0	1.340	19.96	11.27	1.531	1.377	21.32	1.538	1.23:	2.356	0.297

Table A.17—*Continued*

Name	Cluster/ Group	Type	r–band				B–band					
			$\log r_{\rm eff}$ ($''$)	$\langle\mu\rangle_{\rm eff}$ (mag/$''$)	$r_{\rm tot}$ (mag)	$\log D_r$ ($''$)	$\log r_{\rm eff}$ ($''$)	$\langle\mu\rangle_{\rm eff}$ (mag/$''$)	$\log D_B$ ($''$)	$B-r$ (mag)	$\log\sigma_0$ (km s^{-1})	Mg_2 (mag)
(1)	(2)	(3)	(4)	(5)	(6)	(7)	(8)	(9)	(10)	(11)	(12)	(13)
N2513	OTHER	E	1.350	20.14	11.39	1.481	1.527	22.05	1.458	1.27:	2.434	0.314
N2974	OTHER	E4	1.370	19.35	10.51	1.731	1.567	21.27	1.728	1.21:	2.372	0.290
N6849	OTHER	SB0	1.520	21.21	11.62	1.311	1.717	23.03	1.318	1.11:	2.293	0.262
N7144	OTHER	E0	1.470	20.09	10.74	1.621	1.607	21.78	1.618	1.19:	2.261	0.284
N7145	OTHER	E0	1.430	20.24	11.10	1.541	1.587	21.90	1.548	1.09:	2.113	0.252
N7385	OTHER	E	1.500	21.12	11.62	1.341	1.637	22.89	1.298	1.27:	2.426	0.325
N7785	OTHER	E5	1.340	19.88	11.19	1.561	1.427	21.43	1.548	1.24:	2.462	0.292
N7507	OTHER	E0	1.420	19.14	10.04	1.841	1.497	20.62	1.848	1.20:	2.364	0.321

Table A.18: Comparisons of r–band Quantities from Jørgensen *et al.* (1995a) and V–band Quantities from Lucey & Carter (1988) and Lucey *et al.* (1991a,b; 1997)

Name	Cluster/ Group	Type	r–band				V–band					
			$\log r_{\rm eff}$ ($''$)	$\langle\mu\rangle_{\rm eff}$ (mag/$''$)	$r_{\rm tot}$ (mag)	$\log D_r$ ($''$)	$\log r_{\rm eff}$ ($''$)	$\langle\mu\rangle_{\rm eff}$ (mag/$''$)	$\log D_V$ ($''$)	$V-r$ (mag)	$\log\sigma_0$ (km s^{-1})	Mg_2 (mag)
(1)	(2)	(3)	(4)	(5)	(6)	(7)	(8)	(9)	(10)	(11)	(12)	(13)
E160G37	COMA	E	0.630	19.06	13.91	1.071	0.599	19.18	1.063	0.23:	2.354	0.302
TT41	COMA	E	0.660	20.17	14.88	0.781	0.674	20.44	0.785	0.21:	2.004	0.261
N4839	COMA	E	1.470	21.18	11.84	1.281	1.425	21.29	1.272	0.27:	2.420	0.313
N4840	COMA	E1	0.810	19.35	13.30	1.171	0.793	19.59	1.152	0.30:	2.377	0.320
N4926	COMA	S0	1.040	19.79	12.60	1.281	0.995	19.90	1.258	0.27:	2.420	0.321
N4854	COMA	SB0	1.150	21.13	13.38	0.991	1.102	21.22	0.969	0.26:	2.263	0.311
D65	COMA	S0	0.820	20.55	14.46	0.811	0.798	20.85	0.773	0.38:	2.070	0.252
D67	COMA	S0	0.380	18.81	14.91	0.881	0.437	19.41	0.832	0.39:	2.178	0.277
I3963	COMA	S0	0.890	20.58	14.13	0.901	0.854	20.73	0.885	0.28:	2.120	0.269
I3959	COMA	E3	0.730	19.42	13.78	1.081	0.769	19.86	1.053	0.30:	2.295	0.307
I3957	COMA	S0	0.630	19.51	14.37	0.951	0.637	19.84	0.926	0.31:	2.179	0.292
I3947	COMA	S0	0.520	19.00	14.40	0.971	0.589	19.58	0.952	0.33:	2.148	0.279
N4923	COMA	S0	0.930	19.88	13.23	1.151	0.865	19.93	1.124	0.28:	2.288	0.307
D101	COMA	S0	0.560	19.42	14.62	0.901	0.520	19.55	0.882	0.27:	2.109	0.269
N4875	COMA	S0	0.520	18.96	14.37	0.991	0.508	19.20	0.971	0.28:	2.269	0.290
N4869	COMA	E3	0.880	19.74	13.35	1.141	0.920	20.16	1.125	0.27:	2.309	0.316
D106	COMA	S0	0.389	18.99	15.04	0.851	0.419	19.40	0.827	0.30:	2.210	0.241
D108	COMA	S0	0.511	19.61	15.06	0.791	0.496	19.89	0.755	0.33:	2.073	0.272
I3960	COMA	S0	0.730	19.77	14.12	0.981	0.698	19.98	0.947	0.32:	2.252	0.336
D116	COMA	SB0	0.850	20.62	14.38	0.851	0.838	20.81	0.842	0.23:	2.123	0.247
N4906	COMA	E3	0.870	20.09	13.74	1.031	0.831	20.19	1.021	0.24:	2.229	0.295
D119	COMA	S0	0.620	19.87	14.78	0.851	0.514	19.73	0.831	0.24:	2.195	0.280
N4876	COMA	E5	0.710	19.47	13.93	1.041	0.689	19.82	1.015	0.42:	2.264	0.248
RB43	COMA	E	0.179	18.06	15.16	0.871	0.219	18.50	0.854	0.29:	2.231	0.267
D128	COMA	S0	0.400	19.30	15.30	0.751	0.409	19.67	0.740	0.33:	2.028	0.250
N4874	COMA	E0	1.850	22.13	10.88	1.311	1.743	22.15	1.282	0.40:	2.377	0.323
N4872	COMA	SB0	0.480	18.53	14.13	1.061	0.482	18.84	1.036	0.30:	2.330	0.301
N4871	COMA	S0	0.920	20.24	13.64	1.021	0.919	20.54	1.001	0.30:	2.234	0.281
N4867	COMA	E3	0.490	18.53	14.09	1.071	0.553	19.11	1.038	0.35:	2.353	0.308
RB257	COMA	E	0.170	17.99	15.14	0.871	0.126	18.11	0.852	0.28:	2.193	0.279
N4850	COMA	S0	0.670	19.07	13.72	1.111	0.738	19.78	1.048	0.46:	2.233	0.269
I4051	COMA	E0	1.260	21.02	12.72	1.121	1.272	21.42	1.075	0.35:	2.355	0.332
I4041	COMA	S0	0.870	20.52	14.18	0.881	0.844	20.76	0.862	0.33:	2.111	0.283
D146	COMA	SB0/a	1.050	21.31	14.06	0.801	1.083	21.73	0.776	0.30:	2.030	0.246
N4889	COMA	E4	1.530	20.64	10.99	1.511	1.484	20.85	1.468	0.37:	2.606	0.351
I4011	COMA	E	0.690	19.98	14.54	0.871	0.624	20.03	0.860	0.29:	2.040	0.280
N4886	COMA	E0	0.970	20.38	13.54	1.041	0.874	20.34	1.018	0.30:	2.194	0.252
I3998	COMA	SB0	0.950	20.73	13.98	0.911	0.880	20.75	0.902	0.27:	2.201	0.272
RB45	COMA	E	0.571	19.58	14.73	0.861	0.536	19.76	0.846	0.30:	2.133	0.282
D157	COMA	S0	0.490	19.48	15.04	0.811	0.483	19.74	0.799	0.28:	2.109	0.251
N4864	COMA	E2	0.890	19.78	13.34	1.141	0.880	20.04	1.114	0.29:	2.294	0.286
I3955	COMA	SB0	0.910	20.36	13.81	0.981	0.831	20.37	0.967	0.29:	2.267	0.300
RB241	COMA	E	0.910	20.07	13.53	1.081	0.879	20.24	1.054	0.28:	2.251	0.303
N4908	COMA	S0/E	0.850	19.60	13.36	1.151	0.867	19.93	1.128	0.27:	2.314	0.265
I4045	COMA	E4	0.640	18.79	13.60	1.151	0.660	19.25	1.115	0.39:	2.331	0.306
I4026	COMA	SB0	0.860	20.38	14.09	0.931	0.888	20.77	0.904	0.29:	2.155	0.289
I4021	COMA	E	0.511	19.02	14.47	0.961	0.486	19.25	0.931	0.32:	2.206	0.300
D173	COMA	S0	0.530	19.52	14.88	0.851	0.527	19.68	0.861	0.17:	2.147	0.287
I4012	COMA	E	0.330	18.23	14.59	0.981	0.363	18.56	0.988	0.21:	2.259	0.292

Table A.18—*Continued*

Name	Cluster/ Group	Type	r–band				V–band					
			$\log r_{\rm eff}$ ($''$)	$\langle\mu\rangle_{\rm eff}$ (mag/$''$)	$r_{\rm tot}$ (mag)	$\log D_r$ ($''$)	$\log r_{\rm eff}$ ($''$)	$\langle\mu\rangle_{\rm eff}$ (mag/$''$)	$\log D_V$ ($''$)	$V-r$ (mag)	$\log\sigma_0$ (km s^{-1})	Mg_2 (mag)
(1)	(2)	(3)	(4)	(5)	(6)	(7)	(8)	(9)	(10)	(11)	(12)	(13)
D175	COMA	S0	0.840	19.91	13.71	1.041	0.785	20.03	1.022	0.32:	2.243	0.297
D176	COMA	S0	0.490	18.98	14.54	0.941	0.671	20.01	0.916	0.37:	2.216	0.282
N4865	COMA	S0	0.710	18.77	13.22	1.231	0.748	19.26	1.193	0.35:	2.379	0.285
D181	COMA	S0	0.511	19.45	14.90	0.851	0.486	19.69	0.820	0.33:	2.161	0.248
RB155	COMA	E	0.620	20.04	14.95	0.771	0.550	19.92	0.808	0.13:	2.083	0.266
N4860	COMA	E2	0.930	19.64	12.99	1.211	0.895	19.82	1.188	0.30:	2.396	0.342
D204	COMA	E	0.780	20.42	14.53	0.871	0.766	20.58	0.849	0.21:	2.109	0.269
N4895	COMA	S0	1.000	19.86	12.87	1.211	1.028	20.12	1.237	0.16:	2.337	0.292
RB167	COMA	E	0.600	19.66	14.66	0.861	0.620	19.92	0.885	0.19:	2.174	0.268
E160G49A	COMA	Ep	0.590	19.26	14.31	0.981	0.539	19.39	0.949	0.31:	2.232	0.271
N4881	COMA	E	1.040	20.24	13.04	1.151	1.022	20.49	1.119	0.31:	2.311	0.292
D238	COMA	E	0.400	18.94	14.95	0.871	0.431	19.33	0.854	0.28:	2.026	0.237
N4841A	COMA	E	1.250	20.39	12.14	1.311	1.170	20.44	1.284	0.34:	2.417	0.320
D52	A194	E	0.630	19.86	14.71	0.861	···	-9.99	0.894	-9.99	1.979	0.204
N0535	A194	S0	1.090	20.47	13.03	1.111	···	-9.99	···	-9.99	2.131	0.240
N0538	A194	Sa	1.150	20.47	12.72	1.181	···	-9.99	1.212	-9.99	2.310	···
N0541	A194	S0	1.330	20.61	11.96	1.331	···	-9.99	1.347	-9.99	2.328	0.312
N0545	A194	S0	1.420	20.63	11.54	1.381	···	-9.99	1.409	-9.99	2.367	0.314
N0547	A194	E1	1.100	19.69	12.20	1.371	···	-9.99	1.411	-9.99	2.326	0.319
N0548	A194	E	1.100	20.91	13.41	1.011	···	-9.99	1.053	-9.99	2.097	0.246
D32	KLEMOLA44	E	0.850	19.64	13.39	1.131	···	-9.99	1.127	-9.99	2.476	0.331
D33	KLEMOLA44	S0	0.670	20.83	15.48	0.581	···	-9.99	···	-9.99	1.928	···
D37	KLEMOLA44	S0	0.690	20.67	15.22	0.631	···	-9.99	···	-9.99	1.948	···
D38	KLEMOLA44	S0	0.511	19.13	14.59	0.931	···	-9.99	···	-9.99	2.165	0.294
D39	KLEMOLA44	S0	0.730	20.43	14.79	0.791	···	-9.99	···	-9.99	2.118	···
D40	KLEMOLA44	S0	0.700	20.98	15.48	0.531	···	-9.99	···	-9.99	1.987	···
D42	KLEMOLA44	D	1.320	21.25	12.65	1.101	···	-9.99	1.106	-9.99	2.338	0.362
D43	KLEMOLA44	S0	0.960	20.46	13.66	1.011	···	-9.99	···	-9.99	2.273	···
D44	KLEMOLA44	E	-0.041	17.37	15.57	0.811	···	-9.99	0.814	-9.99	2.210	0.292
D45	KLEMOLA44	E	0.670	20.20	14.86	0.801	···	-9.99	0.841	-9.99	2.117	0.242
D49	KLEMOLA44	S0	0.439	19.62	15.43	0.731	···	-9.99	···	-9.99	2.100	···
D50	KLEMOLA44	SB0/a	0.950	20.43	13.69	1.011	···	-9.99	···	-9.99	2.310	···
D51	KLEMOLA44	S0	0.260	18.92	15.62	0.721	···	-9.99	···	-9.99	2.185	···
D55	KLEMOLA44	E	0.520	19.05	14.46	0.951	···	-9.99	0.956	-9.99	2.229	0.304
D56	KLEMOLA44	D	1.200	20.54	12.54	1.211	···	-9.99	1.220	-9.99	2.423	0.310
D58	KLEMOLA44	E	0.830	19.52	13.38	1.151	···	-9.99	1.145	-9.99	2.412	0.292
D59	KLEMOLA44	S0	0.730	20.21	14.56	0.851	···	-9.99	···	-9.99	2.230	···
D60	KLEMOLA44	E	0.600	19.64	14.64	0.881	···	-9.99	0.891	-9.99	2.119	0.251
D65	KLEMOLA44	S0	1.030	20.48	13.34	1.071	···	-9.99	···	-9.99	2.335	···
D66	KLEMOLA44	S0	0.511	20.11	15.56	0.651	···	-9.99	···	-9.99	2.030	···
D68	KLEMOLA44	E	0.230	19.25	16.11	0.631	···	-9.99	0.638	-9.99	2.095	···
D70	KLEMOLA44	E	0.090	18.47	16.02	0.681	···	-9.99	0.686	-9.99	2.131	0.286
D76	KLEMOLA44	S0	0.620	20.01	14.91	0.791	···	-9.99	···	-9.99	2.142	···
D77	KLEMOLA44	S0	0.880	19.70	13.30	1.151	···	-9.99	···	-9.99	2.314	···
D83	KLEMOLA44	S0	0.830	20.51	14.37	0.871	···	-9.99	···	-9.99	2.106	···
N3305	HYDRA	E0	0.970	19.18	12.34	1.391	···	-9.99	1.397	-9.99	2.368	···
N3308	HYDRA	S0	1.510	20.94	11.39	1.401	···	-9.99	1.409	-9.99	2.287	0.293
N3309	HYDRA	E3	1.340	20.00	11.30	1.531	···	-9.99	1.545	-9.99	2.409	0.329
N3311	HYDRA	E2	2.060	22.53	10.23	1.331	···	-9.99	1.332	-9.99	2.292	0.309

Table A.19: Comparisons of R_C–band Quantities from Smith *et al.* (1997) and V–band Quantities from Lucey & Carter (1988) and Lucey *et al.* (1991a,b; 1997)

Name	Cluster/ Group	Type	R_C–band				V–band					
			$\log r_{\rm eff}$ ($''$)	$\langle\mu\rangle_{\rm eff}$ (mag/$''$)	$R_{\rm C,tot}$ (mag)	$\log D_R$ ($''$)	$\log r_{\rm eff}$ ($''$)	$\langle\mu\rangle_{\rm eff}$ (mag/$''$)	$\log D_V$ ($''$)	$V-R_C$ (mag)	$\log\sigma_0$ (km s^{-1})	Mg_2 (mag)
(1)	(2)	(3)	(4)	(5)	(6)	(7)	(8)	(9)	(10)	(11)	(12)	(13)
I3963	COMA	S0	0.965	20.50	13.68	0.887	0.854	20.73	0.885	0.63:	2.120	0.269
I3959	COMA	E3	0.773	19.27	13.41	1.065	0.769	19.86	1.053	0.60:	2.295	0.307
I3957	COMA	S0	0.573	18.99	14.13	0.934	0.637	19.84	0.926	0.62:	2.179	0.292
N4875	COMA	S0	0.502	18.51	14.01	0.998	0.508	19.20	0.971	0.67:	2.269	0.290
N4869	COMA	E3	0.914	19.48	12.91	1.148	0.920	20.16	1.125	0.66:	2.309	0.316
N4876	COMA	E5	0.671	18.99	13.64	1.044	0.689	19.82	1.015	0.76:	2.264	0.248
RB43	COMA	E	0.182	17.71	14.80	0.876	0.219	18.50	0.854	0.65:	2.231	0.267
D128	COMA	S0	0.378	18.96	15.07	0.754	0.409	19.67	0.740	0.60:	2.028	0.250
N4874	COMA	E0	1.811	21.68	10.63	1.303	1.743	22.15	1.282	0.71:	2.377	0.323
N4872	COMA	SB0	0.508	18.33	13.79	1.050	0.482	18.84	1.036	0.60:	2.330	0.301
N4871	COMA	S0	0.843	19.66	13.45	1.012	0.919	20.54	1.001	0.60:	2.234	0.281
D132	COMA	S0	0.604	19.85	14.84	0.727	0.649	20.60	0.730	0.59:	2.113	0.263
N4889	COMA	E4	1.509	20.30	10.76	1.489	1.484	20.85	1.468	0.64:	2.606	0.351
I4011	COMA	E	0.687	19.67	14.24	0.863	0.624	20.03	0.860	0.58:	2.040	0.280
N4886	COMA	E0	0.915	19.89	13.32	1.021	0.874	20.34	1.018	0.60:	2.194	0.252
I3998	COMA	SB0	0.809	19.89	13.85	0.914	0.880	20.75	0.902	0.60:	2.201	0.272
D157	COMA	S0	0.561	19.44	14.64	0.802	0.483	19.74	0.799	0.58:	2.109	0.251
L113	A2199	E	0.316	18.74	15.16	0.750	0.302	19.22	0.761	0.53:	2.218	0.268
L114	A2199	S0	0.265	18.15	14.82	0.849	0.208	18.47	0.852	0.53:	2.290	0.301
S26	A2199	E	0.964	20.38	13.56	0.924	0.959	20.93	0.925	0.57:	2.246	0.286
S30	A2199	E	0.301	17.96	14.46	0.931	...	-9.99	0.935	-9.99	2.394	0.261
L145	A2199	S0/a	0.907	20.35	13.82	0.870	0.942	21.05	0.873	0.57:	2.169	0.285
S34	A2199	E	0.403	18.96	14.95	0.779	0.283	19.03	0.778	0.50:	2.195	0.273
N6166	A2199	E2	1.893	22.17	10.71	1.201	1.927	22.82	1.194	0.53:	2.487	0.323
Z34A	A2199	E	0.950	19.95	13.21	1.035	0.909	20.38	1.042	0.58:	2.314	0.285
Z34ACOMP	A2199	S0	0.474	18.55	14.19	0.953	0.363	18.71	0.949	0.56:	2.353	0.327
N7720	A2634	E	1.279	20.22	11.83	1.272	1.288	20.83	1.273	0.57:	2.494	0.331

Table A.20: Comparisons of I_C–band Quantities from Scodeggio *et al.* (1997) and V–band Quantities from Lucey & Carter (1988) and Lucey *et al.* (1991a,b; 1997)

Name	Cluster/ Group	Type	I_C–band			V–band				
			$\log r_{\rm eff}$ ($''$)	$\langle\mu\rangle_{\rm eff}$ (mag/$''$)	$r_{\rm tot}$ (mag)	$\log r_{\rm eff}$ ($''$)	$\langle\mu\rangle_{\rm eff}$ (mag/$''$)	$V-I_C$ (mag)	$\log\sigma_0$ (km s^{-1})	Mg_2 (mag)
(1)	(2)	(3)	(4)	(5)	(6)	(7)	(8)	(9)	(10)	(11)
E159G83	COMA	U	0.956	18.66	11.89	0.993	20.45	1.65:	2.307	···
E159G89	COMA	U	0.867	18.86	12.53	0.973	20.64	1.39:	2.231	···
I0832	COMA	E	0.890	18.81	12.36	0.981	20.63	1.49:	2.321	···
N4789	COMA	S0	1.213	18.87	10.81	1.188	20.37	1.59:	2.423	0.287
N4807	COMA	S0	0.831	18.12	11.97	0.835	19.65	1.51:	2.328	0.275
I3900	COMA	SB0	0.704	17.60	12.08	0.708	19.40	1.78:	2.432	···
N4816	COMA	S0	1.390	20.17	11.23	1.236	21.00	1.39:	2.365	0.306
E160G22	COMA	U	1.009	19.01	11.97	0.785	19.75	1.55:	2.415	···
E160G23	COMA	U	1.101	20.35	12.85	0.601	19.55	1.00:	2.250	···
E160G27	COMA	E	0.721	18.62	13.02	0.766	20.15	1.37:	2.235	0.282
N4827	COMA	S0	1.094	19.01	11.54	1.010	20.18	1.47:	2.448	···
E160G37	COMA	E	0.588	17.61	12.68	0.599	19.18	1.52:	2.354	0.302
N4839	COMA	E	1.519	20.07	10.48	1.425	21.29	1.56:	2.420	0.313
N4841A	COMA	E	0.834	18.57	12.40	1.170	20.44	0.66:	2.417	0.320
N4840	COMA	E1	0.823	18.22	12.11	0.793	19.59	1.47:	2.377	0.320
D238	COMA	E	0.427	17.66	13.53	0.431	19.33	1.65:	2.026	0.237
N4850	COMA	S0	0.774	18.44	12.58	0.738	19.78	1.47:	2.233	0.269
N4854	COMA	SB0	1.134	19.96	12.30	1.102	21.22	1.37:	2.263	0.311
D181	COMA	S0	0.632	18.53	13.37	0.486	19.69	1.69:	2.161	0.248
I3947	COMA	S0	0.740	18.50	12.81	0.589	19.58	1.62:	2.148	0.279
D136	COMA	E	0.114	16.11	13.54	0.126	18.11	1.95:	2.200	0.279
N4860	COMA	E2	0.885	18.28	11.86	0.895	19.82	1.50:	2.396	0.342
I3955	COMA	SB0	1.048	19.74	12.50	0.831	20.37	1.41:	2.267	0.300
I3957	COMA	S0	0.568	18.11	13.27	0.637	19.84	1.48:	2.179	0.292
I3960	COMA	S0	0.684	18.40	12.98	0.698	19.98	1.53:	2.252	0.336
I3959	COMA	E3	0.663	17.88	12.57	0.769	19.86	1.60:	2.295	0.307
I3963	COMA	S0	1.130	20.27	12.63	0.854	20.73	1.46:	2.120	0.269
N4864	COMA	E2	0.952	18.80	12.05	0.880	20.04	1.50:	2.294	0.286
N4867	COMA	E3	0.664	17.90	12.59	0.553	19.11	1.61:	2.353	0.308
N4865	COMA	S0	0.941	18.20	11.50	0.748	19.26	1.75:	2.379	0.285
N4869	COMA	E3	0.919	18.65	12.06	0.920	20.16	1.50:	2.309	0.316
D106	COMA	S0	0.540	18.33	13.63	0.419	19.40	1.51:	2.210	0.241
D67	COMA	S0	0.530	17.85	13.20	0.437	19.41	1.90:	2.178	0.277
D157	COMA	S0	0.797	19.34	13.36	0.483	19.74	1.53:	2.109	0.251
D132	COMA	S0	0.827	19.73	13.60	0.649	20.60	1.51:	2.113	0.263
D156	COMA	E/S0	0.724	19.52	13.90	0.512	20.28	1.52:	2.019	0.231
N4871	COMA	S0	1.146	19.88	12.16	0.919	20.54	1.48:	2.234	0.281
D176	COMA	S0	0.882	19.08	12.68	0.671	20.01	1.69:	2.216	0.282
N4872	COMA	SB0	0.512	17.38	12.83	0.482	18.84	1.57:	2.330	0.301
N4874	COMA	E0	1.724	20.71	10.10	1.743	22.15	1.37:	2.377	0.323
N4875	COMA	S0	0.626	18.04	12.91	0.508	19.20	1.59:	2.269	0.290
D128	COMA	S0	0.871	19.73	13.38	0.409	19.67	1.61:	2.028	0.250
D153	COMA	E	0.418	17.77	13.68	0.536	19.76	1.56:	2.133	0.280
N4876	COMA	E5	0.915	18.93	12.36	0.689	19.82	1.70:	2.264	0.248
D152	COMA	SB0	1.052	19.88	12.62	0.880	20.75	1.49:	2.190	0.264
D193	COMA	E	0.751	19.26	13.51	0.550	19.92	1.39:	2.083	0.264
N4883	COMA	S0	0.945	19.13	12.41	0.785	20.03	1.48:	2.232	0.289
N4881	COMA	E	0.956	18.93	12.15	1.022	20.49	1.32:	2.311	0.292
N4886	COMA	E0	0.964	19.41	12.60	0.874	20.34	1.25:	2.194	0.252

Table A.20—*Continued*

Name	Cluster/ Group	Type	I_C–band			V–band				
			$\log r_{\rm eff}$ ($''$)	$\langle\mu\rangle_{\rm eff}$ (mag/$''$)	$r_{\rm tot}$ (mag)	$\log r_{\rm eff}$ ($''$)	$\langle\mu\rangle_{\rm eff}$ (mag/$''$)	$V-I_C$ (mag)	$\log\sigma_0$ (km s^{-1})	Mg_2 (mag)
(1)	(2)	(3)	(4)	(5)	(6)	(7)	(8)	(9)	(10)	(11)
D65	COMA	S0	1.183	20.53	12.62	0.798	20.85	1.71:	2.070	0.252
I4011	COMA	E	0.750	19.12	13.38	0.624	20.03	1.36:	2.040	0.280
N4889	COMA	E4	1.553	19.47	9.71	1.484	20.85	1.63:	2.606	0.351
I4012	COMA	E	0.417	17.02	12.94	0.363	18.56	1.73:	2.259	0.292
D207	COMA	E	0.862	19.18	12.88	0.620	19.92	1.61:	2.174	0.266
D173	COMA	S0	0.629	18.39	13.25	0.527	19.68	1.66:	2.147	0.287
N4895	COMA	S0	1.387	19.58	10.65	1.028	20.12	1.83:	2.337	0.292
I4026	COMA	SB0	0.906	19.39	12.86	0.888	20.77	1.44:	2.155	0.289
D27	COMA	E	0.773	19.33	13.47	0.674	20.44	1.46:	2.009	0.260
D119	COMA	S0	0.726	19.11	13.48	0.514	19.73	1.38:	2.195	0.280
D146	COMA	SB0/a	1.303	20.94	12.43	1.083	21.73	1.58:	2.030	0.246
N4906	COMA	E3	0.856	18.81	12.54	0.831	20.19	1.47:	2.229	0.295
I4041	COMA	S0	1.100	19.97	12.48	0.844	20.76	1.71:	2.111	0.283
D116	COMA	SB0	0.838	19.30	13.12	0.838	20.81	1.51:	2.123	0.247
I4045	COMA	E4	0.865	18.31	11.99	0.660	19.25	1.68:	2.331	0.306
N4908	COMA	S0/E	0.920	18.51	11.92	0.867	19.93	1.61:	2.314	0.265
I4051	COMA	E0	1.321	20.13	11.53	1.272	21.42	1.46:	2.355	0.332
E160G92	COMA	E	0.814	19.50	13.43	0.810	20.90	1.41:	2.182	0.266
D204	COMA	E	0.699	18.84	13.35	0.766	20.58	1.50:	2.109	0.269
N4923	COMA	S0	0.792	18.18	12.23	0.865	19.93	1.48:	2.288	0.307
I0843	COMA	S0	1.198	19.18	11.20	0.978	20.34	1.95:	2.392	...
E160G100	COMA	E	0.524	17.86	13.25	0.651	19.80	1.48:	2.269	0.285

Table A.21: Comparisons of I_C–band Quantities from Scodeggio *et al.* (1997) and r–band Quantities from Jørgensen *et al.* (1995a)

Name	Cluster/ Group	Type	I_C–band			r–band				
			$\log r_{\rm eff}$ ($''$)	$\langle\mu\rangle_{\rm eff}$ (mag/$''$)	$r_{\rm tot}$ (mag)	$\log r_{\rm eff}$ ($''$)	$\langle\mu\rangle_{\rm eff}$ (mag/$''$)	$r - I_C$ (mag)	$\log\sigma_0$ (km s^{-1})	Mg_2 (mag)
(1)	(2)	(3)	(4)	(5)	(6)	(7)	(8)	(9)	(10)	(11)
E160G37	COMA	E	0.588	17.61	12.68	0.630	19.06	1.30:	2.354	0.302
N4839	COMA	E	1.519	20.07	10.48	1.470	21.18	1.29:	2.420	0.313
N4841A	COMA	E	0.834	18.57	12.40	1.250	20.39	0.32:	2.417	0.320
N4840	COMA	E1	0.823	18.22	12.11	0.810	19.35	1.18:	2.377	0.320
N4841B	COMA	E	1.199	19.18	11.19	0.930	19.88	1.67:	2.355	0.295
D238	COMA	E	0.427	17.66	13.53	0.400	18.94	1.38:	2.026	0.237
N4850	COMA	S0	0.774	18.44	12.58	0.670	19.07	1.01:	2.233	0.269
N4854	COMA	SB0	1.134	19.96	12.30	1.150	21.13	1.11:	2.263	0.311
D181	COMA	S0	0.632	18.53	13.37	0.510	19.45	1.36:	2.161	0.248
I3947	COMA	S0	0.740	18.50	12.81	0.520	19.00	1.29:	2.148	0.279
N4860	COMA	E2	0.885	18.28	11.86	0.930	19.64	1.20:	2.396	0.342
I3955	COMA	SB0	1.048	19.74	12.50	0.910	20.36	1.12:	2.267	0.300
I3957	COMA	S0	0.568	18.11	13.27	0.630	19.51	1.18:	2.179	0.292
I3960	COMA	S0	0.684	18.40	12.98	0.730	19.77	1.20:	2.252	0.336
I3959	COMA	E3	0.663	17.88	12.57	0.730	19.42	1.30:	2.295	0.307
I3963	COMA	S0	1.130	20.27	12.63	0.890	20.58	1.18:	2.120	0.269
N4864	COMA	E2	0.952	18.80	12.05	0.890	19.78	1.20:	2.294	0.286
N4867	COMA	E3	0.664	17.90	12.59	0.490	18.53	1.26:	2.353	0.308
N4865	COMA	S0	0.941	18.20	11.50	0.710	18.77	1.40:	2.379	0.285
N4869	COMA	E3	0.919	18.65	12.06	0.880	19.74	1.23:	2.309	0.316
D106	COMA	S0	0.540	18.33	13.63	0.390	18.99	1.20:	2.210	0.241
D67	COMA	S0	0.530	17.85	13.20	0.380	18.81	1.50:	2.178	0.277
D157	COMA	S0	0.797	19.34	13.36	0.490	19.48	1.25:	2.109	0.251
N4871	COMA	S0	1.146	19.88	12.16	0.920	20.24	1.17:	2.234	0.281
I3973	COMA	S0/a	0.577	17.54	12.66	0.640	19.06	1.29:	2.338	0.306
D176	COMA	S0	0.882	19.08	12.68	0.490	18.98	1.32:	2.216	0.282
N4873	COMA	S0	1.136	19.96	12.29	0.870	20.09	1.09:	2.194	0.290
N4872	COMA	SB0	0.512	17.38	12.83	0.480	18.53	1.27:	2.330	0.301
N4874	COMA	E0	1.724	20.71	10.10	1.850	22.13	0.96:	2.377	0.323
N4875	COMA	S0	0.626	18.04	12.91	0.520	18.96	1.30:	2.269	0.290
D128	COMA	S0	0.871	19.73	13.38	0.400	19.30	1.27:	2.028	0.250
N4876	COMA	E5	0.915	18.93	12.36	0.710	19.47	1.28:	2.262	0.248
N4881	COMA	E	0.956	18.93	12.15	1.040	20.24	1.01:	2.311	0.292
N4886	COMA	E0	0.964	19.41	12.60	0.970	20.38	0.95:	2.194	0.252
D65	COMA	S0	1.183	20.53	12.62	0.820	20.55	1.33:	2.070	0.252
I4011	COMA	E	0.750	19.12	13.38	0.690	19.98	1.08:	2.040	0.280
N4889	COMA	E4	1.553	19.47	9.71	1.530	20.64	1.25:	2.606	0.351
I4012	COMA	E	0.417	17.02	12.94	0.330	18.23	1.52:	2.259	0.292
D173	COMA	S0	0.629	18.39	13.25	0.530	19.52	1.49:	2.147	0.287
N4894	COMA	S0	1.150	20.38	12.63	0.680	19.93	1.25:	1.976	0.233
N4895	COMA	S0	1.387	19.58	10.65	1.000	19.86	1.68:	2.337	0.292
I4026	COMA	SB0	0.906	19.39	12.86	0.860	20.38	1.16:	2.155	0.289
D119	COMA	S0	0.726	19.11	13.48	0.620	19.87	1.14:	2.195	0.280
D146	COMA	SB0	1.303	20.94	12.43	1.050	21.31	1.28:	2.030	0.246
N4906	COMA	E3	0.856	18.81	12.54	0.870	20.09	1.23:	2.229	0.295
I4041	COMA	S0	1.100	19.97	12.48	0.870	20.52	1.38:	2.111	0.283
I4042	COMA	S0/a	0.783	18.45	12.54	0.860	19.96	1.23:	2.229	0.281
D116	COMA	SB0	0.838	19.30	13.12	0.850	20.62	1.28:	2.123	0.247
D191	COMA	S0	1.192	20.54	12.58	0.360	18.95	1.41:	1.966	0.254

Table A.21—*Continued*

Name	Cluster/ Group	Type	I_C–band			r–band				
			$\log r_{\rm eff}$ ($''$)	$\langle\mu\rangle_{\rm eff}$ (mag/$''$)	$r_{\rm tot}$ (mag)	$\log r_{\rm eff}$ ($''$)	$\langle\mu\rangle_{\rm eff}$ (mag/$''$)	$r - I_C$ (mag)	$\log \sigma_0$ (km s^{-1})	Mg_2 (mag)
(1)	(2)	(3)	(4)	(5)	(6)	(7)	(8)	(9)	(10)	(11)
I4045	COMA	E4	0.865	18.31	11.99	0.640	18.79	1.29:	2.331	0.306
N4908	COMA	S0/E	0.920	18.51	11.92	0.850	19.60	1.34:	2.314	0.265
I4051	COMA	E0	1.321	20.13	11.53	1.260	21.02	1.11:	2.355	0.332
N4919	COMA	S0	0.970	18.77	11.93	0.760	19.30	1.29:	2.219	...
D204	COMA	E	0.699	18.84	13.35	0.780	20.42	1.29:	2.109	0.269
N4923	COMA	S0	0.792	18.18	12.23	0.930	19.88	1.20:	2.288	0.307